IKM 2012

Weimar, July 04 - 06

19th International Conference on the Applications of Computer Science and Mathematics in Architecture and Civil Engineering

digital PROCEEDINGS

Proceedings of the 19th International Conference on the Applications of Computer Science and Mathematics in Architecture and Civil Engineering

Weimar, July 04-06, 2012

ISSN 1611-4086

Editors: K. Gürlebeck, T. Lahmer, F. Werner

Contents

19th International Conference on the Application of Computer
Science and Mathematics in Architecture and Civil Engineering
K. Gürlebeck, T. Lahmer and F. Werner (eds.)
Weimar, Germany, 04–06 July 2012

MODEL COMBINATIONS FOR ASSESSING THE FLUTTER STABILITY OF SUSPENSION BRIDGES

Tajammal Abbas*, **Guido Morgenthal**

**Research Training Group, Graduate College 1462, Department of Civil Engineering,*
Bauhaus University Weimar
Berkaer Strae 9, 99423 Weimar, Germany
E-mail: tajammal.abbas@uni-weimar.de, Fax: +49 3643 58 4101

Keywords: Coupling, suspension bridge, flutter, CFD, aerodynamic derivatives

Abstract. *Long-span cable supported bridges are prone to aerodynamic instabilities caused by wind and this phenomenon is usually a major design criterion. If the wind speed exceeds the critical flutter speed of the bridge, this constitutes an Ultimate Limit State. The prediction of the flutter boundary therefore requires accurate and robust models. This paper aims at studying various combinations of models to predict the flutter phenomenon.*

Since flutter is a coupling of aerodynamic forcing with a structural dynamics problem, different types and classes of models can be combined to study the interaction. Here, both numerical approaches and analytical models are utilised and coupled in different ways to assess the prediction quality of the hybrid model. Models for aerodynamic forces employed are the analytical Theodorsen expressions for the motion-induced aerodynamic forces of a flat plate and Scanlan derivatives as a Meta model. Further, Computational Fluid Dynamics (CFD) simulations using the Vortex Particle Method (VPM) were used to cover numerical models.

The structural representations were dimensionally reduced to two degree of freedom section models calibrated from global models as well as a fully three-dimensional Finite Element (FE) model. A two degree of freedom system was analysed analytically as well as numerically. Generally, all models were able to predict the flutter phenomenon and relatively close agreement was found for the particular bridge. In conclusion, the model choice for a given practical analysis scenario will be discussed in the context of the analysis findings.

1 INTRODUCTION

Long-span bridges are highly flexible, light weight and have low structural damping. They can be subjected to large dynamic motion due to wind actions. The assessment of aerodynamic behaviour, therefore, plays very important role in the design of long-span bridges. For this reason, flutter is also viewed as an essential aeroelastic phenomenon to be studied for these structures. The aeroelastic stability of long-span bridges against flutter is checked by calculating a wind speed at which flutter occurs which is known as the flutter limit. The required aeroelastic properties of the bridge deck section are usually determined in wind tunnel tests.

Scanlan introduced mathematical treatment of flutter in 1960s whereas for the last couple of decades, numerical methods are becoming more popular due to the increasing use of computers in the field of Structural Engineering. In this paper, the study is made on the aerodynamic phenomena, the methods available for flutter analysis for bridges, and to apply the analytical and numerical based analysis on the Lillebælt suspension bridge to calculate ultimately its flutter limit.

2 METHODS OF AERODYNAMIC ANALYSIS

Analytical approaches play very important role in Wind Engineering whereas numerical methods are gaining more importance. All methods apply simplifications to a certain extent such as assuming two-dimensionality of the flow or the shedding process like the wake oscillator model for the case of vortex induced vibration [**?**]. There are three main types of analysis to deal with the aerodynamic problems:

- Experimental methods
- Analytical methods
- Numerical methods

The last two methods have been used in this study. Analytical solution based on potential flow theory for the motion induced forces on a flat plate exerting sinusoidal heave and pitch motion was given by Theodorsen [**?**]. In most cases, the empirical models are available which are based on the results of experimental studies. These models are mostly for 2D situations but in reality the 3D effects are present. Also in analytical models, the basic physical causes are attended but the Fluid-structure Interaction is not addressed. The experimental methods are considered relatively accurate compared to the other methods. Wind tunnel testing and full scale models are the examples of experimental methods.

The wind tunnel testing is very expensive for parametric studies but the numerical approach makes it relatively cheaper. With the advancement in the computer modelling and the processing power and by using the principles of CFD, it is now possible to study wind effects on structures in relatively less time. These methods are also efficient, repeatable and economical. Numerical simulations can be used in place of wind tunnel investigation for the fundamental studies. The accuracy of results from these methods not only depends on the quality of the solver but also on the modelling itself. Therefore, the numerical method must be reliable and robust to be used in place of wind tunnel tests.

3 REFERENCE OBJECT

The Lillebælt suspension bridge, Denmark, has been used as a reference object to employ the various model combinations. The data about the bridge is available in [**?**] and the structural parameters used for this reference object are given in Table **??**. For simplicity in the calculation, the railing and other attachments on the deck are not considered in this study.

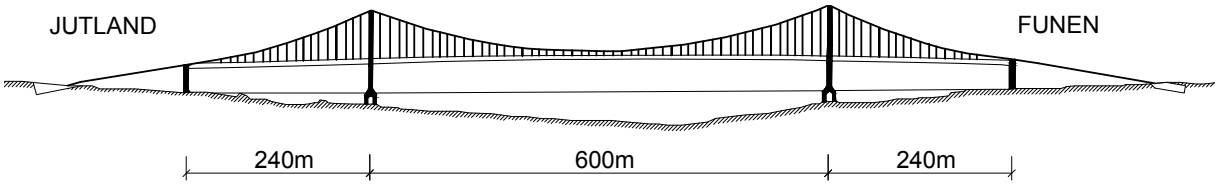

Figure 1: Elevation of the Lillebælt suspension bridge, Denmark used as a reference object in this study.

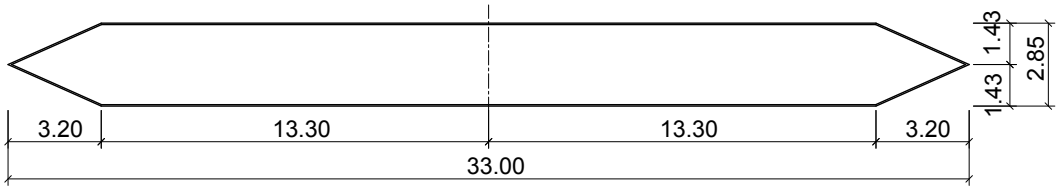

Figure 2: Simplified Lillebælt suspension bridge deck section geometry used in this study (Dimensions: [m]).

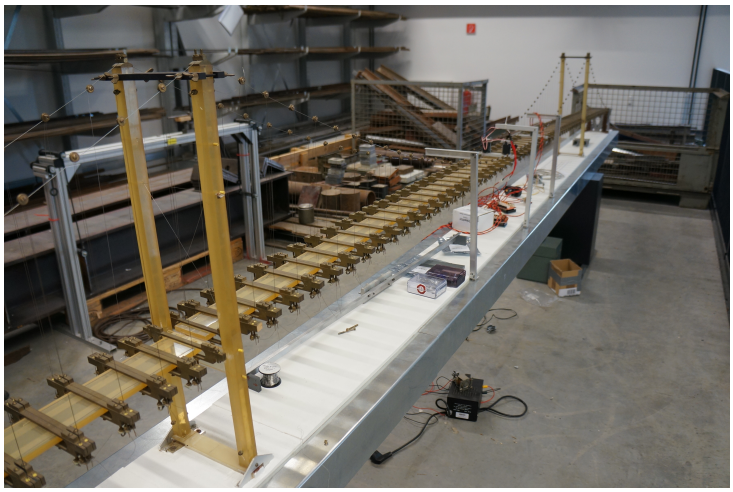

Figure 3: Physical model of the Lillebælt suspension bridge.

Table 1: Basic data and structural properties of the Lillebælt suspension bridge section used in this study.

Section width B [m]	Mass m [kg/m]	Inertial mass I [kgm^2/m]	Bending Frequency f_h [Hz]	Torsional Frequency f_α [Hz]	Damping ratio ξ [-]
33	11667	1017778	0.156	0.500	0.01

4 COUPLING OF MODELS

Flutter is a coupling of aerodynamic forcing with a structural dynamics problem. Therefore, different types and classes of models can be combined to study the interaction. In this study, both numerical approaches and analytical models are utilised and coupled in different ways to assess the prediction quality of the hybrid model.

The structural representations were dimensionally reduced to two degree of freedom section models calibrated from global models as well as a fully three-dimensional Finite Element (FE) model. A two degree of freedom system was analysed analytically as well as numerically. The following models were thus derived and analysed: Fully analytical, CFD Derivatives-Analytical and Numerical 2D Structural, CFD Derivatives-Numerical 3D Structural, Fully coupled CFD Numerical 2D Structural. This has allowed to investigate a very broad range of model combinations and to study their merits and drawbacks.

Table 2: Model coupling for the flutter analysis used in this study.

Structural \ Aerodynamic			Analytical		Numerical	
			Flat Plate		Flat Plate	Lillebælt Section
Analytical		2D	o	•	•	•
Numerical	VPM (CFD)	2D	-		o	o
	FE Software	2D	-		•	•
		3D	-		•	•

o Simple/ Regular model • Meta model

4.1 Analytical Approach (Theodorsen Theory)

Theodorsen investigated the flutter phenomenon for aircraft wings and gave a very popular approach for the flutter analysis. This approach is independent of the shape of the body but on the other hand it neglects the effect originating from the simplification to the flat plate. From the basic principle of potential flow theory, Theodorsen showed that for thin airfoils in incompressible flow, the expressions for lift F_L and moment F_M are linear in displacement h and rotation α and their first and second derivatives [**?**].

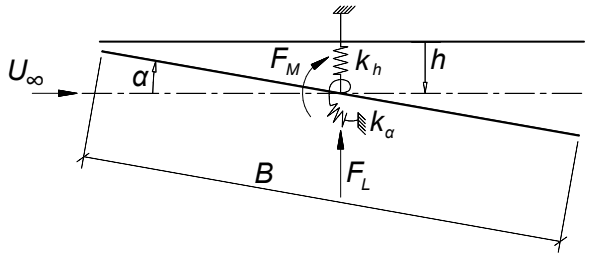

Figure 4: Definition of degrees of freedom (heave h and pitch α) for flutter analysis.

where F_L and F_M are the lift and moment, k_h and k_α are the vertical and rotational spring stiffness and h and α are the vertical displacement and rotation respectively. U_∞ is the oncoming

wind speed. The equations of motion can be written as

$$F_L = m\ddot{h} + 2m\xi_h\omega_h\dot{h} + m\omega_h^2 h \tag{1}$$

$$F_M = I\ddot{\alpha} + 2I\xi_\alpha\omega_\alpha\dot{\alpha} + I\omega_\alpha^2\alpha \tag{2}$$

where ω_h and ω_α are the natural circular frequencies in heave and pitch degree of freedom respectively. The theoretical expressions on a flat plate airfoil for sinusoidal oscillating lift F_L and moment F_M are

$$F_L = -\rho b^2 U_\infty \pi\dot{\alpha} - \rho b^2\pi\ddot{h} - 2\pi\rho C U_\infty^2 b\alpha - 2\pi\rho C U_\infty b\dot{h} - 2\pi\rho C U_\infty b^2\frac{1}{2}\dot{\alpha} \tag{3}$$

$$F_M = -\rho b^2\pi\frac{1}{2}U_\infty b\dot{\alpha} - \rho b^4\pi\frac{1}{8}\ddot{\alpha} + 2\rho U_\infty b^2\pi\frac{1}{2}CU_\infty\alpha + 2\rho U_\infty b^2\pi C\dot{h} + 2\rho\frac{1}{2}U_\infty b^3\pi C\dot{\alpha} \tag{4}$$

where ρ is the air density, $C(k)$ is the Theodorsens circulation function and $b = B/2$. The system of differential equations (1), (2), (3) and (4) can be written as

$$\begin{bmatrix} \dot{h} \\ \ddot{h} \\ \dot{\alpha} \\ \ddot{\alpha} \end{bmatrix} = \begin{bmatrix} 0 & 1 & 0 & 0 \\ a_{21} & a_{22} & a_{23} & a_{24} \\ 0 & 0 & 0 & 1 \\ a_{41} & a_{42} & a_{43} & a_{44} \end{bmatrix} \begin{bmatrix} h \\ \dot{h} \\ \alpha \\ \dot{\alpha} \end{bmatrix} \tag{5}$$

This is of the form

$$\dot{X} = AX \tag{6}$$

and assuming the response X is of the form

$$X = \boldsymbol{R}e^{\lambda t} \tag{7}$$

where $\boldsymbol{R}$ is real. This simplifies to Eigenvalue problem as follows:

$$\left[\boldsymbol{A} - \lambda\boldsymbol{I}\right]\boldsymbol{R}e^{\lambda t} = 0 \tag{8}$$

The solution for $h(t)$ and $\alpha(t)$ is of an exponential form. The Eigenvalues of λ_i of the matrix $\boldsymbol{A}$ characterize the response of the system as follows:

- Positive real part: Increasing response
- Negative real part: Decaying response
- Imaginary part: Oscillating response

The system will become unstable when an Eigenvalue has a positive real part. When the imaginary part goes towards zero, the oscillatory part vanishes and the phenomenon of static divergence is observed. In this situation, there will be pure heave or pitch motion which can be interpreted as loss of vertical stiffness. The system is solved successively for increasing U_∞ until at least one Eigenvalue becomes positive real. The code for solving the Theodorsens equations was written in Matlab. Using the structural parameters for the Lillebælt bridge (see Table **??**), the flutter limit was found 93.8m/s.

4.2 Meta Model (Scanlan Approach)

Scanlan proposed a set of expressions for the aerodynamic forces on a bridge cross section. It assumes that the self-excited lift F_L and moment F_M for a bluff body may be treated as linear in displacement h and rotation α and their first derivatives [**?**]. Below is commonly used linearised form.

$$F_L = \frac{1}{2}\rho U_\infty^2 B \left[K H_1^* \frac{\dot{h}}{U_\infty} + K H_2^* \frac{B\dot{\alpha}}{U_\infty} + K^2 H_3^* \alpha + K^2 H_4^* \frac{h}{B} \right] \tag{9}$$

$$F_M = \frac{1}{2}\rho U_\infty^2 B^2 \left[K A_1^* \frac{\dot{h}}{U_\infty} + K A_2^* \frac{B\dot{\alpha}}{U_\infty} + K^2 A_3^* \alpha + K^2 A_4^* \frac{h}{B} \right] \tag{10}$$

$$K = \frac{B\omega}{U_\infty} \tag{11}$$

where the non-dimensional coefficients H_i^* and A_i^* are known as aerodynamic or flutter derivatives. The frequency of the bridge oscillation under aerodynamic forcing is known as reduced frequency. As the aerodynamic derivatives are the function of this frequency therefore they can only be measured when the bridge is in the oscillatory state. Normally these are measured in special wind tunnel tests.

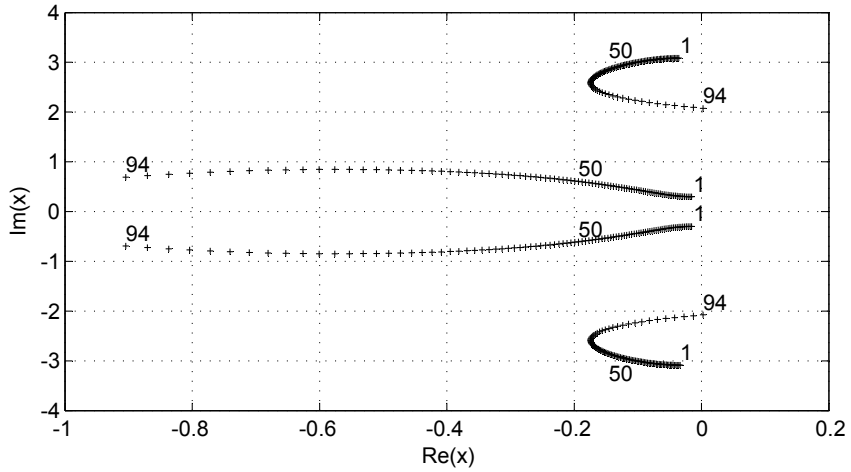

Figure 5: Eigenvalue paths for increasing wind speed U_∞.

The formulation to the Eigenvalue problem in this case is similar as described in Section **??**. The flutter limit is determined when the real part of at least one Eigenvalue becomes positive as shown in Figure **??**. The flutter limit was determined as 93.8m/s using the structural parameters of the Lillebælt bridge given in Table **??**.

4.3 Forced Vibration Simulation

Forced vibration simulations are used to determine motion-induced forces. The resulting lift and moment time histories are used to compute the aerodynamic derivatives. A computer code, VXFlow, based on VPM has been used here to compute these derivatives. Forced vibration simulations were performed on the Lillebælt section and the flat plate (aspect ratio 1:100) in

sinusoidal heave and pitch motion over a range of reduced frequencies. The reduced frequency is controlled by changing the period of heave and pitch forcing motion.

$$v_r = \frac{2\pi U_\infty}{b\omega} \tag{12}$$

where v_r is reduced frequency. These simulations are performed in heave and pitch motion separately and the aerodynamic derivatives are computed from the resulting force time histories. The simulation gives time histories for $\bar{\boldsymbol{F}}_L$ and $\bar{\boldsymbol{F}}_M$ corresponding to known displacement traces $\boldsymbol{h}$. Equations (9) and (10) (with α=0) thus constitutes a system of equations as

$$\bar{\boldsymbol{F}}_L = \boldsymbol{C}_h^L \boldsymbol{H}_h^* \tag{13}$$

$$\bar{\boldsymbol{F}}_M = \boldsymbol{C}_h^M \boldsymbol{A}_h^* \tag{14}$$

where

$$\boldsymbol{C}_h^L = \frac{1}{2}\rho U_\infty^2 BK \begin{bmatrix} \frac{\dot{\boldsymbol{h}}}{U_\infty} & K\frac{\boldsymbol{h}}{B} \end{bmatrix} \tag{15}$$

and

$$\boldsymbol{C}_h^M = B\boldsymbol{C}_h^L \tag{16}$$

$$\boldsymbol{H}_h^* = \begin{bmatrix} H_1^* \\ H_4^* \end{bmatrix}, \boldsymbol{A}_h^* = \begin{bmatrix} A_1^* \\ A_4^* \end{bmatrix} \tag{17}$$

System (13) and (14) can be solved in the least-squares sense by left-multiplying with the $\boldsymbol{C}$ matrix:

$$\boldsymbol{C}_h^{L^T} \bar{\boldsymbol{F}}_L = \boldsymbol{C}_h^{L^T} \boldsymbol{C}_h^L \boldsymbol{H}_h^* \tag{18}$$

$$\boldsymbol{C}_h^{M^T} \bar{\boldsymbol{F}}_M = \boldsymbol{C}_h^{M^T} \boldsymbol{C}_h^M \boldsymbol{A}_h^* \tag{19}$$

This gives two sets of derivatives in lease-square sense. The procedure to calculate these aerodynamic derivatives can be found in [**?**] and is summarized as follows:

• perform forced vibration tests in either heave or pitch motion

• calculate a best-fit harmonic of the same forcing frequency to obtain lift coefficient and phase shift

• calculate derivatives

The resulting aerodynamic derivatives can be used to calculate flutter limit of the bridge. The forced vibration simulation was performed for the Lillebælt section shown in Figure **??** and the flat plate of the same width (with aspect ratio of 100). For both these cases, structural parameters given in Table **??** were used. The flutter limit for the Lillebælt section was calculated as 94.2m/s and for flat plate as 88.7m/s.

4.4 Fluid-structure Interaction Simulation

VXFlow has been used here for the coupled analysis of the vertical motion and rotation of a two-degree of freedom spring supported section model. The coupling of fluid dynamics solution and the structural dynamics is done at every time step. The pressure on the surface of the body is integrated to get the resultant force in terms of lift and twisting moment. These are associated with the two degrees of freedom of the structural system. The equations of motion for the system are solved by time marching structural dynamics solution. A stiffness matrix is

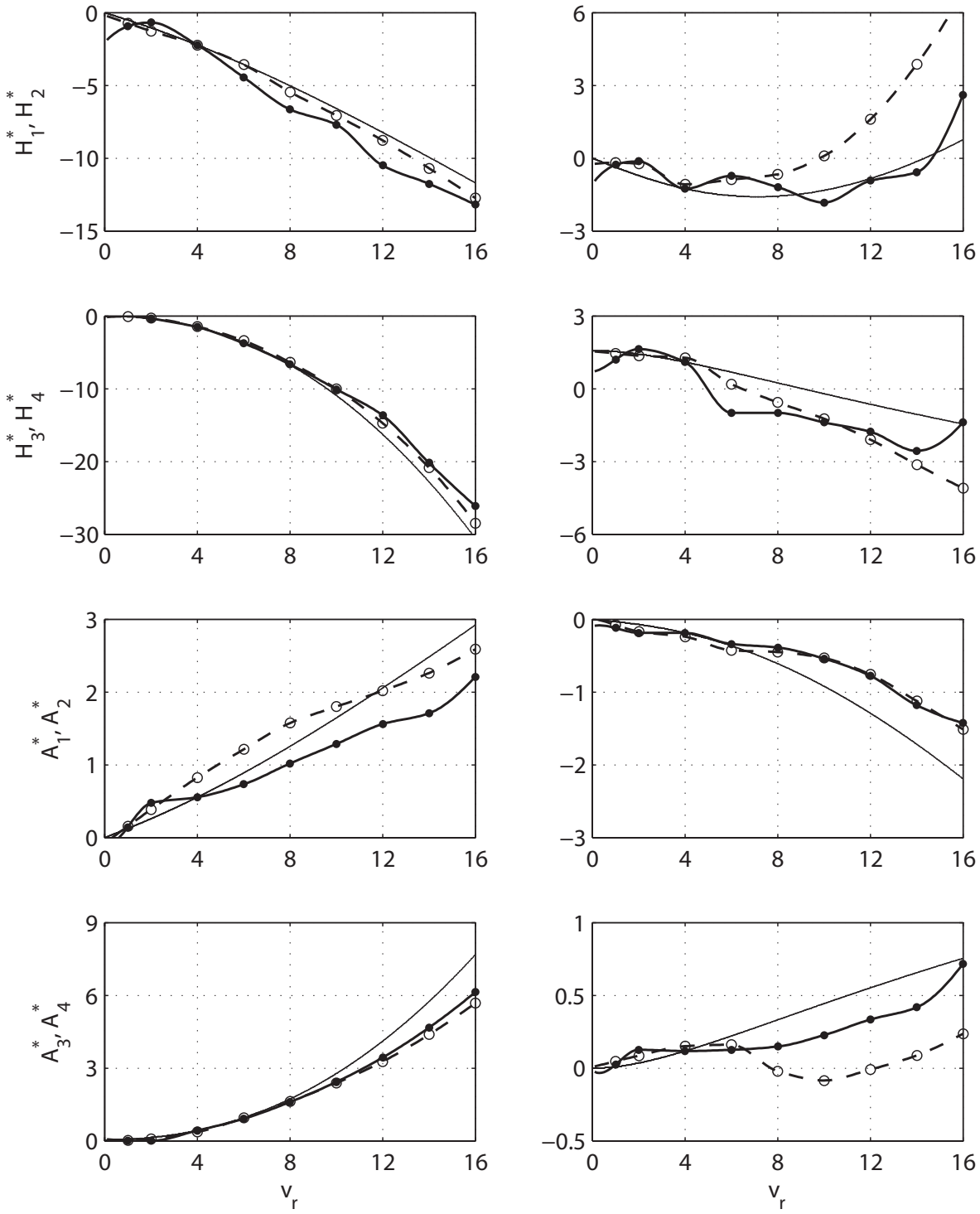

Figure 6: Aerodynamic derivatives (H_i^* and A_i^* where i =1, 2, 3, 4) w.r.t. the reduced speed (v_r): flat plate by Theodorsen theory (——), interpolated values from forced vibration analysis on the Lillebælt section (—•—) and the flat plate (- -○- -).

then created and solution is performed. Rayleigh damping is used to model structural damping, for which the damping matrix is proportional to the combination of mass and stiffness matrices.

Structural parameters, given in Table **??** for the Lillebælt suspension bridge, were used for the bridge section (see Figure **??**) and the flat plate of aspect ratio 100. The simulations were performed at various wind speed to identify the flutter instability. It was observed that just before the flutter limit, the section goes into the loss of vertical stiffness stage having extreme heave condition. At 95m/s the bridge section becomes unstable after a few hundred time steps. The flutter limit for the plate section was found as 98m/s.

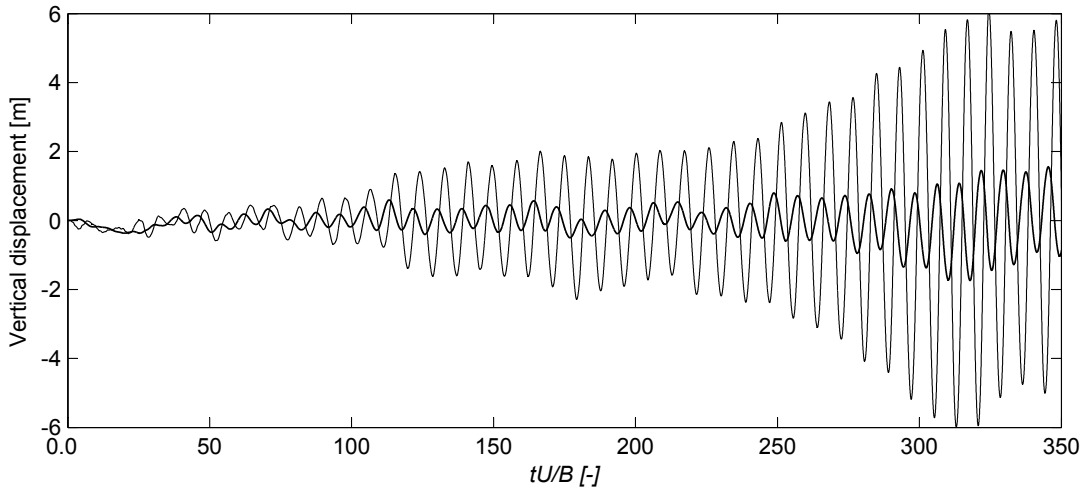

Figure 7: Lillebælt section in Fluid-structure Interaction, displacement time histories at U_∞= 95m/s: leading edge (——), trailing edge (——).

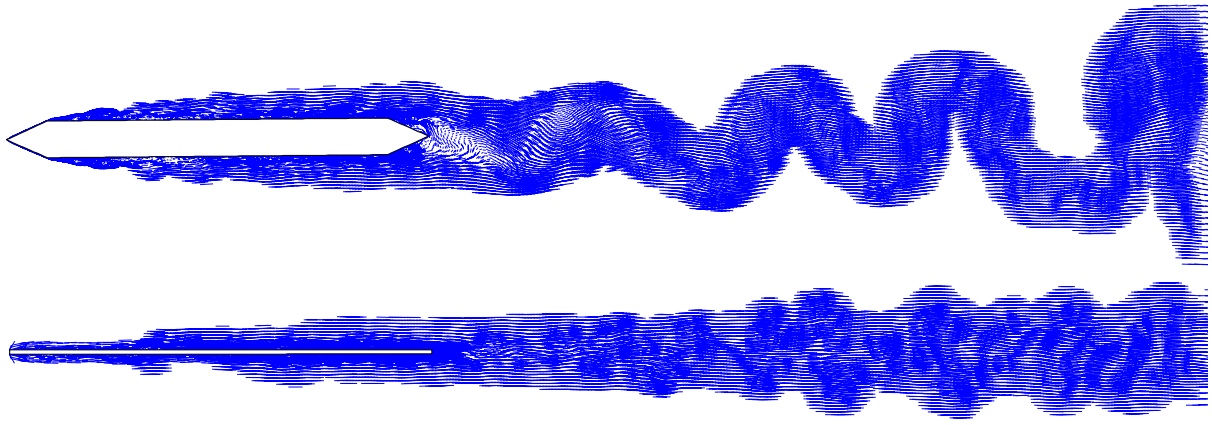

Figure 8: Instantaneous vortex pattern with streak lines for the Lillebælt section (Top) and the flat plate (Bottom).

4.5 Finite Element Model

The section of the Lillebælt suspension bridge deck was modelled as a two degree of freedom beam element of unit length in a Finite Element software. The system was supported on springs with vertical and rotational degrees of freedom. The reduced model was calibrated to represent

the first bending and first torsional mode of the full bridge model. The dimensional reduction to a two-degree of freedom system is a simplification but on the other hand it neglects the effects coming from the higher modes. The aerodynamic derivatives obtained through forced vibration analysis (see Section **??**), for the Lillebælt section and the flat plate, were used to calculate the aerodynamic forces. Dynamic wind history analysis was performed on the system. The flutter limit both for the Lillebælt section and the flat plate was found to be 58.5m/s.

A 3D Finite Element model of the Lillebælt suspension bridge was made and calibrated to represent the structural properties of the bridge given in Table **??**. In the calibration process some discrepancies were found and the target frequencies were not achieved exactly. The mode shapes of first bending and first torsional mode with their achieved frequencies are shown in Figure **??**. The approach from the two degree of freedom model was implemented to the full 3D model of the bridge and the resulting flutter limits were calculated. The effect of higher modes was observed in the deformed model of the bridge at flutter limit. The flutter limit calculated was 49.0m/s both for the Lillebælt section and the flat plate.

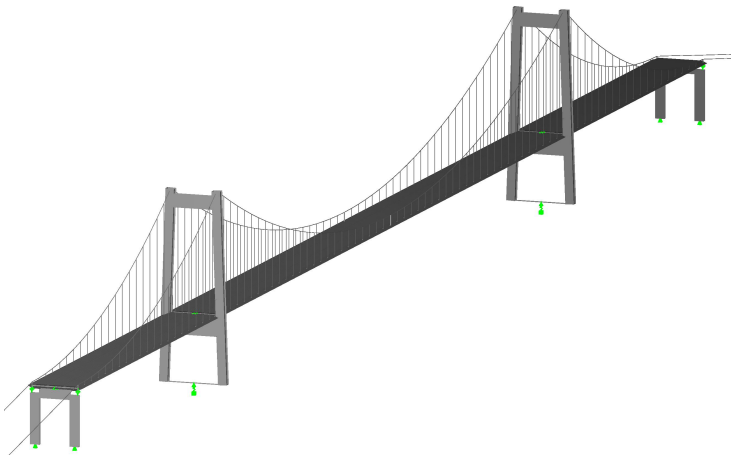

Figure 9: View of full 3D Finite Element bridge model.

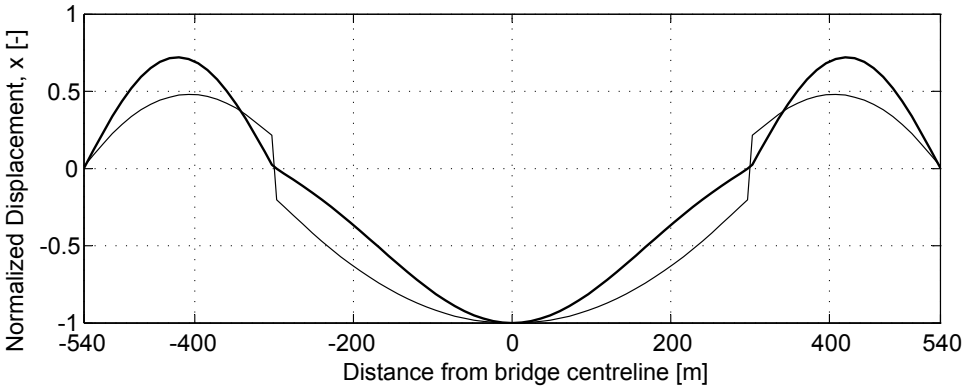

Figure 10: First bending mode (——) (achieved frequency = 0.151 Hz) and first torsional mode (——) (achieved frequency = 0.502 Hz) of full 3D Finite Element bridge model.

5 CONCLUSIONS

The flutter phenomenon was studied employing various combinations of analytical and numerical prediction models. Lillebælt suspension bridge was used as a study object. Generally, all models were able to predict the flutter phenomenon and relatively close agreement was found for the particular bridge. Fully coupled CFD analyses have the advantage that no prior knowledge as to the phenomenon needs to be inserted into the model. Three-dimensional structural representations are superior over dimensionally reduced models in that no prior knowledge as to the modes participating in the flutter coupling is required. Fully analytical models are more direct models and allow a better insight into the force coupling. Simplified aerodynamic models need to be critically assessed with respect to their ability to predict the aerodynamic behaviour of the real cross section. The summary of the results is preseneted in Table **??**.

Table 3: Summary of flutter limits from different model coupling (see Table **??**).

Structural \ Aerodynamic			Analytical		Numerical	
			Flat Plate		Flat Plate	Lillebælt Section
Analytical		2D	93.8	93.8	88.7	94.2
Numerical	VPM (CFD)	2D	-		98.0	95.0
	FE Software	2D	-		58.5	58.5
		3D	-		49.0	49.0

ACKNOWLEDGMENT

This research is supported by the German Research Institute (DFG) via Research Training Group "Evaluation of Coupled Numerical Partial Models in Structural Engineering (GRK 1462)", which is gratefully acknowledged by the authors.

REFERENCES

[1] G. Morgenthal, *Comparison of Numerical Methods for Bridge-Deck Aerodynamics*, MPhil Thesis, 2000.

[2] T. Theodorsen, *General theory of aerodynamic instability and the mechanism of flutter*, TR 496, NACA, 1935.

[3] Chr. Ostenfeld, A. G. Frandsen, J. J. Jessen and G. Hass, *Motorway Bridge Across Lillebælt, Publication III: Design and Construction of the Bridge*, Report, 1970.

[4] R. H. Scanlan and J. J. Tomko, *Airfoil and bridge deck flutter derivatives*, ASCE J. of Eng. Mech. 97 (1971), 17171737.

[5] G. Morgenthal, *Aerodynamic Analysis of Structures Using High-resolution Vortex Particle Methods*, PhD Thesis, 2002.

19th International Conference on the Application of Computer
Science and Mathematics in Architecture and Civil Engineering
K. Gürlebeck and C. Könke (eds.)
Weimar, Germany, 04–06 July 2012

WAVELET-BASED INDICATORS FOR RESPONSE SURFACE MODELS IN DAMAGE IDENTIFICATION OF STRUCTURES

S. Ahmad*, **V. Zabel*** **and C. Könke***

**Institute of Structural Mechanics, Bauhaus University Weimar*
address
E-mail: sofyan.ahmad@uni-weimar.de

Keywords: Damage detection, Structural health monitoring, Response surface methodology

Abstract. *In this paper, wavelet energy damage indicator is used in response surface methodology to identify the damage in simulated filler beam railway bridge. The approximate model is addressed to include the operational and surrounding condition in the assessment. The procedure is split into two stages, the training and detecting phase. During training phase, a so-called response surface is built from training data using polynomial regression and radial basis function approximation approaches. The response surface is used to detect the damage in structure during detection phase. The results show that the response surface model is able to detect moderate damage in one of bridge supports while the temperatures and train velocities are varied.*

1 INTRODUCTION

Damage in civil engineering structures can be defined by changes of structural properties that lead to degradation of performance. A robust approach to identify structural damages is by analyzing the vibration responses. The degradation of material or structural properties lead to change in dynamics properties. However, changes in dynamics properties could be the outcomes of environmental condition changes. The structural health monitoring (SHM) systems will not be accepted in practical applications unless robust techniques are developed to explicitly account for environmental and operational conditions, [7].

Response surface methodology (RSM) approach seems able to take into account all damaged and environmental or operational factors that has significant effects on dynamics response of structure. However, the capability of meta models to identify damage is also depend on damage indicator. Low sensitivity damage indicator causes identification procedures more difficult. The difference between damage and non-damage response is too small and can be hidden by noise, model error, or minor parameters that are not included in the models.

Wavelet transform is well known powerful tool in signal analysis. Wavelet reveals hidden information in signals. Instead of wavelet package and wavelet entropy that have been suggested by many researcher e.g. [6, 8, 9], total wavelet energy can be an alternative indicators. The alteration of dynamics response signals due to damage is indicated by the change of energy distribution over frequency sub bands.

In this paper, the response surface methodology was applied to numerical simulated train passage over a filler beam railway bridge. The dynamic response was computed using Newmark method while the damping matrix was constructed using Rayleigh method. The temperature and train speed were chosen as the environmental and operational variables respectively. Wavelet energy was employed as damage indicator while the polynomial regression model and radial basis function approximation were used to construct the surrogate model.

2 WAVELET DAMAGE INDICATOR

2.1 Wavelet Analysis

The history of wavelet transform was started in the 1909 when Alfred Haar introduced rectangular basis function. However the term wavelet was firstly used by Jean Morlet to describe the resulting waveforms of varying window width in short time fourier transform, [1]. The theoretical formulation of wavelet transform was first proposed by Jean Morlet and Alex Grossmann, [15]. The important breakthrough of wavelet analysis emerged in late 1990s. Ingrid Daubechies introduced a so-called Daubechies wavelet bases and Stephane Mallat proposed a general method to construct wavelet bases. The theory of wavelet transform described in many literatures e.g. [10, 12]. A short summary of wavelet analysis is presented here.

The wavelet transform of a function $f(t)$ is written as:

$$W_{\psi}^{f}(a,b) = |a|^{-1/2} \int_{-\infty}^{\infty} f(t)\psi\left(\frac{t-b}{a}\right) \mathrm{d}t \tag{1}$$

The function ψ is often called "mother wavelet" where its value can be real or complex. In this application, ψ is assumed to be real, otherwise the complex conjugate should be introduced to the equation. In the equation (1), it is obvious that the function $f(t)$ is multiplied by a function

of two variables (a,b) which is shown in equation (2).

$$\psi_{a,b}(t) = |a|^{-1/2}\,\psi\left(\frac{t-b}{a}\right) \tag{2}$$

The term *wavelets* is used to the function $\psi_{a,b}$, which is actually the dilated (stretched or compressed) and translated versions of *mother wavelet* ψ. a dan b are called scaling parameter and translation parameter respectively. Several types of wavelet families have been known such as Haar, Mexican Hat, Morlet, Meyer, Daubechies etc. Figure (1) shows mother wavelet examples.

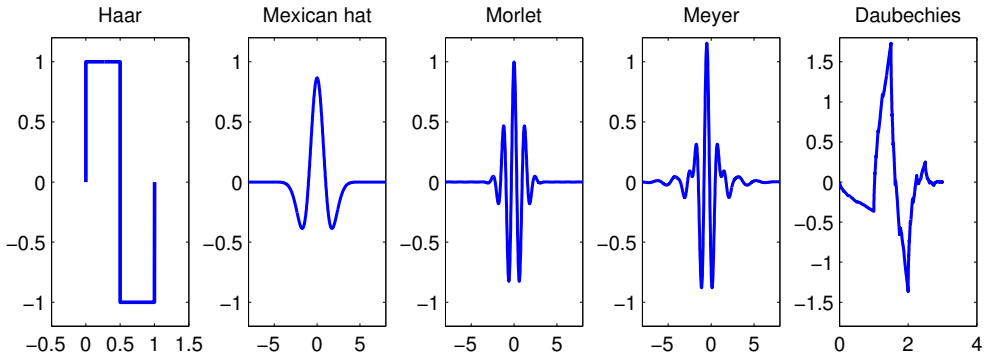

Figure 1: mother wavelet

For discrete wavelet transform, the parameter a and b in equation (2) become discrete and are chosen to be a constant, where $a_m = a_0^m$ and $b_{m,n} = nb_0a_0^m$. $m, n \in \mathbb{Z}$ and $a_0 > 1, b_0 > 0$, [12]. By substituting these constants, the equation (2) becomes:

$$\psi_{m,n} = a_0^{-\frac{m}{2}}\,\psi\left(a_0^{-m}t - nb_0\right) \tag{3}$$

A well-known group of discrete wavelet is given by dyadic wavelet. They are formed by setting $a_0 = 2$ and $b_0 = 1$. By considering these values, the equation (3) can be written as:

$$\psi_{m,n} = 2^{-\frac{m}{2}}\,\psi\left(2^{-m}t - n\right) \tag{4}$$

The numerical implementation of discrete wavelet transform is done by means of the fast wavelet transform (FWT) which is a set of algorithm developed by [14]. The algorithm is based on multiresolution analysis. A short description of wavelet transform is presented here.

A signal f in the subspace V_{-1} in $L^2(\mathbb{R})$ is separated into a high and low frequency part. The low frequency part is the projection $\mathcal{P}_0 f$ onto a lower space V_0. The complement is the projection $\mathcal{Q}_0 f$ into W_0.

$$f = \mathcal{P}_0 f + \mathcal{Q}_0 f, \quad V_{-1} = V_0 \oplus W_0 \tag{5}$$

Therefore a signal f in $L^2(\mathcal{R})$ can be described by the following decomposition:

$$f = \mathcal{P}_M f + \sum_{k=m+1}^{M} \mathcal{Q}_k f, \quad V_m = V_M \oplus \bigoplus_{k=m+1}^{M} W_k \tag{6}$$

which is graphically shown in figure (2).

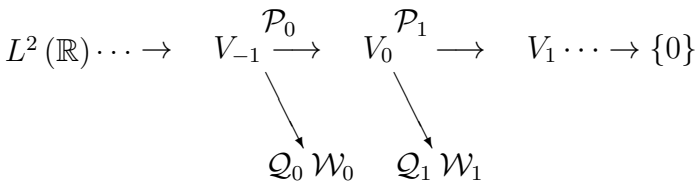

Figure 2: Scheme of a multi-scale analysis

The multi-scale analysis in the context of orthogonal wavelet transformation assumes the existence of scaling function φ.

$$\varphi_{m,n} = 2^{-\frac{m}{2}} \varphi\left(2^{-m}t - n\right) \tag{7}$$

The scaling function φ satisfies the scaling condition;

$$\varphi(t) = \sqrt{2} \sum_{k \in \mathbb{Z}} a_k \varphi(2t - k), \quad a_k \in \mathbb{R} \tag{8}$$

Based on such a scaling function φ a mother wavelet ψ can be written:

$$\psi(t) = \sqrt{2} \sum_{k \in \mathbb{Z}} b_k \varphi(2t - k), \quad b_k \in \mathbb{R} \tag{9}$$

φ and ψ hold properties,

$$\int_{-\infty}^{\infty} \varphi(t)dt = 1, \quad \int_{-\infty}^{\infty} \psi(t)dt = 0 \tag{10}$$

a_k and b_k follow the conditions,

$$\sum_{k \in \mathbb{Z}} a_k = \sqrt{2}, \quad \sum_{k \in \mathbb{Z}} b_k = 0 \tag{11}$$

By using fast wavelet transform, a signal $f \in V_0 \subset L^2(\mathbb{R})$ defined by equations(5) and (6) can be decomposed as:

$$f(t) = \sum_{k \in \mathbb{Z}} C_{M,k} \varphi_{M,k} + \sum_{m=1}^{M} \sum_{k \in \mathbb{Z}} D_{m,k} \psi_{m,k} \tag{12}$$

Where $C_{m,n}$ and $C_{m,n}$ are approximation coefficients and detail coefficients respectively, which are calculated using the following equations:

$$C_{m,n} = \sum_{k \in \mathbb{Z}} a_{k-2n} C_{m-1,k}, \quad D_{m,n} = \sum_{k \in \mathbb{Z}} b_{k-2n} C_{m-1,k} \tag{13}$$

The algorithm fast wavelet transform based on multi resolution analysis that proposed by [14] has been implemented in SLang software Package, [3] and was used in this study.

2.2 Wavelet Energy Damage Indicator

In signal processing, the energy of a given signal x(t) is defined as :

$$E = \int_t |x(t)|^2 \, \mathrm{d}t \tag{14}$$

Wavelet also has orthonormal basis, therefore the concept of energy in signal processing can also be applied in wavelet. Based on equation (12), the total energy of the decomposition signal up to level M can be calculated from equation (15).

$$\Pi_0 = \sum_k 2^M C_{M,k}^2 + \sum_{m=1}^{M} \sum_k 2^m D_{m,k}^2 \tag{15}$$

C and D indicate the approximation and details of respective wavelet decomposition. The factor 2^m guarantees the energy conservation at each level. Consequently, the absolute wavelet energy of the approximation and detail of a level m is given by equation (16) and (17) respectively.

$$\Pi_{C,m} = 2^m \sum_k C_{m,k}^2 \tag{16}$$

$$\Pi_{D,m} = 2^m \sum_k D_{m,k}^2 \tag{17}$$

3 RESPONSE SURFACE METHODOLOGY

3.1 Overview

Response Surface Methodology (RSM) is a collection of statistical and mathematical techniques useful for developing, improving, and optimizing processes, [4]. The RSM emerged in 1951 when G. E. P. Box and K. B. Wilson proposed empirical model to study the relationship between some variables in chemical experimental study, [16]. Three decades later, this approach was also applied in numerical or computer experiments. RSM has been applied to optimize the high-speed mass transport, [11]. In [5] and [13], the RSM approach was used for reliability analysis. This paper presents the application of RSM in structural health monitoring (SHM) systems.

3.2 Damage Detection Response Surface

In damage identification, the RSM is used to take into account all variables that contribute the variation of structural response including the operational and environmental conditions. The procedure is split into two stages, the *Learning Phase* and the *Detection Phase* which are elaborated in the following subsections.

3.2.1 Learning Phase

The learning phase is commenced by a basic assumption that no damage is present in the structure. The vibration response of structure is measured including its corresponding operational and surrounding condition. The measured or simulated response signal is further processed to obtain the damage indicator values. The indicator values will be used to train the

approximation model. Therefore, this phase is also known as *Training Phase*. The model is called *Reference Surface*, the benchmark of healthy structure responses in various environmental and operational conditions. Figure (3) illustrates the approximation models and its observation points.

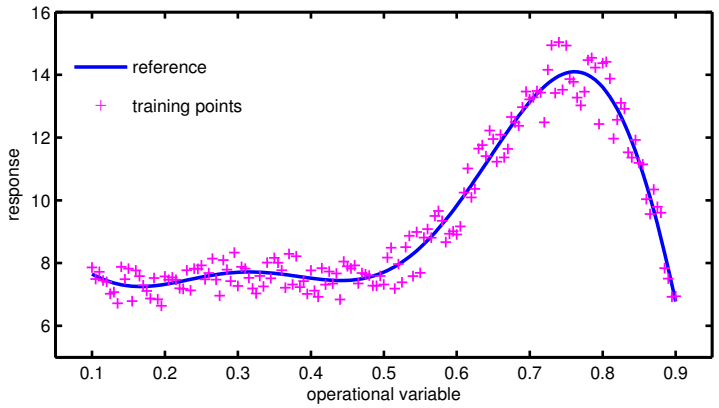

Figure 3: Training phase: the reference surface is built from observation points using scattered data approximation

In numerical simulation, the training points can be set by using design of experiments (DoE) such as full factorial design, fractional factorial design or latin hypercube sampling. Both stationer and non-stationer data can be generated. However, in real application the stationer space filling is generally not possible. The data spread irregularly because most of the variation of environmental or operational variables are uncontrollable. Furthermore, it also possible to have support points that are concentrated in certain regions. In this case, the effect of influence radius in approximation with weighting function should be carefully observed. Poor approximation can be achieved in the neighboring area of dense support points.

For model selection and validation, the observation data is split into two parts, the training and testing data sets. The first is used to fit the model while the second is used to compute the model error. It is importance to assess the model quality in non-sampled region. The simple way to assess the quality of approximation model is by using coefficient determination (R^2). Better model has higher R^2. Another approach that is also very popular is called cross validation. Furthermore, the sensitivity analysis is employed to improve the surrogate model. Some variables possibly do not have significant impact on model response. Therefore, omitting these variables is useful to reduce model complexity and improve model quality.

Several methods are available to construct reference surface from scattered points. Polynomial regression is very famous because of its simplicity. However, high order polynomials are required to approximate a surface with many peaks and troughs. Combination of many variables and higher order increase the complexity in model selection. Furthermore, high order polynomial order can lead to over fitting in noise data. More local representative is obtained by weighting method such as radial basis function or moving least square. Artificial neural networks can also be an option in model approximation. Polynomial and radial basis function is applied in this study. More detail elaboration about these method is described in section (3.3).

3.2.2 Detection Phase

The detection phase is started after the reference surface is built. The damage identification is done by comparing damage indicator value from actual measurement to the reference surface. Significant deviation from reference indicates the presence of damage. Figure (4) illustrates the responses of damage structures and it respective benchmark.

The capability of the reference surface to detect damages is depend on the sensitivity of damage indicator. Less sensitivity indicator are not able to support the response surface model to identify the damage. The reason is because the distinction between damaged and non-damaged response is too narrow. In real application this small discrepancy is potentially obscured by noise of measurement or approximation error. Another requirement for damage indicator is stability with respect to damage severity. It means no sudden change of gradient sign when the damage becomes more severe.

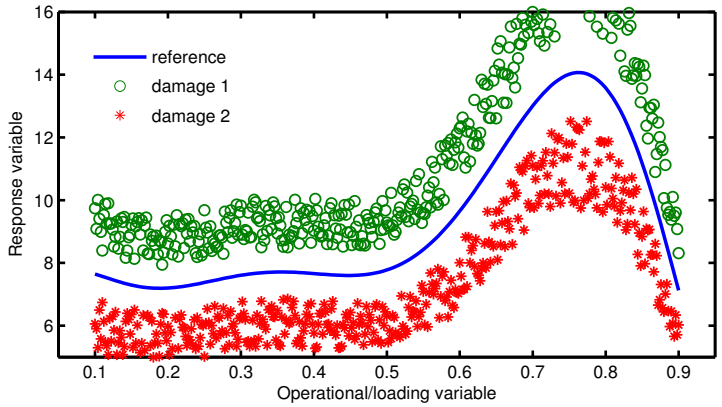

Figure 4: Detection phase: the actual response is compared to reference surface

Basically, RSM approximation approach is very suitable for damage detection of structures after extreme loading event. The structural condition can immediately assess by using ambient excitation from vehicles, winds, or pedestrian steps. However, application for long term monitoring also gives a great advantage. The RSM damage identification can be used to monitor the degradation of structural performance or damage growth. Therefore this phase also known as *monitoring phase*.

3.3 Scattered Data Approximation

As mentioned earlier, several methods are available to construct the reference surface from scattered data. Polynomial and radial basis function are used in this study. Short review about these approaches is described in the following sub subsection.

3.3.1 Polynomial Model Regression

Basically, the polynomial approximation of a function is similar to a Taylor series expansion of function f after m+1 terms, Box:1987. The flexibility of the estimation function increases as a new higher polynomial order is included in the model. A polynomial approximation of a

function $y = f(x)$ of order m is written in equation (18).

$$y = \beta_0 + \beta_1 + \beta_2 x^2 + \cdots + \beta_m x^m + \varepsilon \tag{18}$$

In a matrix form the equation (18) can be written as (19), where X is known as *Vandermonde matrix*.

$$y = X\beta + \varepsilon \tag{19}$$

$$\begin{Bmatrix} y_0 \\ y_1 \\ y_2 \\ \vdots \\ y_n \end{Bmatrix} = \begin{bmatrix} 1 & x_1 & x_1^2 & \dots & x_1^m \\ 1 & x_2 & x_2^2 & \dots & x_2^m \\ 1 & x_3 & x_3^2 & \dots & x_3^m \\ \vdots & \vdots & \vdots & \ddots & \vdots \\ 1 & x_n & x_n^2 & \dots & x_n^m \end{bmatrix} \begin{Bmatrix} \beta_0 \\ \beta_1 \\ \beta_2 \\ \vdots \\ \beta_n \end{Bmatrix} + \begin{Bmatrix} \varepsilon_0 \\ \varepsilon_1 \\ \varepsilon_2 \\ \vdots \\ \varepsilon_n \end{Bmatrix} \tag{20}$$

The estimation variables β are solved through least square solution of equation (20), which give $\beta = X^+ y$, where $X^+ = (X^{\mathrm{T}}X)^{-1}X^{\mathrm{T}}$ is known as *Moore-Penrose pseudo-inverse*.

The polynomial model approximation can also apply to multivariable systems by expanding the equation (18). For second order, multivariable polynomial model with interaction terms has general form:

$$\begin{aligned} y = \beta_0 + \beta_1 x_1 + \beta_2 x_2 + \cdots + \beta_k x_k + \beta_{11} x_1^2 + \cdots + \beta_{kk} x_k^2 \\ + \beta_{12} x_1 x_2 + \beta_{13} x_1 x_3 + \cdots + \beta_{k-1,k} x_{k-1} x_k + \varepsilon \end{aligned} \tag{21}$$

$$y = \beta_0 + \sum_{i=1}^{k} \beta_i x_i + \sum_{i=1}^{k} \beta_{ii} x_i^2 + \sum \sum_{i<j=2}^{k} \beta_{ij} x_i x_j + \varepsilon \tag{22}$$

3.3.2 Radial Basis Function Approximation

The general equation of RBF interpolation in space dimension *s* can be written as:

$$F(x) = \sum_{k=1}^{N} c_k \varphi(\parallel x - x_k \parallel), \quad x \in \mathbb{R}^s \tag{23}$$

Where, φ is basis function. $(\parallel x - x_k \parallel)$ is a matrix of Euclidean distance, for n points this matrix becomes:

$$\begin{Bmatrix} f(x_1) \\ f(x_2) \\ \vdots \\ f(x_n) \end{Bmatrix} = \begin{Bmatrix} c_1 \\ c_2 \\ \vdots \\ c_n \end{Bmatrix} \begin{bmatrix} \varphi(\parallel x_1 - x_1 \parallel) & \varphi(\parallel x_1 - x_2 \parallel) & \dots & \varphi(\parallel x_1 - x_n \parallel) \\ \varphi(\parallel x_2 - x_1 \parallel) & \varphi(\parallel x_2 - x_2 \parallel) & \dots & \varphi(\parallel x_2 - x_n \parallel) \\ \vdots & \vdots & \ddots & \vdots \\ \varphi(\parallel x_n - x_1 \parallel) & \varphi(\parallel x_n - x_2 \parallel) & \dots & \varphi(\parallel x_n - x_n \parallel) \end{bmatrix} \tag{24}$$

Coefficient c_k are obtained by solving the linear equation system in (23). The solution of this equation is unique if the Euclidean distance matrix is non-singular. Certain type of basis function can be used to develop a positive definite weighting matrix. Several basis function can be used in RBF e.g. the truncated power function, multiquadratic or inverse multiquadratic. A widely used basis function is *Gaussian fuction* as described in equation (25). This type of basis function also used in this study.

$$\varphi(r) = e^{-(\epsilon r)^2} \tag{25}$$

The shape parameter ϵ in equation (25) is used to adjust the local influence of support points. Figure (5) illustrates how a shape parameter has a profound influence on how flat or peak (localize) is the basis function. Smaller value of ϵ that also means larger variance results a flatter surface while larger value of ϵ tend to have more peaked plot. Furthermore, it affects the accuracy and numerical stability of the approximation.

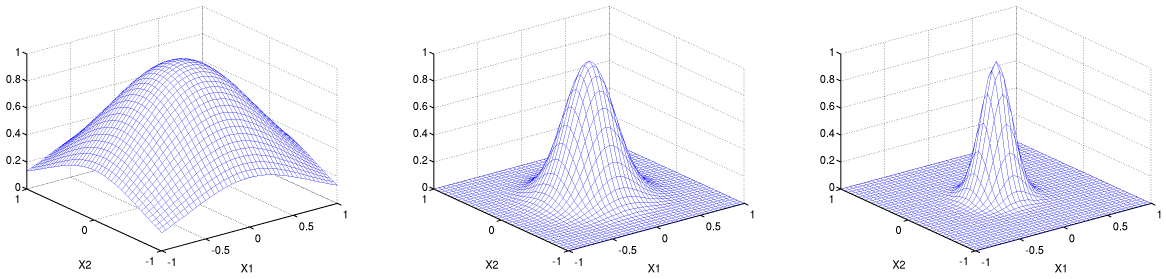

Figure 5: Shape parameter ϵ is used to adjust the local influence. Shape parameter in gaussian basis function, ϵ = 1 (left), ϵ = 3 (middle) and ϵ = 5 (right).

4 CASE STUDY AND RESULTS

4.1 Simple Supported Steel Beam

Simple supported steel beam is modeled using finite element package to observe the sensitivity of wavelet energy damage indicator. The beam is a modification of standard IPE 80 section. The additional 40 mm thickness plate is attached to its bottom flanges. The section with extra plate is considered as non-damaged structure. The damage scenario is carried on by turning back the section to its original section. The beam is illustrates in figure (6). The natural frequencies and their corresponding shape of vertical bending mode are shown in figure (7).

The beam was excited by single impulse in vertical direction. The responses signals were monitored in 5 locations as indicates in figure (7). The extracted vertical acceleration signals were decomposed using wavelet. The energies content in the decomposed signals were calculated using equations (15, 16, and 17).

The performance of eigen frequencies and modal displacement to identify the damage is summarized in figure (8). There are no significant differences in frequencies from damaged and non-damaged scenarios. Only 0.3 % approximately of frequency changes is obtained from these two scenarios. More clear differences are shows by modal displacement amplitude. However

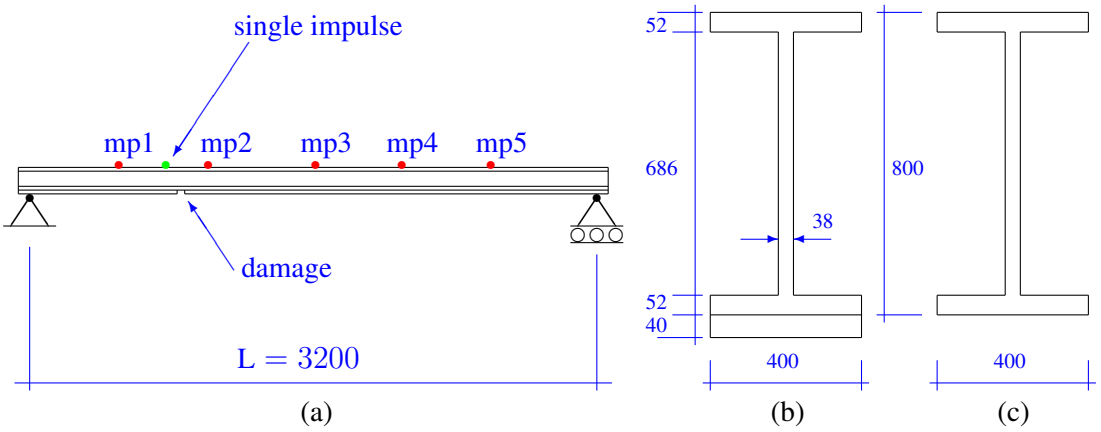

Figure 6: (a) Simple supported steel beam model, (b) Non-damaged section, (c) Damaged section.

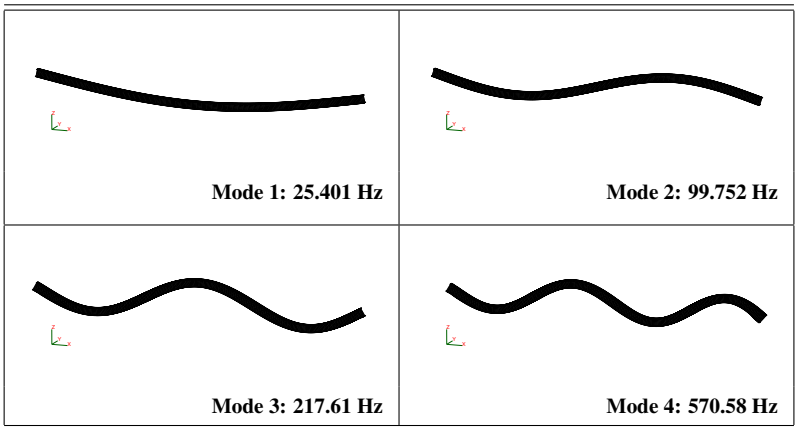

Figure 7: Vertical bending mode shapes of simulated simple supported beam

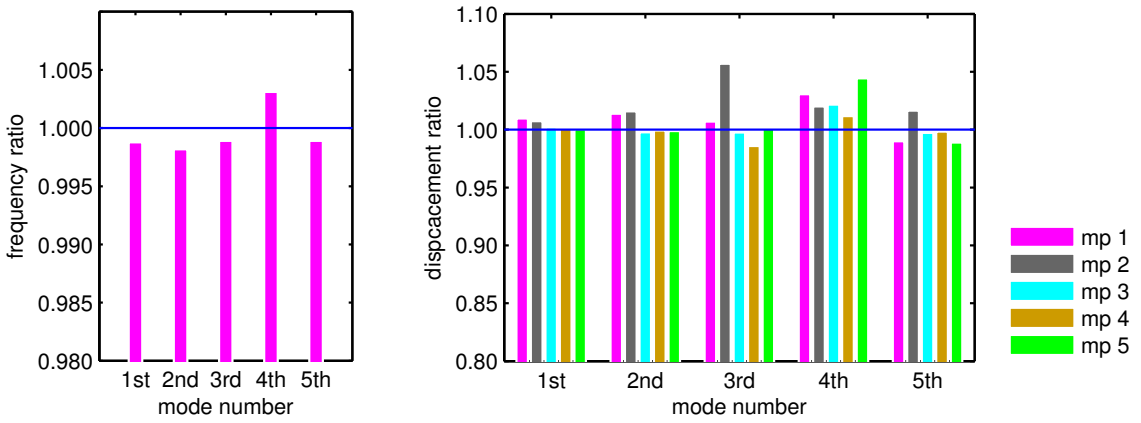

Figure 8: frequencies and modal displacement comparison

this trend appears in higher frequencies mode shapes. In practice, high frequency mode shape is difficult to be extracted.

In general, wavelet energy show much better result compared to frequencies or modal displacement amplitude. The difference between wavelet energy in damaged and non-damage scenario exceed 3 % in all extracted signals. Therefore this indicator is more suitable to be applied in RSM damage identification. The energy ratio between damage and non-damage structure is shown in figure(9).

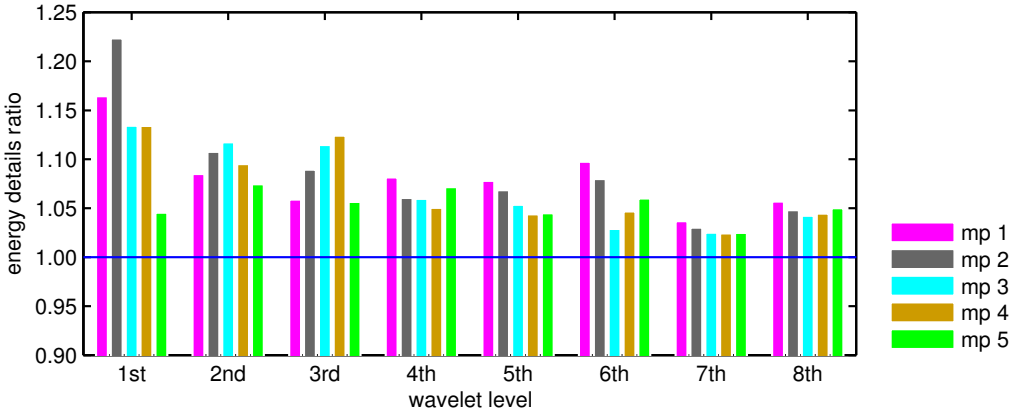

Figure 9: comparison of wavelet energy details in damaged and nondamaged structure

4.2 Railway Bridge

The response surface model for damage detection was applied to filler beam bridge through numerical simulation. The bridge has 24.60 m span and 5.39 m width. The main structure consists of girder and deck slab which are modeled by beam and shell elements respectively. The 3D spring elements are used to model the elastomeric bearings which are directly support the steel I-shape main girders. The similar elements also are used to model the ballast, where five spring elements are allocated to support each sleeper. Figure (10) shows the finite element model of the bridge. Three of the lowest eigen frequencies of the bridge model are 3.63 Hz, 5.53 Hz, and 9.18 Hz.

A collective of moving loads was built and shifted for each time step to develop the dynamic excitation. This collective load represents a series of ICE3 train, one load for each wheel. It means 64 vertical point loads were applied to the structure with sampling rate 500 Hz. Possible effects due to rail-roughness, train-bridge-interaction or wheel irregularities were neglected for simplification.

The speed of the loading train and temperature were chosen as operational and environmental condition respectively. The train speed varies from 200 to 300 km/h. The temperature is assumed to affect the elastomeric material only. The temperature effects model is adopted from [2]. The relation between temperature and shear modulus is described as $G = 4.06574 - 0.0271153T - 0.00503455T^2, \quad -5°C \leq T \leq 21°C$, where G and T are shear modulus and temperature respectively. The temperature-shear modulus model was obtained from long term dynamics experimental test of the similar bridge.

Full factorial design was adopted for design of experiments to generate 42 regular training points. The same approach was also applied to obtain 30 testing points for model selection and

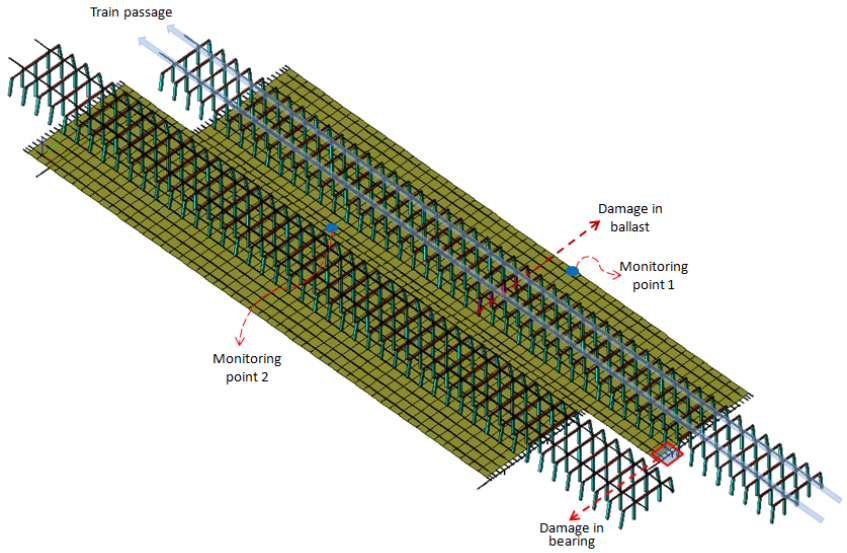

Figure 10: Finite element model of the bridge.

validation. The support points and its correspond response surface that was generated using *polynomial model* is shown in figure (11a). It shows that the 1st level wavelet energy fitted well by polynomial model. The response surface generated by RBF is show in figure (11b).

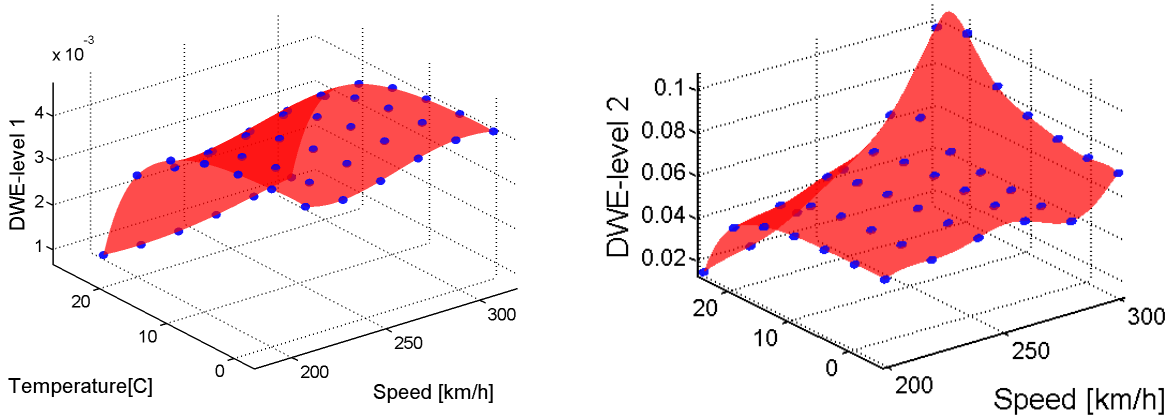

(a) (b)

Figure 11: (a) Reference surface of wavelet energy level 1 generated using polynomial regression. (b) Reference surface of wavelet energy level 2 generated using radial basis fuction approximation.

The damage is prescribed by reducing 50 % stiffness of one elastomeric support. 5 variation of train speed and surrounding temperature are selected using *Latin Hypercube Sampling* method. The level 2 wavelet energy of the testing points are plot together with its reference in figure(12a). A clear distinction of damage and non-damaged wavelet energy is obtained in 3 points. The energy ratio of these 3 points changed up to 25 % while only 10 % changes is monitored from the rest 2 points. However, these 2 points indicates much better differentiation in the next wavelet energy level. Therefore, the change of wavelet energy should be observed in

all level in order to have comprehensive assessment of structural condition. The comparison of wavelet energy in the damage and healthy condition in all level of wavelet is presented in figure (12b).

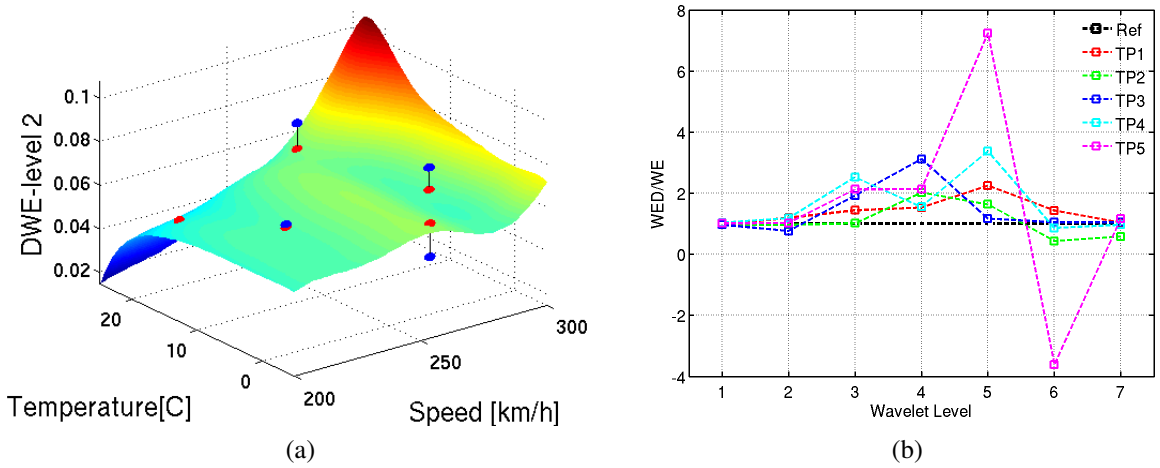

Figure 12: Response surface method for damage identification. (a) Response of damage structure and its reference at level 2. (b) Comparison wavelet energy in all level

5 CONCLUSIONS

The paper describes an approximation procedure to assess the structural health in assorted operational and environmental condition by using wavelet energy as response indicator. The response surface methodology is a potential approach to deal with damage detection problem in a situation where the non-damaged variables also affect the data response. A quite sensitive damage indicator is also very substantial to increase the capability of the method.

From the simulation results, wavelet energy is a good candidate for an indicator in combination with response surface damage identification. Its sensitivity allows to distinguish the alteration between two scenarios of numerical simulation. However, more effort is needed to be spent in observation of each wavelet level because the sensitivity is different from one to other level. As the signal becomes longer, more level will be acquired from the decomposition.

Both polynomial and RBF model show a good performance for model approximation in this study. However, the polynomial models are not able generate a good approximation in higher level of wavelet energy. The complexity of searching the best polynomial model increase significantly as new variables are introduced to the surrogate model while in RBF new variables only add new term in calculation of Euclidean distances. Therefore, the RBF model is more suitable as the number of variable increase.

REFERENCES

[1] R. X. Gao and R. Yan, Wavelets: Theory and Applications for Manufacturing. Springer, New York, 2011.

[2] V. Zabel, M. Brehm, and S. Nikulla, The influence of temperature varying material parameters on the dynamic behavior of short span railway bridge. In Proc. International Conference on Noise and Vibration Engineering (ISMA), Leuven, Belgium, 2010.

[3] Dynardo GmbH, Bauhaus University Weimar, SLang - The Structural Language. Weimar, Germany, 2009.

[4] R. H. Myers, D. C. Montgomery and C. M. Anderson-Cook, Response Surface Methodology: Process and Product Optimization Using designed Experiment. Wiley & Sons, New Jersey, 2009.

[5] T. Most, An adaptive response surface approach for reliability analysis of discontinuous limit state functions. In Proc. International probabilistic workshop, Darmstadt, Germany, 2008.

[6] W. X. Ren, Z. S. Sun, Structural damage identification by using wavelet entropy. *Engineering Structures*, **30**, 2840–2849, 2008.

[7] H. Sohn, Effects of Environmental and Operational Variability on Structural Health Monitoring. *Phil. Trans. R. Soc. A*, **365**, 539–560, 2007.

[8] V. Zabel, Applications of Wavelet Analysis in System Identification, PhD Thesis, Bauhaus University Weimar, 2003.

[9] Z. Sun, G. De Roeck, Structural damage assessment based on wavelet packet transform. *Journal of Structural Engineering*, **128**, 1354–1361, 2002.

[10] D. E. Newland, An Introduction to Random Vibrations, Spectral and Wavelet Analysis. Longman, Singapore, 1993.

[11] D. L. Knill, A. A. Giunta, C. A. Baker, B. Grossman, W. H. Mason, R. T. Haftka and L. T. Watson, Response surface models combining linear and Euler aerodynamics for HSCT design. *American Institute of Aeronautics and Austonautics, Inc.*, Virginia, 1998.

[12] I. Daubechies, Ten Lectures on Wavelets. Society for Industrial and Applied Mathematics (SIAM), Philadelphia, 1992.

[13] C. G. Bucher, A fast and efficient response surface approach for structural reliability analysis. *Structural Safety*, **7(1)**, 57–66, 1990.

[14] S. G. Mallat, A theory for multiresolution signal decomposition: The wavelet representation. *IEEE Transactions on Pattern Analysis and Machine Intelligence*, **25**, 47–68, 1989.

[15] A. Grossmann and J. Morlet, Decomposition of functions into wavelets of constant shape, and related transforms. Lecture on recent results, Mathematics and Physics. World scientific publishing, 1984.

[16] G. E. P. Box, K. B. Wilson, On the experimental attainment of optimum conditions. *Journal of The Royal Statistical Society, Series B*, **13**, 1–45, 1951.

19th International Conference on the Application of Computer
Science and Mathematics in Architecture and Civil Engineering
K. Gürlebeck, T. Lahmer and F. Werner (eds.)
Weimar, Germany, 04–06 July 2012

ILLUSTRATING DIFFERENTIAL GEOMETRY VIA GEOMETRIC ALGEBRA OF COLOR SPACE

W. Benger[1,2] **and M. Ritter**[2]

[1]*Center for Computation & Technology*
Louisiana State University
Baton Rouge, LA-70803
Louisiana, USA
werner@cct.lsu.edu

[2]*Institute for Astro- and Particle Physics/*
Inst. of Basic Sciences in Civil Engineering
University of Innsbruck
Technikerstraße 15/13
A-6020 Innsbruck, Austria
Werner.Benger@uibk.ac.at
Marcel.Ritter@uibk.ac.at

Keywords: differential geometry, geometric algebra, color models, high-dimensional spaces, visualization, color patterns, vision research, perception theory

Abstract. *Both Geometric Algebra (GA) and Differential Geometry (DG) distinguish among different kinds of vectors of the same dimensionality, leading to a higher expressiveness of algebraic objects than usual vector calculus based on Euclidean geometry. The distinct semantics of different kinds of vectors vector, co-vector, bi-vector, bi-co-vector - is obscured in the framework of Euclidean vector calculus, but they can be reasonably associated with a specific visual representation. However, in just three dimensions various ambiguities arise which question the requirement to distinguish these vector types. Higher dimensions help to illustrate this requirement, but only in five dimensions all these four vector types become unambiguous. A spatial representation in five dimension is unfortunately hard to comprehend. In this article we consider colors as dimensions instead of spatial coordinates, leading to considerations that allow improved understanding of the differences between vectors, co-vectors, bi-vectors and bi-co-vectors. This discussion is primarily intended for didactic purposes, but may have actual applications in image processing.*

1 INTRODUCTION

1.1 Related Work

D. Hestenes [6, 7] introduced Geometric Algebra as a tool providing more insight into mathematical formalisms, in particular (but not only) the spinor formalism in quantum mechanics. Geometric Algebra applies to arbitrary dimensions and when applied to a four-dimensional spacetime allows to express special and general relativity within this framework [5]. In spacetime algebra (STA) space and time have different properties which impedes understanding of four-dimensional structures. The four-dimensional computer graphics presented by A. Hansons [4] considers a fully spatial four-dimensional situation where all coordinates are equivalent. Unfortunately such a four-dimensional space is less intuitive since it is unphysical and therefore beyond human experience. However, higher dimensional spaces are still intuitive when considering colors instead of spatial dimensions, as will be demonstrated in this article. It is not uncommon to consider colors as elements of a vector space, and such approaches may be useful for image processing [3]. In previous work [1] we discussed the properties of using the framework of geometric algebra in conjunction with differential geometry without performing the frequently done identifications between vector-valued objects. In this article we introduce texturing as additional dimension to a color space, leading to color patterns as the basic objects of consideration instead of geometric objects. A metric on color patterns as a measure of perceptual similarity has been investigated by Mojsilovic et.al. [8]; however, they did not express their findings in vision research using a mathematical framework such as the one presented here.

1.2 Outline

Section 2 reviews the mathematical framework introducing the notation and terminology used throughout this article. While each of the reviewed theories can be found in standard text books, they are usually presented in their own, often incompatible or sometimes even obscure notation which impacts insight. Section 2.1 reviews the basic definitions of a vector space, which is the sufficient for defining the Grassmann algebra in section 2.2. Section 2.3 reviews the definition of tangential and co-tangential vectors as well as the definition of a metric. The metric is essential for defining the geometric algebra, reviewed in section 2.4. Section 2.5 finally discusses applying the Grassmann and Geometric algebra on the tangential and co-tangential vectors. Section 3 discusses the abstract relationships introduced in section 2 in virtue of colors instead of geometrical objects: Section 3.1 discusses the three-dimensional case using the RGB color model, section 3.2 the four-dimensional case and section 3.3 presents the extension to five dimensions.

2 MATHEMATICAL FRAMEWORK

Differential Geometry is a most fundamental mathematical framework crucial to physics as it describes the concept of a manifold with charts. Many formalism in physics and in particular simplifications used in engineering are based on vector calculus in euclidean space, which can be seen as a special case of the more general framework. Only in certain application domains such as general relativity or computational modeling using curvilinear grids it is evident that a more powerful framework than Euclidean vector calculus is required. In such more general cases the actual structures that are implicitly assumed in Euclidean vector algebra become visible and explicit. The awareness of such otherwise implicitly used structures is helpful for

understanding the mathematical framework and to ease generalizing algorithms. This section follows mostly the introduction of [1].

2.1 Vector Spaces

The concept of a vector space is most fundamental, as it considers abstract objects with certain constraining properties: A vector space over a field F is a set V together with two binary operations, called scalar multiplication and vector addition, satisfying the vector space axioms. A significant consequence is that a vector space is closed under these operations, i.e. for arbitrary $u, v \in V$ and $a, b \in F$, then it follows that $au + bv \in V$.

An element of V is called a "vector", commonly illustrated via an arrow. However, the vector space elements may have a variety of other properties distinguishing them and the representation as an arrow is not always appropriate to them.

Some formalisms may be implied directly on vector spaces such as the grassmann algebra, others such as geometric algebra require additional structures, for instance a metric. The concept of a space-time, fundamental to physics, is not a vector space, though in simplifications it is treated as such. In general however the full framework of differential geometry needs to be applied, which in addition to a metric also may require more structures such as an orientation-form and possibly a connection form, as will be discussed below.

2.2 Grassmann Algebra

Grassmann Algebra [2] introduces another binary operation to a vector space, the Grassmann product "$\wedge$", also called the wedge, alternating or exterior product. It can be seen as the anti-symmetric subset of the direct product of two vectors $v \wedge u = v \otimes u - u \otimes v$ and provides the important property

$$v \wedge u = -v \wedge u \tag{1}$$

The Grassmann product introduces a new type of vectors, so-called bi-vectors, which form their own vector space distinct, but related to, vectors. When vectors are illustrated by an arrow, a bi-vector is appropriatly illustrated by the plane that is spun by two vectors as in Fig. 1. Bi-vectors

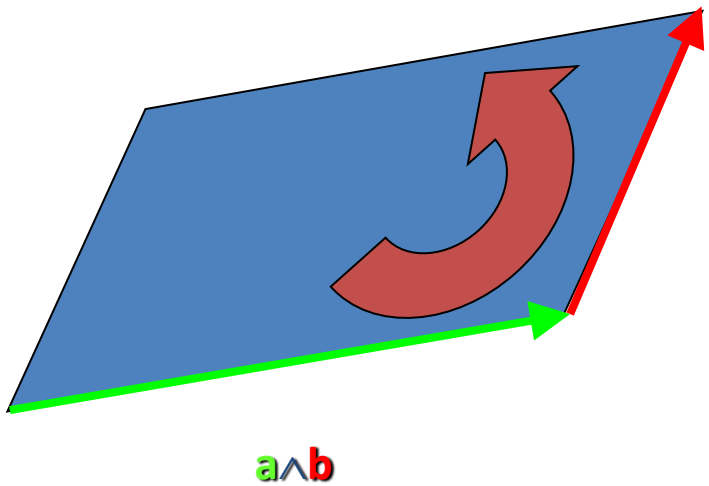

Figure 1: A bi-vector is represented by an (oriented) area element spun by its two generating vectors.

form their own vector space, called $\Lambda^2(V)$ or $V \wedge V$. With n the dimensions of a vector space V, the dimension of $\Lambda^2(V)$ is $n(n-1)/2$.

Higher order wedge products are defined by applying the wedge product to bi-vectors and vectors etc., leading to the k-th power $\Lambda^k(V)$ of a vector space V. Its element is a k-vectors with $\binom{n}{k}$ components. However, since $v \wedge v = 0$ due to eqn. (1), the highest power can only be $k = n$ for an n-dimensional vector space as there are at most n linearly independent vectors. $\Lambda^n(V)$ is a one-dimensional vector space as all elements, the so-called pseudo-scalars, are scalar multiples of the basis vector $v_1 \wedge v_2 \dots v_n$ where $v_1, v_2 \dots v_n$ are the n basis vectors of V. Pseudo-scalars represent oriented (n-dimensionial) volumes, and - in contrast to a actual scalars - depend on the used coordinate system. For instance, they change sign under reflections.

These dimensionality of k-vectors are illustrated by the Pascal's triangle, with the row representing the dimensionality n (starting with 0D in the first row) of the underlying vector space and the column the power k of the k-vector:

$$\begin{array}{ccccccccc} & & & & 1 & & & & \\ & & & 1 & & 1 & & & \\ & & 1 & & 2 & & 1 & & \\ & 1 & & 3 & & 3 & & 1 & \\ 1 & & 4 & & 6 & & 4 & & 1 \end{array} \tag{2}$$

For a three-dimensional vector space, there are three vectors as well as three bi- vectors. Therefore, in three dimensions vectors and bi-vectors can be identified. Bi- vectors describing a surface area are known as "normal vector" in usual Euclidean vector calculus. For a four-dimensional vector space this identification of vectors with bi-vectors is no longer possible, as there will be four 1-vectors, six bi-vectors, four tri-vectors and one 4-vector.

2.3 Differential Geometry

Differential Geometry (DG) identifies derivatives along curves in a manifold as tangential vectors. Given a curve $q : \mathbb{R} \to M : s \mapsto q(s)$, the derivative d/ds along the curve can be written as a linear combination of basis vectors (e.g. $\{\partial_x, \partial_y, \partial_z\}$), which each are derivatives in the direction of a (local) coordinate system (e.g. given by coordinate functions $\{x, y, z\}$):

$$d/ds = \dot{q}^x \partial_x + \dot{q}^y \partial_y + \dot{q}^z \partial_z \quad . \tag{3}$$

The numbers $\{\dot{q}^x, \dot{q}^y, \dot{q}^z\}$ represent the tangential vector $\dot{q}$ in the coordinate system $\{x, y, z\}$. The notation "∂_x" hereby stands for "derivation into the direction of the coordinate function x" and is a shortcut for the partial derivative $\partial/\partial x$. The set of all tangential vectors at a certain point $P \in M$ is called the tangential space $T_p(M)$. The tangential space is a vector space regardless whether the underlying manifold M is a vector space itself or not.

In addition to tangential vectors differential geometry considers linear functions on tangential vectors $df : T_p(M) \to \mathbb{R}$, which constitute a vector space by itself. They can be constructed from scalar functions $f : M \to \mathbb{R}$ such that for any tangential vector $v \in T_p(M)$

$$df(v) := v(f) \equiv (v^x \partial_x + v^y \partial_y + v^z \partial_z)(f) \quad . \tag{4}$$

These linear functions on tangential vectors are called co-vectors and their space is the co-tangential space $T_p^*(M)$. The basis of the co-tangential space in a coordinate system $\{x, y, z\}$ is denoted $\{dx, dy, dz\}$ following the notation of a scalar function's total differential

$$df = \frac{\partial f}{\partial x}\, dx + \frac{\partial f}{\partial y}\, dy + \frac{\partial f}{\partial z}\, dz \quad . \tag{5}$$

Tangential vectors and co-vectors are dual to each other, i.e. when applying the k^{th} basis co-vector as dx^k to the i^{th} basis vector ∂_i the result will be 1 only if $i = k$, otherwise 0. This property is intrinsic to the tangential and co-tangential spaces on an arbitrary manifold.

Additional properties that may be specified on a certain manifold are in particular the metric tensor field $g : T_p(M) \times T_p(M) \to \mathbb{R}$ that allows to define the inner product of two vectors and therefore means to compute the norm (magnitude) of tangential vectors (a co-metric $g : T_p^*(M) \times T_p^*(M) \to \mathbb{R}$ is required to compute the norm of co-vectors). Given an (invertible) metric tensor allows identifying vectors and co-vectors via the so-called musical isomorphisms. In Euclidean geometry the metric tensor is represented by a unity matrix at each point such that vectors and co-vector are represented by the same numerical values and thus usually not considered as distinct objects. However, treatment of non-Euclidean spaces requires distinguishing between vectors and co-vectors.

2.4 Geometric Algebra

Geometric Algebra [6, 7] extends the usual vector calculus using vector addition and scalar multiplication by introducing the geometric product as the combination of the inner product and the exterior (Grassmann) product. For two vectors $u, v \in V$ of a vector space V with metric $g : V \times V \to \mathbb{R}$ the geometric product uv (by convention denoted without explicit operator symbol) is given by $uv = g(u, v) + u \wedge v$. The geometric product provides useful properties such as being associative and invertible, whereas it is not commutative in general. It is closed within the space of multi-vectors, which is formed by linear combinations of k-vectors:

$$\Lambda(\mathcal{V}) = \bigoplus_{k=0}^{n} \Lambda^k(\mathcal{V}) \tag{6}$$

where n is the dimension of the underlying vector space V. The dimensionality of $\Lambda(\mathcal{V})$ is 2^n.

The Geometric Algebra (GA) requires a metric given on the underlying vector space, in contrast to the Grassmann algebra which is independent from any metric. Given the concept of a "norm" through the metric, GA allows to identify k-vectors with $n - k$ vectors using the hodge-star operator $\star : \Lambda^k(\mathcal{V}) \to \Lambda^{n-k}(\mathcal{V})$ since the dimensionality of $\Lambda^k(\mathcal{V})$ and $\Lambda^{n-k}(\mathcal{V})$ is equal.

2.5 Geometric Algebra on the Tangent Space

Given a manifold M with tangent space $T_p(M)$ and co-tangent space $T_p^*(M)$ we can apply the Grassmann and Geometric algebra on each of these vector spaces. The multi-vector space constructed from tangential vectors is then $\Lambda\big(T_p(M)\big)$, the multi-vector space of co-vectors $\Lambda\big(T_p^*(M)\big)$. The multi-vector space of tangential vectors hereby corresponds to "multiple directions", such as a bi-vector defining an (oriented) area. In contrast, co-vectors describe a direction that is "not to be used", as they represent a scalar function on just this direction. A co-vector can be seen as a "cut out" function which removes a direction from the n-dimensional volume. For instance, in three dimensions a co-vector "cuts off" one direction, thus leaving the plane defined by the two remaining directions. Thus, a bi-co-vector is an operation that "cuts off" two directions.

A bi-co-vector corresponds to the subspace of an n-dimensional hyperspace where a plane is "cut out". In three dimensions these visualizations overlap: both, a bi-tangential vector and a co-vector correspond to a plane, and both a tangential vector and a bi-co-vector correspond to an one-dimensional direction ("arrow"). In four dimensions, these visuals are more distinct

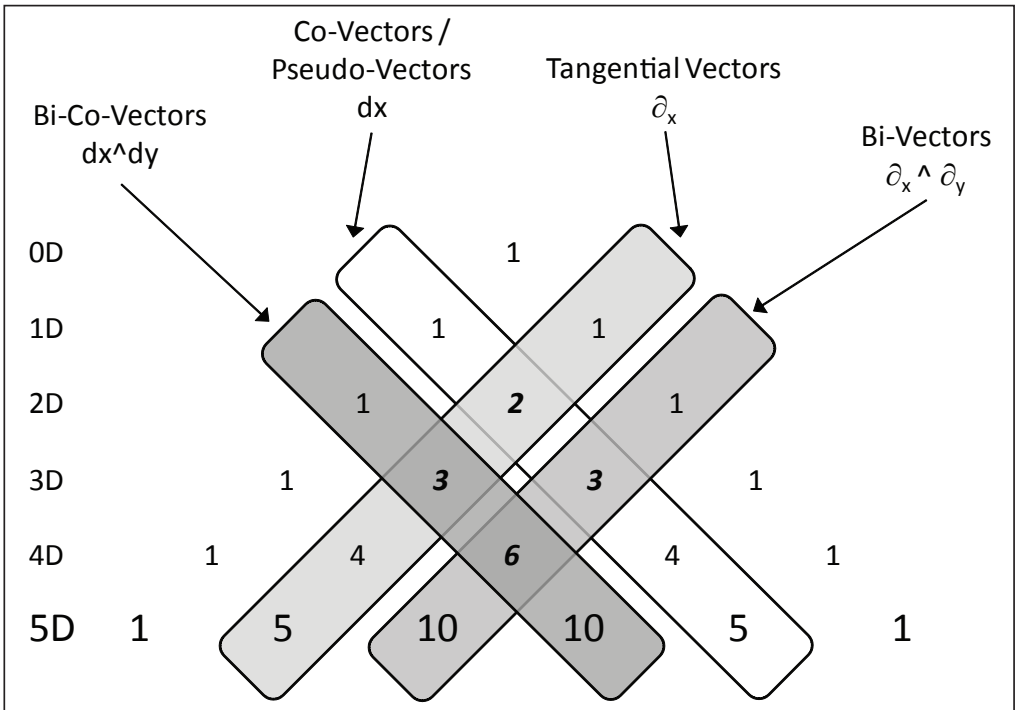

Figure 2: Pascal's triangle depicting tangential vectors, bi-vectors, co-vectors and bi-covectors for the Grassmann algebra of tangential and co-tangential spaces. In three dimensions there are many ambiguities where all vectorial objects are of the same dimensionality 3. In four dimensions there are less ambiguities , but only in 5D all vector types become unambiguous.

but still overlap: a co-vector corresponds to a three-dimensional volume, but a bi-tangential vector is represented by a plane similar to a bi-co-vector, since cutting out a 2D plane from four-dimensional space yields a 2D plane again. Only in higher dimensions these graphical representations become unique, as indicated by Fig. 2. In any case a co-vector and a pseudo-vector will have the same appearance as an $n-1$ dimensional hyperspace, same as a tangential vector corresponds to an pseudo-co-vector: The difference between a co-vector and a pseudo-vector however is their orientation: a co-vector does not provide any orientation information, it is just a "cut-off" operation. In contrast, a pseudo-vector is constructed from alternating products of tangential vectors with relevance to its ordering. In 3D, we can therefore visualize a co-vector as non-oriented planar area element and a bi-vector as an oriented planar area element.

3 GEOMETRIC ALGEBRA OF COLOR SPACE

3.1 Three-dimensional Color Space - RGB

Colors form a vector space same as spatial dimensions due to the linear properties[1] of the Maxwell equations, allowing to superpose electromagnetic waves, i.e. light. Colors in particular form a three-dimensional space due to the biophysical properties of the human eye being sensitive to three fundamental colors. There are many ways to represent a color space such as RGB, HSV, CIE etc..; a metric given on a color space may for instance be used to determine color similarities when comparing images [3].

[1] In contrast, gravitational waves cannot be superposed due to the non-linearity of the Einstein equations.

A most simple color space is RGB, using the red, green and blue primary colors to construct other colors, similar to the x,y,z coordinates in Euclidean vector calculus. It is common to associate xyz coordinates with RGB colors for illustration purposes in computer graphics. The RGB color space describes the additive color system as it represents light being added to darkness, for instance, relevant to LED displays or computer/TV monitors. Complementary to RGB is the CMY color space describing the subtractive color system where color filtering is applied to a white background, such as in painting or printing colors on a white sheet of paper. The primary colors of the CMY color space are cyan, magenta and yellow, which are complementary to red, green and blue in the additive color system.

When considering the notion of tangential and co-tangential vectors in differential geometry, it seems quite fitting to associate RGB colors with tangential vectors and CMY colors with co-vectors: RGB colors "add" directional information, like tangential vectors, whereas CMY colors "subtract" directional information, like co-vectors. The intrinsic duality between vectors and co-vectors corresponds to the complementarity of RGB and CMY colors. We may denote the basis vectors of the RGB space as $\{\partial_r, \partial_g, \partial_b\}$ and of the CMY space as $\{\partial_c, \partial_m, \partial_y\}$ to support this interpretation. Duality between RGB and CMY then means in this notation:

$$\star\, \partial_r = dr \quad \equiv \quad \partial_c \tag{7}$$
$$\star \partial_g = dg \quad \equiv \quad \partial_m \tag{8}$$
$$\star \partial_b = db \quad \equiv \quad \partial_y \tag{9}$$
$$\star \partial_c = dc \quad \equiv \quad \partial_r \tag{10}$$
$$\star \partial_m = dm \quad \equiv \quad \partial_g \tag{11}$$
$$\star \partial_y = dy \quad \equiv \quad \partial_b \tag{12}$$

The exterior product of color vectors then corresponds to the mixing of colors in this interpretation, allowing for additive and subtractive mixing. For instance, mixing red and green light yields yellow light, described as $\partial_r \wedge \partial_g$, a bivector in the additive color space. Yellow (∂_y) in the CMY system can be seen as removing blue from white and is thus identified with a co-vector in the RGB system, $db \equiv \partial_y$. This co-vector is identified with the dual of the blue color, i.e. $\star\partial_b \cong \partial_r \wedge \partial_g$. This identification is the same as relating the cross product "$\times$" of vectors with a "normal" vector in Euclidean vector calculus $\partial_z \cong \partial_x \times \partial_y = \star(\partial_x \times \partial_y)$. Identifying the same "colors" in the additive (RGB) color systems with colors in the subtractive (CMY) color system is the same as identifying vectors with co-vectors and bi-vectors. This is only possible within a three-dimensional vector space.

3.2 Four-dimensional Color Space - RGBA

While human vision is limited to only three primary colors, in computer graphics color is frequently described using four components. The fourth component is transparency. Considering transparency as an additional property of a color space allows to consider a four-dimensional space. The property complementary to transparency is opacity, or "blackness", which may be expressed via the CMYK color model where "k" stands for an additional blackness component, similar to opacity of the overall color. Starting from the four-dimensional RGBA color space

with four basis vectors $\{\partial_r, \partial_g, \partial_b, \partial_a\}$ we may construct six color bi-vectors

$$\begin{aligned}
\partial_r \wedge \partial_a &\rightarrow \text{transparent red} \\
\partial_g \wedge \partial_a &\rightarrow \text{transparent green} \\
\partial_b \wedge \partial_a &\rightarrow \text{transparent blue} \\
\partial_r \wedge \partial_g &\rightarrow \text{yellow (non-transparent)} \\
\partial_g \wedge \partial_b &\rightarrow \text{cyan (non-transparent)} \\
\partial_b \wedge \partial_r &\rightarrow \text{magenta (non-transparent)}
\end{aligned}$$

four three-vectors

$$\begin{aligned}
\partial_r \wedge \partial_g \wedge \partial_a &\rightarrow \text{transparent yellow} \\
\partial_g \wedge \partial_b \wedge \partial_a &\rightarrow \text{transparent cyan} \\
\partial_b \wedge \partial_r \wedge \partial_a &\rightarrow \text{transparent magenta} \\
\partial_r \wedge \partial_g \wedge \partial_b &\rightarrow \text{gray (non-transparent)}
\end{aligned}$$

and last not least one pseudo-scalar

$$\partial_r \wedge \partial_g \wedge \partial_b \wedge \partial_a \rightarrow \text{transparent white} \quad .$$

These various wedge products allow to express all possible combinations to be built from RGBA. Using the relationships eqn.(7), (8) and (9) we can express mixed colors via their dual counterparts from the CMYK space, e.g.

$$\partial_r \wedge \partial_g = dc \wedge dm = \star(\partial_c \wedge \partial_m) \tag{13}$$

where we can interpret using the co-vector as indicating a color that "must not" be used. The star-operator hereby plays the role of a "not" operator, i.e. the indicated color blue in the subtractive color model, expressed as $\partial_c \wedge \partial_m$ (mixing cyan and magenta gives blue) must not be used for printing the additive color yellow $\partial_r \wedge \partial_g$. Using vectors, the $\wedge$ -operator means "both", using co-vectors, the $\wedge$ operator means "neither". Thus we can identify RGBA colors with their dual counterparts from the CMYK space by considering "color that should not be printed" on a white canvas, whereby "transparency" corresponds to some "light" or "bright" color in this case:

$$\begin{aligned}
\partial_r \wedge \partial_a = \star(\partial_c \wedge \partial_k) &\rightarrow \text{light red means printing neither black nor cyan} \\
\partial_g \wedge \partial_a = \star(\partial_m \wedge \partial_k) &\rightarrow \text{light green means printing neither black nor magenta} \\
\partial_b \wedge \partial_a = \star(\partial_y \wedge \partial_k) &\rightarrow \text{light blue means printing neither black nor yellow} \\
\partial_r \wedge \partial_g = \star(\partial_c \wedge \partial_m) &\rightarrow \text{intense yellow means printing neither cyan nor magenta} \\
\partial_g \wedge \partial_b = \star(\partial_m \wedge \partial_y) &\rightarrow \text{intense cyan means printing neither magenta nor yellow} \\
\partial_b \wedge \partial_r = \star(\partial_y \wedge \partial_c) &\rightarrow \text{intense magenta means printing neither yellow nor cyan}
\end{aligned}$$

Expressing a rule "to print colors" means that all CMYK colors are printed except those specified to not be printed. The four tri-vector colors relate to the RGBA/CMYK color space as

follows:

$$\begin{aligned}
\partial_r \wedge \partial_g \wedge \partial_b = da = dc \wedge dm \wedge dy = \star dk = \partial_k &\rightarrow \text{gray - no white - print black} \\
\partial_r \wedge \partial_g \wedge \partial_a = db = dc \wedge dm \wedge dk = \star dy = \partial_y &\rightarrow \text{light yellow - no blue - print yellow} \\
\partial_g \wedge \partial_b \wedge \partial_a = dr = dm \wedge dy \wedge dk = \star dc = \partial_c &\rightarrow \text{light cyan - no red - print cyan} \\
\partial_b \wedge \partial_r \wedge \partial_a = dg = dy \wedge dc \wedge dk = \star dm = \partial_m &\rightarrow \text{light magenta - no green - print magenta}
\end{aligned}$$

The relationships between RGBA color vectors and their CMYK counterparts may therefore be interpreted as "rules" on how to print additive colors using the subtractive color model. The inverse rules, not shown here explicitly, can be interpreted as rules how to produce subtractive colors using a light projector. Arbitrary colors are created via linear combinations of these base vectors. The pseudo-scalars represents white and black:

$$\begin{aligned}
\partial_r \wedge \partial_g \wedge \partial_b \wedge \partial_a = dc \wedge dm \wedge dy \wedge dk &\rightarrow \text{white - do not print any color} \\
dr \wedge dg \wedge db \wedge da = \partial_c \wedge \partial_m \wedge \partial_y \wedge \partial_k &\rightarrow \text{black - do print all colors}
\end{aligned}$$

In this four-dimensional RGBA color space, vectors (i.e. primary colors in the additive color system: red, green, blue, transparent) can no longer be identified with bi-vectors (light red, light green, light blue, intense yellow, intense cyan, intense magenta) as it was possible in the three-dimensional RGBA color space. We can however identify tri-vectors with co-vectors, since using three colors means not using the fourth color, whereby "color" hereby also includes the transparency/black channel.

This illustration of the base vectors of four-dimensional space is similar to the case of space-time algebra (STA) [5] where we have three spacelike and three timelike, i.e. six, bi-vectors. Using these color vectors, the transparency (alpha channel, black channel for printing) playes the same role as time in STA, hereby distinguishing "bright" and "dark" colors.

The $2^4 = 16$ colors that can be produced by a system of four light emitting diodes (LEDs) (red, green, blue and white) are summarized in the following table, where color vectors indicate the LEDs to be switched on and co-vectors indicate LEDs that must not be used:

RGBA vector *LED's to use*	RGBA covector *LED's not to use*	color
0	$dr \wedge dg \wedge db \wedge da$	black
∂_r	$dg \wedge db \wedge da$	dark red
∂_g	$dr \wedge db \wedge da$	dark green
∂_b	$dr \wedge dg \wedge da$	dark blue
∂_a	$dr \wedge dg \wedge db$	transparency / brightness
$\partial_r \wedge \partial_a$	$dg \wedge db$	bright red
$\partial_g \wedge \partial_a$	$dr \wedge db$	bright green
$\partial_b \wedge \partial_a$	$dr \wedge dg$	bright blue
$\partial_r \wedge \partial_g$	$db \wedge da$	dark yellow
$\partial_g \wedge \partial_b$	$dr \wedge da$	dark cyan
$\partial_b \wedge \partial_r$	$dg \wedge da$	dark magenta
$\partial_r \wedge \partial_g \wedge \partial_b$	da	gray
$\partial_r \wedge \partial_g \wedge \partial_a$	db	bright yellow
$\partial_g \wedge \partial_b \wedge \partial_a$	dr	bright cyan
$\partial_b \wedge \partial_r \wedge \partial_a$	dg	bright magenta
$\partial_r \wedge \partial_g \wedge \partial_b \wedge \partial_a$	0	white

It should be pointed out that both ∂_a and $\partial_r \wedge \partial_g \wedge \partial_b$ represent gray; this corresponds to the two alternative ways of a CMYK printer to produce a gray color: either using all of CMY inks, or using just the black ink. In theory, both methods would yield gray. In practice, there will be slight deviations in the gray tone. The ambiguity among these two approaches may therefore be resolved by assuming that ∂_a yields an overall intensity different from $\partial_r \wedge \partial_g \wedge \partial_b$, for instance "bright gray" vs. "dark gray".

When identifying bright and dark colors, i.e. ignoring the alpha channel/intensity, we arrive at the three-dimensional color space as before where vectors and co-vectors can be identified with each other. This, again, relates to identifying vectors and bi-vectors in 3D ("bright red" $\approx$ "dark red").

3.3 Five-dimensional Color Space - RGBAT/CMYKU

The four-dimensional RGBA color space could easily be extended to a five-dimensional scheme by introducing different levels of gray, introducing infra-red or ultra-violet, but this would become rather confusing and less intuitive since these extensions are not easily accessible to the perception of the human eye and thus our experiences. A more suitable approach is to add texturing as a fifth parameter to the color space, now considering not just single dots of colors, but some spatially extend elements that may or may not provide some additional pattern. Denoting this texturing property as a "t" coordinate, we have the following basis vectors for a five-dimensional RGBAT color space:

$$\begin{aligned} \partial_r &\rightarrow \text{red} \\ \partial_g &\rightarrow \text{green} \\ \partial_b &\rightarrow \text{blue} \\ \partial_a &\rightarrow \text{brightness} \\ \partial_t &\rightarrow \text{textured} \end{aligned}$$

These five base vectors produce $2^5 = 32$ combinations for colored patterns, encompassing 10 bi-vectors, 10 tri-vectors, 5 four-vectors and one pseudoscalar. Instead of listing each of these cases, the main purpose of considering a five-dimensional color space is to show that each of these objects is different in 5D as pointed out in Fig. 2, and none of them can be identified with each other any more like in 3D or 4D.

In 3D we could say "red is not cyan" ($\partial_r = dc$), "red light means using neither green and blue light" ($\partial_r = \star(\partial_g \wedge \partial_b)$), "printing red means mixing magenta and yellow colors" ($\partial_r = \star(\partial_m \wedge \partial_y)$), allowing for alternative ways to produce the same color in RGB space, i.e. identifying vectors (primary RGB colors) with bi-vectors (specifying which lights not to use) and co-vectors (specifying which inks to use for printing): pure or mixed color in the three-dimensional scheme is a primary color in either the RGB ("tangential") or CMY ("co-tangential") space. Thus for each color we have the option to uniquely specify it by just giving one colorization vector (i.e. any of "red","green","blue", "magenta","cyan" or "yellow").

In 4D, any primary color ("dark red") can only be expressed by three complementary properties (e.g. $\partial_r = dg \wedge db \wedge da$). Any mixed color can only be expressed by a mix of complementary colors as well (e.g. bright red $\partial_r \wedge \partial_a = dg \wedge db$), but never as a primary color in either RGBA or CMYK. This corresponds to identifying vectors with tri-covectors and bi-vectors with bi-co-vectors in 4D, e.g.

dark red	∂_r	$dg \wedge db \wedge da$	vector / tri-co-vector
bright red	$\partial_r \wedge \partial_a$	$dg \wedge db$	bi-vector / bi-co-vector
bright magenta	$\partial_r \wedge \partial_b \wedge \partial_a$	dg	tri-vector / co-vector

Thus in 4D space we have a unique choice to express primary colors, but alternative options to express mixed colors if we want to specify only two color properties from either RGBA or CMYK.

In 5D, we can still express each k-vector via its dual $n-k$ co-vector (adding colors/textures vs. removing colors/textures), but the descriptions will no longer be equivalent. For instance, a "dark red textured" pattern is the bi-vector $\partial_r \wedge \partial_t$, "bright red textured" is the tri-vector $\partial_r \wedge \partial_a \wedge \partial_t$ and "bright magenta textured" is the four-vector $\partial_r \wedge \partial_b \wedge \partial_a \wedge \partial_t$, see Fig. 3.

black	0	$dr \wedge dg \wedge db \wedge da \wedge dr$	scalar
dark red	∂_r	$dg \wedge db \wedge da \wedge dr$	vector
dark red textured	$\partial_r \wedge \partial_t$	$dg \wedge db \wedge da$	bi-vector
bright red textured	$\partial_r \wedge \partial_a \wedge \partial_t$	$dg \wedge db$	bi-co-vector
bright magenta textured	$\partial_r \wedge \partial_b \wedge \partial_a \wedge \partial_t$	dg	co-vector
bright white textured	$\partial_r \wedge \partial_g \wedge \partial_b \wedge \partial_a \wedge \partial_t$	0	pseudo-scalar

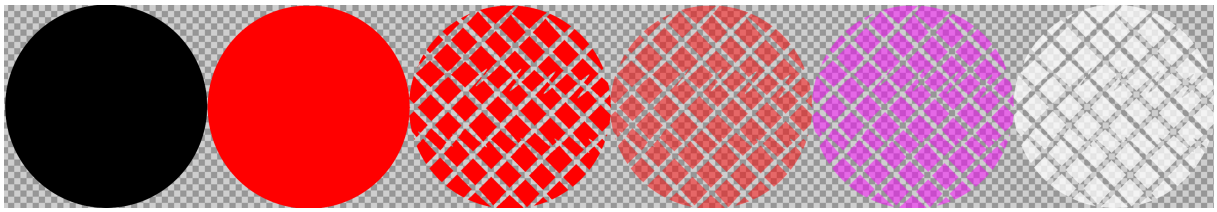

Figure 3: Six exemplary and unique 5D multi-vector elements illustrated in 5D color space using red, green, blue, alpha and texture (RGBAT). From left to right: scalar, vector, bi-vector, bi-co-vector, co-vector and pseudo-scalar.

In this 5D space we may still express any color via just two properties from either RGBAT or its complementary CMYKU ("U" meaning "untextured") space, but in contrast to the 3D and 4D space this choice will be unique now: A mixed color must either be expressed via RGBAT quantities or CMYKU quantities such that two basis vectors are sufficient for identifying the color. This property of the five-dimensional texture color space disables the ability to identify vectors with co-vectors, bi-vectors and bi-co-vectors.

4 SUMMARY

Considering the properties of colors is an alternative to geometry for illustrating the notion of tangential vectors and co-vectors in differential geometry in conjunction with Grassman and geometric algebra. This approach eases intuition for higher-dimensional spaces. A tangential vector can be understood as a "adding" a property to a colorization scheme, a co-vector can be understood as a rule to "remove" a property from a color. The wedge product is the join of these properties, leading to objects such as bi-vectors, co-vectors and bi-co-vectors. In 3D and 4D these objects can be described in alternative ways, only in 5D the "most easy" description in terms of a "minimal number of properties to be specified" becomes unique.

5 FUTURE WORK

The discussion on applying geometric algebra and differential geometry to color spaces is intended to be of primarily didactic purpose; it may lead to inspirations and further applications, for instance in image processing where the choice of color/pattern metric plays a relevant role for similarity assessments based on perception theory such as in [8, 3]. The provided discussion does not utilize the full mathematical framework of geometric algebra considering such a metric. For a meaningful interpretation of colors as vectors and bi-vectors one would also have to consider the ordering of colors ($\partial_r \wedge \partial_g = -\partial_g \wedge \partial_r$), i.e negative intensities for color values.

6 ACKNOWLEDGEMENT

This research employed resources of the Center for Computation and Technology at Louisiana State University, which is supported by funding from the Louisiana legislature's Information Technology Initiative. This work was supported by the Austrian Science Foundation FWF DK+ project *Computational Interdisciplinary Modeling* (W1227) and by the Austrian Ministry of Science BMWF as part of the UniInfrastrukturprogramm of the Forschungsplattform Scientific Computing at LFU Innsbruck..

REFERENCES

[1] W. Benger, A. Hamilton, M. Folk, Q. Koziol, S. S. Princeton, E. Schnetter, M. Ritter, and G. Ritter. Using geometric algebra for navigation in riemannian and hard disc space. In V. Skala and D. Hildebrand, editors, *GraVisMa 2009 - Computer Graphics, Vision and Mathematics for Scientific Computing*. UNION Agency, Na Mazinach 9, CZ 322 00 Plzen, Czech Republic, 2010.

[2] A. Bossavit. Differential geometry for the student of numerical methods in electromagnetism. Technical report, Tampere University of Technology, 1991.

[3] A. Doloc-mihu, V. Raghavan, and P. Bollmann-sdorra. Color retrieval in vector space model. In *In Proceedings of the 26 th International ACM SIGIR Workshop on Mathematical/Formal Methods in Information Retrieval MF/IR*, 2003.

[4] A. J. Hanson and R. A. Cross. Interactive visualization methods for four dimensions. In *Proceedings of the 4th conference on Visualization '93*, VIS '93, pages 196–203, Washington, DC, USA, 1993. IEEE Computer Society.

[5] D. Hestenes. *Space-Time Algebra*. Routledge, 1966.

[6] D. Hestenes. *New Foundations for Classical Mechanics, 2nd ed.* Springer Verlag., 1999.

[7] D. Hestenes. Oersted Medal Lecture: Reforming the Mathematical Language of Physics. *American Journal of Physics*, 71(2):104–121, 2002.

[8] A. Mojsilovic, J. Kovacevic, R. J. S. J. Hu, and K. Ganapathy. Matching and retrieval based on the vocabulary and grammar of color patterns. *IEEE Trans. on Image Processing*, 9(1):pp. 38–54, 2000.

19th International Conference on the Application of Computer Science and Mathematics in Architecture and Civil Engineering
K. Gürlebeck, T. Lahmer and F. Werner (eds.)
Weimar, Germany, 04–06 July 2012

COMPUTATION OF THE REFLECTANCE AND TRANSMITTANCE FOR AN INHOMOGENEOUS LAYERED MEDIUM WITH TURNING POINTS USING THE WKB AND SPPS METHODS

R. Castillo-Pérez*[,1], A. del C. Cedillo-Díaz[2], V. V. Kravchenko[3] and H. Oviedo-Galdeano[1]

*[,1]*SEPI ESIME, National Polytechnic Institute*
Av. IPN s/n, C.P. 07738, Mexico City, Mexico
[2]*SEPI UPIITA, National Polytechnic Institute, Av. IPN 2580, C.P. 07340, Mexico City, Mexico*
[3]*Department of Mathematics, CINVESTAV del IPN, Campus Querétaro, Apartado Postal 1-798, Arteaga # 5, Col. Centro, Santiago de Querétaro, Qro., C.P. 76001 Mexico*
E-mail: rcastillo@ipn.mx

Keywords: Pseudoanalytic functions, transmittance, reflectance, turning points.

Abstract. *Electromagnetic wave propagation is currently present in the vast majority of situations which occur in everyday life, whether in mobile communications, HDTV, satellite tracking, broadcasting, etc. Because of this the study of increasingly complex means of propagation of electromagnetic waves has become necessary in order to optimize resources and increase the capabilities of the devices as required by the growing demand for such services.*

Within the electromagnetic wave propagation different parameters are considered that characterize it under various circumstances and of particular importance are the reflectance and transmittance. There are several methods for the analysis of the reflectance and transmittance such as the method of approximation by boundary condition, the plane-wave expansion method (PWE), etc., but this work focuses on the WKB and SPPS methods.

The implementation of the WKB method is relatively simple but is found to be relatively efficient only when working at high frequencies. The SPPS method (Spectral Parameter Powers Series) based on the theory of pseudoanalytic functions, is used to solve this problem through a new representation for solutions of Sturm-Liouville equations and has recently proven to be a powerful tool to solve different boundary value and eigenvalue problems. Moreover, it has a very suitable structure for numerical implementation, which in this case took place in the Matlab software for the evaluation of both conventional and turning points profiles.

The comparison between the two methods allows us to obtain valuable information about their performance which is useful for determining the validity and propriety of their application for solving problems where these parameters are calculated in real-life applications.

1 INTRODUCTION

When a wave traveling from a medium to another is considered, some parameters such as reflectance and transmittance can be identified. They are defined as the ratio of the amplitude of the reflected wave and the transmitted wave with respect to the incident wave amplitude respectively.

The study of these parameters is necessary in many areas of science for increasingly complex media. For example, most modern optical systems could not function without inhomogeneous optical coatings. The telecommunications industry uses various types of layers such as antireflective layers, polarizers and dichroic layers in personal displays, optical filters, inhomogeneous planar waveguides [1], inhomogeneous photonic crystals [2], devices for splitting and combining optical communication channels, and so on. Also the knowledge of the reflectance and transmittance has important applications in ionospheric communications and in the analysis of radiation of antennas [3]. Other areas of study include applications such as environmental studies, precision agriculture, ecology, etc. [4].

There are numerous methods for the analysis of the reflectance and transmittance having different degrees of precision, complexity and efficiency. Some examples of them are the WKB method [5], the method of approximation by boundary condition, the plain wave expansion method PWE [6], the transfer matrix method TMM [7], the variational method [8], the perturbation method [9], differential TMM, etc. (see, e.g., [10, 11, 12, 13, 14]). A recently developed method is the SPPS method (Spectral Parameter Powers Series method [15, 16, 17]).

This work focuses on the WKB [5] and SPPS [18] methods because the WKB method is well known and has been extensively studied, in addition it is relatively easy to implement and efficient especially when working at high frequencies. The SPPS method, which in this particular case is associated with the solutions of a Sturm-Liouville problem, has proven a powerful tool for solving various types of boundary and eigenvalue problems [19, 20, 21] and has a structure which is very suitable for its numerical implementation.

The particular problem discussed in this paper is calculating the reflectance and transmittance of an electromagnetic wave with perpendicular polarization that propagates through an inhomogeneous layered medium with normal incidence. Inhomogeneous media are those for which one or more of their material parameters depend on space and are defined here by means of a refractive index profile, which in this case depends on a single space coordinate. In addition to traditional profiles, profiles with turning points are considered.

We proceeded with the programming of both methods and with the evaluation of different profiles. We used some profiles with known exact solutions (linear, exponential and hyperbolic profiles) as test problems to verify the correct operation of the methods. Then the study of turning points profiles was carried out with both methods.

The organization of this paper is as follows. In Section 2 we introduce the problem to be solved and propose the elements for calculating the reflectance and transmittance. In Section 3 the WKB method is developed and the considerations under which it can be adapted for the analysis of a turning points profile are described. Section 4 introduces the SPPS method and it is shown how the solutions of a Sturm-Liouville equation can be used to construct the solution to our problem. In Section 5 the results of the computations are presented and the performance of the methods is analyzed.

2 WAVE PROPAGATION IN INHOMOGENOUS LAYERED MEDIA

In general the characteristics of wave propagation and dispersion in a non homogeneous medium cannot be described in a simple manner. However, there are special cases where asymptotic methods may apply as, for example, when working with high or low frequency fields [5]. The low frequency approach is applicable whenever the size of a dielectric body is much smaller than a wavelength. The high-frequency approach is useful when the refractive index variation is negligibly small over the distance of one wavelength.

The inhomogeneous media under consideration will have the layered structure shown in Figure 1.

where T is the transmission coefficient and $k_3 = k_0 n_3$. In this case and for non-absorbent media the following energy conservation relation holds

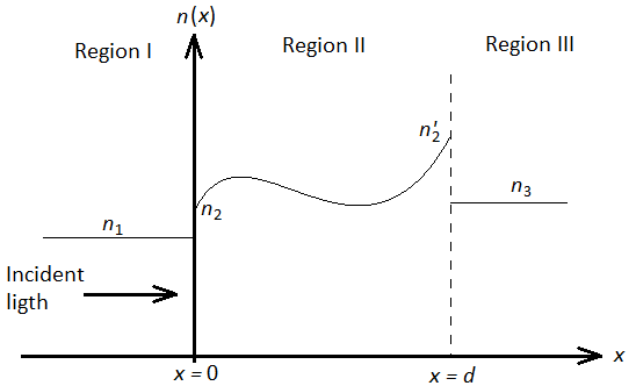

Figure 1. Inhomogeneous layered medium.

The refractive index n has constant values n_1 and n_3 in the regions I and III respectively and is an arbitrary continuous function in the region II. If we suppose an incident wave in region I represented by the scalar function u which stands for a transverse component of the electric field of an s-polarized electromagnetic wave, the following Helmholtz equation is satisfied

$$(x) + [q(x) \qquad]u(x) \tag{1}$$

where $q(x) = k_0^2 n^2(x)$, k_0 is the free-space circular wavenumber and $\beta = k_0 \sin\theta$, θ being the angle of incidence (for the sake of simplicity normal incidence is considered, so in what follows $\theta = 0°$, and β vanishes). If the incident wave is supposed to have the form $e^{-ik_1 x}$, where $k_1 = k_0 n_1$, then together with the reflected wave the whole solution for $x < 0$ is

$$u(x)$$

where the constant R is the reflection coefficient whose absolute value is less than 1. The solution corresponding to the transmitted wave in region III has the form

$$u(x)$$

$$|R| \qquad \frac{}{_3|T|^2} \qquad 1. \tag{2}$$

The general solution of (1) for $0 < x < d$ is proposed to have the form

and consists of two linearly independent solutions u_1 and u_2 in the interval $0 \le x \le d$ such that

$$(0) = 1, \qquad u_1'(0) \tag{3}$$

$$(0) \quad 0, \qquad (0) \tag{4}$$

and with c_1 and c_2 being arbitrary constants. So, from the continuity and initial conditions the expressions for R and T were found to be [18]

$$\frac{(d) - u_1'(d) - ik_3u_1(d) + ik_1u_2'(d)}{[u_1'(d) \qquad u\ (d)] \quad i[k \quad (d) \qquad (d)]} \tag{5}$$

$$\frac{[u_1(d)u_2'(d) - \quad (d)u_2(d)]e}{[u_1'(d) - k_1k_3u_2(d)] + i[k_3u_1(d) + k_1u_2'(d)]} \tag{6}$$

These are the formulas for the reflectance and transmittance in an inhomogeneous layered medium.

3 WKB METHOD

3.1 WKB method for profiles without turning points

Initially we work with (1) considering normal incidence

$$\left[— \qquad (x)\right] u(x) \quad 0. \tag{7}$$

The following solution is proposed

$$u(x) = \ ^{\varphi(x)} \tag{8}$$

where $\varphi(x)$ is given by the following expression

$$\varphi(x) = \int \phi(x)dx$$

It is worth mentioning that $\phi(x)$ will be found later. Now, replacing (8) in (7) we get

$$— \ ^{\varphi(x)} \qquad (x)e^{\varphi(x)} \quad 0. \tag{9}$$

Equation (9) can be expressed as a Riccati equation

$$\phi'(x) + \phi^2(x) + q^2(x) \quad 0. \tag{10}$$

Knowing that $q(x) \qquad n(x)$, (10) becomes

$$\phi'(x) + \phi^2(x) + {k_0}^2n^2(x) = \quad . \tag{11}$$

Now, $\phi(z)$ can be written as an inverse power series of

$$\phi(x) = \left[\phi_0(x)k \quad \phi_1(x) \quad \underline{\phi_2(x)} \quad \underline{\phi_3(x)} \qquad \right].$$

Taking into account the power series of $\phi^2(x)$, (11) becomes

$$\left[\phi_0^2(x) \qquad (x)\right]k \quad \left[\phi_0'(x) \quad \phi_0(x)\phi_1(x)\right]k \quad \left[\phi_1'(x) \quad \phi_1^2(x) + 2\phi_0(x)\phi_2(x)\right] +$$

where when considering high frequencies, the large value of allows us to neglect the terms in which it appears in the denominator.

Equating the coefficients of each power of to zero, we obtain an infinite number of equations, but we only took the first three

$$\phi_0^2(x) \qquad (x) \tag{12}$$

$$\phi\ (x) \qquad \phi_0(x)\phi_1(x) \tag{13}$$

$$\phi_1'(x) + \phi_1^2(x) \qquad \phi_0(x)\phi_2(x) \quad 0. \tag{14}$$

From (12) we can get the value of $\phi_0(x)$

$$\phi_0(x) \qquad in(x). \tag{15}$$

In order to find $\phi_1(x)$, using $\frac{d}{}(\ln u)$ $\overline{\quad}$ equation (14) turns out to be

$$\phi_1 \qquad \frac{\phi_0'}{\phi_0} \qquad -\frac{\phi_0}{} \qquad \frac{\phi_0}{}^{1/2}. \tag{16}$$

Now, from (8) for

$$\phi(x) \quad \phi_0 \qquad \phi_1 \quad \underline{\phi_2} \quad \underline{\phi_3}$$

we get

$$u(x) \qquad \int[\phi \qquad \phi_1 \ \underline{\phi_2} \ \underline{\frac{\phi_3}{2}}]dx$$

Neglecting all the terms which have k in the denominator and replacing the values of (15) and (16) we get

$$u(x) = \frac{1}{\sqrt{\phi_0}} \cdot e^{\pm i \int k_0 n(x) dx}. \tag{17}$$

Developing the previous expression we can state it in terms of $q(x)$

$$u(x) = \frac{1}{(x)^{1/}}\left[a \cdot e^{-i \int q(x)} \qquad\qquad \int q(x)dx\right]. \tag{18}$$

The constants *a* and *b* can be found using the initial conditions. Then the solution consists of a wave traveling in the *+z* direction and a wave traveling in the direction of *–z*

$$(x) \qquad \frac{}{1/2} \quad i \int q \tag{19}$$

$$(x) \qquad \frac{}{1/2} \quad i \int q \quad . \tag{20}$$

After obtaining the solutions (19) and (20) that are solutions of the quadratic equation with inhomogeneous parameters (7), we proceed to find the value of the constants, which together with the above equations will constitute the complete solution *v* which will allow us to satisfy the initial conditions (3) and (4).

In order to do this we propose two linearly independent solutions given by

$$(x) \qquad (x) \qquad (x) \tag{21}$$

and

$$(x) \qquad (0) \qquad (x). \tag{22}$$

The constants for the conditions (3) were found to be

$$- \ ^{/2}(0)\left(1 \quad - \quad (0) \quad (0)\right) \tag{23}$$

and

$$= q \ ^{/}{}_{2}(0) \quad - \quad ^{/}{}_{2}(0)\left(1 \quad - \quad (0) \quad (0)\right). \tag{24}$$

For the conditions (4) we found

$$\overline{\ ^{/}{}_{2}(0)} \tag{25}$$

and also

$$\overline{\ ^{/}{}_{2}(0)}\ . \tag{26}$$

Solutions (21) and (22) can be used for calculating the reflectance and transmitance using (5) and (6).

3.2 WKB method for profiles with turning points

The solutions found with the WKB method (19) and (20) in Section 3.1 for the Helmholtz equation (7) can be used to find the reflectance and transmittance of profiles that do not have a zero crossing singularity, i.e., when the function $q^2(x)$ (which depends on the refractive index) does not pass through zero. In the case of profiles having such zero crossing, the point where they cross zero (here denoted by x_0) is called the turning point. (Figure 2).

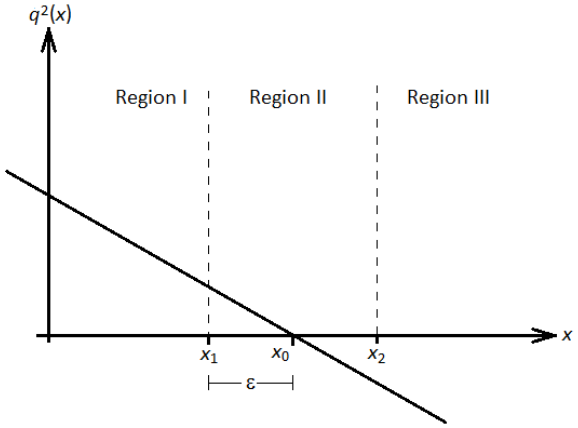

Figure 2. Profile with turning points.

In order to study the above problem, the inhomogeneous region of the medium is in its turn divided into three regions. Let x_1 delimit the region II by the left hand side and x_2 delimit the region II by the right hand side. This region is a ε-neighburhood of the turning point x_0. In region I and region III, the solutions found in Section 3.1, (19) and (20) are valid, but in region II, the one where the turning points lie, a different solution should be calculated.

In order to find the solution in region II [5] one can go back to the Helmholtz equation (7) for which $q^2(x)$ can then be expanded around x_0 using the Taylor series. In this case only the first term will be used

$$(x) \qquad a(x \qquad), \tag{27}$$

where a is the slope at x_0:

$$\underline{d(q^2)}\Big|$$

Then (7) becomes

$$\left[- \quad a(x \qquad) \right] u(x) \quad 0. \tag{28}$$

To see what happens around the turning point, one must find the solution of (28). This is possible, using the solutions in the Region I (21) and (22) in order to calculate the solutions in region II that we will denote by $\widetilde{v_1}(x)$ and $\widetilde{v_2}(x)$. In addition, it is necessary to connect the solutions found for the Region I with the solutions in the Region II, for which new initial conditions are introduced (Cauchy problem). The following continuity conditions are to be imposed

$$\widetilde{v_1}(x_1) \qquad (x_1), \qquad \widetilde{v_1}'(x_1) \qquad '(x_1) \tag{29}$$

$$\widetilde{v_2}(x_1) \qquad (x_1), \qquad \widetilde{v_2}'(x_1) \qquad (x_1). \tag{30}$$

It is possible to solve this system using the mathematical package Matlab, which in its turn uses an internal process based on Maple. The command used to obtain the solutions is *dsolve* and it allows the solution of a quadratic equation with initial conditions to be found. The command used in Matlab to solve (28) for the initial conditions (29) was

$$e(' \qquad\qquad (x \quad 0) \qquad v(x1) \qquad\qquad Dv(x1) \qquad\qquad ').$$

The resulting expression after applying the *simplify* command is:

$$\widetilde{v_1} \quad \frac{Bi(\zeta_2) \cdot \left(v_1'(x_1) \qquad (\zeta_1) \qquad (x_1) \qquad '(\zeta_1) \cdot \left(- - \right)^{-} \right)}{a\left(Ai(\zeta_1) \qquad '(\zeta_1) \qquad '(\zeta_1) \quad Bi(\zeta_1) \right) \cdot \left(- - \right)^{-}}$$

$$\frac{Ai(\zeta_2) \cdot \left(v_1'(x_1) \quad Bi(\zeta_1) \qquad (x_1) \qquad '(\zeta_1) \cdot \left(- - \right)^{-} \right)}{a\left(Ai(\zeta_1) \qquad '(\zeta_1) \qquad '(\zeta_1) \quad Bi(\zeta_1) \right) \cdot \left(- - \right)^{-}} \tag{31}$$

where

$$\left(- - \right)^{-} \qquad \left(- - \right)^{-}$$

$$ax \left(- - \right)^{-} - \; ax_0 \left(- - \right)^{-}$$

and for the initial conditions (30) the solution is the following expression

$$\widetilde{v_2} \quad \frac{Bi(\zeta_2) \cdot \left(v_2'(x_1) \qquad (\zeta_1) \qquad (x_1) \qquad '(\zeta_1) \cdot \left(- - \right)^{-} \right)}{a\left(Ai(\zeta_1) \qquad '(\zeta_1) \qquad '(\zeta_1) \quad Bi(\zeta_1) \right) \cdot \left(- - \right)^{-}}$$

$$\frac{Ai(\zeta_2)\cdot\left(v_2'(x_1)\quad Bi(\zeta_1)\qquad (x_1)\qquad '(\zeta_1)\cdot\left(--\right)^{-}\right)}{a\left(Ai(\zeta_1)\qquad '(\zeta_1)\qquad '(\zeta_1)\quad Bi(\zeta_1)\right)\cdot\left(--\right)^{-}} \tag{32}$$

For Region III we take up the solutions found with the WKB method (19) and (20) and proceed to find the constants that will complement the proposed final solutions

$$\widetilde{\widetilde{v_1}}(x)\qquad (x)\qquad (x) \tag{33}$$

$$\widetilde{\widetilde{v_2}}(x)\qquad (x)\qquad (x) \tag{34}$$

for which with similar initial conditions to those used in Region II were imposed that lead to the following constants

$$\frac{(x_2)\cdot\widetilde{v_1}'(x_2)-\widetilde{v_1}(x_2)\qquad (x_2)}{(x_2)\qquad (x_2)\qquad (x_2)\qquad (x_2)} \tag{35}$$

$$\frac{\widetilde{v_1}(x_2)\qquad (x_2)}{u\ (x_2)} \tag{36}$$

$$\frac{(x_2)\cdot\widetilde{v_2}'(x_2)-\widetilde{v_2}(x_2)\qquad (x_2)}{(x_2)\qquad (x_2)\qquad (x_2)\qquad (x_2)} \tag{37}$$

$$\frac{\widetilde{v_2}'(x_2)\qquad (x_2)}{(x_2)} \tag{38}$$

Equations (33) and (34) are the final solutions needed to find the reflectance and transmittance for a turning points profile.

In Section 4 we will work with these profiles using the SPPS method. This will later allow us to stablish a comparison of the performance of both methods.

4 SPPS METHOD

An application of the theory of pseudoanalytic functions corresponds to the theory of linear ordinary differential equations of second order. One of them is the Sturm-Liouville equation, which is of fundamental importance because of the many situations in mathematical physics where it arises, and that has the following form

$$(pv') \tag{39}$$

for which p, q, r and v are complex-valued functions of an independent real variable $x \in [0, d]$ and β is an arbitrary complex constant. The coefficients p, q and r depend on the considered problem and are proposed so that there is a particular solution v_0 (which is also a complex-valued function of a real variable x) of the homogeneous equation

$$(p\quad) \tag{40}$$

such that the functions and $\mathbf{1}/(\boldsymbol{v}\ \boldsymbol{p})$ are continuous in the interval $[\mathbf{0}\ \boldsymbol{d}]$.

The general solution for (39) takes the form [18]

(41)

where are arbitrary complex constants, are defined in the following way

$$\sum \quad \tilde{X}^{(n)} \tag{42}$$

$$\sum \quad {}^{(n)} \tag{43}$$

where $\tilde{X}^{(n)}$ and $X^{(n)}$ are defined as

$$\tilde{X}^{(0)} \qquad {}^{(0)} \tag{44}$$

and for $n \in \mathbb{N}$,

$$\tilde{X}^{(n)}(x) \quad \begin{matrix} \int \tilde{X}^{(n-1)}(s) v_0^2(s) r(s) ds \\ \int \tilde{X}^{(n-1)}(s) \dfrac{}{(s)p(s)} \end{matrix} \tag{45}$$

$$X^{(n)}(x) \quad \begin{matrix} \int {}^{(n\ )}(s) \dfrac{}{v\ (s)p(s)} \\ \int X^{(\ \ )}(s) v_0^2(s) r(s) ds \end{matrix} \tag{46}$$

With the above recursive formulas, the solution *v* can be found. The solution consisting of the equations (41)-(43) is a power series in β that is really attractive for the numerical solution of spectral problems, initial value and boundary value problems. Both series in (42) and (43), which are called Spectral Parameter Power Series (SPPS), converge uniformly on [0, *d*] and as shown in [16] it is easy to obtain a rough but useful estimate of the rest of the series. This estimate provides a simple tool to calculate the number of powers *N* which guarantees an a priori established accuracy.

The required non vanishing particular solution v_0 of (42) and (43), at least in the case of a regular equation with real-valued coefficients, always exists and and can be easily constructed as follows [18]: take any two linearly independent solutions $v_{0,1}$ y $v_{0,2}$ of (40), then their zeros do not coincide (otherwise their Wronskian is zero and are not linearly independent) and then can be chosen as .

Then v_0 can be constructed in a manner similar to the solutions v_1 and v_2 considering a special case of the already presented result when $q \equiv 0$ and $\beta = 1$, which was already known to Weyl [22]. That is, let $1/p$ and *r* be continuous on [0, *d*]. The general solution of equation $(pv')' = rv$ in (0, d) has the form (41) where c_1 and c_2 are arbitrary constantsand v_1 and v_2 are defined by equations (42)-(46) with $v_0 \equiv \beta = 1$.

As a special case another important situation is considered. Very often in electromagnetic theory (see for example [8]) it is necessary to solve the equation

$$\frac{v(x)}{} \qquad q(x)v(x) \tag{47}$$

for different values of the complex constant . It can be seen that the above equation is practically the same as (7). Its general solution can be represented as follows

(48)

where

$$\sum \quad \widetilde{W}^{(n)}$$

$$\sum \quad {}^{(n)}$$

with $\widetilde{W}^{(n)}$ and $W^{(n)}$ defined by

$$\widetilde{W}^{(0)} \quad 1, \qquad {}^{(0)} \quad 1, \tag{49}$$

and for $\mathbb{N}$,

$$\widetilde{W}^{(n)}(x) \quad \begin{matrix} \int \widetilde{W}^{(n-1)}(s)q(s)ds \\ \int \widetilde{W}^{(n-1)}(s)ds \end{matrix} \tag{50}$$

$$W^{(n)}(x) \quad \begin{matrix} \int \quad {}^{(n\ )}(s)ds \\ \int \quad {}^{(n\ )}(s)q(s)ds \end{matrix} \tag{51}$$

and for c_1 and c_2 two arbitrary complex constants. Thus, once $\widetilde{W}^{(n)}$ and $W^{(n)}$ are calculated up to a certain power N, an approximate solution of (47) is simply a polynomial on k with its calculated coefficients $\widetilde{W}^{(n)}$ and $W^{(n)}$. This observation is also valid for the case of solution (41), (42) and (43) of equation (39). Furthermore this property is very useful for the numerical solution of the corresponding spectral problems, which reduces to finding the zeros of the polynomials with respect to k and β respectively [18].

5 CALCULATIONS

5.1 Calculation for profiles without turning points

Initially, to ensure that the programs developed for the WKB and SPPS methods were functioning correctly, we studied some well known profiles having analytic solutions based on Bessel functions [23, 24]. Such profiles are the linear, exponential and hyperbolic profiles.

For example for the exponential profile its refractive index profile is described by

$$n(x) \qquad \exp\left[-\ \mathrm{n}\left(\frac{2}{}\right)\right] \ . \tag{52}$$

The following data were used in our programs:

- Incidence angle °, that is, normal incidence
- Size of the non homogeneous medium m
- Number of points in the evaluated interval $[0\ d]$
- Refractive index of medium in region I,
- Refractive index of medium in region III,
- Refractive index of the boundary of medium 1,

- Refractive index of the boundary of medium 3, ′
- Wavelengths, approximately from 2 to 100
- Frequencies, approximately from 3 THz to 150 THz.

The program used to implement the SPPS method performed the calculations using 31 formal powers, approximating the functions needed to calculate the recursive integrals by splines of order two and using 500 segments for integrating. From the parameters (p, q and r) in (39) one can obtain a particular solution v_0 for (40). The same parameters are used to calculate the formal powers (45)-(46), with which two linearly independent solutions are found according to formulas (42) and (43) which in turn are used to find the solution (41) that will be a solution of (39).

The obtained results are shown in the following figures.

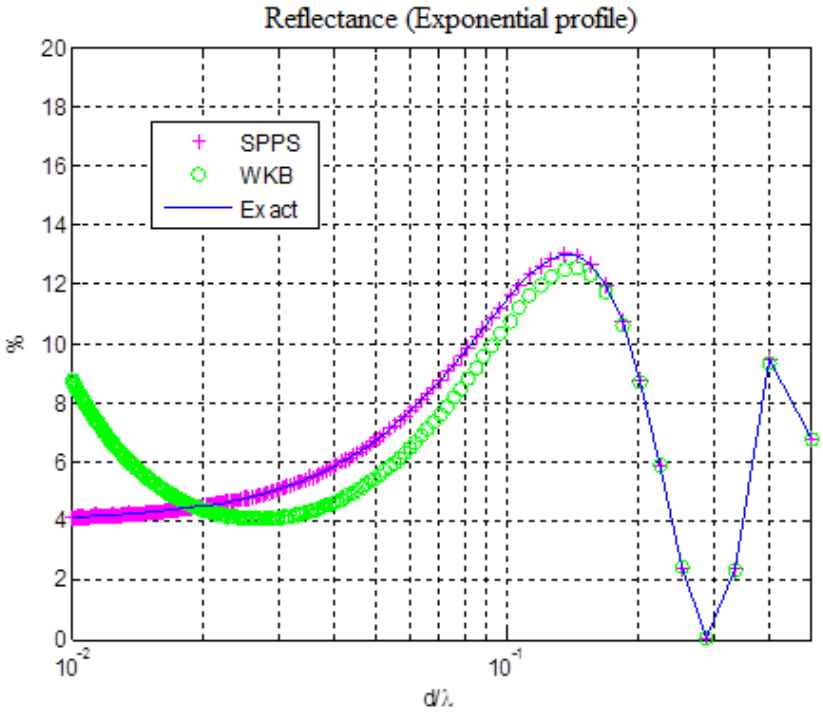

Figure 3. Reflectance for the exponential profile.

The elapsed time for the program which implemented the WKB method was approximately of 1.5 seconds, using a laptop computer with an Intel Core i7 2.8 GHz processor, with 8 GB of RAM. The SPPS method for its execution needed a time of around 11 minutes.

Another comparison which was performed was estimating the absolute error of the two methods in comparison with the exact solutions for each of the profiles. Some of the resulting graphs are shown in Figures 5 and 6.

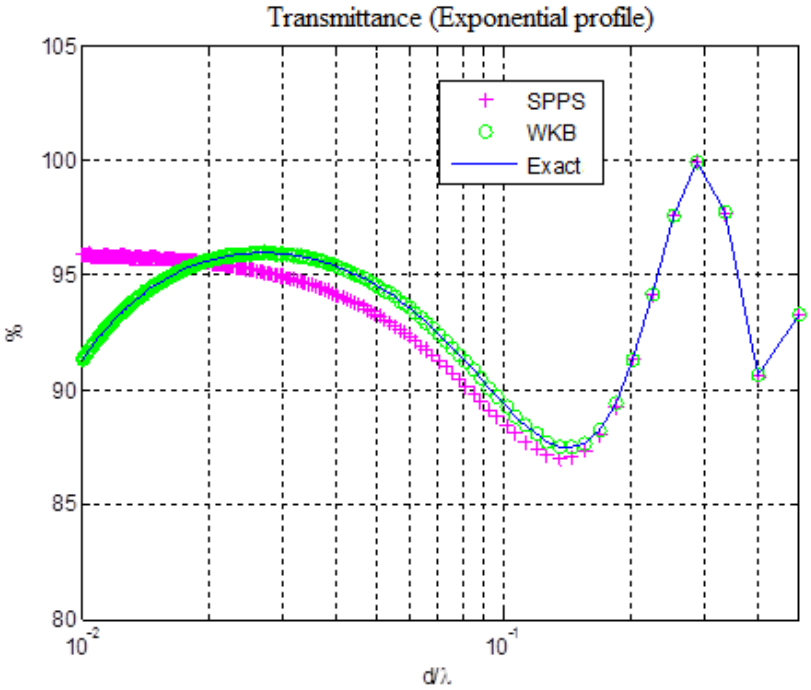

Figure 4. Transmittance for the exponential profile.

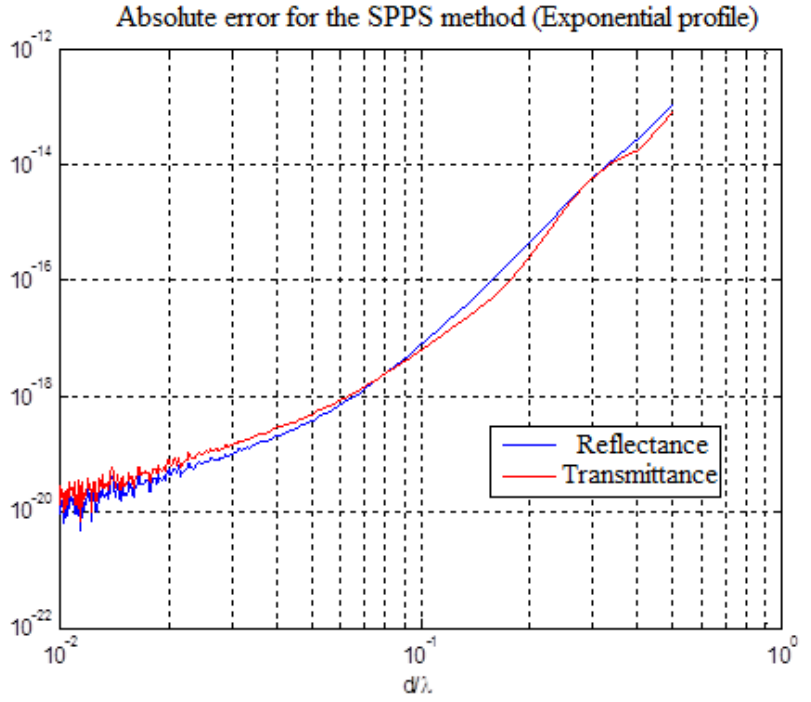

Figure 5. Absolute error for the exponential profile using the SPPS method.

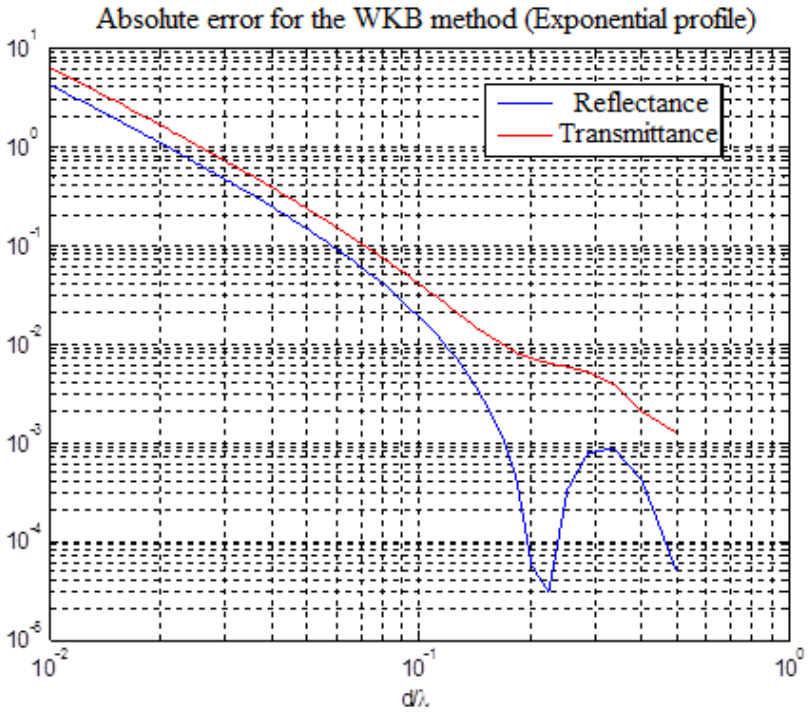

Figure 6. Absolute error for the exponential profile using the WKB method.

5.2 Calculation for profiles with turning points

In order to study profiles with turning points we proceeded to enter into the program that implements the WKB solution a profile $n(x)$ with a zero crossing. It is shown in Figure 7.

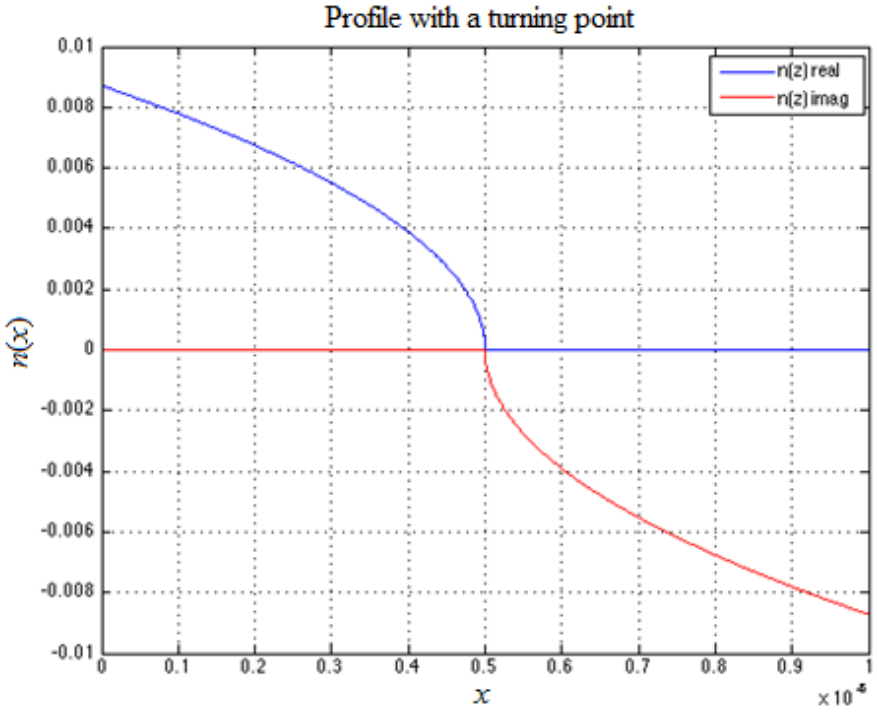

Figure 7. Profile for $n(x)$ with turning points with .

The percentage of the reflectance and transmittance was obtained with the modified WKB method for a profile with turning points replacing (33) and (34) in the expressions (5) and (6) and their values are shown in Figure 8.

The same profile with turning points was tested with the use of the SPPS method. The results are shown in Figure 9.

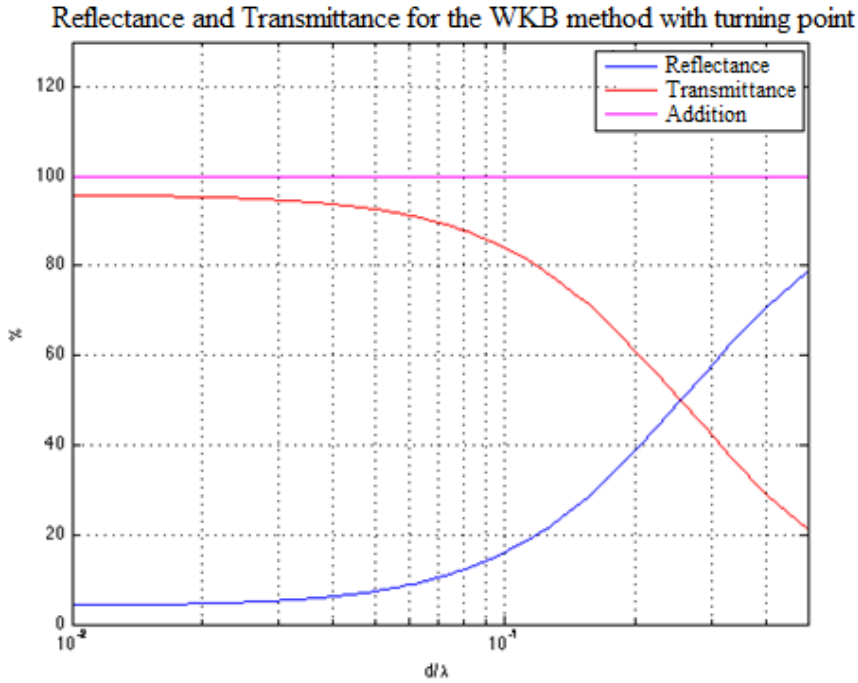

Figure 8. Reflectance and transmittance calculated with the modified WKB method for turning points.

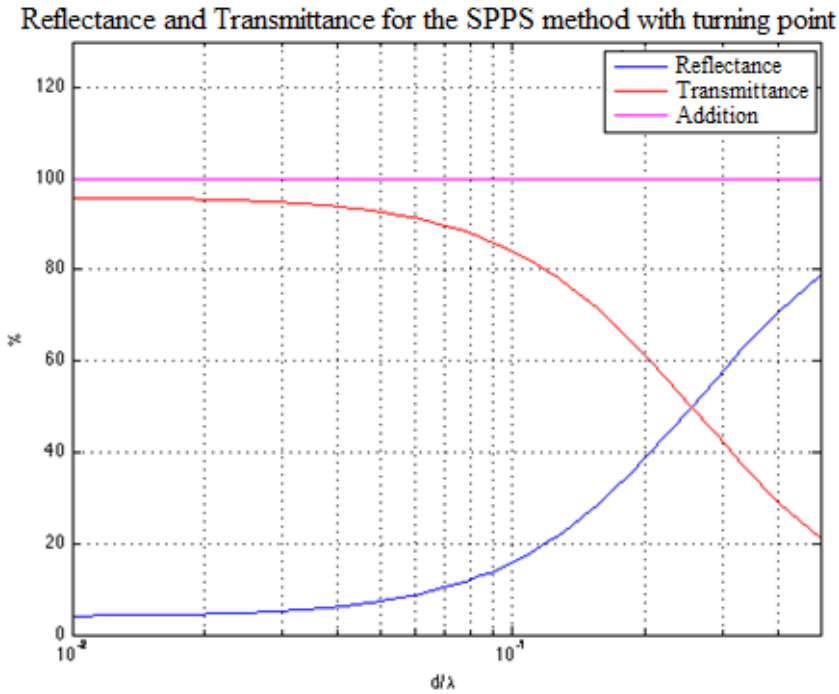

Figure 9. Reflectance and transmittance calculated with the modified SPPS method for turning points.

It is worth noting that for the SPPS method no changes at all are needed for its implementation (which implies another advantage of it). The WKB method should be specifically adjusted in order to work with profiles with turning points in which $q^2(x)$ is arbitrary.

6 CONCLUSIONS

Up to date there was no comparative analysis between the SPPS method and the WKB method, and it was presented in this paper. The numerical implementation of both methods does not represent any difficulty.

For the first time different profiles with turning points were analyzed using the SPPS method. Note that the SPPS method has very few limitations in terms of the profiles it can evaluate compared with the WKB method which requires a more thorough work. As an example, unlike the WKB method, no modifications are required in the case of the profile with turning points for the SPPS method.

Talking about computation time, the WKB method is much faster (2 seconds) compared with the SPPS method (11 minutes). The SPPS method's precision was much higher because in comparison with the exact solutions, in the worst case an accuracy of 10^{-13} was obtained. In contrast, we found that the WKB method in the best case could only deliver an accuracy of

.

Acknowledgements. R. Castillo would like to thank the support of the SIBE and EDI programs of the IPN as well as of the project SIP 20120438. V. Kravchenko acknowledges the support by Conacyt via the project 166141. H. Oviedo would like to thank the support of the SIBE and EDI programs of the IPN as well as of the project SIP 20120524.

REFERENCES

[1] de J. C. G. Sande, G. Leo and G. Assanto: Phase-matching engineering in birefringent AlGaAs waveguides for difference frequency generation. J. Lightwave Technol. **20**, 651–660, 2002.

[2] K. Sakoda: Optical properties of photonic crystals. Springer-Verlag, New York, 2001.

[3] J. R. Wait: Electromagnetic Waves in Stratified Media. IEEE Press, Piscataway, NJ, 1996.

[4] J. Sandoval: Biología, Agricultura, Producción: aportes de la Radiometría. Conference-Colloquium, Universidad de Alicante, Alicante, Spain, 2007.

[5] A. Ishimaru: Electromagnetic Wave Propagation, Radiation, and Scattering. Prentice Hall, Englewood Cliffs, NJ, 1991.

[6] M. Chamanzar, K. Mehrany and B. Rashidian. Legendre polynomial expansion for analysis of linear one-dimensional inhomogeneous optical structures and photonic crystals. J. Opt. Soc. Am. B, vol. **23**, No. 5, 969-977, 2006.

[7] C. C. Katsidis and D. I. Siapkas: General Transfer-Matrix Method for Optical Multilayer Systems with Coherent, Partially Coherent, and Incoherent Interference. Appl. Opt. **41**, 3978–3987, 2002.

[8] J. B. Pendry and A. MacKinnon: Calculation of photon dispersion relations. Phys. Rev. Lett. **69**, 2772–2775, 1992.

[9] A. N. Furs and T. A. Alexeeva: Reflection and transmission of weakly inhomogeneous anisotropic and bianisotropic layers calculated by perturbation method. J. Phys. A: Math. Theor. **41** no. 6, 2008.
[10] M. Hébert and R. D. Hersch: Reflectance and transmittance model for recto-verso halftone prints. J. Opt. Soc. Am. A, **23**, No. 10, 2415–2432, 2006.
[11] D. Myers: ASTM WK29032 Standard draft under development - New Test Method for Solar Absorptance, Reflectance, and Transmittance of Materials Using Integrating Spheresres, 2010.
[12] E. Nichelatti and R. M. Montereali: Optical reflectance and transmittance of a multilayer coating affected by refractive-index inhomogeneity, interface roughness, and thickness wedge. J. of Non-crystalline Solids, **355**, no. 18, 1115–1118, 2009.
[13] J. A. Pradeep and P. Agarwal: Determination of thickness, refractive index, and spectral scattering of an inhomogeneous thin film with rough interfaces. J. Appl. Phys. **108**, no. 4, 2010.
[14] C. Thompson and B. L. Weiss: Modal characteristics of graded multilayer optical waveguides. J. Lightwave Technol. **14**, 849–900, 1996.
[15] V. V. Kravchenko: A representation for solutions of the Sturm–Liouville equation. Complex Var. Elliptic Equ. **53**, 775–89, 2008.
[16] V. V. Kravchenko and R. M. Porter: Spectral parameter power series for Sturm–Liouville problems. Math. Methods Appl. Sci, **33**, issue 4, 459–468, 2010.
[17] V. V. Kravchenko: Applied pseudoanalytic function theory. Birkhauser, Basel, 2009.
[18] R. Castillo-Pérez, K. V. Khmelnytskaya, V. V. Kravchenko and H. Oviedo-Galdeano: Efficient calculation of the reflectance and transmittance of finite inhomogeneous layers. J. Opt. A: Pure Appl. Opt. **11**, 2009.
[19] H. M. Campos, R. Castillo-Pérez and V. V. Kravchenko: Construction and application of Bergman-type reproducing kernels for boundary and eigenvalue problems in the plane. Complex Variables and Elliptic Equations, published online, 2011.
[20] R. Castillo-Pérez, V. V. Kravchenko, H. Oviedo-Galdeano and V. Rabinovich: Dispersion equation and eigenvalues for quantum wells using spectral parameter power series. Journal of Mathematical Physics **52**, no. 4, 2011.
[21] R. Castillo-Pérez, V. V. Kravchenko and R. Reséndiz-Vázquez: Solution of boundary and eigenvalue problems for second order elliptic operators in the plane using pseudoanalytic formal powers. Math. Meth. Appl. Sci. **34**, no. 4, 455–468, 2011.
[22] H. Weyl: Über gewöhnliche Differentialgleichungen mit Singularitäten und die zugehörigen Entwicklungen willkürlicher Funktionen. Math. Ann. **68** 220–69, 1910.
[23] S. F. Monaco: Reflectance of an inhomogeneous thin film. J. Opt. Soc. Am. **51**, no. 3 280–282, 1961.
[24] P. Yeh: Optical Waves in Layered Media, Wiley & Sons, 2005.

19th International Conference on the Application of Computer
Science and Mathematics in Architecture and Civil Engineering
K. Gürlebeck, T. Lahmer and F. Werner (eds.)
Weimar, Germany, 04–06 July 2012

INFLUENCE OF DIFFERENT DATA TYPES FOR THE ESTIMATION OF HYDROMECHANICAL PARAMETERS FOR A WATER RETAINING DAM USING SYNTHETIC DATA

José G. De Aguinaga

Research Training Group 1462, Bauhaus-Universität Weimar
Berkaer Str. 9, 99423 Weimar, Germany
E-mail: jose.de.aguinaga@uni-weimar.de

Keywords: Sensitivity analysis, Parameter identification, Particle Swarm Optimization, Embankment.

Abstract. *The present research analyses the error on prediction obtained under different data availability scenarios to determine which measurements contribute to an improvement of model prognosis and which not.*

A fully coupled 2D hydromechanical model of a water retaining dam is taken as an example. Here, the mean effective stress in the porous skeleton is reduced due to an increase in pore water pressure under drawdown conditions.

Relevant model parameters are ranked by scaled sensitivities, Particle Swarm Optimization is applied to determine the optimal parameter values and model validation is performed to determine the magnitude of error forecast. We compare the predictions of the optimized models with results from a forward run of the reference model to obtain actual prediction errors.

The analyses presented here were performed to 31 data sets of 100 observations of varying data types. Calibrating with multiple information types instead of only one sort, brings better calibration results and improvement in model prognosis. However, when using several types of information the number of observations have to be increased to be able to cover a representative part of the model domain; otherwise a compromise between data availability and domain coverage prove best.

Which type of information for calibration contributes to the best prognoses, could not be determined in advance. For the error in model prognosis does not depends on the error in calibration, but on the parameter error, which unfortunately can not be determined in reality since we do not know its real value. Excellent calibration fits with parameters' values near the limits of reasonable physical values, provided the highest prognosis errors. While models which included excess pore pressure values for calibration provided the best prognosis, independent of the calibration fit.

1 INTRODUCTION

There has been a growing need to better understand model quality of numerical models in all branches of science. This issue has been recently addressed by [1, 2, 3, 4, 5] among others.

Models have grown in complexity and scope. In civil engineering, different models have to be coupled to simulate behavior of complex structures. Type, location and quality of measurements significantly impact model calibration and validation in these coupled models. This information either contributes to model quality by improving model forecast or to model uncertainty when neglecting important information. Models have to be parameterized; however, the values of the parameters are usually not known and have to be calibrated by inverse methods using observations [6]. This study focus on the influence of using different observation types for calibration on model prediction.

An advantage of calibrating with different observation types is to overcome systematic errors. Systematic errors are difficult to detect and cannot be analyzed statistically, because all of the data is off in the same direction, either too high or too low. The approach to overcome this is similar to that of investing in stokes of different branches, the risk of having the wrong numbers is disperse. Experience with the specific data type and measurement conditions are required to detect this errors. A way around this is to use different types of observations for calibration. If one set is wrong the others will push the values still in the right direction. By working with many data sets, even if you do not notice that one of them is wrong, the model could still be calibrated properly by the weight of other ”correct” data sets.

To analyze the effects of the observation types in the numerical model, the drawdown of an embankment will serve as illustrative example. This is a typical flow and deformation coupled problem in geotechnical engineering.

It is not the goal of this paper to find the best model description for hydromechanical models, but to quantify the error related to model calibration with different data type availability. The objective is to identify the data relationships which are necessary to correctly predict deformation, strain and excess pore pressure development within a coupled hydromechanical model.

2 METHODOLOGY

A reference model of a water retaining dam is generated to assess the impact of data availability to model error prognosis. Such a model provides different types of synthetic measurements, in this case, under slow drawdown conditions. The same model can be then, calibrated to all possible combinations of these measurement sets. Finally, the models with the optimized sets of parameters can be validated under rapid drawdown conditions and the prognosis error be compared.

With the reference model we create a total of five different data sets: horizontal and vertical deformation, horizontal and vertical strain and excess pore pressure. Based on these sets we generate 31 combinations ($2^{5\ \text{data types}}$ - 1 = 31 data sets) of equal number of observations but different type of data. In order to determine the effect of ”data type” in model forecast, we calibrate the more important parameters to the different 31 data sets using the same model which generated the data. This is necessary to avoid external influences other than data type, and compare their forecasts to the reference model.

Before calibration, a sensitivity analysis is performed to determine the most important parameters of the model. The optimal parameter values are identified with Particle Swarm Op-

timization on a surrogate model. Finally, the calibrated models are validated under a rapid drawdown scenario and the actual forecast errors are determined.

3 THEORY

Single scaled sensitivities ($ss_{i,j}$) are used to determine the most relevant parameters of the model. They provide the ratio of difference in model response at each *i* measuring point (y_i) to a small change in parameter value of every *j* parameter (p_j) where *i,j* $\in \mathbb{N}$. They are calculated as follow [7]:

$$ss_{i,j} = \frac{\partial y_i}{\partial p_j} p_j \tag{1}$$

In matrix form the scaled sensitivity matrix (SS) can be calculated as

$$\mathrm{SS} = \frac{\partial \mathrm{y}}{\partial \mathrm{p}} \mathrm{p} \tag{2}$$

where y is the calculated model response vector $\{y_1, y_2, ..., y_i\}$ and p is the model parameter vector $\{p_1, p_2, ..., p_j\}$. The partial derivatives are approximated by forward finite difference:

$$\frac{\partial \mathrm{y}}{\partial \mathrm{p}} \approx \frac{\mathrm{y(p} + \Delta \mathrm{p)} - \mathrm{y(p)}}{\Delta \mathrm{p}} \tag{3}$$

The resulting sensitivities are ranked calculating the variance-covariance matrix, $(\mathrm{SS^T SS})^{-1}$, which is the inverted product of the transposed scaled sensitivity matrix times itself. The smaller the value of the respective parameter in the main diagonal of the variance covariance matrix, the more influential the parameter is.

The divergence between model response and reference measured values is quantified by the objective function as follows:

$$F(\mathrm{p}) = \sqrt{\sum_{i=1}^{n} \frac{(y_{i,meas} - y_i(p_1, p_2, ..., p_n)_{calc})^2}{\sum_{j=1}^{n} y_{i,meas}^2} w_i} \tag{4}$$

where $F(\mathrm{p})$ is the average error sum, $i = 1, 2, ..., n$ counts each measurement of a time series, and w is a weighting factor, in this case equal to one. In $F(\mathrm{p})$ the absolute error of all observation types is sumed and then squared to get an average. The objective funtion sums unitless values. This is achieved for each type of data by norming the squared residuals of a given type at each measuring point, by the squared sum of the measurements at the given point.

An automated calibration is performed with Particle Swarm Optimization [8] using the following surrogate model:

$$y(\mathrm{p})_{calc} = \hat{y}(\mathrm{p}, \beta) + \hat{\epsilon} \tag{5}$$

by this means the numerical model is approximated with a fully quadratic function, $\hat{y}(\mathrm{p}, \beta)$, for each time step [9]. Where β are the coefficients of the fully quadratic approximation and $\hat{\epsilon}$ is the error between numerical and surrogate model.

During optimization the sum of the objective function for each measurement series is minimized:

$$F_{total}(\mathrm{p}) = \frac{1}{m}\sum_{j=1}^{m} F_j(\mathrm{p}) \rightarrow min. \tag{6}$$

where m stands for the amount of test series.

4 ILLUSTRATIVE EXAMPLE: WATER RETAINING DAM

A numerical model of a water retaining dam under drawdown conditions is used to illustrate the data availability influence on error prognosis of coupled numerical models in constructive civil engineering. The simulations were performed with PLAXIS 2D [10], a commercial Finite Element Program.

4.1 Geometry and boundary conditions

The earth dam is of trapezoidal form (Figure 1), 30 m high, trapezoid upper side is only 5 m long while the bottom side is 172.5 m long, from which 20 m correspond to the core. The underline block is 260 m long and also 30 m height. The extension of this block was conceived large enough to avoid effects of the boundary conditions inside the dam.

The mesh was constructed with 6-node triangular elements refined on the embankment itself and consists of around 500 elements and ca. 1100 nodes. On Figure 1 it is also marked the initial water level at 25 m (straight line) and the final water level at 5 m (dashed line).

Furthermore, the boundary condition at the bottom of the rectangular block is of full fixity, no deformation in horizontal or vertical direction allowed. At the sides just vertical deformation is allowed while the entire upper boundary is a free surface with a time dependent water level.

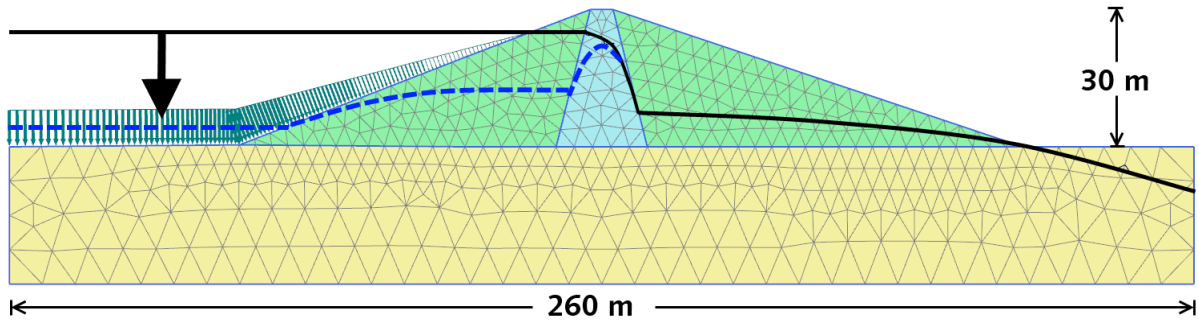

Figure 1: Mesh of water retaining dam with core (trapezoid in the center), fill (lateral triangles) and subsoil (rectangular basement), showing schematic drawdown and water pressure distribution

4.2 Material model

The embankment has three distinctive parts of different materials which have to be parameterized: 1) an almost impermeable clay core to prevent flow through it; 2) the fill, normally constructed of local material to protect the core from erosion and forces applied by the water; and 3) the subsoil which is the foundation in which the dam is built on.

For all three soil materials, the Mohr-Coloumb model (MC) is used to represent the elastic-plastic soil behavior. MC is suitable to analyze the stability of slopes and embankments [11].

The hydraulic model is parameterized using the Hypres data set available in PLAXIS with Van Genuchten parameterization. This parameterization is of coarse subsoil type for fill and subsoil material and of very fine type for the core.

The values of the parameters are given in Table 1 and are synthetic since they were not determined from an existing object.

Table 1: Soil parameter values for the three different materials

Soil parameters		Core	Fill	Subsoil
		Undrained	Drained	Drained
Saturated soil unit weight	γ_{unsat} [kN/m^3]	16	16	17
Unsaturated soil unit weight	γ_{sat} [kN/m^3]	18	20	21
Shear Modulus	G [kN/m^2]	555.60	7518.80	19230.77
Poisson's ratio	ν' [-]	0.35	0.33	0.30
Cohesion	C'_{ref} [kN/m^2]	5	5	1
Friction angle	φ' [°]	25	31	35
Dilatancy angle	ψ [°]	0	1	5
Hydraulic conductivity (isotropic)	k_{xy} [m/d]	0.0001	0.25	0.01

4.3 Simulation

The hydraulics in PLAXIS are simulated with the Darcy law for fully saturated soil and with the Richards equation which describes unsaturated groundwater flow. They are fully coupled to the mechanical model using Biot's theory of consolidation. This formulation contains a coupled hydromechanical behaviour represented by both the equilibrium equation and the continuity equation of the water-soil mixture [12].

Calculations are performed in classical mode, which uses Terzaghi's definition of stress. In a first phase, the initial stress due to soil and material weight is calculated, as well as the initial pore water pressure under undrained behaviour and steady state groundwater flow conditions.

To the previous Gravity loading phase follows a Nil-Step phase. This phase improves the accuracy of the equilibrium stress field with a plastic drained long term calculation in which no additional loading is applied [13]. Finally, the effect of the drawdown can be simulated as a consolidation phase with transient groundwater flow in which the dam is submitted to a linear drawdown of 40 cm/d.

5 RESULTS AND CONCLUSIONS

5.1 Sensitivities

The Parameters of interest for the present study are those of the soft soil core, specially the isotropic hydraulic conductivity (k_{xy}), two parameters from Hooke's law: shear modulus (G) and Poisson's ratio (ν') and also the parameter to describe the flow rule, the dilatancy angle (ψ). Since we are working on the range of values where the dam is stable and cannot sample data about its collapse, the parameters to define failure are not of interest for this study, these are the friction angle and cohesion.

Eight nodes and five stress points within the core and the fill (Figure 2) were selected for

measurements of five different types of data: horizontal and vertical deformation (u_x, u_y), horizontal and vertical strain ($\varepsilon_{xx}, \varepsilon_{yy}$) and excess pore pressure (*EPP*)

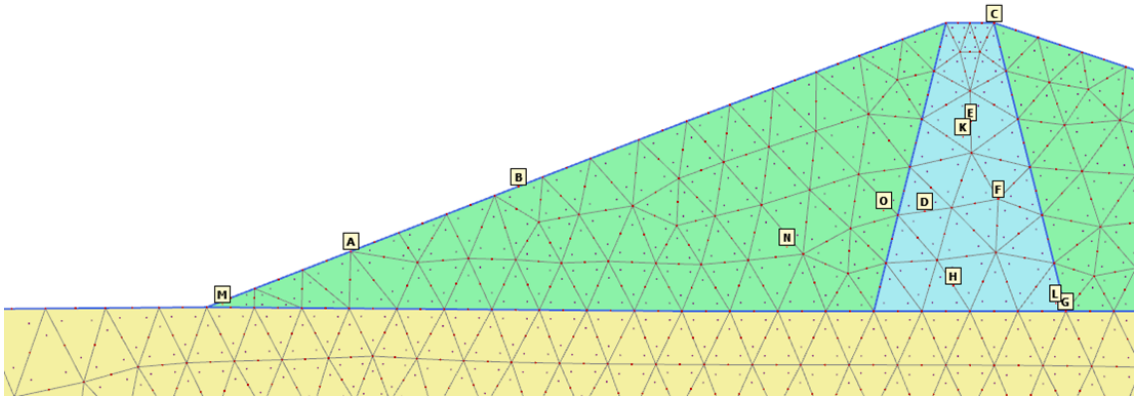

Figure 2: Observation points at the embankment

The Sensitivities were calculated with respect to the five different types of model answers at those observation points using the equations presented on Section 3. The resulting variance-covariance matrix is shown on Table 2. The smaller the value on the diagonal, the more sensitive the respective parameter is.

Table 2: Variance-Covariance Matrix $(SS^TSS)^{-1}$ of the most relevant parameters of the impermeable core

		G	ν'	ψ	$\lg(k_{xy})$	
G	[	$\mathbf{4 \cdot 10^{-4}}$	$-8 \cdot 10^{-5}$	$2 \cdot 10^{-3}$	$-3 \cdot 10^{-6}$	]
ν'	[		$\mathbf{7 \cdot 10^{-5}}$	$7 \cdot 10^{-5}$	$-1 \cdot 10^{-7}$	]
ψ	[			$\mathbf{1 \cdot 10^{-1}}$	$-1 \cdot 10^{-6}$	]
$\lg(k_{xy})$	[		symmetric		$\mathbf{6 \cdot 10^{-7}}$	]

The more influential parameter is k_{xy} from the hydraulic model followed by G and ν' from Hooke's law of the material model.

5.2 Calibration

The four previous parameters, which were sensitive to a set of model answers of diverse type in 13 different points, were calibrated to different data type availability. 31 data sets, shown in Table 3, each with 100 observations were generated from the combinations of $u_x, u_y, \varepsilon_{xx}, \varepsilon_{yy}$ and *EPP*.

The resulting combinations have a constant number of observations and vary in data type. This generates a tradeoff between data type coverage and spatial domain coverage. The spatial coverage of the first data set, considering all data types is shown at the left side of Figure 3. Measured in nodes A and B are u_x and u_y, *EPP* in nodes B and C, and $\varepsilon_{xx}, \varepsilon_{yy}$ in the stress points K and L. In contrast, at the right side of Figure 3, data set 31, which uses just *EPP* observations, shows a good spatial coverage of *EPP* in the core. As data type increases, spatial coverage decreases and vice versa.

The model was calibrated to the 31 data sets with an automated algorithm using the Particle Swarm Optimization method on a surrogate model. The resulting deviations to the respective data sets are also given on Table 3 as average error sum in percent.

Table 3: Combinations of data type availability for calibration purpose using 100 observations; number of points per data type (10 measurements in time per point) and resulting average error sum [%]

	1	2	3	4	5	6	7	8	9	10	11	12	13	14	15	16
u_x	2	3	2	2	3		3	3	3	4	3	3				
u_y	2	2	2	2		3	3	3	3				4	3	3	
ε_{xx}	2	3	3		2	2	4			3	3		3	3		3
ε_{yy}	2	2		3	2	2		4		3		3	3		3	3
EPP	2		3	3	3	3			4		4	4		4	4	4
Error	0.8	0.2	0.6	0.9	0.9	1.0	0.1	0.1	0.9	0.3	0.9	0.3	0.0	1.1	0.7	1.4

	17	18	19	20	21	22	23	24	25	26	27	28	29	30	31
u_x	5	5	5	5							10				
u_y	5				5	5	5					10			
ε_{xx}		5			5			5	5				10		
ε_{yy}			5			5		5		5				10	
EPP				5			5		5	5					10
Error	0.2	0.0	0.2	0.1	0.1	0.6	0.7	0.2	1.1	1.7	0.1	0.2	0.9	0.7	1.5

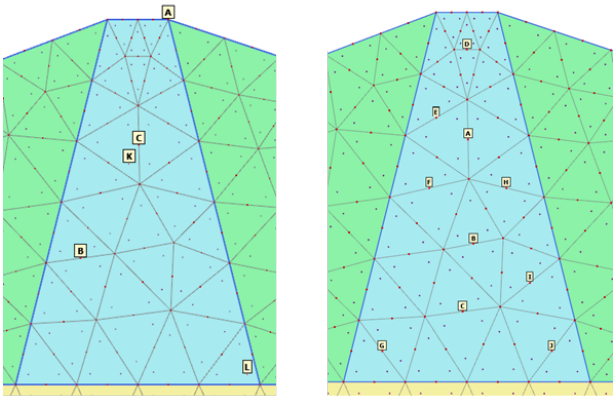

Figure 3: Left: Observation points for data set 1, ; Right: Observation points for data set 31

The average error sum for all different calibrations is small, lower than 2 %. After sorting the average error three classes were identified, as shown in Figure 4. These are, a first class with excellent fit, up to 0.3 % average error (green oval), a second class with good fits on the range 0.5 - 1.2 % average error (orange oval) and a third class with relative bad fits from 1.4 to 1.7 % average error (red oval). Most of the calibrations fall within the first two classes.

Furthermore, by sorting Figure 4 additionally by number of data types, see Figure 5, we can determine that the best results are obtained by using 1 to 3 data types, however, also the worst values. The choice of data type makes then the difference between best or worst case. It must be noticed that most of the best calibration results can be attained with 2 and 3 data types. This reflects the tradeoff between using different data types for calibration vs. the spatial coverage of each single data type. For our case with 100 observations, a set with two or three data types, might allow for variety in information for calibration while maintaining some representative spatial coverage of the domain.

Every data type is used 16 times in different combinations. The calibrations using combinations of data sets with u_x show the best fits, see Figure 6. In contrast, the worst fits are obtained

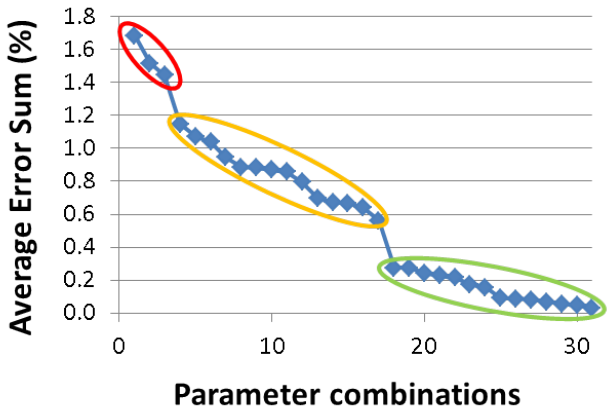

Figure 4: Sorted average error sum of calibration results for different parameter combinations

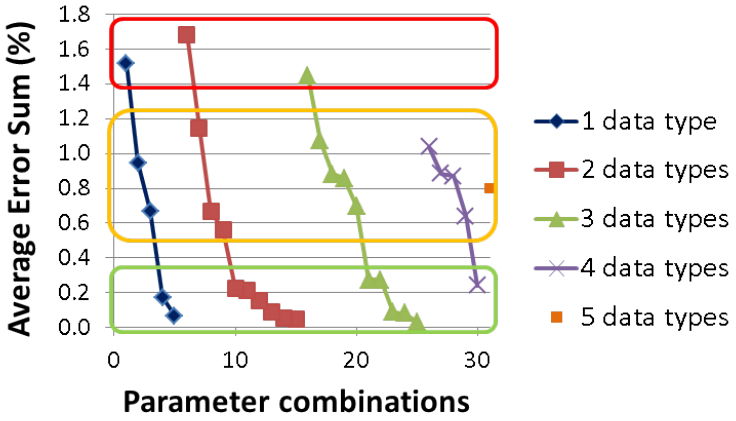

Figure 5: Sorted average error sum of calibration results by number of data types used

when *EPP* is considered.

5.3 Validation

The model was validated for each of the resulting optimal parameter values. For this, 90 observations were taken on the 5 days period in which the water table decreased at a linear rate of 4 m per day.

The average error sums of the validations were lower than those obtained during calibration. However, the average error sums of both graphs are not comparable in magnitude, since the validation values were measured at different points, at different times, with fewer measurements and what is more important with other boundary conditions (under rapid falling water table). What can be compared are the tendencies to analyze if there are correlations between them.

The maximum prediction average error sum was around 1 %, see Figure 7. Most of the validation results fall within the range 0.3 and 0.7 % average error sum.

When the average error sum of the prognosis is sorted also by number of data types, see Figure 8 we see a similar trend as with the calibration results. The best and worst fits are obtained with 2 or 3 types of data.

Which parameters are responsible for the best and worst cases is appreciable in Figure 9,

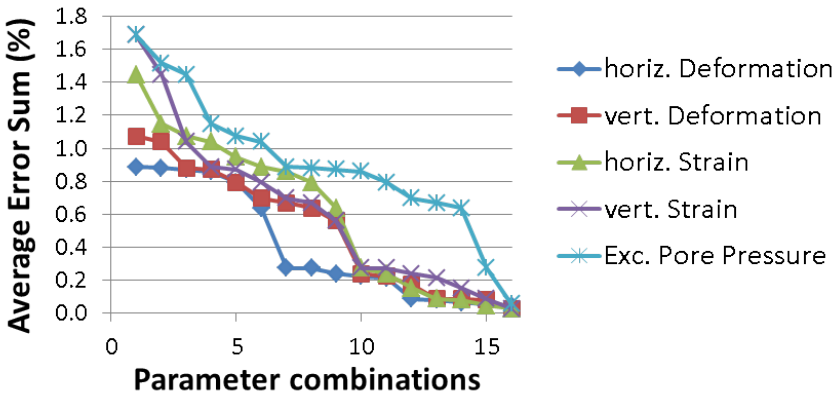

Figure 6: Sorted average error sum of calibration results by data type

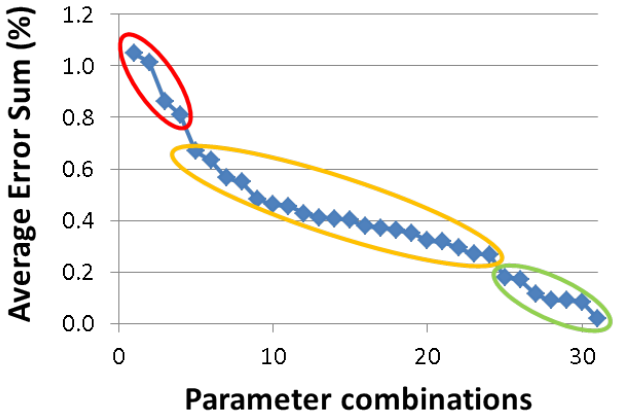

Figure 7: Sorted average error sum of validation results for different parameter combinations

where the results are sorted by type of observation used for calibration. Surprisingly the worst prognosis were made by considering deformation or strain observations during calibration. In contrast, a guarantee for good prognosis seemed to be attained by calibrating with *EPP* information. This is the opposite as deducted from Figure 6, in which calibrating with deformation while excluding *EPP* information is recommended to obtain best calibration results.

By plotting the sorted calibration results against the actual errors of the prognosis (left side of Figure 10), we observe that a decrease in calibration error does not improve the prognosis accuracy. The prognosis error seems to be normal distributed around 0.4 % average error sum. However, for the case of excellent calibration fits with average error sums lower than 0.3 % the validation error becomes more variable, and the parameter set is susceptible of giving prognosis with higher errors.

The right side of Figure 10 shows the corresponding parameter error of the optimized parameter sets at the left side of the Figure. By very small calibration errors, the optimized parameter values can be driven to values close to the limit of reasonable physical values, as it was here the case for several combinations for k_{xy}, which is the most sensitive parameter in this model.

5.4 Conclusion

The fit obtained by the automated Particle Swarm Optimization calibration was very good, with an average error sum at all cases lower than 2 %. However, the error in prognosis does not

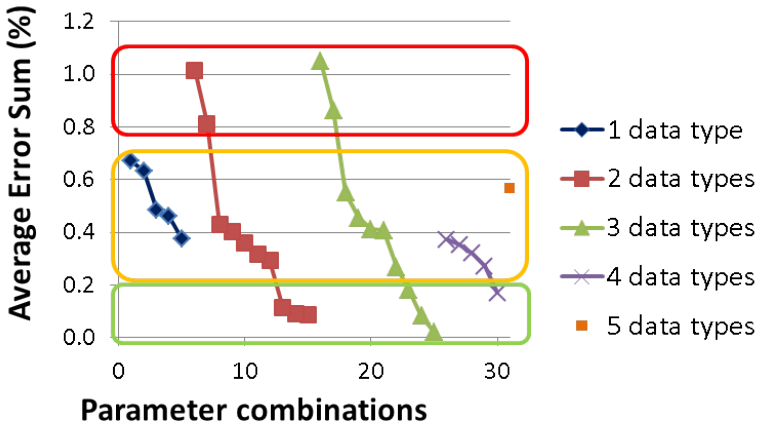

Figure 8: Sorted average error sum of validation results by number of data types used

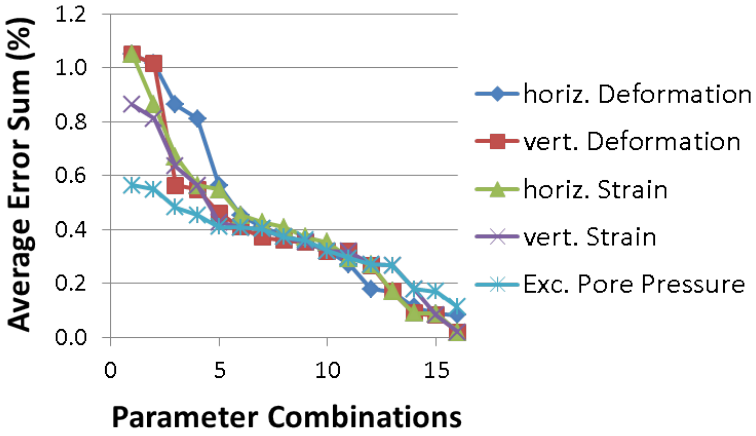

Figure 9: Sorted average error sum of validation results by data type

correlate with the calibration effort, since when calibration error decreases, validation error does not. Excellent calibration values, interestingly increased the variation in prognosis error. These calibrations, with very small errors can drive the value of the optimized parameters to the limit of reasonable physical values, as it is here the case. The error of the prognosis depends on the parameter error. Unfortunately, the parameter error can not be determined since we normally do not know the real value of the parameter.

Surprisingly, the model calibrated to all five different types did not provide the best results. This could be explained by the reduction of the spatial coverage. Using 2 or 3 types of information, both, best and worst calibrations were obtained. Depending on which data sets are considered, either the best or the worst results are obtained. The best calibrations usually were obtained considering u_x while the worst calibrations included a data set of *EPP*. The opposite was the case for the prognosis. Good prognosis were attained with the data sets which considered *EPP* for calibration, while the worst prognosis were given by those considering u_x for calibration. The information that contributes to the best prognoses, could not be determined in advance. Information diversity for calibration and a good coverage of model domain is important for a good prognosis. In order to obtain better prognosis it is preferable to accept higher calibration errors and obtain optimized parameter values which are more likely to be expected

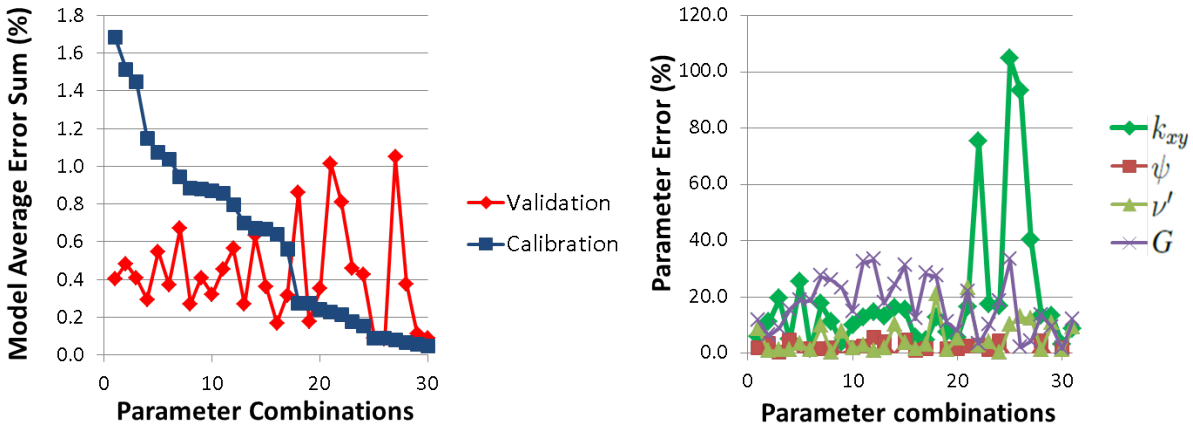

Figure 10: Left: sorted average error sum of calibration results with corresponding validation error. Right: Corresponding parameter errors

than excellent calibration fits with unreasonable parameter values. This could be implemented in an automated optimization algorithm by using the expected value of the parameters as prior information for calibration [14].

6 ACKNOWLEDGMENTS

The author would like to acknowledge the support of Dr. Martin Zimmerer for allowing the use of his optimization code VARO^{2}PT, which interacts with PLAXIS and the support by the German Research Council (DFG) through the Research Training Group 1462.

REFERENCES

[1] S. Nishat, Y. Guo and B. W. Baetz, Relative Importance of Input Parameters in the Modeling of Soil Moisture Dynamics of Small Urban Areas. *Journal of Hydrologic Engineering*. **17** (3), 2012. ISSN 1084-0699/2012/3-359-367.

[2] H. Keitel and A. Dimmig-Osburg, Uncertainty and sensitivity analysis of creep models for uncorrelated and correlated input parameters. *Engineering Structures*, 2010. doi:10.1016/j.engstruct.2010.08.020

[3] T. Most, Estimating uncertainties from inaccurate measurement data using maximum entropy. K. Gürlebeck and C. Könke eds. *18th International Conference on the Application of Computer Science and Mathematics in Architecture and Civil Engineering*, Weimar, Germany, 07-09 July 2009.

[4] L. J. Lucas, H. Owhadi and M. Ortiz, Rigorous verification, validation, uncertainty quantification and certification. *Comput. Methods Appl. Mech. Engrg.*, **197**, 4591–4609, 2008. doi:10.1016/j.cma.2008.06.008.

[5] I. Babuška, F. Nobile and R. Tempone, Reliability of Computational Science. *Numerical Methods for Partial Differential Equations*, **23** (4), 753–784, 2007. doi: 10.1002/num.20263.

[6] T. Lahmer, Crack identification in hydro-mechanical systems with applications to gravity water dams. *Journal of Inverse Problems in Science and Engineering*, **18** (8), 1083–1101, 2010. doi:10.1080/17415977.2010.500495.

[7] M. M. Zimmerer, Identifikation konstitutiver Parameter von weichen feinkörnigen Böden, Beitrag zum Konsolidationsverhalten von Ton. Dissertation, Bauhaus-Universität Weimar, *Schriftenreihe des DFG Graduiertenkollegs 1462 Modellqualitäten*, **1**, 2010.

[8] J. Kennedy, R. Eberhard, Particle Swarm Optimization. *Proc. IEEE International Conference on Neuronal Networks*, 1942–1948, Perth, Australia, 27 Nov. - 01 Dec. 1995.

[9] M. M. Zimmerer, T. Schanz, Y.Lins and V. Bettzieche, Numerical Analysis of Water Reservoir Dam - Prediction of Long Term Performance of Versetal Dam (Germany). *79th ICOLD Annual Meeting*, Lucerne, Switzerland, May 29 - June 3, 2011.

[10] R. B. J. Brinkgreve, W. M. Swolfs, E. Engin, D. Waterman, A. Chesaru, P. G. Bonnier and V. Galavi, PLAXIS 2D 2010 (Version 2010.01). Delft, Netherlands: PLAXIS b.v., 1997-2010. Available at http://www.plaxis.nl

[11] K. S. Ti, B. B. K. Huat, J.Noorzaei, M. S. Jaafar, and G. S. Sew, A Review of Basic Soil Constitutive Models for Geotechnical Application. *Electronic Journal of Geotechnical Engineering*, **14** (J), 1–18, 2010.

[12] V. Galavi, Groundwater flow, fully coupled flow deformation and undrained analyses in PLAXIS 2D and 3D. Internal Report, Delft, Netherlands: PLAXIS b.v. Research Department, January 2010. Available at: http://kb.plaxis.nl/author/v-galavi

[13] PLAXIS b.v., PLAXIS Scientific Manual 2010. Delft, Netherlands: PLAXIS b.v., 2010. Available at http://www.plaxis.nl/shop/135/info/manuals/

[14] A.J. Jakeman, R.A. Letcher and J.P. Norton, Ten iterative steps in development and evaluation of environmental models. *Environmental Modelling & Software*, **21** (5), 602–614, May 2006. doi: 10.1016/j.envsoft.2006.01.004

19th International Conference on the Application of Computer
Science and Mathematics in Architecture and Civil Engineering
K. Gürlebeck, T. Lahmer and F. Werner (eds.)
Weimar, Germany, 04–06 July 2012

THE APPLICATION OF POD CURVES TO DAMAGE DETECTION BASED ON PARTIAL MODELS- A NUMERICAL AND EXPERIMENTAL STUDY

Maher Deeb*, **Volkmar Zabel**

**Bauhaus-Universität Weimar, Graduiertenkolleg GRK 1462 "Modellqualitäten"*
Berkaer Str. 9, 99423 Weimar, Deutschland
E-mail: maher.deeb@uni-weimar.de

Keywords: Partial Models, Global Models, Model Quality Assessment, POD, POD Curves, Numerical and Experimental.

Abstract. *Non-destructive techniques for damage detection became the focus of engineering interests in the last few years. However, applying these techniques to large complex structures like civil engineering buildings still has some limitations since these types of structures are unique and the methodologies often need a large number of specimens for reliable results. For this reason, cost and time can greatly influence the final results.*
***M**odel- **A**ssisted **P**robability Of **D**etection (MAPOD) has taken its place among the ranks of damage identification techniques, especially with advances in computer capacity and modeling tools. Nevertheless, the essential condition for a successful MAPOD is having a reliable model in advance. This condition is opening the door for model assessment and model quality problems.*
*In this work, an approach is proposed that uses Partial Models (PM) to compute the **P**robability **O**f damage **D**etection (POD). A simply supported beam, that can be structurally modified and tested under laboratory conditions, is taken as an example. The study includes both experimental and numerical investigations, the application of vibration-based damage detection approaches and a comparison of the results obtained based on tests and simulations.*
Eventually, a proposal for a methodology to assess the reliability and the robustness of the models is given.

1 INTRODUCTION

The main objective of damage identification is to detect the damage in the early stages, so as to reduce the risks of stability failure and serviceability issues. Since civil engineering structures possess characteristics that make them different than systems in other engineering fields, this goal is not easily attained. In most cases, given that each structure is unique, the results from a certain method applied to one structure are not valid for other structures. These structures also cannot be moved or isolated in order to perform ideal damage detection tests, such as those conducted in the laboratory. In addition, the detection tests should be conducted while the structure is operational, making some areas of the structure inaccessible, and precluding anything other than non-destructive testing.

Although simulation tools have developed significantly in the last few years, the quality of models remains a serious problem that faces engineers. This is due to of different sources of uncertainty. In general, uncertainty can be classified as either: aleatoric or epistemic. The former one represents the randomness of the phenomenon and the second is related to lack of the knowledge and the data. This categorization helps deal with uncertainties in the proper way e.g. to reduce the epistemic uncertainty, further and deeper studies or more data collection is needed. However, the aleatoric uncertainty can be included in the model stochastically.

In the case of damage identification, uncertainty included in specimens and uncertainty in experiments are the two main components of total uncertainty. Uncertainties related to specimens include dimensions, supporting conditions and loading conditions. Furthermore, noise because of sensors can be addressed as an uncertainty included in experiments.

In most cases, it is neither easy nor practical to give an absolute answer for appearance of damage in a structure. This is due to uncertainties. Furthermore, trying to eliminate the noise completely requires much time and efforts. Therefore, it is very important to define a minimum level of confidence which can be the balance between sufficient accuracy and required effort. Choosing a reliable confidence level can be done based on the acceptable risk criteria.

An overview of previous research, which focused on using statistical information for damage assessment in civil engineering structures using vibrational based inspection can be found in [1].However, only since 2004 has the MAPOD working group started to develop strategies to couple the physics-based and empirical understanding guided by draft protocols. This group was formed by the Air Force Research Laboratory, the FAA Technical Center and NASA. The motivations of a Model-Assisted Probability of Detection (MAPOD) approach are presented in [2]. It was mentioned that a wave of new inspection requirements is anticipated in the coming years to reduce the cost and time spent. The MAPOD approach was defined as an alternate approach which is sorely needed to reduce the amount of empirical tests. This approach depends on physics-based models to determine the POD. The POD is based on distributions of signal (from flaw of the same nominal size) and noise. These distributions are controlled by several factors that can be predicted by simulation tools such as MAPOD. However, empirical tests are still needed because many variabilities can not be described by well-understood physical phenomena. It is mentioned that the major goal of current activities is to codify methods that are less time/cost intensive than in MIL-HDBK-1823 (Nondestructive Evaluation System Reliability Assessment). The ideas and strategies to develop the MAPOD approach are introduced. In [3] the recent work and development as well as future work of the MAPOD working group are presented. In [4] a modified MAPOD approach is used to detect the damage in the case of an two-layer airframe structure. In [5] the MAPOD approach is applied to validate the reliability of an automated ultrasonic inspection used for crack detection at fastener holes in the lower wing

skins of F-111 aircraft. A transfer function method is used to predict the POD for an angle-beam ultrasonic inspection of cracks in fastener holes within a complex structure. The MAPOD for ultrasonic structural health monitoring SHM is discussed in [6] as an effective technique for monitoring fatigue-induced damage. The paper introduces the differences between the traditional POD approaches as used for non-destructive evaluation and for SHM. In [7] a new Model-Assisted probabilistic reliability assessment methodology is described. The feasibility of applying this approach to typical sensing methods found in SHM systems is discussed. The POD is used in [8] to assess vibration-based damage identification techniques using different types of indicators, which depend, in general, on mode shapes. In [9], a POD model is used with a reliability-based crack growth model to assess fatigue damage in bridges.

In this work, a simply supported beam, that can be modified and tested under laboratory conditions, is studied including both experimental and numerical investigations, (figure 1). It has a length of 3300 mm and a cross section of type IPE 80 and typical steel material properties. The beam is simply supported at 50 mm from each end. In order to perform non-destructive tests, the beam is backed up with plates of size $150 \times 46 \times 2.5\ mm^3$. The damage is simulated by removing one or more of these plates. Three damage cases are studied: case 1: one plate is removed near the middle of the beam; case 2: a plate is removed near the support of the beam; case 3 two plates are removed near the middle and a support of the beam. The work uses vibration-based method for damage detection. 16 accelerometers are used to record acceleration at the top of the beam.

2 PARTIAL MODELS

2.1 Structure Model

There are different possibilities to model the studied beam. It can be modeled using beam, shell or solid elements. This is dependent on the uncertainty types that one wants to include in these models. For example, in reality, supports are at the bottom of the cross section; however, in the case of using beam elements to simulate the beam, the supports are at the center of the cross section. Therefore, to include this uncertainty, a more sophisticated model is needed,(figure 2).

2.2 Damage Model

The types of damage that structures can suffer vary depending on different conditions e.g. the material, operation task, quality of construction, the effect of the surrounding environment, etc. For instance, in concrete structures damage can appear as a crack which can be harmful or harmless according to its position, type, propagation opportunity and also the type of structure itself which will be the final judge of the accepted tolerance e.g. crack tolerance for dams is more conservative than for normal buildings.

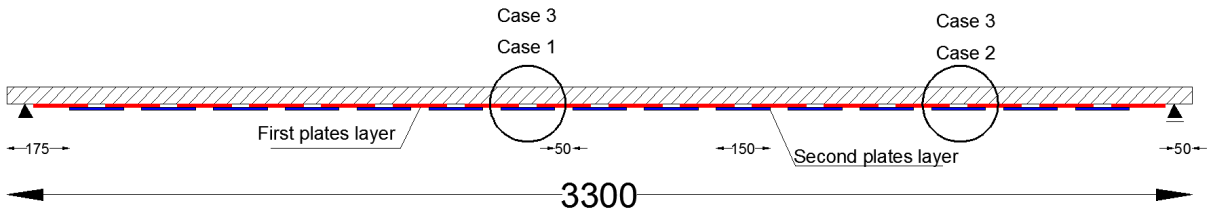

Figure 1: The studied beam sketch showing some dimensions and the distribution of the plates. Dimensions in mm

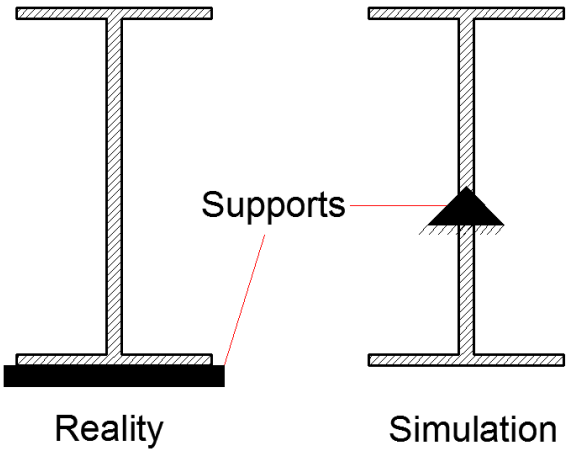

Figure 2: A cross section of the studied beam at place of the support, uncertainty because of support place in case of using beam elements to model the beam

Non-destructive techniques only allow non-destructive damage. In this example, the non-destructive damage will be represented by the removal of one or more plates, (figure 1). However, this damage model is not the real damage that should be detected in the structure.

Nevertheless, if the global model can be validated for different types of non-destructive damage at different locations with differing severities, this will produce a strong argument that the real damage would be represented correctly using this model. In this work, two types of real damage are used: decreasing the thickness of the bottom flange of the beam and E modulus degradation.

2.3 Indicator

In general, the data which is recorded from a damaged structure contains information about damage as well as noise from different sources of uncertainty. In order to extract this damage information, appropriate indicators are needed. In general, indicators are categorized according to the level of damage information that they can provide as following,[1]:

1- Level1: identification of damage;

2- Level2: level1 and the location of damage;

3- Level3: level2 and severity of damage;

4- Level4: level3 and prediction of the remaining service life.

The computational method of POD value is dependent on the level of information that indicators can provide. For instance, if the indicator shows damage in the correct location, it has truly detected damage. Conversely, if the indicator shows damage, but this damage is in the false location, it is only a false alarm and this damage has not been detected on the existing structure.

In general, two types of indicators can be used in the case of the vibration-based method. The first depends on the mode shapes and their derived features. The second is based on analyzing the signal directly e.g. stochastic subspace identification method (SSI). In this work, only the first type will be presented.

2.3.1 Indicators Based on Mode Shapes

This group of indicators utilizes post-processed data. In other words, the mode shapes should be calculated either by modal analysis or records analysis. After that, the mode shapes are processed to find if it is possible to distinguish between damage and noise. Three indicators are used: mode shapes, mode shape curvatures and model strain energy. The mode shape is calculated using equation (1)

$$Ind_j = (\phi_{0i}^2 - \phi_{ji}^2)^2 \tag{1}$$

where:
Ind: the indicator's value
j: the damage case
ϕ_{0i}: the mode shape i of non damaged beam
ϕ_{ji}: the mode shape i of the damaged beam case j

Mode shapes curvatures are calculated approximately by finding the second derivative of the mode shapes with respect to position. The model strain energy indicator is derived from the Euler-Bernoulli beam of length l as shown in equation (2)

$$U_i = \frac{1}{2}\int_0^l (EI)(\frac{d^2\phi_i}{dx^2})^2 dx \tag{2}$$

where:
U: the strain energy i: index of the mode shape
EI: the structure rigidity
ϕ_i is the mode shape number i

Other indicators can be found in the literature, such as Yuen functions, Dynamic Flexibility, etc...

2.3.2 Indicators Based Signal Analysis

This group of indicators utilizes pre-processed data. Stochastic subspace identification method (SSI) is an example for this type of indicator. The main advantages of this type of indicator are that they are more sensitive and present less data analysis uncertainty. However, the level of information that they provide is low.

2.4 Sensor Position

Since the indicators in this example depend on the quality of the mode shapes, mode shapes errors can be used as an objective function for the optimization process. The number of sensors used in these experiments is limited by availability in the laboratory and therefore 16 accelerometers are used. Since there are a limited number of accelerometers, the optimization process involves finding the best 16 nodes that will lead to a minimum value of the objective function,f, as represented by equation (3).

$$f = \|\phi_{133} - \phi_{16}\| \tag{3}$$

where:
ϕ_{133}: the mode shapes generated using the total number of nodes of the model
ϕ_{16}: the mode shapes generated using only 16 nodes

2.5 Excitation

An excitation partial model is used when the experiments are simulated. In this work, only impulse excitation is used. Since a force sensor is available in the lab, it was possible to determine the range of the force value and its duration.

2.6 Threshold

Another essential element in calculating POD value is threshold level. Generally, when the indicator value crosses the threshold, this is a sign the damage exists. This value should be chosen carefully since the POD will be calculated based on its value. In this work, threshold is taken as a percentage of the maximum value of the indicator. The following levels are chosen: 70%, 75%, 80%, 85%, 90% and 95%. Furthermore, threshold plays an important role in evaluating the robustness of the global model, as will be shown later.

3 PRINCIPLES OF SELECTION AND ASSESSMENT METHODOLOGY

Since a large number of partial models can be developed as shown above, the number of combinations or global models will be much larger. As a result, it is impractical to apply the assessment process to each global model, especially if the complexity increases meaning more computational time and higher computer efforts are required. Therefore, it is necessary to develop a strategy to selectively limit the number of models in order to increase the efficiency of model quality assessment.

3.1 Model Selection

In the case of damage identification, the number of partial models can be minimized based on POD value decomposition. The decomposition process can be completed by classifying the uncertainty's sources into different independent types. The idea behind the decomposition is that some sources of uncertainty are easy to estimate and to apply and others are too complicated. As a result, checking models for each independent type of uncertainty helps to reduce the amount of models each time. In the decomposition stage, the quality of the models is not assessed but rather the quality of coupling.

In this example, the calculation of POD is decomposed into two independent types. The first is caused by the uncertainty between the samples or specimens, POD_s, and the second is caused by the uncertainty included in experiments, POD_e. POD_s is calculated as the ratio between the number of samples that show damage and the total number of samples. POD_e is calculated as the ratio between the number of the experiments that show damage and the total number of experiments. The final POD value is computed by multiplying both POD components together.

3.2 Model Assessment

In general, reliability and robustness are used to assess the quality of studied global models. However, in case of no existing damage, the model should show low probability of detection otherwise the model is unreliable. Furthermore, the model is considered reliable if damage is detected early with a high probability of detection.

The global model is considered robust if the following conditions are satisfied: the POD increases when damage level increases and changing an input parameter by a small amount does not lead to failure or unacceptable variation of the outcomes.

4 NUMERICAL RESULTS

In the following sections, only a few results are presented in order to show the application of the methodology that is given in the previous section. Since uncertainty between samples is easier to estimate and POD_s is more quickly calculated in this case, all possible global models that can be created by coupling partial models are checked for POD_s. Consequently, only few coupled partial models or global models are needed to be checked for the POD_e and finally assess their quality based on POD curves.

4.1 POD_s of Non-destructive Damage

Figure(3) shows POD_s results of two global models. The vertical axis represents POD_s and the horizontal axis represents threshold level. Threshold level is computed as a percentage of the maximum value that is given by the indicator. Damage is detected when the value of the indicator coincides with damage over the threshold level at the damage location. At other locations, the indicator's value is under this threshold level. The colors represent the type of beam partial model which is used in this global model. Blue represents the beam elements model, red represents the shell elements model and green represents the solid elements model. The results show that the solid elements model is not suitable for this model combination since the POD_s value did not cross 50% in the best case. In addition, for the low threshold level, coupled partial models with the shell elements model of the beam had low POD_s values, which means that this global model is not robust. However, the beam elements model correlated best with the other partial models.

Although some coupled partial models produced poor results, the quality of the these partial models is not necessarily a factor. It just means that the combination(s) used resulted in poor data. New partial models could be developed to produce better results or one could select only those models that produced the best results, eliminating all others.

4.2 POD_e of Non-destructive Damage

Although it is not easy to determine all sources of uncertainty in the experiments and the POD_e requires more time to calculate, POD_s results minimized the amount of partial model combinations that need to be checked. Only the beam elements model, strain energy and mode shape curvature will be considered in this part. Damage model and sensor positions remain the same as in the first part.

In order to excite a large number of mode shapes as much as possible, the beam is excited about $0.15L$ from one of its supports. Excitation location remains the same for all tests. A high frequency rate is used to capture high order mode shapes. The signal is computed where the

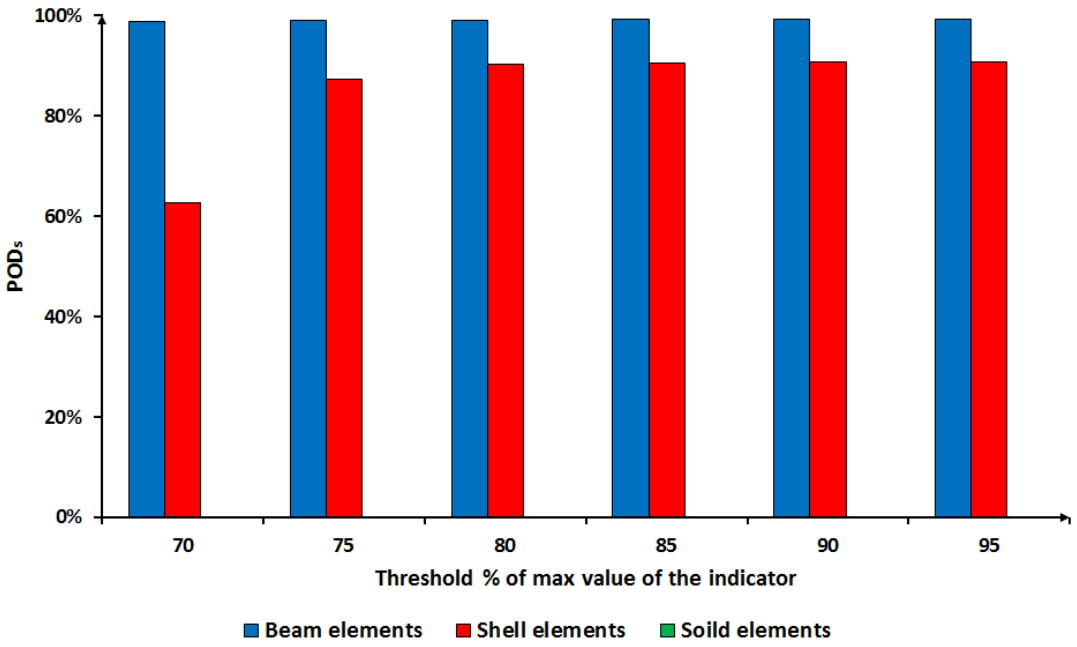

(a) POD_s, damage case 1, mode shapes curvature indicator

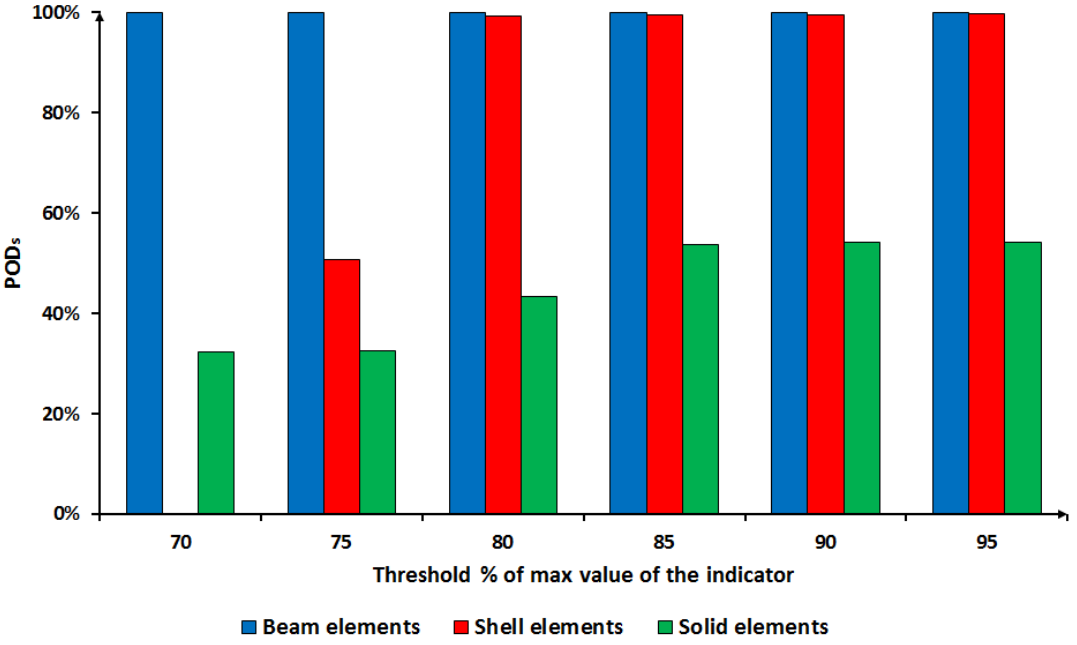

(b) POD_s, damage case 1,strain energy indicator

Figure 3: POD_s value, damage case 1

sensors are supposed to be placed before the addition of noise to it. The noise is considered white Gaussian noise. The amplitude of the noise is estimated directly from the sensors.

One of model reliability conditions is that the POD value should be low in places where no damage exists. Therefore, the POD_e is calculated at each point where the sensors supposed to be placed. Figure(4) shows the results for coupled partial models using the strain energy indicator for both damage cases 1 and 2. The vertical axis represents POD_e and the horizontal axis represents the length of the beam. Red triangles represent the position of the sensors. It shows a high POD_e value where damage exists. However, in places where no damage exists, POD_e can reach 50%. As a result, the reliabity of the selected global model is low. The reasons could be that using an inappropriate noise model or uncertainty in the mode shape extraction and data analysis affected the results. In addition, the number of experiments can influnce the results.

Figure(5) shows the POD_e for both damage case 1 and 2 using the strain energy indicator. The vertical axis represents POD_e and the horizontal axis represents the threshold level. The results show that the selected global models are robust where damage exists because the POD_e value does not change significantly by changing the threshold level.

4.3 POD_s Curves

As mentioned before, if the global model can be validated for different types of non-destructive damage in different locations with differing severities, this will result in a strong argument that the real damage would be represented correctly using this model. Furthermore, in order to assess the global models, POD curves should be created by replacing non-destructive damage with real damage detected in a structure. In the case of the E modulus degradation damage model, the damage increases from 0% to 20% with an interval of 1%. In the case of decreasing the thickness of the bottom flange,the damage increases from 0% to 80% with an interval of 4%. The POD_s is calculated in each step. The same procedure can be followed when creating POD_e curves.

After producing the POD curves, model assessment principles can be applied again to evaluate the final global models not only for a certain damage level, but for the whole damage range. In figure (6) (a), if the E modulus degradation damage model is used, the global model is not robust since changing the threshold value leads to large variation in POD_s values e.g. if E modulus decreased about 12.5%, the POD_s value varies about 60% in the case of different threshold levels. The robustness of the model is improved if the model where damage is simulated by decreasing the thickness of bottom flange is used, figure (6) (b).

In figure (7) (b), if mode shape curvature is used, the global model is not robust since the POD_s value decreases by increasing the damage level. However, using the strain energy indicator, instead of mode shape curvature, improved the robustness of the model, figure (7) (a).

Model reliability can be estimated by the level of the damage that can be detected with high probability. Consequently, the model with results shown in figure (6) (b) is more reliable than the one with results shown in figure (7) (a).

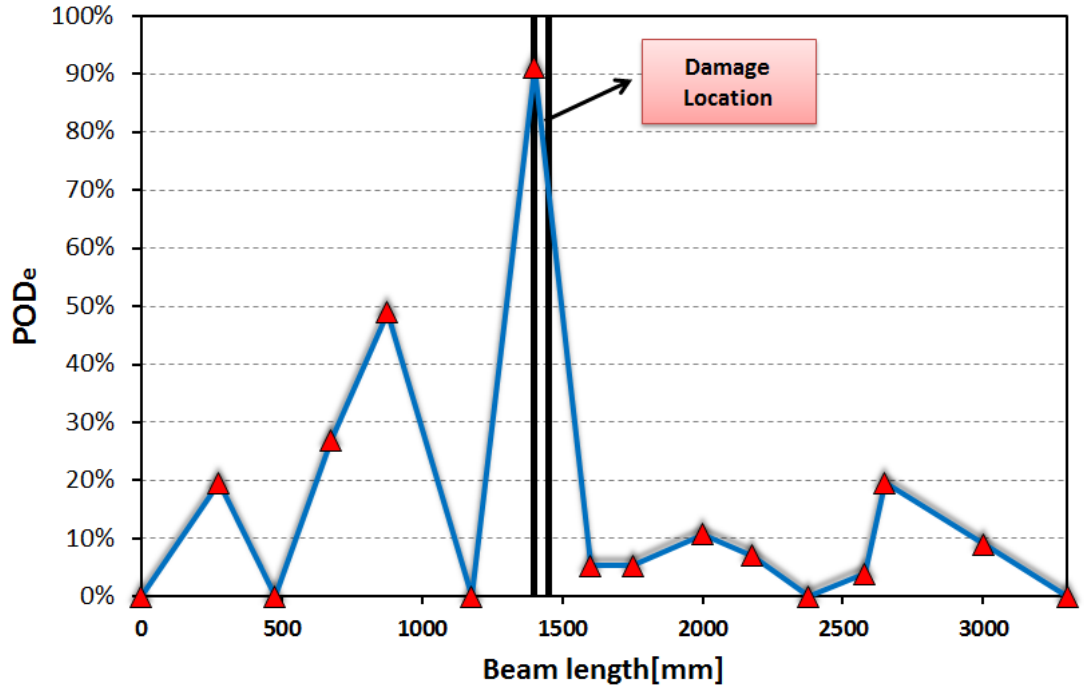

(a) POD_e in damage case 1, simulated experiments, strain energy indicator

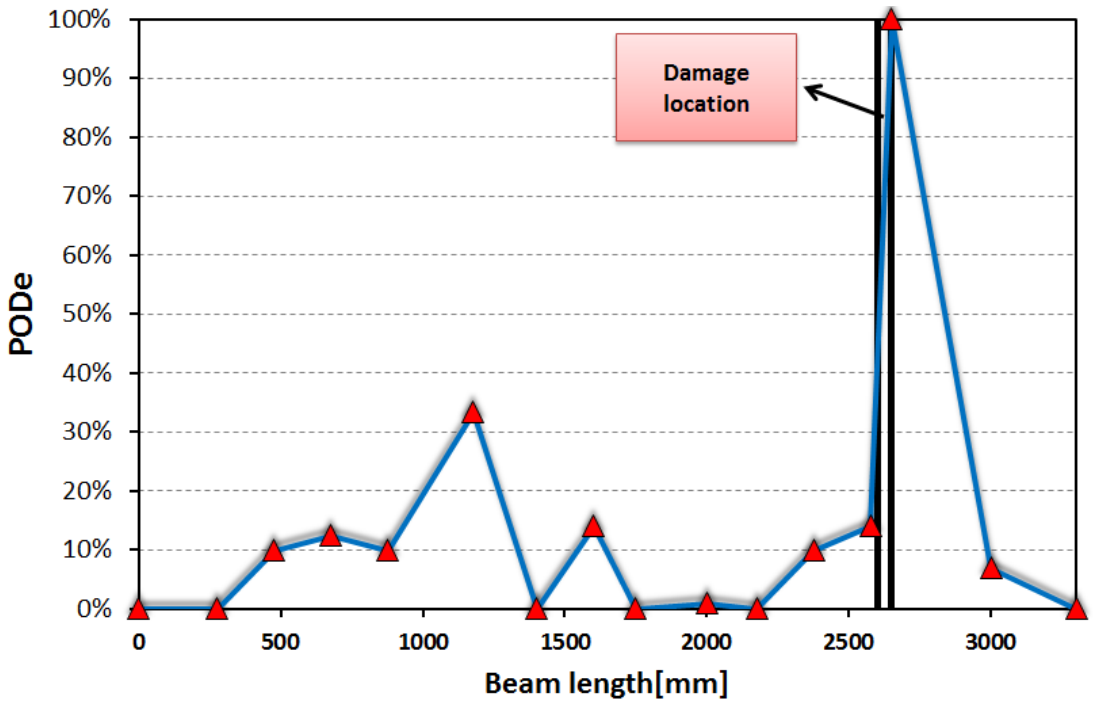

(b) POD_e in damage case 2, simulated experiments, strain energy indicator

Figure 4: Checking model reliability

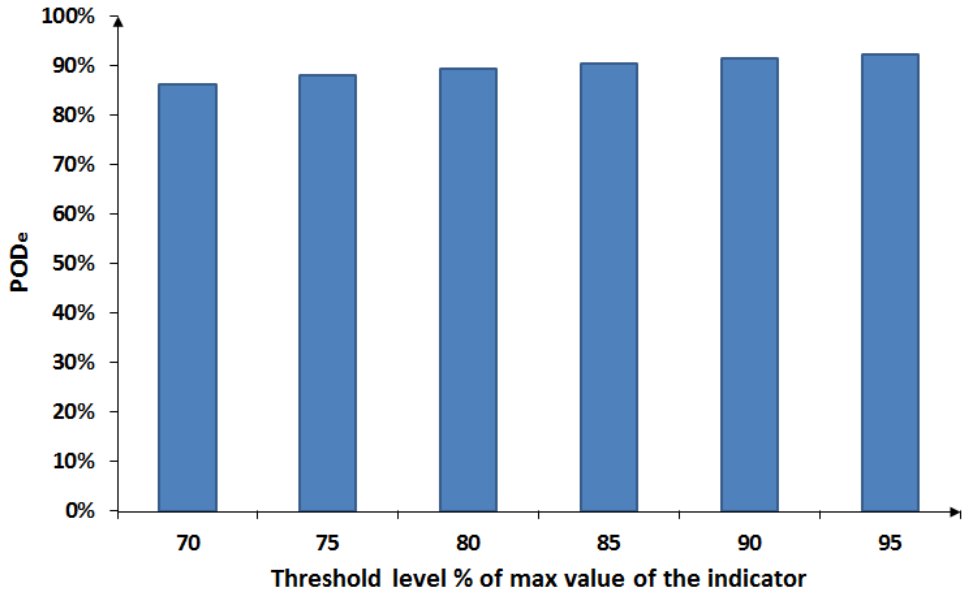

(a) POD_e, damage case 1, strain energy indicator

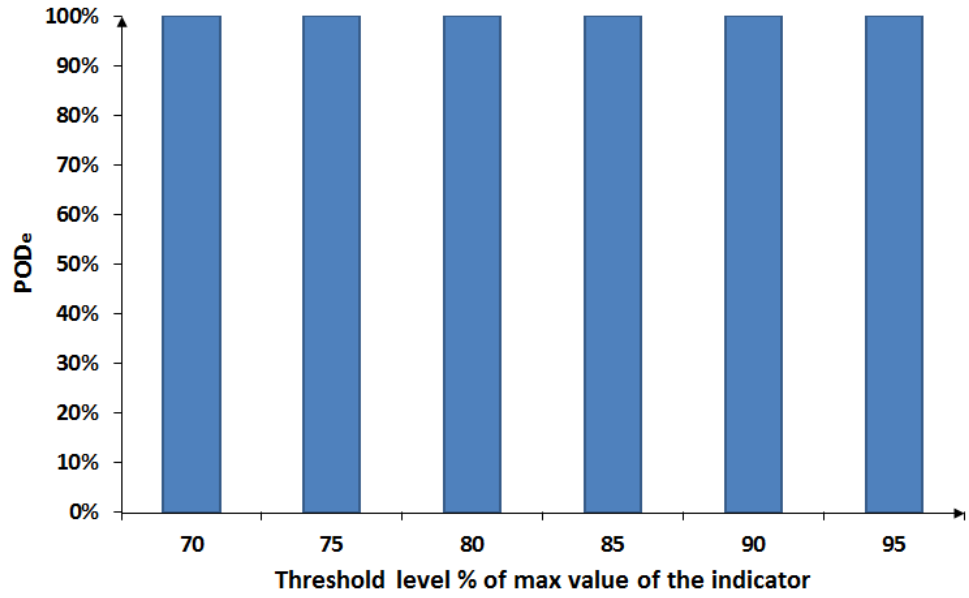

(b) POD_e, damage case 2, strain energy indicator

Figure 5: POD_e value, damage case 1

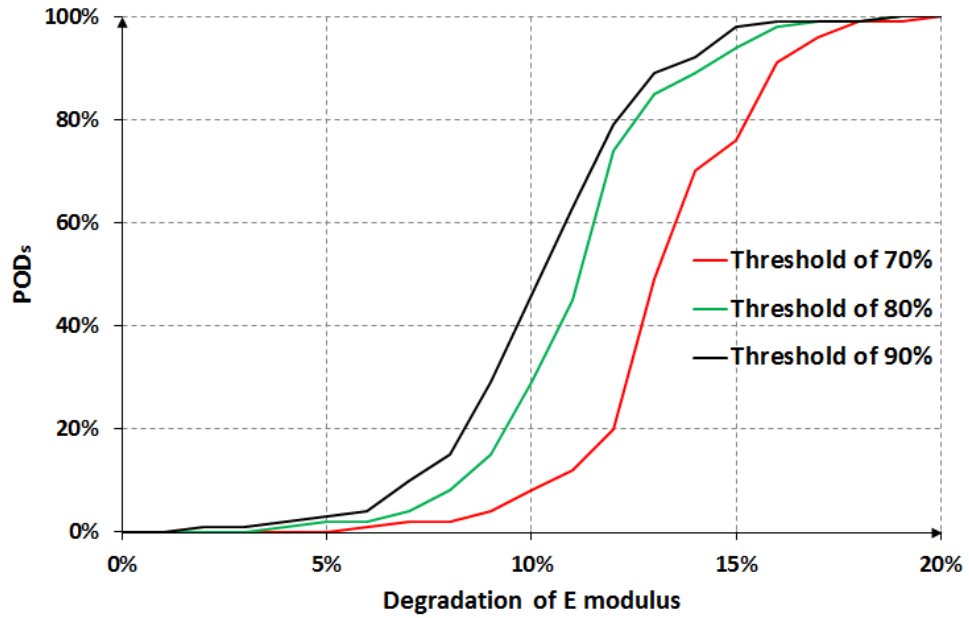

(a) POD_s curves, damage case 2, mode shapes curvature indicator, beam elements model, E modulus degradation model

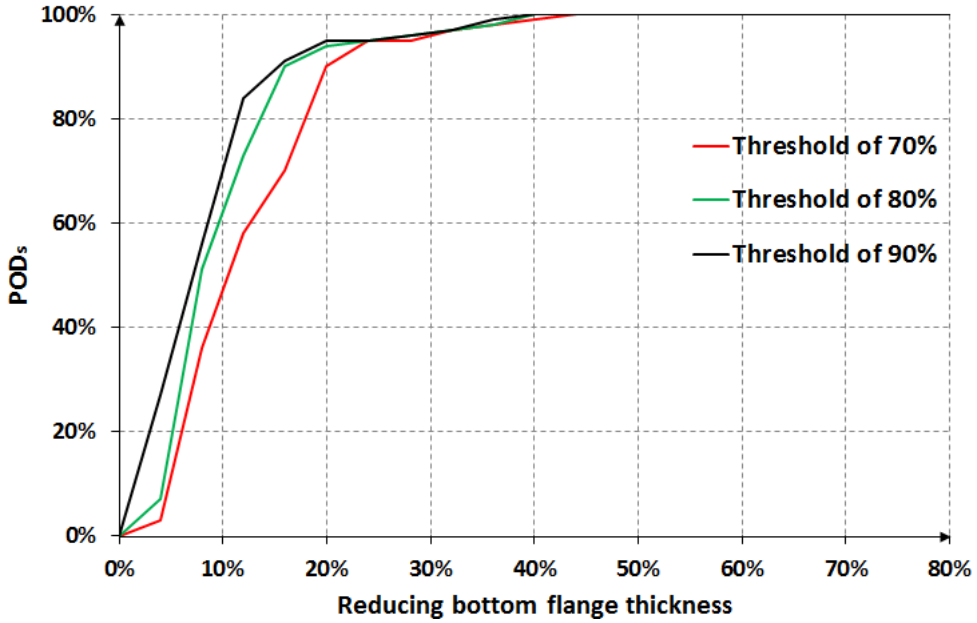

(b) POD_s curves, damage case 2, mode shapes curvature indicator, beam elements model, decrease the thickness of the bottom flange damage model

Figure 6: POD_s curves, Damage case 2

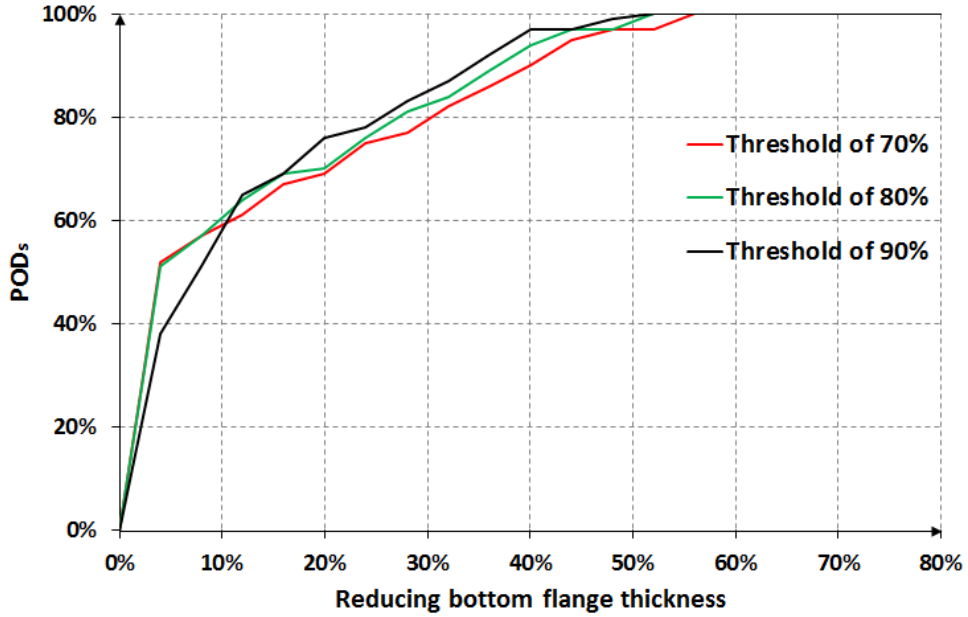

(a) POD_s curves, damage case 3, strain energy indicator, beam elements model, decrease the thickness of the bottom flange damage model

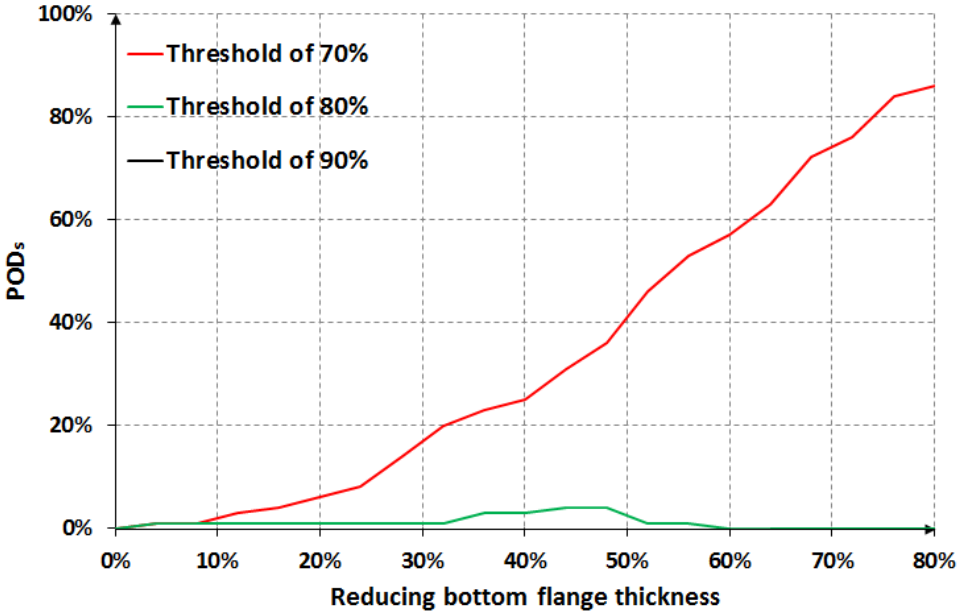

(b) POD_s curves, damage case 3, mode shapes curvature indicator, beam elements model, decrease the thickness of the bottom flange damage model

Figure 7: POD_s curves, Damage case 3

5 EXPERIMENTAL RESULTS

Experiments are performed based on numerical results using 16 accelerometers. A high frequency rate is used to capture high order modes. An impulse force is applied about $0.15L$ from one of the beam supports to excite a large number of mode shapes. The excitation point remains the same in all tests. The damage of the first and second cases is produced by removing one plate in the damage area. In the third case, two plates are removed. In order to keep the mass constant, the plates are placed again on the beam in such way that they do not contribute to the stiffness anymore.

The recorded data is analyzed using the Stochastic Subspace Identification method (SSI) to extract the dynamic properties of the beam. After that, the indicators are applied to mode shapes to calculate the POD_e.

5.1 Global Physical Model Quality

In the case of real experiments, as well as in simulated experiments, the reliability of the model should be checked. Therefore, the POD_e is calculated in each point where the sensors are placed. Figure(8) shows the results for coupled physical partial models using the strain energy indicator for both damage cases 1 and 2. The Vertical axis represents POD_e and the horizontal axis represents the length of the beam. Red triangles represent the position of the sensors. It shows that in damage case 1, the POD_e is as high as in simulated experiments but damage location is differs by more than half meter, or 17% of the length of the beam, to the left. In damage case 2, the damage location is correct but the POD_e is not more than 70%, while in simulated experiments it is 100%. However, in places where no damage exists, the POD_e can reach 30%. The reason could be data analysis uncertainty. In addition, the number of experiments can influnce the results.

Figure(9) shows the POD_e for both damage case 1 and 2 using the strain energy indicator. The vertical axis represents POD_e and the horizontal axis represents threshold level. The results show that the selected global model is robust for damage case 1 but it is not for damage case 2, since the POD_e value changes significantly when the threshold from 70% to 80%.

6 CONCLUSIONS

The application of POD curves to damage detection based on partial models is discussed. The work proposed an approach to calculate the **P**robability **O**f damage **D**etection (**POD**) based on **P**artial **M**odels (**PM**). However, the quality of the model is a problem that should be investigated if a Model assisted tool is used. Therefore, the work proposed a methodology to select and assess coupled partial models. The methodology is applied to a simply supported beam that can be modified and tested under laboratory conditions. Non-destructive damage is produced by removing one or more plates based on studied damage cases. The work uses a vibration-based method for damage detection. 16 accelerometers are used to record acceleration at the top of the beam.

The results show that the efficiency of model selection and assessment is increased when the POD is decomposed into two independent types: POD_s and POD_e, since the number of models is minimized. After the validation process, the POD curves can be created by replacing non-destructive damage with real damage that should be detected. In this work, two types of damage are used: E modulus degradation and reduction of bottom flange thickness.

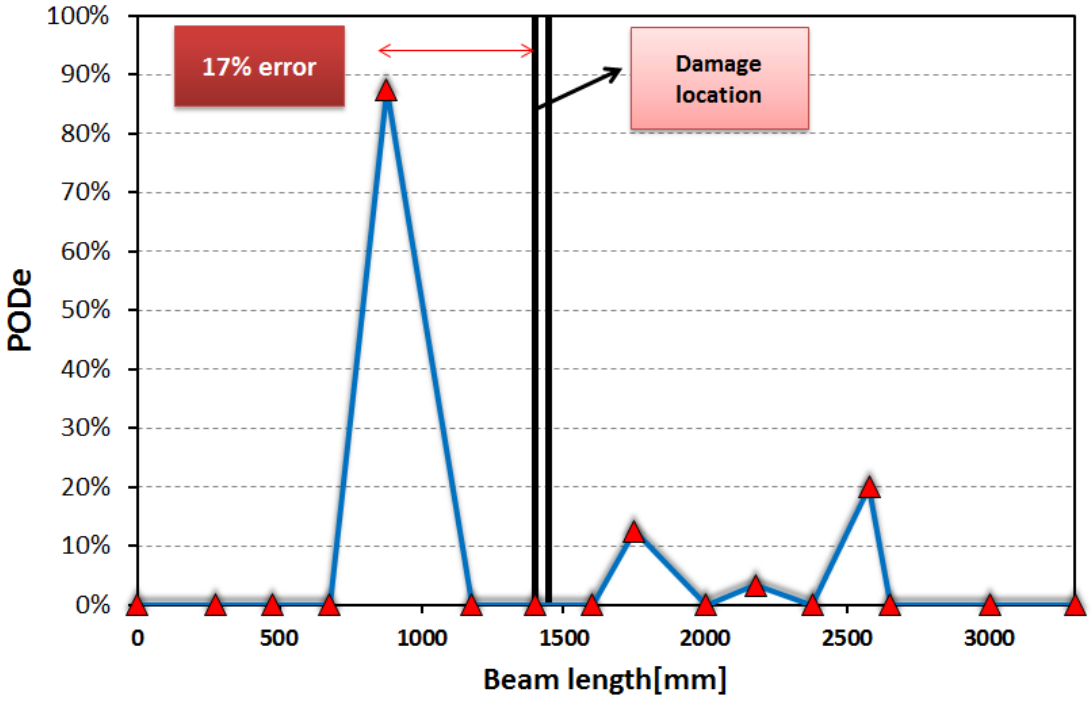

(a) POD_e in damage case 1, real experiments, strain energy indicator

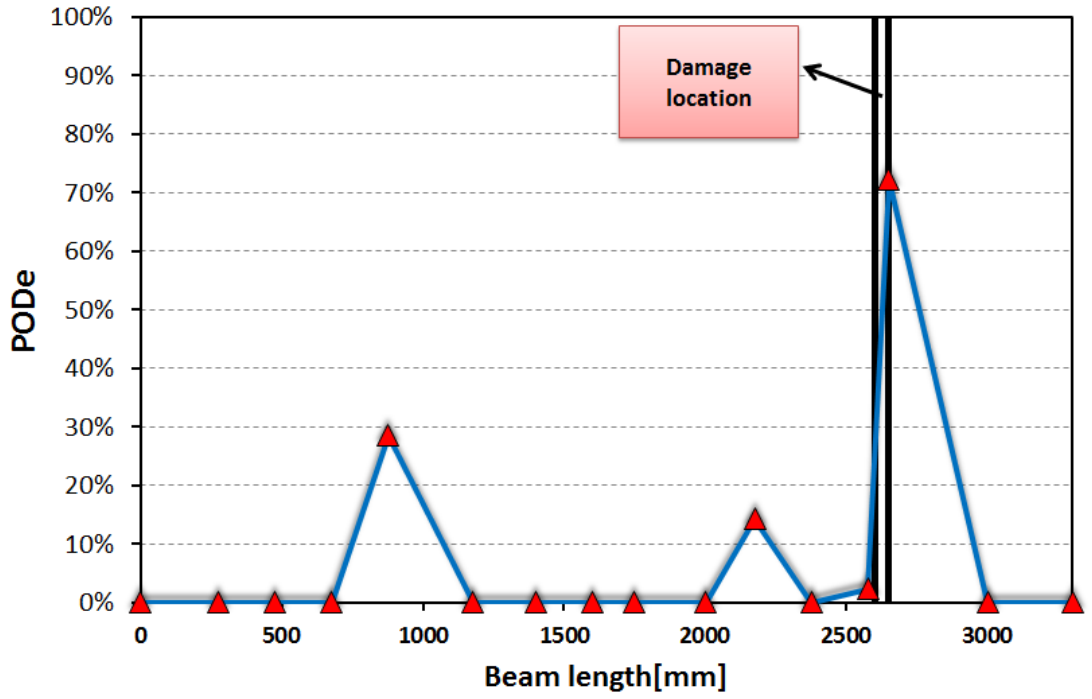

(b) POD_e in damage case 2, real experiments, strain energy indicator

Figure 8: Checking data quality

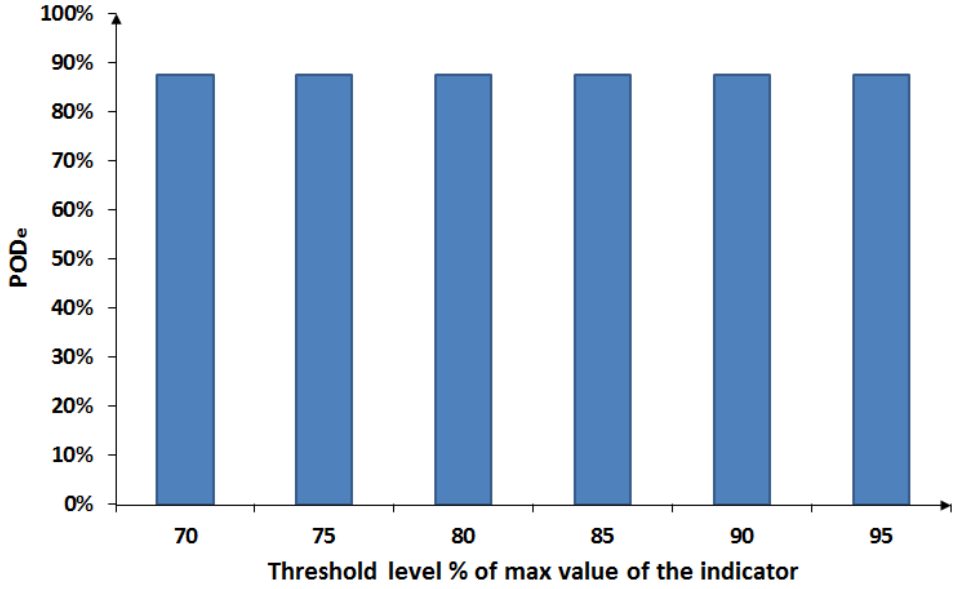

(a) POD_e, damage case 1, strain energy indicator

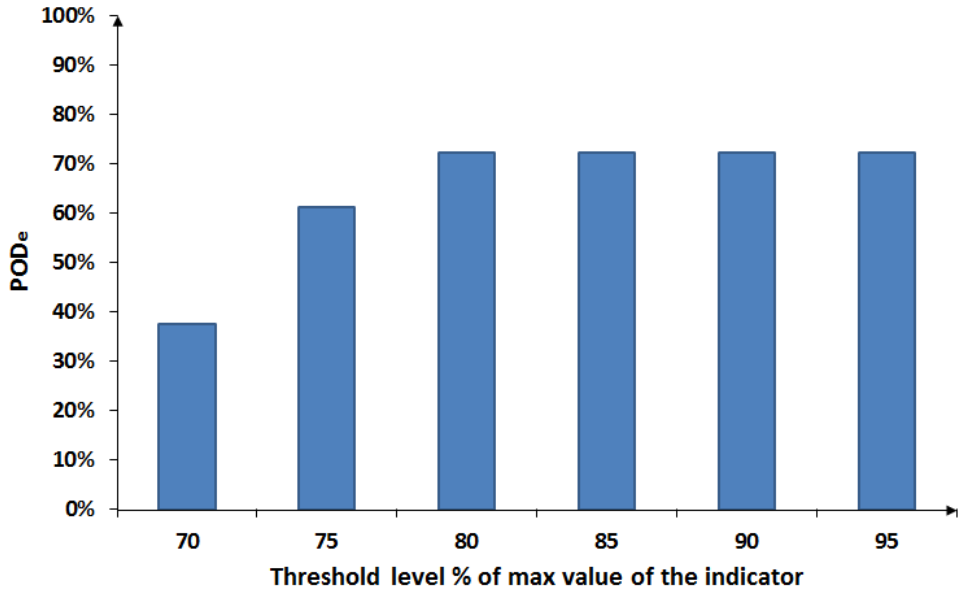

(b) POD_e, damage case 2, strain energy indicator

Figure 9: POD_e value, damage case 1

7 OUTLOOK

For future work, more partial models should be included, especially excitation, damping and noise models. More caution should be taken during the coupling of partial models in order to reduce coupling problems and their effect on the final results e.g. coupling the impulse which has a high amplitude with a very short duration with the beam could cause singularity problems. In addition, further development of the methodology for model selection and assessment based on the principles presented above is needed in order to deal with larger civil engineering structures. In addition, coupling numerical and real data should be investigated in order to solve the inverse problem.

ACKNOWLEDGEMENTS

The author would like to express his gratitude towards the German Research Foundation (DFG) that is supporting his research through the Graduiertenkolleg GRK 1462 "Modellqualitäten". Furthermore the support by the European Regional Development Fund (ERDF), for use of technical equipment necessary for the project is highly appreciated.

REFERENCES

[1] P. H. Kirkegaard, P. Andersen, *Use of statistical information for damage assessment of civil engineering structures*, *Proceedings of the International Modal Analysis Conference IMAC (2002)*, Volume: 1, Publisher: SEM, Bethel, CT, United States, Pages: 363-368

[2] R. B. Thompson, L. Brasche, *News From From NTIAC*, Analysis (2005), Volume: 30, Issue: 3.

[3] R. B. Thompson, LJ. Brasche, DS. Forsyth, E. Lindgren, P. Swindell, W. Winfree, *Recent Advances in Model-Assisted Probability of Detection*, *the Proceedings of the 4th European American Workshop on the Reliability of NDE Berlin Germany (2009)*, Pages: 23-26

[4] J. S. Knopp, J. C. Aldrin, E. Lindgren, C. Annis, *Investigation of a Model-Assisted Approach to Probability of Detection Evaluation*, *Aip Conference Proceedings (2006)*, Volume: 894, Publisher: Aip, Pages: 1775-1782

[5] C. Harding, G. Hugo, S. Bowles *Model-Assisted Probability of Detection Validation of Automated Ultrasonic Scanning for Crack Detection at Fastener Holes*, *10th Joint Conference on Aging Aircraft Palm Springs CA USA (2007)*

[6] A. C. Cobb, J. Fisher, J. E. Michaels, *Model-Assisted Probability of Detection for Ultrasonic Structural Health Monitoring*, *4th European American Workshop on Reliability of NDE (2009)* , Pages: 1-8

[7] J.C. Aldrin, E. A. Medina, E. A. Lindgren, C. Buynak, G. Steffes, M. Derriso, *Model-Assisted Probabilistic Reliability Assessment for Structural Health Monitoring Systems*, *American Institute of Physics Conference Series (2010)*, Pages: 1965-1972

[8] A. Alvandi, C. Cremona, *Assessment of Vibration-Based Damage Identification Techniques*, Journal of Sound and Vibration(2006), Volume: 292, Issue: 1-2, Pages: 179-202.

[9] A. Alvandi, C. Cremona, *Bridge Fatigue Assessment and Management Using Reliability-Based Crack Growth and Probability of Detection Models*, Probabilistic Engineering Mechanics (2011) , Volume: 26, Issue: 3, Publisher: Elsevier Ltd, Pages: 471-480

Hyperbolic Laplace Operator and the Weinstein Equation in $\mathbb{R}^3$

Sirkka-Liisa Eriksson
Department of Mathematics
Tampere University of Technology
P.O.Box 553, FI-33101 Tampere, Finland
email: Sirkka-Liisa.Eriksson@tut.fi

Heikki Orelma
Department of Mathematics
Tampere University of Technology
P.O.Box 553, FI-33101 Tampere, Finland
email:Heikki.Orelma@tut.fi

June 19, 2012

Abstract

We study the Weinstein equation

$$\Delta u - \frac{k}{x_2}\frac{\partial u}{\partial x_n} + \frac{l}{x_2^2}u = 0,$$

on the upper half space $\mathbb{R}^3_+ = \left\{(x_0, x_1, x_2) \in \mathbb{R}^3\right\}$ for $4l \leq (k+1)^2$. If $l = 0$, the operator $x_2^{2k}\left(\Delta u - \frac{k}{x_2}\frac{\partial u}{\partial x_2}\right)$ is the Laplace-Beltrami operator with respect to the Riemannian metric $ds^2 = x_2^{-2k}\left(\sum_{i=0}^{2} dx_i^2\right)$. In case $k = 1$ the Riemannian metric is the hyperbolic distance of Poincaré upper half space. The Weinstein equation is connected to the axially symmetric potentials. We compute solutions of the Weinstein equation depending on the hyperbolic distance and x_2. These results imply the explicit mean value properties. We also compute the fundamental solution. The main tools are the hyperbolic metric and its invariance properties.

1 Introduction

Weinstein introduced axially symmetric potential theory in [12]. The idea was to consider the following simple elliptic differential equation with variable coefficients

in the neighborhood of the singular plane $x_n = 0$

$$x_n \triangle h + p\frac{\partial h}{\partial x_n} = 0,$$

where as usual

$$\triangle h = \frac{\partial^2 h}{\partial x_0^2} + ... + \frac{\partial^2 h}{\partial x_n^2}.$$

Note that if p is an integer then a axially symmetric harmonic function in $p+2$-dimensional space satisfies the preceding equation in the meridian plane (see for example [9])

We consider the solutions of the generalized Weinstein equation

$$x_2^2 \triangle h - kx_2\frac{\partial h}{\partial x_2} + lh = 0 \tag{1}$$

in an open domain whose closer is contained in the upper half space

$$\mathbb{R}^3_+ = \{(x_0, x_1, x_2) \mid x_0, x_1, x_2 \in \mathbb{R},\, x_2 > 0\}.$$

Our general technical assumption is that the constants $l, k \in \mathbb{R}$ satisfy $4l \leq (k+1)^2$. This equation has been researched for example by Leutwiler and Akin in [10] and in [1]. We transfer solutions of this equation to solutions of Laplace-Beltrami equation of the hyperbolic metric in the Poincaré upper half space. In the main result, we present the fundamental solution of the equation (1) in terms of the hyperbolic distance function.

We recall that the operator

$$\Delta_h f = x_2^2 \Delta f - x_2\frac{\partial f}{\partial x_2}$$

is the hyperbolic Laplace-Beltrami operator with respect to the hyperbolic Riemannian metric

$$ds^2 = \frac{dx_0^2 + dx_1^2 + dx_2^2}{x_2^2}$$

in the Poincaré upper half space model.

The hyperbolic distance may be computed as follows (see the proof for example in [11]).

Lemma 1 *The hyperbolic distance $d_h(x, a)$ between the points $x = (x_0, x_1, x_2)$ and $a = (a_0, a_1, a_2)$ in $\mathbb{R}^3_+$ is*

$$d_h(x, a) = \operatorname{arcosh}\, \lambda(x, a),$$

where

$$\lambda(x, a) = \frac{(x_0 - a_0)^2 + (x_1 - a_1)^2 + x_2^2 + a_2^2}{2x_2a_2} = \frac{|x - a|^2}{2x_2a_2} + 1$$

and $|x - a|$ is the usual Euclidean distance between the points a and x.

We also apply the simple calculation rules of the hyperbolic distance stated next.

Lemma 2 *If $x = (x_0, x_1, x_2)$ and $a = (a_0, a_1, a_2)$ are points in $\mathbb{R}^3_+$ then*

$$|x-a|^2 = 2x_2a_2\left(\lambda(x,a)-1\right), \tag{2}$$

$$|x-\hat{a}|^2 = 2x_2a_2\left(\lambda(x,a)+1\right), \tag{3}$$

$$\frac{|x-a|^2}{|x-\hat{a}|^2} = \frac{\lambda(x,a)-1}{\lambda(x,a)+1} = \tanh^2(\frac{d_h\left(x,a\right)}{2}), \tag{4}$$

where $\widehat{a} = (a_0, a_1, -a_2)$.

We also note the relation between the Euclidean and hyperbolic balls.

Proposition 3 *The hyperbolic ball $B_h\left(a, r_h\right)$ with the center $a = (a_0, a_1, a_2)$ and the radius r_h is the same as the Euclidean ball with the Euclidean center $(a_0, a_1, a_2 \cosh r_h)$ and the Euclidean radius $r_e = a_2 \sinh\, r_h$.*

2 The hyperbolic Laplace operator depending on the hyperbolic distance in $\mathbb{R}^3_+$

We need the computations of the hyperbolic Laplace operator of functions depending on λ, computed in [2].

Lemma 4 *If f is twice continuously differentiable depending only on $\lambda = \lambda\left(x, e_n\right)$ then*

$$\triangle_h f\left(x\right) = \left(\lambda^2-1\right)\frac{\partial^2 f}{\partial\lambda^2} + 3\lambda\frac{\partial f}{\partial\lambda}.$$

Using this it is relatively easy to compute the result.

Lemma 5 *If f is twice continuously differentiable depending only on $r_h = d_h\left(x, e_n\right)$ then the hyperbolic Laplace in $\mathbb{R}^3_+$ is given by*

$$\triangle_h f\left(r_h\right) = \frac{\partial^2 f}{\partial r_h^2} + 2\coth r_h\frac{\partial f}{\partial r_h}.$$

Proof. Using $r_h = \operatorname{arcosh}\, \lambda(x, e_n)$, we compute

$$\frac{\partial r_h}{\partial\lambda} = \frac{1}{\sinh r_h}$$

and

$$\frac{\partial^2 r_h}{\partial\lambda^2} = -\frac{\cosh r_h}{\sinh^3 r_h}.$$

Hence applying the chain rule we obtain

$$\begin{aligned}\frac{\partial f(r_h)}{\partial \lambda} &= \frac{\partial f}{\partial r_h}\frac{\partial r_h}{\partial \lambda} = \frac{\partial f}{\partial r_h}\frac{1}{\sinh r_h},\\ \frac{\partial^2 f(\lambda)}{\partial \lambda^2} &= \frac{\partial^2 f}{\partial r_h^2}\left(\frac{\partial r_h}{\partial \lambda}\right)^2 + \frac{\partial f}{\partial r_h}\frac{\partial^2 r_h}{\partial \lambda^2}\\ &= \frac{\partial^2 f}{\partial r_h^2}\frac{1}{\sinh^2 r_h} - \frac{\partial f}{\partial r_h}\frac{\cosh r_h}{\sinh^3 r_h},\end{aligned}$$

completing the proof by the preceding lemma. ■

If we know one strictly positive solution depending on r_h, we may compute all the solutions depending on r_h.

Theorem 6 *If μ is a strictly positive solution of the equation*

$$\triangle_h f + \gamma f = \frac{\partial^2 f}{\partial r_h^2} + 2\frac{\partial f}{\partial r_h}\frac{\cosh r_h}{\sinh r_h} + \gamma f = 0 \tag{5}$$

depending on $r_h = d_h(x, e_n)$ then the general solution of this equation is

$$f(r_h) = \left(C\int_{r_0}^{r_h} \sinh^{-2} u\mu^{-2}(u)\,du + C_0\right)\mu(r_h)$$

for some real constants C and C_0.

Proof. Assume that $\mu(r_h)$ is a particular positive solution of (5). Setting $f(r_h) = g(r_h)\,\mu(r_h)$ we obtain

$$\begin{aligned}0 &= \mu\frac{d^2 g}{dr_h^2} + 2\frac{d\mu}{dr_h}\frac{dg}{dr_h} + g\frac{d^2\mu}{dr_h^2}\\ &\quad + 2\frac{\cosh r_h}{\sinh r_h}g\frac{d\mu}{dr_h} + 2\frac{\cosh r_h}{\sinh r_h}\mu\frac{dg}{dr_h} + \gamma\mu g\\ &= \mu\frac{d^2 g}{dr_h^2} + 2\frac{d\mu}{dr_h}\frac{dg}{dr_h} + 2\frac{\cosh r_h}{\sinh r_h}\mu\frac{dg}{dr_h}.\end{aligned}$$

Denoting $\frac{dg}{dr_h} = h$, we deduce

$$\mu\frac{dh}{dr_h} + \left(2\frac{d\mu}{dr_h} + 2\frac{\cosh r_h}{\sinh r_h}\mu\right)h = 0.$$

Hence we solve

$$\frac{d}{dr_h}\left(\log h + 2\log\mu + 2\log(\sinh r_h)\right) = 0$$

and therefore

$$\frac{\partial g}{\partial r_h} = h = C\sinh^{-2} r_h\mu^{-2}(r_h).$$

Consequently, the general solution is$\frac{n^2-(k+1)^2}{4}$

$$f(r_h) = \left(C \int_{r_0}^{r_h} \sinh^{-2} u\mu^{-2}(u)\, du + C_0 \right) \mu(r_h).$$

We recall the relation between solutions of (1) and eigenfunctions of the hyperbolic Laplace-Beltrami operator.

Proposition 7 ([10]) *Let $\Omega \subset \mathbb{R}^3_+$ be an open subset Ω of $\mathbb{R}^3_+$. If u is a solution of (1) in Ω, then $f(x) = x_2^{\frac{1-k}{2}} u(x)$ is an eigenfunction of the hyperbolic Laplace operator corresponding to the eigenvalue $\frac{1}{4}\left((k+1)^2 - 4l - 4\right)$. Conversely, if f is the an eigenfunction of the hyperbolic Laplace operator corresponding to the eigenvalue γ in Ω then $u(x) = x_2^{\frac{k-1}{2}} f(x)$ is the solution of the equation (1) in Ω with $l = \frac{1}{4}\left((k+1)^2 - 4\gamma - 4\right)$.*

The mean value property for the solutions of (1) can be stated in terms of the hypergeometric functions. We recall their definition:

$$_2F_1(a, b; c; x) = \sum_{m=0}^{\infty} \frac{(a)_m (b)_m}{(c)_m} \frac{x^m}{m!},$$

where $(a)_m = a(a+1)...(a+m-1)$ and $(a)_0 = 1$. This series converges for x satisfying $|x| < 1$. We recall also an important Euler's integral formula valid for $a, b, c \in \mathbb{C}$ satisfying $0 < \operatorname{Re} b < \operatorname{Re} c$

$$_2F_1(a, b; c; z) = \frac{1}{B(b, c-b)} \int_0^1 t^{b-1}(1-t)^{c-b-1}(1-tz)^{-a} dt.$$

where the Beta funtion has the representation

$$B(x, y) = \frac{\Gamma(x)\Gamma(y)}{\Gamma(x+y)}.$$

The mean value property for solutions of (1) with respect to the hyperbolic surface measure was proved in [8].

Theorem 8 *Let l and k be real numbers satisfying $4l \leq (k+1)^2$ and $U \subset \mathbb{R}^3_+$ be open. If*

$$\psi_{2,k,l}(r_h) = e^{-\frac{1+\sqrt{(k+1)^2-4l}}{2} r_h} {}_2F_1\left(1 + \frac{\sqrt{(k+1)^2-4l}}{2}, 1; 2; 1 - e^{-2r_h}\right)$$

then $\psi_{2,k,l}(r_h)$ is an eigenfunction of the hyperbolic Laplace operator corresponding to the eigenvalue $\frac{1}{4}\left((k+1)^2 - 4l - 4\right)$. Moreover, if $u : U \to \mathbb{R}$ is a solution of the Weinstein equation

$$\Delta u - \frac{k}{x_2}\frac{\partial u}{\partial x_2} + \frac{l}{x_2^2} u = 0$$

in U then

$$u(a)=\frac{a_2^{\frac{k-1}{2}}}{4\pi\sinh^2(r_h)\psi_{2,k,l}(r_h)}\int_{\partial B_h(a,r_h)}u(x)\frac{d\sigma}{x_2^{\frac{3+k}{2}}}$$

for all hyperbolic balls satisfying $\overline{B_h(a,r_h)}\subset U$.

In our special case $\mathbb{R}^3_+$, we can give a simple formula for the function $\psi_{2,k,l}(r_h)$ as follows.

Theorem 9 *Let l and k be real numbers satisfying $4l\leq(k+1)^2$ and $U\subset\mathbb{R}^3_+$ be open. Denote*

$$a=1+\frac{\sqrt{(k+1)^2-4l}}{2}$$

and $r_h=d_h(x,e_n)$. Then

$$\begin{aligned}\psi_{2,k,l}(r_h)&=e^{-ar_h}{}_2F_1(a,1;2;1-e^{-2r_h})\\&=\begin{cases}\frac{\sinh(r_h(a-1))}{(a-1)\sinh r_h}, & \text{if } 4l\neq(k+1)^2,\\ \frac{r_h}{\sinh r_h}, & \text{if } 4l=(k+1)^2,\end{cases}\end{aligned}$$

is the eigenfunction of the hyperbolic Laplace operator corresponding to the eigenvalue $\frac{1}{4}\left((k+1)^2-4l-4\right)$.

For the sake of completeness, we first prove the lemma.

Lemma 10 *If $|x|<1$ then*

$${}_2F_1(a,1;2;x)=\begin{cases}\frac{1-(1-x)^{-a+1}}{x(-a+1)} & \text{if } a\neq1,\\ -\frac{\log(1-x)}{x} & \text{if } a=1.\end{cases}$$

Proof. If we replace t with $1-s$ in Euler's integral we obtain

$$\begin{aligned}{}_2F_1(a,b;c;x)&=\frac{\Gamma(c)}{\Gamma(b)\Gamma(c-b)}\int_0^1(1-x+xs)^{-a}(1-s)^{b-1}s^{c-b-1}ds\\&=\frac{(1-x)^{-a}\Gamma(c)}{\Gamma(b)\Gamma(c-b)}\int_0^1\left(1+\frac{xs}{1-x}\right)^{-a}(1-s)^{b-1}s^{c-b-1}ds.\end{aligned}$$

In case $a\neq1$ we infer

$$\begin{aligned}{}_2F_1(a,1;2;x)&=(1-x)^{-a}\int_0^1\left(1+\frac{xs}{1-x}\right)^{-a}dt\\&=(1-x)^{-a}\frac{1-x}{x(-a+1)}\left(\left(1+\frac{x}{1-x}\right)^{-a+1}-1\right)\\&=(1-x)^{-a}\frac{x-1}{x(-a+1)}\left(\frac{1}{(1-x)^{-a+1}}-1\right)\\&=\frac{1-(1-x)^{-a+1}}{x(-a+1)}.\end{aligned}$$

If $a = 1$ we compute

$$\begin{aligned}
{}_2F_1(a,1;2;x) &= (1-x)^{-a}\int_0^1 \left(1+\frac{xs}{1-x}\right)^{-1} dt \\
&= (1-x)^{-1}\,\frac{1-x}{x}\log\left(1+\frac{x}{1-x}\right) \\
&= -\frac{\log(1-x)}{x}.
\end{aligned}$$

We are ready to verify the preceding theorem.

Proof. Setting $a = 1 + \frac{\sqrt{(k+1)^2-4\ell}}{2} \neq 1$ we obtain

$$\begin{aligned}
\psi_{2,k,l}(r_h) &= e^{-ar_h}{}_2F_1(1+\frac{\sqrt{(k+1)^2-4\ell}}{2},1;2;1-e^{-2r_h}) \\
&= e^{-ar_h}\left(\frac{e^{2r_h(a-1)}-1}{(1-e^{-2r_h})(a-1)}\right) \\
&= e^{-ar_h}e^{r_h(a-1)}e^{r_h}\frac{\frac{e^{r_h(a-1)}-e^{-r_h(a-1)}}{2}}{\frac{\left(e^{r_h}-e^{-r_h}\right)}{2}(a-1)} \\
&= \frac{\sinh(r_h(a-1))}{(a-1)\sinh r_h}.
\end{aligned}$$

If $a = 1$ then

$$\psi_{2,k,l}(r_h) = -e^{-r_h}\frac{\log e^{-2r_h}}{(1-e^{-2r_h})} = \frac{2r_h}{(e^{r_h}-e^{-r_h})} = \frac{r_h}{\sinh r_h}.$$

Note also that

$$\lim_{r_h\to 0}\psi_{2,k,l}(r_h) = 1$$

and with this extension $\psi_{2,k,l}$ is a continuously differential function.

Substituting the values of $\psi_{2,k,l}$ for the mean value theorem we immediately obtain the result.

Theorem 11 *Let k be a real number and $U \subset \mathbb{R}^3_+$ be open. If $u : U \to \mathbb{R}$ is a solution of the Weinstein equation*

$$x_2^2\Delta u - kx_2\frac{\partial u}{\partial x_n} = 0$$

in U then

$$u(a) = \frac{a_n^{\frac{k-1}{2}}|k+1|}{8\pi\sinh(r_h)\sinh\left(\frac{r_h|k+1|}{2}\right)}\int_{\partial B_h(a,r_h)} x_2^{-\frac{k+3}{2}}u(x)d\sigma$$

in case $k \neq -1$ and in case $k = -1$

$$u(a) = \frac{1}{4\pi a_2 r_h\sinh(r_h)}\int_{\partial B_h(a,r_h)} x_n^{-1}u(x)d\sigma.$$

Similarly, the general solution of the equation (5) has the representation.

Theorem 12 *If* $\gamma = \frac{1}{4}(4-(k+1)^2)$ *and* $k \neq -1$ *the general solution of the equation (5) is*

$$f(r_h) = C_1 \frac{\cosh\left(\frac{|k+1|r_h}{2}\right)}{\sinh r_h} + C_0 \frac{\sinh\left(\frac{r_h|k+1|}{2}\right)}{\sinh r_h}$$

for some real constants C_1 *and* C_0. *If* $k=-1$ *the general solution for* $\gamma = 1$ *is*

$$f(r_h) = C_1 \frac{1}{\sinh r_h} + C_0 \frac{r_h}{\sinh r_h}.$$

Proof. Assuming $k \neq -1$ and substituting

$$\mu(r_h) = \frac{\sinh\left(\frac{r_h|k+1|}{2}\right)}{\sinh r_h}$$

in

$$f(r_h) = \left(C\int_{r_0}^{r_h} \sinh^{-2} u\mu^{-2}(u)\,du + C_0\right)\mu(r_h),$$

we obtain

$$\begin{aligned} f(r_h) &= \left(C\int_{r_0}^{r_h} \sinh^{-2} u \frac{(k+1)^2 \sinh^{-2}\left(\frac{u|k+1|}{2}\right)}{4\sinh^{-2} u}du + C_0\right)\frac{2\sinh\left(\frac{r_h|k+1|}{2}\right)}{|k+1|\sinh r_h} \\ &= \left(C\int_{\frac{|k+1|r_0}{2}}^{\frac{|k+1|r_h}{2}} \sinh^{-2}(s)\,ds + C_0\right)\frac{\sinh\left(\frac{r_h|k+1|}{2}\right)}{\sinh r_h} \\ &= \left(C\coth\left(\frac{|k+1|r_0}{2}\right) - C\coth\left(\frac{|k+1|r_h}{2}\right) + C_0\right)\frac{\sinh\left(\frac{r_h|k+1|}{2}\right)}{\sinh r_h}. \end{aligned}$$

completing the proof, if we choose the constants properly. The case $k=-1$ is proved similarly.

Corollary 13 *The particular solution of (5) with* $\gamma = \frac{1}{4}(4-(k+1)^2)$ *outside the point* e_2 *is*

$$F(x) = \frac{\cosh\left(\frac{|k+1|d_h(x,e_2)}{2}\right)}{\sinh d_h(x,e_2)} = \frac{\cosh\left(\frac{|k+1|d_h(x,e_2)}{2}\right)}{|x-\cosh d_h(x,e_2)\,e_2|}$$

and $x_2^{\frac{k-1}{2}} F(r_h)$ *is* k*-hyperbolic harmonic.*

Denote

$$F(x,a) = \frac{\cosh\left(\frac{|k+1|d_h(x,a)}{2}\right)}{\sinh d_h(x,a)}.$$

We obtain this function by transforming the preceding function with the transformation $\tau(x) = a_2 x + Pa$.

Corollary 14 *The function $F_h(x,a)$ satisfies the equation*

$$\frac{\partial^2 f}{\partial r_h^2}+2\frac{\partial f}{\partial r_h}\frac{\cosh r_h}{\sinh r_h}+\gamma f=0$$

with $\gamma=\frac{1}{4}(4-(k+1)^2)$ outside $x=a$ and $x_2^{\frac{k-1}{2}}F_h(x,a)$ is k-hyperbolic harmonic outside $x=a$.

Proof. Since the hyperbolic distance is invariant under Möbius transformation mapping the upper half space onto itself, applying $\tau(x)=a_2x+Pa$ we infer

$$d_h(\tau(x),a)=d_h(x,e_2)$$

and

$$F(x)=\frac{\cosh\left(\frac{|k+1|d_h(\tau(x),a)}{2}\right)}{\sinh d_h(\tau(x),a)}.$$

Since the hyperbolic Laplace operator is invariant under Möbius transformation mapping the upper half space onto itself the function

$$F\left(\tau^{-1}(x)\right)=\frac{\cosh\left(\frac{|k+1|d_h(x,a)}{2}\right)}{\sinh d_h(x,a)}$$

is the eigenfunction of the hyperbolic Laplace operator with the eigenvalue with $\gamma=\frac{1}{4}(4-(k+1)^2)$, completing the proof.

Lemma 15 *The function $F_h(x,a)$ is Lebesgue integrable in the hyperbolic ball $B_h(a,r_h)$ and*

$$\int_{B_h(a,r_h)}x_2^{-\frac{5k+1}{2}}F_h(x,a)\,dx\leq M(a,r_h)\left(\frac{(\cosh r_h-1)^2}{6}+\frac{\sinh^2 r_h}{2}\right),$$

for some function $M(a,r_h)>0$ with a bounded limit when $r_h\to 0$.

Proof. It is enough to prove the statement for $a=e_2$. Note that

$$\frac{|x|^2+1}{2x_2}=\lambda(x,e_2)=\cosh d_h(x,e_2).$$

Since $e^{-r_h}<x_2<e^{r_h}$ in $B_h(e,r_h)=B(\cosh r_he_2,\sinh r_h)$ we obtain

$$\begin{aligned}\frac{x_2^{-\frac{1+5k}{2}}\cosh\left(\frac{|k+1|d_h(x,a)}{2}\right)}{\sinh d_h(x,e_2)}&=\frac{x_2^{-\frac{1+5k}{2}}\cosh\left(\frac{|k+1|d_h(x,a)}{2}\right)}{\sqrt{\lambda-1}\sqrt{\lambda+1}}\\&\leq\frac{x_2^{-\frac{1+5k}{2}}\cosh\left(\frac{|k+1|r_h}{2}\right)}{\sqrt{\lambda-1}}\\&\leq\frac{\sqrt{2}e^{\frac{5k}{2}r_h}\cosh\left(\frac{|k+1|r_h}{2}\right)}{\sqrt{|x|^2+1-2x_2}}\end{aligned}$$

in $B_h(a, r_h)$ it is enough to consider the integral

$$\int_{B_h(e_r, r_h)} \frac{dx}{\sqrt{|x|^2 + 1 - 2x_2}}$$

$$\int_{B(\cosh r_h e_2, \sinh r_h)} \frac{dx}{\sqrt{|x|^2 + 1 - 2x_2}}.$$

Denote $c = \cosh r_h e_2$. Changing the variables

$$\begin{aligned} x_0 &= r \sin\theta \cos\phi, \\ x_1 &= r \sin\theta \sin\phi, \\ x_2 &= r \cos\theta + c, \end{aligned}$$

we obtain

$$\begin{aligned} &\int_{B(\cosh r_h e_2, \sinh r_h)} \frac{dx}{\sqrt{|x|^2 + 1 - 2x_2}} \\ &= \int_0^{\sinh r_h} \int_0^{2\pi} \int_0^{\pi} \frac{r^2 \sin\theta d\theta d\phi dr}{\sqrt{r^2 + 2r(c-1)\cos\theta + (c-1)^2}} \\ &= 2\pi \int_0^{\sinh r_h} -\frac{1}{c-1} \left(r\left(|r - c + 1|\right) - r\left(r + c - 1\right)\right) dr \\ &= 2\pi \int_0^{c-1} -\frac{1}{c-1} \left(r\left(c - 1 - r\right) - r\left(r + c - 1\right)\right) dr \\ &+ 2\pi \int_{c-1}^{\sinh r_h} -\frac{1}{c-1} \left(r\left(r - c + 1\right) - r\left(r + c - 1\right)\right) dr \\ &= 2\pi \int_0^{c-1} \frac{2r^2}{c-1} dr + 2\pi \int_{c-1}^{\sinh r_h} r dr \\ &= 2\pi \left(\frac{2}{3}(c-1)^2 + \frac{\sinh^2 r_h}{2} - \frac{1}{2}(c-1)^2 \right) \\ &= 2\pi \left(\frac{1}{6}(c-1)^2 + \frac{\sinh^2 r_h}{2} \right), \end{aligned}$$

completing the proof.

We recall the Green formula in some Riemannian manifolds.

Proposition 16 ([1]) *Let $R \subset \mathbb{R}^3_+$ be a bounded open set with the smooth boundary contained $\mathbb{R}^3_+$ and denote the volume element corresponding to the Riemannian metric*

$$ds^2 = \frac{dx_0^2 + dx_1^2 + dx_2^2}{x_2^{2k}}$$

by $dm_{(k)} = x_2^{-3k} dm$, the surface elements by $d\sigma_{(k)} = x_2^{-2k} d\sigma$ and the outer normal $\frac{\partial u}{\partial n_{(k)}} = x_2^k \frac{\partial u}{\partial n}$. where n is the outer normal to the the surface ∂R. Then the Laplace-Beltrami operator is

$$\triangle_k = x_2^{2k} \left(\triangle - \frac{k}{x_2} \frac{\partial}{\partial x_2} \right)$$

and

$$\int_R \left(u\triangle_k v dm_{(k)} - v\triangle_k u dm_{(k)}\right) = \int_{\partial R}\left(u\frac{\partial v}{\partial n_k} - v\frac{\partial u}{\partial n_k}\right) d\sigma_{(k)}$$

for any functions u and v that are twice continuously differentiable functions in an open set containing the closure $\overline{\Omega}$ of Ω.

A function $f : \Omega \to \mathbb{R}$ is called *k-hyperbolic harmonic* if

$$\triangle_k f = 0$$

in Ω. The theory of *k-hyperbolic harmonic functions* was developed in [3]. Denote

$$H(x,y) = y_2^{\frac{k-1}{2}} x_2^{\frac{k-1}{2}} \frac{\cosh\left(\frac{|k+1|d_h(x,y)}{2}\right)}{\sinh d_h(x,y)}.$$

We will show that $H(x,y)$ is the fundamental k-hyperbolic harmonic functions with a pole in x. We need following lemma.

Lemma 17 *Let $\Omega \subset \mathbb{R}^3_+$ be open and x a point with $\overline{B_h(x,r_h)} \subset \Omega$. Then*

$$\lim_{r_h\to 0} \frac{\int_{\partial B_h(x,r_h)} u\frac{\partial H(x,y)}{\partial n_k} d\sigma_{(k)}(y)}{4\pi} = -u(x)$$

for any hyperbolic balls $B_h(x,r_h)$ satisfying $\overline{B_h(x,r_h)} \subset \Omega$.

Proof. Using Proposition 3 we infer that in $\partial B_h(x,r_h)$ the outer normal at y is

$$n = (n_0, n_1, n_2) = \frac{(y_0 - x_0, y_1 - x_1, y_2 - x_2\cosh r_h)}{x_2 \sinh r_h}.$$

Denote $r_h = d(x,y)$. We first compute

$$\begin{aligned}
\frac{\partial H(x,y)}{\partial n_k} &= y_2^k \frac{\partial H(x,y)}{\partial n} = y_2^k (n, \operatorname{grad} v). \\
&= y_2^{\frac{3k-1}{2}} x_2^{\frac{k-1}{2}} \frac{\partial}{\partial r_h} \frac{\cosh\left(\frac{|k+1|r_h}{2}\right)}{\sinh r_h} \sum_{i=1}^{2} n_i \frac{\partial r_h}{\partial y_i} + \frac{k-1}{2} y_2^{k-1} n_2 H(x,y) \\
&= y_2^k H(x,y)\left(\frac{|k+1|}{2}\tanh\left(\frac{|k+1|r_h}{2}\right) - \coth r_h\right)\sum_{i=1}^{2} n_i \frac{\partial r_h}{\partial y_i} \\
&+ \frac{k-1}{2} y_2^{k-1} n_2 H(x,y).
\end{aligned}$$

Applying Lemma 1 we infer

$$\frac{\partial r_h}{\partial y_i} = \frac{\partial \operatorname{arcosh}\lambda(x,y)}{\partial y_i} = \frac{y_i - x_i - x_2(\cosh r_h - 1)\delta_{in}}{y_2 x_2 \sinh r_h},$$

and therefore we conclude

$$\sum_{i=1}^{2} n_i \frac{\partial r_h}{\partial y_i} = \frac{1}{y_2}.$$

Hence we have

$$\frac{\partial H}{\partial n_k}(x,y) = y_2^{k-1} H(x,y) \left(\frac{|k+1|}{2} \tanh\left(\frac{|k+1| r_h}{2} \right) - \coth r_h + \frac{k-1}{2} n_2 \right).$$

Since $B_h(x, r_h) = B(x_e, x_2 \sinh r_h)$ for $x_e = (x_0, x_1, x_2 \cosh r_h)$ and $u y_2^{\frac{3k-3}{2}}$ is continuous we obtain

$$\lim_{r_h \to 0} \frac{|k+1| x_2^{\frac{k-1}{2}}}{8\pi} \frac{\sinh\left(\frac{|k+1| r_h}{2}\right)}{\sinh r_h} \int_{\partial B_h(x,r_h)} u(y) y_2^{\frac{3k-3}{2}} d\sigma_{(k)}(y) = 0.$$

Similarly we deduce that

$$\lim_{r_h \to 0} \frac{k-1}{8\pi} \int_{\partial B_h(x,r_h)} \frac{y_2^{k-1} u(y) n_2 H(x,y)}{x_2 \sinh r_h} d\sigma_{(k)}(y)$$

$$= \lim_{r_h \to 0} \frac{(k-1) x_2^{\frac{k+1}{2}}}{8\pi x_2^2 \sinh^2 r_h} \int_{\partial B_h(x,r_h)} u(y) y_2^{\frac{3k-1}{2}} (y_2 - x_2 \cosh r_h) \cosh \frac{|k+1| r_h}{2} d\sigma_{(k)} = 0.$$

Lastly we infer

$$\lim_{r_h \to 0} -\frac{x_2^{\frac{k+3}{2}} \cosh r_h \cosh\left(\frac{|k+1| r_h}{2}\right)}{4\pi x_2^2 \sinh^2 r_h} \int_{\partial B_h(x,r_h)} \frac{u(y)}{y_2^{\frac{k+3}{2}}} d\sigma(y) = -u(x),$$

completing the proof.

Theorem 18 *Let $\Omega \subset \mathbb{R}^3_+$ be open and R a bounded open set with a smooth boundary satisfying $\overline{R} \subset \Omega$. If u is twice continuously differentiable functions in Ω and $x \in R$ then*

$$u(x) = \frac{1}{4\pi} \int_{\partial R} \left(u \frac{\partial H}{\partial n_k} - H \frac{\partial u}{\partial n_k} \right) d\sigma_k(y) - \frac{1}{4\pi} \int_R H \triangle_k u dm_{(k)}$$

where $d\sigma_k$, $dm_{(k)}$ and $\frac{\partial}{\partial n_k}$ are the same as in Lemma 16. Moreover, if $u \in \mathcal{C}_0^2(R)$ then

$$u(x) = -\frac{1}{4\pi} \int_R H \triangle_k u dm_{(k)}.$$

Proof. Applying Green formula in the set $R \backslash B_h(x, r_h)$ we obtain

$$\begin{aligned} \int_{R \backslash B_h(x,r_h)} (H \triangle_k u - u \triangle_k H) dm_{(k)} &= \int_{\partial R \backslash B_h(x,r_h)} \left(H \frac{\partial u}{\partial n_k} - u \frac{\partial H}{\partial n_k} \right) d\sigma_k \\ &= \int_{\partial R} \left(H \frac{\partial u}{\partial n_k} - u \frac{\partial H}{\partial n_k} \right) d\sigma_k \\ &\quad - \int_{\partial B_h(x,r_h)} \left(H \frac{\partial u}{\partial n_k} - u(y) \frac{\partial H}{\partial n_k} \right) d\sigma_k. \end{aligned}$$

Since H is k-hyperbolic harmonic in $R\backslash B_h(x,r_h)$ we obtain

$$\int_{R\backslash B_h(x,r_h)} H(x,y)\triangle_k u(y)\,dm_{(k)}(y) = \int_{\partial R}\left(H\frac{\partial u}{\partial n_k} - u\frac{\partial H}{\partial n_k}\right)d\sigma_k(y) - \int_{\partial B_h(x,r_h)}\left(H\frac{\partial u}{\partial n_k} - u\frac{\partial H}{\partial n_k}\right)d\sigma_k.$$

Since

$$\int_{\partial B_h(x,r_h)} H\frac{\partial u}{\partial n_k}d\sigma_k = x_2^{\frac{k-1}{2}}\frac{\cosh\left(\frac{|k+1|r_h}{2}\right)}{\sinh r_h}\int_{\partial B_h(x,r_h)}\frac{\partial u}{\partial n_k}y_2^{-\frac{3k+1}{2}}d\sigma$$

and $\frac{\partial u}{\partial n_k}y_2^{-\frac{3k+1}{2}}$ is bounded in $\partial B_h(x,r_h)$ we obtain

$$\int_{\partial B_h(x,r_h)}\left|H\frac{\partial u}{\partial n_k}\right|d\sigma_k \le m(x,r_h)\,x_2^{\frac{k-1}{2}}4\cosh\left(\frac{|k+1|\,r_h}{2}\right)\pi\sinh r_h$$

for some founction $m>0$ with bounded limit when $r_h\to 0$ and therefore

$$\lim_{r_h\to 0}\int_{\partial B_h(x,r_h)} H\frac{\partial u}{\partial n_k}d\sigma_k = 0.$$

Since the function $\triangle_k u(y)$ is a continuous function and by Lemma 15 $H(x,y)$ is integrable in a bounded set R we obtain

$$\lim_{r_h\to 0}\int_{R\backslash B_h(x,r_h)} H\triangle_k uydm_{(k)} = \int_R H\triangle_k udm_{(k)}.$$

Combining all the preceding steps and applying Lemma 17 we conclude the result.

Corollary 19 *Let $\Omega\subset\mathbb{R}^3_+$ be open and R a bounded open set with a smooth boundary satisfying $\overline{R}\subset\Omega$. If u is k-hyperbolic harmonic in Ω and $x\in R$ then*

$$u(x) = \frac{1}{4\pi}\int_{\partial R}\left(u\frac{\partial H}{\partial n_k} - H\frac{\partial u}{\partial n_k}\right)d\sigma_k(y)$$

where $d\sigma_k$, $dm_{(k)}$ and $\frac{\partial}{\partial n_k}$ are the same as in Lemma 16.

Note that if $k=1$, then

$$H(x,y) = \coth\left(d_h(x,y)\right) = \int_{d_h(x,y)}^{\infty} -\frac{du}{\sinh^2 u}$$

and if $k=-1$, then

$$H(x,y) = \frac{1}{x_2y_2\sinh d_h(x,y)} = \frac{1}{x_2y_2\sqrt{\lambda^2-1}} = \frac{2}{|x-y|\,|x-\widehat{y}|}.$$

These kernels were already used in integral formulas for hypermonogenic functions, see for example in [2] and [6]. Mean value properties for hyperbolic harmonic functions were verified in [7] .

We may prove also similar results for eigenfunctions of the hyperbolic Laplace operator.

Theorem 20 *Let $\Omega \subset \mathbb{R}^3_+$ be open and R a bounded domain with a smooth boundary satisfying $\overline{R} \subset \Omega$. Denote $\gamma = \frac{1}{4}(4-(k+1)^2$. If u is twice continuously differentiable functions in Ω and $x \in R$ then*

$$u(x) = \frac{1}{4\pi}\int_{\partial R}\left(u\frac{\partial F}{\partial n_h} - F\frac{\partial u}{\partial n_h}\right)d\sigma_h(y) - \frac{1}{4\pi}\int_R F\left(\triangle_h u - \gamma u\right)dm_h,$$

where $d\sigma_h = \frac{d\sigma}{y_2^2}$, $dm_h = \frac{dm}{y_2^3}$ and $\frac{\partial}{\partial n_h} = y_2\frac{\partial}{\partial n}$. Moreover. if $u \in \mathcal{C}_0^2(R)$ then

$$u(x) = -\frac{1}{4\pi}\int_R F\left(\triangle_h u - \gamma u\right)dm_h.$$

Proof. Using Green formula in the set $R\backslash B_h(x,r_h)$ we obtain

$$\begin{aligned}\int_{R\backslash B_h(x,r_h)}\left(F\left(\triangle_h u-\gamma u\right)-u\left(\triangle_h F-\gamma F\right)\right)dm_h &= \int_{\partial R\backslash B_h(x,r_h)}\left(F\frac{\partial u}{\partial n_h}-u\frac{\partial F}{\partial n_h}\right)d\sigma_h\\ &= \int_{\partial R}\left(F\frac{\partial u}{\partial n_h}-u\frac{\partial F}{\partial n_h}\right)d\sigma_h\\ &- \int_{\partial B_h(x,r_h)}\left(F\frac{\partial u}{\partial n_h}-u\frac{\partial F}{\partial n_h}\right)d\sigma_h.\end{aligned}$$

From $\triangle_h F(x,y) - \gamma F(x,y) = 0$ in $R\backslash B_h(x,r_h)$, it follows that

$$\begin{aligned}\int_{R\backslash B_h(x,r_h)} F\left(\triangle_h u-\gamma u\right)dm_h &= \int_{\partial R}\left(F\frac{\partial u}{\partial n_h}-u\frac{\partial F}{\partial n_h}\right)d\sigma_h\\ &- \int_{\partial B_h(x,r_h)}\left(F\frac{\partial u}{\partial n_h}-u\frac{\partial F}{\partial n_h}\right)d\sigma_h.\end{aligned}$$

Since $\frac{\partial u}{\partial n_k}$ is bounded in $\partial B_h(x,r_h)$ we obtain

$$\int_{\partial B_h(x,r_h)}\left|F(x,y)\frac{\partial u(y)}{\partial n_h}\right|d\sigma_h(y) \le 4m(x,r_h)\cosh\frac{|k+1|\,r_h}{2}\pi x_2\sinh r_h$$

for some function $m>0$ with a bounded limit when $r_h \to 0$ and therefore

$$\lim_{r_h\to 0}\int_{\partial B_h(x,r_h)} F(x,y)\frac{\partial u(y)}{\partial n_h}d\sigma_h(y) = 0.$$

Since the function $\triangle_h u - \gamma u$ is a continuous function and by Lemma 15 $F(x,y)$ is integrable in a bounded set R we obtain

$$\lim_{r_h\to 0}\int_{R\backslash B_h(x,r_h)} F(x,y)\left(\triangle_h u-\gamma u\right)dm_h(y) = \int_R F(x,y)\left(\triangle_h u-\gamma u\right)dm_h(y).$$

The proof is completed when we verify that

$$\lim_{r_h \to 0} \frac{\int_{\partial B_h(x,R_h)} u \frac{\partial F(x,y)}{\partial n_h} d\sigma_h(y)}{4\pi} = -u(x).$$

This follows from the preceding calculations similarly as earlier proof, since

$$\frac{\partial F}{\partial n_h} = F(x,y)\left(\frac{|k+1|}{2}\tanh\left(\frac{|k+1|\, r_h}{2}\right) - \coth r_h\right)$$

and

$$\begin{aligned}\lim_{r_h \to 0} \int_{\partial B_h(x,r_h)} u \frac{\partial F(x,y)}{\partial n_h} d\sigma_h &= -\lim_{r_h \to 0} \frac{\cosh\left(\frac{|k+1|r_h}{2}\right)\cosh r_h}{\sinh^2 r_h} \int_{\partial B_h(x,r_h)} \frac{u d\sigma}{y_2^2} \\ &= -4\pi u(x).\end{aligned}$$

Corollary 21 *Let $\Omega \subset \mathbb{R}^3_+$ be open and R a bounded open set with a smooth boundary satisfying $\overline{R} \subset \Omega$. If u is an eigenfunction corresponding to the eigenvalue $\gamma = \frac{1}{4}(4-(k+1)^2$ in Ω and $x \in R$ then*

$$u(x) = \frac{1}{4\pi}\int_{\partial R}\left(u\frac{\partial F(x,y)}{\partial n_h} - F(x,y)\frac{\partial u}{\partial n_h}\right) d\sigma_h.$$

References

[1] Akin, Ö., Leutwiler, H.,*On the invariance of the solutions of the Weinstein equation under Möbius transformations.* In Classical and modern potential theory and applications (Chateau de Bonas, 1993), 19 - 29, NATO Adv. Sci. Inst. Ser. C Math. Phys. Sci., 430, Kluwer , Dordrecht, 1994.

[2] Eriksson, S.-L., *Hyperbolic Extensions of Integral Formulas*, Adv. appl. Clifford alg. 20, Numbers 3-4, (2010), 575-586.

[3] Eriksson-Bique, S.-L., *k-hypermonogenic functions,* In Progress in analysis: proceedings of the 3rd International ISAAC Congress (2003), 337-348.

[4] Eriksson, S-L. and H. Leutwiler, *Hyperbolic harmonic functions and their function theory*, in Potential theory and Stochatics in Albac, Theta 2009, 85–100.

[5] Eriksson,S.-L., H. Orelma, *A Mean-Value Theorem for Some Eigenfunctions of the Laplace-Beltrami Operator on the Upper-Half Space*, Ann. Acad. Sci. Fenn. 36, 2011, 101–110.

[6] Eriksson, S-L., Orelma, H., *A Hyperbolic Interpretation of Cauchy-Type Kernels in Hyperbolic Function Theory*, Hypercomplex Analysis and Applications Trends in Mathematics, 2011, 43 - 59.

[7] Eriksson,S.-L., H. Orelma, *A Mean-Value Theorem for Some Eigenfunctions of the Laplace-Beltrami Operator on the Upper-Half Space*, Ann. Acad. Sci. Fenn. 36, 2011, 101–110.

[8] Eriksson, S-L. and H. Orelma, *Mean value properties for the Weinstein equation using the hyperbolic metric.* Submitted for a publication.

[9] Huber, A., *A Uniqueness of Generalized Axially Symmetric Potentials*, Ann. of Math. 60, no 2, 1954, 351-368.

[10] Leutwiler, H., *Best constants in the Harnack inequality for the Weinstein equation*, Aequationes Math. 34, no. 2 - 3, 1987, 304 – 315. .

[11] Leutwiler, H., *Appendix: Lecture notes of the course "Hyperbolic harmonic functions and their function theory"*. Clifford algebras and potential theory, 85–109, Univ. Joensuu Dept. Math. Rep. Ser., 7, Univ. Joensuu, Joensuu, 2004.

[12] Weinstein, A., *Generalized Axially Symmetric Potential Theory*, Bul. Amer. Math. Soc. 59 , 1953, 20–38.

19th International Conference on the Application of Computer
Science and Mathematics in Architecture and Civil Engineering
K. Gürlebeck, T. Lahmer and F. Werner (eds.)
Weimar, Germany, 04–06 July 2012

T-SPLINE BASED XIGA FOR ADAPTIVE MODELING OF CRACKED BODIES

S. Sh. Ghorashi*, T. Rabczuk, J. J. Ródenas and T. Lahmer

**Research Training Group 1462, Bauhaus-Universität Weimar*
Berkaer Str. 9, 99423 Weimar, Germany
E-mail: shahram.ghorashi@uni-weimar.de

Keywords: Crack, EXtended IsoGeometric Analysis (XIGA), T-spline Basis Functions, Local Refinement, Stress Intensity Factor.

Abstract. *Safety operation of important civil structures such as bridges can be estimated by using fracture analysis. Since the analytical methods are not capable of solving many complicated engineering problems, numerical methods have been increasingly adopted. In this paper, a part of isotropic material which contains a crack is considered as a partial model and the proposed model quality is evaluated. EXtended IsoGeometric Analysis (XIGA) is a new developed numerical approach [1, 2] which benefits from advantages of its origins: eXtended Finite Element Method (XFEM) and IsoGeometric Analysis (IGA). It is capable of simulating crack propagation problems with no remeshing necessity and capturing singular field at the crack tip by using the crack tip enrichment functions. Also, exact representation of geometry is possible using only few elements. XIGA has also been successfully applied for fracture analysis of cracked orthotropic bodies [3] and for simulation of curved cracks [4]. XIGA applies NURBS functions for both geometry description and solution field approximation. The drawback of NURBS functions is that local refinement cannot be defined regarding that it is based on tensor-product constructs unless multiple patches are used which has also some limitations. In this contribution, the XIGA is further developed to make the local refinement feasible by using T-spline basis functions. Adopting a recovery based error estimator in the proposed approach for evaluation of the model quality and performing the adaptive processes is in progress. Finally, some numerical examples with available analytical solutions are investigated by the developed scheme.*

1 INTRODUCTION

Increasingly development of computers made the possibility to apply numerical methods for simulation of civil structures as an alternative to analytical methods which are not feasible in resolving complex problems. This has attracted many researchers' interests for developing more accurate and efficient computational approaches in the last decades.

Fracture analysis of structures is of great importance for estimation of their safety operation. A reliable and efficient numerical method is required for analysis of cracked part of a structure.

The remeshing necessity and existence of a singular field around a crack tip in simulation of crack propagation problems led to the development of a new generation of computational approaches such as meshfree methods [5-14] and the extended FEM (XFEM) [15-20] which belongs to the class of Partition of Unity Methods (PUM). Moving discontinuous problems such as crack propagation can be analyzed by these methods without the requrirement of remeshing or rearranging of the nodal points. In the XFEM, a priori knowledge of the solution is locally added to the approximation space. This enrichment allows for capturing particular features such as discontinuities and singularities which are present in the solution exactly.

More recently, a numerical approach called extended isogeometric analysis (XIGA) [1, 2] has been developed for simulation of stationary and propagating cracks by incorporating the concepts of the XFEM into the isogeometric analysis [21, 22]. Some superiorities of the isogeometric analysis in comparison with the conventional FEM are: simple and systematic refinement strategies, an exact representation of common and complex engineering shapes, robustness and higher accuracy. XIGA has also been successfully applied for fracture analysis of cracked orthotropic bodies [3] and for simulation of curved cracks [4].

XIGA applies NURBS functions for both geometry description and solution field approximation. The drawback of NURBS functions is that local refinement cannot be defined regarding that it is based on tensor-product constructs unless multiple patches are used which has also some limitations. In this contribution, T-spline basis functions are applied in the XIGA to make local refinement feasible.

Finally, for quality evaluation of the proposed model, some numerical simulations with available analytical solutions are studied.

2 BASIS FUNCTIONS

2.1 NURBS

Non-uniform rational B-splines (NURBS) are a generalization of piecewise polynomial B-spline curves. The B-spline basis functions are defined in a parametric space on a knot vector $\boldsymbol{\Xi}$. A knot vector in one dimension is a non-decreasing sequence of real numbers:

$$\boldsymbol{\Xi} = \{\xi_1, \xi_2, \ldots, \xi_{n+p+1}\} \tag{1}$$

where ξ_i is the i^{th} knot, i is the knot index, $i = 1, 2, \ldots, n + p + 1$, p is the order of the B-spline, and n is the number of basis functions. The half open interval $[\xi_i, \xi_{i+1})$ is called the i^{th} knot span and it can have zero length since knots may be repeated more than once, and the

interval $[\xi_1, \xi_{n+p+1}]$ is called a patch. In the isogeometric analysis, always open knot vectors are employed. A knot vector is called open if it contains $p+1$ repeated knots at the two ends.

With a certain knot span, the B-spline basis functions are defined recursively as,

$$N_i^0(\xi) = \begin{cases} 1 & \text{if } \xi_i \leq \xi \leq \xi_{i+1} \\ 0 & \text{otherwise} \end{cases} \tag{2}$$

and

$$N_i^p(\xi) = \frac{\xi - \xi_i}{\xi_{i+p} - \xi_i} N_i^{p-1}(\xi) + \frac{\xi_{i+p+1} - \xi}{\xi_{i+p+1} - \xi_{i+1}} N_{i+1}^{p-1}(\xi) \quad p = 1, 2, 3, \ldots \tag{3}$$

where $i = 1, 2, \ldots, n$.

A B-spline curve of order p is defined by:

$$\mathbf{C}(\xi) = \sum_{i=1}^{n} N_i^p(\xi) \mathbf{P}_i \tag{4}$$

where $N_i^p(\xi)$ is the i^{th} B-spline basis function of order p and $\{\mathbf{P}_i\}$ are control points, given in d-dimensional space $\mathbf{R}^d$.

The non-uniform rational B-spline (NURBS) curve of order p is defined as:

$$\mathbf{C}(\xi) = \sum_{i=1}^{n} R_i^p(\xi) \mathbf{P}_i \tag{5}$$

$$R_i^p(\xi) = \frac{N_i^p(\xi) w_i}{\sum_{j=1}^{n} N_j^p(\xi) w_j} \tag{6}$$

where $\{R_i^p\}$ are the NURBS basis functions, $\{\mathbf{P}_i\}$ are the control points and w_i is the i^{th} weight that must be non-negative. In the two dimensional parametric space $[0,1]^2$, NURBS surfaces are constructed by tensor product through knot vectors $\boldsymbol{\Xi}^1 = \left\{\xi_1^1, \xi_2^1, \ldots, \xi_{n+p+1}^1\right\}$ and $\boldsymbol{\Xi}^2 = \left\{\xi_1^2, \xi_2^2, \ldots, \xi_{n+p+1}^2\right\}$. It yields to:

$$R_{i,j}^{p,q}\left(\xi^1, \xi^2\right) = \frac{N_i^p(\xi^1) M_j^q(\xi^2) w_{i,j}}{\sum_{k=1}^{n} \sum_{l=1}^{m} N_k^p(\xi^1) M_l^q(\xi^2) w_{k,l}} \tag{7}$$

For more details on NURBS, refer to [23].

2.2 T-splines

T-splines is a generalization of NURBS enabling local refinement [26, 27]. For defining the T-spline basis functions, an index space called T-mesh is defined. It is similar to the index space representation of a NURBS, with the difference that T-junctions, which are vertices connecting three edges, are allowed. An example of T-mesh is illustrated in Fig. 1. It is noted that each line

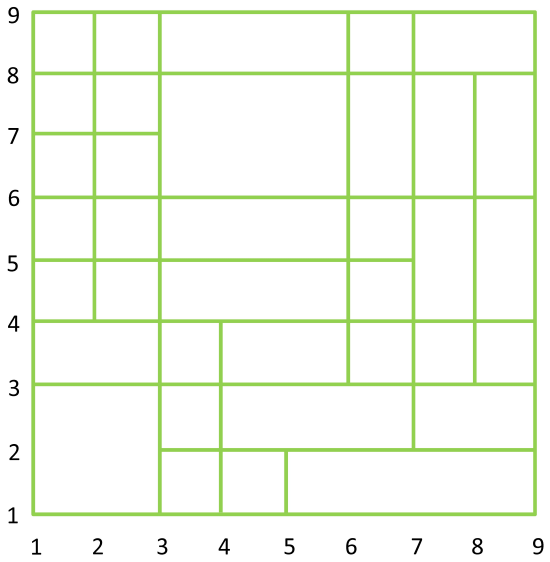

Figure 1: A sample of T-mesh.

in the mesh corresponds to a knot value. Then, anchors are defined on the T-mesh to identify the location of each basis function. They are located at the intersections of knot lines if the polynomial order is odd, otherwise their location are in the center of the cells. Regardless of degree, an anchor location is at the center of the support of a function in the index space.

For definition of T-splines, local knot vectors are defined instead of using the global knot vectors since each basis function has the compact support of $(p+1) \times (q+1)$ knots. As illustrated in Fig. 2, local knot vectors in each direction are defined by horizontally or vertically marching from the anchors backward and forward [27]. Afterwards, each basis function can be defined using the Eqs. 2, 3 and 7 and its corresponding local knot vectors.

In order to refine the mesh, knot insertion process is performed. It consists of adding new knots to the present mesh/T-mesh and correspondingly, modifying and adding some control points. For more information about T-spline and local refinement, readers are referred to [26, 27].

3 EXTENDED ISOGEOMETRIC ANALYSIS

Extended isogeometric analysis (XIGA) is a newly developed computational approach which uses the superiorities of the extended finite element method (XFEM) within the isogeometric analysis. It is capable of crack propagation simulation without the remeshing necessity since element edges are defined independent of the crack location.

Solution field approximation is extrinsically enriched by the Heaviside and branch functions for crack face and singular field (around the crack tip) modeling, respectively.

$$\begin{aligned}\mathbf{u}^h\left(\xi^1,\xi^2\right) = &\sum_{i=1}^{n_{en}} R_i^{p,q}\left(\xi^1,\xi^2\right)\mathbf{u}_i + \sum_{j=1}^{n_H} R_j^{p,q}\left(\xi^1,\xi^2\right) H\mathbf{a}_j \\ &+ \sum_{k=1}^{n_Q} R_k^{p,q}\left(\xi^1,\xi^2\right)\sum_{\alpha=1}^{4} Q_\alpha \mathbf{b}_k^\alpha\end{aligned} \tag{8}$$

The first term in the right hand side is standard IGA approximation. $\{R_i^{p,q}\left(\xi^1,\xi^2\right)\}$ are the T-Spline basis functions of orders p and q in ξ^1 and ξ^2 directions, respectively, at the point (ξ^1,ξ^2)

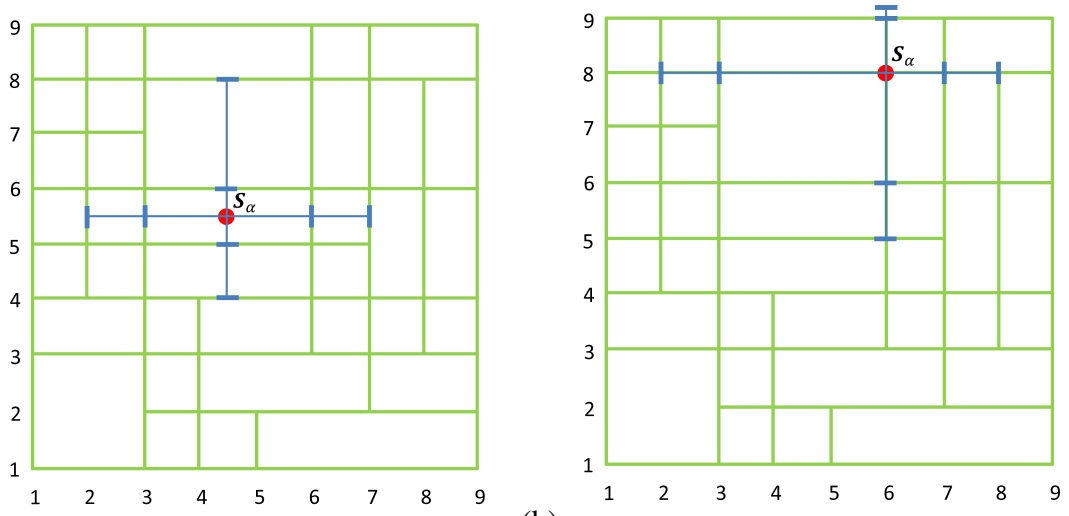

Figure 2: Schematic view of defining local knot vectors for the anchor $\mathbf{S}_\alpha$: (a) quadratic polynomial order: $\mathbf{\Xi}_\alpha^1 = \left\{\xi_2^1, \xi_3^1, \xi_6^1, \xi_7^1\right\}$ and $\mathbf{\Xi}_\alpha^2 = \left\{\xi_4^2, \xi_5^2, \xi_6^2, \xi_8^2\right\}$; (b) cubic polynomial order: $\mathbf{\Xi}_\alpha^1 = \left\{\xi_2^1, \xi_3^1, \xi_6^1, \xi_7^1, \xi_8^1\right\}$ and $\mathbf{\Xi}_\alpha^2 = \left\{\xi_5^2, \xi_6^2, \xi_8^2, \xi_9^2, \xi_9^2\right\}$.

in the parametric space $[0,1] \times [0,1]$. $\{\mathbf{a}_j\}$ are the vectors of additional degrees of freedom which are related to the modeling of crack faces, $\{\mathbf{b}_k^\alpha\}$ are the vectors of additional degrees of freedom for modeling the crack tip, n_{en} is the number of nonzero basis functions for a given knot span, n_Q is the number of n_{en} basis functions which have been selected as branch enriched basis functions. They can be selected using the topological enrichment strategy or geometrical enrichment one. In topological enrichment scheme, the basis functions which contain the crack tip in their influence domains are selected as the branch enriched basis functions while in geometrical enrichment method, branch enriched basis functions consist of the basis functions chosen from the previous strategy and the ones which are selected according to considering a constant domain around the crack tip. In this contribution, geometrical enrichment method is adopted and a circular domain with a predefined radius at the center crack tip is considered and basis functions whose influence domains contain the crack tip and whose anchors located in the circle are selected as branch enriched basis functions. n_H is the number of n_{en} basis functions that have crack face in their support domains and have not been selected as branch enriched basis functions. H is the generalized Heaviside function [24],

$$H\left(\mathbf{X}\right) = \begin{cases} +1 & \text{if } \left(\mathbf{X} - \mathbf{X}^*\right).\mathbf{e}_n > 0 \\ -1 & \text{otherwise} \end{cases} \tag{9}$$

where $\mathbf{e}_n$ is the unit normal vector of crack alignment in point $\mathbf{X}^*$on the crack surface which is the nearest point to $\mathbf{X}\left(\xi^{\mathbf{1}}, \xi^{\mathbf{2}}\right)$.

In Eq. 8, $Q_\alpha\left\{\alpha = 1,2,3,4\right\}$ are the crack tip enrichment functions whose roles are reproducing the singular field around crack tips,

$$\left\{Q_\alpha\right\}_{\alpha=1}^4 = \left\{\sqrt{r}\sin\frac{\theta}{2}, \sqrt{r}\cos\frac{\theta}{2}, \sqrt{r}\sin\theta\sin\frac{\theta}{2}, \sqrt{r}\sin\theta\cos\frac{\theta}{2}\right\} \tag{10}$$

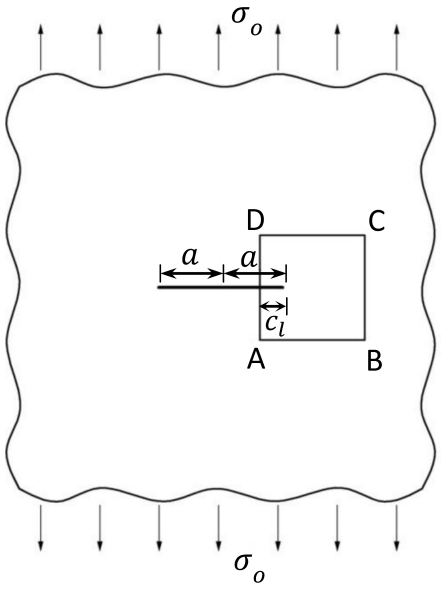

Figure 3: A mode I crack model in an infinite plate.

where (r, θ) are the local crack tip polar coordinates with respect to the tangent to the crack tip in the physical space.

Readers are referred to [2] for more information about XIGA formulation and implementation.

4 NUMERICAL EXAMPLES

In this section, two numerical examples are investigated by the proposed approach. The first one contains a mode I crack while the other includes a mixed mode crack. New knots added for refinement satisfy the conditions of analysis-suitable T-splines [28]. Basis functions of cubic order are considered. Gauss quadrature rule with 4x4 Gauss points for normal elements is utilized. For integration over split and tip elements, sub-triangles and almost polar techniques with 13 and 7x7 Gauss points for each sub-triangles are adopted.

4.1 Mode I crack model in the infinite plate

An infinite plate including a straight crack under pure fracture mode I is considered, as depicted in Figure 3. The plate is in plane strain state. Then, a local finite square domain ABCD which includes the crack tip in the center is defined. The domain ABCD, which includes the $c_l = 5$ mm part of the crack, is smaller than the crack length $2a = 200$ mm in the infinite plate. The size of this analytical domain ABCD is 10×10 mm. Other parameters are: Young's modulus $E = 10^7$ N/mm^2, Poisson's ratio $\nu = 0.3$ and prescribed uniaxial stress $\sigma_o = 10^4$ N/mm^2.

The analytical solution for the displacement and stress fields in terms of local polar coordinates in a reference frame (r, θ) centered at the crack tip are:

$$\begin{aligned} u_x(r,\theta) &= \tfrac{2(1+\nu)}{\sqrt{2\pi}} \tfrac{K_I}{E} \sqrt{r} \cos\tfrac{\theta}{2} \left(2 - 2\nu - \cos^2\tfrac{\theta}{2}\right) \\ u_y(r,\theta) &= \tfrac{2(1+\nu)}{\sqrt{2\pi}} \tfrac{K_I}{E} \sqrt{r} \sin\tfrac{\theta}{2} \left(2 - 2\nu - \cos^2\tfrac{\theta}{2}\right) \end{aligned} \tag{11}$$

Table 1: Error norms (in percent) of the three models before and after local refinement using NURBS and T-splines.

model	local refined	basis functions	control points	elements	DOFs	error norm (%)	
						L_2	energy
I	no	NURBS	64	25	272	0.1341	2.4945
	yes	NURBS	140	77	500	0.0698	2.1441
	yes	T-spline	112	77	444	0.0706	2.1595
II	no	NURBS	324	225	1044	0.0516	1.6823
	yes	NURBS	680	527	2488	0.0101	0.9486
	yes	T-spline	442	391	1820	0.0101	0.9252
III	no	NURBS	784	625	2592	0.0230	1.2012
	yes	NURBS	1620	1377	5864	0.0039	0.6358
	yes	T-spline	972	891	3848	0.0040	0.6238

$$\begin{aligned} \sigma_{xx}(r,\theta) &= \tfrac{K_I}{\sqrt{2\pi r}} \cos\tfrac{\theta}{2}\left(1-\sin\tfrac{\theta}{2}\sin\tfrac{3\theta}{2}\right) \\ \sigma_{yy}(r,\theta) &= \tfrac{K_I}{\sqrt{2\pi r}} \cos\tfrac{\theta}{2}\left(1+\sin\tfrac{\theta}{2}\sin\tfrac{3\theta}{2}\right) \\ \sigma_{xy}(r,\theta) &= \tfrac{K_I}{\sqrt{2\pi r}} \sin\tfrac{\theta}{2}\cos\tfrac{\theta}{2}\cos\tfrac{3\theta}{2} \end{aligned} \tag{12}$$

where $K_I = \sigma_o\sqrt{\pi a}$ is the mode I stress intensity factor. Analytical displacement field (Eq. 11) is prescribed on the boundaries except for the crack boundary. Unlike homogeneous essential boundary conditions, inhomogeneous boundaries can not be imposed in a straightforward approach in isogeometric analysis; because the non-interpolating natures of NURBS and T-splines do not allow for satisfaction of the kronecker delta property. For imposition of essential boundary conditions, the least-squares minimization method [1] is applied.

Three models with uniformly distributed elements are considered: model I with 5×5 elements, model II with 15×15 elements, and model III with 25×25 elements. For this purpose, the h-refinement (knot insertion) process is utilized. In order to locally refine the mesh around the crack, the elements intersected with the crack are chosen for uniform refinement in a 3×3 mesh. Both NURBS and T-spline basis functions are applied for each model. Mesh and elements for the model III before and after local refinement are displayed in Fig. 4.

The exact L_2 (of displacement) and energy error norms (in percent) of all models are given in Table 1. It is observed that in some cases the models which are locally refined by using T-splines result in even more accurate results than those obtained by using NURBS, although much less number of control points and degrees of freedom are applied.

4.2 Inclined center crack in a square plate under uniaxial tension

Mixed mode stress intensity factors for a square plate with a center inclined crack under remote uniaxial tensile stress (Fig. 5) are investigated. The plate is in plane stress state, with $L = D = 10$ and $2a = 0.7$. Since the plate dimensions are large in comparison to the crack length, the numerical results can be reasonably compared with the analytical solution of infinite plate. For the predefined loading σ_o, the exact mixed mode stress intensity factors are:

$$K_I = \sigma_o\sqrt{\pi a}\cos^2\phi, \quad K_{II} = \sigma_o\sqrt{\pi a}\sin\phi\cos\phi \tag{13}$$

which ϕ is the crack inclination angle with respect to the horizontal line.

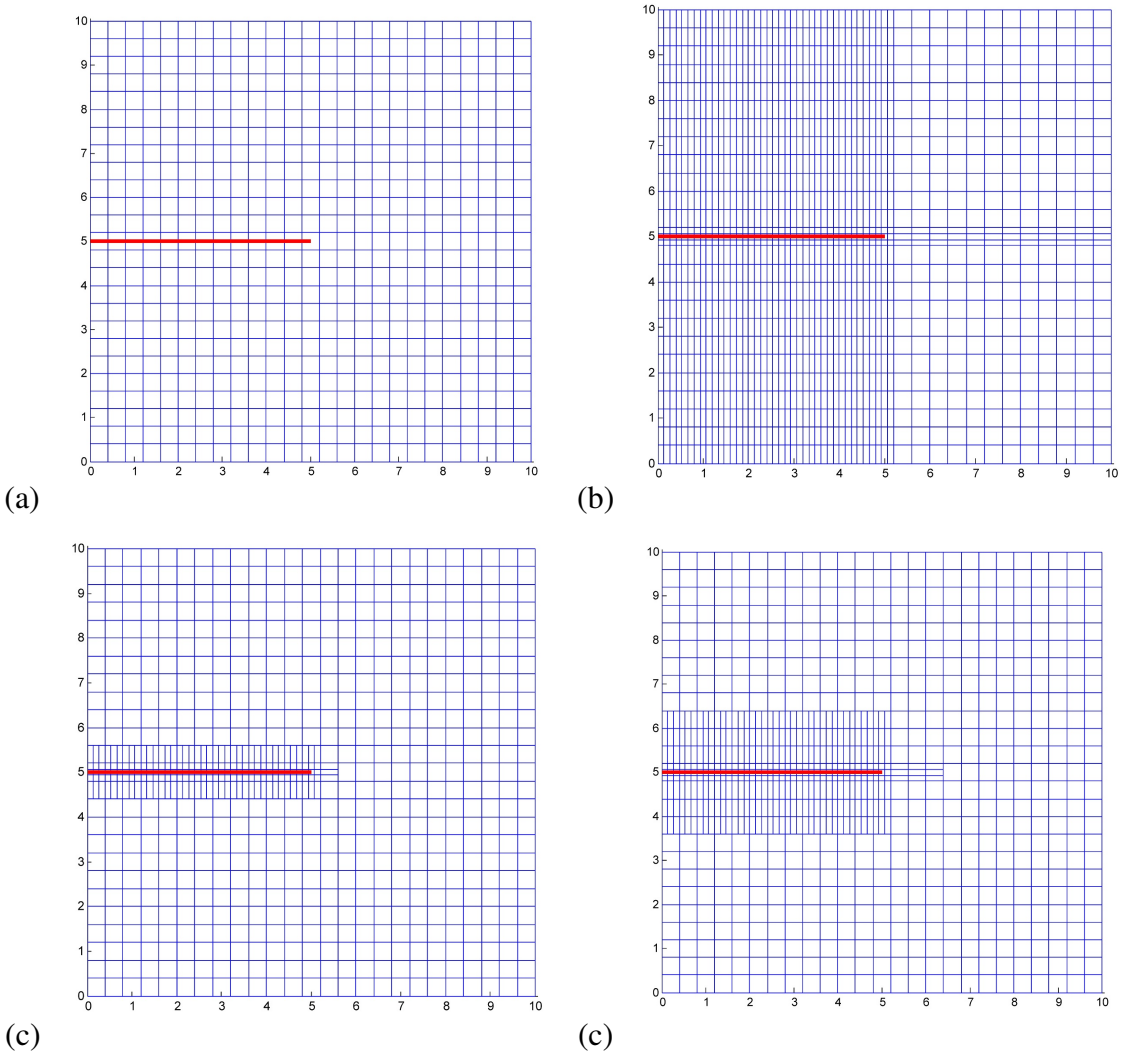

Figure 4: Mesh and elements of the model III before and after local refinement: (a) mesh/elements before local refinement; (b) mesh/elements after local refinement using NURBS; (c) mesh after local refinement using T-splines; (c) elements (for integration) after local refinement using T-splines.

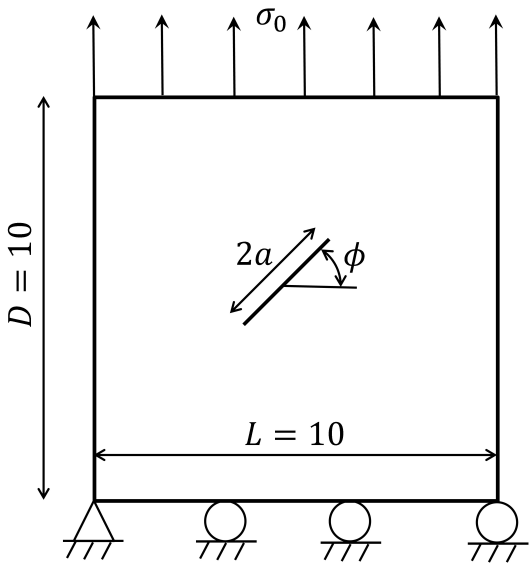

Figure 5: Geometry and loading of a square plate with a center inclined crack.

Table 2: Errors (%) of computed mixed-mode SIFs for different crack inclination angles, ϕ (degree).

	K_I		K_{II}	
ϕ	NURBS	T-spline	NURBS	T-spline
0	0.4339	0.4339	-	-
15	0.3786	0.3786	0.2912	0.2913
30	0.477	0.477	1.0711	1.07
45	0.4759	0.4759	1.0388	1.0387
60	0.6498	0.6526	1.3027	1.3039
75	0.4746	0.4746	1.1389	1.1389

Since Dirichlet boundary condition is homogeneous in this example, no specific technique is utilized for imposition of essential boundary conditions. For discretizing the model, firstly 25×25 uniformly distributed elements are constructed using the h-refinement, then the elements located in $[4,6]\times[4,6]$ are selected for uniform refinement in a 5×5 mesh. Both NURBS and T-spline basis functions are applied for analysis. Model discretizations for models which use NURBS and T-spline basis functions are illustrated in Figs. 6 and 7, respectively.

Different inclination angles have been modeled using the two aforementioned discretizations. It is interesting to note that the both resulted in very similar mixed mode SIFs while 2304 control points and 2025 elements are modeled for the first discretization and 1504 control points and 1465 elements are modeled for the second one. Errors (%) of the computed SIFs are given in Table 2 and the exact and computed normalized mixed mode SIFs are illustrated in Fig. 8. The computed SIFs are close to the exact SIFs.

5 CONCLUSION

In this contribution, the XIGA method has been further developed by using the T-spline basis functions. This method is capable of local refinement which is necessary for adaptive procedure.

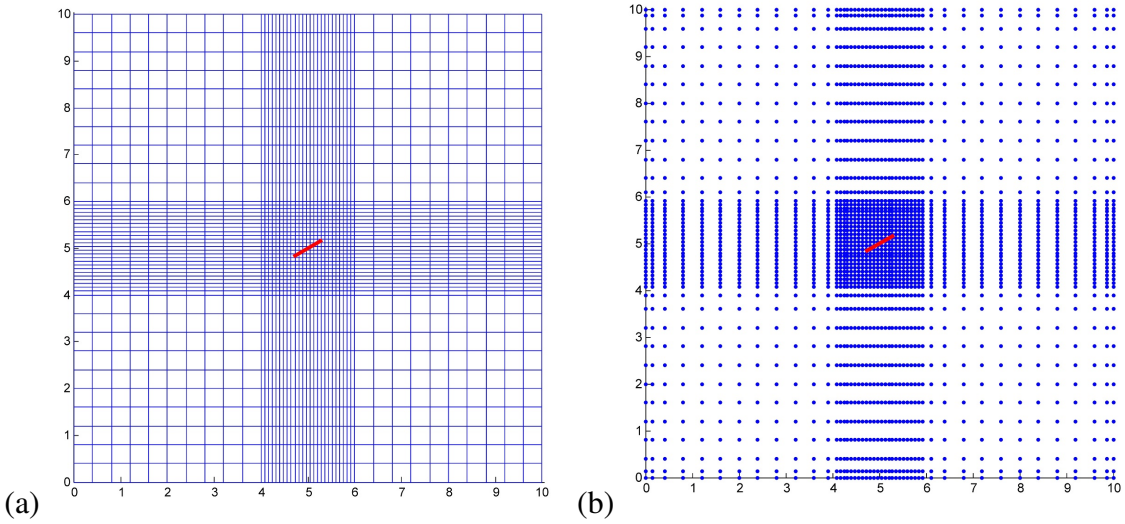

Figure 6: Discretization of a square plate with a center inclined crack using NURBS: (a) mesh; (b) control points.

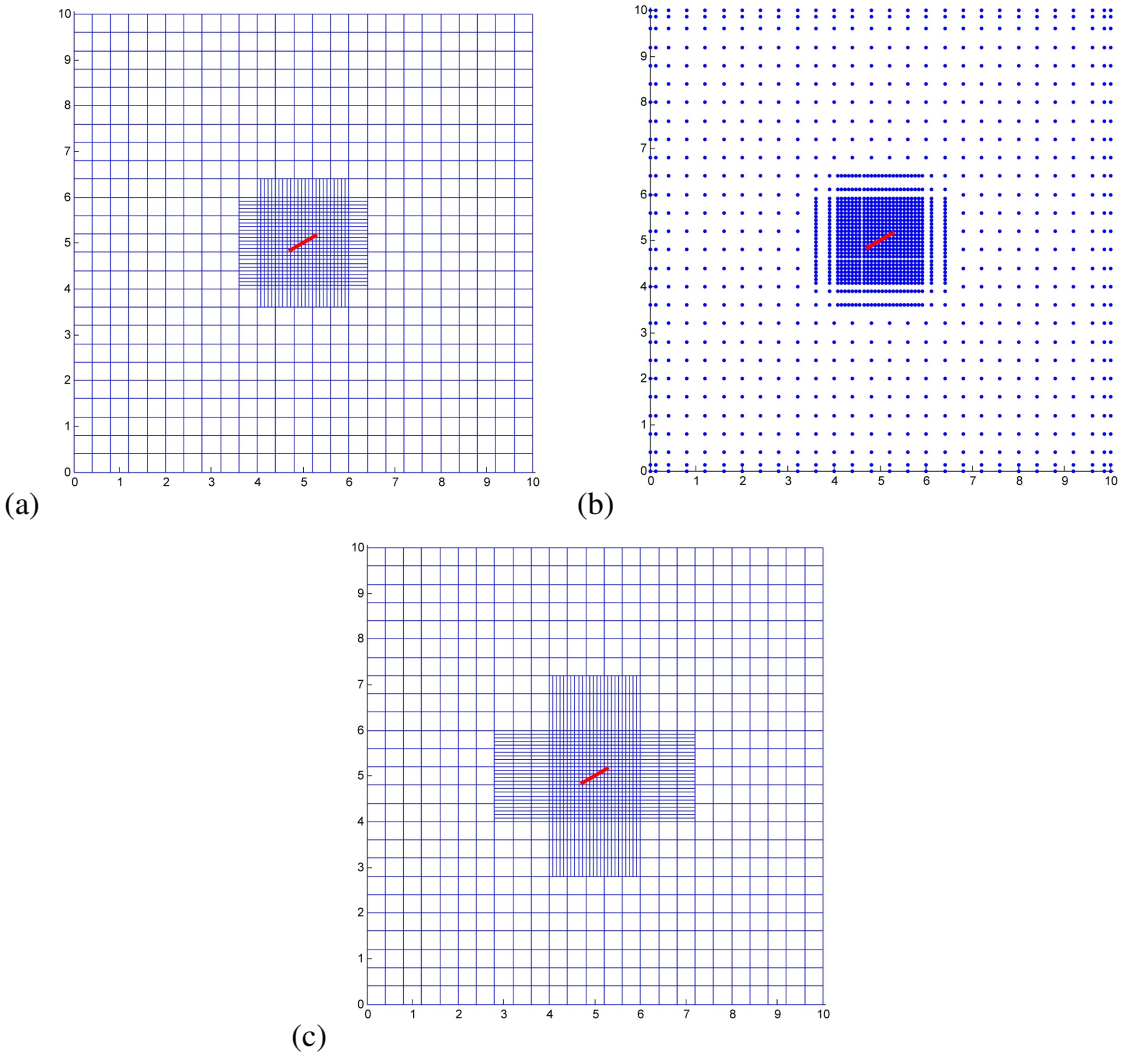

Figure 7: Discretization of a square plate with a center inclined crack using T-splines: (a) mesh; (b) control points; (c) elements for integration.

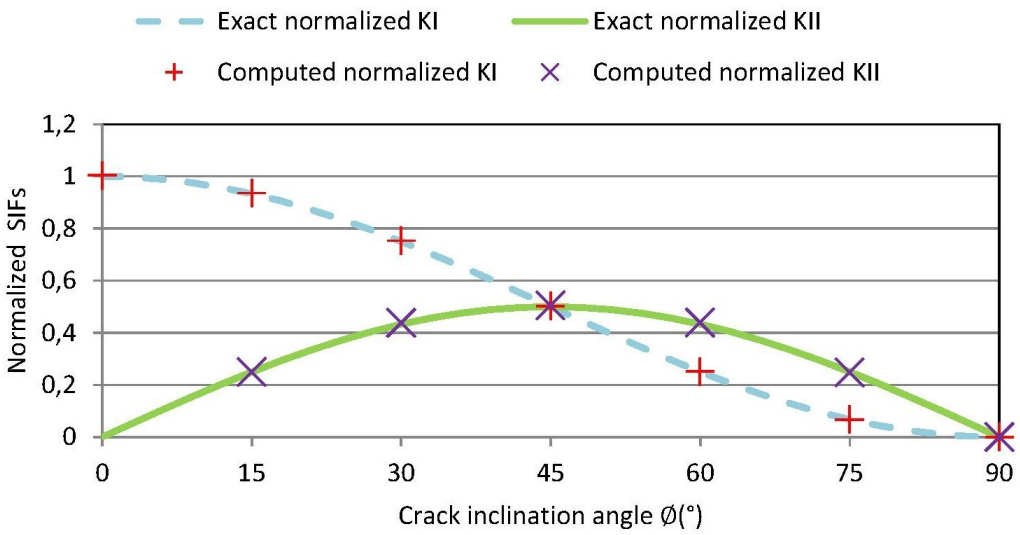

Figure 8: Analytical and computed normalized mixed mode SIFs for several crack inclination angles

Adopting a recovery based error estimator in the proposed approach (which is in progress by the authors), can make XIGA a robust and practical method for fracture analysis of structures.

ACKNOWLEDGEMENT

This research is supported by the German Research Institute (DFG) via Research Training Group ”Evaluation of Coupled Numerical Partial Models in Structural Engineering (GRK 1462)”, which is gratefully acknowledged by the authors.

REFERENCES

[1] E. De Luycker, D. J. Benson, T. Belytschko, Y. Bazilevs and M. C. Hsu, X-FEM in Isogeometric Analysis for Linear Fracture Mechanics. *International Journal for Numerical Methods in Engineering*, **87**, 541–565, 2011. DOI: 10.1002/nme.3121

[2] S. Sh. Ghorashi, N. Valizadeh and S. Mohammadi, EXtended IsoGeometric Analysis (XIGA) for Simulation of Stationary and Propagating Cracks. *International Journal for Numerical Methods in Engineering*, **89**, 1069–1101, 2012. DOI: 10.1002/nme.3277

[3] S. Sh. Ghorashi, N. Valizadeh and S. Mohammadi, Analysis of Cracked Orthotropic Media Using the EXtended IsoGeometric Analysis (XIGA). *International Conference on Extended Finite Element Methods - Recent Developments and applications*, XFEM2011, Cardiff, UK, 2011.

[4] S. Sh. Ghorashi, N. Valizadeh, S. Mohammadi and T. Rabczuk, Extended Isogeometric Analysis of Plates with Curved Cracks. *The Eighth International Conference on Engineering Computational Technology*, ECT2012, Dubrovnik, Croatia, 2012.

[5] T. Belytschko, Y.Y. Lu and L. Gu, Element-Free Galerkin Methods. *International Journal for Numerical Methods in Engineering*, **37**, 229–256, 1994.

[6] T. Belytschko, Y. Krongauz, D. Organ, M. Fleming and P. Krysl, Meshless Methods: An Overview and Recent Developments. *Computer Methods in Applied Mechanics and Engineering*, **139**(1-4), 3–47, 1996.

[7] V.P. Nguyen, T. Rabczuk, S. Bordas and M. Duflot, Meshless Methods: A Review and Computer Implementation Aspects. *Mathematics and Computers in Simulation*, **79**(3), 763–813, 2008.

[8] S.Sh. Ghorashi, S. Mohammadi and S.R. Sabbagh-Yazdi, Orthotropic Enriched Element Free Galerkin Method for Fracture Analysis of Composites. *Engineering Fracture Mechanics*, **78**, 1906–1927, 2011.

[9] T. Rabczuk and T. Belytschko, Cracking Particles: A Simplified Meshfree Method for Arbitrary Evolving Cracks. *International Journal for Numerical Methods in Engineering*, **61**(13), 2316–2343, 2004.

[10] T. Rabczuk, G. Zi, S. Bordas and H. Nguyen-Xuan, A Simple and Robust Three-Dimensional Cracking-Particle Method without Enrichment. *Computer Methods in Applied Mechanics and Engineering*, **199**(37-40), 2437–2455, 2010.

[11] T. Rabczuk and T. Belytschko, A Three Dimensional Large Deformation Meshfree Method for Arbitrary Evolving Cracks. *Computer Methods in Applied Mechanics and Engineering*, **196**(29-30), 2777–2799, 2007.

[12] T. Rabczuk, P.M.A. Areias and T. Belytschko, A Meshfree Thin Shell Method for Nonlinear Dynamic Fracture. *International Journal for Numerical Methods in Engineering*, **72**(5), 524–548, 2007.

[13] T. Rabczuk and G. Zi, A Meshfree Method Based on the Local Partition of Unity for Cohesive Cracks. *Computational Mechanics*, **39**(6), 743–760, 2007.

[14] T. Rabczuk, S. Bordas and G. Zi, On Three-Dimensional Modelling of Crack Growth using Partition of Unity Methods. *Computers & Structures*, **88**(23-24), 1391–1411, 2010.

[15] T. Belytschko and T. Black, Elastic Crack Growth in Finite Elements with Minimal Remeshing. *International Journal for Numerical Methods in Engineering*, **45**, 601–620, 1999.

[16] S. Mohammadi, *Extended Finite Element Method for Fracture Analysis of Structures*. Wiley/Blackwell, United Kingdom, 2008.

[17] T.-P. Fries and T. Belytschko, The Extended/Generalized Finite Element Method: An Overview of the Method and Its Applications. *International Journal for Numerical Methods in Engineering*, **84**(3), 253–304, 2010.

[18] A. Asadpoure and S. Mohammadi, Developing New Enrichment Functions for Crack Simulation in Orthotropic Media by the Extended Finite Element Method. *International Journal for Numerical Methods in Engineering*, **69**, 2150–2172, 2007.

[19] D. Motamedi and S. Mohammadi, Dynamic Analysis of Fixed Cracks in Composites by the Extended Finite Element Method. *Engineering Fracture Mechanics*, **77**, 3373–3393, 2010.

[20] S. Esna Ashari and S. Mohammadi, Delamination Analysis of Composites by New Orthotropic Bimaterial Extended Finite Element Method. *International Journal for Numerical Methods in Engineering*, **86**(13), 1507–1543, 2011. doi: 10.1002/nme.3114

[21] T. J. R. Hughes, J.A. Cottrell and Y. Bazilevs, Isogeometric Analysis: CAD, Finite Elements, NURBS, Exact Geometry and Mesh Refinement. *Computer Methods in Applied Mechanics and Engineering*, **194**, 4135–4195, 2005.

[22] J.A. Cottrell, T.J.R. Hughes and Y. Bazilevs, *Isogeometric Analysis: Towards Integration of CAD and FEA*. Wiley, Chichester, 2009.

[23] L. Piegl and W. Tiller, *The NURBS Book*. Springer-Verlag, New York, 1997.

[24] N. Moës, J. Dolbow and T. Belytschko, A Finite Element Method for Crack Growth without Remeshing. *International Journal for Numerical Methods in Engineering*, **46**, 131–150, 1999.

[25] T. Belytschko and T. Black, Elastic Crack Growth in Finite Elements With Minimal Remeshing. *International Journal for Numerical Methods in Engineering*, **45**, 601–620, 1999.

[26] T.W. Sederberg, J. Zheng, A. Bakenov and A. Nasri, T-splines and T-NURCCSs. *ACM Transactions on Graphics*, **22**(3), 477–484, 2003.

[27] Y. Bazilevs, V.M. Calo, J.A. Cottrell, J.A. Evans, T.J.R. Hughes, S. Lipton, M.A. Scott and T.W. Sederberg, Isogeometric analysis using T-splines. *Computer Methods in Applied Mechanics and Engineering*, **199** (5-8), 229–263, 2010.

[28] M. A. Scott, X. Li, T. W. Sederberg and T. J. R. Hughes, Local Refinement of Analysis-Suitable T-splines. *Computer Methods in Applied Mechanics and Engineering*, **213-216**, 206–222, 2012.

19th International Conference on the Application of Computer
Science and Mathematics in Architecture and Civil Engineering
K. Gürlebeck, T. Lahmer and F. Werner (eds.)
Weimar, Germany, 04–06 July 2012

NEW FOUNDATIONS FOR GEOMETRIC ALGEBRA

R. González Calvet

Institut Pere Calders
Campus Universitat Autònoma de Barcelona, 08193 Cerdanyola del Vallès, Spain
E-mail : rgonzalezcalvet@gmail.com

Keywords: geometric algebra, matrix algebra, Clifford algebra, linear algebra, similarity transformation

Abstract. New foundations for geometric algebra are proposed based upon the existing isomorphisms between geometric and matrix algebras. Each geometric algebra always has a faithful real matrix representation with a periodicity of 8. On the other hand, each matrix algebra is always embedded in a geometric algebra of a convenient dimension. The geometric product is also isomorphic to the matrix product, and many vector transformations such as rotations, axial symmetries and Lorentz transformations can be written in a form isomorphic to a similarity transformation of matrices. We collect the idea that Dirac applied to develop the relativistic electron equation when he took a basis of matrices for the geometric algebra instead of a basis of geometric vectors. Of course, this way of understanding the geometric algebra requires new definitions: the geometric vector space is defined as the algebraic subspace that generates the rest of the matrix algebra by addition and multiplication; isometries are simply defined as the similarity transformations of matrices as shown above, and finally the norm of any element of the geometric algebra is defined as the n^{th} root of the determinant of its representative matrix of order $n \times n$. The main idea of this proposal is an arithmetic point of view consisting of reversing the roles of matrix and geometric algebras in the sense that geometric algebra is a way of accessing, working and understanding the most fundamental conception of matrix algebra as the algebra of transformations of multilinear quantities.

1 INTRODUCTION

In his memoir *On multiple algebra* [1], Josiah Willard Gibbs explored the algebras proposed by several authors in the XIX century in order to multiply multiple quantities (vectors), and he reviewed Grassmann's extension theory, Hamilton's quaternions and Cayley's matrices among others as well as the relations between them. Many kinds of products of vectors have been proposed since then, including Gibb's skew product of vectors in the room space [2, p. 21]. What called strongly my attention was the following phrase of Gibbs [3, p.179]:

> "We have, for example, the tensor of the quaternion[1], which has the important property represented by the equation: $\mathrm{T}(q\,r) = \mathrm{T}q\ \mathrm{T}r$.
>
> There is a scalar quantity related to the linear vector operator which I have represented by the notation $|\Phi|$ and called the *determinant* of Φ. It is in fact the determinant of the matrix by which Φ may be represented, just as the square of the tensor of q (sometimes called the *norm*[2] of q) is the determinant of the matrix by which q is represented. It may also be defined as the product of the latent roots[3] of Φ, just as the square of the tensor of q might be defined as the product of the latent roots of q. Again, it has the property represented by the equation $|\Phi.\Psi| = |\Phi|\,|\psi|$ which corresponds exactly with the preceding equation with both sides squared."

That is, he pointed out that the relation between the determinant of the matrix representation of a quaternion and its norm was a power. Gibbs said that the determinant was the square, but it is the 4th power of the present norm for the regular 4×4 matrix representation:

$$q = a\,i + b\,j + c\,k + d \qquad \Rightarrow \qquad \det q = |q|^4 = \left(a^2 + b^2 + c^2 + d^2\right)^2 \tag{1}$$

I wish to quote another phrase of Gibbs [4, p. 157]:

> "The quaternion affords a convenient notation for rotations. The notation $q(\ )q^{-1}$, where q is a quaternion and the operand is to be written in the parenthesis, produces on all possible vectors just such changes as a (finite) rotation of a solid body."

That is, if q is represented by a matrix, a rotation is a similarity transformation. In fact, many vector transformations such as rotations, axial symmetries and Lorentz transformations can be written in the form $v' = q^{-1} v\, q$ [5, 6, 7, 8 p. 19], which is isomorphic to a similarity transformation of matrices. It can be applied not only to vectors, but also to the other elements of geometric algebra.

While searching a square root of the Klein-Fock equation in order to find the relativistic electron equation, Paul Adrien Maurice Dirac [9] surprisingly took a basis of complex matrices for the space-time geometric algebra instead of taking geometric elements (vectors) as the fundamental entities. Later on, Ettore Majorana [10] found a real 4×4 matrix representation[4] equivalent to Dirac's matrices. The isomorphism between geometric algebras and matrix algebras

---

[1] William Rowan Hamilton called *tensor* to what we take as the norm nowadays (See *Elements of Quaternions*, vol. I, p. 163).

[2] Hamilton called *norm* to the square of our norm, that is, to the sum of the squares of the components of a quaternion.

[3] *Latent roots* means *eigenvalues*.

[4] It is curious that the smaller faithful representation of the non-physical Euclidean four dimensional geometric algebra Cl_4 is included in the complex matrices $M_{4\times4}(\mathbf{C})$ or, by expansion, in the real $M_{8\times8}(\mathbf{R})$.

is well known. Each geometric algebra always has a faithful real matrix representation with a periodicity of 8 [11]:

$$Cl_{p,\,q+8} \cong Cl_{p+8,\,q} \cong Cl_{p,q} \otimes M_{16\times 16}(\mathbf{R}) \tag{2}$$

On the other hand, each matrix algebra is embedded in a geometric algebra of a convenient dimension, while the geometric product is isomorphic to the matrix product. For instance, the algebra of square real 2×2 matrices, $M_{2\times 2}(\mathbf{R})$, is isomorphic to the geometric algebra of the Euclidean plane $Cl_{2,0}$ and also to the geometric algebra of the hyperbolic plane $Cl_{1,1}$ in virtue of the general isomorphism [12]:

$$Cl_{p,\,q} \cong Cl_{q+1,\,p-1} \tag{3}$$

Another example is Majorana's representation $M_{4\times 4}(\mathbf{R})$, which is a real representation of the space-time geometric algebra $Cl_{3,1}$.

Since all Clifford algebras are included in matrix algebras, I wondered whether matrices or geometric vectors were the more fundamental concept and if an arithmetic point of view could give us advantage over the geometric point of view with which geometric algebras have been studied until now.

2 GEOMETRIC ALGEBRA *AB INITIO*

Leopold Kronecker stated [13]:

> "God made the integers, and all the rest is the work of man."

I do not wish to be as radical as him[5] but let us suppose for a moment that the multiple quantities of real numbers are the only tangible reality. Let us search for a rule of multiplication of these multiple quantities taking Gibbs' point of view and without any presupposition about this rule, although we expect to have two algebraic properties: the distributive property and the associative property. The first one is always required for any kind of vector multiplication. The second one is not always required, like in the case of the skew (cross) product, but its presence has clear advantages, especially for algebraic manipulations and geometric equation solving [14]. The most elemental outlining of the transformations of multiple quantities leads us to matrices. If $\mathbf{v} = (v_1 \cdots v_n)$ is a multiple quantity with real components, then we can find any other one $\mathbf{v'} = (v_1' \cdots v_n')$ through a linear transformation represented by a matrix $\mathbf{M} = (m_{ij})$:

$$\begin{pmatrix} v_1' \\ \vdots \\ v_n' \end{pmatrix} = \begin{pmatrix} m_{11} & \cdots & m_{1n} \\ \vdots & \ddots & \vdots \\ m_{n1} & \cdots & m_{nn} \end{pmatrix} \begin{pmatrix} v_1 \\ \vdots \\ v_n \end{pmatrix} \qquad \mathbf{v'} = \mathbf{M}\ \mathbf{v} \tag{4}$$

The distinction between operator (matrix) and operand (multiple quantity) is fictitious since any operand is also an operator. So, the multiple quantity is also an operator and also has a matrix representation a column of which is the column here shown. Note that I am talking about "multiple quantities" instead of "vectors" because the word "vector" needs a more precise

[5] Perhaps if the development of quantum gravity destroys the fiction of the continuity of room space we shall then agree with Kronecker.

definition and I wish to avoid confusion between algebraic vectors (elements of a vectorial space) and geometric vectors (generators of the Clifford algebra). The composition of two linear transformation $\mathbf{M} = (m_{ij})$ and $\mathbf{N} = (n_{ij})$ leads us naturally to the matrix product:

$$\begin{pmatrix} v_1'' \\ \vdots \\ v_n'' \end{pmatrix} = \begin{pmatrix} n_{11} & \cdots & n_{1n} \\ \vdots & \ddots & \vdots \\ n_{n1} & \cdots & n_{nn} \end{pmatrix} \begin{pmatrix} m_{11} & \cdots & m_{1n} \\ \vdots & \ddots & \vdots \\ m_{n1} & \cdots & m_{nn} \end{pmatrix} \begin{pmatrix} v_1 \\ \vdots \\ v_n \end{pmatrix} = \begin{pmatrix} p_{11} & \cdots & p_{1n} \\ \vdots & \ddots & \vdots \\ p_{n1} & \cdots & p_{nn} \end{pmatrix} \begin{pmatrix} v_1 \\ \vdots \\ v_n \end{pmatrix} \tag{5}$$

That is:

$$\mathbf{v''} = \mathbf{P}\ \mathbf{v} \qquad \text{with} \qquad \mathbf{P} = \mathbf{N}\ \mathbf{M} \tag{6}$$

and the multiplication rule:

$$p_{ij} = \sum_k n_{ik} m_{kj} \tag{7}$$

Following a similar way, William Rowan Hamilton discovered quaternions, as the operators q which transform geometric vectors:

$$v' = q\ v \tag{8}$$

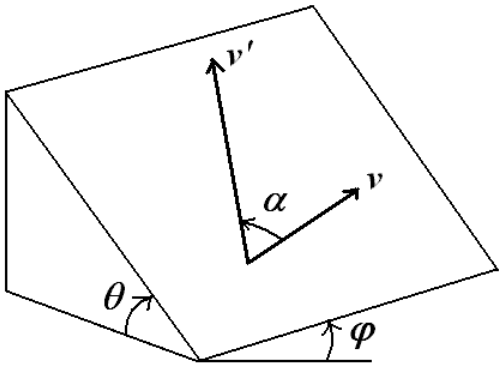

Fig. 1. Quaternion operating upon a vector.

and the rules of their product [15]. He was surprised by the fact that the transformation of three-dimensional vectors required four real quantities, a quaternion, instead of three quantities, which are the inclination θ of the plane, the declination φ, the angle α between both vectors and the ratio of their lengths $|v'|/|v|$ (fig. 1).

Once stated square matrices as the fundamental concept of geometric algebra, which already contain vectors, new definitions must be given in order to work with them.

3 NEW DEFINITIONS IN GEOMETRIC ALGEBRA

The necessary new definitions that I propose are the following:

1) A *complete geometric algebra* is a square matrix algebra $M_{2^n \times 2^n}(\mathbf{R})$. Many geometric algebras are not complete (such as quaternions or $Cl_{4,0}$) because their smallest faithful representation is a subalgebra of a matrix algebra of the same order. The space-time geometric algebra is a complete geometric algebra because $Cl_{3,1} \cong M_{4\times 4}(\mathbf{R})$.
2) The *generator vector space* (the *geometric vector space*) is the set of matrices and their linear combinations (a vectorial subspace) that generate by multiplication the whole geometric algebra. The concept is similar to the set of generators of a discrete group, but applied to a continuous group.
3) The *norm of every element* of a geometric algebra $M_{k\times k}(\mathbf{R})$ is the k^{th} root of the determinant of its representative matrix:

$$\left|\mathbf{M}_{k\times k}\right| = \sqrt[k]{\det \mathbf{M}} \tag{9}$$

For instance, the subalgebra of quaternions is given by:

$$a + b\,i + c\,j + d\,k = \begin{pmatrix} a & -b & -c & -d \\ b & a & -d & c \\ c & d & a & -b \\ d & -c & b & a \end{pmatrix} \tag{10}$$

whose norm is obtained from the 4th root of the matrix determinant:

$$\left|a + b\,i + c\,j + d\,k\right| = \sqrt[4]{\det \begin{pmatrix} a & -b & -c & -d \\ b & a & -d & c \\ c & d & a & -b \\ d & -c & b & a \end{pmatrix}} = \sqrt{a^2 + b^2 + c^2 + d^2} \tag{11}$$

The norm can be a real number, an imaginary number and also zero since all the complete geometric algebras have divisors of zero. According to Frobenius' theorem [16], the only division associative algebras[6] are the real numbers, the complex numbers and quaternions.

4) *Isometries* are defined as the similarity transformations of matrices:

$$\mathbf{M'} = \mathbf{P}^{-1}\mathbf{M}\,\mathbf{P} \quad \text{with} \quad \det \mathbf{P} \neq 0 \qquad \Rightarrow \qquad \det \mathbf{M'} = \det \mathbf{M} \tag{12}$$

because they preserve the determinant and hence the norm.

5) Two elements are said to be *equivalent* if their matrices can be transformed one into the other through an isometry, that is, through a similarity transformation. To have the same norm and determinant does not imply to be equivalent since similar matrices have the same eigenvalues and the determinant is only their product. For instance, in the space-time algebra $Cl_{3,1} \cong M_{4\times 4}(\mathbf{R})$, we have $e_1 \sim e_2 \sim e_3$ but they are not equivalent to e_0 although $\det e_1 = \det e_2 = \det e_3 = \det e_0 = 1$.

6) A *unity* is a matrix whose square power is equal to $\pm\mathbf{I}$, and whose determinant is equal to 1 (from dimension 4 on). The unities can be found through tensor product of the four unities of $M_{2\times 2}(\mathbf{R})$, the smallest complete geometric algebra:

$$1 = \begin{pmatrix} 1 & 0 \\ 0 & 1 \end{pmatrix} \qquad e_1 = \begin{pmatrix} 1 & 0 \\ 0 & -1 \end{pmatrix} \qquad e_2 = \begin{pmatrix} 0 & 1 \\ 1 & 0 \end{pmatrix} \qquad e_{12} = \begin{pmatrix} 0 & 1 \\ -1 & 0 \end{pmatrix} \tag{13}$$

For instance, a unity of $M_{4\times 4}(\mathbf{R})$ is:

$$\begin{pmatrix} 1 & 0 \\ 0 & 1 \end{pmatrix} \otimes \begin{pmatrix} 1 & 0 \\ 0 & -1 \end{pmatrix} = \begin{pmatrix} 1 & 0 & 0 & 0 \\ 0 & -1 & 0 & 0 \\ 0 & 0 & 1 & 0 \\ 0 & 0 & 0 & -1 \end{pmatrix} \tag{14}$$

[6] Algebras without divisors of zero.

Of course, any similar matrix to this one is also a unity.

4 CONSEQUENCES OF THE NEW DEFINITIONS

1) Any set of orthogonal unities fulfils the Pythagorean or pseudo-Pythagorean theorem. Let $\{\mathbf{E}_i\}$ and $\mathbf{M}$ be respectively a set of orthogonal unities and a linear combination of them:

$$i \neq j \Rightarrow \mathbf{E}_i \mathbf{E}_j = -\mathbf{E}_j \mathbf{E}_i \qquad \mathbf{E}_i^2 = \pm \mathbf{I} = \chi_i \mathbf{I} \qquad \mathbf{E}_i \in M_{n\times n}(\mathbf{R}) \tag{15}$$

$$\mathbf{M} = \sum_i \alpha_i \mathbf{E}_i \;\Rightarrow\; \mathbf{M}^2 = \left(\sum_i \alpha_i \mathbf{E}_i \right)^2 = \sum_i \alpha_i^2 \mathbf{E}_i^2 = \mathbf{I} \sum_i \alpha_i^2 \chi_i \tag{16}$$

Then:

$$\det \mathbf{M}^2 = \det\left(\mathbf{I} \sum_i \alpha_i^2 \chi_i \right) = \left(\sum_i \alpha_i^2 \chi_i \right)^n \;\Rightarrow\; \det \mathbf{M} = \pm \left(\sum_i \alpha_i^2 \chi_i \right)^{n/2} \tag{17}$$

$$|\mathbf{M}| = \sqrt[n]{\det \mathbf{M}} = \sqrt{\pm \sum_i \alpha_i^2 \chi_i} \tag{18}$$

For instance, the determinant of a bivector of the space-time geometric algebra $Cl_{3,1}$ does not fulfil the Pythagorean theorem:

$$\det(a\, e_{01} + b\, e_{02} + c\, e_{03} + f\, e_{23} + g\, e_{31} + h\, e_{12}) = \\ (a^2 + b^2 + c^2 - f^2 - g^2 - h^2)^2 + 4(a\, f + b\, g + c\, h)^2 \tag{19}$$

because $e_{01} e_{23} = e_{23} e_{01}$ and so on. However, if the first or the second tern of components vanishes, the norm is then given by the Pythagorean theorem:

$$|a\, e_{01} + b\, e_{02} + c\, e_{03}| = \sqrt{a^2 + b^2 + c^2} \qquad |f\, e_{23} + g\, e_{31} + h\, e_{12}| = \sqrt{f^2 + g^2 + h^2} \tag{20}$$

because the remaining unit bivectors are orthogonal. It happens that the directions e_{01} and e_{23} have the same geometric direction.

2) The expression of isometries as similarity transformation is general and can be applied to any element of the geometric algebra. Let us suppose for a moment that this expression can only be applied to geometric vectors. Then, it can be applied to geometric products of vectors:

$$v' = q^{-1} v\, q \qquad \Rightarrow \qquad v_1' v_2' = q^{-1} v_1 q\; q^{-1} v_2 q = q^{-1} v_1 v_2 q \tag{21}$$

and also to exterior products of vectors and their linear combinations, that is, to any element of second degree:

$$(v_1 \wedge v_2)' = v_1' \wedge v_2' = \frac{1}{2}(v_1' v_2' - v_2' v_1') = \frac{1}{2} q^{-1} (v_1 v_2 - v_2 v_1)\, q = q^{-1}\; v_1 \wedge v_2\; q \tag{22}$$

and so on for any degree, that is, for any element of the geometric algebra. Nowadays, certain isometry operators are written in a form that is only valid for vectors but not for other elements of the algebra. For instance, a rotation of angle θ of a vector in the plane can be written as [17, p. 52]:

$$v' = v\left(\cos\theta + e_{12}\sin\theta\right) \qquad v = v_1 e_1 + v_2 e_2 \tag{23}$$

but the application of this operator to a complex number turns its direction. However, complex numbers are geometric products (or quotients) of two plane vectors. Both vectors are turned through the same angle of rotation θ, so that the angle α between both vectors is preserved, and therefore complex numbers must be preserved [7, p. 27] (fig. 2). We can only obtain this result with the half angle operator:

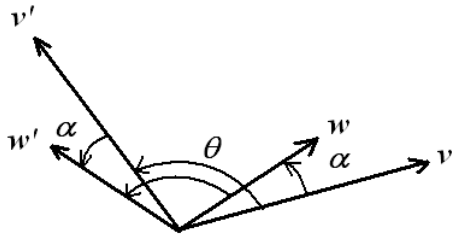

Fig. 2. Preservation, upon a rotation, of the angle between two plane vectors and their lengths, and therefore of their product or quotient, a complex number.

$$v' = \left(\cos\frac{\theta}{2} - e_{12}\sin\frac{\theta}{2}\right) v \left(\cos\frac{\theta}{2} + e_{12}\sin\frac{\theta}{2}\right) \tag{24}$$

which is a similarity transformation. Now complex numbers are preserved because of their commutative property:

$$z' = \left(\cos\frac{\theta}{2} - e_{12}\sin\frac{\theta}{2}\right) z \left(\cos\frac{\theta}{2} + e_{12}\sin\frac{\theta}{2}\right) = z \qquad z = a + b\, e_{12} \tag{25}$$

3) Isometries transform orthogonal vectors into orthogonal vectors, which can be easily proven:

$$\mathbf{E}_i\mathbf{E}_j = -\mathbf{E}_j\mathbf{E}_i \;\Rightarrow\; \mathbf{P}^{-1}\mathbf{E}_i\mathbf{P}\,\mathbf{P}^{-1}\mathbf{E}_j\mathbf{P} = -\mathbf{P}^{-1}\mathbf{E}_j\mathbf{P}\,\mathbf{P}^{-1}\mathbf{E}_i\mathbf{P}$$
$$\Rightarrow \quad \mathbf{E}_i'\mathbf{E}_j' = -\mathbf{E}_j'\mathbf{E}_i' \tag{26}$$

because $\mathbf{P}\,\mathbf{P}^{-1} = \mathbf{I}$. Both vectors can lie in an Euclidean plane or in a hyperbolic plane. In the second case, two vectors are orthogonal if we "see" their directions as being symmetric with respect to the quadrant bisectors [7, p. 156]. Fig. 3 shows how an isometry, such as a Lorentz transformation, transforms a pair of orthogonal vectors u, v into another pair of orthogonal vectors u', v'.

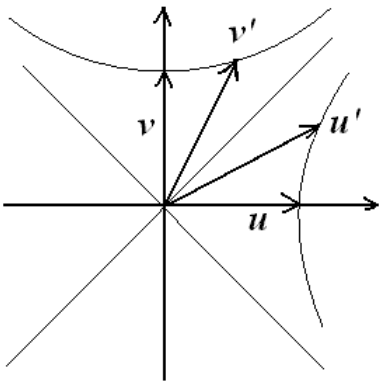

Fig. 3. Transformation of two orthogonal vectors *u*, *v* into another pair of orthogonal vectors *u'*, *v'* under an isometry in a hyperbolic plane.

4) Any product of distinct orthogonal unities is linearly independent of them and has no intersection with the subspace generated by the unities and other products of lower degree. It follows immediately from the identity between geometric and exterior product:

$$\forall i \neq j \qquad \mathbf{E}_i\mathbf{E}_j = -\mathbf{E}_j\mathbf{E}_i \quad \Rightarrow \quad \mathbf{E}_i \cdots \mathbf{E}_k = \mathbf{E}_i \wedge \cdots \wedge \mathbf{E}_k \qquad i < \cdots < k \tag{27}$$

because the exterior product is the product by the orthogonal component. We can also prove this linear independence in another way. For instance, the complete geometric algebra $M_{2\times 2}(\mathbf{R})$ has two orthogonal generator unities $\mathbf{E}_1$ and $\mathbf{E}_2$:

$$\mathbf{E}_1\mathbf{E}_2 = -\mathbf{E}_2\mathbf{E}_1 \qquad\qquad \mathbf{E}_i^2 = \chi_i = \pm 1 \tag{28}$$

Let us suppose that their product is a linear combination of them and the identity:

$$\mathbf{E}_1\mathbf{E}_2 = \alpha_0\mathbf{I} + \alpha_1\mathbf{E}_1 + \alpha_2\mathbf{E}_2 \tag{29}$$

If we multiply the equality by $\mathbf{E}_1$ on the left and on the right we obtain:

$$\left.\begin{aligned}\mathbf{E}_1^2\mathbf{E}_2 = \chi_1\mathbf{E}_2 = \alpha_0\mathbf{E}_1 + \alpha_1\chi_1 + \alpha_2\mathbf{E}_{12}\\ \mathbf{E}_1\mathbf{E}_2\mathbf{E}_1 = -\chi_1\mathbf{E}_2 = \alpha_0\mathbf{E}_1 + \alpha_1\chi_1 - \alpha_2\mathbf{E}_{12}\end{aligned}\right\} \quad\Rightarrow\quad \begin{cases}\alpha_0 = \alpha_1 = 0\\ \alpha_2^2 = \chi_1\end{cases} \tag{30}$$

If we multiply the equality by $\mathbf{E}_2$ on the left and on the right we obtain:

$$\left.\begin{aligned}\mathbf{E}_2\mathbf{E}_1\mathbf{E}_2 = -\chi_2\mathbf{E}_1 = \alpha_0\mathbf{E}_2 - \alpha_1\mathbf{E}_{12} + \alpha_2\chi_2\\ \mathbf{E}_1\mathbf{E}_2^2 = \chi_2\mathbf{E}_1 = \alpha_0\mathbf{E}_2 + \alpha_1\mathbf{E}_{12} + \alpha_2\chi_2\end{aligned}\right\} \quad\Rightarrow\quad \begin{cases}\alpha_0 = \alpha_2 = 0\\ \alpha_1^2 = \chi_2\end{cases} \tag{31}$$

a result which comes in contradiction with the former result. Therefore, this proves that our hypothesis that $\mathbf{E}_1\mathbf{E}_2$ is a linear combination of $\{\mathbf{I}, \mathbf{E}_1, \mathbf{E}_2\}$ is a falsehood, whence it follows that the set $\{\mathbf{I}, \mathbf{E}_1, \mathbf{E}_2, \mathbf{E}_1\mathbf{E}_2\}$ is a basis of $M_{2\times 2}(\mathbf{R})$.

5) Reflections need a special mention. When talking with Prof. L. Dorst and Prof. H. Pijls during the ECM 2008 conference in Amsterdam about my supposition that isometries are similarity transformations, they replied to me that the expression for reflections is not a similarity transformation since [18]:

$$v' = -a^{-1}\, v\, a \tag{32}$$

where v is a geometric vector and a is a vector perpendicular to the plane of reflection (fig. 4). The first objection to this expression is the fact that it can only be applied to vectors but not to other elements of the geometric algebra such as bivectors. The modification which I have proposed [8, p. 36] is to write it as a similarity transformation in the following way:

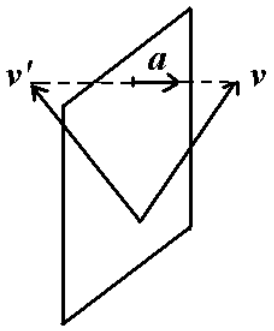

Fig. 4. Reflection of a vector in a plane.

$$r = e_0 a \qquad\Rightarrow\qquad r^{-1} = -a^{-1}e_0 \tag{33}$$

$$v' = r^{-1}v\, r = -a^{-1}e_0 v\, e_0 a = -a^{-1}\, v\, a \tag{34}$$

Of course it has a consequence: this operator changes the sign of the time component:

$$e_0' = r^{-1}e_0\, r = -a^{-1}\, e_0 e_0\, e_0 a = a^{-1}e_0 a = -a^{-1}a\, e_0 = -e_0 \tag{35}$$

That is, a reflection would be an isometry reversing one spatial direction and also the time direction. We can discuss widely about whether the reversal of one spatial and the temporal components must be linked or not in a reflection. The physical world does not remain invariant under reflections because there are physical processes, driven by weak interactions, whose mirror image has a very much lower probability [19]. However, physical invariance is preserved under the CPT transformation[7] [20], that is, if time is also reversed. On the other hand, the biological world has chosen one side of the mirror: all the proteins of the superior species are built with the L-amino acids while their mirror images, D-amino acids, are absent from the most biological structures. Anyway, we may wonder whether a reflection without reversal of the time can be a similarity transformation. Let us see how a generic element of the space-time geometric algebra $Cl_{3,1}$:

$$\begin{aligned} w = a + b\,e_0 + c\,e_1 + d\,e_2 + e\,e_3 + f\,e_{01} + g\,e_{02} + h\,e_{03} + i\,e_{23} + j\,e_{31} + k\,e_{12} \\ + l\,e_{023} + m\,e_{031} + n\,e_{012} + o\,e_{123} + p\,e_{0123} \end{aligned} \tag{36}$$

changes under a reflection in the plane e_{23}, which produces the reversal $e_1 \to -e_1$:

$$\begin{aligned} w' = a + b\,e_0 - c\,e_1 + d\,e_2 + e\,e_3 - f\,e_{01} + g\,e_{02} + h\,e_{03} + i\,e_{23} - j\,e_{31} - k\,e_{12} \\ + l\,e_{023} - m\,e_{031} - n\,e_{012} - o\,e_{123} - p\,e_{0123} \end{aligned} \tag{37}$$

The characteristic polynomials of both elements[8] are:

$$\det(w-\lambda) = \begin{vmatrix} a+d+h-l-\lambda & b+e-g+i & f+j+n+o & -c+k-m+p \\ -b+e-g-i & a-d-h-l-\lambda & c+k-m-p & f-j-n+o \\ f-j+n-o & c-k-m+p & a+d-h+l-\lambda & -b+e+g+i \\ -c-k-m-p & f+j-n-o & b+e+g-i & a-d+h+l-\lambda \end{vmatrix} \tag{38}$$

$$\det(w'-\lambda) = \begin{vmatrix} a+d+h-l-\lambda & b+e-g+i & -f-j-n-o & c-k+m-p \\ -b+e-g-i & a-d-h-l-\lambda & -c-k+m+p & -f+j+n-o \\ -f+j-n+o & -c+k+m-p & a+d-h+l-\lambda & -b+e+g+i \\ c+k+m+p & -f-j+n+o & b+e+g-i & a-d+h+l-\lambda \end{vmatrix} \tag{39}$$

In fact, it reduces to a change of sign of all the matrix elements in the highest right square and in the lowest left square. Both determinants are equal, and the characteristic polynomials are identical. Therefore, the existence of a similarity transformation for this reflection cannot be discarded although it is necessary that both matrices have the same invariant factors [21]. This question must be clarified soon. In the case that this reflection be a similarity transformation, the operator may not have a simple form, and I believe that it will be a combination of elements with different degree and temporal components. That is the reason why reflections cannot be written as similarity transformation in the room space geometric algebra Cl_3.

[7] Charge conjugation, parity or spatial inversion, and time reversal.

[8] I have built these determinants with the matrix basis given in [8, p. 11]. Notwithstanding this, all the bases of $Cl_{3,1}$ are equivalent and they therefore have the same characteristic polynomial (38) although the matrix elements can change depending on the chosen basis.

6) In a complete geometric algebra $M_{2^n\times 2^n}(\mathbf{R})$ the maximum number of orthogonal unities is $k=2n$. It is well known that a geometric algebra generated by a geometric space of dimension k has dimension 2^k because:

$$\dim Cl_{p,q}=\binom{k}{0}+\binom{k}{1}+\cdots+\binom{k}{k}=2^k \qquad k=p+q \tag{40}$$

Then, the dimension of this geometric algebra must be equal to the dimension of the linear space of the matrix algebra so that:

$$2^k=2^n\times 2^n \qquad \Rightarrow \qquad k=2n \tag{41}$$

For instance, in $M_{4\times 4}(\mathbf{R})$ the maximum number of orthogonal unities is 4 while in $M_{8\times 8}(\mathbf{R})$ the maximum number of orthogonal unities is 6 because $2^6=8\times 8$. However, in virtue of the isomorphisms $Cl_{p,q}\cong Cl_{q+1,p-1}$ and $Cl_{p,q}\cong Cl_{p-4,q+4}$ for $p\geq 4$ [12], there are two or more non-equivalent sets of unities generating these geometric algebras [11]:

$$M_{4\times 4}(\mathbf{R})\cong Cl_{3,1}\cong Cl_{2,2} \tag{42}$$

$$M_{8\times 8}(\mathbf{R})\cong Cl_{0,6}\cong Cl_{3,3}\cong Cl_{4,2} \tag{43}$$

Those statements outlined in this section but not proven yet should be rigorously demonstrated as well as some definitions given in section 3 should be improved in future work. The knowledge we have on Clifford algebras will be very helpful in this task.

5 CONCLUSIONS

If we take multiple quantities as the fundamental entities, then the matrix theory follows naturally from their transformations, and the matrix product from the composition of transformations. In this framework, a geometric algebra is defined as a matrix algebra or subalgebra that is closed under addition and multiplication of a set of generating unities obtained from tensor product of the unities of $M_{2,2}(\mathbf{R})$. A complete geometric algebra is defined as a matrix algebra isomorphic to a geometric algebra over the real numbers, which only happens for $M_{2^n\times 2^n}(\mathbf{R})$. Searching for a generalization of the norm of a complex numbers or a quaternion, we wish that the norm of a product of two elements be equal to the product of their norms. The unique quantity that fulfils this equality is the determinant, because the determinant of a product of two matrices is equal to the product of their determinants. In order to fit this new norm to the norms of complex numbers or quaternions, or to the length of a vector, the k^{th} root of the determinant must be taken, where $k\times k$ are the dimensions of the matrix algebra. Since k is always an even number, the norm $|\mathbf{M}|$ of a matrix $\mathbf{M}$ can be a real or an imaginary positive number, which fulfils $|\mathbf{M}\,\mathbf{N}|=\pm|\mathbf{M}|\,|\mathbf{N}|$. This definition of the norm of an element of a geometric algebra fills a void in Clifford algebras theory, since the norm of elements with mixed degree have not been unambiguously defined until now, except for special cases such as quaternions.

On the other hand, an isometry is defined as a matrix similarity transformation, which preserves the determinant and therefore the norm. The advantage of this definition is the fact that

the same operator can be applied to any element of geometric algebra. A new definition for unities is also given as matrices with square power equal to $\pm\mathbf{I}$ and determinant equal to 1 (for $n \geq 4$). In fact, they are obtained by tensor product of the unities of $M_{2\times 2}(\mathbf{R})$. Any matrix equivalent (through a similarity transformation) to a given unity is also a unity.

Two elements (matrices) of a geometric algebra are said to be orthogonal if they anticommute. In this case, it is deduced that their norm fulfils the Pythagorean or pseudo-Pythagorean theorem. In a complete geometric algebra $M_{2^n\times 2^n}(\mathbf{R})$ there are a maximum of $2n$ orthogonal unities. Isometries transform orthogonal vectors into orthogonal vectors. Finally, it is shown that these $2n$ orthogonal unities and their products induce the structure of Clifford algebra inside the matrix algebra (which we are calling geometric algebra) and form a basis of the algebra.

REFERENCES

[1] J. W. Gibbs: On Multiple Algebra. Proceedings of the American Association for the Advancement of Science, **XXXV,** 37-66. 1886. Reproduced in Scientific papers of J. Willard Gibbs **II**, 91-117. Dover, New York, 1961.

[2] J. W. Gibbs: Elements of Vector Analysis. Privately printed, New Haven, 1881. *Ibidem* 17-90.

[3] J. W. Gibbs: Quaternions and Vector Analysis. Nature, **XLVIII,** 364-367. Aug. 17, 1893. *Ibidem* 173-181.

[4] J. W. Gibbs: On the Rôle of Quaternions in the Algebra of Vectors. Nature, **XLIII**, 511-513. April 2, 1891. *Ibidem* 155-160.

[5] D. Hestenes: Space-Time Algebra, p. 49. Gordon and Breach, New York, 1966.

[6] S. Gull, Ch. Doran, A. Lasenby: Dynamics. Clifford (Geometric) Algebras, p. 83, W. E. Baylis (ed.). Birkhäuser, Boston, 1996.

[7] R. González Calvet: Treatise of Plane Geometry through Geometric Algebra, p. 27. Cerdanyola del Vallès, 2007.

[8] R. González Calvet: El álgebra geométrica del espacio y tiempo. http://www.xtec.cat/~rgonzal1/espacio.htm. 2011.

[9] P. A. M. Dirac: The Quantum Theory of Electron. Proc. Roy. Soc. Ser. A **117**, 610, 1928.

[10] E. Majorana: Teoria simetrica dell'elettrone e del positrone. Nuovo Cimento, **5**, 171-184, 1937. Reproduced in La Vita e l'opera di Ettore Majorana (1906-1938), pp. 67-79. Academia Nazionale dei Lincei, Roma, 1966.

[11] P. Lounesto: Clifford Algebras and Spinors, p. 216. Cambridge University Press, Cambridge, 1997.

[12] P. Lounesto, *ibidem* p. 215.

[13] C. B. Boyer: A History of Mathematics, 2nd edition, p. 570. Wiley, New York 1991.

[14] R. González Calvet: Applications of Geometric Algebra and the Geometric Product to Solve Geometric Problems. Talk held at the AGACSE 2010 conference (14th-16th July 2010), http://www.xtec.cat/~rgonzal1/proceedings.pdf.

[15] W. R. Hamilton: First Motive for naming the Quotient of two Vectors a Quaternion. Elements of Quaternions, 3rd ed., **I**, 110-113. Chelsea, New York, 1969.

[16] L. S. Pontriaguin: Grupos continuos, p. 170. Mir, Moscow, 1978.

[17] G. Peano: Gli elementi di calcolo geometrico. 1891. Opere Scelte, **III**, pp 41-69. Ed. Cremonese, Roma, 1959.

[18] L. Dorst, D. Fontijne, S. Mann: Geometric Algebra for Computer Science, p. 168, Elsevier, Amsterdam, 2007.
[19] P. Renton: Electroweak Interactions, 35-36. Cambridge Univ. Press, Cambridge,1990.
[20] L. Landau, E. Lifchitz : Physique théorique, **4**, Électrodynamique quantique, p. 68. Mir, Moscow, 1989.
[21] S. Perlis, Theory of Matrices, p. 143. Dover, New York, 1991.

19th International Conference on the Application of Computer
Science and Mathematics in Architecture and Civil Engineering
K. Gürlebeck, T. Lahmer and F. Werner (eds.)
Weimar, Germany, 04–06 July 2012

THE CLIFFORD FOURIER TRANSFORM IN REAL CLIFFORD ALGEBRAS

E. Hitzer*

**University of Fukui*
910-8507 Fukui, Japan
E-mail: hitzer@mech.u-fukui.ac.jp

Keywords: Clifford Fourier transform, Clifford algebra, signal processing, square roots of -1.

Abstract. *We use the recent comprehensive research [15, 17] on the manifolds of square roots of -1 in real Clifford's geometric algebras $Cl(p,q)$ in order to construct the Clifford Fourier transform. Basically in the kernel of the complex Fourier transform the imaginary unit $j \in \mathbb{C}$ is replaced by a square root of -1 in $Cl(p,q)$. The Clifford Fourier transform (CFT) thus obtained generalizes previously known and applied CFTs [7,11,12], which replaced $j \in \mathbb{C}$ only by blades (usually pseudoscalars) squaring to -1. A major advantage of real Clifford algebra CFTs is their completely real geometric interpretation. We study (left and right) linearity of the CFT for constant multivector coefficients $\in Cl(p,q)$, translation ($\boldsymbol{x}$-shift) and modulation (ω-shift) properties, and signal dilations. We show an inversion theorem. We establish the CFT of vector differentials, partial derivatives, vector derivatives and spatial moments of the signal. We also derive Plancherel and Parseval identities as well as a general convolution theorem.*

1 INTRODUCTION

Quaternion, Clifford and geometric algebra Fourier transforms (QFT, CFT, GAFT) [6, 12, 13, 16] have proven *very useful* tools for applications in non-marginal color image processing, image diffusion, electromagnetism, multi-channel processing, vector field processing, shape representation, linear scale invariant filtering, fast vector pattern matching, phase correlation, analysis of non-stationary improper complex signals, flow analysis, partial differential systems, disparity estimation, texture segmentation, as spectral representations for Clifford wavelet analysis, etc.

All these Fourier transforms essentially analyze scalar, vector and multivector signals in terms of sine and cosine waves with multivector coefficients. For this purpose the imaginary unit $i \in \mathbb{C}$ in $e^{i\phi} = \cos\phi + i\sin\phi$ can be replaced by any *square root of* -1 *in a Clifford algebra* $Cl(p,q)$. The replacement by pure quaternions and blades with negative square [6, 13] has already yielded a wide variety of results with a clear geometric interpretation. It is well-known that there are elements other than blades, squaring to -1. Motivated by their special relevance for new types of CFTs, they have recently been studied thoroughly [15, 17, 21].

We therefore tap into these new results on square roots of -1 in Clifford algebras and fully general construct CFTs, with one general square root of -1 in $Cl(p,q)$. Our new CFTs form therefore a more general class of CFTs, subsuming and generalizing previous results. A further benefit is, that these new CFTs become *fully steerable* within the continuous Clifford algebra submanifolds of square roots of -1. We thus obtain a comprehensive *new mathematical framework* for the investigation and application of Clifford Fourier transforms together with *new properties* (full steerability). Regarding the question of the *most suitable* CFT for a certain application, we are only just beginning to leave the terra cognita of familiar transforms to map out the vast array of possible CFTs in $Cl(p,q)$.

This paper is organized as follows. We first review in Section 2 key notions of Clifford algebra, *multivector signal functions*, and the recent results on *square roots of* -1 in Clifford algebras. Next, in Section 3 we define the central notion of *Clifford Fourier transforms* with respect to any square root of -1 in Clifford algebra. Then we study in Section 4 (left and right) linearity of the CFT for constant multivector coefficients $\in Cl(p,q)$, translation ($\boldsymbol{x}$-shift) and modulation (ω-shift) properties, and signal dilations, followed by an inversion theorem. We establish the CFT of vector differentials, partial derivatives, vector derivatives and spatial moments of the signal. We also show Plancherel and Parseval identities as well as a general convolution theorem.

2 CLIFFORD'S GEOMETRIC ALGEBRA

Definition 2.1 (Clifford's geometric algebra [10, 19]) *Let* $\{e_1, e_2, \ldots, e_p, e_{p+1}, \ldots, e_n\}$*, with* $n = p+q$*,* $e_k^2 = \varepsilon_k$*,* $\varepsilon_k = +1$ *for* $k = 1, \ldots, p$*,* $\varepsilon_k = -1$ *for* $k = p+1, \ldots, n$*, be an orthonormal base of the inner product vector space* $\mathbb{R}^{p,q}$ *with a geometric product according to the multiplication rules*

$$e_k e_l + e_l e_k = 2\varepsilon_k \delta_{k,l}, \qquad k,l = 1, \ldots n, \tag{1}$$

where $\delta_{k,l}$ *is the Kronecker symbol with* $\delta_{k,l} = 1$ *for* $k = l$*, and* $\delta_{k,l} = 0$ *for* $k \neq l$*. This non-commutative product and the additional axiom of associativity generate the* 2^n*-dimensional Clifford geometric algebra* $Cl(p,q) = Cl(\mathbb{R}^{p,q}) = Cl_{p,q} = \mathscr{G}_{p,q} = \mathbb{R}_{p,q}$ *over* $\mathbb{R}$*. The set* $\{e_A : A \subseteq \{1, \ldots, n\}\}$ *with* $e_A = e_{h_1} e_{h_2} \ldots e_{h_k}$*,* $1 \leq h_1 < \ldots < h_k \leq n$*,* $e_\emptyset = 1$*, forms a graded (blade)*

basis of $Cl(p,q)$. The grades k range from 0 for scalars, 1 for vectors, 2 for bivectors, s for s-vectors, up to n for pseudoscalars. The vector space $\mathbb{R}^{p,q}$ is included in $Cl(p,q)$ as the subset of 1-vectors. The general elements of $Cl(p,q)$ are real linear combinations of basis blades e_A, called Clifford numbers, multivectors or hypercomplex numbers.

In general $\langle A\rangle_k$ denotes the grade k part of $A \in Cl(p,q)$. The parts of grade 0 and $k+s$, respectively, of the geometric product of a k-vector $A_k \in Cl(p,q)$ with an s-vector $B_s \in Cl(p,q)$

$$A_k * B_s := \langle A_k B_s\rangle_0, \qquad A_k \wedge B_s := \langle A_k B_s\rangle_{k+s}, \tag{2}$$

are called *scalar product* and *outer product*, respectively.

For Euclidean vector spaces ($n = p$) we use $\mathbb{R}^n = \mathbb{R}^{n,0}$ and $Cl(n) = Cl(n,0)$. Every k-vector B that can be written as the outer product $B = \boldsymbol{b}_1 \wedge \boldsymbol{b}_2 \wedge \ldots \wedge \boldsymbol{b}_k$ of k vectors $\boldsymbol{b}_1, \boldsymbol{b}_2, \ldots, \boldsymbol{b}_k \in \mathbb{R}^{p,q}$ is called a *simple* k-vector or *blade*.

Multivectors $M \in Cl(p,q)$ have k-vector parts ($0 \le k \le n$): scalar part $Sc(M) = \langle M\rangle = \langle M\rangle_0 = M_0 \in \mathbb{R}$, vector part $\langle M\rangle_1 \in \mathbb{R}^{p,q}$, bi-vector part $\langle M\rangle_2$, ..., and pseudoscalar part $\langle M\rangle_n \in \bigwedge^n \mathbb{R}^{p,q}$

$$M = \sum_A M_A \boldsymbol{e}_A = \langle M\rangle + \langle M\rangle_1 + \langle M\rangle_2 + \ldots + \langle M\rangle_n . \tag{3}$$

The *principal reverse* of $M \in Cl(p,q)$ defined as

$$\widetilde{M} = \sum_{k=0}^{n} (-1)^{\frac{k(k-1)}{2}} \langle \overline{M}\rangle_k, \tag{4}$$

often replaces complex conjugation and quaternion conjugation. Taking the *reverse* is equivalent to reversing the order of products of basis vectors in the basis blades e_A. The operation $\overline{M}$ means to change in the basis decomposition of M the sign of every vector of negative square $\overline{e_A} = \varepsilon_{h_1} e_{h_1} \varepsilon_{h_2} e_{h_2} \ldots \varepsilon_{h_k} e_{h_k}$, $1 \le h_1 < \ldots < h_k \le n$. Reversion, $\overline{M}$, and principal reversion are all involutions.

The principal reverse of every basis element $e_A \in Cl(p,q)$, $1 \le A \le 2^n$, has the property

$$\widetilde{e_A} * e_B = \delta_{AB}, \qquad 1 \le A, B \le 2^n, \tag{5}$$

where the Kronecker delta $\delta_{AB} = 1$ if $A = B$, and $\delta_{AB} = 0$ if $A \ne B$. For the vector space $\mathbb{R}^{p,q}$ this leads to a reciprocal basis e^l, $1 \le l,k \le n$

$$e^l := \widetilde{e_l} = \varepsilon_l e_l, \quad e^l * e_k = e^l \cdot e_k = \begin{cases} 1, & \text{for } l = k \\ 0, & \text{for } l \ne k \end{cases} . \tag{6}$$

For $M, N \in Cl(p,q)$ we get $M * \widetilde{N} = \sum_A M_A N_A$. Two multivectors $M, N \in Cl(p,q)$ are *orthogonal* if and only if $M * \widetilde{N} = 0$. The modulus $|M|$ of a multivector $M \in Cl(p,q)$ is defined as

$$|M|^2 = M * \widetilde{M} = \sum_A M_A^2. \tag{7}$$

2.1 Multivector signal functions

A multivector valued function $f:\mathbb{R}^{p,q}\to Cl(p,q)$, has 2^n blade components $(f_A:\mathbb{R}^{p,q}\to\mathbb{R})$

$$f(\boldsymbol{x})=\sum_A f_A(\boldsymbol{x})\boldsymbol{e}_A,\qquad \boldsymbol{x}=\sum_{l=1}^n x_l e^l=\sum_{l=1}^n x^l e_l. \tag{8}$$

We define the *inner product* of two functions $f,g:\mathbb{R}^{p,q}\to Cl(p,q)$ by

$$(f,g)=\int_{\mathbb{R}^{p,q}} f(\boldsymbol{x})\widetilde{g(\boldsymbol{x})}\,d^n\boldsymbol{x}=\sum_{A,B}\boldsymbol{e}_A\widetilde{\boldsymbol{e}}_B\int_{\mathbb{R}^{p,q}} f_A(\boldsymbol{x})g_B(\boldsymbol{x})\,d^n\boldsymbol{x}, \tag{9}$$

with the *symmetric scalar part*

$$\langle f,g\rangle=\int_{\mathbb{R}^{p,q}} f(\boldsymbol{x})*\widetilde{g(\boldsymbol{x})}\,d^n\boldsymbol{x}=\sum_A\int_{\mathbb{R}^{p,q}} f_A(\boldsymbol{x})g_A(\boldsymbol{x})\,d^n\boldsymbol{x}, \tag{10}$$

and the $L^2(\mathbb{R}^{p,q};Cl(p,q))$*-norm*

$$\|f\|^2=\langle(f,f)\rangle=\int_{\mathbb{R}^{p,q}}|f(\boldsymbol{x})|^2 d^n\boldsymbol{x}=\sum_A\int_{\mathbb{R}^{p,q}} f_A^2(\boldsymbol{x})\,d^n\boldsymbol{x}, \tag{11}$$

$$L^2(\mathbb{R}^{p,q};Cl(p,q))=\{f:\mathbb{R}^{p,q}\to Cl(p,q)\mid\|f\|<\infty\}. \tag{12}$$

The *vector derivative* ∇ of a function $f:\mathbb{R}^{p,q}\to Cl(p,q)$ can be expanded in a basis of $\mathbb{R}^{p,q}$ as [23]

$$\nabla=\sum_{l=1}^n e^l\partial_l\quad\text{with}\quad\partial_l=\partial_{x_l}=\frac{\partial}{\partial x_l},\ 1\le l\le n. \tag{13}$$

2.2 Square roots of -1 in Clifford algebras

Every Clifford algebra $Cl(p,q)$, $s_8=(p-q)\bmod 8$, is isomorphic to one of the following (square) matrix algebras[1] $\mathscr{M}(2d,\mathbb{R})$, $\mathscr{M}(d,\mathbb{H})$, $\mathscr{M}(2d,\mathbb{R}^2)$, $\mathscr{M}(d,\mathbb{H}^2)$ or $\mathscr{M}(2d,\mathbb{C})$. The first argument of $\mathscr{M}$ is the dimension, the second the associated ring[2] $\mathbb{R}$ for $s_8=0,2$, $\mathbb{R}^2$ for $s_8=1$, $\mathbb{C}$ for $s_8=3,7$, $\mathbb{H}$ for $s_8=4,6$, and $\mathbb{H}^2$ for $s_8=5$. For even n: $d=2^{(n-2)/2}$, for odd n: $d=2^{(n-3)/2}$.

It has been shown [15,17] that $Sc(f)=0$ for every square root of $-\mathbf{1}$ in every matrix algebra $\mathscr{A}$ isomorphic to $Cl(p,q)$. One can distinguish *ordinary* square roots of $-\mathbf{1}$, and *exceptional* ones. All square roots of $-\mathbf{1}$ in $Cl(p,q)$ can be computed using the package CLIFFORD for Maple [1,3,18,20].

In all cases the *ordinary* square roots f of $-\mathbf{1}$ constitute a *unique conjugacy class* of dimension $\dim(\mathscr{A})/2$, which has *as many connected components as the group* $\mathrm{G}(\mathscr{A})$ of invertible elements in $\mathscr{A}$. Furthermore, we have $\mathrm{Spec}(f)=0$ (zero pseudoscalar part) if the associated ring is $\mathbb{R}^2$, $\mathbb{H}^2$, or $\mathbb{C}$. The exceptional square roots of $-\mathbf{1}$ *only* exist if $\mathscr{A}\cong\mathscr{M}(2d,\mathbb{C})$. The manifolds of square roots of -1 in $Cl(p,q)$, $n=p+q=2$, compare Table 1 of [15], are visualized in Fig. 1.

For $\mathscr{A}=\mathscr{M}(2d,\mathbb{R})$, the centralizer (set of all elements in $Cl(p,q)$ commuting with f) and the conjugacy class of a square root f of $-\mathbf{1}$ both have $\mathbb{R}$-dimension $2d^2$ with *two connected components*. For the simplest case $d=1$ we have the algebra $Cl(2,0)$ isomorphic to $\mathscr{M}(2,\mathbb{R})$, pictured in Fig. 2 for $d=1$.

[1] Compare chapter 16 on *matrix representations and periodicity of 8*, as well as Table 1 on p. 217 of [19].

[2] Associated ring means, that the matrix elements are from the respective ring $\mathbb{R}$, $\mathbb{R}^2$, $\mathbb{C}$, $\mathbb{H}$ or $\mathbb{H}^2$.

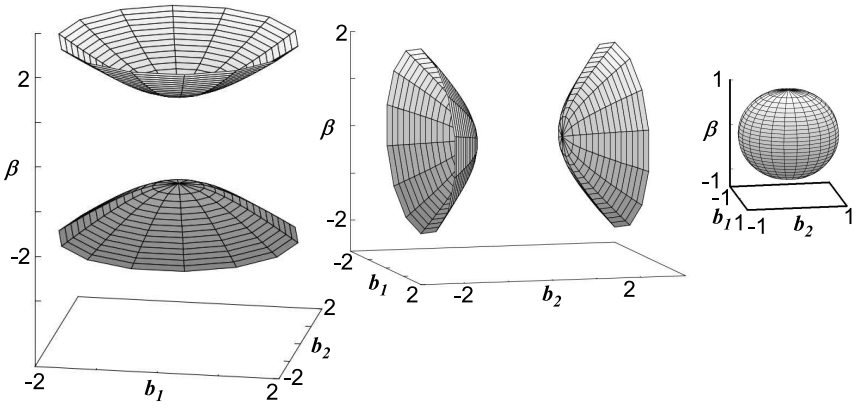

Figure 1: Manifolds [17] of square roots f of -1 in $Cl(2,0)$ (left), $Cl(1,1)$ (center), and $Cl(0,2) \cong \mathbb{H}$ (right). The square roots are $f = \alpha + b_1 e_1 + b_2 e_2 + \beta e_{12}$, with $\alpha, b_1, b_2, \beta \in \mathbb{R}$, $\alpha = 0$, and $\beta^2 = b_1^2 e_2^2 + b_2^2 e_1^2 + e_1^2 e_2^2$.

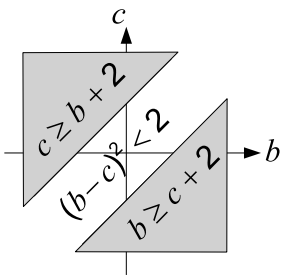

Figure 2: Two components of square roots of $-\mathbf{1}$ in $\mathscr{M}(2,\mathbb{R}) \equiv Cl(2,0)$, see [17] for details.

For $\mathscr{A} = \mathscr{M}(2d, \mathbb{R}^2) = \mathscr{M}(2d, \mathbb{R}) \times \mathscr{M}(2d, \mathbb{R})$, the square roots of $(-\mathbf{1}, -\mathbf{1})$ are pairs of two square roots of $-\mathbf{1}$ in $\mathscr{M}(2d, \mathbb{R})$. They constitute a unique conjugacy class with *four connected components*, each of dimension $4d^2$. Regarding the four connected components, the group of inner automorphisms $\mathrm{Inn}(\mathscr{A})$ induces the permutations of the Klein group, whereas the quotient group $\mathrm{Aut}(\mathscr{A})/\mathrm{Inn}(\mathscr{A})$ is isomorphic to the group of isometries of a Euclidean square in 2D. The simplest example with $d = 1$ is $Cl(2,1)$ isomorphic to $M(2, \mathbb{R}^2) = \mathscr{M}(2, \mathbb{R}) \times \mathscr{M}(2, \mathbb{R})$.

For $\mathscr{A} = \mathscr{M}(d, \mathbb{H})$, the submanifold of the square roots f of $-\mathbf{1}$ is a *single connected conjugacy class* of $\mathbb{R}$-dimension $2d^2$ equal to the $\mathbb{R}$-dimension of the centralizer of every f. The easiest example is $\mathbb{H}$ itself for $d = 1$.

For $\mathscr{A} = \mathscr{M}(d, \mathbb{H}^2) = \mathscr{M}(d, \mathbb{H}) \times \mathscr{M}(d, \mathbb{H})$, the square roots of $(-\mathbf{1}, -\mathbf{1})$ are pairs of two square roots (f, f') of $-\mathbf{1}$ in $\mathscr{M}(d, \mathbb{H})$ and constitute a *unique connected conjugacy class* of $\mathbb{R}$-dimension $4d^2$. The group $\mathrm{Aut}(\mathscr{A})$ has two connected components: the neutral component $\mathrm{Inn}(\mathscr{A})$ connected to the identity and the second component containing the swap automorphism $(f, f') \mapsto (f', f)$. The simplest case for $d = 1$ is $\mathbb{H}^2$ isomorphic to $Cl(0,3)$.

For $\mathscr{A} = \mathscr{M}(2d, \mathbb{C})$, the square roots of $-\mathbf{1}$ are in *bijection to the idempotents* [2]. First, the *ordinary* square roots of $-\mathbf{1}$ (with $k = 0$) constitute a conjugacy class of $\mathbb{R}$-dimension $4d^2$ of a *single connected component* which is invariant under $\mathrm{Aut}(\mathscr{A})$. Second, there are $2d$ *conjugacy classes* of *exceptional* square roots of $-\mathbf{1}$, each composed of a *single connected component*, characterized by the equality $\mathrm{Spec}(f) = k/d$ (the pseudoscalar coefficient) with $\pm k \in \{1, 2, \ldots, d\}$, and their $\mathbb{R}$-dimensions are $4(d^2 - k^2)$. The group $\mathrm{Aut}(\mathscr{A})$ includes conjugation of the pseudoscalar $\omega \mapsto -\omega$ which maps the conjugacy class associated with k to the class associated with $-k$. The simplest case for $d = 1$ is the Pauli matrix algebra isomorphic to the geometric algebra $Cl(3,0)$ of 3D Euclidean space $\mathbb{R}^3$, and to complex biquaternions [21]. See Table 2.2 for representative exceptional ($k \neq 0$) square roots of $-\mathbf{1}$ in conformal geometric algebra $Cl(4,1)$ of three-dimensional Euclidean space [17].

k	f_k	$\Delta_k(t)$
2	$\omega = e_{12345}$	$(t-i)^4$
1	$\frac{1}{2}(e_{23} + e_{123} - e_{2345} + e_{12345})$	$(t-i)^3(t+i)$
0	e_{123}	$(t-i)^2(t+i)^2$
-1	$\frac{1}{2}(e_{23} + e_{123} + e_{2345} - e_{12345})$	$(t-i)(t+i)^3$
-2	$-\omega = -e_{12345}$	$(t+i)^4$

Table 1: Square roots of $-\mathbf{1}$ in conformal geometric algebra $Cl(4,1) \cong \mathscr{M}(4, \mathbb{C})$, $d = 2$, with characteristic polynomials $\Delta_k(t)$. See [17] for details.

With respect to any square root $i \in Cl(p,q)$ of -1, $i^2 = -1$, every multivector $A \in Cl(p,q)$ can be split into *commuting* and *anticommuting* parts [17].

Lemma 2.2 *Every multivector $A \in Cl(p,q)$ has, with respect to a square root $i \in Cl(p,q)$ of -1, i.e., $i^{-1} = -i$, the unique decomposition*

$$A_{+i} = \frac{1}{2}(A + i^{-1}Ai), \qquad A_{-i} = \frac{1}{2}(A - i^{-1}Ai)$$
$$A = A_{+i} + A_{-i}, \qquad A_{+i}\,i = iA_{+i}, \qquad A_{-i}\,i = -iA_{-i}. \tag{14}$$

3 THE CLIFFORD FOURIER TRANSFORM

The *general Clifford Fourier transform* (CFT), to be introduced now, can be understood as a generalization of known CFTs [12] to a general real Clifford algebra setting. Most previously known CFTs use in their kernels specific square roots of -1, like bivectors, pseudoscalars, unit pure quaternions, or blades [6]. We will *remove all these restrictions* on the square root of -1 used in a CFT.

Definition 3.1 (CFT with respect to one square root of -1) *Let $i \in Cl(p,q)$, $i^2 = -1$, be any square root of -1. The general Clifford Fourier transform (CFT) of $f \in L^1(\mathbb{R}^{p,q}; Cl(p,q))$, with respect to i is*

$$\mathscr{F}^i\{f\}(\omega) = \int_{\mathbb{R}^{p,q}} f(\boldsymbol{x})\, e^{-iu(\boldsymbol{x},\omega)} d^n\boldsymbol{x}, \tag{15}$$

where $d^n\boldsymbol{x} = dx_1 \ldots dx_n$, $\boldsymbol{x}, \omega \in \mathbb{R}^{p,q}$, and $u : \mathbb{R}^{p,q} \times \mathbb{R}^{p,q} \to \mathbb{R}$.

Since square roots of -1 in $Cl(p,q)$ populate *continuous submanifolds* in $Cl(p,q)$, the CFT of Definition 3.1 is generically *steerable* within these manifolds. In Definition 3.1, the square roots $i \in Cl(p,q)$ of -1 may be from any component of any conjugacy class.

4 PROPERTIES OF THE CFT

We now study important properties of the general CFT of Definition 3.1.

4.1 Linearity, shift, modulation, dilation, and powers of f, g

Regarding *left and right linearity* of the general two-sided CFT of Definition 3.1 we can establish with the help of Lemma 2.2 that for $h_1, h_2 \in L^1(\mathbb{R}^{p,q}; Cl(p,q))$, and constants $\alpha, \beta \in Cl(p,q)$

$$\mathscr{F}^i\{\alpha h_1 + \beta h_2\}(\omega) = \alpha \mathscr{F}^i\{h_1\}(\omega) + \beta \mathscr{F}^i\{h_2\}(\omega), \tag{16}$$

$$\begin{aligned}\mathscr{F}^i\{h_1\alpha + h_2\beta\}(\omega) = {} & \mathscr{F}^i\{h_1\}(\omega)\alpha_{+i} + \mathscr{F}^{-i}\{h_1\}(\omega)\alpha_{-i} \\ & + \mathscr{F}^i\{h_2\}(\omega)\beta_{+i} + \mathscr{F}^{-i}\{h_2\}(\omega)\beta_{-i}.\end{aligned} \tag{17}$$

For *i power factors* in $h_{a,b}(\boldsymbol{x}) = i^a h(\boldsymbol{x}) i^b$, $a, b \in \mathbb{Z}$, we obtain as an application of linearity

$$\mathscr{F}^i\{h_{a,b}\}(\omega) = i^a \mathscr{F}^i\{h\}(\omega) i^b. \tag{18}$$

Regarding the *$\boldsymbol{x}$-shifted* function $h_0(\boldsymbol{x}) = h(\boldsymbol{x} - \boldsymbol{x}_0)$ we obtain with constant $\boldsymbol{x}_0 \in \mathbb{R}^{p,q}$, assuming linearity of $u(\boldsymbol{x}, \omega)$ in its vector space argument $\boldsymbol{x}$,

$$\mathscr{F}^i\{h_0\}(\omega) = \mathscr{F}^i\{h\}(\omega)\, e^{-iu(\boldsymbol{x}_0,\omega)}. \tag{19}$$

For the purpose of *modulation* we make the special assumption, that the function $u(\boldsymbol{x}, \omega)$ is linear in its frequency argument ω. Then we obtain for $h_m(\boldsymbol{x}) = h(x)\, e^{-iu(\boldsymbol{x},\omega_0)}$, and constant $\omega_0 \in \mathbb{R}^{p,q}$ the modulation formula

$$\mathscr{F}^i\{h_m\}(\omega) = \mathscr{F}^i\{h\}(\omega + \omega_0). \tag{20}$$

Regarding *dilations*, we make the special assumption, that for constants $a_1,\ldots,a_n \in \mathbb{R}\setminus\{0\}$, and $\boldsymbol{x}' = \sum_{k=1}^n a_k x^k \boldsymbol{e}_k$, we have $u(\boldsymbol{x}',\omega) = u(\boldsymbol{x},\omega')$, with $\omega' = \sum_{k=1}^n a_k \omega^k \boldsymbol{e}_k$. We then obtain for $h_d(\boldsymbol{x}) = h(\boldsymbol{x}')$ that

$$\mathscr{F}^i\{h_d\}(\omega) = \frac{1}{|a_1\ldots a_n|}\mathscr{F}^i\{h\}(\omega_d), \qquad \omega_d = \sum_{k=1}^n \frac{1}{a_k}\omega^k \boldsymbol{e}_k. \tag{21}$$

For $a_1 = \ldots = a_n = a \in \mathbb{R}\setminus\{0\}$ this simplifies under the same special assumption to

$$\mathscr{F}^i\{h_d\}(\omega) = \frac{1}{|a|^n}\mathscr{F}^i\{h\}(\frac{1}{a}\omega). \tag{22}$$

Note, that the above assumption would, e.g., be fulfilled for $u(\boldsymbol{x},\omega) = \boldsymbol{x} * \widetilde{\omega} = \sum_{k=1}^n x^k\omega^k = \sum_{k=1}^n x_k\omega_k$.

4.2 CFT inversion , moments, derivatives, Plancherel, Parseval

For establishing an inversion formula, moment and derivative properties, Plancherel and Parseval identities, certain *assumptions* about the phase function $u(\boldsymbol{x},\omega)$ need to be made. One possibility is, e.g., to assume

$$u(\boldsymbol{x},\omega) = \boldsymbol{x} * \widetilde{\omega} = \sum_{l=1}^n x^l\omega^l = \sum_{l=1}^n x_l\omega_l, \tag{23}$$

which will be assumed for the current subsection.

We then get the following *inversion* formula

$$h(\boldsymbol{x}) = \mathscr{F}^i_{-1}\{\mathscr{F}^i\{h\}\}(\boldsymbol{x}) = \frac{1}{(2\pi)^n}\int_{\mathbb{R}^{p,q}} \mathscr{F}^i\{h\}(\omega)\, e^{iu(\boldsymbol{x},\omega)} d^n\omega, \tag{24}$$

where $d^n\omega = d\omega_1\ldots d\omega_n$, $\boldsymbol{x},\omega \in \mathbb{R}^{p,q}$. For the existence of (24) we need $\mathscr{F}^i\{h\} \in L^1(\mathbb{R}^{p,q};\ Cl(p,q))$.

Additionally, we get the transformation law for *partial derivatives* $h'_l(\boldsymbol{x}) = \partial_{x_l} h(\boldsymbol{x})$, $1 \le l \le n$, for h piecewise smooth and integrable, and $h, h'_l \in L^1(\mathbb{R}^{p,q};\ Cl(p,q))$ as

$$\mathscr{F}^i\{h'_l\}(\omega) = \omega_l\, \mathscr{F}^i\{h\}(\omega)i, \quad \text{for } 1 \le l \le n. \tag{25}$$

The *vector derivative* of $h \in L^1(\mathbb{R}^{p,q};\ Cl(p,q))$ with $h'_l \in L^1(\mathbb{R}^{p,q};\ Cl(p,q))$ gives therefore

$$\mathscr{F}^i\{\nabla h\}(\omega) = \mathscr{F}^i\{\sum_{l=1}^n e^l h'_l\}(\omega) = \omega\mathscr{F}^i\{h\}(\omega)i. \tag{26}$$

For the transformation of the *spatial moments* with $h_l(\boldsymbol{x}) = x_l h(\boldsymbol{x})$, $1 \le l \le n$, $h, h_l \in L^1(\mathbb{R}^{p,q};\ Cl(p,q))$, we obtain

$$\mathscr{F}^i\{h_l\}(\omega) = \partial_{\omega_l}\mathscr{F}^i\{h\}(\omega)i, \tag{27}$$

and for the *spatial vector moment*

$$\mathscr{F}^i\{\boldsymbol{x}h\}(\omega) = \nabla_\omega\mathscr{F}^i\{h\}(\omega)i, \tag{28}$$

Moreover, for the functions $h_1, h_2, h \in L^2(\mathbb{R}^{p,q};\ Cl(p,q))$ we obtain the *Plancherel* identity

$$\langle h_1, h_2\rangle = \frac{1}{(2\pi)^n}\langle\mathscr{F}^i\{h_1\}, \mathscr{F}^i\{h_2\}\rangle, \tag{29}$$

as well as the *Parseval* identity

$$\|h\| = \frac{1}{(2\pi)^{n/2}}\left\|\mathscr{F}^i\{h\}\right\|. \tag{30}$$

4.3 Convolution

We define the *convolution* of two multivector signals $a, b \in L^1(R^{p,q}; Cl(p,q))$ as

$$(a \star b)(\boldsymbol{x}) = \int_{\mathbb{R}^{p,q}} a(\boldsymbol{y}) b(\boldsymbol{x}-\boldsymbol{y}) d^n\boldsymbol{y}. \tag{31}$$

We assume that the function u is linear with respect to its first argument. The *CFT of the convolution* (31) can then be expressed as

$$\mathscr{F}^i\{a \star b\}(\omega) = \mathscr{F}^{-i}\{a\}(\omega)\mathscr{F}^i\{b_{-i}\}(\omega) + \mathscr{F}^i\{a\}(\omega)\mathscr{F}^i\{b_{+i}\}(\omega) \tag{32}$$

5 CONCLUSIONS

We have established a comprehensive *new mathematical framework* for the investigation and application of Clifford Fourier transforms (CFTs) together with *new properties*. Our new CFTs form a more general class of CFTs, subsuming and generalizing previous results. We have applied new results on square roots of -1 in Clifford algebras to fully general construct CFTs, with a general square root of -1 in real Clifford algebras $Cl(p,q)$. The new CFTs are *fully steerable* within the continuous Clifford algebra submanifolds of square roots of -1. We have thus left the terra cognita of familiar transforms to outline the vast array of possible CFTs in $Cl(p,q)$.

We first reviewed the recent results on *square roots of* -1 in Clifford algebras. Next, we defined the central notion of the *Clifford Fourier transform* with respect to any square root of -1 in Clifford algebra. Finally, we investigated important *properties* of these new CFTs: linearity, shift, modulation, dilation, moments, inversion, partial and vector derivatives, Plancherel and Parseval formulas, as well as a convolution theorem.

Regarding numerical implementations, usually 2^n complex Fourier transformations (FTs) are sufficient. In some cases this can be reduced to $2^{(n-1)}$ complex FTs, e.g., when the square root of -1 is a pseudoscalar. Further algebraic studies may widen the class of CFTs, where $2^{(n-1)}$ complex FTs are sufficient. Numerical implementation is then possible with 2^n (or $2^{(n-1)}$) discrete complex FTs, which can also be fast Fourier transforms (FFTs), leading to fast CFT implementations.

A well-known example of a CFT is the quaternion FT (QFT) [4, 5, 8, 9, 13, 16, 22], which is particularly used in applications to partial differential systems, color image processing, filtering, disparity estimation (two images differ by local translations), and texture segmentation. Another example is the spacetime FT, which leads to a multivector wave packet analysis of spacetime signals (e.g. electro-magnetic signals), applicable even to relativistic signals [13, 14].

Depending on the choice of the phase functions $u(\boldsymbol{x}, \omega)$ the multivector basis coefficient functions of the CFT result carry information on the symmetry of the signal, similar to the special case of the QFT [4].

The convolution theorem allows to design and apply multivector valued filters to multivector valued signals.

ACKNOWLEDGMENT

E. H. thanks God: *Soli deo gloria!*, his family, J. Helmstetter, R. Abłamowicz, S. Sangwine, R. Bujack and the IKM 2012 organizers.

REFERENCES

[1] R. Abłamowicz, *Computations with Clifford and Grassmann Algebras*, Adv. Appl. Clifford Algebras **19**, No. 3–4 (2009), 499–545.

[2] R. Abłamowicz, B. Fauser, K. Podlaski, J. Rembieliński, *Idempotents of Clifford Algebras*. Czechoslovak Journal of Physics, **53** (11) (2003), 949–954.

[3] R. Abłamowicz and B. Fauser, CLIFFORD with Bigebra – A Maple Package for Computations with Clifford and Grassmann Algebras, http://math.tntech.edu/rafal/ (©1996-2012).

[4] T. Bülow, *Hypercomplex Spectral Signal Representations for the Processing and Analysis of Images*. Ph.D. Thesis, University of Kiel, 1999.

[5] T. Bülow, M. Felsberg and G. Sommer, *Non-commutative Hypercomplex Fourier Transforms of Multidimensional Signals*. In G. Sommer (ed.), Geometric Computing with Clifford Algebras: Theoretical Foundations and Appli- cations in Computer Vision and Robotics. Springer-Verlag, Berlin, 2001, 187–207.

[6] R. Bujack, G. Scheuermann, E. Hitzer, *A General Geometric Fourier Transform*, In: K. Gürlebeck (ed.), Proc. of The 9th Int. Conf. on Clifford Algebras and their Applications, (2011).

[7] J. Ebling, G. Scheuermann, *Clifford Fourier Transform on Vector Fields*, IEEE Transactions on Visualization and Computer Graphics, **11**(4) July/August (2005), 469-479.

[8] T. A. Ell, *Quaternion-Fourier Transforms for Analysis of Two-Dimensional Linear Time-Invariant Partial Differential Systems*. In Proc. of the 32nd Conf. on Decision and Control, IEEE (1993), 1830–1841.

[9] T. A. Ell, S. J. Sangwine, *Hypercomplex Fourier Transforms of Color Images.* IEEE Transactions on Image Processing, **16**(1), (2007), 22-35.

[10] M.I. Falcao, H.R. Malonek, *Generalized Exponentials through Appell sets in* $\mathbb{R}^{n+1}$ *and Bessel functions*, AIP Conference Proceedings, Vol. 936, pp. 738–741 (2007).

[11] M. Felsberg, *Low-Level Image Processing with the Structure Multivector*, PhD Thesis, University of Kiel, Germany, 2002.

[12] E. Hitzer, B. Mawardi, *Clifford Fourier Transform on Multivector Fields and Uncertainty Principles for Dimensions* $n = 2 \pmod 4$ *and* $n = 3 \pmod 4$. Adv. Appl. Clifford Algebras, **18** (3-4) (2008), 715–736.

[13] E. Hitzer, *Quaternion Fourier Transformation on Quaternion Fields and Generalizations*, Adv. in App. Cliff. Alg., **17**, (2007) 497–517.

[14] E. Hitzer, *Directional Uncertainty Principle for Quaternion Fourier Transforms*, Adv. in App. Cliff. Alg., **20**(2), pp. 271–284 (2010),

[15] E. Hitzer, R. Abłamowicz, *Geometric Roots of* -1 *in Clifford Algebras* $Cl(p,q)$ *with* $p+q \leq 4$. Adv. Appl. Clifford Algebras, **21**(1), (2011) 121–144, DOI: 10.1007/s00006-010-0240-x.

[16] E. Hitzer, *OPS-QFTs: A New Type of Quaternion Fourier Transforms Based on the Orthogonal Planes Split with One or Two General Pure Quaternions*. Numerical Analysis and Applied Mathematics ICNAAM 2011, AIP Conf. Proc. 1389 (2011), 280–283; DOI: 10.1063/1.3636721.

[17] E. Hitzer, J. Helmstetter, R. Ablamowicz, *Square roots of* -1 *in real Clifford algebras*, In: K. Gürlebeck (ed.), Proc. of The 9th Int. Conf. on Clifford Algs. and their Applications, (2011). Preprints: `http://arxiv.org/abs/1204.4576`, `http://www.tntech.edu/files/math/reports/TR_2012_3.pdf`.

[18] E. Hitzer, J. Helmstetter, and R. Abłamowicz, Maple worksheets created with `CLIFFORD` for a verification of results in [17], http://math.tntech.edu/rafal/publications.html (©2012).

[19] P. Lounesto, *Clifford Algebras and Spinors*, CUP, Cambridge (UK), 2001.

[20] Waterloo Maple Incorporated, *Maple, a general purpose computer algebra system*. Waterloo, `http://www.maplesoft.com` (©2012).

[21] S. J. Sangwine, *Biquaternion (Complexified Quaternion) Roots of* -1. Adv. Appl. Clifford Algebras **16**(1) (2006), 63–68.

[22] S. J. Sangwine, *Fourier transforms of colour images using quaternion, or hypercomplex, numbers*, Electronics Letters, **32**(21) (1996), 1979–1980.

[23] G. Sobczyk, *Conformal Mappings in Geometric Algebra*, Notices of the AMS, **59**(2) (2012), 264–273.

19th International Conference on the Application of Computer
Science and Mathematics in Architecture and Civil Engineering
K. Gürlebeck, T. Lahmer and F. Werner (eds.)
Weimar, Germany, 04–06 July 2012

ASSESSMENT OF INTEGRAL BRIDGES USING QUANTITATIVE MODEL EVALUATION

B. Jung*, **G. Morgenthal**

**Research Training Group 1462 Model Quality*
Berkaer Straße 9
99423 Weimar
Germany
E-mail: bastian.jung@uni-weimar.de

Keywords: sensitivity analysis, coupled models, global model quality, integral bridge, restraint effects

Abstract. *Numerical simulations in the general field of civil engineering are common for the design process of structures and/or the assessment of existing buildings. The behaviour of these structures is analytically unknown and is approximated with numerical simulation methods like the Finite Element Method (FEM). Therefore the real structure is transferred into a global model (GM, e.g. concrete bridge) with a wide range of sub models (partial models PM, e.g. material modelling, creep). These partial models are coupled together to predict the behaviour of the observed structure (GM) under different conditions. The engineer needs to decide which models are suitable for computing realistically and efficiently the physical processes determining the structural behaviour. Theoretical knowledge along with the experience from prior design processes will influence this model selection decision. It is thus often a qualitative selection of different models.*

The goal of this paper is to present a quantitative evaluation of the global model quality according to the simulation of a bridge subject to direct loading (dead load, traffic) and indirect loading (temperature), which induce restraint effects. The model quality can be separately investigated for each partial model and also for the coupled partial models in a global structural model. Probabilistic simulations are necessary for the evaluation of these model qualities by using Uncertainty and Sensitivity Analysis. The method is applied to the simulation of a semi-integral concrete bridge with a monolithic connection between the superstructure and the piers, and elastomeric bearings at the abutments. The results show that the evaluation of global model quality is strongly dependent on the sensitivity of the considered partial models and their related quantitative prediction quality. This method is not only a relative comparison between different models, but also a quantitative representation of model quality using probabilistic simulation methods, which can support the process of model selection for numerical simulations in research and practice.

1 EVALUATION METHOD FOR GLOBAL MODEL QUALITY ASSESSMENT

Global models (GM) for numerical simulation approaches utilize different model classes (M) with subordinate partial models (PM). Material descriptions, creep, and/or shrinkage models are defined as possible M for concrete structures within this paper. Interactions and couplings of their PM are necessary for determining an appropriate structural behaviour. Therefore, the following evaluation method enables to assess the Global Model Quality. For detailed information the author recommends KEITEL et al. [11].

1.1 Sensitivity according a model class

The first step is to quantify whether the model class M has an influence on a certain target value. This is evaluated by using Sensitivity Analysis [12] which, in general, is the study of how the output of a model (Y) is related to the model input (X). By using discrete random variables for selecting the model class, the Sensitivity Study in this case is not an estimation of uncertainty, but a quantified value of the influence of the model class (X_i). The First Order Sensitivity Index is:

$$S_i = \frac{V\left(E\left(Y|X_i\right)\right)}{V\left(Y\right)}. \tag{1}$$

This index S_i illustrates the exclusive influence of model X_i. Due to interactions in complex engineering problems higher order Sensitivity Indices are needed. The Total Effect Index is defined as:

$$S_{Ti} = 1 - \frac{V\left(E\left(Y|X_{\sim i}\right)\right)}{V\left(Y\right)}. \tag{2}$$

A finite number of possible model class combinations n_{comb} are necessary for the indices:

$$n_{comb} = 2^{n_M} \tag{3}$$

with n_M random variables (model classes). A measure of the interaction between X_i and other model classes is the difference between S_i and S_{Ti}. High values of these Sensitivity Indices highlight a significant influence of this partial model class on the response of the global model. Models with values smaller than a given threshold (here: $S_{Ti} \leq 0.03$) shall be neglected for the next evaluation method step. In other words, no further investigations about their Partial Model Quality are performed.

1.2 Sensitivity according the choice in a model class

The second method step quantifies the importance of selecting a partial model from one model class. It is also based on Sensitivity Studies [11, 12]. The choice of each PM within a model class is controlled by X_i. The Total Effect Sensitivity Index indicates how this choice leads to a variation of the global model response according to a certain output value. Low values show that different partial models within the same model class give a similar contribution to the structural response value and do not significantly affect these response values. These indices are used as weighting factors for the importance of the quality of a PM in a model class.

1.3 Quality of coupled partial models

The Global Model Quality (MQ_{GM}) of coupled partial models is quantified by a path on a graph (graph theory see [3, 4, 9, 10]) with the vertex as the quality of the partial model MQ_{PM}

and the edges as the coupling quantities. A number between 0 and 1 expresses this quality. 0 signifies a poor and 1 a high MQ_{PM}. These quantitative values come from the evaluation of the PM itself, using Uncertainty, Complexity or Robustness criterias [8]. Assuming a perfect data coupling between each model classes the model quality of a global structural model is defined as [11]:

$$MQ_{GM} = \sum_{i=1}^{n_{M,red}} \frac{S_{Ti}^{MC} \cdot MQ_{PM_j}}{\sum_{i=1}^{n_{M,red}} S_{Ti}^{MC}}. \tag{4}$$

PM_j is one partial model of the model class M_i. The variable $n_{M,red}$ is the number of non-negligible partial model classes influecing the global response, determined by method step one. This Global Model Quality Evaluation method is applied to a reinforced and prestsressed semi-integral concrete bridge below.

2 APPLICATION TO SEMI-INTEGRAL CONCRETE BRIDGE

2.1 Geometry, material properties and loading

The geometry of the longitudinal and vertical direction of the bridge and the prestressing steel is shown in Fig. 1. The cross sections of the superstructure and the pier are shown in Fig. 2a and Fig. 2b and the material properties are listed in Table 1.

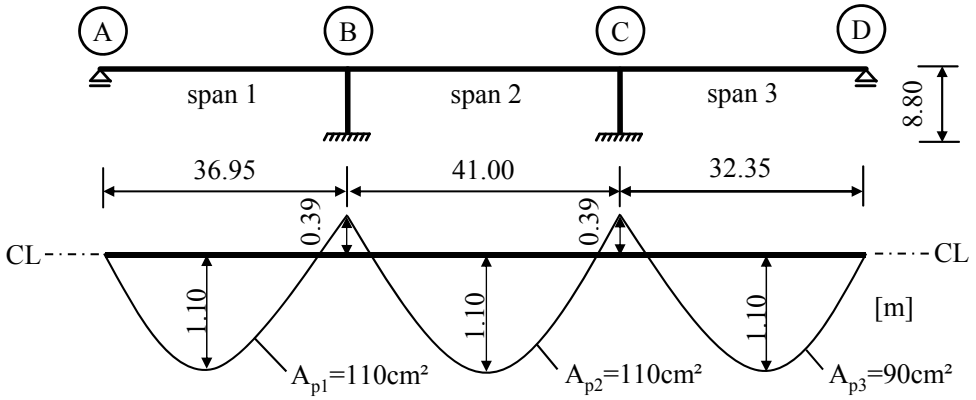

Figure 1: Bridge and prestressing geometry

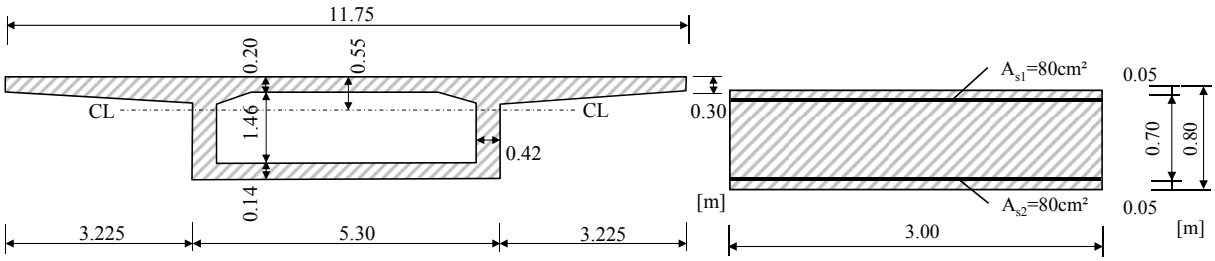

(a) Superstructure (b) Piers

Figure 2: Cross sections of the superstructure and the piers

Table 1: Material properties for the superstructure and the piers

	Unit	Superstructure	Piers
Concrete		C50/60	C35/45
CEM	-	II 52.5N	II 42.5N
E_{c0m}	[MN/m^2]	35,500	33,300
E_{cm}	[MN/m^2]	32,800	28,300
f_{cm}	[MN/m^2]	58	43
f_{ctm}	[MN/m^2]	4.1	3.2
Steel		Y1770	B500B
E_s	[MN/m^2]	190,000	200,000
f_y	[MN/m^2]	1,500	500

The commonly decoupled connection between the piers and the superstructure (differential bridge) is adjusted to a coupled semi-integral bridge. Therefore the overall structural load-deformation behaviour is affected by the interaction within the piers and superstructure, particularly in case of restraint effects. Hence, the interference between the partial models is investigated.
The structural behaviour is simulated under quasi-permanent loading [5] for 100 years of service life (see Table 2).

Table 2: Loading for quasi-permanent loading according [5]

Loading category	Loading value
dead load (G_k)	G_{k1} = 142 kN/m (superstructure) G_{k2} = 24 kN/m (pavement) G_{k3} = 6.75 kN/m (piers)
prestressing (P_k)	σ_{pk} = 1295 MN/m^2
imposed traffic (Q_{k1})	$Q_{k1,UDL}$ = 46.4 kN/m, $Q_{k1,TL}$ = 400 kN (span 1) $\Psi_{2,1}$ = 0.20
temperature load (Q_{k2})	T_0 = 10°C, T_{min} = -24°C, $T_{e,min}$ = -16° C, ΔT_N = -26K, ΔT_M = -8.8K $\Psi_{2,2}$=0.50

2.2 Considered partial models

The material description (Model Class A) for the concrete compression range is modelled with linear-elastic relation between strains and stresses. Because of the prestressing and the quasi-permanent loading, the compression stresses are smaller than $\sigma_c \leq 0.40 \cdot f_{cm}$. Therefore, linear-elastic material behaviour can be assumed. In the range of tensile concrete parts the concrete can either sustain stresses until f_{ctm} (A-1: linear-elastic material modelling) or cracking shall be considered through the application of a tension-stiffening model as $\beta_{ct} \cdot f_{ctm}$ until $\epsilon_{ct} \leq \epsilon_{sy}$ (A-2: tension-stiffening model).
In order to describe the time-dependent increase of the creep compliance two creep models (Model Class B) are investigated. These are the models according to Model Code 2010 (B-1:

MC 10 [2]) and GARDNER and LOCKMAN (B-2: GL2000 [7]).
Geometrical nonlinearities (Model Class D) can affect displacement values and section forces. The nonlinear kinematic (D-1) and the p-Δ (D-2) approaches are considered in this model class.
Restraint effects in concrete structures may occur as a result of imposed deformations such as thermal actions (Model Class E). In the standard code EN 1991 [6] specific values are stated for temperature conditions and temperature distributions. One possibility to take thermal actions on bridges into account is to assume constant temperature (ΔT_N) and linearly shift values over the cross section height (ΔT_M). Alternatively, thermal actions can also be considered by the temperature (ΔT_N) and nonlinear varying values (ΔT) over the cross section height. Combination factors for the concurrent occurrence of both temperature parts are included to account for their coincident probability. Four temperature distributions are considered as partial models in the model class temperature:

- E-1 TEMP 1 constant with linear shifting $0.35 \cdot \Delta T_N + \Delta T_M$
- E-2 TEMP 2 constant with linear shifting $\Delta T_N + 0.75 \cdot \Delta T_M$
- E-3 TEMP 3 constant with nonlinear distribution $0.35 \cdot \Delta T_N + \Delta T$
- E-4 TEMP 4 constant with nonlinear distribution $\Delta T_N + 0.75 \cdot \Delta T$

The creep $\epsilon_{c,cr}(t)$, shrinkage $\epsilon_{c,sh}(t)$ and temperature $\epsilon_{c,t}(t_0)$ strains are expressed by additional strain components of the concrete, which leads to the total strains of the concrete:

$$\epsilon_{c,tot}(t) = \epsilon_{c,el}(t) + \epsilon_{c,pl}(t) + \epsilon_{c,da}(t) + \epsilon_{c,cr}(t) + \epsilon_{c,sh}(t) + \epsilon_{c,t}(t_0) \tag{5}$$

with $\epsilon_{c,el}(t)$, $\epsilon_{c,pl}(t)$ and $\epsilon_{c,da}(t)$ as the time-dependent elastic, plastic and damage strains.

2.3 Structural response values for the quantification

In case of the first step in the evaluation method, the Sensitivity is quantified for the vertical deformations in all spans, horizontal deformations at each bridge axis, concrete compression and prestressing steel tensile stress in the superstructure, concrete and reinforcement stresses in the piers and axial and bending moment section forces at different positions. The 8 model classes lead to 256 model combinations (n_{comb} = 2^8) independent of the target values for the structural behaviour.

2.4 Sensitivity according the model class

The discrete random variables control, whether the model class is activated or deactivated. In terms of the material behaviour, either tension-stiffening or purely linear-elastic material is modelled. In terms of creep or shrinkage, either creep or shrinkage strains are computed or neglected. In terms of geometric nonlinearity, either the second order or the first order kinematic is used. Finally, in terms of temperature, either temperature strains occurring from constant and shifting parts are considered or zero. Table 3 shows the First Order and Total Effects Sensitivity Indices for a selection of target values.

The creep phenomenon increases the strains for the quasi-permanent loading for 100 years design life. The vertical displacements in the superstructure are almost exclusively sensitive to this model class. Non activated creep modelling will reduce the predicted vertical displacement

Table 3: Sensitivity indices for the model classes according target values, first row for each target value: First Order Effect S_i^M, second row for each target value: Total Effects S_{Ti}^M

Model Class	σ-ϵ super-struct. A	σ-ϵ piers A	creep super-struct. B	creep piers B	shrink. super-struct. C	shrink. piers C	geom. kine-matic D	tem-pera-ture E
Vertical dis.	0.000	0.000	**0.975**	0.001	0.000	0.012	0.000	0.000
span 1	0.000	0.000	**0.976**	0.012	0.001	0.012	0.000	0.001
Horizontal dis.	0.000	0.000	**0.076**	0.000	**0.850**	0.000	0.000	**0.074**
axis C	0.000	0.000	**0.076**	0.000	**0.850**	0.000	0.000	**0.074**
concrete stress	0.000	0.004	**0.054**	**0.265**	0.002	0.022	0.000	**0.514**
superstr. span 2	0.000	0.023	**0.098**	**0.355**	**0.072**	0.025	0.000	**0.580**
concrete stress	0.000	0.003	0.014	**0.296**	**0.548**	0.004	0.000	**0.045**
pier axis C	0.000	0.013	0.016	**0.382**	**0.620**	0.004	0.000	**0.059**
bending moment	0.000	0.003	**0.132**	**0.170**	0.001	0.023	0.000	**0.424**
right axis B	0.000	0.016	**0.316**	**0.230**	**0.047**	0.025	0.000	**0.622**
Axial force superstr.	0.000	0.002	0.006	**0.164**	**0.732**	0.001	0.000	0.047
right axis B	0.000	0.010	0.008	**0.208**	**0.770**	0.001	0.000	0.056
Bending moment	0.000	0.003	0.018	0.207	**0.663**	0.000	0.000	**0.057**
pier bottom axis C	0.000	0.016	0.020	0.252	**0.700**	0.001	0.000	**0.070**
Axial force	0.000	0.001	0.000	**0.091**	**0.631**	0.016	0.000	**0.217**
pier bottom axis C	0.000	0.004	0.024	**0.110**	**0.647**	0.016	0.000	**0.245**

significantly. The creep phenomenon regarding the vertical displacements can thus not be neglected.
In case of horizontal displacements, the major impact occurs from the shrinkage model class. Shrinkage strains must be included without any reduction factors. Temperature strains for the quasi-permanent loading are reduced by the combination factor $\Psi_{2,2} = 0.50$. This leads to:

- Shrinkage MC10 $\quad \epsilon_{c,sh}(36510\ d) \qquad\qquad = -4.204\ e^{-4}$
- $\Delta T_N = -26$ K $\quad \epsilon_{c,t}(36510\ d) = -26\ \text{K} \cdot 1.0\ e^{-5} \cdot 0.5 \quad = -1.300\ e^{-4}$

and therefore to higher sensitivity of the shrinkage phenomenon according the horizontal displacement.
The difference between S_i and S_{Ti} such as the concrete stress in span 2 clarify a strong interaction between model classes ($S_{Ti} - S_i > 0.05$). The deformation behaviour of the piers and superstructure affect each other and therefore the coupling of their model classes has a strong influence on the structural response. The influence of choice of different partial models in each model class is quantified for the bolted structural response value in the first column of Table 3 (horizontal displacement at the axis c, concrete stress in the superstructure in span 2, bending moment right axis B).

2.5 Sensitivity according the model choice in a model class

The analysis of the Total Effect Sensitivity Index enables the quantification of the model choice importance (comparable as weighting factors). For example, the prognosis of the models

MC10 and GL2000 for creep and shrinkage are different, and the influence of it can be computed by Sensitivity Analysis. Table 4 shows these weighting factors, which quantify the impact of model selection according to the chosen structural response values.

Table 4: Total Effect Sensitivity Indexes S_{Ti}^{MC} for the model choice according the important model classes for different target values, * model classes with no significant influence according the target value

Model Class	σ-ϵ super-struct. A	σ-ϵ piers A	creep super-struct. B	creep piers B	shrink. super-struct. C	shrink. piers C	geom. kine-matic D	tem-pera-ture E
Horizontal dis. axis C	*	*	0.405	*	**0.496**	*	*	0.099
concrete stress superstr. span 2	*	*	0.121	0.341	0.007	*	*	**0.622**
bending moment right axis B	*	*	0.285	**0.490**	0.010	*	*	0.252

2.6 Global Model Quality

The Partial Model Quality for the creep models is analysed by uncertainty analysis including model and parameter uncertainty and is stated in [11]. The Partial Model Quality of the shrinkage models is assessed on the variation of the error of the prediction. This uncertainty is $CV_{MC10} = 0.481$ and $CV_{GL2000} = 0.433$ [1]. In relation to the lowest model uncertainty of $CV_{B3} = 0.374$ the Partial Model Quality is defined as:

- MC10 $MQ_{PM}^{MC10} = 0.374/0.481 = 0.78$
- GL2000 $MQ_{PM}^{GL2000} = 0.374/0.433 = 0.86$

Linear and nonlinear temperature models [6] are quantified by their prognosis of the induced strains. The complexity of the nonlinear temperature distributions is higher in comparison to the linear approaches. It can be assumed, that their Partial Model Quality is highest (of the considered) and the linear distributions are quantified relatively by the model outputs for the concrete stress in span 2, which is selected for the next method step (Global Model Quality Evaluation).
The important model classes with their respective partial models are shown in Fig. 3. The unimportant model classes are excluded for the Global Model Quality Evaluation. The influence of the model selection in every model class is expressed by the Total Effect Sensitivity Index (bottom of Fig. 3). Partial Model Qualities mentioned above, are expressed in the vertices. The coupling (edges) is without any loss of data information.
The grey highlighted partial models express one admissible path through the graph. Because of practical reason, the structural engineer would not chooce a different creep model for the superstructure and the piers. Thats why the possible combinations is reduced ensuing from $n_{M,red}^{theoretical} = 32$ to $n_{M,red}^{practical} = 16$. The selected combination of partial models in the global

Figure 3: Global Model Quality Evaluation according the concrete stress in span 2 for the application of a semi-integral bridge, count model combination i = 7 regarding Table 5

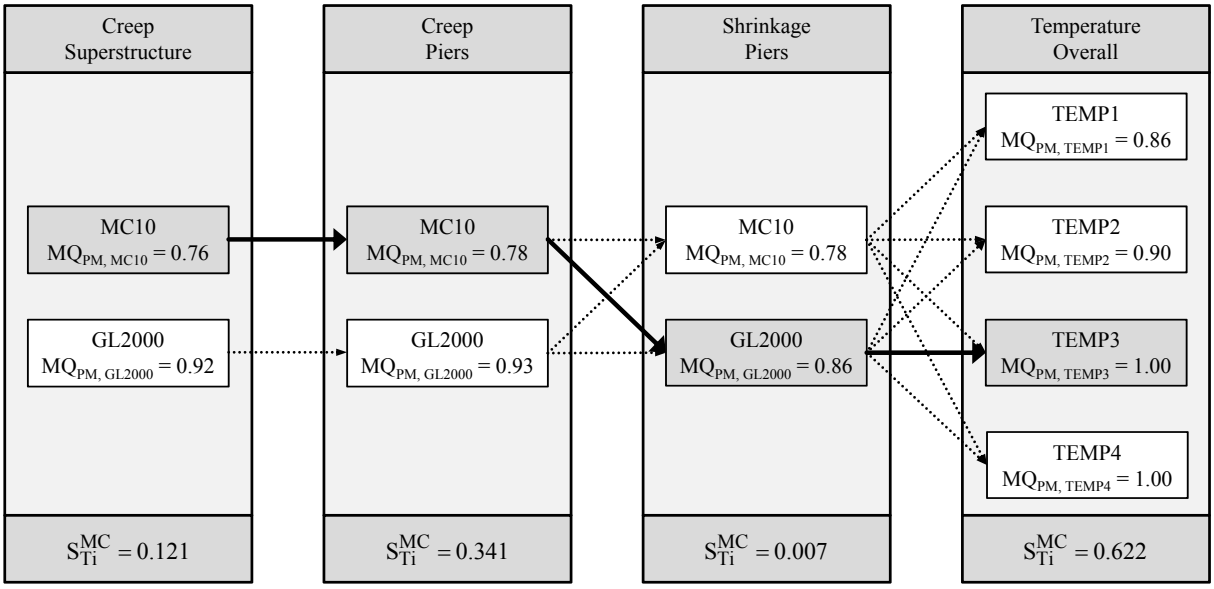

model (see Fig. 3) will lead to the following Global Model Quality:

$$MQ_{GM} = \frac{0.12 \cdot 0.76 + 0.341 \cdot 0.78 + 0.007 \cdot 0.86 + 0.622 \cdot 1.00}{0.121 + 0.341 + 0.007 + 0.622} = 0.90 \tag{6}$$

For any other possible model combination the resulting Global Model Quality MQ_{GM} is stated in Table 5. Selecting a different Partial Model for the prediction of the creep phenomenon will mainly lead to a changed Global Model Quality. This sensitivity is forced by the high difference of the creep compliance between the MC10 and GL2000 creep model, which is expressed by the associated Partial Model Quality. The target value for this evaluation is the concrete compression strength in span 2 of the semi-integral concrete bridge. The additional strain occurring from both shrinkage models has a minor influence (very low S_{Ti}^{MC}), according this target value, in relation to the other effects. In this case, selecting a different shrinkage model, ensues an unchanged MQ_{GM}.

Table 5: Global Model Quality $MQ_{GM,i}$ for the possible model combinations, application of a semi-integral concrete concrete, target value: concrete stress in span 2, ✓... Partial Model PM_i is activated, ⊖ ... Partial Model PM_i is deactivated

Count i	Creep Superstr.		Creep Piers		Shrinkage Piers		Temperature Overall				$MQ_{GM,i}$
	MC10	GL2000	MC10	GL2000	MC10	GL2000	TEMP1	TEMP2	TEMP3	TEMP4	
1	✓	⊖	✓	⊖	✓	⊖	✓	⊖	⊖	⊖	**0.82**
2	✓	⊖	✓	⊖	✓	⊖	⊖	✓	⊖	⊖	0.85
3	✓	⊖	✓	⊖	✓	⊖	⊖	⊖	✓	⊖	0.90
4	✓	⊖	✓	⊖	✓	⊖	⊖	⊖	⊖	✓	0.90
5	✓	⊖	✓	⊖	⊖	✓	✓	⊖	⊖	⊖	**0.82**
6	✓	⊖	✓	⊖	⊖	✓	⊖	✓	⊖	⊖	0.85
7	✓	⊖	✓	⊖	⊖	✓	⊖	⊖	✓	⊖	0.90
8	✓	⊖	✓	⊖	⊖	✓	⊖	⊖	⊖	✓	0.90
9	⊖	✓	⊖	✓	✓	⊖	✓	⊖	⊖	⊖	0.89
10	⊖	✓	⊖	✓	✓	⊖	⊖	✓	⊖	⊖	0.91
11	⊖	✓	⊖	✓	✓	⊖	⊖	⊖	✓	⊖	**0.97**
12	⊖	✓	⊖	✓	✓	⊖	⊖	⊖	⊖	✓	**0.97**
13	⊖	✓	⊖	✓	⊖	✓	✓	⊖	⊖	⊖	0.89
14	⊖	✓	⊖	✓	⊖	✓	⊖	✓	⊖	⊖	0.91
15	⊖	✓	⊖	✓	⊖	✓	⊖	⊖	✓	⊖	**0.97**
16	⊖	✓	⊖	✓	⊖	✓	⊖	⊖	⊖	✓	**0.97**

3 CONCLUSIONS

The evaluation method for accessing the Global Model Quality for coupled partial models [11] is applied on a semi-integral bridge. Sensitivity Analyses quantify in the first step the influence of the phenomenona (model classes) like creep, shrinkage, material description, geometrical nonlinearities and temperature distributions. They depend on the structural output value (displacements, stresses, section forces). In a second step the impacts of the model choice of a partial model in the same model class are analysed. Global Model Quality is evaluated by a path through the graph of partial models whereby each possible combination of the models will lead to a changed Global Model Quality.

The structural application of a semi-integral bridge shows the applicability of the evaluation method and quantifies the important model classes and the model selection process. The Global Model Qualities are useful to compare different simulations in a quantitative manner.

REFERENCES

[1] Z. P. Bazánt, *Unbiased statistical comparison of creep and shrinkage prediction models*, ACI Material Journal (2008) No. 6, pp. 610-621.

[2] CEB-Comit Euro-International du Beton, *Structural concrete: textbook on behaviour, design and performance*, updated knowledge of the CEB/FIB Model Code 90. tech. rep. (1999) and CEP-FIP Model Code 2010 First complete draft (2010).

[3] G. Chartrand, *Introductory graph theory*, New York: Dover Paperbacks (1985)

[4] R. Diestel, *Graph theory*, Springer (2005)

[5] DIN-Fachbericht 101, *Actions on bridges*, Beuth (2009).

[6] EN 1991-1-5, *Actions on structures General actions Thermal actions*, Beuth (2010).

[7] N. Gardner, M. Lockman, *Design provisions for drying shrinkage and creep of normal-strength concrete*, ACI Mater (2001) No. 98, pp. 159-165

[8] T. Lahmer et al., *Bewertungsmethoden für Modelle des konstruktiven Ingenieurbaus*, Bautechnik Sonderheft (2011) No.6.

[9] A. Kaveh, *Structural mechanics: Graph and matrix methods*, 3rd ed. Exeter (UK): Research Studies Press, John Wiley (2004)

[10] A. Kaveh, *Optimal structural analysis*, 2nd ed. Chichester (UK): John Wiley (2006)

[11] H. Keitel, G. Karaki, T. Lahmer, S. Nikulla, V. Zabel, *Evaluation of coupled partial models in structural engineering using graph theory and sensitivity analysis*, Engineering Structures (2011) No. 33, pp. 3726-3736.

[12] A. Saltelli, M. Ratto, T. Andres, F. Campolongo, J. Cariboni, D. Gatelli, M. Saisana, S. Tarantola, *Global sensitivity analysis*, The Primer, John Wiley and Sons (2008).

19th International Conference on the Application of Computer
Science and Mathematics in Architecture and Civil Engineering
K. Gürlebeck, T. Lahmer and F. Werner (eds.)
Weimar, Germany, 04–06 July 2012

THE DISCRETE MODEL OF CRACKS ACCORDING TO BORCZ'S THEORY IN ORDER TO CALCULATE THE DEFLECTIONS OF BENDING REINFORCED CONCRETE BEAMS

M. Kamiński *, **M. Musiał, B. Hydayatullah and A. Ubysz**

* *Institute of Building Engineering, Wroclaw University of Technology, Poland address*
E-mail: michal.musial @ pwr.wroc.pl

Keywords: computational model, the rigidity of beams, beam with cracks

Abstract.
In the design of the reinforced concrete beams loaded by the bending moment, it is assumed that the structure can be used at a level of load, that there are local discontinuities - cracks. Designing the element demands checking two limit states of construction, load capacity and usability. Limit states usability include also the deflection of the element.
Deflections in the reinforced concrete beams with cracks are based on actual rigidity of the element. After cracking there is a local change in rigidity of the beam. The rigidity is variable in the element's length and due to the heterogeneous structure of concrete, it is not possible to clearly describe those changes. Most standards of testing methods tend to simplify the calculations and take the average value of the beam's rigidity on its entire length. The rigidity depends on the level of the maximal load of the beam. Experimental researches verify the value by inserting the coefficients into the formulas used in the theory of elasticity. The researches describe the changes in rigidity in the beam's length more precisely. The authors take into consideration the change of rigidity, depending on the level of maximum load (continuum models), or localize the changes in rigidity in the area of the cracks (discrete models).
This paper presents one of the discrete models. It is distinguished by the fact that the left side of the differential equation, that depends on the rigidity, is constant, and all effects associated with the scratches are taken as the external load and placed on the right side of the equation. This allows to generalize the description.
The paper presents a particular integral of the differential equation, which allow analyzing the displacement and vibration for different rigidity of the silo's walls, the flow rate and type of the flowing material.

1 INTRODUCTION

In construction statics, beam deflections are inversely proportional to their rigidity. The dependence, though, is true in the case of material, the rigidity of which does not depend on the load level and des not change in time. Such a dependence is, for instance, to a large extent true for the steel beams.

In the case of another kind of material, such as concrete or reinforced concrete, the rigidity is reduced as a result of loading of the beam. Initially, the extended sections get plasticised, and finally, in the extension stress zone cracks appear. In the cracked sections, the beam rigidity is considerably decreased. It causes a noticeable, disproportionate deflection increase.

The computational methods most frequently include it directly through implementing a function changing the rigidity into the formula (the continuum method). In the presented method, always a constant primal stiffnes of the element is assumed, and it enables calculating the increase of deflections caused by the cracks in the structure and rheological effects (the discrete method).

In the following chapters, the assumptions made for the calculations and the method of their practical use is presented.

2. MODELS OF CALCULATING RIGIDITY IN THE REINFORCED CONCRETE BEAMS

In the construction statics, the differential equation of a deflected axis is derived from the geometrical dependences and balance equations. For small shifts, the differential equation of the deflection line of the bent beam is:

$$\frac{1}{L^2}\frac{\partial^2}{\partial \xi^2}\left[\frac{1}{L} EI(\xi,t)\frac{\partial^2 v(x,t)}{\partial \xi^2}\right] = p(\xi) \qquad (1)$$

Deflections of cracked reinforced concrete beams depend on factual element's rigidity. After cracking a local change of rigidity occurs. The rigidity changes along the element length. For reasons of inhomogeneity of structure of concrete an explicit description of these changes is impossible. Most of the codes' methods are aimed at simplicity of calculations and assume mean value of rigidity in whole length of a beam. It depends on load level of a beam. The experimental studies verify the computational value of rigidity by introducing coefficients to the formulae applying in theory of elasticity. The investigative theories describe changes of rigidity along a beam length in more precise way. Authors take rigidity changes into account depending on load level (continual models) or localize rigidity changes near by cracks (discrete models) – figure 1.

According to EC 2 and most of the Authors the rigidity change of bending beam is taken into account with the term describing rigidity:

$$\frac{\partial^2}{\partial x^2}\left[EJ_{I,II}\frac{\partial^2 v(\xi,t)}{\partial x^2}\right]=p(\xi) \tag{2}$$

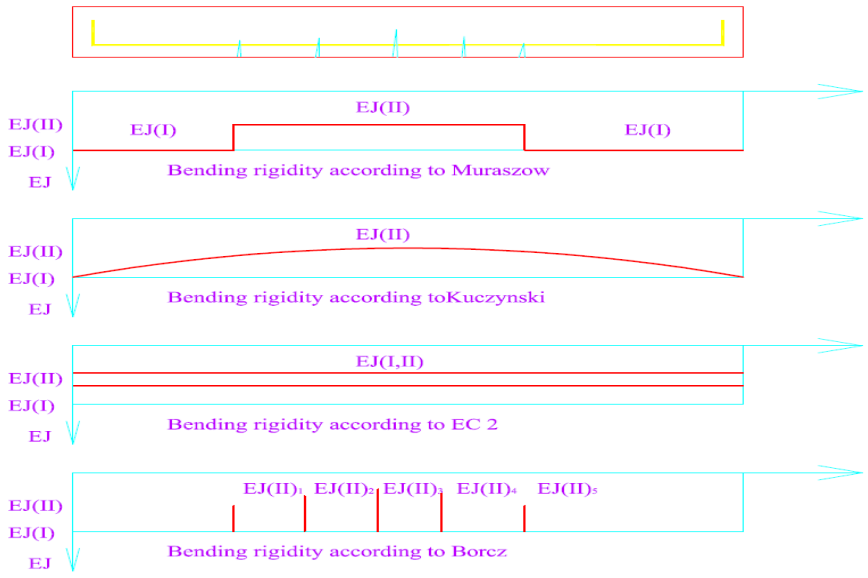

Fig. 1. The beam's rigidity according to the different Authors and EC2

In terms of quality, different is a proposal implied by the Borcz theory, according to which the left side of the differential equation does not depend on the maximum load of the beam. The form of the left side is identical with the one of the classical elasticity theory (the linearly elastic material and the infinite strength). The model takes into account both the permanent deformations in the material, the rheological deformations, and the maximum load of a section. The model is presented in chapter 3.

3. MODELS OF CALCULATING RIGIDITY IN THE REINFORCED CONCRETE BEAMS ACCORDING TO BORCZ

3.1. The bent element

According to Borcz the rigidity of beam after cracking is the same as before. Each effects connected with cracking are assumed as external load.

$$\frac{\partial^2}{\partial x^2}\left[EJ_I\frac{\partial^2 v(\xi)}{\partial x^2}\right]=p(\xi)+\sum_r r_i\delta_{,\xi\xi}(\xi-\zeta_r) \tag{3}$$

r_i – pitch angle in the area of the crack, $\delta_{,\xi\xi}(\xi-\zeta_r)$ – the second Dirac delta derivative.

Part of a deflection resulting from the existing cracks is expressed on the right side of the equation (3) as the change of angular displacement in the place of crack occurrence. In the place of crack, elastic strains and plastic deformations are localized. The model has been to some extent experimentally verified.

In the model of Borcz general solution of the equation (3) does not depend on the occurrence of cracks in element. It allows to apply the solution of classic theory of elasticity for static analysis of reinforced concrete structure with cracks.

After fourfold integration, equation (3) will assume the form of a polynomial,the constant results of which result from the boundary conditions:

$$v(\xi)=\frac{1}{L}\delta_0+\xi\varphi_0-\frac{\xi^2 L}{2EJ}M_0-\frac{\xi^3 L^2}{6EJ}T_0+\bar{v}(\xi)+\sum_i r_i(\xi-\zeta_i)h(\xi-\zeta_i) \tag{4}$$

$v(\xi)$ - special integral of the differential equation $h(\xi-\zeta_i)$ – Heaviside's function

The curve formula:

$$v_{,\xi\xi}(\xi)=-\frac{L}{EJ}M_0-\frac{\xi L^2}{EJ}T_0+\overline{v_{,\xi\xi}}(\xi)+\sum_i\left\{\left[-r_{0i}+r_{1i}v_{,\xi\xi}\left(\zeta_i^-\right)\right]\delta\left(\xi-\zeta_i^-\right)\right\}, \tag{5}$$

and after substitution with the coordinates of the crack:

$$v_{,\xi\xi}\left(\zeta_i^-\right)=-\frac{L}{EJ}M_0-\frac{\xi L^2}{EJ}T_0+\overline{v_{,\xi\xi}}\left(\zeta_i^-\right), \tag{6}$$

After implementation of equation (6) into equation (3):

$$\begin{aligned}v(\xi)=&\frac{1}{L}\delta_0+\xi\varphi_0+\left[-\frac{\xi^2 L}{2EJ}-\sum_i r_{1i}\frac{L}{EJ}(\xi-\zeta_i)h(\xi-\zeta_i)\right]M_0\\&+\left[-\frac{\xi^3 L^2}{6EJ}-\sum_i r_{1i}\zeta_i\frac{L^2}{EJ}(\xi-\zeta_i)h(\xi-\zeta_i)\right]T_0\\&+\left[\bar{v}(\xi)+\sum_i r_{1i}\bar{v}_{,\xi\xi}(\xi-\zeta_i)h(\xi-\zeta_i)+\sum_i -r_{0i}(\xi-\zeta_i)h(\xi-\zeta_i)\right]\end{aligned} \tag{7}$$

Differentiating the shift resulting from it (7) in relation to ξ one gets vector**{u(ξ)}**. The solution canalso be expressed in a form of a matrix as a sum of the solution of the homogenous and the cracked structure model:

$$\mathbf{\{u(\xi)\}=[F_E(\xi)+F_{res}(\xi)]\{u_0\}+\{u'(\xi)\}} \tag{8}$$

$$[\mathbf{F}_E(\xi)]=\begin{bmatrix}\frac{1}{L} & \xi & \frac{-\xi^2 L}{2EJ} & \frac{-\xi^3 L^2}{6EJ}\\ 0 & 1 & \frac{-\xi^2 L}{2EJ} & \frac{-\xi^2 L^2}{2EJ}\\ 0 & 0 & L & \xi L^2\\ 0 & 0 & 0 & L^2\end{bmatrix}$$ - matrix for the elastic system (9)

$$[\mathbf{F}_{res}(\xi)]=\begin{bmatrix}0 & 0 & -\sum_i r_{1i}(\xi-\zeta_i)h(\xi-\zeta_i) & -\sum_i r_{1i}\zeta_i(\xi-\zeta_i)h(\xi-\zeta_i)\\ 0 & 0 & -\sum_i r_{1i}h(\xi-\zeta_i) & -\sum_i r_{1i}\zeta_i h(\xi-\zeta_i)\\ 0 & 0 & 0 & 0\\ 0 & 0 & 0 & 0\end{bmatrix}$$

matrix complementation by the non-elastic deformations (9a)

$$[\mathbf{u}'(\xi)]=\begin{bmatrix} v_1(\xi)+\sum_i\left(-r_{0i}+r_{1i}v_{1,\xi\xi}\right)\left(\zeta_i^-\right)(\xi-\zeta_i)h(\xi-\zeta_i) \\ \varphi_1(\xi)+\sum_i\left(-r_{0i}+r_{1i}v_{1,\xi\xi}\right)\left(\zeta_i^-\right)h(\xi-\zeta_i) \\ M_1(\xi) \\ T_1(\xi) \end{bmatrix} \tag{10}$$

The transfer matrix is derived from the substitution of the matrix values **[$\mathbf{F_E}(\xi)$] ; [$\mathbf{F_{res}}(\xi)$]** at the end of the bracket for $\xi = 1$:

$$[\mathbf{F}_E]=\begin{bmatrix} \frac{1}{L} & 1 & \frac{-L}{2EJ} & \frac{-L^2}{6EJ} \\ 0 & 1 & \frac{-L}{2EJ} & \frac{-L^2}{2EJ} \\ 0 & 0 & L & L^2 \\ 0 & 0 & 0 & L^2 \end{bmatrix} \text{ - transfer matrix for the elastic system} \tag{11}$$

$$[\mathbf{R}]=\begin{bmatrix} 0 & 0 & -\sum_i r_{1i}(1-\zeta_i) & -\sum_i r_{1i}\zeta_i(1-\zeta_i) \\ 0 & 0 & -\sum_i r_{1i} & -\sum_i r_{1i}\zeta_i \\ 0 & 0 & 0 & 0 \\ 0 & 0 & 0 & 0 \end{bmatrix} \text{ matrix complementation of the transfer matrix by the non-elastic deformations} \tag{12}$$

If a beam has only one continuum bracket, four starting conditions can be calculated using the system of equations:

$$\mathbf{v_k} = \mathbf{F}\mathbf{v_0} \tag{13}$$

where: $\mathbf{v_0} = \{\mathrm{v}_0\ \Phi_0\ \mathrm{M}_0\ \mathrm{T}_0\}$ - parameters at the beginning of the section;

$\mathbf{v_k} = \{\mathrm{v}_\mathrm{k}\ \Phi_\mathrm{k}\ \mathrm{M}_\mathrm{k}\ \mathrm{T}_\mathrm{k}\}$ - parameters at the end of the section;

F is a matrix which in general is a sum of the elastic bar solution effects and of the permanent bar deformation effects:

$$\mathbf{F} = \mathbf{F_E} + \mathbf{F_{res}} \tag{14}$$

3.2. Compressed element

The task can also be extended by the case in which, axial force is introduced into the structure (eg. prestressing reinforcement or a pillar). To the equation of the bent axis of the bar, a formula describing influence of the axial force is introduced:

$$\frac{\partial^4 v(\xi)}{\partial\xi^4}+\frac{Nl^2}{EJ}\frac{\partial^2 v(\xi)}{\partial\xi^2}=\frac{1}{EJ}\sum_i r_N\delta_{,\xi\xi}\left(\xi-\zeta_i\right) \tag{15}$$

The solution then has a form of recurrence formulae [2]:

$$v_n(\xi)=R_N v_{n-1}(\xi) \tag{16}$$

where: $\mathrm{R_N}$ – recurrence factor of the equation (15).

The transfer matrix is derived from the substitution of the general differential equation:

$$v(\xi) = v(0) + \frac{1}{k} v_{,\xi}(0) + \left[\frac{1}{k^2}(1 - \cos k\xi)\right] v_{,\xi\xi}(0) + \left[\frac{1}{k^3}\left(\xi - \frac{\sin k\xi}{k}\right)\right] v_{,\xi\xi\xi}(0) + \frac{1}{k}\sum_{i=1}^{n}\left[r_0 + r_1 v_{,\xi\xi}\left(\zeta_i^-\right)\right][\sin k(\xi - \zeta_i)]h(\xi - \zeta_i) \quad (17)$$

where: $k = \sqrt{\frac{Nl^2}{EJ}}$ (18)

The unknown value $v_{,\xi\xi}(\zeta_i\text{-})$ is calculated from the recurrence formula:

$$v_{,\xi\xi}(z_i^-) = |A_i|\ v_{,\xi\xi}(0) + |B_i|\ v_{,\xi\xi\xi}(0) - |C_i| \quad , \quad (19)$$

the derivative of which is presented in detail in [2]. Matrices A_i ; B_i ; C_i are formed by substituting the i column of matrix A with vectors {a}; {b}; {c}. Matrix A is a triangular matrix.

$\mathbf{A} = [a_{ij}]_{i=1, \ldots n}$
$\{a\} = (a_j)_{j=1, \ldots n}$
$\{b\} = (b_j)_{j=1, \ldots n}$
$\{c\} = (c_j)_{j=1, \ldots n}$

where:

$$a_{ij} = \begin{cases} 1 & \text{dla } i = j \\ 0 & \text{dla } i < j \\ kr_{1j} \sin k(\zeta_i - \zeta_j) & \text{dla } i > j \end{cases}$$

$a_j = \cos k\zeta_j$

$b_j = \sin k\zeta_j$

$$c_j = \begin{cases} 0 & i = 1 \\ kr_{0i} \sin k(\zeta_i - \zeta_j) & i > 1 \end{cases}$$

Hence, the following recurrence formulae can be derived for the matrices' determinants:

$$|A_i| = a_i - \sum_{j=1}^{i-1} |A_{i-j}| a_{i,i-j} \quad (20)$$

$$|B_i| = b_i - \sum_{j=1}^{i-1} |B_{i-j}| a_{i,i-j} \quad (21)$$

$$|C_i| = c_i - \sum_{j=1}^{i-1} |C_{i-j}| a_{i,i-j} \quad (22)$$

By means of the presented formulae, the algorithms for the numerical calculations can be formulated. The transfer matrix of the entire structure then will be:

$$v_k = C_n\ H_{n-1}\ C_{n-1} \text{K}\ C_2\ H_1\ C_1\ v_0 = C_{glob}\ v_0 \quad (23)$$

where: $\mathbf{C_i}$ – transfer matrix for the pillar (4.81):

b = l / l' ;

a = EJ / EJ'

l' ; EJ' - randomly selected comparative values

To solve the system of equations (23), known boundary conditions at both ends of the system are used. For a one-element articulated ends bar, the system of equations is:

$$C=\begin{bmatrix} 1 & \frac{\beta}{k} & -\frac{1}{\alpha}\left(\frac{\beta}{k}\right)^2\left[(1-\cos k)-\frac{1}{k}\sum_{i=1}^{n} r_{1i}|A_i|\sin k(1-\zeta_i)\right] \\ 0 & 1 & -\frac{1}{\alpha}\frac{\beta}{k}\left[\sin k-\frac{1}{k}\sum_{i=1}^{n} r_{1i}|A_i|\cos k(1-\zeta_i)\right] \\ 0 & 0 & \left[\cos k-\frac{1}{k}\sum_{i=1}^{n} r_{1i}|A_i|\sin k(1-\zeta_i)\right] \\ 0 & 0 & \frac{k}{\beta}\left[-\sin k-\frac{1}{k}\sum_{i=1}^{n} r_{1i}|A_i|\cos k(1-\zeta_i)\right] \\ 0 & 0 & 0 \end{bmatrix}$$

$$\begin{bmatrix} -\frac{1}{\alpha}\left(\frac{\beta}{k}\right)^3\left[\left(1-\frac{\sin k}{k}\right)-\frac{1}{k}\sum_{i=1}^{n} r_{1i}|B_i|\sin k(1-\zeta_i)\right] & \frac{1}{k}\sum_{i=1}^{n}(r_0-r_1|C_i|)\sin k(1-\zeta_i) \\ -\frac{1}{\alpha}\left(\frac{\beta}{k}\right)^2\left[(1-\cos k)-\frac{1}{k}\sum_{i=1}^{n} r_{1i}|B_i|\cos k(1-\zeta_i)\right] & \sum_{i=1}^{n}(r_0-r_1|C_i|)\cos k(1-\zeta_i) \\ \frac{\beta}{k}\left[\sin k-\frac{1}{k}\sum_{i=1}^{n} r_{1i}|B_i|\sin k(1-\zeta_i)\right] & \alpha k\sum_{i=1}^{n}(r_0-r_1|C_i|)\sin k(1-\zeta_i) \\ \left[\cos k-\frac{1}{k}\sum_{i=1}^{n} r_{1i}|B_i|\cos k(1-\zeta_i)\right] & \alpha k^2\sum_{i=1}^{n}(r_0-r_1|C_i|)\cos k(1-\zeta_i) \\ 0 & 1 \end{bmatrix} \tag{24}$$

$$c_{12}\, j_0 + c_{14}\, T_0 = c_{15} \tag{25}$$

$$c_{32}\, j_0 + c_{34}\, T_0 = c_{35}$$

The critical force informs about the instability of the structure. The state will correspond with the indeterminacy of the equation system, which can be expressed by condition:

$$\det\begin{bmatrix} c_{12}(k) & c_{14}(k) \\ c_{32}(k) & c_{34}(k) \end{bmatrix}=0 \tag{26}$$

The equation has a lot of elements on critical values k_n , from which values of critical foces N_{kr} can be derived. For a one-element articulated boundary conditions bar, the age equation has a form:

$$\left(\frac{\beta}{k}\right)^2\left[\sin k-\frac{1}{k}\sum_{i=1}^{n} r_{1i}|B_i|\sin k(1-\zeta_i)\right]-\frac{1}{\alpha}\frac{1}{k}\sum_{i=1}^{n} r_{1i}|B_i|\sin k(1-\zeta_i)=0 \tag{27}$$

after transformation:

$$\beta^2 \sin k = \left(\frac{\beta^2}{k} + \frac{1}{\alpha} \right) \sum_{i=1}^{n} r_{1i} |B_i| \sin k(1-\zeta_i) \tag{28}$$

where: $|B_i|$ – defined by a recurrence formula.

3.3. A dynamically loaded element

Similar solution is observed in the task of determining the proper vibration of the bar and the generalized shifts and internal forces. They are obtained from a general differential equation describing vibration of the bar with the elastic and permanent dislocations [3]:

$$\frac{\partial^4 v(\xi,t)}{\partial \xi^4} - \frac{ml^4}{EJ} \frac{\partial^2 v(\xi,t)}{\partial t^2} = \sum_i r_K \quad \delta_{,\xi\xi}(\xi - \zeta_i) \tag{29}$$

The solution is obtained in a form of recurrence formulae:

$$v_n(\xi,t) = R_K v_{n-1}(\xi,t) \tag{30}$$

where: R_K – the recurrence factor of the equation (29).

For one element, the homogenous equation is:

$$\left. \frac{\partial^4 v(\xi,t)}{\partial \xi^4} - \frac{ml^4}{EJ} \frac{\partial^2 v(\xi,t)}{\partial t^2} \right|^e = 0 \tag{30}$$

For the set vibration it can be assumed that the solution has a form of a ratio (variables separation method). The solution has a form :

$$v^e(x,t) = T(t)\, V^e(x) \tag{31}$$

At the harmonic vibration:

$$T(t) = e^{iwt} \tag{32}$$

where: w – circular frequency of the harmonic vibration of the bar

The timeless equation can then have a form of:

$$\left. V_{,\xi\xi\xi\xi} - k^4 V \right|^e = 0 \tag{33}$$

$$k^4 = \omega^2 \frac{ml^2}{EJ} \tag{34}$$

The general integral of the differential equation (33) is:

$$V^e(\xi) = A \cos k\xi + B \sin k\xi + C \operatorname{ch} k\xi + D \operatorname{sh} k\xi \tag{35}$$

Based on the solution, it is possible to build a function which will also be a solution of the differential equation (33). The solution can be obtained using the shift method, the force method, or the mixed method. In the static task, the integral of a differential equation expressed by means of the initial parameters was presented. Now, a solution by means of the shift method is shown. Constant equations are then kinematic boundary conditions:

$$V^e(\xi) = d_i Z_1(k\xi) + j_i Z_2(k\xi) + d_j Z_3(k\xi) + j_j Z_4(k\xi) \tag{36}$$

where: $d_i = V^e(0)$

$j_i = V^e{}_{,x}(0)$

$d_j = V^e(1)$
$j_j = V^e{}_{,x}(1)$

The solution of the amplitude equation with their derivatives can be shown in a form of a matrix:

$$\mathbf{V^e(\xi) = Z(k\xi)\, d^e} \tag{37}$$

where: $\mathbf{V^e(\xi)} = \{V(\xi);\ V_{,x}(\xi);\ M(\xi);\ T(\xi)\}^e$

$\mathbf{d^e} = [\{\ d_i\ ;\ j_i\ ;\ d_j\ ;\ j_j\ \}^e]^T$.

Matrix of the shape can be described by:

$$\mathbf{Z}(k\xi) = \begin{bmatrix} Z^1(k\xi) & Z^2(k\xi) & Z^3(k\xi) & Z^4(k\xi) \\ Z^1_{,\xi}(k\xi) & Z^2_{,\xi}(k\xi) & Z^3_{,\xi}(k\xi) & Z^4_{,\xi}(k\xi) \\ -EJZ^1_{,\xi\xi}(k\xi) & -EJZ^2_{,\xi\xi}(k\xi) & -EJZ^3_{,\xi\xi}(k\xi) & -EJZ^4_{,\xi\xi}(k\xi) \\ -EJZ^1_{,\xi\xi\xi}(k\xi) & -EJZ^2_{,\xi\xi\xi}(k\xi) & -EJZ^3_{,\xi\xi\xi}(k\xi) & -EJZ^4_{,\xi\xi\xi}(k\xi) \end{bmatrix} \tag{38}$$

where:

$$Z^1(k\xi) = S(k\xi) + \frac{K^2 - SU}{U^2 - KT}U(k\xi) + \frac{KU - ST}{KT - U^2}K(k\xi)$$

$$Z^2(k\xi) = \frac{1}{k}T(k\xi) + \frac{SK - TU}{U^2 - KT}U(k\xi) + \frac{SU - T^2}{KT - U^2}K(k\xi)$$

$$Z^3(k\xi) = \frac{U}{U^2 - KT}U(k\xi) + \frac{T}{KT - U^2}K(k\xi)$$

$$Z^4(k\xi) = -\frac{K}{U^2 - KT}U(k\xi) + \frac{U}{KT - U^2}K(k\xi)$$

$$Z^1_{,\xi}(k\xi) = k\left[K(k\xi) + \frac{K^2 - SU}{U^2 - KT}T(k\xi) + \frac{KU - ST}{KT - U^2}U(k\xi)\right]$$

$$Z^2_{,\xi}(k\xi) = k\left[\frac{1}{k}S(k\xi) + \frac{SK - TU}{U^2 - KT}T(k\xi) + \frac{SU - T^2}{KT - U^2}U(k\xi)\right]$$

.....

.....

$$Z^4_{,\xi\xi\xi}(k\xi) = k^3\left[-\frac{K}{U^2 - KT}K(k\xi) + \frac{U}{KT - U^2}S(k\xi)\right] \tag{39}$$

whereas Krylow's functions:

$$\begin{aligned} K(k\xi) &= 0{,}5(\mathrm{sh}k\xi - \sin k\xi), \quad K = K(k) \\ U(k\xi) &= 0{,}5(\mathrm{ch}k\xi - \cos k\xi) \quad U = U(k) \\ T(k\xi) &= 0{,}5(\mathrm{sh}\,k\xi + \sin k\xi), \quad T = T(k) \\ S(k\xi) &= 0{,}5(\mathrm{ch}k\xi + \cos k\xi), \quad S = S(k) \end{aligned} \tag{40}$$

are in a form of tables and have the following values:

$$K(0) = U(0) = T(0) = 0;\ S(0) = 1; \tag{41}$$

$K_{,xxxx}(kx) = k\,K_{,xxx}(kx) = k^2\,T_{,xx}(kx) = k^3\,S_{,x}(kx) = k^4\,K(kx)$

The transfer matrix in the static task enables the determination of deformations and forces at the end of the bracket by means of the initial parameters, whereas here the static values in any point of the bracket are expressed by means of deformations at its ends. In order to maintain a uniform solution it is necessary to determine the generalized deformations and forces at the ends of the bracket and find a mutual relation between them:

$$\mathbf{V^e(0) = Z(0)\ \delta^e} \tag{42}$$

$$\mathbf{V^e(1) = Z(k)\ \delta^e} \tag{43}$$

Determining vector $\boldsymbol{\delta}^e$ from fomula (42) and substituting it in equation (43) one obtains:

$$\boldsymbol{\delta}^e = \mathbf{Z^{-1}(0)\ V^e(0)} \tag{44}$$

$$\mathbf{V^e(1) = Z(k)\ Z^{-1}(0)\ V^e(0)} \tag{45}$$

The transfer matrix is then:

$$\mathbf{F = Z(k)\ Z^{-1}(0)} \tag{46}$$

$$\mathbf{F} = \begin{bmatrix} S & \frac{\beta}{k}T & -\frac{1}{\alpha}\left(\frac{\beta}{k}\right)^2 U & -\frac{1}{\alpha}\left(\frac{\beta}{k}\right)^3 V \\ \frac{k}{\beta} & S & -\frac{1}{\alpha}\frac{\beta}{k}T & -\frac{1}{\alpha}\left(\frac{\beta}{k}\right)^2 U \\ -\alpha\left(\frac{k}{\beta}\right)^2 U & -\alpha\frac{k}{\beta}V & S & \frac{\beta}{k}T \\ -\alpha\left(\frac{k}{\beta}\right)^3 T & -\alpha\left(\frac{k}{\beta}\right)^2 U & \frac{k}{\beta}V & S \end{bmatrix} \tag{47}$$

where: $a = EJ^e / EJ'$;

$b = l^e / l'$;

EJ' ; l' - comparative rigidity and length

4. SUMMARY

Presented method allows to analyse the construction based on the solution of the elementar differential equation

$$G_{,xxxx} = \delta(\xi - \zeta)$$

If the function G (ξ - ζ) will be multiplied (inside the integral) by the right side of the differential equation, than we obtain a solution that takes into account the impact of the permanent and rheologycal deformations.

$$v_1(\xi) = \int_0^1 G(\xi, \zeta) p^O(\xi) d\xi$$

where: $p^O(\xi)$ – load and impact of the permanent and rheologycal deformations.

This presentation of problem allows in a wider aspect to use the solutions from the classical theory of elasticity for materials with variable characteristics.

REFERENCES:

[1]. Borcz A.: Teoria konstrukcji żelbetowych, wybrane badania wrocławskie.t.2. Wyd. Politechniki Wroclawskiej. Wrocław 1986

[2]. Kiedroń K.: Siła krytyczna ściskanych słupów żelbetowych. Archiwum Inżynierii Lądowej t.XXVII, z.3/1981, s.221-231.

[3]. Łuczak-Romanów R., Metoda obliczania drgań prętów żelbetowych z rysami, praca doktorska, Wrocław 1980.

[4]. Ubysz A.: Plastic strains and self-stresses in reinforced concrete, bar construction. Edit. TU Wrocław. Wrocław 1999

19th International Conference on the Application of Computer
Science and Mathematics in Architecture and Civil Engineering
K. Gürlebeck, T. Lahmer and F. Werner (eds.)
Weimar, Germany, 04–06 July 2012

DEPENDENCY OF THE INFLUENCE OF INPUT PARAMETERS OF BVI MODELS ON THE INITIAL EXCITATIONS AND SPEED RANGES OF THE VEHICLE

G. Karaki*

**Civil Engineering Department, Birzeit University*
Birzeit, P.O. Box 14, West Bank
E-mail: gkaraki@birzeit.edu

Keywords: sensitivity analysis, functional input, joint meta-modeling, bridge-vehicle interaction.

Abstract. *Bridge vibration due to traffic loading has been subject of extensive research in the last decades. Such studies are concerned with deriving solutions for the bridge-vehicle interaction (BVI) and analyzing the dynamic responses considering randomness of the coupled model's (BVI) input parameters and randomness of road unevenness. This study goes further to examine the effects of such randomness of input parameters and processes on the variance of dynamic responses in quantitative measures. The input parameters examined in the sensitivity analysis are, stiffness and damping of vehicle's suspension system, axle spacing, and stiffness and damping of bridge. This study also examines the effects of the initial excitation of a vehicle on the influences of the considered input parameters. Variance based sensitivity analysis is often applied to deterministic models. However, the models for the dynamic problem is a stochastic one due to the simulations of the random processes. Thus, a setting using a joint meta-model; one for the mean response and other for the dispersion of the response is developed. The joint model is developed within the framework of Generalized Linear Models (GLM). An enhancement of the GLM procedure is suggested and tested; this enhancement incorporates Moving Least Squares (MLS) approximation algorithms in the fitting of the mean component of the joint model. The sensitivity analysis is then performed on the joint-model developed for the dynamic responses caused by BVI.*

1 INTRODUCTION

Structural systems can be represented by various mathematical models implemented and solved using complex computer codes, which may be referred to as numerical models. Developed numerical models are often employed to identify influential input parameters that affect responses of interest. This identification is carried out by methods of sensitivity and uncertainty analyses. Such studies can be used for model validation, model calibration, and decision making processes. Variance sensitivity analysis is one of the efficient methods to study global sensitivities where main and higher order effects of input parameter can be quantitatively measured. Furthermore, sampling-based techniques for estimating the variance-based sensitivity indices are frequently used for complex engineering problems for their ease in implementation. However, their main drawback is the demand of high computational time. Therefore, meta-models are used as an alternative for the complex computer codes, and the sensitivity analysis is performed efficiently on fitted meta-models [1]. Such a procedure applies to deterministic models that produces always the same output for the same set of input. Unfortunately, this is not the case in all engineering applications where random processes or unknown input parameters may be over-looked.

Stochastic computer codes are the ones were simulations of random processes are included in every run of the analysis, thus, the output values depend on the realizations of these random processes. Applying variance-based sensitivity analysis for such models is a challenge and has attracted the attention of researchers in the recent years. *Tarantola et al.* [2] suggested a solution to consider the effects of random processes by introducing a scalar input parameter ($\xi \sim U(0,1)$) controlling the simulation of random processes and including them in the computer model, this require performing the sensitivity analysis directly on the numerical model, which means high computational time. More recently, [3] introduced building a joint model for the output of stochastic computer codes. The joint model is then used for the sensitivity analysis. The procedure for joint modeling followed by [3] is within the framework of generalized linear models. Later the same authors suggested non-parametric models, e.g. generalized additive models and joint Gaussian process modeling, as they proved to be more efficient in estimating the sensitivity indices [4]. A similar idea is to be used and tested for the engineering problem at hand.

The engineering problem of interest is bridge-vehicle interaction. There has been an increasing attention to develop procedures for solving the bridge-vehicle interaction, which is encouraged by the advent computational power of digital computers and the increasing number and weights of vehicles traveling on bridges. Therefore, researchers and modelers had been concerned with deriving solutions of the dynamic problem of bridge-vehicle interaction. *F. Yang et al.* [5] and [6] reviewed the different methods with their corresponding mathematical and computational descriptions. Moreover, probabilistic studies had also been employed to assess the effects of random input parameters and road unevenness on the dynamic response. *Hwang and Nowak* [7] presented a procedure to calculate statistical parameters for the dynamic loading of bridges. These parameters were based on surveys and tests and included vehicle mass, suspension system, tires and road roughness, which were simulated by stochastic processes. *Kirkegaard and Nielsen* [8, 9] studied the randomness of vehicle input parameters and the randomness of road unevenness in two separate studies. One conducted for vehicle input parameters and the other for the effects of random road profiles on the dynamic response of highway bridges. Moreover, solutions for the statistical characteristics of a bridge's response to the passage of a vehicle over a random rough surface have been of interest in a number of

research works, such as [11, 12, 13]. More recently, [14] considered both the randomness of the vehicle input parameters and road unevenness, and calculated the statistical characteristics of the bridge response by using the random variable functional moment method.

This study aims to extend probabilistic studies and use them for purposes of sensitivity and uncertainty analyses. One of the main challenges of such an analyses is considering the effect of road unevenness on the variance of the bridge displacements. Further, the effect of the initial excitations on the influence of vehicle and bridge dynamics on variances of bridge displacements is also examined.

The first section of the paper deals with the general description of the enhanced generalized linear models and their use to determine the sensitivity indices followed by presenting the main solution algorithm of the bridge-vehicle interaction. An academic example is illustrated to validate the presented approach followed by the application on the influences of vehicle dynamics, bridge dynamics and initial excitations on the variance of a bridge's response.

2 ENHANCED GENERALIZED LINEAR MODELS

The numerical models of interest are the ones that are stochastic in nature, e.g. having functional inputs which cannot be captured by scalar ones. For such a problem and where no replications is preferred for computational time reduction, it is useful to model both the output's mean and variance jointly, which leads to the use of generalized linear models. Generalized linear models generalizes linear regression by allowing the linear model to relate to the response variable using a link function and by allowing the variance at each observation point to be a function of its prediction at the same position. Each generalization model has three components; response variable distribution, linear predictor, link function. A full description of the such models and their extension can be found in [15, 16]. In short the followings describe the mean and dispersion components of the joint model.

$$E(Y_i) = \mu_i, \quad \eta_i = g(\mu_i) = \Sigma_j x_{ij}\beta_j; \tag{1}$$

$$var(Y_i) = \phi_i v(\mu_i), \tag{2}$$

where $(Y_i)_i = 1, \ldots, n$ are random variables with mean μ_i; x_{ij} are samples of covariate vectors X_j; β are the regression coefficients; η_i is the linear predictor of the mean; $g(.)$ is the link function; ϕ_i is the dispersion parameter, and $v(.)$ is the variance function. The dispersion is assumed to vary and dependent on the predicted mean values, hence a model is built for ϕ_i:

$$E(d_i) = \phi_i, \quad \xi_i = h(\phi_i) = \Sigma_j u_{ij}\gamma_j; \tag{3}$$

$$var(d_i) = \tau v_d(\phi_i), \tag{4}$$

where $(d_i)_i = 1, \ldots, n$ are estimates of dispersion, error of prediction is used; u_{ij} are samples of covariate vectors U_j; γ are the regression coefficients; ξ_i is the linear predictor of the dispersion; $h(.)$ is the link function; τ is a constant, and $v_d(.)$ is the variance function for dispersion. The choice of the linear predictor has a strong effects on the joint model and its quality. In the case where the distribution for the responses of the mean model is chosen to be normal, an identity link function follows the choice of this distribution and (1) becomes $E(y) = \mu$, which is the general formulation of simple linear regression.

This paper is concerned with enhancing the procedure of generalized linear models by using local approximation algorithms for the predictor of the mean. Not only a weighting function dependent on the variance distribution is introduced to estimate the regression coefficients β but also a weighting function dependent on the position of the approximation point relative to the observation (support) points is used. Moving least squares (MLS) is proposed to be the predictor in GLM procedure.

Furthermore, the base of the variance model is the squared residuals $\epsilon_i^2 = (y_i - \mathbf{X_i}\beta)^2$ for the $i = 1, 2, \ldots, n$, where n is number of observations. For the mean component of joint model, the meta-models coefficients β are evaluated as

$$\beta = (X'V^{-1}X)^{-1}X'V^{-1}y, \tag{5}$$

where $Var(\epsilon) = V_{n\times n}$ with $\sigma_i^2 = e^{\grave{u}_i\gamma}$. It can be noticed that the maximum likelihood (MLE) estimator of β involves γ through V matrix and the MLE of γ clearly involves β since the data in the variance involves β. As a result an iterative procedure is carried out.

The enhanced GLM procedure using MLS is as follows:

1. Ordinary linear regression models is used to obtain β_0 for the mean model $y_i = X_i'\beta_0 + \epsilon_i$
2. β_0 is used to compute n residuals, $\epsilon_i = y_i - X_i'\beta_0$
3. The residuals ϵ_i^2 are used as data to fit the variance model with regressors u and a log link function, the regression coefficients γ are determined
4. The variance weighting matrix V is formulated to be used in updating β_0 to β_1 for the iteration step
5. The moving least squares (MLS) is concurrently applied on the approximation point
6. Step 2 is repeated with the updated data, and analysis is continued till convergence

The Gaussian weighting function is used for MLS algorithm, which is an exponential function described as

$$w_G(s) = e^{-s^2/\alpha^2}, \tag{6}$$

with α as a shape factor and $s = \|x - x_i\| / D$, where s is the normalized distance between the approximation point and the supporting point considered and D is the influence radius. Furthermore, for the above procedure cross validation is used to find the residuals, which eliminates the over-fitting of noise in the fitting

3 SENSITIVITY INDICES

Sensitivity analysis is the study of how uncertainties or variances in the output of a model is apportioned to uncertainties or variances of the inputs. Variance based methods have been chosen due to their independence from the investigated model, and the influence of groups or sets of input parameters may be examined. Moreover, such an analysis provides the importance ranking of the input parameters as well as quantifying their contribution to the output variance [17]. The main idea of variance-based methods is to estimate the amount of variance that would disappear if the true value of the input parameter X_i is known. This can be described by the conditional variance of Y fixing X_i at its true value $V(Y|X_i)$, and is obtained by varying

over all parameters, except X_i. Since the true value of X_i in complex engineering problems is unknown, the average of the conditional variance for all possible values of X_i is used, i.e. $E(V(Y|X_i))$. Having the unconditional variance of the output $V(Y)$ and the expectation of the conditional variance $E(V(Y|X_i))$, the following relation holds, which is known as the law of total variance:

$$V(Y) = V(E(Y|X_i)) + E(V(Y|X_i)), \tag{7}$$

From equation (7) the variance of the conditional expectation $V(E(Y|X_i))$ is determined. This term is often referred to as the main effect, as it estimates the main effect contribution of the X_i to the variance of the output. Normalizing the main effect by the unconditional variance $V(Y)$ results in:

$$S_i = \frac{V(E(Y|X_i))}{V(Y)} \tag{8}$$

The ratio S_i is known as a first order sensitivity index [18], which is also known as the importance measure [19]. The value of S_i is less than 1, further the sum of all first order indices corresponding to multiple input parameters is an indicator of the additivity of the model. The model is considered additive when the sum equals to one (no interactions between the input parameters), and non-additive when the sum is less than one. Hence, the difference $1 - \sum S_i$ is an indicator for the presence of interactions between the input parameters. For example, the interaction between two parameters X_i and X_j on the output Y in terms of conditional variance is expressed as:

$$V_{ij} = V(E(Y|X_i, X_j)) - V(E(Y|X_i)) - V(E(Y|X_j)), \tag{9}$$

where $V(E(Y|X_i, X_j))$ describes the joint effect of the pair (X_i, X_j) on Y. This is known as a second order effect. Higher order effects can be computed in a like manner. The total effect index S_{Ti} is used to represent the total contribution of the input parameter X_i to the output, i.e. the first order effects, in addition to all higher order effects.

The above formulations applies to deterministic computer codes, where the same set of data produces the same output repeatedly. However, such a statement cannot be said when considering functional inputs, e.g. random processes, for the numerical models at hand, which are called stochastic models as mentioned before.

The work of [4] suggested the family of generalized linear models (GLM) and generalized additive models (GAM) to model the mean and dispersion of model's output and use the joint model to estimate the sensitivity indices. This general approach is adopted in this study using GLM with moving least squares MLS as the fitting algorithm of the mean component of join model, having the identity as the link function.

The procedure starts with assuming the existence of an uncontrollable input parameter X_ϵ in addition to the scaler inputs $X = (X_1, X_2, \ldots, X_k)$. Thus, the output of the numerical models can be written as $Y = f(\mathbf{X}, X_\epsilon)$. The joint meta-models using enhanced GLM are used to formulate the relation for the mean (f_m) and dispersion (f_{ds}) with respect to the scaler inputs $(\mathbf{X})$, which can be written as [4]:

$$f_m(\mathbf{X}) = E(Y|\mathbf{X}) \tag{10}$$

$$f_{ds}(\mathbf{X}) = V(Y|\mathbf{X}) \tag{11}$$

The total variance of Y is defined by (7), hence, the sensitivity indices for the scalar inputs can be estimated on the mean component of the joint model using classical sampling methods having $S_i = V_i(f_m)/V(Y)$. At the same time the dispersion component of the joint

model f_{ds} is developed. $E(V(Y|\mathbf{X}))$ presents the expected value of the variance caused by X_ϵ and its interaction with $\mathbf{X}$, thus, the total effect sensitivity index of X_ϵ is estimated as $S_{T\epsilon} = E(V(Y|\mathbf{X}))/V(Y)$.

4 MODELING OF BVI

The engineering problem of interest is the vibration of bridges caused by a moving heavy vehicle. A general description of the vehicle and the bridge models as well as the used solution algorithms are explained.

4.1 Vehicle model

The equations of motion for the vehicle can be written in the following general form:

$$\mathbf{M}_v\ddot{\mathbf{U}}_v + \mathbf{C}_v\dot{\mathbf{U}}_v + \mathbf{K}_v\mathbf{U}_v = \mathbf{P}_v, \tag{12}$$

where $\mathbf{M}_v$ is the mass matrix of the vehicle, $\mathbf{C}_v$ is the damping matrix of the vehicle, $\mathbf{K}_v$ is the stiffness matrix of the vehicle, $\mathbf{P}_v$ is the dynamic force vector of the vehicle, and $\mathbf{U}_v$ is the generalized coordinate vector describing the dynamics of the vehicle model (degrees of freedom).

The chosen vehicle model is an eight-degree-of-freedom model representing a typical configuration of a common heavy truck traveling on road networks [20]. The vehicle consists of a two-axle tractor and a three-axle semi-trailer linked by a hinge. It is assumed that the three axles of the semi-trailer share the rear static load equally since load-sharing mechanisms are common in multi-axle heavy vehicle suspensions [21]. The generalized coordinates used to describe the vehicle dynamics are tractor vertical displacement y_T, tractor pitch angle θ_T, semi-trailer vertical displacement y_S, semi-trailer pitch angle θ_S, tractor front unsprung mass vertical displacement y_1, tractor rear unsprung mass vertical displacement y_2, and semi-trailer unsprung masses vertical displacements $y_3,\ y_4,$ and y_5, as shown below:

$$\mathbf{U}_v = \left\{ \begin{array}{ccccccccc} y_T & \theta_S & \theta_S & y_1 & y_2 & y_3 & y_4 & y_5 \end{array} \right\}^T \tag{13}$$

The mass, damping and stiffness matrices can be found in [20].

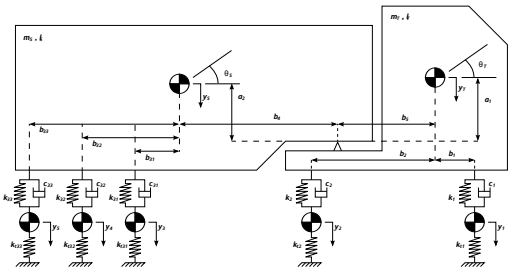

Figure 1: Schematic for the five-axle vehicle model

The interaction force F_i^{int} can be expressed as:

$$F_i^{int} = k_{ti}\left[y_i(t) - y_b(x_i,t) - r_i(t)\right],\ \ i = 1,\ 2,\ 3,\ 4,\ 5 \tag{14}$$

where $y_b(x_i,t)$ and $r_i(t)$ are the displacements of the bridge and road unevenness respectively, at the contact point corresponding to the i^{th} axle at instant t.

The vibration of such a heavy vehicle has two distinctive frequency ranges; the first range is 1.5 Hz to 4 Hz, representing the sprung mass bounce involving some pitching, and the second range is 8 Hz to 15 Hz, representing the unsprung mass bounce involving suspension pitch modes [21].

4.2 Bridge model

The equations of motion of the bridge considering time varying forces can be expressed in the following matrix notation:

$$\mathbf{M}_b\ddot{\mathbf{U}}_b + \mathbf{C}_b\dot{\mathbf{U}}_b + \mathbf{K}_b\mathbf{U}_b \;=\; \mathbf{P}_b \;, \tag{15}$$

with $\mathbf{M}_b$, $\mathbf{C}_b$, $\mathbf{K}_b$ are the mass, damping and stiffness matrices of the bridge, $\ddot{\mathbf{U}}_b$, $\dot{\mathbf{U}}_b$, $\mathbf{U}_b$ are the accelerations, velocities and displacements of the bridge, and $\mathbf{P}_b$ is the vector of forces acting on each bridge node at time t, which has two components, as shown below:

$$\mathbf{P}_b \;=\; \mathbf{F}^g + \mathbf{F}^{int} \;, \tag{16}$$

where $\mathbf{F}^g$ is the force acting on the bridge due to the weight of the vehicle, which is independent of the interaction, and $\mathbf{F}^{int}$ is the time-variant force acting on the bridge, which depends on the interaction between the bridge and the vehicle. The damping of the bridge is assumed to be viscous, which means that it is proportional to the nodal velocities.

4.3 Bridge-vehicle interaction

The equations of motion for the vehicle and the bridge are written as (12) and (15), respectively. Assuming perfect contact, the solution of these equations is governed by satisfying the compatibility equation and imposing the equality of displacement at the contact point, as expressed below:

$$y_w(x_i, t) \;=\; y_b(x_i, t) + r_i(t) \;, \tag{17}$$

where $y_w(x_i, t)$ is the displacement of the tire of the vehicle at i^{th} contact point at instant t. In addition, the force equilibrium conditions at the contact point i must be satisfied, which can be shown as:

$$P_b^i \;=\; F_i^g + F_i^{int} \;, \tag{18}$$

where F_i^g is the static weight of the i^{th} axle and F_i^{int} is the interaction force at the i^{th} axle. The i^{th} contact point usually does not coincide with the a DOF of the bridge model. Therefore, the forces F_i^g and F_i^{int} are converted to equivalent nodal forces associated with the bridge's DOF.

The solution algorithm described in [10] is used in the analysis. It is a non-iterative solution conditioning over a sufficiently small time step. With such a time step, the force acting on the vehicle at the current time step is estimated from the previous step. The choice of the time step should be *small enough* to capture the highest desired frequency of the bridge, the vehicle passage, and the excitation from road unevenness. Moreover a factor of $\frac{1}{10}$ is introduced into the Δt selected to secure reasonable integration accuracy.

In general, many DOFs are involved in the FE model of the bridge system, but only the first modes of vibration make the significant contribution to the dynamic response. Therefore, the modal superposition method has been used to solve the equations of motion of the bridge, which reduces the computational effort considerably, which is regarded as advantageous [22].

4.4 Road unevenness

Road unevenness is often treated as a realization of a stationary Gaussian homogeneous random process described by its power spectral density function in space domain $S_{f_0 f_0}(\kappa)$ with κ as the wavenumber [23].

However, the dynamic analysis is performed in time domain, and a description of the road unevenness in time domain is needed. Therefore, the temporal power spectral density function $S_{f_0 f_0}(\omega)$ is to be computed. Assuming a constant speed for the vehicle v, $S_{f_0 f_0}(\omega)$ and $S_{f_0 f_0}(\kappa)$ can be related using the following:

$$S_{f_0 f_0}(\omega = v\kappa) = \frac{1}{v} S_{f_0 f_0}(\kappa) \tag{19}$$

When performing the analysis in time domain, one can deduce that the excitation of the vehicle due to road unevenness can be described as non-stationary when the vehicle speed is time dependent [25]. Even when the speed is constant and the vehicle excitation is stationary, the dynamic responses of the bridge are non-stationary due to the movement of the vehicle [11]. This observation is of importance in deriving the stochastic characteristics when the dynamic problem is solved in frequency domain.

The model for generating realizations of road unevenness is a series of cosine terms with random phase angles, and described in (20).

$$\begin{aligned} f(t) &= \sum_{k=0}^{N_d-1} \left[C_k cos(\omega_k t + \Phi_k) \right] , \\ \omega_k &= \omega_l + k\Delta\omega , \\ k &= 0, 1, 2, \ldots, N_d - 1 , \end{aligned} \tag{20}$$

where Φ_ks are independent random phase angles uniformly distributed in the range $[0, 2\pi]$ and C_ks are random variables following Rayleigh distribution with a mean value of $\beta_k \sqrt{\frac{\pi}{2}}$ and a variance of $\beta_k^2(2 - \frac{\pi}{2})$ taking β_k as $\sqrt{S_{FF}(\omega_k)\Delta\omega}$. S_{FF} is the one sided power spectral density function (PSD) used to describe the road unevenness. Further, the realized road surfaces reflect the prescribed probabilistic characteristics of the random process accurately as the number N_d gets larger.

It is noticed from (20) that the PSD is discretized into temporal frequency bands of a width of $\Delta\omega$, and the corresponding discretized frequencies are used in the realization of the stochastic process. However, the entire frequency domain of the PSD cannot be used in the realization for mathematical and physical reasons [26]. For the realizations of road surfaces, cut-off frequencies are needed. The discretizing frequency band is defined as

$$\Delta\omega = (\omega_u - \omega_l)/N_d , \tag{21}$$

with ω_u and ω_l (rad/s) as the upper and the lower cut-off frequencies. The long wavelength irregularities correspond to low frequency components in the time domain and short wavelength irregularities correspond to high frequency components [27].

5 NUMERICAL EXAMPLES

5.1 Ishigami test function

The described joint modeling combined with sensitivity analysis have been applied to Ishigami function [24]:

$$Y(X1, X2, X3) = \sin(X_1) + a\sin(X_2)^2 + bX_3^4 \sin(X_1), \tag{22}$$

where $a = 7$, $b = 0.1$, and $X_i \sim U[-\pi; \pi]$ for $i = 1, 2, 3$. The sensitivity indices for this function are well documented in [1]. A similar setting that of [4] is used in this example. The input parameters X_1 and X_2 are considered as the known input parameters, whereas X_3 is an uncontrollable or unknown input parameter which is not considered in the joint modeling of the function's output.

For Joint modeling support samples are obtained by running a Monte Carlo simulation. One thousand samples of (X_1, X_2, X_3) are simulated to obtain the support observations. Latin hypercube is used for efficiency in sampling. A joint model using the enhanced GLM procedure is applied, the properties of the fit for the mean and dispersion of the joint models are given in Table 1. As mentioned before, cross validation has been used in the determinations of the predictions errors which are used in GLM procedure. Fig. 2 depicts the better fit when GLM procedure is used in building the meta model.

Table 1: Properties of the fitted joint model for Ishigami function

	Formula
Joint GLM enhanced with MLS	$f_m = f(X_1, X_2^2, X_1^3, X_2^4)$ $\text{radius}_{MLS} = 0.77$, $\alpha_{MLS} = 0.4$ $f_d = f(X_1^2, X_2^3)$

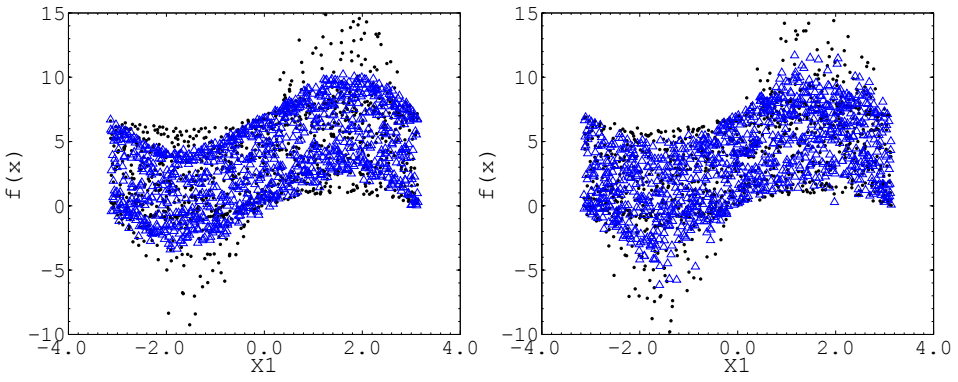

(a) using MLS (b) using GLM procedure with MLS

Figure 2: Comparison between fitting the data with and without GLM procedure: • observations (supports) △ approximated

The sensitivity indices are calculated using the developed joint model, thousands of samples are run on the joint model to ensure convergence in the estimation of the sensitivity indices. A comparison between the exact indices [1], estimated by [4], and the procedure suggested here

are shown in Table 2. The results by [4] were estimated using generalized additive models that employs spline smoothing algorithms based on 100 repetitions of the joint models fitting process. Whereas, the suggested enhanced GLM with MLS has been performed using 10 repetitions of the joint models fitting process.

Table 2: Exact and estimated sensitivity indices

SI	Exact [1]	Joint GAM [4]	Joint GLM$_{MLS}$
S_1	0.314	0.310	0.32
S_2	0.442	0.452	0.41
S_{T3}	0.244	0.236	0.22

It can be noticed from Table 2 that an agreement in the estimated indices exists, which proves the efficiency of the application of the proposed joint models and their use in estimating the sensitivity indices.

5.2 Effects of bridge-vehicle interaction

The engineering problem at hand is the effects of bridge and vehicle dynamics on the bridge displacements considering the excitations of the vehicle due to road unevenness, which can be described as an uncontrollable parameter rendering the dynamic model to stochastic.

The vehicle model presented by [20] is used. The characteristics of the vehicle are found in [29]. The bridge model is a single span simply supported beam model for the Pirton Lane Highway bridge in Gloucester (United Kingdom) [21]. The bridge has a length $L = 40$m, an estimated mass per unit length of $m = 12000$ kg/m and a bending stiffness of EI = $1.26 \times 10^5\ MNm^2$. The bridge's first natural frequency is $f_1 = 3.20$ Hz with a modal damping ratio $\zeta_1 = 0.02$.

Road unevenness is considered in the dynamic analysis, its realization follows (20) where $\omega_l = 1.74$ rad/s and $\omega_u = 75.54$ rad/s with $\Delta\omega = 0.104$ rad/s. The dynamic model's output is the displacements at mid-span that are normalized by the corresponding static displacements, which is known as the Dynamic Incremental Factor (DIF).

A sensitivity analysis is carried out to identify the influence of the input parameters of the vehicle dynamics; stiffness (k_t) and damping (c_t) of suspension system and spacing of fifth axle (S), and the bridge dynamics; flexural stiffness (EI) and damping ratio (ζ). Further, the excitation of the vehicle by the road profile of the approach leading to the bridge is examined and its effects on the variance of the dynamic response is studied.

In order to build the joint model, 1000 random vectors of input parameters are generated and the dynamic model is run for each sample to obtain the support observations. The uncontrollable input parameter X_ϵ represents the random processes of road unevenness. For the scaler input parameters (X), the first order indices are determined from the mean component of joint model, whereas, for X_ϵ the total effect index is estimated. The results are presented for two speeds, these are critical speeds derived for the examined bridge and vehicle models, which had been documented in a previous work by the author [30]. The critical speeds for the vehicle are 57km/h and 84km/h; these speeds cause the highest dynamic effects on the bridge.

Two scenarios are examined; one considers the vehicle traveling over the bridge with initial excitation (WI), and another ignores the initial excitation (WoI). The corresponding sensitivity indices are presented in Table 3. It can be noticed that the initial excitation has a limit influence

on the identified input parameters from the vehicle and bridge dynamics affecting the variance of the bridge's displacement. Whereas, studying the effect of the speed on the sensitivity indices in Table 4 one can see that higher speeds shadow the influence of vehicle dynamics and power the influence of road unevenness on the variance of the bridge's displacement. In other words, the higher the speed, the higher is the amplification in the dynamic response, however, the scatter of the output is also higher. Such an observation is of significance in the modeling of the dynamic problem as more attention must be given when higher speeds are considered in the analysis as higher variations in the response are expected.

Table 3: Estimated sensitivity indices estimated for the displacements due to a vehicle traveling at 57km/h

	1st order WoI	1st order WI
k_s	0.14	0.16
c_s	0.03	0.02
S	0.00	0.02
EI	0.09	0.09
ζ	0.01	0.03
$S_{T\epsilon}$	0.72	0.68

Table 4: Estimated sensitivity indices estimated for the displacements considering the initial excitations by the approach

	1st order v_{cr}=57km/h	1st order v_{cr}=84km/h
k_s	0.16	0.05
c_s	0.02	0.03
S	0.02	0.01
EI	0.09	0.05
ζ	0.03	0.10
$S_{T\epsilon}$	0.68	0.80

6 CONCLUSIONS

The study is concerned with performing sensitivity analysis for responses retrieved from stochastic models of bridge-vehicle interaction. The main presented and tested methods are based on building a joint model using GLM procedure and enhancing the fitting by suggesting MLS approximation algorithms within the framework of GLM. Hence, a meta-model is built for the mean and the dispersion jointly. The described method is applied on an academic example and proved efficient. Later it has been used for the engineering problem of interest. It can be said that considering the initial excitation of the vehicle by road unevenness of the bridge's approach has a limited effect on the identified parameters from the vehicle and bridge dynamics

affecting the variances of the bridge's displacement. However, the speed has a prominent effect as higher speeds leads to higher amplifications in the bridge's displacements accompanied with higher variances caused mainly by the uncontrollable parameter of road unevenness, which has been qualitatively measured.

REFERENCES

[1] A. Saltelli, M. Ratto, T. Andres, F. Campolongo, J. Cariboni, D. Gatelli, M. Saisana, S. Tarantola, Global Sensitivity Analysis, John Wiley & Sons Ltd, 2008.

[2] S. Tarantola, N. Giglioli, N. Jesinghaus, A. Saltelli, Can Global Sensitivty Analysis steer the Implementation of Models for Environmental Assessments and Decision-Making?, Stochastic Environmental Research and Risk Assessment 16 (2002) 63–76.

[3] R. Iooss, M. Ribatet, Global Sensitivity Analysis of Computer Models with Functional Inputs, Reliability Engineering System Safety 94 (2009) 1194–1204.

[4] A. Marrel, B. Iooss, S. Veiga, Global Sensitivity Analysis of Stochastic Computer Models with Joint Metamodels, Statics and Computing 22 (2012) 833–847.

[5] F. Yang, G. Fonder, An Interative Solution Method for Dynamic Resposne of Bridge-Vehicle Systems, Earthquake Engineering and Structural Dynamics 25 (1996) 195–215.

[6] Y. Yang, J. Yau, Y. Wu, Vehicle-Bridge Interaction Dynamics, World Scientific Publishing Co. Pte. Ltd., 2004.

[7] E. Hwang, A. Nowak, Simulation of Dynamic Load for Bridges, Journal of Structural Engineering ASCE , 117(5) (5) (1991) 1413–1434.

[8] P. Kirkegaard, S. Nielsen, Influence of Uncertainty of Vehicle Dynamics on the Dynamic Response of Minor Highway Bridges, in: Proceedings of the 4th International Conference on Stochastic Dynamics, University of Notre Dame, USA, 1998, pp. 507–512.

[9] S. Nielsen, P. Kirkegaard, Influence of Surface Irregularities on the Dynamic Response of Minor Highway Bridges, in: Proceedings of the 4th International Conference on Stochastic Dynamics, University of Notre Dame, USA, 1998, pp. 507–512.

[10] K. Liu, G. D. Roeck, G. Lombaert, The Effect of Dynamic Train-Bridge Interaction on the Bridge Resposne during a Train Passage, Journal of Sound and Vibration 325 (2009) 240–251.

[11] F. Lu, J. Lin, D. Kennedy, F. Williams, An Algorithm to Study Non-stationary Random Vibrations of Vehicle-Bridge Systems, Computers and Structures 87 (2009) 177–185.

[12] G. Lombaert, J. Conte, Vehicle-Bridge Interaction in the Presence of Random Track Unevenness, Tech. rep., Structural Mechanics Division, Katholieke Universiteit Leuven, Belgium (2010).

[13] S. Law, S. Wu, Dynamic Analysis of Bridge with Non-Gaussian Uncertainties under a Moving Vehicles, Probabilistic Engineering Mechanics 26 (2011) 281–293.

[14] N. Liu, W.Gao, C. Song, N. Zhang, Probabilistic Dynamic Analysis of Vehicle-Bridge Interaction with Uncertain Parameters, Computer Modeling in Engineering & Sciences 72 (2) (2011) 72–102.

[15] P. McCullagh,J.A. Nelder, Generalized Linear-Models, Chapman and Hall, 1989.

[16] R.H. Myers,D.C. Montgomery,G.G. Vining, Generalized Linear-Models: with applications in engineering and the sciences, Chapman and Hall, 2002.

[17] A. Saltelli, S. Tarantola, F. Campolongo, M. Ratto, Sensitivity Analysis in Practice: A Guide to Assessing Scientific Models., John Wiley & Sons Ltd, 2004.

[18] I. Sobol, On Freezing Unessential Variables, Vestnik Moskovskogo Universiteta Serija Matematika 6 (1996) 9294.

[19] S. Hora, R. Iman, A Comparison of Maximum/Bounding and bayesian/monte carlo for Fault Tree Uncertainty Analysis, Tech. rep., Report SAND85-2839, Sandia Laboratories (1986).

[20] N. Harris, E. OBrien, A.González, Reduction of Bridge Dynamic Amplification through Adjustment of Vehicle Suspension Damping, Journal of Sound and Vibration 302 (2007) 471–485.

[21] D. Cebon, Handbook of Vehicle-Road Interaction, Taylor & Francis, 1999.

[22] W. Clough, J. Penzien, Dynamics of Structures, McGraw-Hill, 1993.

[23] C. Dodds, J. Robson, The Description of Road Surface Roughness, Journal of Sound and Vibration 31(2) (1973) 175–183.

[24] T. Homma, A. Saltelli, Importance Measures in Global Sensitivty Analysis of Non Linear Models, Reliability Engineering and System Safety 52 (1996) 1–17.

[25] W. Schiehlen, Colored Noise Excitation of Engineering Structures, in: Computational Methods in Structural Dynamics and Earthquake Engineering, 2009.

[26] M. Shinozuka, G. Deodatis, Simulation of Stochastic Processes by Spectral Representation, Applied Mechanics Reviews 44 (4) (1991) 191–204.

[27] D. Newland, An Introduction to Random Vibrations, Spectral and Wavelet Analysis, Dover Publications, Inc., 1993.

[28] D. Newland, The Effect of a Footprint on Perceived Surface Roughness, Proceedings of the Royal Society of London, Series A : Mathematical, Physical sciences & Engineering Sciences 405 (1986) 303–327.

[29] S. Brady, E. O'Brien, A. Žnidarič, The Effect of Vehicle Velocity on the Dynamic Amplification of a Vehicle Crossing a Simply Supported Bridge, American Society of Civil Engineering 11 (2006) 241–249.

[30] G. Karaki, Assessment of Coupled Models of Bridges considering Time-Dependent Vehicular Loading, PhD Thesis, Fakultät Bauingenieurwesen, Bauhaus-Universität Weimar 2012.

19th International Conference on the Application of Computer
Science and Mathematics in Architecture and Civil Engineering
K. Gürlebeck, T. Lahmer and F. Werner (eds.)
Weimar, Germany, 04–06 July 2012

QUANTIFYING THE QUALITY OF PARTIAL MODEL COUPLING AND ITS EFFECT ON THE SIMULATED STRUCTURAL BEHAVIOR

H. Keitel *

* *Research Training Group 1462*
Berkaer Str. 9
99423 Weimar, Germany
E-mail: holger.keitel @ uni-weimar.de

Keywords: Coupling Quality, Interaction, Model Evaluation, Uncertainty Quantification.

Abstract. *The process of analysis and design in structural engineering requires the consideration of different partial models, for example loading, structural materials, structural elements, and analysis types. The various partial models are combined by coupling several of their components. Due to the large number of available partial models describing similar phenomena, many different model combinations are possible to simulate the same aspects of a structure. The challenging task of an engineer is to select a model combination that ensures a sufficient, reliable prognosis. In order to achieve this reliable prognosis of the overall structural behavior, a high individual quality of the partial models and an adequate coupling of the partial models is required.*
Several methodologies have been proposed to evaluate the quality of partial models for their intended application, but a detailed study of the coupling quality is still lacking. This paper proposes a new approach to assess the coupling quality of partial models in a quantitative manner. The approach is based on the consistency of the coupled data and applies for uni- and bidirectional coupled partial models. Furthermore, the influence of the coupling quality on the output quantities of the partial models is considered.
The functionality of the algorithm and the effect of the coupling quality are demonstrated using an example of coupled partial models in structural engineering.

1 INTRODUCTION

The models used in structural engineering to design for serviceability and the ultimate limit state are composed of several partial models (PM) and their couplings (C). A partial model describes a component of the global model, e.g. loading, material, or the level of abstraction. For each class of PMs, e.g. the material behavior of steel, several possibilities of modeling are available. If the material model is relevant for the structural behavior, the structural engineer needs to decide, whether a linear or a non-linear material model should be used and whether further effects, e.g. long-term behavior, have to be considered. Apart from the selection of appropriate partial models the coupling of the individual PMs is a key issue. Some partial models might interact with each other, thus a coupling is substantial and the quality of this coupling influences the quality of the global model.

In recent years, strategies to estimate the quality of partial models, [1], [2], and to quantify the influence of the partial models on the global model prognosis [3] have been developed. Furthermore, the quantification of the prognosis quality of a global model, neglecting the influence of coupling quality, is described in [3]. The assessment of software coupling has been shown in [4], but does not apply to partial models directly. Altogether, the evaluation of partial model coupling and its influence on the prognosis of a global model has not been addressed so far.

In the scope of this paper a method to quantify the quality of data coupled partial models is presented. The basis of the procedure is the consistency of data belonging to the coupled partial models. Besides the pure data integrity the influence of the coupling on the partial models' output is taken into account within the framework of the evaluation algorithm.

In the next section some basic principles and methods are introduced. Section three presents the method of evaluation and section four gives an example of coupling quality evaluation. Finally, conclusions are drawn.

2 BASIC METHODS AND PRINCIPLES

2.1 Graphical Representation of Coupled Partial Models

Global models used in engineering consist of several partial models. Figure 1 depicts a structure of a simply supported beam, connected to a clamped column with a footing. On the left side the overall structure is presented all in one, on the right side the structural parts are decoupled. The partial models that are exemplarily depicted are: load models for dead load, live load, and wind load, material models, models of geometric non-linear kinematics, and soil.

Stein, Lahmer, and Bock [5] show that a global model can be represented schematically by a graph, consisting of vertices – symbolizing the partial models – and edges – symbolizing the coupling. This idea is extended within the scope of this paper. The global model in Figure 1, represented by the graph in Figure 2, is separated into its structural components; beam, column, and foundation. Due to the numerical calculation, a discretization of the structural parts is necessary, for example using 1D-beam or 3D-volume elements. Each of the structural parts consist of several classes of partial models, which are arranged according to the sequence of the analysis. These classes of partial models may include several different representations – partial models - of a phenomenon, for example material behavior. Only one partial model of a class can be used at the same time when modeling a global system.

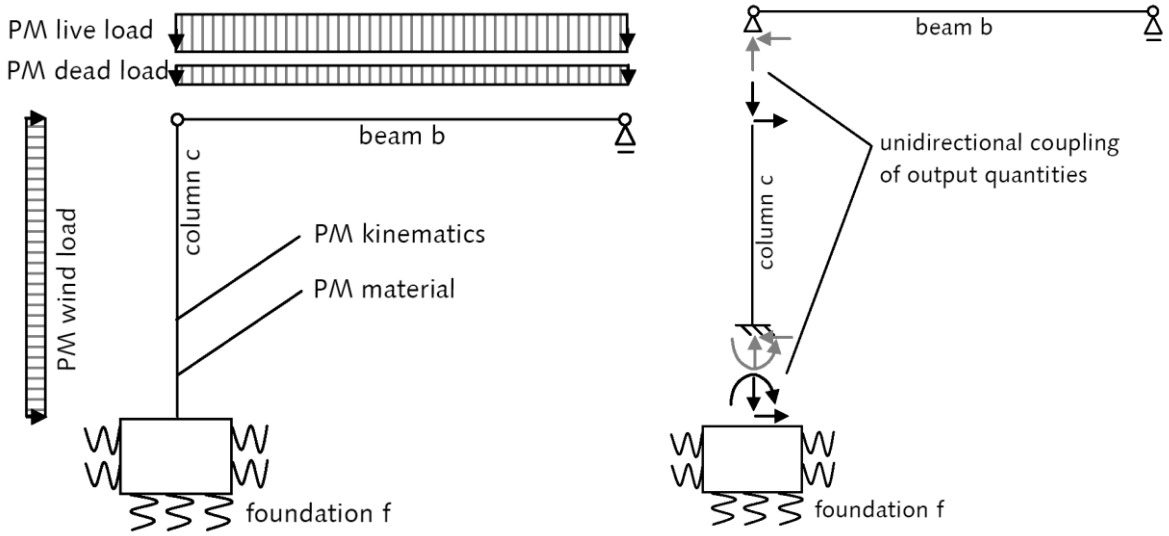

Figure 1: System of coupled partial models (PM), complete coupled system (left), decoupled system (right)

Within Figure 2 the coupling of partial models or structural parts is illustrated by arrows. These coupling are distinguished into unidirectional and bidirectional coupling [4]. If unidirectional coupling is applied, for example coupling beam and column, the output of the beam, in this case support forces, is the input of the column, but the output of the column, in this case deformations, is not the input of the beam. In case of bidirectional coupling, the output (deformations) of the column is also considered as input (pre-deformations of the support) of the beam. For some model combinations bidirectional coupling is essential, e.g. coupling of the material model. The output of the material model, the stresses, is required for the calculation of the column, thus backward coupling is substantial.

2.2 Sensitivity Analysis applied to Partial Models

Sensitivity analyses quantify the influence of input parameters on the output of a model. As proposed in [3], variance-based global sensitivity analysis can also be used to study the influence of partial models on the output of the global model. This procedure detects the most influential classes of the partial models. Consequently, when evaluating the quality of the global model, the individual quality of the partial models with high influences on the system's behavior is crucial for the overall prognosis quality. This algorithm to quantify the influence of classes of partial models is the basis of this investigation of coupling quality and is described in the following.

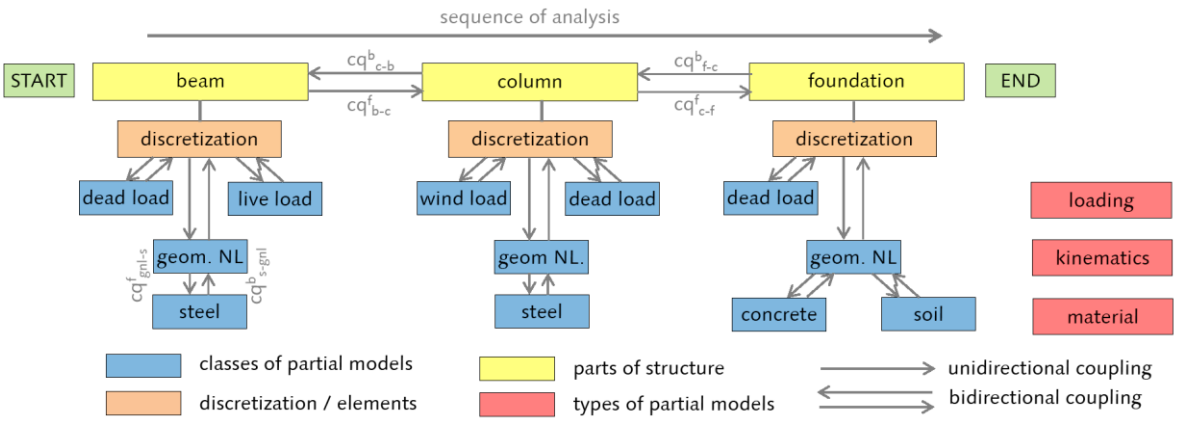

Figure 2: Representation of coupled partial models by a graph

Each of the classes of partial models *i, j* is represented by a uniformly distributed, discrete random parameter

$$X_i \in \{0,1\}, X_j \in \{0,1\}, \ldots \tag{1}$$

A value of $X_i=0$ denotes the deactivated class of partial models *i*, for example geometric non-linearity is not included, and $X_i=1$ denotes the activated class of partial models *i*. The global model *Y* is calculated for all possible combinations of the number of N_p partial model classes, which is in case of the discrete parameters a total of

$$N = 2^{N_p} \tag{2}$$

combinations. The first-order sensitivity index quantifies the exclusive influence of the parameter X_i and is defined as follows [6]:

$$S_i = \frac{V\left(E\left(Y \mid X_i\right)\right)}{V(Y)} = \frac{V_i}{V(Y)}. \tag{3}$$

Herein, $V(E(Y|X_i))$ is the variance of the expected value of the model response *Y* when conditioning to X_i and $V(Y)$ is the variance of the system response when all parameters vary simultaneously. If the sum of all S_i is close to one, the model is purely additive and no interactions of parameters exist. A sum smaller than one denotes that parts of the variance cannot be explained when the interactions of parameters or coupling effects are neglected.

In order to take into account coupling effects, the total-effects sensitivity index S_{Ti} was introduced [7]

$$S_{Ti} = 1 - \frac{V\left(E\left(Y \mid \boldsymbol{X}_{\sim i}\right)\right)}{V(Y)}, \tag{4}$$

with the variance of the expected value $V(E(Y|\boldsymbol{X}_{\sim i}))$ for the case that all parameters but X_i itself are fixed, denoted as $\boldsymbol{X}_{\sim i}$. Besides the exclusive influence of the parameter X_i on the variance of the response, the S_{Ti} index considers the interaction of X_i with all other parameters $\boldsymbol{X}_{\sim i}$.

Differences among first-order and total-effects sensitivity indices indicate interaction of parameter X_i with all other parameters $\boldsymbol{X}_{\sim i}$. When using high-order indices these interactions can be directly apportioned to specific parameters/classes of partial models. The definition of the high-order index of parameter X_i and X_j is the following [8]:

$$S_{ij} = \frac{V\left(E\left(Y \mid X_i, X_j\right)\right) - V_i - V_j}{V(Y)} = \frac{V\left(E\left(Y \mid X_i, X_j\right)\right)}{V(Y)} - S_i - S_j, \tag{5}$$

wherein $V(E(Y|X_i,X_j))$ is the variance of the expected value of *Y* when conditioning to X_i and X_j simultaneously. High-order indices can be calculated for all combinations of input parameters. Summing up all high-order indices of a single variable results in the total-effects indices.

In the present case of discrete input parameters all first-order, total-effects, and high-order indices can be calculated directly from the results of model *Y* for the *N* combinations of input parameters without the usual need of specific sensitivity estimators, which require high computational effort.

3 COUPLING QUALITY

3.1 Quality of Data Coupling

Within the scope of this paper, coupling is defined as data coupling and the quality of coupling is related to the quality of data transfer. Let α and β be quantities appearing in both partial models k and l at the same point on the structure, for example forces or displacements. A perfect data coupling ensures consistent data in both models, e.g. $\alpha^k=\alpha^l$, which refers to data coupling quality of $cq^f_{\alpha,k-l}=1$. The index f denotes the forward coupling according to the sequence of partial models within the graph, whereas b denotes the backward-coupling, for example $cq^b_{\beta,l-k}$. As the differences in transferred data increases, the quality of the coupling decreases down to a quality of zero when no data is transferred. This leads to the following definition of data coupling quality:

$$cq^{\mathrm{f}}_{\alpha\ ,k-l} = 1 - \frac{\left|\alpha^k - \alpha^l\right|}{\max\left\{\left|\alpha^k\right|,\left|\alpha^l\right|\right\}} \quad \text{and} \quad cq^{b}_{\beta\ ,l-k} = 1 - \frac{\left|\beta^k - \beta^l\right|}{\max\left\{\left|\beta^k\right|,\left|\beta^l\right|\right\}}. \tag{6}$$

The data coupling quality depends on the quantity being compared. As a coupling might consist of numerous data, the mean quality of N_f forward and N_b backward transferred data is derived with

$$\overline{cq}^{f}_{k-l} = \sum_{\alpha=1}^{N_f} cq^{\mathrm{f}}_{\alpha\ ,k-l} \quad \text{and} \quad \overline{cq}^{b}_{l-k} = \sum_{\beta=1}^{N_b} cq^{b}_{\beta\ ,l-k}. \tag{7}$$

An example of coupling is the data transfer of the support forces of the column to the foundation in Figure 1, when both structural parts are analyzed seperately. The forward quantities normal force, shear force, and bending moment are transferred to the foundation, and the backward quantities deformation in vertical direction u_z and horizontal direction u_x as well as the rotation φ_y, that occur due to the flexibility of the soil, are transferred back to the column support and are considered pre-deformations of the column at the support.

3.2 Influence of Coupling on Data

Independent from the quality of data coupling, the question of the influence of coupling on the data needs to be answered. For this reason, variance-based sensitivity analysis according to Section 2 is applied. In the current section the sensitivity of the forward coupled data quantities with respect to the partial models is explored, which is in contrast to the usual algorithms used when the sensitivity of certain structural quantities of the global system is determined.

For this analysis the partial models need to be distinguished based on their position in the sequence of the analysis: partial models arranged before the investigated coupling, denoted as $PM\leq k$, and models arranged after the investigated coupling, denoted as $PM\geq l$. If the coupling quality of column-foundation needs to be determined for the graph in Figure 2, $PM\leq k$ refers to all models directly linked to the beam and the column, and $PM\geq l$ refers to all models directly linked to the foundation.

Using high-order indices, the influence of partial models on the transferred data can be apportioned to each model and to several groups of models. In the present case we are interested in the sensitivity of the transferred data with respect to all $PM\leq k$ and all $PM\geq l$. The sum of high-order indices for the groups of models becomes

$$\sum_{PM\leq k} S_\alpha = \sum_{i\leq k}\sum_{j\leq k} S_{ij,\alpha} \quad \text{and} \quad \sum_{PM\geq l} S_\alpha = \sum_{i=1}^{N_p} S_{Ti,\alpha} - \sum_{PM\leq k} S_\alpha \ . \tag{8}$$

In $\sum_{PM\leq k} S_\alpha$ no first-order or higher-order indices referring to any $PM\geq l$ are included. This value is a measure of the importance of forward coupling for quantity α. In contrast to this, $\sum_{PM\geq l} S_\alpha$ indicates the importance of backward coupling and includes all first-order for $PM\geq l$ and all high-order terms referring to any $PM\geq l$. The need for bidirectional coupling increases with an increasing influence of backward coupling. Hence, the coupling quality is more and more dependent on the quality of the backward coupling.

3.3 Quality of Partial Model Coupling

In order to derive the quality of PM coupling, the data coupling quality and the influence of coupling are combined. The final application of the derived coupling quality is the consideration of it within the framework of model evaluation, thus the quality of coupling is defined with this motive. In order to do so, the coupling quality depends on the position of the output quantity in the graph, for which the influence of coupling is investigated for.

When the coupling quality is evaluated for coupled PMs that are after the investigated output quantity in the sequence of the analysis, a backward coupling is essential; otherwise no information of the partial models arranged after the coupling can be transferred back to the PMs that are before in the sequence of the analysis. In this case, quality of coupling becomes

$$CQ_{k-l} = \overline{cq}^{\,f}_{k-l} \times \overline{cq}^{\,b}_{l-k}. \tag{9}$$

If one of the forward or backward data coupling quality is zero, the total quality of coupling becomes zero as well.

When coupling quality is evaluated for coupled PMs that are arranged before the investigated output quantity, the backward coupling might influence the coupled quantities to some extent, but it is not obligatory. In this case the quality is defined as

$$CQ_{k-l} = \frac{\sum_{\alpha=1}^{N_f}\left(cq^{f}_{\alpha\ ,k-l} \sum_{PM\leq k} S_{\alpha_f}\right) + \overline{cq}^{\,b}_{l-k}\ \frac{1}{N_f} \sum_{\alpha=1}^{N_f}\left(\sum_{PM\geq l} S_\alpha\right)}{\sum_{PM} \overline{S}_{ij}}. \tag{10}$$

The forward data coupling quality $cq^f{}_\alpha$ is directly linked to the sensitivity indices of α. For backward data coupling quality this is not possible, because it cannot be determined which of the backward coupling quantities β has an influence on α. Furthermore, the number of forward and backward coupling quantities might differ. Hence, the mean value of sensitivity indices of α is multiplied with the mean of backward data coupling quality $\overline{cq}^{\,b}_{l-k}$.

4 EXAMPLE

4.1 Partial Models and First Results

In the following, an example depicted in Figure 3 is analyzed with respect to coupling quality. The considered partial models are: live load beam (PM1), non-linear material behavior

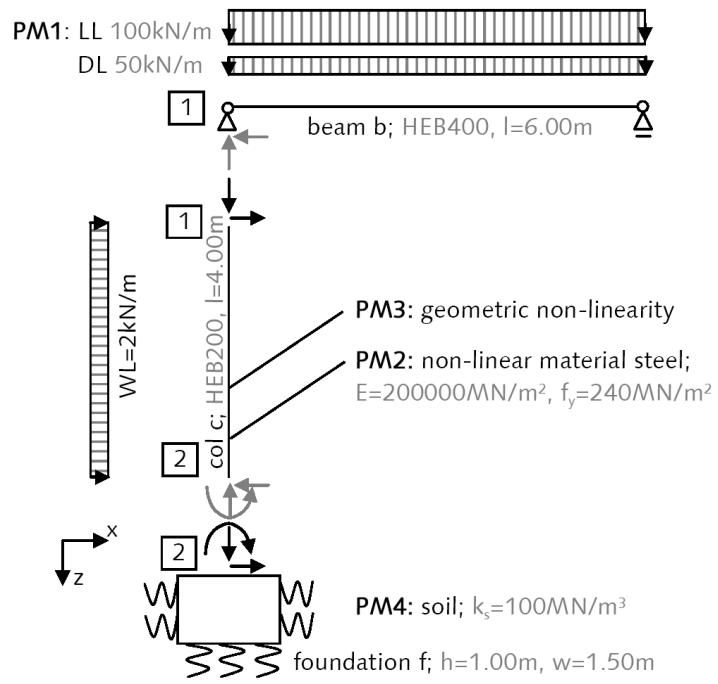

Figure 3: Example of coupled partial models

of the steel columns (PM2), geometric non-linear behavior of the steel column (PM3), and elastic behavior of soil (PM4). Coupling positions of the structural parts are between beam and column, denoted as 1, and between column and foundation, denoted as 2. Further parameters are depicted in the figure.

First, the system is calculated considering perfect model coupling and the resulting major forces, moment, displacements, and rotations of the three structural parts are given in Table 1. From these numbers the qualitative influence of the several classes of partial models is derived, e.g. the influence of geometric non-linearity PM3 on the bending moment at column support, $M_{y2,c}$.

Second, Table 2 shows the results of different couplings of the structural parts, distinguished into uni- and bidirectional coupling. Furthermore, bidirectional coupling with a limited number of iterations between the structural subsystems is given. From these numbers the relationship between the couplings are found. For example the support force of the beam $F_{z1,b}$ is independent from these couplings. This is in contrast to the support moment of the column $M_{y2,c}$, which depends on the type of column-foundation foundation.

X_{PM1}	X_{PM2}	X_{PM3}	X_{PM4}	$F_{z1,b}$ [kN]	$F_{z2,c}$ [kN]	$M_{y2,c}$ [kNm]	$u_{x1,c}$ [mm]	$\varphi_{y2,c}$ [E-3]	$\varphi_{y2,f}$ [E-3]
0	0	0	0	150	150	16.0	5.5	0.0	0.0
1	0	0	0	450	450	16.0	5.5	0.0	0.0
1	0	1	0	450	450	19.3	7.3	0.0	0.0
1	0	0	1	450	450	16.0	9.9	-0.86	-0.97
1	0	1	1	450	450	21.7	13.8	-1.06	-1.06
1	1	1	1	450	450	21.7	13.8	-1.06	-1.06

Table 1: Results for different model classes, perfect bidirectional coupling

coupling b-c	coupling c-f	$F_{z1,b}$ [kN]	$F_{z1,c}$ [kN]	$M_{y2,c}$ [kNm]	$M_{y2,f}$ [kNm]	$\varphi_{y2,c}$ [E-3]	$\varphi_{y2,f}$ [E-3]
unidirectional	unidirectional	450	450	19.3	19.3	0.00	-0.97
bidirectional	unidirectional	450	450	19.3	19.3	0.00	-0.97
unidirectional	bidirectional	450	450	21.7	21.7	-1.06	-1.06
bidirectional	bidirectional	450	450	21.7	21.7	-1.06	-1.06
bidirectional	bidirectional, only 1 iteration	450	450	21.5	21.5	-0.97	-1.05

Table 2: Results for different coupling types, all partial models considered

4.2 Influence of Partial Models

The influence of the partial models is determined by means of sensitivity analysis according to [3], applying a perfect data coupling. The resulting high-order sensitivity indices for selected output quantities are given in Table 3. The output $F_{z1,b}$ depends only on PM1 live load beam, thus no interaction effects with other PMs occur. Contradictory to this, $M_{y2,c}$ depends on several partial models and an interaction of these PMs is quantified by the high-order indices, for example an interaction of live load PM1 and geometric non-linearity PM3 with S_{13}=0.181. The quantity $M_{y2,c}$ depends also on the soil model PM4. This effect can only occur when backward coupling from the foundation to the column exists, thus a higher demand for this coupling is present, in contrast to the beam-column coupling.

	$F_{z1,b}$	$F_{z2,c}$	$M_{y2,c}$	$u_{x1,c}$	$\varphi_{y2,f}$
S_1	1.000	1.000	0.181	0.035	0.002
S_2	0.000	0.000	0.000	0.000	0.000
S_3	0.000	0.000	0.536	0.104	0.005
S_4	0.000	0.000	0.037	0.801	0.984
$S_{13} = S_{31}$	0.000	0.000	0.181	0.035	0.002
$S_{14} = S_{41}$	0.000	0.000	0.014	0.005	0.002
$S_{34} = S_{43}$	0.000	0.000	0.037	0.014	0.005
$S_{134} = S_{314} = S_{413}$	0.000	0.000	0.014	0.005	0.002
S_{T1}	1.000	1.000	0.389	0.081	0.007
S_{T2}	0.000	0.000	0.000	0.000	0.000
S_{T3}	0.000	0.000	0.768	0.158	0.013
S_{T4}	0.000	0.000	0.102	0.826	0.992
$\Sigma S_{PM \leq k}$	1.000	1.000	1.079	0.209	1.011
$\Sigma S_{PM \geq l}$	0.000	0.000	0.181	0.856	0.000
ΣS_T	1.000	1.000	1.260	1.065	1.011

Table 3: Sensitivity indices of specific model responses

coupling b-c	cq^f_{Fz1}	cq^b_{uz1}	$\sum_{PM\leq 1} S_{Fz1}$	$\sum_{PM\geq 2} S_{Fz1}$	$\frac{1}{2}\sum_{f=1}^{2}\left(\sum_{PM\geq 2} S_{\alpha_f}\right)$	$CQ^b_{b\text{-}c}$	$CQ^c_{b\text{-}c}$
unidirectional	1.00	0.00	1.00	0.00	0.00	0.00	1.00
bidirectional	1.00	1.00				1.00	1.00

Table 4: Results for coupling quality beam-column

coupling c-f	cq^f_{My2}	$cq^b_{\varphi y2}$	$\sum_{PM\leq 3} S_{My2}$	$\sum_{PM\geq 4} S_{My2}$	$\frac{1}{3}\sum_{f=1}^{3}\left(\sum_{PM\geq 4} S_{\alpha_f}\right)$	$CQ^c_{c\text{-}f}$	$CQ^f_{c\text{-}f}$
unidirectional	1.00	0.00	1.08	0.18	0.06	0.00	0.94
bidirectional	1.00	1.00				1.00	1.00
bidirectional, only 1 iteration	1.00	0.92				0.92	0.99

Table 5: Results for coupling quality column-foundation

4.3 Coupling Quality

Within this section the coupling quality is estimated considering all four partial models of the example. Different couplings of beam-column and column-foundation are investigated. The further couplings, e.g. the material behavior with the kinematics, do not provide any data loss and have a quality of one. The qualities for specific quantities are given in the Tables 4 and 5. As mentioned earlier, the quality of partial model coupling CQ depends on the quantity of interest, in particular on the position of the quantity of interest within the sequence of the analysis. Hence, CQ is calculated for the different involved partial models/structural parts, denoted for example as CQ^c for coupling quality of the column.

The coupling beam-column consists of two output quantities of the beam, $F_{z1,b}$ and $F_{x1,b}$, and two output quantities of the column, $u_{z1,b}$ and $u_{x1,c}$. The forward coupling quality is always one, as the output quantities of the beam are directly applied to the column and no data loss occurs. In case of unidirectional coupling the data coupling quality of the backward coupling is zero. Analyzing the sensitivity indices reveals that the output quantity $F_{z1,b}$ depends only on PM1, thus no backward coupling is necessary when CQ is analyzed for the column and this results to $CQ^c_{b\text{-}c}=1.0$ according to Eq. (10). When analyzing the quality for quantities of the beam according to Eq. (9), values of $CQ^b_{b\text{-}c}=0.0$ and $CQ^b_{b\text{-}c}=1.0$ for the unidirectional and bidirectional case are obtained. The zero coupling quality for unidirectional interaction results from necessity of backward coupling for the beam in order to take into account output quantities of the column.

The coupling column-foundation consists of three output quantities of the column, $F_{z2,c}$, $F_{x2,c}$ and $M_{y2,c}$, as well as three output quantities of the foundation, $u_{z2,f}$, $u_{x2,f}$ and $\varphi_{y2,f}$. The forward coupling quality is still always one and the backward coupling quality is always zero in case of unidirectional coupling. As already mentioned, $M_{y2,c}$ depends to some extent on PM4. This is pointed out when comparing the sum of the sensitivity indices of all $PM\leq 3$ before and all $PM\geq 4$ after the coupling, 1.08 and 0.18. Hence, the coupling quality of the partial models depends on the quality of the forward and backward coupling even for response quantities that are after the coupling. The data coupling quality of the support moment is given in Table 5. The resulting coupling qualities are also shown in this Table 5 for two response quantities: first belonging to the column $CQ^c_{c\text{-}f}$, which is before coupling and calculated according to Eq. (9), and second for the foundation $CQ^f_{c\text{-}f}$, which is after the coupling analyzed according to

Eq. (10). The value of $CQ^{c}_{c\text{-}f}$ is zero in the unidirectional case, as no information of PM4 can be transferred back to the column. When analyzing $CQ^{f}_{c\text{-}f}$ it is observed that a unidirectional coupling still leads to a quality of $CQ^{f}_{c\text{-}f}$=0.94, as the output quantities of the column are mainly defined by the forward coupling and only relatively small parts of the output quantities are influenced by the backward coupling. In case of bidirectional coupling with only one iteration between the structure of the column and foundation, a high value of $CQ^{f}_{c\text{-}f}$=0.99 is determined, thus one iteration already gives satisfying results.

5 CONCLUSIONS

This paper presented a method to calculate data coupling quality and to quantify the influence of coupling on the output data in the case of coupled partial models. By doing so the determination of coupling quality of partial models in the context of a global system is acconted for.

The method provides a useful tool to determine the necessity to couple partial models in a uni- or bidirectional manner. Hence, the algorithm allows for a reduction of complexity of global systems when bidirectional coupling is less important. Furthermore, the understanding of the system's behavior increases when the results of the method are analyzed.

The defined coupling quality can be considered within a framework of model evaluation in order to provide a total measure for the quality of coupled partial models. This global measure should take into account the influence of partial models on the global response, the quality of the partial models, and the quality of their coupling.

ACKNOWLEDGEMENTS

This research is supported by the German Research Institute (DFG) via Research Training Group "Evaluation of Coupled Numerical Partial Models in Structural Engineering (GRK 1462)", which is gratefully acknowledged by the author.

REFERENCES

[1] T. Most, Assessment of structural simulation models by estimating uncertainties due to model selection and model simplification. Computers and Structures, **89**, 1664-1672, 2011.

[2] T. Lahmer, T. Knabe, S. Nikulla, and M. Reuter, Bewertungsmethoden für Modelle des konstruktiven Ingenieurbaus. Bautechnik Sonderheft, **88**, 60-64, 2011.

[3] H. Keitel, G. Karaki, S. Nikulla, T. Lahmer, and V. Zabel, Evaluation of coupled partial models in structural engineering using graph theory and sensitivity analyses. Engineering Structures, **33**, 3726-3736, 2011.

[4] T. Fröbel, Data coupled civil engineering applications: modeling and quality assessment methods. Dissertation, Bauhaus-Universität Weimar, 2012.

[5] P. Stein, T. Lahmer, and S. Bock, Synthese und Analyse von gekoppelten Modellen im konstruktiven Ingenieurbau. Bautechnik Sonderheft, **88**, 8-11, 2011.

[6] I. Sobol, Sensitivity estimates for nonlinear mathematical models. Mathematical Modeling & Computational Experiment, **1**, 407-414, 1993.

[7] T. Homma and A. Saltelli, Importance measures in global sensitivity analysis of nonlinear models. Reliability Engineering and System Safety, **52**, 1-17, 1996.

[8] A. Saltelli, M. Ratto, T. Andres, F. Campolongo, J. Cariboni, D. Gatelli, M. Saisana, and S. Tarantola, Global sensitivity analysis. The primer. John Wiley and Sons, 2008.

Some Harmonic analysis on the Klein bottle in $\mathbb{R}^n$

by R.S. Kraußhar

Arbeitsgruppe Algebra, Fachbereich Mathematik, Technische Universität Darmstadt, Schloßgartenstr. 7, 64289 Darmstadt, Germany, E-mail: krausshar@mathematik.tu-darmstadt.de

Abstract

The aim of this paper we discuss explicit series constructions for the fundamental solution of the Helmholtz operator on some important examples non-orientable conformally flat manifolds. In the context of this paper we focus on higher dimensional generalizations of the Klein bottle which in turn generalize higher dimensional Möbius strips that we discussed in preceding works. We discuss some basic properties of pinor valued solutions to the Helmholtz equation on these manifolds.

1 Introduction

Clifford and Harmonic analysis deal with the analysis of the Dirac operator resp. the Laplace operator on manifolds in n variables. A lot of progress has been made for orientable manifolds over the past three decades. In particular, much attention has been paid to orientable conformally flat manifolds with spin structures, such as oriented cylinders and tori as their simplest representants.

In contrast to the cases of the oriented tori and cylinder that we discussed extensively in a series of papers, see for example, [8, 3, 5], which indeed are all examples of spin manifolds, we cannot construct the fundamental solution of the Helmholtz equation on higher dimensional generalizations of the non-oriented Klein bottle in terms of spinor valued sections that are in the kernel of $D - i\alpha$.

One obstacle is the lack of orientability. This does does not allow us to construct spinor bundles over these manifolds. Secondly, it is not possible either to construct non-vanishing solutions in the class Ker $D - i\alpha$ in $\mathbb{R}^n$ that have the additional pseudo periodic property to descend properly to

these manifolds. A successful way is to start directly from special classes of harmonic functions that take values in bundles of the ${}^{+}Pin(n)$ group or ${}^{-}Pin(n)$ group.

By means of special classes of pseudo-multiperiodic harmonic functions we develop series representations for the Green's kernel of the Helmholtz operator for some n-dimensional generalizations of Klein bottle with values in different pin bundles. These functions represent a generalization of the Weierstraß $\wp$-function to the context of these geometries.

This functions that can be used to present Green type integral formulas that provide us with the basic stones for doing harmonic analysis in this geometrical context. This has been worked out in detail in [6].

The case of the Klein bottle has interesting particular features. In contrast to the Möbius strips considered earlier in our paper [7] the Klein bottle is a compact manifold.

The compactness allows us to prove that every solution of the Helmholtz operator having atmost unsessential singularities can be expressed as a finite linear combination of the fundamental solution and a finite amount of its partial derivatives. The proof of this statement represents also a central topic in our forthcoming paper [6].

In this paper here we focus ourselves to establish that the only entire solution of the Helmholtz equation on the Klein bottle is reduced to the constant function $f \equiv 0$.

2 Pin structures on conformally flat manifolds

Conformally flat manifolds are n-dimensional Riemannian manifolds that possess atlases whose transition functions are conformal maps in the sense of Gauss. For $n > 3$ the set of conformal maps coincides with the set of Möbius transformations. In the case $n = 2$ the sense preserving conformal maps are exactly the holomorphic maps. So, under this viewpoint we may interpret conformally flat manifolds as higher dimensional generalizations of holomorphic Riemann surfaces. On the other hand, conformally flat manifold are precisely those Riemannian manifolds which have a vanishing Weyl tensor.

As mentioned for instance in the classical work of N. Kuiper [10], concrete examples of conformally flat orbifolds can be constructed by factoring out a

simply connected domain X by a Kleinian group Γ that acts discontinuously on X. In the cases where Γ is torsion free, the topological quotient X/Γ, consisting of the orbits of a pre-defined group action $\Gamma \times X \to X$, is endowed with a differentiable structure. We then deal with examples of conformally flat manifolds.

In the case of oriented manifolds it is natural to consider spin structures. In the non-oriented case, this is not possible anymore. However, one can consider pin structures instead. For details about the description of pin structures on manifolds that arise as quotients by discrete groups. we refer the reader for instance to [1]. See also [2] and [4] where in particular the classical Möbius strip and the classical Klein bottle has been considered.

A classical way of obtaining pin structures for a given Riemannian manifold is to look for a lifting of the principle bundle associated to the orthogonal group $O(n)$ to a principle bundle for the pin groups ${}^{\pm}Pin(n)$. As described in the above cited works, the group ${}^{+}Pin(n) := Pin(n.0)$ is associated to the Clifford algebra $Cl_{n,0}$ of positive signature $(n, 0)$. The Clifford algebra $Cl_{n,0}$ is defined as the free algebra modulo the relation $x^2 = q_{n,0}(x)$ $(x \in \mathbb{R}^n)$ where $q_{n,0}$ is the quadratic form defined by $q_{n,0}(e_i) = +1$ for all basis vectors $e_1, \ldots, e_n$ of $\mathbb{R}^n$. For particular details about Clifford algebras and their related classical groups we also refer the reader to [14]. Next we recall that the group ${}^{-}Pin(n) := Pin(0, n)$ is associated to the Clifford algebra $Cl_{0,n}$ of negative signature $(0, n)$. Here the quadratic form $q_{n,0}$ is replaced by the quadratic form $q_{0,n}$ defined by $q_{0,n}(e_i) = -1$ for all $i = 1, \ldots, n$. Topologically both groups are equivalent, however algebraically they are not isomorphic, cf. for example [4]. The more popular $Spin(n)$ group is a subgroup of ${}^{\pm}Pin(n)$ of index 2. Here we have $Spin(n) := Spin(0, n) \cong Spin(n, 0)$. $Spin(n)$ consists exactly of those matrices from ${}^{\pm}Pin(n)$ whose determinant equals $+1$. The groups ${}^{\pm}Pin(n)$ double cover the group $O(n)$.

So there are surjective homomorphisms ${}^{\pm}\theta :^{\pm} Pin(n) \to^{\pm} Pin(n)$ with kernel $\mathbb{Z}_2 = \{\pm 1\}$. Adapting from Appendix C of [13], where spin structures have been discussed, this homomorphism gives rise to a choice of two local liftings of the principle $O(n)$ bundle to a principle ${}^{\pm}Pin(n)$ bundle. The number of different global liftings is given by the number of elements in the cohomology group $H^1(M, \mathbb{Z}_2)$. See [11] and elsewhere for details. These choices of liftings give rise to different pinor bundles over M. We shall explain their explicit construction on the basis of the examples that we consider in the next section.

3 n-dimensional generalizations of the Klein bottle

In this main section we present basic series constructions for the fundamental solution of the Helmholtz operator on a class of higher dimensional generalizations of the Klein bottle. For simplicity we consider an n-dimensional normalized lattice of the form $\Lambda_n := \mathbb{Z}e_1 + \cdots + \mathbb{Z}e_n$.

We introduce higher dimensional generalization of the classical Klein bottle by the factorization

$$\mathcal{K}_n := \mathbb{R}^n / \sim^*$$

where the equivalence relation $\sim^*$ is defined by the map

$$(\underline{x} + \sum_{i=1}^{n-1} m_i e_i + (x_n + m_n)e_n) \mapsto (x_1, \cdots, x_{n-1}, (-1)^{m_n} x_n).$$

The manifolds $\mathcal{K}_n$ can be described as the set of orbits of the group action $\Lambda_n \times \mathbb{R}^n \to \mathbb{R}^n$ where the action here is defined by

$$v \circ x := (\sum_{i=1}^{k-1} x_i e_i + \sum_{i=1}^{k-1} m_i e_i + ((-1)^{m_k} x_k + m_k)e_k, x_{k+1}, \ldots, x_{n-1}, x_n),$$

where $v = m_1 e_1 + \cdots + m_n e_n$ is a lattice point from Λ_n. Here, and in the remaining part of this section, $\underline{x}$ denotes a shortened vector in $\mathbb{R}^{n-1}$. In the case $n = 2$ we re-obtain the classical Klein bottle. Notice that in contrast to the Möbius strips treated in our previous paper [7], here the minus sign switch occurs in one of the component on which the period lattice acts, too. As for the Möbius strips we can again set up distinct pinor bundles. See also [2] where pin structures of the classical four-dimensional Klein-bottle have been considered.

By decomposing the complete n-dimensional lattice Λ_n into a direct sum of two sublattices $\Lambda_n = \Omega_l \oplus \Lambda_{n-l}$ we can construct in analogy to the oriented torus case treated in [8], 2^n distinct pinor bundles by considering the maps

$$(\underline{x} + \sum_{i=1}^{n-1} m_i e_i, x_n + m_n, X) \mapsto (x_1, \cdots, x_{n-1}, (-1)^{m_n} x_n, (-1)^{m_1 + \cdots + m_l} X).$$

In order to describe the fundamental solution of the Helmholtz operator on the Klein bottlr we recall from standard literature (see for instance [15]) that

the fundamental solution to the Klein-Gordon operator $\Delta - \alpha^2$ in Euclidean flat space $\mathbb{R}^n$ is given by

$$E_\alpha(x) = -\frac{i\pi}{2\omega_n \Gamma(n/2)} (\frac{1}{2} i\alpha)^{\frac{1}{2}n-1} |x|^{1-\frac{1}{2}n} H^{(1)}_{\frac{n}{2}-1}(i\alpha|x|). \tag{1}$$

In this formula, ω_n stands for the surface measure of the unit sphere in $\mathbb{R}^n$ while $H^{(1)}_m$ denotes the first Hankel function with parameter m. Furthermore, we choose the root of α^2 such that $\alpha > 0$. Then, as proposed in [6] we may introduce the following generalized version of Weierstrass $\wp$-function adapted to this class of Klein bottles by

$$\wp^{\mathcal{K}_n}_\alpha(x) := \sum_{v \in \Lambda_n} E_\alpha(\sum_{i=1}^{n-1} (x_i + m_i) e_i, (-1)^{m_n} x_n + x_m). \tag{2}$$

By similar arguments as applied in the cases of the Möbius strips described in [7] one may establish

Theorem 3.1. *Consider the decomposition of the lattice $\Lambda_n = \Lambda_l \oplus \Lambda_{n-l}$ for some $l \in \{1, \ldots, n\}$ and write a lattice point $v \in \Lambda_n$ in the form $v = m_1 e_1 + \cdots + m_l e_l + m_{l+1} e_{l+1} + \cdots + m_n e_n$ with integers $m_1, \ldots, m_n \in \mathbb{Z}$. Let $\mathcal{E}^{(q)}$ be the pinor bundle on $\mathcal{K}_n$ defined by the map*

$$(\underline{x} + \sum_{i=1}^{n-1} m_i e_i, x_n + m_n, X) \mapsto (x_1, \cdots, x_{n-1}, (-1)^{m_n} x_n, (-1)^{m_1 + \cdots + m_l} X).$$

The fundamental solution of the Helmholtz operator on $\mathcal{K}_n$ (induced by $p_*(\Delta - \alpha^2)$) for sections with values in the pinor bundle $\mathcal{E}^{(q)}$ can be expressed by

$$E'_{\alpha,q}(x') = p_* \left(\sum_{v \in \Lambda_l \oplus \Lambda_{n-l}} (-1)^{m_1 + \cdots + m_l} E_\alpha(\sum_{i=1}^{n-1} (x_i + m_i) e_i, (-1)^{m_n} x_n + x_m) \right), \tag{3}$$

where p_* denotes the projection from $\mathbb{R}^n$ to $\mathcal{K}_n = \mathbb{R}^n / \sim^*$. The symbol $'$ represents the image under p_*.

The detailed proof is given in our forthcoming paper [6]. To recall the main idea of proof, without loss of generality we may consider the trivial bundle, as the arguments can easily be adapted to the other bundles that we also considered, namely by taking into account the parity factor $(-1)^{m_1 + \cdots + m_l}$.

This parity factor has no influence on the convergence property of the series. Now one can apply the same argumentation as applied for the Möbius strips to estimate each term of the series which turn out to be asymptotically exponentially decreasing, as a consequence of the Bessel functions. Further, it is a simple exercise to establish that the function $\wp_\alpha^{\mathcal{K}_n}$ is an element from Ker $\Delta - \alpha^2$ in $\mathbb{R}^n \backslash \Lambda_n$.

An important feature however is to show:

Lemma 3.2. *For all $k := k_1 e_1 + \cdots + k_n e_n \in \Lambda_n$ we have*

$$\wp_\alpha^{\mathcal{K}_n}(x+k) = \wp_\alpha^{\mathcal{K}_n}(x_1, \ldots, x_{n-1}, (-1)^{k_n} x_n).$$

Proof. To prove this statement it is important to use the following decomposition

$$\begin{aligned}
\wp_\alpha^{\mathcal{K}_n}(x) &= \sum_{(m_1,\ldots,m_n)\in\mathbb{Z}^n} E_\alpha(x_1+m_1, \ldots, x_{n-1}+m_{n-1}, (-1)^{m_n} x_n + m_n) \\
&= \sum_{(m_1,\ldots,m_{n-1})\in\mathbb{Z}^{n-1}, m_n\in 2\mathbb{Z}} E_\alpha(x_1+m_1, \ldots, x_{n-1}+m_{n-1}, x_n + m_n) \\
&= \sum_{(m_1,\ldots,m_{n-1})\in\mathbb{Z}^{n-1}, m_n\in 2\mathbb{Z}+1} E_\alpha(x_1+m_1, \ldots, x_{n-1}+m_{n-1}, -x_n + m_n).
\end{aligned}$$

First we note that

$$\wp_\alpha^{\mathcal{K}_n}(x_1+k_1, \ldots, x_{n-1}+k_{n-1}, x_n) = \wp_\alpha^{\mathcal{K}_n}(x_1, \ldots, x_n)$$

for all $(k_1, \ldots, k_{n-1}) \in \mathbb{Z}^{n-1}$. This follows by the direct series rearrangement

$$\begin{aligned}
&\wp_\alpha^{\mathcal{K}_n}(x_1+k_1, \ldots, x_{n-1}+k_{n-1}, x_n) \\
= &\sum_{(m_1,\ldots,m_n)\in\mathbb{Z}^n} E_\alpha(x_1+k_1+m_1, \ldots, x_{n-1}+k_{n-1}+m_{n-1}, (-1)^{m_n} x_n + m_n) \\
= &\sum_{(p_1,\ldots,p_n)\in\mathbb{Z}^n} E_\alpha(x_1+p_1, \ldots, x_{n-1}+p_{n-1}, (-1)^{p_n} x_n + p_n)
\end{aligned}$$

where we put $p_i := m_i + k_i \in \mathbb{Z}$ for $i = 1, \ldots, n-1$ and $p_n := m_n$. Notice that rearrangement is allowed because the series converges normally on $\mathbb{R}^n \backslash \Lambda_n$.

It thus suffices to show

$$\wp_\alpha^{\mathcal{K}_n}(x_1, \ldots, x_{n-1}, x_n + 1) = \wp_\alpha^{\mathcal{K}_n}(x_1, \ldots, x_{n-1}, -x_n).$$

We observe that

$$\begin{aligned}
& \wp_\alpha^{\mathcal{K}_n}(x_1,\ldots,x_{n-1},x_n+1) \\
= & \sum_{(m_1,\ldots,m_n)\in\mathbb{Z}^n} E_\alpha(x_1+m_1,\ldots,x_{n-1}+m_{n-1},(-1)^{m_n}(x_n+1)+m_n) \\
= & \sum_{(m_1,\ldots,m_{n-1})\in\mathbb{Z}^{n-1},m_n\in 2\mathbb{Z}} E_\alpha(x_1+m_1,\ldots,x_{n-1}+m_{n-1},x_n+\underbrace{m_n+1}_{odd}) \\
+ & \sum_{(m_1,\ldots,m_{n-1})\in\mathbb{Z}^{n-1},m_n\in 2\mathbb{Z}+1} E_\alpha(x_1+m_1,\ldots,x_{n-1}+m_{n-1},-x_n+\underbrace{m_n-1}_{even}) \\
= & \sum_{(p_1,\ldots,p_{n-1})\in\mathbb{Z}^{n-1},p_n\in 2\mathbb{Z}+1} E_\alpha(x_1+p_1,\ldots,x_{n-1}+p_{n-1},x_n+p_n) \\
= & \sum_{(p_1,\ldots,p_{n-1})\in\mathbb{Z}^{n-1},q_n\in 2\mathbb{Z}} E_\alpha(x_1+p_1,\ldots,x_{n-1}+p_{n-1},-x_n+q_n) \\
= & \wp_\alpha^{\mathcal{K}_n}(x_1,\ldots,x_{n-1},-x_n).
\end{aligned}$$

The fact that

$$\wp_\alpha^{\mathcal{K}_n}(x_1,\ldots,x_{n-1},x_n+k_n)=\wp_\alpha^{\mathcal{K}_n}(x_1,\ldots,x_{n-1},(-1)^{k_n}x_n)$$

is true for all $k_n\in\mathbb{Z}$ now follows by a direct induction argument on k_n. □

With this property we may infer that $\wp_\alpha^{\mathcal{K}_n}$ descends to a well-defined pinor section on $\mathcal{K}_n$ by applying the projection $p_*(\wp_\alpha^{\mathcal{K}_n})$. The result of this projection will be denoted by $E'_\alpha(x')$. $E'_\alpha(x')$ is the canonical skew symmetric periodization of $E_\alpha(x)$ that is constructed in such a way that it descends to the manifold. Therefore, the reproduction property of $E'_\alpha(x'-y')$ on $\mathcal{K}_n$ follows from the reproduction property of the usual Green's kernel $E_\alpha(x-y)$ in Euclidean space, where we apply the usual Green's integral formula for the Helmholtz operator.

Remarks. The fundamental solution of the Helmholtz operator on the usual Klein bottle in two real variables (for pinor sections with values in the trivial bundle) has the form

$$p_*\left(\sum_{v\in\Lambda_2} E_\alpha((x_1+m_1),(-1)^{m_2}x_2+m_2)\right).$$

In terms of this formula for the fundamental solution of the Helmholtz operator on the manifolds $\mathcal{K}_n$ we can deduce similar representation formulas

for the solutions to the general inhomogeneous Helmholtz problem with prescribed boundary conditions on these manifolds as presented in the context of the Möbius strips in [7]. This is also a topic treated in detail in [6].

The fact that the manifolds $\mathcal{K}_n$ are compact manifolds has some interesting special function theoretical consequences. As also shown in our forthcoming paper [6], one can express any arbitrary solution of the Helmholtz equation with unessential singularities on these manifolds as a finite sum of linear combinations of the fundamental solution ${E'}_\alpha$ and its partial derivatives.

In this paper we restrict ourselves to show that there are no non-vanishing entire solutions to the Helmholtz equation on the Klein bottle. To establish the latter statement one first has to show

Lemma 3.3. *Let $\alpha \neq 0$. Suppose that $f : \mathbb{R}^n \to \mathbb{C}$ is an entire solution of $(\Delta - \alpha^2)f = 0$ on the whole $\mathbb{R}^n$. If f additionally satisfies*

$$f(x_1 + m_1, \cdots, x_n + m_n) = f(x_1, \ldots, x_{n-1}, (-1)^{m_n} x_n) \tag{4}$$

for all $(m_1, \ldots, m_n) \in \mathbb{Z}^n$, then f vanishes identically on $\mathbb{R}^n$.

Proof. Since f satisfies the relation

$$f(x_1 + m_1, \cdots, x_n + m_n) = f(x_1, \ldots, x_{n-1}, (-1)^{m_n} x_n),$$

it takes all its values in the n-dimensional period cell $[0,1]^{n-1} \times [0,2]$, because

$$f(x_1 + m_1, x_2 + m_2, \ldots, x_{n-1} + m_{n-1}, x_n + 2m_n) = f(x_1, x_2, \ldots, x_{n-1}, x_n)$$

for all $(m_1, \ldots, m_n) \in \mathbb{Z}^n$. The set $[0,1]^{n-1} \times [0,2]$ is compact. Since f is an entire solution of $(\Delta - \alpha^2)f = 0$ on the whole $\mathbb{R}^n$, it is in particular continuous on $[0,1]^{n-1} \times [0,2]$. Consequently, f must be bounded on $[0,1]^{n-1} \times [0,2]$ and therefore it must be bounded over the whole $\mathbb{R}^n$, too.

Since f is an entire solution of $(\Delta - \alpha^2)f = 0$, it can be expanded into a Taylor series of the following form, compare with [3],

$$f(x) = \sum_{q=0}^{\infty} |x|^{1-q-n/2} J_{q+n/2-1}(\alpha|x|) H_q(x).$$

This Taylor series representation holds in the whole space $\mathbb{R}^n$.

Here, $H_q(x)$ are homogeneous harmonic polynomials of total degree q. These are often called spherical harmonics, cf. for example [12].

Since the Bessel J functions are exponentially unbounded away from the real axis, f can only be bounded if all spherical harmonics H_q vanish identically. Hence, $f \equiv 0$. □

Notice that all constant functions $f \equiv C$ with $C \neq 0$ are not solutions of $(\Delta - \alpha^2)f = 0$. As a direct consequence we obtain

Corollary 3.4. *There are no non-vanishing entire solutions of* $(\Delta-\alpha^2)f = 0$ *on the manifolds* $\mathcal{K}_n$ *(in particular on the Klein bottle* $\mathcal{K}_2$*).*

This is a fundamental consequence of the compactness of the manifolds $\mathcal{K}_n$. Notice that this argument cannot be carried over to the context of the manifolds that we considered in the previous section, since those are not compact.

Remark. The statement can be adapted to the harmonic case $\alpha = 0$. In this case one has a Taylor series expansion of the simpler form

$$f(x) = \sum_{q=0}^{\infty} H_q(x),$$

where only the spherical harmonics of total degree $q = 0, 1, \ldots$ are involved. The only bounded entire harmonic functions are constants. Applying the same argumentation leads to the fact that the only harmonic solutions on $\mathcal{K}_n$ are constants.

References

[1] M. Blau, L. Dabrowski, *Pin structures on manifolds quotiented by discrete groups*, J. Geom. Phys. 6 No.1, 1989, 143–157.

[2] L. Bonora, F.Ferrari Ruffino, R, Savelli, *Revisiting pinors, spinors and orientability*, SISSA 47, 2009, EP-FM, arXiv: 0907.4334v2

[3] D. Constales and R.S. Kraußhar, *Multiperiodic eigensolutions to the Dirac operator and applications to the generalized Helmholtz equation on flat cylinders and on the n-torus*, Mathematical Methods in the Applied Sciences 32, 2009, 2050–2070.

[4] R.C. Kirby, L.R. Taylor, *Pin Structures on Low-dimensional Manifolds*, London Math. Soc. Lecture Note Ser., 151, Cambridge Univ. Press, Cambridge, 1990, 177–242.

[5] R.S. Kraußhar, *On the Klein-Gordon equation on some examples of conformally flat spin* 3*-manifolds*, Recent Advances in Computational Mathematics, (eds. T.E. Simos), Springer, Dordrecht-Heidelberg-London-New York, 2011, p.209–226

[6] R.S. Kraußhar, *The Klein-Gordon operator on Möbius strip domains and the Klein bottle in* $\mathbb{R}^n$.

[7] R.S. Kraußhar, *The Helmholtz operator on higher dimensional Möbius strips embedded in* $\mathbb{R}^4$, to sppear in Advances in Applied Clifford Algebras (2012).

[8] R.S. Kraußhar and J. Ryan, *Some conformally flat spin manifolds, Dirac operators and Automorphic forms*, J. Math. Anal. Appl. 325 (1), 2007, 359–376.

[9] V.V. Kravchenko, and P. R. Castillo: *On the kernel of the Klein-Gordon operator*, Zeitschrift für Analysis und ihre Anwendungen 17 No. 2 (1998), 261–265.

[10] N.H. Kuiper, *On conformally flat spaces in the large*, Ann. Math., (2) 50, 1949, 916–924.

[11] H. B. Lawson, Jr and M.-L. Michelson, *Spin Geometry*, Princeton University Press, Princeton, NJ, 1989.

[12] C. Müller, *Spherical Harmonics*, Lecture Notes in Mathematics 17, Springer, New York, 1966.

[13] P. Petersen, *Riemannian Geometry*, Graduate Texts in Mathematics, 171, Springer Verlag, New York, 1997.

[14] I. Porteous, *Clifford Algebras and Classical Groups*, Cambridge University Press, Cambridge, 1995.

[15] Zhenyuan Xu, *Helmholtz equations and boundary value problems*, in: Partial differential equations with complex analysis, Pitman Res. Notes, Math. Ser. 262 Longman Sci. Tech., Harlow, 1992, 204–214.

19th International Conference on the Application of Computer
Science and Mathematics in Architecture and Civil Engineering
K. Gürlebeck, T. Lahmer and F. Werner (eds.)
Weimar, Germany, 04–06 July 2012

SOLAR UPDRAFT POWER TECHNOLOGY FROM STRUCTURAL ENGINEERING TO MULTI-PHYSICS SIMULATION

Wilfried B. Krätzig

Krätzig & Partner Ingenieurgesellschaft mbH, Buscheyplatz 9-13, D-44801 Bochum
wilfried.b.kraetzig@kraetzigundpartner.de

Keywords: Solar energy, solar chimneys, numerical simulations, multi-field coupling.

Abstract. *After an introduction the lecture will start with an explanation of the working scheme of solar updraft power plants, in the course of the manuscript abbreviated by SUPPs. Some of the response problems of the solar chimney are elucidated, the high tower-like construction in the centre of a SUPP. After this, we change to fluid-thermodynamic simulations of the entire plant to derive a software tool for the determination of the power harvest. Further, as an important part the transition of the solar irradiation into heat-flux in the collector is modelled. All together, elements of different physical fields are combined, such as thermodynamics, fluid-mechanics and electro-magnetism, which alone are represented by linear or quasi-linear fields. However, by combining of these single fields the then coupled problem turns out to become highly nonlinear, followed by numerical expenditures. Finally, some computed results demonstrate the applicability of the derived software.*

1 INTRODUCTION

Our material world is multi-physics, using a modern caption. One of the great achievements in the history of science was the separation of observed physical phenomena into sub-theories, which then were treated independently, like mechanics, optics, theory of heat, electricity. This separation went along with many simplifications, keys to application of physics in modern technology. As an example: Structural engineers use linear elasticity for their strength problems, mostly neglecting thereby inelastic behaviour, geometrical non-linearities, or thermo-effects of deformation.

But for more complex problems and in modelling attempts closer to reality, we find many sub-problems coupled, so-called multi-field coupling. Often strong nonlinearities arise thereby, which make multi-physics-problems in general numerically difficult. This shall be demonstrated to the reader by example of an advanced type of solar power plants, so-called SUPPs.

How did the author come to be engaged with numerical models of these SUPPs, Solar Updraft Power Plants? One of the reasons was my life-long involvement with natural draft cooling towers in many parts of the world. There thin RC shell structures offer extremely complex engineering problems in their design, and it is a high challenge for me and my colleagues from Krätzig & Partners to design and analyze structures of such extreme height [7].

From these power plant components it is only a small step to solar updraft energies. The energy irradiated from the sun onto the earth exceeds the entire world energy demand for more that a factor of 10 000. So for all engineers it should be an enthusiastic challenge to find new ways to exploit solar energies, and to make it useful for human energy demands.

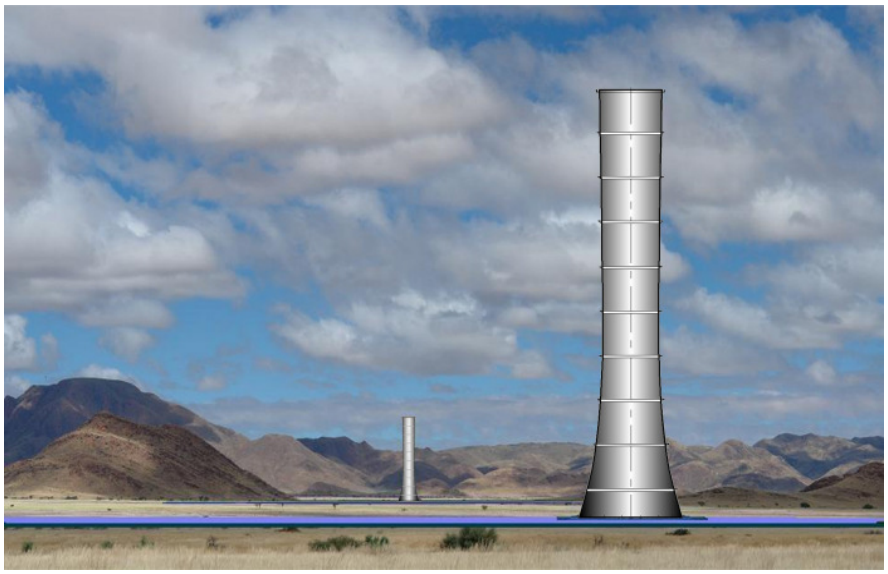

Fig. 1: Computer vision of SUPPs with 1000 m high solar chimneys

2 WORKING SCHEME OF SOLAR UPDRAFT POWER PLANTS: SUPPs

The general working principle of SUPPs will be explained in the lecture. Such plant like in Fig. 1 essentially consists of the collector area (CA), the turbo-generators as power conversion units (PCUs), and the solar chimney (SC). In the CA, a large glass-covered area like a

greenhouse, solar irradiation heats the ground absorber. By this process, the air inside the collector warms up, expands, and streams towards its elevated centre. There, in the PCUs, the kinetic energy of the flow of warm air is partly transformed into electric power. Source of this kinetic energy is the buoyancy of the warm air in the SC, the plant's engine, creating a pressure sink at the PCUs' outlet. This draws permanently fresh air into the collector from the CA rim creating a continuous flow of air through the power plant.

As elucidated, SUPPs are wind power generators [1] which produce their required wind themselves by use of thermal conversion of solar irradiation [12, 13]. Thus the first job of the glass roof over the CA thereby is to let a maximum of short wave solar irradiation (UV radiation) pass through, heating up the absorber - in simplest case the soil - to highest possible temperatures. From the absorber soil, the internal airflow is warmed up. Thus the second scope of the collector glass roof is to prevent the heat of the internal airflow (IR radiation) to escape into the outer ambient environment: Altogether, a high-tech glass coating problem!

SUPPs are supposed to work efficiently in locations with solar irradiation of >2.0 MWh/m²a, occurring between the tropics of the globe. But also countries on the north rim of the Mediterranean Sea, like Southern Italy, Southern Spain or South Turkey, with irradiation values of ≈1.95 MWh/m²a offer fair locations. The efficiency of a SUPP depends on the size of the CA (air temperature) and on the height of the SC (air pressure difference). For example, a plant with CA diameter of 7000 m and SC height of 1000 m in a North African location is estimated to deliver a maximum of electric power of ≈200 MW_p, on mid-days in summer, and an annual energy output of 650 GWh/a.

The paper will explain this working principle, show the best locations world-wide and give elucidations for the gained electric work over day and year.

3 RESPONSE PROBLEMS OF SOLAR CHIMNEYS

This part of the lecture will concentrate on the solar chimney SC, the huge tower structure in the centre of a SUPP [4]. Some of the pre-designed SC are pictured on Fig. 2, in comparison to the world-highest natural draft cooling tower in Niederaussem/Germany and the world-highest skyscraper, the Burj Chalifa in Dubai. The SC consists of a thin shell structure, fabricated of RC, and stiffened by a suitable number of stiffening rings. To increase their stiffnesses, the latter should be pre-stressed.

At first, the loads acting on the chimney are explained [6]. Clearly, besides dead weight D most important is the wind-loading W, but also service temperatures T and possible seismic forces E act on the structure. Concentrating on wind loads, they are decisive for the safety estimation of the structure, and have carefully determined in wind-tunnels [9, 10].

The already mentioned stiffening rings shall constraint the original shell-like stress distributions towards more beam-like ones. The lecture will demonstrate this for a typical wind load distribution, showing that small stiffening members leads to high meridional tension forces for the design state of failure D + 1.50 W, which require large amounts of reinforcement steel. Larger stiffening rings with a wider cranking are much more favourable, but costly and enormously difficult to construct.

The paper then will investigate, if a more realistic shell modelling including the crack-formation for determination of the internal forces on the nonlinear way from load initiation to structural failure will lead to more favourable internal forces and thus to less reinforcement. In the lecture this crack evolution is demonstrated in detail. As a result, we observe much smaller reinforcements compared to a linear elastic model (around 15%), but the arising crack-widths

are much larger than for elastic models (around 300%!). However, since the RC codes world-wide have no crack-limitations in the design state of failure, this seems to be a concept for saving steel without reducing the structural safety [8].

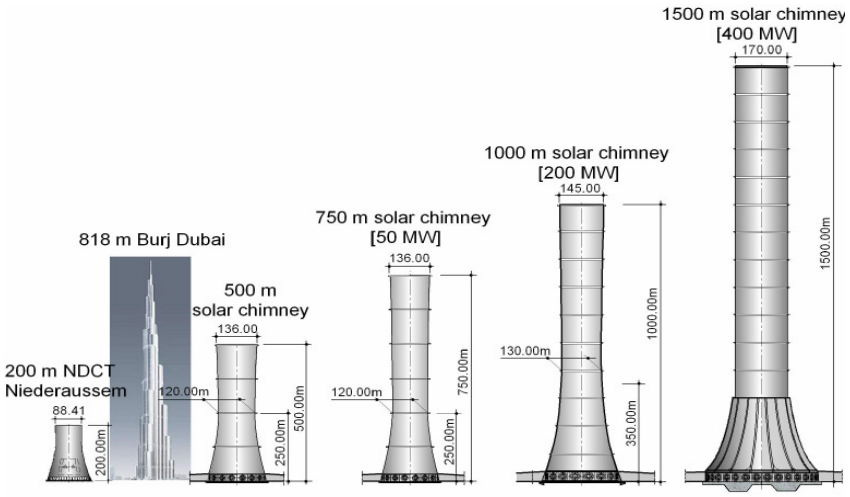

Fig. 2: From the world-highest structures to pre-designs of future SUPPs

4 BASIC FLUID-THERMODYNAMIC SIMULATION OD SUPPS

Coding a simulation software which shall portray the service states of a SUPP, the following physical problems have to be combined:

- The solar heat transfer from the sun into the collector air;
- The heated air movement through the collector;
- The work extraction in the turbines;
- The updraft of heated air in the chimney, coupled by the air velocity at the turbine outlets.

The future computer model for this purpose is based on one-dimensional flow-tube theory, and we apply the following assumptions:

- The collector bottom is horizontal with equal ambient air pressure everywhere;
- All fluid-thermodynamics is approximated as one-dimensional;
- This present model is approximated as stationary.

Beginning with the mass flow through the CA, we start our derivation with a collector ring cell with ground/top surfaces $\Delta A_{coll\ i} = \pi\ (r_{i+1}^2 - r_i^2)$. Its nodal points i, i+1 describe cross-sections $A_i = 2\ \pi\ r_i\ h_i$, $A_{i+1} = 2\ \pi\ r_{i+1}\ h_{i+1}$ of the air stream, in which r_i, r_{i+1} denote distances from the chimney axis, h_i, h_{i+1} the respective collector heights. The fluid-thermodynamics in the collector is then described by the following basic conditions [3]:

- *Conservation of mass*: $\dot{m} = \text{const.},$ (1)
- *Conservation of momentum*: $\dot{m}u_i - \dot{m}u_{i+1} + p_i A_{coll\,i} - p_{i+1} A_{coll.i+1} = 0\,,$ (2)
- *Conservation of energy*: $\Delta\dot{Q}_i = \dot{m}\ c_p\ \Delta T_i\,.$ (3)

Herein, $\dot{m}$ stands for the mass flow rate of air (kg/s) through the plant, u for the air velocity (m/s), p for the stagnation air pressure (N/m²), $\Delta\dot{Q}_i$ for the specific heat flux increase (W), and ΔT_i for the temperature increase (K). c_p abbreviates specific heat capacity of the air (J/kg K). The solar irradiation G (W/m²) is coupled with the heat flux increment $\Delta\dot{Q}_i$ in the cell ring element, and by the total heat flux $\dot{Q}_i$ as follows:

$$\Delta\dot{Q}_i = \alpha_i \, G \, \Delta A_{coll.i}, \dot{Q}_i = \Sigma_i \Delta\dot{Q}_i \, . \qquad (4)$$

Herein α_i denotes the efficiency of the collector ring cells $\Delta A_{coll.i}$ in transforming solar irradiation G into collector heat flux $\Delta\dot{Q}_i$. Presently α_i is still unknown, it will be determined in the next chapter and may be assumed for the moment by guessed values.

For the solar chimney SC we use the following conditions:

• *Conservation of mass*: $\dot{m} = \text{const.}, \qquad (5)$

• *Conservation of momentum*: The SC transforms the heat of the air, gathered in the CA by solar irradiation, with temperature increase ΔT_{turb} and pressure p_{turb} into kinetic energy, using the difference in air density as buoyancy:

$$\Delta p = g \int_0^H \{\rho_o(h) \div \rho_i(h)\} \, dh \, . \qquad (6)$$

Herein $\rho_o(h)$ and $\rho_i(h)$ stand for the height-depending mass density of the air (kg/m³) outside and inside the chimney, g for the gravitational acceleration (m/s²). Obviously, both density profiles influence the chimney's buoyancy. With the standard barometric pressure dependence on height, air assumed as an ideal gas, and ΔT assumed as constant over h, we evaluate equation (6) over tower height H and find:

$$\Delta p = g \, \rho_0 \, H \;\; \Delta T / (T_0 + \Delta T). \qquad (7)$$

The 0-indexed quantities characterize the plant's ambience at chimney foot. BERNOULLI's equation finally delivers the important formula for the maximum air velocity at the chimney's entrance:

$$u_{max} = \sqrt{2 g \; H \;\; \Delta T / (T_0 + \Delta T)} \, . \qquad (8)$$

If we now consider all flow losses in the collector and in the solar chimney [4], we are finally able to find the electric power delivered by the turbines:

$$P_{eff} = \eta_{turb} \, \Delta p_{turb} \;\; \dot{m} / \rho \; = \eta_{turb} \, \kappa \;\; \dot{m} \, u_{max}^2 / 2 \, . \qquad (9)$$

Herein η_{turb} stands for the turbines' efficiency, and κ characterizes their working point.

These formulae form for given irradiation G and thus collector efficiency α_i from equation (4), a nonlinear initial value problem – coupled to the buoyancy velocity at the chimney entrance - for the mass flow of air $\dot{m}$. The single physical constituents stem from fluid-mechanics and thermodynamics. Solving all equations in a discretized concept for finite collector ring cells by application of increments of $\dot{m}$ and suitable iterations, P_{eff} can be determined. This solution process uses an optimization solver and is described in the oral presentation.

5. RADIATION AND HEAT POWER INTERACTION IN THE COLLECTOR

The collector efficiency α_i, a function of the radial distance r from chimney axis, is still unknown and has now to be determined. For this aim, the complicated physical process of transformation of solar irradiation G into temperature increase $\Delta T(r)$ - equations (3) and (4) - of the collector air flux $\dot{m}$ has to be modelled. This requires knowledge in the fields of thermodynamics and of radiation optics.

Between the different collector components - single or double glass sheets, the air flow, possible heat storage devices and the soil absorber – there exist manifold exchanges of heat and

radiation, which have to be taken into account in the formulation of the heat balance equations of all single collector components. For this sophisticated task, in which optical parameters of the translucent as well as opaque materials and the heat transfer coefficients of all components play an important role, we refer the interested reader to [5].

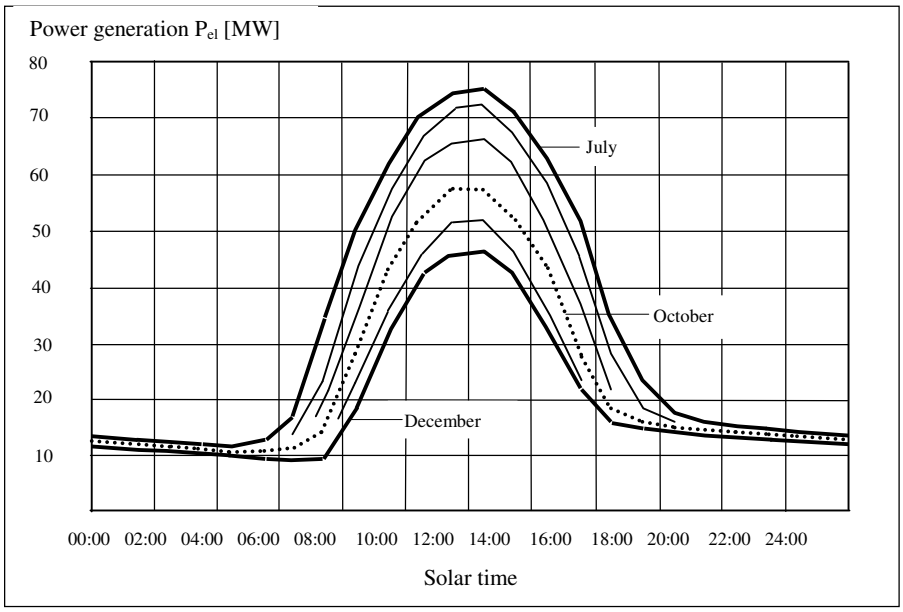

Fig. 3. Generated power P_{el} for typical months July to December, 750/3500-plant

For a short introduction into this task we apply the simplest collector construction, namely one sheet of glass (Temperature: T_1), the heated air-flow (T_2) and the soil absorber (T_3), distinguishing the following thermal transfers q, all depending on their respective temperatures:

$qr_{ou\ gl}$ thermal transfer by radiation (qr) from outer air (ou) into glass (gl), …,

$qc_{ou\ gl}$ thermal transfer by convection (qc) from outer air into glass, …,

$si_{su\ gl}$ solar irradiation from the sun into glass sheet.

In the oral lecture all 11 thermal transfers will be identified, and it will be demonstrated that for this simple collector construction we arrive at three coupled algebraic heat balance conditions, depending on fourth (qr) and first (qc) powers of the mentioned temperatures T_1, T_2 and T_3. Such highly nonlinear algebraic conditions have to be solved for each collector cell element $\Delta A_{coll,i}$ iteratively, simultaneously with the solution process of the above mentioned nonlinear initial value problem for the entire SUPP. This requires considerable computing effort, and for even more complicated collector constructions (double glazing, water-filled heat reservoirs), this generally is the bottle-neck of high computing times [3, 11].

Interesting again is that each of the sub-problems, the convective heat transfers and the radiation heat transfers, are (quasi-)linear if separated, but the coupled problem is highly nonlinear [11]. For solution of the nonlinear algebraic equations of each cell, again an optimization solver is applied.

6. SIMULATION RESULTS: POWER AND ENERGY HARVEST

In the lecture we then will present certain analyzed results as examples, e.g.:

- Temperature distributions of the glazing, the soil and the internal air over the collector distance r from rim to turbine entrance;

• The collector distributions of the degrees of efficiency α_I for different collector constructions, like single glazing, double glazing, blackened soil, and water covered soil;
• The power harvest of a certain analyzed SUPP over typical solar days for half a year, Fig. 3.

Finally, to approach the real world of power generation again, results for detailed cost calculations for two power plants are presented. These calculations demonstrate the high efficiency of SUPPs: A plant with a SC of 750m of height and a CA diameter of 3 500m of diameter delivers electricity for levelled electricity costs LED of less than 0.10 € /kWh [2].

REFERENCES

[1] Backström, T.W. von, Harte R., Höffer R., Krätzig W.B., Kröger D.G., Niemann H.-J., Zijl G.P. van, 2008. State and Recent Advances of Solar Chimney Power Plant Technology. PowerTech, 88 Vol. 7: 64-71.

[2] Bergermann, R., Weinrebe, G., 2010: Realization and costs of solar updraft towers. Proceedings of the SCPT 2010 – Solar Chimney Power Technology International Conference, 63-68. Ruhr-University Bochum.

[3] Bernardes, M.A. dos Santos, 2004: Technische, ökonomische und ökologische Analyse von Aufwindkraftwerken. Dr.-Ing.-Dissertation U Stuttgart, Institut für Energiewirtschaft und Rationelle Energieanwendung.

[4] Bottenbruch H., Krätzig WB.: Optimum design concepts for solar power plants. Proceedings of the SCPT 2010 – Solar Chimney Power Technology International Conference, 35-42. Ruhr-University Bochum, 2010.

[5] Duffie, J.A., Beckman, W.A.: Solar Engineering of Thermal Processes. 3rd Edition, John Wiley & Sons Inc. Hoboken New Jersey, 2006.

[6] Harte, R., Höffer, R., Krätzig, W.B., Mark, P., Niemann, H.-J., 2012: Solare Aufwindkraftwerke: Ein Beitrag zur nachhaltigen und wirtschaftlichen Energieerzeugung (SUPPs: A structural engineering contribution for sustainable and economic power generation). Bautechnik 89, Vol. 3, 173-181.

[7] Krätzig, W.B., Harte, R., Montag, U., Woermann, R., 2009: From large natural draft cooling tower shells to chimneys of solar upwind power plants. In: A. Domingo, C. Lazaro (eds.), IASS Symposium on Evolutions and Trends in Design, Analysis and Construction of Shells. CD-Rom, University of Valencia.

[8] Krätzig W.B., Graffmann M., Harte R., Montag U., 2008: Load Response and Design of Giga Towers. In: Bottenbruch, H.: Proc. CICIND Symposium on Giga Towers, Ratingen.

[9] Lupi, F., 2011: Structural behaviour, optimization and design of a solar chimney prototype under wind loading and other actions. Master Thesis, Università degli studi di Firenze.

[10] Niemann, H.-J., Hölscher, N., Hubert, W., 2010: Static, quasi-static and resonant wind effects on solar towers. In Bottenbruch H. et al. (eds): Proc. 2nd Int. Conf. on Solar Chimney Power Technology SCPT, Bochum, Germany, 207-211.

[11] Pretorius, J.P., 2007. Optimization and Control of a Large-Scale Solar Chimney Power Plant. PhD-thesis, University of Stellenbosch.

[12] Schlaich, J., Bergermann, R., Schiel, W., Weinrebe, G., 2005. Design of Commercial Solar Updraft Tower Systems. ASME J. Solar Energy Engineering, 127: 117-124.

[13] Schlaich, J., 1995. The Solar Chimney, Electricity from the Sun. Edition A. Menges, Stuttgart.

19th International Conference on the Application of Computer
Science and Mathematics in Architecture and Civil Engineering
K. Gürlebeck, T. Lahmer and F. Werner (eds.)
Weimar, Germany, 04–06 July 2012

THE INFLUENCE OF LOCAL DIMPLES ON THE FUNCTION OF BEARING SHELL CYLINDRICAL HIGH-RISE STRUCTURES

A. Kulchytskyy*, Ye. Horokhov, V. Gubanov and A. Golikov

**Donbas National Academy of Civil Engineering and Architecture*
Derzhavin str., 2,
86123 Makeyevka, Ukraine

**Research Training Group 1462, Bauhaus-University Weimar,*
Research Training Group "Model Validation in Structural Engineering"
Berkaer Str. 9,
99425 Weimar, Germany
E-mail:artem.kulchytskyy@meta.ua

Keywords: Shell, dimple, bearing capacity, the zone of influence, imperfection.

Abstract. *Areas with various defects and damages, which reduce carrying capacity, were examined in a study of metal chimneys. In this work, the influence of the local dimples on the function of metal chimneys was considered. Modeling tasks were completed in the software packages LIRA and ANSYS. Parameters were identified, which characterize the local dimples, and a numerical study of the influence of local dimples on the stress-strain state of shells of metal chimneys was conducted. A distribution field of circular and meridional tension was analyzed in a researched area. Zones of influence of dimples on the bearing cover of metal chimneys were investigated. The bearing capacities of high-rise structures with various dimple geometries and various cover parameters were determined with respect to specified areas of the trunk. Dependent relationships are represented graphically for the decrease in bearing capacity of a cover with respect to dimples. Diameter and thickness of covers of metal chimneys were constructed according to the resulting data.*

1 INTRODUCTION

A survey of a series of metal chimneys showed that many chimneys operate with various defects and damages, thus reducing the load carrying capacity. This paper shows the influence of local dimples on the function of metal chimneys. Parameters were identified, which characterize the local dimples. Additionally, results of numerical research on the influence of local dimples on the stress-strain state of cylindrical shells of metal chimneys are provided. The researched areas consist of distribution fields of circular and meridional tension. Zones of influence of the concavity on the bearing shell of metal chimneys and also the carrying capacity of high-altitude areas of the trunk of cylindrical structures with different geometry and the concavity of the various parameters of the investigated cylindrical shell were identified. Loss of stability (buckling) was investigated for studied sites. Diagrams of dependence of reduction of bearing capacity of cylindrical shells from the extent of concavity, diameters, and thickness of shells of metal chimneys, were constructed from the received data.

2 RESEARCH TOPIC

2.1 Relevance of the Research

Metal chimneys are used in different industries, but are particularly widespread in the energy industry. A metal chimney is a high-rise sheet construction, intended for the removal of exhaust gases into the atmosphere for further dispersion. Geometric deviations include concavity and the eccentricity of docking drawer side and ellipse form, which reduce the carrying capacity. These areas are the foci of this study of metal chimneys. These geometric deviations or their combination can cause a decrease in efficiency, or lead to the destruction of the site or of the whole structure. These effects can not only have great financial impact, but they can also result in casualties. The existing principles of design for metal chimneys as compressed-bent rods does not account for the influence of geometric variations on the stress-strain state. By modeling the chimney shell as a cantilever rod, we cannot take into account the reduced tension in the area with geometric deviation. For example, reducing the cross section and then calculating the resistance of the steel indirectly.

It is difficult to estimate the influence of geometric variations on the stress-strain state of such structures in the normative literature [1, 2, 3], but there are indications of the need for such accounting in the design of structures. This fact requires a precise professional knowledge of the real work and the stress-strain state of this type of structure. Research in this area would develop new and improved engineering methods for calculating local stresses and considering their influence on the overall stress-strain state of the structure.

2.2 The Object of the Research

The objects of the research are areas of chimneys with geometrical deviation in the form of dimples. As a constructive solution, metal chimneys are divided into free-standing elements, supported by braces or rigid braces, or in a lattice frame (extraction tower). The main types of constructive solutions for metal chimneys are shown in Figure 1.

a) *b)* *c)* *d)*

Figure 1. The main types of constructive solutions for metal chimneys. a) freestanding; b) with braces; c) with rigid braces; d) in a lattice frame;

Geometric deviation of this type of structure translates to deviation of the actual shape of the object from the ideal (reference). This research will consider one of the types of geometric deviations - the concavity of the shell of metal chimneys.

Concavity of shell structures for the deviation is defined by the deviation of the actual profile from the ideal. When this occurs, points of the real profile from the adjacent segment expand from the edges to the middle. (Figure 2)

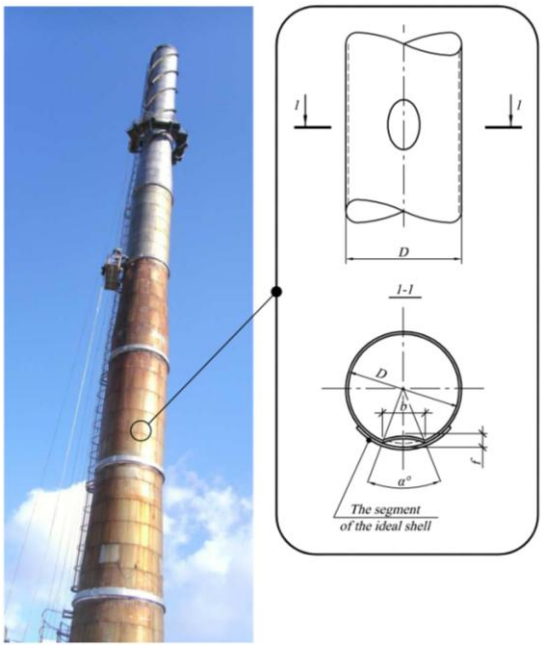

Figure 2. General view of the site with the dimple of the shell of metal chimney

The concavity is characterized by the following parameters:

- An angle of coverage of the concavity ($\alpha°$)
- Opening width of the concavity (b)
- Depth of the lesion (f)

2.3 Purpose of the Study

Analysis of the influence on the local concavity of the stress-strain state of metal chimneys and the improvement of engineering methods of calculation of such structures, taking into account the local concavity.

2.4 Research Task

- To characterize the geometric parameters of the concavity;
- To determine the influence of geometry of the concavity on the stress-strain state of cylindrical shells;
- To determine the carrying capacity of the trunk sections of high-rise structures with different concave geometry, and with various parameters of the investigated membranes.

2.5 Method of Study

This paper will examine the influence of the concavity of the high shell and the shell of medium length, which, according to [7] chimneys with a ratio of length L to the radius r and equals $L/r > 20$ relate to. Metal chimney with a height of 60 m with different parameters of the diameter and thickness of the shell was investigated in this work.

To solve this problem, computational schemes in the software packages Lira (The Ukraine) and ANSYS (USA) have been developed. The calculation was performed taking into account the wind load with characteristic value, which equals 600 Pa according to [4], and also taking into account the self-weight of the structure.

Four settlement schemes were compared to determine the stress-strain state of the stack.

The first computational scheme is adopted as a cantilever rod with an analytical calculation according to [4];

The second computational scheme is adopted as the dimensional sheet structure with analytical calculations according to [4];

The third computational scheme is adopted as the dimensional sheet structure in the form of a perfect shell in the software package ANSYS.

The fourth computational scheme is adopted as the dimensional sheet structure in the form of a perfect shell with a local dimple.

Local dimple takes the size *150x150mm* and depth of the concavity equal to the shell thickness (t). The location of the dimple - *0.5m* from the base of the compressed shell of the chimney - was chosen as the most unfavorable (Figure 3) according to calculations by the third calculation scheme (Figure 4).

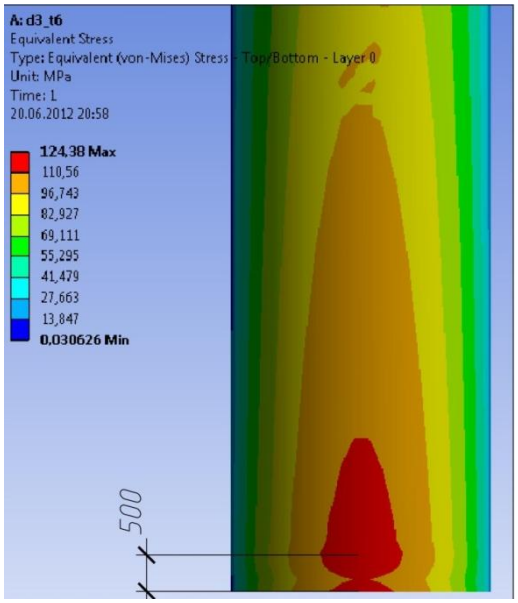

Figure 3. The zone with the proof stress (calculation of Ansys)

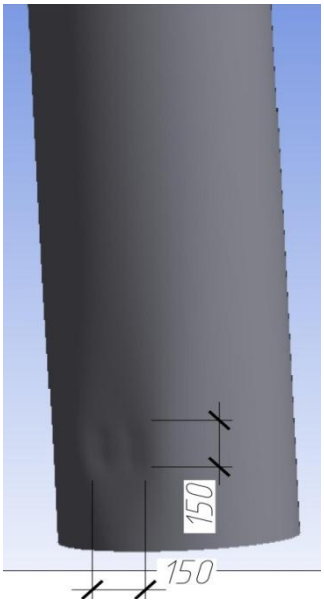

Figure 4. The general form and location of the dimple

Analysis of the stress-strain state of the four calculation schemes showed the next proof stress given in Table 1.

Table 1. The proof stresses in the chimney for different variants of calculation

		Core model	Sheet construction	Sheet construction (Ansys)	Sheet construction + dimple
Ø, mm	t, mm	σ, MPa	σ, MPa	σ, MPa	σ, MPa
2400	6	193,1	167,8	179,2	315,2
	8	146,5	125,1	134,2	275,4
3000	6	125,3	105,1	116,4	209,1
	8	95,6	81,2	87,5	170,8

Stresses by the third calculation scheme were taken as a standard, because the computational scheme was most appropriate for the ideal structure. Modeling the chimney as a cantilever rod, the technique presented in [4] is therefore used to calculate the chimney at the design stage. This calculation shows excessive stress of about 10% margin. In the zone of the local dimple, bursts of local stresses were observed. The stresses of these bursts were twice as high as the standard calculation scheme and were not included in the calculation of the first and second design schemes.

3 FEATURES OF THE STRESS DISTRIBUTION IN THE CONCAVITY ZONES

The software package LIRA was used for the numerical investigation of the influence of the concavity on the stress-strain state of the metal chimneys. Qualitative changes in the stresses of the concave chimney shell were obtained (Figure 5). On the basis of these results,

the stress distribution on the ring of the shell was constructed (Figure 6) and the height of 4 m of the computational model of a cylindrical shell (Figure 7).

Characteristic of the object: *D – 3м, α° = 10°*

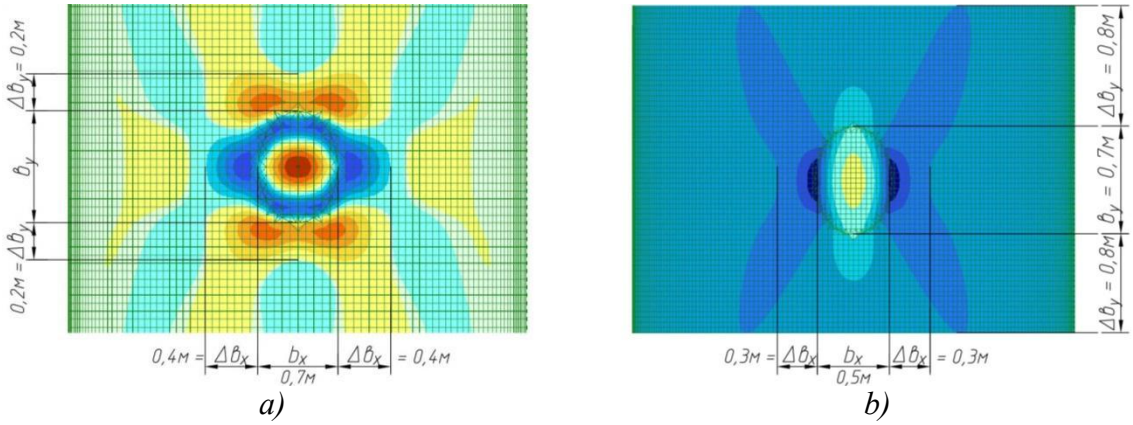

Figure 5. Changes in stresses on the concave part of the shell. a) circular strain); b) meridional strain

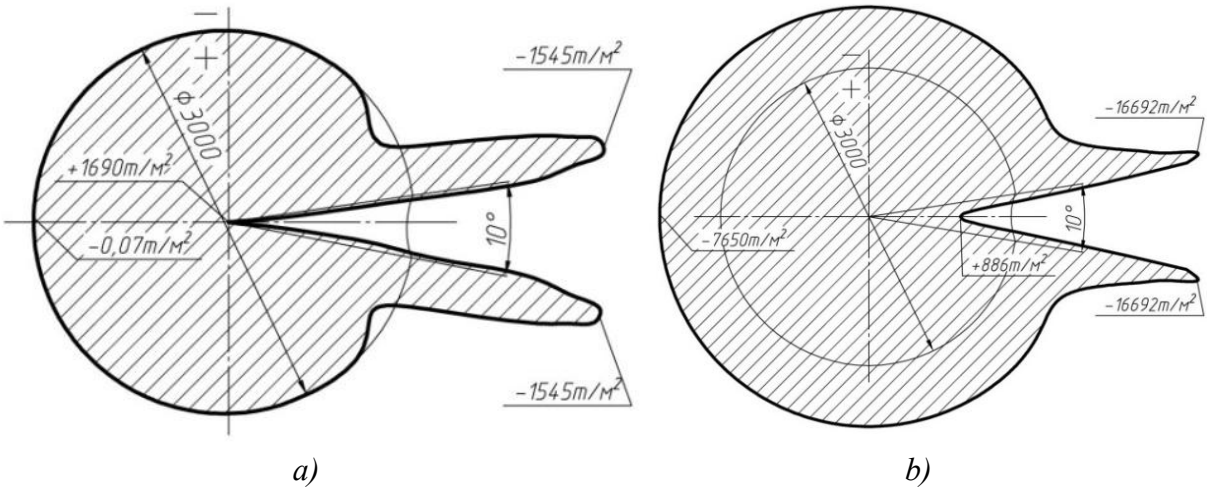

Figure 6. The stress distribution on the ring of a cylindrical shell.a) circular strain( ); b) meridional strain

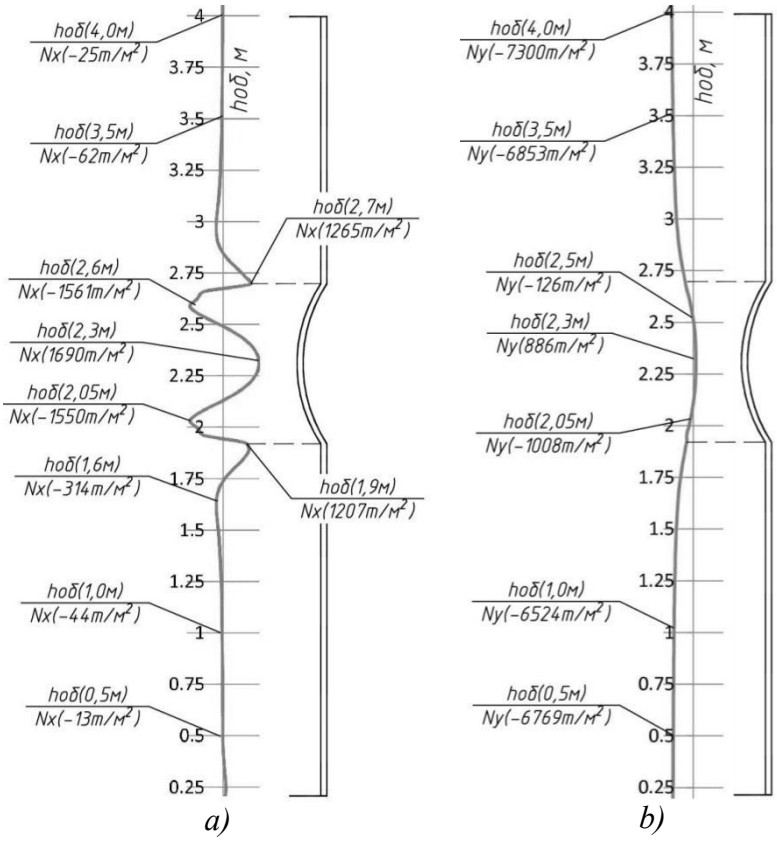

Figure 7. The stress distribution on the height of the computational model membranes. a) circular strain( ); b) meridional strain

From these results, we can see that local stress peaks occur in concaved areas of the chimneys' shell. We also can conclude that the stress peaks at an angle of coverage of the concavity of $\alpha° = 10°$, observed at a distance of *0.2m* to *0.8m* from the boundary concavity.

3.1 The Stress-strain State Chimneys with a Concave Shell

Establishing the dependencies of influence of various factors on the stress-strain state of parts of high-rise structures with a concave shell.

Matrix of research:

D, м	1.2	1.5	1.8	2.1	2.4	2.7	3	3.3	3.6	3.9	4.2
t, мм	4	6	8	10	12	14	16				
	10	20	30	40	50	60					

1. Dependence of the stress σ_{pr} on the diameter (D_{shell}) of the computational model on the site with the concave shell (Figure 8).

The initial parameters of the calculation: $D_{shell} = 1.2 – 4.2m$ with a step $0.3m, t_{shell} = 10mm$, $\alpha° = 10°$.

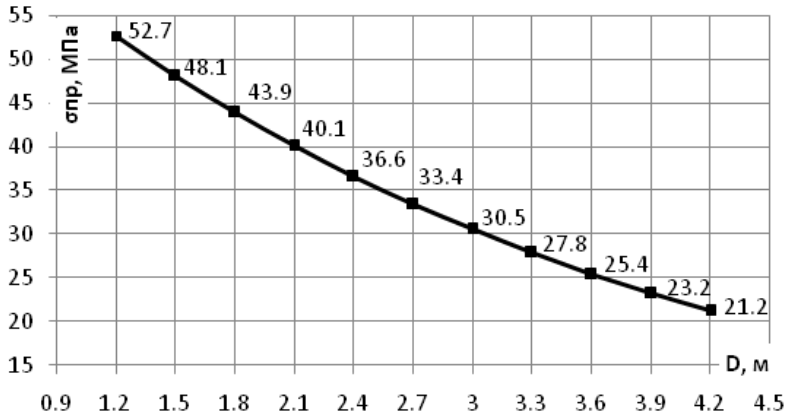

Figure *8*. Change in stress (σ_{pr}) from the diameter of the computational model

2. Dependence of the stress σ_{pr} of thickness (t_{shell}) of calculation model in the section with the concavity of the shell (Figure 9).

The initial parameters of the calculation: D_{shell} *=2,1м;* t_{shell} *= 4 –16mm* with a step *2mm*.

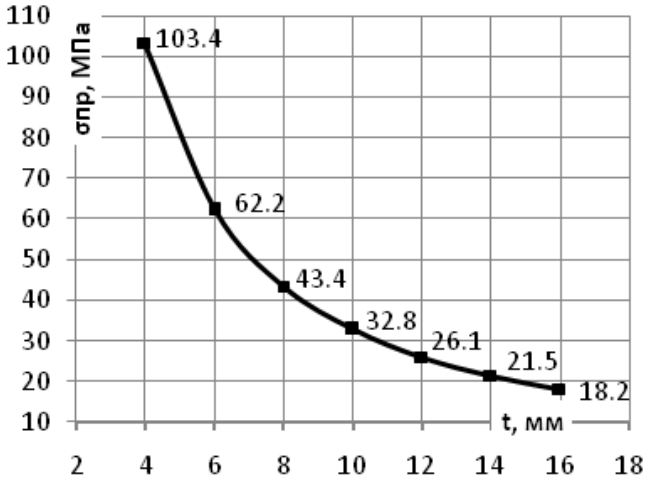

Figure *9*. Change the stress (σ_{pr}) from the thickness of the computational model

3. The dependence of the stress variation from the angle of coverage of the concavity ($\alpha°$) (Figure 10)

The initial parameters of the calculation: D_{shell}*=2.1м;* t_{shrll}*= 10мм,* $\alpha° = 10° – 60°$ with a step *10°*.

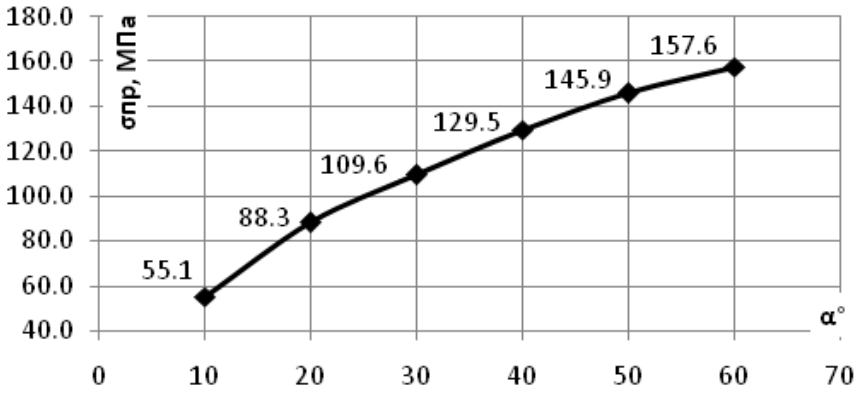

Figure 10. Change in stress (σ_{pr}) from the angle coverage of the concavity

The calculations revealed that:

1. The influence of concavity is reduced with increasing diameter of the computational model; approximating curve has a quadratic dependence of the results given by the formula $\sigma_{pr} = a+bD_{shell} +cD_{shell}^{2}$.
2. The influence of concavity is reduced with increasing thickness of the computational model; approximating curve of the results has the dependence: $\sigma_{pr} =at_{shell}^{b}$.
3. The local stresses in the shell increases with increasing angle of coverage of the concavity; approximating curve of the results has the dependence: $\sigma_{pr} = a\alpha^{\circ b}$.

4. CONCLUSIONS

1. Parameters characterizing the concavity are defined - angle of coverage of the concavity ($a°$), width of opening concavity (b) and lesion depth (f).

2. On the basis of numerical studies of the work of shells of metal chimneys, the dependences between changes of stress from the size of concavity, diameter and thickness of the shell were obtained. We also established that:

- At the concavity of the shell with an angle of coverage of the concavity from 10° to 60°, reduces stresses in the local area by factors of 1.4 - 3.9.
- At changing of the diameter of the computational model from 1.2 m to 4.2 m and the angle of coverage of the concavity α° = 10°, results in a 2.5 decrease in the local area reduced.
- Changing the thickness of the computational model from 4mm up to 16mm and the angle of coverage of the concavity α° = 10°, decreased the stress in the local area by a factor of 5.7.

3. It is necessary to analyze the impact of the concavity on the stability of the shell in order to create engineering techniques that consider the influence of concavity on the stress-strain state while examining the high-rise structures.

4. Bursts of local stresses exceed the stress on the three different design schemes by about 2 orders of magnitude in the zone of local dimple. These stresses are not included in the calculation by the regulatory procedure of Building Code. Thus, taking into account the local stresses, while projecting the chimneys with random dimples, is an urgent scientific task.

REFERENCES

[1] Standard 2.09.03-85. Industrial facilities /Gosstroy Russia. —M.. FGUP, 2006. — 66 p.

[2] Standard 3.03.01-87. Bearing and enclosing structures /Gosstroy Russia. —M.. FGUP, 2007. — 192 p.

[3] Standard III-18-75. Steel structures structures /— M.: CITP Gosstroy of the USSR, 1977. — 101 p.

[4] Standard B.1.2-2:2006. Loads and actions /– Kyiv: Minstroy of Ukraine, 2006. – 78 p.

[5] A. Golikov. Calculation of gas flow tubes with the defects of geometrical form. // – Visnyk DonNABA 2009-5 (79). –P. 18-21.

[6] V. Gubanov. Calculation and gas pipes with local stresses. // Visnyk DonNABA 2009-4 (78). –P. 215-220.

[7] E. Lessig, A. Lileev, A. Sokolv. Sheet Metal Structures. /— M. 1970. — 488 p.

[8] Lanster E.R., Calladine C.R. Paradoxical buckling behaviour of a thin cylindrical shell under axial compression / International Journal of Mechanical Sciences. Vol. 42. pp. 843-865, (2000).

[9] Model Code for Concrete / Steel Chimneys Part D - GRP Liners (April 2009) ISBN 1902998030.

[10] Schneider W., Marco G. Imperfection sensitivity of cylindrical shells subject to hoop compression - numerical buckling analyses versus experimental results / 8th. World Congress on Computational Mechanics (WCCM8) 5th. European Congress on Computational Methods in Applied Sciences and Engineering (ECCOMAS 2008).

[11] Structural design rules for steel chimneys - the preparation of Eurocode 3, Part 3.2 B.W. Smith et al ; Vol. 13, No. 1, 1997.

19th International Conference on the Application of Computer
Science and Mathematics in Architecture and Civil Engineering
K. Gürlebeck, T. Lahmer and F. Werner (eds.)
Weimar, Germany, 04–06 July 2012

EXTENDED ISOGEOMETRIC ANALYSIS BASED CRACK IDENTIFICATION APPLYING MULTILEVEL REGULARIZING METHODS

T. Lahmer*, **S. Sh. Ghorashi**

* *Bauhaus University Weimar*
Research Training Group „Modelquality“
Berkaer Str. 9, 99423 Weimar
E-mail: tom.lahmer@uni-weimar.de

Keywords: Crack Identification, XIGA, Inverse Problem, Regularization

Abstract. *Many structures in different engineering applications suffer from cracking. In order to make reliable prognosis about the serviceability of those structures it is of utmost importance to identify cracks as precisely as possible by non-destructive testing. A novel approach (XIGA), which combines the Isogeometric Analysis (IGA) and the Extended Finite Element Method (XFEM) is used for the forward problem, namely the analysis of a cracked material, see [1]. Applying the NURBS (Non-Uniform Rational B-Spline) based approach from IGA together with the XFEM allows to describe effectively arbitrarily shaped cracks and avoids the necessity of remeshing during the crack identification problem. We want to exploit these advantages for the inverse problem of detecting existing cracks by non-destructive testing, see e.g. [2]. The quality of the reconstructed cracks however depends on two major issues, namely the quality of the measured data (measurement error) and the discretization of the crack model. The first one will be taken into account by applying regularizing methods with a posteriori stopping criteria. The second one is critical in the sense that too few degrees of freedom, i.e. the number of control points of the NURBS, do not allow for a precise description of the crack. An increased number of control points, however, increases the number of unknowns in the inverse analysis and intensifies the ill-posedness. The trade-off between accuracy and stability is aimed to be found by applying an inverse multilevel algorithm [3, 4] where the identification is started with short knot vectors which successively will be enlarged during the identification process.*

1 INTRODUCTION

Many materials like concrete or brittle smart materials suffer from cracking caused due to intensive dynamic loadings. Cracked piezoelectric specimens have e.g. been investigated by X-Ray inspection, see Figure 1. Due to the very thin and often sharp forms of the cracks, discrete

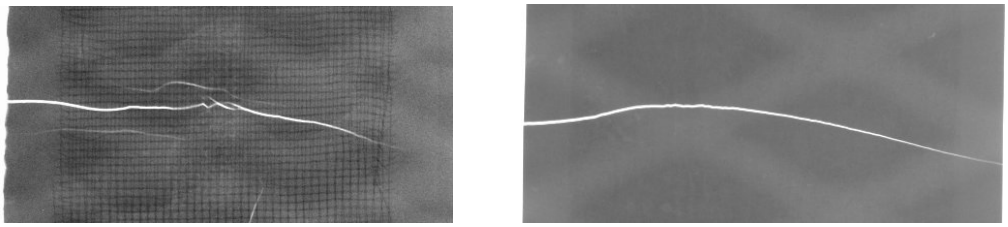

Figure 1: Cracks inside anisotropic smart materials

crack models are advantagueous to smeared crack approaches. Often, the cracks result from some extensional and rare loads, e.g. impacts due to accidents or on buildings after earthquakes while thinking of civil engineering objects. Now after a structure or specimen has been damaged, it is of high importance to know the degree of the damage (e.g. the length and shape of a crack) to derive whether the structure still has full capacity or not. By non-destructive testing, e.g. applying moderate loads, one can compare the behavior of the damaged structure to the behaviour of an undamaged one in means of displacements, accelerations, modal values and draw conclusions about the severity of the damage.

Previous works on identifying discrete cracks are e.g. reported in [2] where the authors use an XFEM approach and apply genetic algorithms to detect the cracks from some measurements on the boundaries of the specimens where the cracks are assumed to be straight lines. This may in many cases be a sufficient approximation. In some cases however, see e.g. Figure 1, the cracks exhibit some curved forms.

The aim of this work is to develop a strategy to uniquely identify cracks of arbitrary shape. In this work we propose an efficient strategy which shall allow to identify cracks without branching. The model itself consits of an extended isogeometric analysis which allows to model moving cracks without the need of remeshing.
For the identification one has to consider the ill-posedness of the problem, which will be done by applying regularizing iterative methods in a multilevel setting.

2 XIGA ANALYSIS

Recently, two papers appeared which treat the combination of the Extended Finite Element Method with Isogeometric Analysis [1, 5]. In these works advantages of the XFEM and IGA approaches to a so called Extended Isogeometric Analysis (XIGA) are brought together. While XFEM is capable of describing discontinuities by enriching the shape functions along the crack by the Heaviside function and analytical solutions around the crack tip, the IGA allows for a very flexible geometrical description of both, the computational domain and the crack [6]. Further, the IGA has been shown to be superior to classsical FEM in terms of robustness and accuracy for may problems.

The approximated displacement field u^h in case of an XIGA is given by

$$\begin{aligned} u^h(\xi^1,\xi^2) &= \sum_{i=1}^{n_{en}} R_i^{p_s,q_s}(\xi^1,\xi^2)u_i + \sum_{j=1}^{n_H} R_j^{p_s,q_s}(\xi^1,\xi^2)Ha_j \\ &+ \sum_{k=1}^{n_Q} R_k^{p_s,q_s}(\xi^1,\xi^2)\sum_{\alpha=1}^{4} Q_\alpha b_k^\alpha, \end{aligned} \tag{1}$$

where R are the spline based ansatz functions of order p_s and q_s and (ξ^1,ξ^2) coordinates in parametric space. With $n_{en},\ n_H,\ n_Q$ the numbers of non-zero basis functions, the number of n_{en} basis functions that have a crack face (but no crack tip) and the number of n_{en} basis functions around the crack tip are denoted, respectively.
The H - Heaviside function is a common tool in XFEM analysis, taking values $+1$ if the point under consideration is above the crack and -1 in the opposite case. For the crack tip enrichment functions the following basis is appropriate

$$Q(r,\theta) = \{Q_1,Q_2,Q_3,Q_4\} = \left\{\sqrt{r}\sin\frac{\theta}{2}, \sqrt{r}\cos\frac{\theta}{2}, \sqrt{r}\sin\theta\sin\frac{\theta}{2}, \sqrt{r}\sin\theta\cos\frac{\theta}{2}\right\},$$

where polar coordinates are considered with $r = \sqrt{x_1^2 + x_2^2}$ being the distance to the crack and $\theta = \arctan(x_2/x_1)$, see Figure 2.

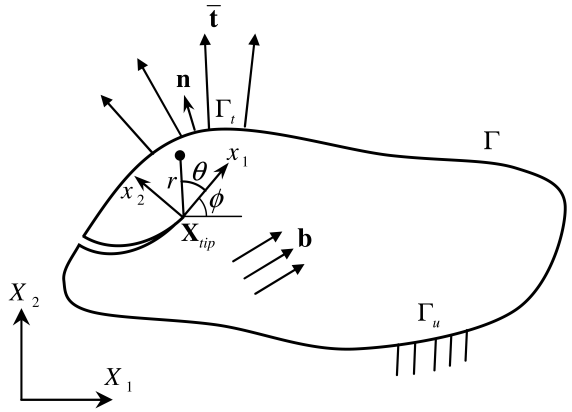

Figure 2: A two dimensional medium with a crack, previously published in [1].

The NURBS - functions $\{R_i^p\}$ are defined as

$$R_i^p(\xi) = \frac{N_{i,p}(\xi)w_i}{\sum_{ii=1}^{n} N_{ii,p}(\xi)w_{ii}} \tag{2}$$

with the recursive definition of the B-spline basis functions

$$N_{i,0}(\xi) = \begin{cases} 1 & \text{if } \xi_i \le \xi \le \xi_{i+1} \\ 0 & \text{otherwise} \end{cases} \tag{3}$$

and

$$N_{i,p}(\xi) = \frac{\xi - \xi_i}{\xi_{i+p} - \xi_i} N_{i,p-1}(\xi) + \frac{\xi_{i+p+1} - \xi}{\xi_{i+p+1} - \xi_{i+1}} N_{i+1,p-1}(\xi), \quad \text{for } p = 1,2,3,.... \tag{4}$$

For more details we refer to [1]. The physical model is a two-dimensional elastostatic problem derived from the following equilibrium equations

$$\mathcal{B}^T\sigma + b = 0 \quad \text{in } \Omega,$$

together with natural boundary conditions

$$\sigma n = \overline{T}, \quad \text{on } \Gamma_t$$

and essential boundary conditions

$$u = \overline{u}, \quad \text{on } \Gamma_u$$

compare with Fig. 2
A point on a crack is modelled with the help of NURBS curves C. Those are defined by a set of N control points $\pi_i := (X_{i,1}, X_{i,2})$, i.e.

$$C(\xi) = \sum_{i=1}^{N} R_i(\xi)(\pi_i)$$

The vector of control points handling the geometrical description of the crack is denoted by $p_N := (\pi_1, ..., \pi_i, ...\pi_N)$. This vector will the sought-for quantity in the inverse crack analysis.

3 CRACK IDENTIFICATION

In the sequel it will be assumed that some structure suffered from cracking due to an extreme load. The task is now, to identify the position and form of the crack, i.e. the exact determination of the entries of the set of control points p_N of the crack by measurements on the boundary of the structure which is assumed to be stressed by moderate loads which do not cause the crack further to grow. We define the following forward operator which maps the control points to displacements on the boundary of the structure

$$F : X \rightarrow Y \tag{5}$$

$$p_N \mapsto (u_1, u_2)_{|\Gamma}. \tag{6}$$

Assuming that y^δ contains measured data with data error level δ, the inverse problems corresponds to solving for p_N in

$$F(p_N) = y^\delta. \tag{7}$$

In (5) X denotes the parameter space, i.e. the space of all possible crack forms and Y the space of measurements (here displacements) which are assumed to in $L^2(\Omega)$. In the sequel, the forward operator or parameter-to-solution map F is assumed to be continuous, differentiable and its Frechét derivative F' to be Lipschitz continuous and normalized such that $||F'(p)|| \leq 1, \ \forall\, p \in D(F)$. For the measured data we further assume, that the following condition holds

$$||y - y^\delta|| \leq \delta,$$

where y are exact data and δ is an upper bound of the data error, assumed to be estimable.
Solving equations of type (7) is not only an inverse but also an ill-posed problem, as existence and uniqueness of the solution are not guaranteed. Additionally, high instability may be introduced due to errors in the data, i.e. small perturbations in the data lead to large perturbations and oscillations in the solution.

This requires the three strategies:

- As existence is not guaranteed, a solutions in the sense of „least-squares" is sought-for,
- As uniqueness is not guaranteed, a close initial guess of the solution needs to be provided,
- As stability is not guaranteed, regularizing methods have to be applied.

3.1 Identification procedure and regularization

In order to solve (7) iterative regularizing methods will be applied. The regularization follows two strategies

1. Regularization by discretization, see e.g. [7, 8]
2. Regularization by early stopping (a posteriori discrepancy principles), see e.g. [8, 9].

Now, for the solution of (7) modified Landweber Methods are run on finite dimensional subspaces X_N of X, i.e. $X_N := Proj_N X$ of X, where $Proj_N$ denotes an orthogonal projection, i.e.

$$X_N \subseteq X, \quad \text{with} \quad X_0 \subseteq X_1 \subseteq ... \subseteq X_N \quad \text{and} \quad \overline{\bigcup_{N\in\mathbb{N}} X_N} = X. \tag{8}$$

Let the union $\cup_{N\in\mathbb{N}} X_N$ be dense in X. The initial guess is denoted by p_0^0 and the first iterate at level N by $p_N^{0,\delta}$, $p^\dagger$ denotes the exact solution. The following local condition is assumed to hold on each discrete subspace X_N

$$||F(p) - F(Proj_N p^\dagger) - F'(p)(p - Proj_N p^\dagger)|| \leq \eta_N ||F(p) - F(Proj_N p^\dagger)|| \tag{9}$$
$$\text{for all } p \in X_N \cap \mathcal{B}_{\rho/2}(Proj_N p^\dagger) \subseteq D(F) \text{ with } \eta_N \leq \frac{1}{4}.$$

Iterations on every level are defined as follows

$$p_N^{k+1,\delta} = p_N^{k,\delta} + \omega_N^{k,\delta} s_N^{k,\delta}, \qquad s_N^{k,\delta} := Proj_N F'(p_N^{k,\delta})^*(y^\delta - F(p_N^k)) \tag{10}$$

where the step-size $\omega_N^{k,\delta}$ is chosen as

$$\omega_N^{k,\delta} := \frac{||y^\delta - F(p_N^{k,\delta})||^2}{||s_N^{k,\delta}||^2}, \tag{11}$$

which renders the discrete classical Landweber iteration a discrete version of the minimal error method, see also [10, 11, 12]. The method can be regarded as a gradient-type iteration with optimal step-length choice. Convergence results and regularizing properties are worked out in [4, 13] under the given conditions, where an application of the same strategy to recover material nonlinearities approximated by cubic splines is reported. Instead of the minimal error update $s_N^{k,\delta}$ an update according to quasi Newton - Methods (Broyden, BFGS) is easily implemented (as we work in finite dimensional spaces). A convergence theory for Broyden's method for ill-posed problems is given in [8], for the BFGS method corresponding results are not known to the author.

The multilevel algorithm is now implemented as follows

1. Start the iterations (10) with an initial guess on the coarsest level (e.g. 2 control points for a straight line approximation of the crack).

2. Run the iterations until an inner discrepancy principle of the type

$$||F(p_N^{k+1,\delta}) - y^\delta|| \leq \tilde{C}_1(\delta + ||(Proj_N - I)p^\dagger||) \tag{12}$$

becomes active or until a maximal number of iterations is reached.

3. Refine, i.e. include additional control points for the crack description and switch to the next finer level.

4. Use the last iterate from the preceding level as initial value, i.e. $p_{N+1}^{0,\delta} := p_N^{k_*(N,\delta),\delta}$.

5. Continue the iterations (10) on the new level.

6. Stop, if on level N the outer discrepancy principle

$$||y^\delta - F(p_N^{k_*(N,\delta),\delta})|| \leq C\delta \leq ||y^\delta - F(p_N^{k,\delta})||, \quad C > 2\frac{1+\eta_N}{1-2\eta_N} > 2.$$

tells to stop or when a maximal number of iterations is reached.

The inner discrepancy principle (12) contains both, an estimate on the data error δ and an estimate of the approximation error as we work on finite dimensional subspace of the true crack forms. For details, see [10, 13].
Quantities like the number of control points, the degree of the splines and measures on the curvature of $p^\dagger$ allow to estimate the term $||(Proj_N - I)p^\dagger||$.
Additional refinements are possible, e.g. the refinement of the number of control points used for the XIGA analysis and increase in the spline orders p_s, q_s.
Remark: The assumed error in the data are genereally not only due to measurement errors but also due to shortcomings of the model. However, in the language of inverse problem theory both measurement and model error are simultaneously estimated by the data error δ.

4 NUMERICAL RESULTS

First numerical results are presented in the following. The shape and loading of the double cantilever beam is according to Fig. 3, where a plane stress state is considered with elasticity modulus $E = 3.0 \times 10^7 \mathrm{N/mm^2}$ and Possion's ratio $\nu = 0.3$. Vertical tensile loads are applied for $X = 0$, $X = \frac{1}{4}L$ and $X = \frac{1}{2}L$. Derivatives of the forward operator with respect to changes in the input parameters (the coordinates of the control points) are computed numerically. A derivation of the linearization and the adjoint operator of it, is work in progress, with which the parameter-updates s_N^k can be implemented more efficiently. Nevertheless, the numerical approach already helps to get an understanding of model-based reconstruction of crack having arbirtrary shapes. For the inner iterations a maximal number of 10 is prescribed. After four refinements, the algorithm stops in case of no data noise, else according to the discrepancy principle. The initially assumed crack, the exact crack and its reconstruction are shown in Figure 4. Figure 5 replots Figure 4 under different scaling together with intermediate solutions at the switch of a coearser to the next finer level.
The following table summarizes error norms ($l2$) for the reconstructed crack and the coresponding residuals for different data noise levels δ.

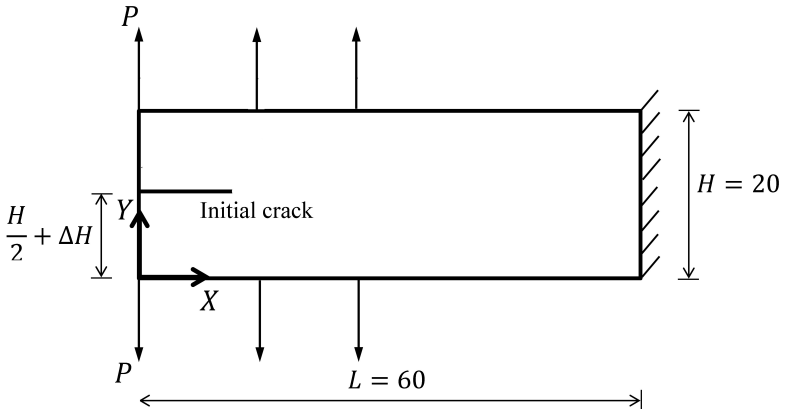

Figure 3: Geometry and loading of the double cantilever beam, previously published in [1].

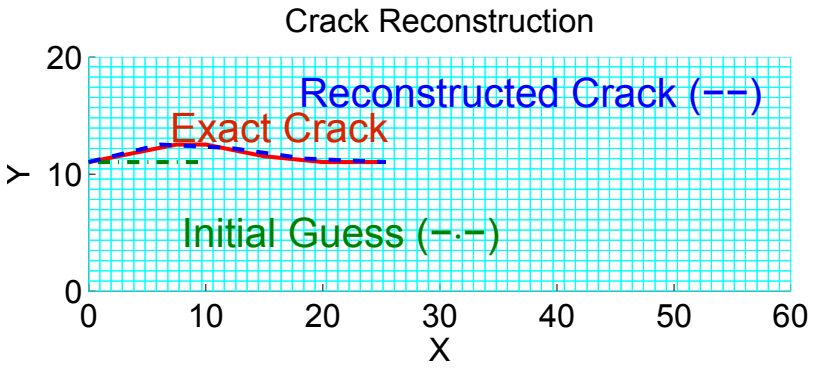

Figure 4: Initial, Exact and Reconstructed Crack

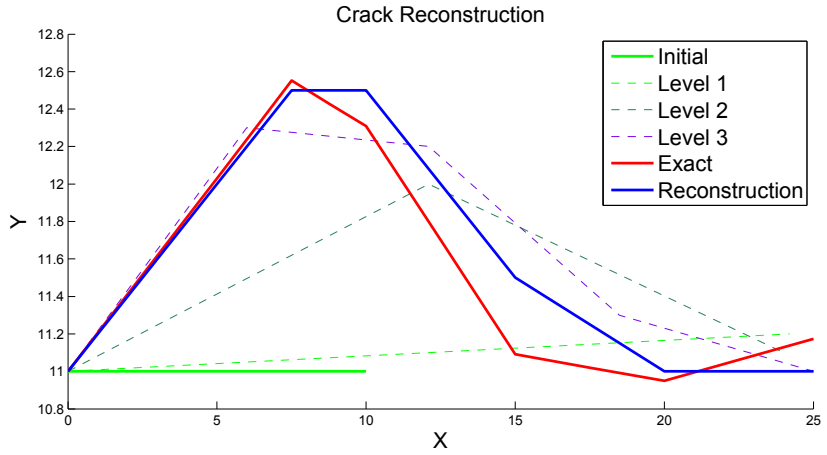

Figure 5: Same as Figure 4 with reconstructed crack a level 4 with intermediate solutions at the end of the iterations on levels $1, 2, 3$.

δ in %	$\|\|p_N^k - Proj_N p^\dagger\|\|$	$\|\|F(p_N^k) - y^\delta\|\|$
0	0.49	0.00075
0.5	0.51	0.00114
1	0.53	0.0015
2	0.62	0.0018
5	1.1	0.0024

Table 1: Errors in parameter and image space between reconstructed and exact solution for different noise level terms

5 SUMMARY, CONCLUSIONS AND OUTLOOK

The combination of the Isogeometric Analysis with the Extended Finite Element Method provides a tool which is extremely useful for inverse crack analysis. The flexibility in geometric descriptions of crack and computational domain and the missing need of remeshing make it a very efficient tool. From the numerical examples, instability during the reconstruction of crack is a critical issue. More pronounced seems however the question of unique identifiability. Analytic answers to this are of utmost importance, in particular for designing the experiment properly. Application of BFGS Newton's method to ill-posed problems needs to be analysed.

6 ACKNOWLEDGMENT

This research is supported by the German Research Institute (DFG) via Research Training Group "Evaluation of Coupled Numerical Partial Models in Structural Engineering (GRK 1462)", which is gratefully acknowledged by the authors.

REFERENCES

[1] S. Sh. Ghorashi, N. Valizadeh, and S. Mohammadi. Extended isogeometric analysis for simulation of stationary and propagating cracks. *Int. J. Numer. Meth. Engng*, 89:1069–1101, 2012.

[2] D. Rabinovich, D. Givoli, and S. Vigdergauz. XFEM-based crack detection scheme using a genetic algorithm. *International Journal for Numerical Methods In Engineering*, (71):1051–1080, 2007.

[3] O. Scherzer. An iterative multi level algorithm for solving nonlinear illposed problems. *Numerische Mathematik*, 80:579–600, 1998. 10.1007/s002110050379.

[4] T. Lahmer. Modified landweber iterations in a multilevel algorithm applied to inverse problems in piezoelectricity. *Journal of Inverse and Ill-Posed Problems*, 17(1), 2009.

[5] E. De Luycker, D. J. Benson, T. Belytschko, Y. Bazilevs, and M. C. Hsu. X-fem in isogeometric analysis for linear fracture mechanics. *International Journal for Numerical Methods in Engineering*, 87(6):541–565, 2011.

[6] S. Sh. Ghorashi, N. Valizadeh, S. Mohammadi, and T. Rabczuk. Extended isogeometric analyis of plates with curved cracks. In *The Eighth International Conference on Engineering Computational Technology, ECT2012, Dubrovnik, Croatioa, 2012*.

[7] B. Kaltenbacher. Regularization by projection with a posteriori discretization level choice for linear and nonlinear ill-posed problems. *Inverse Problems*, 16:1523–1539, 2000. DOI:10.1088/0266-5611/16/5/322.

[8] B. Kaltenbacher, A. Neubauer, and O. Scherzer. *Iterative Regularization Methods for Nonlinear Ill-Posed Problems*. Radon Series on Computational and Applied Mathematics 6. de Gruyter, Berlin - New York, May 2008.

[9] H. W. Engl, M. Hanke, and A. Neubauer. *Regularization of Inverse Problems*. Kluwer, Dordrecht, 1996.

[10] O. Scherzer. An iterative multi level algorithm for solving nonlinear ill-posed problems. *Numer. Math.*, pages :579–600, 1998.

[11] A. Neubauer and O. Scherzer. A convergence rate result for a steepest descent method and a minimal error method for the solution of nonlinear ill-posed problems. *Z. Anal. Anwend.*, 14:369–377, 1995.

[12] O. Scherzer. A convergence analysis of a method of steepest descent and a two-step algorithm for nonlinear ill-posed problems. *Numer. Funct. Anal. and Optimiz.*, pages 197–214, 1996.

[13] T. Lahmer. *Forward and Inverse Problems in Piezoelectricity*. PhD thesis, Friedrich-Alexander University Erlangen-Nuremberg, Germany, 2008.

Binary and ternary Clifford analysis

on

Nonion algebra and su(3)

By

J.Larynowicz*, K.Nouno **, D. Nagayama* and O. Suzuki *****

* *Institute of physics, Lodz University , ul. Pomorska 153/156,Lodz, Poland, Email: jlawryno @uni.lodz, pl*

** *Department of Mathematics, Fukuoka Education University, Munakata Fukuoka, Japan, Email:nouno@fukuoka-edu.ac.jp*

*** *Department of Compute rand System Analysis College of Humanities and Sciences, Nihon University 156 Setagaya,Tokyo,Japan E-mail: osuzuki@cssa.chs.nihon-u.ac.jp*

Keywords: Non-commutative Galois extension, ternary Clifford algebra and analysis

Abstract. *A concept of non-commutative Galois extension is introduced and binary and ternary extensions are chosen. Non-commutative Galois extensions of Nonion algebra and su(3) are constructed. Then ternary and binary Clifford analysis are introduced for non-commutative Galois extensions and the corresponding Dirac operators are associated.*

1. BINARY AND TERNARY NON-COMMUTATIVE GALOIS EXTENSIONS

We introduce a concept of non-commutative Galois extension of binary type and ternary type and state some basic facts on the extensions ([6]).

Basic notations on non-commutative Galois extensions

Let A be an algebra and A' be a subalgebra of A. We make the following definition:

DEFINITION 1

(1) We take an element $\tau \in A$ with the following condition $\tau^k = 1$. The following subalgebra $A'[\tau]$ of A is called non-commutative Galois extension of k-nary type:

$$A'[\sqrt[k]{1}] = \{\sum_{\rho=0}^{k-1} \varsigma_\rho \tau^\rho \mid \varsigma_\rho \in A'\}$$

The extension is called proper when $\tau^\rho \notin A' (\rho = 1,..,k-1)$. In this paper we are

concerned with only proper extensions without mentioning it.

(2)We assume that $A_i = A[\tau_i](i=1,2)$ are subalgebras in a common algebra A_3. When the ismorphism is given by the following multiplication operator: $\theta : A'[\tau_1] \to A'[\tau_2]$, $\theta(\xi) = \xi(\xi \in A')$, $\theta\,\tau_1 = \tau_2(\theta \in A_3)$, it is called θ -equivalent.

(3) We assume the same condition in (2). When the isomorphism is given by the Adjoint operator: $Ad_g\xi\ (\exists g \in A_3)$, $Ad_g\xi = g\,\xi\,g^{-1}., Ad_g\xi' = \xi'\ (\xi' \in A')$. it is called Ad-equivalent.

(4) When $A'[\tau_1] = A'[\tau_2]$ holds, they are called identical each other. When $\tau_1 = \tau_2^2$, then we have the identical extension: $A'[\tau_1] = A'[\tau_2]$.

REMARKS (1) To define the Galois extension structure, we put some additional condition on the algebra: for example, $\xi\,\tau^l = \sum_\alpha \tau^\alpha \xi_\alpha$ holds with some $\xi_\alpha \in A$ for any $\xi \in A, \alpha, l = 1,2,..,k-1$. In this paper we are concerned with the algebra with this condition.

(2) The Galois extension is not unique depending on the choice of τ. We are concerned with the Galois extension which does not depend on the choice $\tau(\neq 1)$.

Examples of binary and ternary extensions

Next we proceed to examples of binary and ternary extensions. We obtain binary and ternary Clifford algebras from Galois extensions $A'[\sqrt[k]{1}]$ (see S.4).

Example 1(Complex numbers)

The first one is the complex number field $R[\sqrt{-1}]$:

$$R[\sqrt{-1}] = \{\theta_1 1 + \theta_2\sqrt{-1} \mid \theta_1, \theta_2 \in R\}$$
$$= \left\{ \begin{pmatrix} \theta_1 & \theta_2 \\ -\theta_2 & \theta_1 \end{pmatrix} \mid \theta_1, \theta_2 \in R \right\}$$

Example 2 (Quaternion number)

The quaternion number field can be obtained by the non-commutative Galios extension of the complex number field $R[\sqrt{-1}]$:

$$C[\sqrt{-1_2}] = \{\theta_1 1 + \theta_2\sqrt{-1_2} \mid \theta_1, \theta_2 \in C\}$$
$$= \left\{ \begin{pmatrix} \theta_1 & \theta_2 \\ \theta_2 & -\theta_1 \end{pmatrix} \mid \theta_1, \theta_2 \in C \right\}$$
$$= \left\{ \begin{pmatrix} \theta_1 & \theta_2 & \theta_3 & \theta_4 \\ -\theta_2 & \theta_1 & \theta_4 & -\theta_3 \\ \theta_3 & \theta_4 & -\theta_1 & -\theta_2 \\ \theta_4 & -\theta_3 & +\theta_2 & -\theta_1 \end{pmatrix} \mid \theta_1, \theta_2, \theta_3, \theta_4 \in R \right\}$$

Example 3 (Cubic root numbers)

We give a basic ternary Galois extension. The simplest example is the complex cubic numbers $R[\sqrt[3]{1}]$

$$R[\sqrt[3]{1}] = \{\theta_1 1 + \theta_2 j + \theta_{32} j^2 \mid \theta_1, \theta_2, \theta_3 \in R\}$$
$$= \left\{ \begin{pmatrix} \theta_1 & \theta_2 & \theta_3 \\ \theta_3 & \theta_1 & \theta_2 \\ \theta_2 & \theta_3 & \theta_1 \end{pmatrix} \mid \theta_1, \theta_2, \theta_3 \in R \right\}$$

In the next section we give ternary extensions in Nonion algebra.

Successive extensions

We consider successive Galois extensions. We take an extension: $A_1 = A_0[\tau_1]$ and make an extension $A_2 = A_1[\tau_2]$. Then we have the successive extension $A_2 = (A_0[\tau_1])[\tau_2]$ as follows: $A_2 = \{\sum x_{i,j} \tau^i{}_1 \tau^j{}_2 \mid x_{i,j} \in A_0\}$ .We can also make the tensor product extension. Namely we can define $A_2 = A_0[\tau_1 \otimes \tau_2]$ by $A_2 = \{\sum x_{i,j} \tau^i{}_1 \otimes \tau^j{}_2 \mid x_{i,j} \in A_0\}$. The example 2 is the tensor product extension.

2. THE GALOIS EXTENSION STRUCTURE ON NONION ALGEBRA

We introduce a concept of Nonion algebra N and discuss ternary Galois extension structures on it. We begin with the definition of Nonion algebra ([1],[4]):

DEFINITION 2

(1)The matrix algebra which is generated by the following 3 matrices over $R[\sqrt[3]{1}]$ is called Nonion algebra:

$$Q_1 = \begin{pmatrix} 0 & j & 0 \\ 0 & 0 & j^2 \\ 1 & 0 & 0 \end{pmatrix} \quad Q_2 = \begin{pmatrix} 0 & j^2 & 0 \\ 0 & 0 & j \\ 1 & 0 & 0 \end{pmatrix} \quad Q_3 = \begin{pmatrix} 0 & 1 & 0 \\ 0 & 0 & 1 \\ 1 & 0 & 0 \end{pmatrix}$$

(2) The matrix algebra which is generated by the following 3 matrices over the real field R is called basic algebra B:

$$T_4 = \begin{pmatrix} 0 & 0 & 1 \\ 0 & 1 & 0 \\ 1 & 0 & 0 \end{pmatrix} \quad T_5 = \begin{pmatrix} 0 & 1 & 0 \\ 1 & 0 & 0 \\ 0 & 0 & 1 \end{pmatrix} \quad T_6 = \begin{pmatrix} 1 & 0 & 0 \\ 0 & 0 & 1 \\ 0 & 1 & 0 \end{pmatrix}$$

(3)The algebra generated by $T_2 (or \ T_3)$ is called cubic algebra and is denoted by B':

$$T_2 = \begin{pmatrix} 0 & 1 & 0 \\ 0 & 0 & 1 \\ 1 & 0 & 0 \end{pmatrix} \qquad T_3 = \begin{pmatrix} 0 & 0 & 1 \\ 1 & 0 & 0 \\ 0 & 1 & 0 \end{pmatrix}$$

(4) The algebra $\tilde{N}$ generated by the following four elements over $R[\sqrt[3]{1}]$ is called the binary extension of N:

$$Q_1 = \begin{pmatrix} 0 & j & 0 \\ 0 & 0 & j^2 \\ 1 & 0 & 0 \end{pmatrix}, \quad Q_2 = \begin{pmatrix} 0 & j^2 & 0 \\ 0 & 0 & j \\ 1 & 0 & 0 \end{pmatrix}, \quad Q_3 = \begin{pmatrix} 0 & 1 & 0 \\ 0 & 0 & 1 \\ 1 & 0 & 0 \end{pmatrix}, \quad T_4 = \begin{pmatrix} 0 & 0 & 1 \\ 0 & 1 & 0 \\ 1 & 0 & 0 \end{pmatrix}$$

Then we can prove the following proposition:

PROPOSITION 3

(1)The following 9 elements constitute linear basis of Nonion algebra:

$$Q_1=\begin{pmatrix}0&j&0\\0&0&j^2\\1&0&0\end{pmatrix}\quad Q_2=\begin{pmatrix}0&j^2&0\\0&0&j\\1&0&0\end{pmatrix}\quad Q_3=\begin{pmatrix}0&1&0\\0&0&1\\1&0&0\end{pmatrix}$$

$$\overline{Q}_1=\begin{pmatrix}0&0&1\\j^2&0&0\\0&j&0\end{pmatrix},\quad \overline{Q}_2=\begin{pmatrix}0&0&1\\j&0&0\\0&j^2&0\end{pmatrix}\quad \overline{Q}_3=\begin{pmatrix}0&0&1\\1&0&0\\0&1&0\end{pmatrix}$$

$$R_1=\begin{pmatrix}1&0&0\\0&1&0\\0&0&1\end{pmatrix},\quad R_2=\begin{pmatrix}1&0&0\\0&j&0\\0&0&j^2\end{pmatrix},\quad R_3=\begin{pmatrix}1&0&0\\0&j^2&0\\0&0&j\end{pmatrix}$$

(2) The following 6 elements are linear basis of B:

$$T_1=\begin{pmatrix}1&0&0\\0&1&0\\0&0&1\end{pmatrix}\quad T_2=\begin{pmatrix}0&1&0\\0&0&1\\1&0&0\end{pmatrix}\quad T_3=\begin{pmatrix}0&0&1\\1&0&0\\0&1&0\end{pmatrix}$$

$$T_4=\begin{pmatrix}0&0&1\\0&1&0\\1&0&0\end{pmatrix}\quad T_5=\begin{pmatrix}0&1&0\\1&0&0\\0&0&1\end{pmatrix}\quad T_6=\begin{pmatrix}1&0&0\\0&0&1\\0&1&0\end{pmatrix}$$

(3) The following 3 elements are linear basis of B'

$$T_1=\begin{pmatrix}1&0&0\\0&1&0\\0&0&1\end{pmatrix}\quad T_2=\begin{pmatrix}0&1&0\\0&0&1\\1&0&0\end{pmatrix}\quad T_3=\begin{pmatrix}0&0&1\\1&0&0\\0&1&0\end{pmatrix}$$

(4) B' is a subalgebra of N, and B is a subalgebra of $\widetilde{N}$.

PROOF

The proofs are direct calculations by use of the following product tables.

	Q_1	Q_2	Q_3	$\overline{Q}_1$	$\overline{Q}_2$	$\overline{Q}_3$	R_1	R_2	R_3
Q_1	$\overline{Q}_1$	$j^2\overline{Q}_3$	$j\ \overline{Q}_2$	R_1	j^2R_3	$j\,R_2$	Q_1	Q_2	Q_3
Q_2	$j\ \overline{Q}_3$	$\overline{Q}_2$	$j^2\overline{Q}_1$	$j\,R_2$	R_1	j^2R_3	Q_2	Q_3	Q_1
Q_3	$j^2\overline{Q}_2$	$j\ \overline{Q}_1$	$\overline{Q}_3$	j^2R_3	$j\,R_2$	R_1	Q_3	Q_1	Q_2
$\overline{Q}_1$	R_1	R_2	R_3	Q_1	j^2Q_3	$j\,Q_2$	$\overline{Q}_1$	$j^2\overline{Q}_3$	$j\ \overline{Q}_2$
$\overline{Q}_2$	R_3	R_1	R_2	$j\,Q_3$	Q_2	j^2Q_1	$\overline{Q}_2$	$j^2\overline{Q}_1$	$j\ \overline{Q}_3$
$\overline{Q}_3$	R_2	R_3	R_1	j^2Q_2	$j\,Q_1$	Q_3	$\overline{Q}_3$	$j^2\overline{Q}_2$	$j\ \overline{Q}_1$
R_1	Q_1	Q_2	Q_3	$\overline{Q}_1$	$\overline{Q}_2$	$\overline{Q}_3$	R_1	R_2	R_3
R_3	j^2Q_2	j^2Q_3	j^2Q_1	$\overline{Q}_3$	$\overline{Q}_1$	$\overline{Q}_2$	R_2	R_3	R_1
R_3	$j\,Q_3$	$j\,Q_1$	$j\,Q_2$	$\overline{Q}_2$	$\overline{Q}_3$	$\overline{Q}_1$	R_3	R_1	R_2

	T_1	T_2	T_3	T_4	T_5	T_6
T_1	T_1	T_2	T_3	T_4	T_5	T_6
T_2	T_2	T_3	T_1	T_5	T_6	T_4
T_3	T_3	T_1	T_2	T_6	T_4	T_5
T_4	T_4	T_6	T_5	T_1	T_3	T_2
T_5	T_5	T_4	T_6	T_2	T_1	T_3
T_6	T_6	T_5	T_4	T_3	T_2	T_1

The explicit construction of binary extension of Nonion algebra

The binary extension $\widetilde{N}$ of N is given as follows:

$$\widetilde{N}=\{x+yT_4\mid x,y\in N\}$$

Then we can give the linear basis of $\widetilde{N}$ as follows:

$$Q_1=\begin{pmatrix}0&j&0\\0&0&j^2\\1&0&0\end{pmatrix}\qquad Q_2=\begin{pmatrix}0&j^2&0\\0&0&j\\1&0&0\end{pmatrix}\qquad Q_3=\begin{pmatrix}0&1&0\\0&0&1\\1&0&0\end{pmatrix}\ (=T_3)$$

$$\overline{Q}_1=\begin{pmatrix}0&0&1\\j^2&0&0\\0&j&0\end{pmatrix},\qquad \overline{Q}_2=\begin{pmatrix}0&0&1\\j&0&0\\0&j^2&0\end{pmatrix},\qquad \overline{Q}_3=\begin{pmatrix}0&0&1\\1&0&0\\0&1&0\end{pmatrix}(=T_2)$$

$$R_1=\begin{pmatrix}1&0&0\\0&1&0\\0&0&1\end{pmatrix}\qquad R_2=\begin{pmatrix}1&0&0\\0&j&0\\0&0&j^2\end{pmatrix}\qquad R_3=\begin{pmatrix}1&0&0\\0&j^2&0\\0&0&j\end{pmatrix}$$

$$Q'_1=\begin{pmatrix}0&0&1\\j^2&0&0\\0&j&0\end{pmatrix},\qquad Q'_2=\begin{pmatrix}0&0&1\\j&0&0\\0&j^2&0\end{pmatrix},\qquad Q'_3=\begin{pmatrix}0&1&0\\1&0&0\\0&0&1\end{pmatrix}$$

$$\overline{Q'}_1=\begin{pmatrix}0&j&0\\0&0&j^2\\1&0&0\end{pmatrix}\qquad \overline{Q'}_2=\begin{pmatrix}0&j^2&0\\0&0&j\\1&0&0\end{pmatrix}\qquad \overline{Q'}_3=\begin{pmatrix}1&0&0\\0&0&1\\0&1&0\end{pmatrix}$$

$$R'_1=\begin{pmatrix}0&0&1\\0&1&0\\1&0&0\end{pmatrix},\qquad R'_2=\begin{pmatrix}0&0&j^2\\0&j&0\\1&0&0\end{pmatrix},\qquad R'_3=\begin{pmatrix}0&0&j\\0&j^2&0\\1&0&0\end{pmatrix}$$

As for the non-commutative Galois structure of Nonion algebra, we can prove the following theorem:

THEOREM I

(1) Nonion algebra is the Galois extension of the algebra B' : $N=B'[\tau]$ by $\tau=R_i(i=2,3),Q_i,\overline{Q}_i(i=1,2,3)\ (\tau^3=1)$.

(2) The Galois extension $\widetilde{N}=N[\sqrt[2]{1}]$ can be expressed as $\widetilde{N}=B[\sqrt[3]{1}]$.

Hence we have the following commutative diagram:

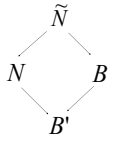

PROOF

(1) We notice that B' is the commutative Galois extension: $B'=R[\sqrt[3]{1}]$.

Choosing $\tau=R_i(i=2,3),Q_i,\overline{Q}_i(i=1,2,3)$, we make the Galois extension $B'[\sqrt[3]{1_3}]$. Then we see that this is identical with N**.**

(2) We notice that B is the non-commutative Galois extension of B' : $B=B'[\sqrt[2]{1}]$, where $\sqrt[2]{1_3}=T_4$. Choosing $\tau=R_2$, we make the Galois extension . Then we see that it is identical with $\widetilde{N}$: $\widetilde{N}=B[\sqrt[3]{1}]$.

THEOREM II

We can prove the following assertions for N :

(1) We have the following ternary Galois extensions which are called basic extension:

$$\begin{cases} A[R]=\{xR_1+yR_2+zR_3 \mid x,y,z\in R[j]\} \\ A[Q_i]=\{xR_1+yQ_i+z\overline{Q}_i \mid x,y,z\in R[j]\}(i=1,2,3) \\ (A[\overline{Q}_i]=\{xR_1+y\overline{Q}_i+zQ_i \mid x,y,z\in R[j]\}(i=1,2,3)) \end{cases}$$

We notice that the extension is unique . Namely we have

$$N=A[R]=A[Q_1]=A[Q_2]=A[Q_3]$$

(2) $Q_i,\overline{Q}_j(i,j=1,2,3)$ give a part of generators of the Galois group of $N:N=B'[\sqrt[3]{1}]$: Namely putting $A_U[R]=\{xR_1+yUR_2+z\overline{U}R_3 \mid x,y,z\in R[j]\}$, where $U=Q_i,\overline{Q}_j(i,j=1,2,3)$, we have Galois extensions (θ -equivalent):

$$\begin{cases} (1) & A_{Q_1}[R]=A[Q_2],\ A_{Q_2}[R]=A[Q_3], \\ & A_{\overline{Q}_1}[R]=A[Q_3],\ A_{\overline{Q}_2}[R]=A[Q_1], \\ (2) & A_{R_2}[Q_1]=A[Q_2],\ A_{R_2}[Q_2]=A[Q_3],\ A_{R_2}[Q_3]=A[Q_1], \\ & A_{\overline{Q}_1}[R]=A[Q_3],\ A_{\overline{Q}_2}[R]=A[Q_1],\ A_{\overline{Q}_3}[R]=A[Q_2], \end{cases}$$

(3) The Ajoint operation gives a part of generators of Galois group of $N=\sqrt[3]{I_n}[B']$ (Ad-equivalent):

$$\begin{cases} Ad_{Q_i}R_1=R_1,\ Ad_{Q_i}R_2=jR_2,\ Ad_{Q_{i1}}R_3=j^2R_3\ (i=1,2,3), \\ Ad_{Q_i}Q_1=Q_1,\ Ad_{Q_i}Q_2=jQ_2,\ Ad_{Q_{i1}}Q_3=j^2Q_3\ (i=1,2,3), \\ Ad_{Q_i}\overline{Q}_1=\overline{Q}_1,\ Ad_{Q_i}\overline{Q}_2=j^2\overline{Q}_2,\ Ad_{Q_{i1}}\overline{Q}_3=j\overline{Q}_3\ (i=1,2,3), \end{cases}$$

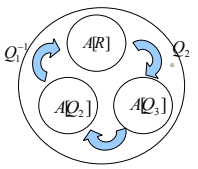

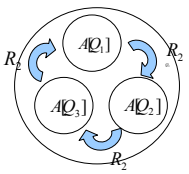

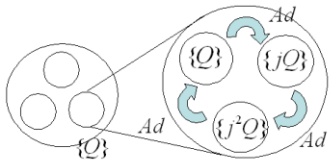

3.THE GALOIS EXTENSION STRUCTRE ON su(3)

In this section we discuss the structure of the Galois extension on su(3).

(1) At first we write up the basis of the algebra ([5]).

$$f_1=\begin{pmatrix} 0 & i & 0 \\ i & 0 & 0 \\ 0 & 0 & 0 \end{pmatrix} \quad f_2=\begin{pmatrix} 0 & -1 & 0 \\ 1 & 0 & 0 \\ 0 & 0 & 0 \end{pmatrix} \quad f_3=\begin{pmatrix} i & 0 & 0 \\ 0 & -i & 0 \\ 0 & 0 & 0 \end{pmatrix}$$

$$f_4=\begin{pmatrix} 0 & 0 & i \\ 0 & 0 & 0 \\ i & 0 & 0 \end{pmatrix},\quad f_5=\begin{pmatrix} 0 & 0 & -1 \\ 0 & 0 & 0 \\ 1 & 0 & 0 \end{pmatrix},\quad f_6=\begin{pmatrix} 0 & 0 & 0 \\ 0 & 0 & i \\ 0 & i & 0 \end{pmatrix} \quad f_7=\begin{pmatrix} 0 & 0 & 0 \\ 0 & 0 & -1 \\ 0 & 1 & 0 \end{pmatrix},\quad f_8=\frac{1}{\sqrt{3}}\begin{pmatrix} 1 & 0 & 0 \\ 0 & 1 & 0 \\ 0 & 0 & -2 \end{pmatrix}$$

(3) We consider the linear subspace L_1 generated by the following 3 elements:

$$L_1: \qquad e_1=\begin{pmatrix}0 & i & 0\\ i & 0 & 0\\ 0 & 0 & 0\end{pmatrix} \qquad e_2=\begin{pmatrix}0 & -1 & 0\\ 1 & 0 & 0\\ 0 & 0 & 0\end{pmatrix} \qquad e_3=\begin{pmatrix}i & 0 & 0\\ 0 & -i & 0\\ 0 & 0 & 0\end{pmatrix}$$

Also we introduce the following two linear subspaces L_2 and L_3:

$$L_2: \qquad e'_1=\begin{pmatrix}0 & 0 & i\\ 0 & 0 & 0\\ i & 0 & 0\end{pmatrix} \qquad e'_2=\begin{pmatrix}0 & 0 & -1\\ 0 & 0 & 0\\ 1 & 0 & 0\end{pmatrix} \qquad e'_3=\begin{pmatrix}i & 0 & 0\\ 0 & 0 & 0\\ 0 & 0 & -i\end{pmatrix}$$

$$L_3: \qquad e''_1=\begin{pmatrix}0 & 0 & 0\\ 0 & 0 & i\\ 0 & i & 0\end{pmatrix}, \qquad e''_2=\begin{pmatrix}0 & 0 & 0\\ 0 & 0 & 1\\ 0 & -1 & 0\end{pmatrix}, \qquad e''_3=\begin{pmatrix}0 & 0 & 0\\ 0 & i & 0\\ 0 & 0 & -i\end{pmatrix}$$

REMARK We notice the following relation $f_8=1/\sqrt{3}(e'_3+e''_3)$. Hence we see that $e_1, e_2, .., e''_3$ constitute the basis of su(3) omitting one of e_3, e'_3, e''_3 .

Then we can prove the following theorem:

THEOREM III

We have the binary and ternary Galois extension structures on su(3):

(1) We have the following Adjoint strucutre on $L_i(i=1,2,3)$.

$$\begin{cases} He_1H^{-1}=-e_2, \ He_2H^{-1}=e_1, \ He_3H^{-1}=e_3, \\ H'e'_1H'^{-1}=e'_2, \ H'e'_2H'^{-1}=-e'_1, \ H'e'_3H'^{-1}=e'_3, \\ H'e''_1H'^{-1}=e''_2, \ H'e''_2H'^{-1}=-e''_1, \ H'e''_3H'^{-1}=e''_3, \end{cases}$$

where

$$H=\begin{pmatrix}1 & 0 & 0\\ 0 & i & 0\\ 0 & 0 & 1\end{pmatrix}, \quad H'=\begin{pmatrix}1 & 0 & 0\\ 0 & 1 & 0\\ 0 & 0 & i\end{pmatrix},$$

(2) We can obtain the following commutation relation:

$$\begin{cases} e_1^2=e_2^2=e_3^2=-1_2 \\ e_1e_2=-e_2e_1=e_3, \ e_2e_3=-e_3e_2=e_1, \ e_3e_1=-e_1e_3=e_2, \end{cases}$$

where $1_2=diag[1,1,0]$. After the central extension, we have the Clifford algebra which is isomorphic to Quaternion algebra. For the case of e'_i and $e''_i(i=1,2,3)$, we have the same assertions. Hence we can define the binary non-commutative Galois structure on $L_i(i=1,2,3)$. We notice that we can introduce three Dirac operators . This is directly connected the three quarks for the Gell-Mann quark model ([5]).

(3) $\{e_i, e'_i, e''_i\}$ $(i=1,2,3)$ constitute the ternary Galois extensions by use of the following Adjoint operators:

$$\begin{cases} G_1e_kG_1^{-1}=e''_k \ (k=1,2,3), \ G_1e'_kG_1^{-1}=e_k \ (k=1,2,3), \\ G_1e''_kG_1^{-1}=e'_k \ (k=1,2), \ G_1e''_3G_1^{-1}=-e'_3 \end{cases}$$

where

$$G_1=\begin{pmatrix}0 & 0 & 1\\ 1 & 0 & 0\\ 0 & 1 & 0\end{pmatrix} (=T_2 \text{ in Proposition 4})$$

(4) Hence su(3) has the following non-commutative Galois extension:

su (3)
$\sqrt[3]{I_3}$
su (2)
$\sqrt[2]{I_3}$
su (1)

(1) $su(3) = L_1 \cup L_2 \cup L_3$

(2) $L_i (i = 1,2,3)$ is isomorphic to su(2) and it is a binary Galois extension $L_i = B_0[\sqrt[2]{1_3}]$ over $B_0 = R[e_3]$

(3) su(3) is a ternary Galois extension $B[\sqrt[3]{1_3}]$ over $B = su(2)$

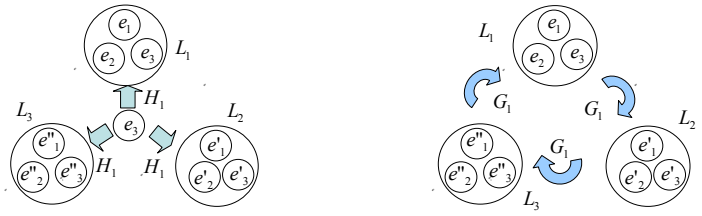

PROOF : The assertions follow from the direct calculations and may be omitted.

4. A METHOD OF NON-COMMUTATIVE GALOIS EXTENSION TO BINARY AND TERNARY CLIFFORD ANALYSIS

In this section we introduce concepts of binary and ternary Clifford algebras and discuss the relationship between the Clifford analysis and non-commutative Galois extensions. We introduce Dirac operators and Klein-Gordon operators for the both Clifford algebras.

(1) Binary Clifford algebras and Galois extensions

We show that a special class of binary Galois extensions introduces binary Clifford algebras. We call the usual Clifford algebra as binary Clifford algebra. Namely we put the following definition:

DEFINITION 4

An algebra with generators $\{T_1, T_2, .., T_n\}$ $(n = 2^r)$ is called binary Clifford algebra, when we have the following commutation relations:

$$T_i T_j + T_j T_i = \pm 2\delta_{ij} 1 \, (i, j = 1,2,..,n) .$$

Then we can introduce the following operators on the n-dimensional Euclidean space:

$$\begin{cases} D = T_1 \dfrac{\partial}{\partial x_1} + T_2 \dfrac{\partial}{\partial x_2} + ... + T_n \dfrac{\partial}{\partial x_n} \\ D^* = T^*_1 \dfrac{\partial}{\partial y_1} + T^*_2 \dfrac{\partial}{\partial y_2} + ... + T^*_n \dfrac{\partial}{\partial y_n} (T^*_j = -T_j (j = 1,2,..,n) \end{cases}$$

The operator is called Dirac operator and its conjugate operators when they satisfy the following condition:

$$\Delta = D^* D = DD^*, \quad \Delta = \mp(\frac{\partial^2}{\partial x_1{}^2} + \frac{\partial^2}{\partial x_2{}^2} + ... + \frac{\partial^2}{\partial x_n{}^2}) \otimes 1_n$$

The operator is called the binary Lapalce operator.

Next we proceed to the connections between non-commutative Galois extensions and binary Clifford algebras. At first we notice that non-commutative Galois extensions do not necessarily define a Clifford algebra (see example below). Hence we can make the following definition:

DEFINITION 5

We take a successive binary non-commutative Galois extension : $\{T_1, T_2, ..., T_n\}(n = 2^p)$. A pair $\{T_a, T_b\}$ is called Clifford pair, when they satisfy the following condition:

$$T_a T_b + T_b T_a = \pm 2\delta^{ab} I_n$$

EXAMPLE: We see that we have only one Clifford pair $\{e_1, e_4\}$ for $C \times C$ Also we see that each pair $\{e_i, e_j\}(i \neq 1, j \neq 1, i \neq j)$ of H is a Clifford pair.

$$C \times C = x_1 e_1 + x_2 e_2 + x_3 e_3 + x_4 e_4$$
$$= \left\{ x_1 \begin{pmatrix} I & 0 \\ 0 & I \end{pmatrix} + x_2 \begin{pmatrix} 0 & J \\ J & 0 \end{pmatrix} + x_3 \begin{pmatrix} J & 0 \\ 0 & J \end{pmatrix} + x_4 \begin{pmatrix} 0 & I \\ -I & 0 \end{pmatrix} \right\}$$

Then we can prove the following theorem:

THEOREM V

When a Clifford algebra A with generators $\{T_1, T_2, ..., T_n\}(n = 2^p)$ is given, then there exists a sequence of successive non-commutative binary Galois extensions which defines the Clifford algebra. Namely we have the following:

$$T_i T_j + T_j T_i = -2\delta_{ij} I_n \Rightarrow A_k = A_{k-1}[\sqrt[2]{-I_n}\,](k = 1,2,..,m)(A = A_m, A_0 = B)$$

PROOF: We prove the assertion by the induction. The quaternion numbers are obtained by the non-commutative Galois extension from the complex numbers. Next we choose a Clifford algebra with generators: $\{T_1, T_2, ..., T_n\}(n = 2^p)$. Putting

$$\hat{T}_i = \begin{pmatrix} T_i & 0 \\ 0 & -T_i \end{pmatrix} (i = 1,2,..,n), \ \hat{T}_{n+1} = \begin{pmatrix} 0 & I \\ -I & 0 \end{pmatrix}, \ \hat{T}_{n+2} = \begin{pmatrix} 0 & J \\ J & 0 \end{pmatrix},$$

we can make a successive binary Galois extension: $A_{n+1} = A_n[\hat{T}_{n+1}], A_{n+2} = A_{n+1}[\hat{T}_{n+2}]$ which also defines a Clifford algebra with the commutation relations: $\hat{T}_i \hat{T}_j + \hat{T}_j \hat{T}_i = -2\delta_{ij} I_{2m}$

(2) Ternary Clifford algebras and Ġalois extensions

Next we proceed to the construction of the ternary Clifford analysis by Galois extensions.

DEFINITION 6

An algebra which is generated by $\{T_1, T_2, T_3\}$ is called ternary Clifford algebra when it satisfies the following commutation relations:

$$\begin{cases} T_a T_b T_c + T_b T_c T_a + T_c T_b T_a = 3\eta^{abc} E_3 \\ \eta^{abc} = \eta^{bca} = \eta^{cab} \\ \eta^{111} = \eta^{222} = \eta^{333} = 1, \eta^{123} = \eta^{231} = \eta^{321} = j^2, \\ \eta^{321} = \eta^{213} = \eta^{132} = j \end{cases}$$

Next we proceed to the derivation of field operators from a ternary Galois extension.

Choosing $\{T_1, T_2, T_3\}$, we introduce the following three operators on the 3-dimensional Euclidean space:

$$\begin{cases} D = T_1 \frac{\partial}{\partial x_1} + T_2 \frac{\partial}{\partial x_2} + T_3 \frac{\partial}{\partial x_3} \\ D^* = T_1 \frac{\partial}{\partial x_1} + j^2 T_2 \frac{\partial}{\partial x_2} + j T_3 \frac{\partial}{\partial x_3} \\ D^{**} = T_1 \frac{\partial}{\partial x_1} + j T_2 \frac{\partial}{\partial x_2} + j^2 T_3 \frac{\partial}{\partial x_3} \end{cases}$$

The operators are called Dirac operator and its conjugate operators when they satisfy the following condition:

$$\Delta = DD^*D^{**}, \quad \Delta = \left(\frac{\partial^3}{\partial x_1^3} + \frac{\partial^3}{\partial x_2^3} + \frac{\partial^3}{\partial x_3^3} - 3\frac{\partial^3}{\partial x_1 \partial x_2 \partial x_3}\right) \otimes 1_3$$

The operator is called the ternary Klein Gordon operator.

(3) Binary and ternary Dirac operators for Nonion algebra:

We begin with introducing the following concept of ternary Clifford triple:

DEFINITION 7

We take a successive ternary non-commutative Galois extension : $\{T_1, T_2, ..., T_n\}\ (n = 3^p)$. A triple $\{T_a, T_b, T_c\}$ is called Clifford triple, when it generate the ternary Clifford algebra:

At first we are concerened with the binary and ternary Dirac operators on B.

PROPOSITION 8

From the linear basis $\{T_1, T_2, T_3\}$ of the algebra B', we can introduce the binary and ternary Dirac operators:

$$\begin{cases} D_t = T_1 \frac{\partial}{\partial y_1} + T_3 \frac{\partial}{\partial y_2} + T_2 \frac{\partial}{\partial y_3} \\ D_t = T_1 \frac{\partial}{\partial y_1} + j T_3 \frac{\partial}{\partial y_2} + j^2 T_2 \frac{\partial}{\partial y_3} \\ D_t = T_1 \frac{\partial}{\partial y_1} + j^2 T_3 \frac{\partial}{\partial y_2} + j T_2 \frac{\partial}{\partial y_3} \end{cases}$$

PROOF: The proof is a direct calculation by use of the table and may be omitted.

We can prove the following theorem:

THEOREM V

(1) The ternary triples $\{X_1, X_2, X_3\}$ which are generated by the linear basis can be listed as follows:

$$\{Q_1,Q_1,Q_1\}\ \{Q_2,Q_2,Q_2\}\ \{Q_3,Q_3,Q_3\}\ \{Q_1,Q_2,Q_3\}\ \{R_2,R_2,R_2\}$$
$$\{R_1,Q_1,\overline{Q}_1\}\ \{R_1,Q_2,\overline{Q}_2\}\ \{R_1,Q_3,\overline{Q}_3\}\ \{R_1,R_1,R_1\}\ \{R_1,R_2,R_3\}$$
$$\{\overline{Q}_1,\overline{Q}_1,\overline{Q}_1\}\ \{\overline{Q}_2,\overline{Q}_2,\overline{Q}_2\}\ \{\overline{Q}_3,\overline{Q}_3,\overline{Q}_3\}\ \{\overline{Q}_1,\overline{Q}_2,\overline{Q}_3\}\ \{\overline{R}_2,\overline{R}_2,\overline{R}_2\}$$

Hence the ternary Dirac operator is defined by the Clifford triple $\{X_1, X_2, X_3\}$:

$$\begin{cases} D_t = X_1\dfrac{\partial}{\partial y_1} + X_3\dfrac{\partial}{\partial y_2} + X_2\dfrac{\partial}{\partial y_3} \\ D_t = X_1\dfrac{\partial}{\partial y_1} + jX_3\dfrac{\partial}{\partial y_2} + j^2X_2\dfrac{\partial}{\partial y_3} \\ D_t = X_1\dfrac{\partial}{\partial y_1} + j^2X_3\dfrac{\partial}{\partial y_2} + jX_2\dfrac{\partial}{\partial y_3} \end{cases}$$

(2) Binary and ternary Dirac operators on su(3)

Next we proceed to the Dirac operators for su(3). From the Clifford structure

$$\begin{cases} e_1^2 = e_2^2 = e_3^2 = -1_2 \\ e_1e_2 = e_2e_1 \quad e_3e_2 = -e_2e_3\,,\ e_1e_3 = -e_3e_1 = e_3, \end{cases}$$

we can introduce the binary Dirac operators: Making the central extension by e_0, we have the Dirac operators for $\{e_0, e_1, e_2, e_3\}$:

$$\begin{cases} D = e_0\dfrac{\partial}{\partial x_0} + e_1\dfrac{\partial}{\partial x_1} + e_2\dfrac{\partial}{\partial x_1}. + e_3\dfrac{\partial}{\partial x_3} \\ \overline{D} = \overline{e}_0\dfrac{\partial}{\partial x_0} + \overline{e}_1\dfrac{\partial}{\partial x_1} + .\overline{e}_2\dfrac{\partial}{\partial x_1} + \overline{e}_3\dfrac{\partial}{\partial x_3} \end{cases}$$

We can obtain the binary Dirac operators for $\{e'_0, e'_1, e'_2, e'_3\}$ in a similar manner. .

Next we proceed to the introduction of the ternary Dirac operator for $\{e_0, e_1, e_2, e_3\}$.

$$\begin{cases} D = T_1\dfrac{\partial}{\partial\theta_1} + G_1\dfrac{\partial}{\partial\theta_2} + G_1^2\dfrac{\partial}{\partial\theta_3} \\ D^* = T_1\dfrac{\partial}{\partial\theta_1} + j^2G_1\dfrac{\partial}{\partial\theta_2} + jG_1^2\dfrac{\partial}{\partial\theta_3} \\ D^{**} = T_1\dfrac{\partial}{\partial\theta_1} + jG_1\dfrac{\partial}{\partial\theta_2} + j^2G_1^2\dfrac{\partial}{\partial\theta_3} \end{cases}$$

For $\{e'_0, e'_1, e'_2, e'_3\}$ and $\{e''_0, e''_1, e''_2, e''_3\}$, we can define the ternary Dirac operator, replacing G_1 with G_2 and G_3 respectively:

$$G_2 = \begin{pmatrix} 0 & j^2 & 0 \\ 0 & 0 & j \\ 1 & 0 & 0 \end{pmatrix}, \qquad G_3 = \begin{pmatrix} 0 & j & 0 \\ 0 & 0 & j^2 \\ 1 & 0 & 0 \end{pmatrix},$$

APPLICATION TO THE THEORY OF ELEMENTARY PARTICLE

We give two applications of a method of non-commutative Galois theory to the theory of elementary particles. The details will be given in another paper.

(1) The generation of elementary particles can be described by use of the Galois extensions. At the very beginning of the universe, there exists only one photon. This can be given the identity matrix. Then particles and anti-particles are produced and mesons are created. This process can be descried by binary extensions. Then the quark-baryon phase transitions happened and baryons are born. This process can be described by the successive binary and ternary Galois extensions . We notice that the following corresponding between the binary and ternary extensions.

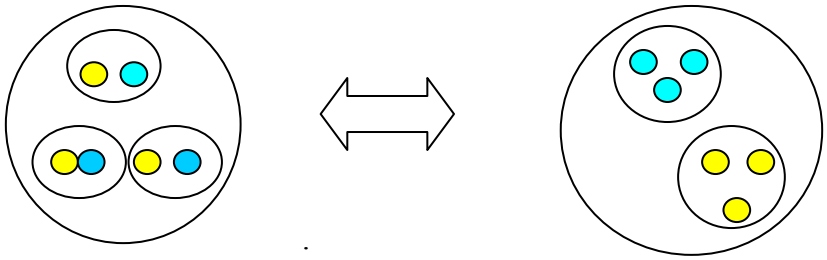

(2) The second application is the construction of quark models. We can realize the Gell-Mann model by use of the Galois extension structure on su(3). In fact we can introduce three quarks by $\{e_0, e_1, e_2, e_3\}$, $\{e'_0, e'_1, e'_2, e'_3\}$ and $\{e''_0, e''_1, e''_2, e''_3\}$. Then we can realize the Gell-Mann model by use of the binary and ternary Galois extensions.

REFERENCE

[1] V.Abramov, R.Kerner, B. Le Roy:Journ. Math. Phys., 38,1650-1669 (1997)

[2]R.Kerner: Journ. Math. Phys. 33, 403-411(1997)

[3] R.Kerner: Class And Quantum Gravity, 14, A203-A 225(2002)

[4] R.Kerner and O.Suzuki:Internal symmetric groups of cubic algebra (To appear)

[5]Gell'Mann and Ne'mann: The eight-fold Way, W.A.Benjamin, INC. New York, Amsterdam (1964)

[6] T.Nakayam and G.Azumaya: Algebra (II) (in Japanese), Iwanami Publisher 1954

19th International Conference on the Application of Computer
Science and Mathematics in Architecture and Civil Engineering
K. Gürlebeck, T. Lahmer and F. Werner (eds.)
Weimar, Germany, 04–06 July 2012

ORTHOGONAL DECOMPOSITIONS AND THEIR APPLICATIONS

H. T. Le*, J. Morais and W. Sprößig

**Freiberg University of Mining and Technology*
Freiberg, Germany
E-mail: lethu@mailserver.tu-freiberg.de

Keywords: Complex quaternion analysis, orthogonal decomposition, boundary value problems.

Abstract. *It is well known that complex quaternion analysis plays an important role in the study of higher order boundary value problems of mathematical physics. Following the ideas given for real quaternion analysis, the paper deals with certain orthogonal decompositions of the complex quaternion Hilbert space into its subspaces of null solutions of Dirac type operator with an arbitrary complex potential. We then apply them to consider related boundary value problems, and to prove the existence and uniqueness as well as the explicit representation formulae of the underlying solutions.*

1 INTRODUCTION AND STATEMENT OF RESULTS

Complex quaternion analysis is an active research subject by itself and it is thought to play an important role in the treatment of 3D and 4D boundary value problems of mathematical physics. A thorough treatment is listed in the bibliography, e.g. K. Gürlebeck and W. Sprößig [4, 6], V. Kravchenko and M. Shapiro [13], V. Kravchenko [14], M. Shapiro and N. Vasilevski [22, 23], and A. Sudbery [30]. This function theory, which involves the study of complex quaternion functions, may also provide the foundations to generalize the classical theory of holomorphic functions of one complex variable onto the multidimensional situation.

During the last years much effort has been done in the study of orthogonal decompositions of quaternion and Clifford Hilbert spaces, starting for example with the works of S. Bernstein [1, 2], B. Goldschmidt [3], K. Gürlebeck and W. Sprößig [4, 5, 6], V. Kravchenko and M. Shapiro [11, 12], E.I. Obolaschvili [16, 17, 18], J. Ryan [19, 20], M. Shapiro and L.M. Tovar [24], F. Sommen and Z. Xu [25], W. Sprößig [26, 28], I. Stern [29], and Z. Xu [33]. Their investigations provide powerful tools to study certain elliptic boundary value problems of partial differential equations within the framework of quaternion and Clifford analyses. So that this research domain has interacted elegantly in numerous problems of mathematical physics (cf. [9, 27, 32]). Those works include, among others, the Laplace, Helmholtz, Maxwell, Schrödinger, Klein-Gordon, Lamé and Stokes (later Navier-Stokes) equations. However, as far as we know, relatively little effort has been done to establish orthogonal decompositions involving complex quaternion Hilbert spaces. Clearly it would be appropriate for us to explore this connection in detail.

This paper is organized as follows. In Section 2 we describe the fundamental solution of the operators $D_{\pm\alpha} = D \pm \alpha$, where D denotes the classical Dirac operator and α is an arbitrary complex constant. As a first step towards we are able to define the Teodorescu and Cauchy-Fueter operators T_α and F_α, which have the same properties as the operators T and F related to the operator D. Let G be a symmetric domain in $\mathbb{R}^3$ with a piecewise smooth Liapunov boundary Γ. In Section 3 we deduce a proper orthogonal decomposition (with complex potential) of the complex quaternion Hilbert space $L^2(G, \mathbb{CH})$:

$$L^2(G, \mathbb{CH}) = \ker D_\alpha \cap L^2(G, \mathbb{CH}) \oplus_{\mathbb{CH}} D_{\overline{\alpha}} \overset{\circ}{W}{}_2^1 (G, \mathbb{CH}). \tag{1}$$

Here $\overset{\circ}{W}{}_2^1(G, \mathbb{CH})$ is the complex quaternion analogue to the Sobolev space $\overset{\circ}{W}{}_2^1(G)$ of functions that vanish on Γ.

We are at liberty to define and give in an explicit manner the corresponding orthoprojections $\mathbf{P}_\alpha$ and $\mathbf{Q}_\alpha$ onto the subspaces of this decomposition. Further investigation shows a closed connection of such decomposition to the following problem:

$$\begin{aligned} (-\Delta + 2Re(\alpha)D + |\alpha|^2)u &= f \quad \text{in } G \\ u &= g \quad \text{on } \Gamma. \end{aligned}$$

In the case of the unique solvability the solution of these boundary value problem can be represented explicitly. Lastly, Section 3 links decomposition (1) to the following Dirichlet problem:

$$\prod_{i=1}^{n\ (l)} D_{\alpha_i} D_{\overline{\alpha}_i} u = f \quad \text{in } G;$$

$$u = g_0,\ D_{\alpha_1} D_{\overline{\alpha}_1} u = g_1, \ldots, D_{\alpha_{n-1}} D_{\overline{\alpha}_{n-1}} \ldots D_{\alpha_1} D_{\overline{\alpha}_1} u = g_{n-1} \quad \text{on } \Gamma$$

where $\prod^{(l)}$ denotes the left product of the underlying sequences. We shall apply the decomposition (1) to prove the existence and uniqueness, and a representation formula for the solution of this boundary value problem, leaving aside for the moment the question of whether the behaviour of the problem is regular and stable. We will follow mainly the notations introduced in [15]. For more details see [4, 26].

2 PRELIMINARIES

We begin by recalling some basic algebraic facts about real and complex quaternions necessary for the sequel. Let $\{e_0, e_1, e_2, e_3\}$ be an orthonormal basis of the Euclidean vector space $\mathbb{R}^4$ with the (quaternionic) product given according to the multiplication rules: $e_1^2 = e_2^2 = e_3^2 = -1$; $e_1e_2 = e_3$, $e_2e_3 = e_1$, and $e_3e_1 = e_2$. This noncommutative product generates the algebra of real quaternions denoted by $\mathbb{H}$. We put $e_0 = 1$, the latter being the identity element. The real vector space $\mathbb{R}^4$ will be embedded in $\mathbb{H}$ by identifying the element $a = (a_0, a_1, a_2, a_3) \in \mathbb{R}^4$ with the element $a = \sum_{j=0}^{3} a_j e_j$ of the algebra. Throughout our presentation, we denote the algebra of quaternions with complex coefficients by $\mathbb{CH}$, where its elements are in the form $a = a^1 + ia^2$, where a^1 and a^2 are real quaternions, and $ie_j = e_j i$, $(j = 1, \ldots, 3)$. In this sense real numbers, complex numbers, and real quaternions can be regarded as special cases of complex quaternions. It is fairly known as the *algebra of complex quaternions* (terminology due to W. Hamilton).

The conjugation corresponding to $\mathbb{CH}$ is readily given by

$$\overline{a}^{\mathbb{CH}} := \overline{a^1} - i\overline{a^2} = \sum_{j=0}^{3} \left(a_j^1 \overline{e_j} - i a_j^2 \overline{e_j}\right), \quad a_j^1, a_j^2 \in \mathbb{R}.$$

We consider functions defined on G and taking values in the algebra of complex quaternions. A complex quaternion-valued function $f : G \longrightarrow \mathbb{CH}$ or, briefly, an $\mathbb{CH}$-valued function will take the following form

$$f(x) = f_0(x) + f_1(x)e_1 + f_2(x)e_2 + f_3(x)e_3 =: f_0(x) + \mathbf{f}(x),$$

where f_l $(l = 0, 1, 2, 3)$, are complex-valued functions defined on G. The spaces $L^2(G, \mathbb{CH})$, $W_2^k(G, \mathbb{CH})$ and $C^{0,\beta}(\Gamma, \mathbb{CH})$ are defined componentwise respectively as the Lebesgue space of all $\mathbb{CH}$-valued functions whose square is Lebesgue integrable in G, the Sobolev space of k-times differentiable $\mathbb{CH}$-valued functions whose k-th derivative belongs to $L^2(G, \mathbb{CH})$, and the Hölder continous $\mathbb{CH}$-valued function space with the exponent β.

We now turn our attention to some simple considerations that are necessary in our study of orthogonal decompositions in complex quaternion Hilbert spaces. Let us denote by $D = \sum_{k=1}^{3} \partial_k e_k$ the classical Dirac operator, and let G be a symmetric domain relative to the origin with a piecewise smooth Liapunov boundary Γ.

In the complex quaternion Hilbert space $L^2(G, \mathbb{CH})$ we consider the following inner product using the complex quaternion conjugation:

$$(u, v)_{\mathbb{CH}} := \int_G \overline{u(x)}^{\mathbb{CH}} v(x) dG_x, \quad u, v \in L^2(G, \mathbb{CH}).$$

Recall the basic fact that two elements u and v are called *orthogonal* if and only if $(u,v)_{\mathbb{CH}}=0$. We proceed by finding the orthogonal decomposition for the Dirac type operator $D_\alpha = D+\alpha$ [10], where α is an arbitrary complex constant. First of all, we describe the fundamental solution of this operator from the well known fundamental solution of the Helmholtz type operator $\Delta+\alpha^2 I$. As usual, I denotes the identity operator.

Recall from [8, 10] (cf. [9, 31]) that in case $\alpha\in\mathbb{C}$ the fundamental solutions of the Helmholtz type operator are given, respectively, by

$$\Theta_\alpha(x):=-\frac{1}{4\pi|x|}e^{-i\alpha|x|},\qquad \widetilde{\Theta}_\alpha(x):=-\frac{1}{4\pi|x|}e^{i\alpha|x|},$$

for $x\in\mathbb{R}^3\setminus\{(0,0,0)\}$. In greater detail, from the factorization of the Helmholtz operator

$$\Delta+\alpha^2=(D+\alpha)(-D+\alpha)$$

it follows $(-D+\alpha)\Theta_\alpha\in\ker(D+\alpha)$, and $-(D+\alpha)\Theta_\alpha\in\ker(D-\alpha)$. We have, in effect, the following fundamental solutions of the Dirac type operators $D_{\pm\alpha}:=D\pm\alpha$ related to $\Theta_\alpha(x)$:

$$K_\alpha(x)=(\alpha+\frac{x}{|x|^2}+i\alpha\frac{x}{|x|})\Theta_\alpha(x),\qquad K_{-\alpha}(x)=(-\alpha+\frac{x}{|x|^2}+i\alpha\frac{x}{|x|})\Theta_\alpha(x),$$

and $\widetilde{\Theta}_\alpha(x)$:

$$\widetilde{K}_\alpha(x)=(\alpha+\frac{x}{|x|^2}-i\alpha\frac{x}{|x|})\widetilde{\Theta}_\alpha(x),\qquad \widetilde{K}_{-\alpha}(x)=(-\alpha+\frac{x}{|x|^2}-i\alpha\frac{x}{|x|})\widetilde{\Theta}_\alpha(x).$$

We proceed by finding the complex quaternion conjugations of the above functions. Keeping in mind that the functions Θ_α and $\widetilde{\Theta}_\alpha$ contain the scalar variable $|x|$ and complex numbers only, then their complex quaternion conjugations are defined as follows:

$$\overline{\Theta_\alpha(x)}^{\mathbb{CH}}=\widetilde{\Theta}_{\overline{\alpha}}(x),\qquad \overline{\widetilde{\Theta}_\alpha(x)}^{\mathbb{CH}}=\Theta_{\overline{\alpha}}(x).$$

That leads to the complex quaternion conjugations of the fundamental solutions $K_\alpha(x)$ and $\widetilde{K}_\alpha(x)$:

$$\overline{K_\alpha(x)}^{\mathbb{CH}}=\widetilde{K}_{\overline{\alpha}}(-x),\qquad \overline{\widetilde{K}_\alpha(x)}^{\mathbb{CH}}=K_{\overline{\alpha}}(-x).$$

In the sequel, let Γ' be an arbitrary parallel surface to Γ. Following [7, 6], the set of functions $\varphi^l:=K_\alpha(y-x^l)$ is complete in $\ker(D+\alpha)\cap L^2(G,\mathbb{CH})$, where $\{x^l\}$ is a dense set on Γ'. We proceed by introducing the operators T_α and F_α with the fundamental solution described beforehand as its kernel:

$$(T_\alpha u)(x):=-\int\limits_G \widetilde{K}_\alpha(x-y)u(y)dG_y,\qquad (F_\alpha u)(x):=\int\limits_\Gamma \widetilde{K}_\alpha(x-y)n(y)u(y)d\Gamma_y.$$

They are known as the *Teodorescu transform* and *Cauchy-Fueter type operator*, respectively. As usual, $n(y)=\sum_{k=1}^3 n_k e_k$ is the outer normal on Γ at the point y. We must bear in mind that the *Plemelj-Sokhotzki formulae* (see e.g. [6, 26]) remain true for the operator F_α. As an aside, we may then define the so called Plemelj projections P_α and Q_α [6, 26] onto the space of square

integrable functions that have a $D_\alpha-$holomorphic extension into the domains G or $\mathbb{R}^3 \setminus \overline{G}$, and vanish at infinity.

Ultimately, let $u \in C^{0,\beta}(\Gamma, \mathbb{CH})$ $(0 < \beta \leq 1)$, it holds

$$n.t. - \lim_{t \to x,\, t \in G} (F_\alpha u)(t) = (P_\alpha u)(x),$$

and

$$n.t. - \lim_{t \to x,\, t \notin \overline{G}} (F_\alpha u)(t) = -(Q_\alpha u)(x)$$

where the notation $n.t.$-limit means nontangential limit.

Remark 2.1. From the above-mentioned relations of the fundamental solutions K_α and $\widetilde{K}_\alpha$, the kernel of the Teodorescu transform and Cauchy-Fueter type operator can also be chosen by K_α with similar results.

3 AN ORTHOGONAL DECOMPOSITION FORMULA WITH COMPLEX POTENTIAL

Let G denote an arbitrary symmetric domain relative to the origin. We begin by introducing an orthogonal decomposition (Theorems 3.1 below) of the complex quaternion Hilbert space $L^2(G, \mathbb{CH})$ into its subspaces of null solutions of the corresponding Dirac operator invoking orthogonality with complex potential.

Using the classical Hopf maximum principle [21], it follows the result.

Theorem 3.1. *The Hilbert space $L^2(G, \mathbb{CH})$ permits the following orthogonal decomposition:*

$$L^2(G, \mathbb{CH}) = \ker D_\alpha \cap L^2(G, \mathbb{CH}) \oplus_{\mathbb{CH}} D_{\overline{\alpha}} \overset{\circ}{W}{}_2^1 (G, \mathbb{CH}).$$

Proof. Following the ideas given in [6, 26], we set $X_1 := \ker D_\alpha \cap L^2(G, \mathbb{CH})$ and $X_2 := L^2(G, \mathbb{CH}) \ominus_{\mathbb{CH}} X_1$. For each function $u \in X_2$ there exists a function $v \in W_2^1(G, \mathbb{CH})$ so that $u = D_{\overline{\alpha}} v$. For an arbitrary $\varphi \in X_1$ we then have

$$\begin{aligned}
0 &= (u, \varphi)_{\mathbb{CH}} := \int_G \overline{u}^{\mathbb{CH}} \varphi dG_y = \int_G \overline{(D + \overline{\alpha})v}^{\mathbb{CH}} \varphi dG_y = \int_G \overline{Dv}^{\mathbb{CH}} \varphi dG_y + \int_G \overline{v}^{\mathbb{CH}} \alpha \varphi dG_y \\
&= \int_G \overline{D(v^1 + iv^2)}^{\mathbb{CH}} \varphi dG_y + \int_G \overline{v}^{\mathbb{CH}} \alpha \varphi dG_y \\
&= \int_G \sum_{k=1}^{3} \sum_{j=0}^{3} \overline{\partial_k e_k v_j^1 e_j + i \partial_k e_k v_j^2 e_j}^{\mathbb{CH}} \varphi dG_y + \int_G \overline{v}^{\mathbb{CH}} \alpha \varphi dG_y \\
&= \sum_{k=1}^{3} \sum_{j=0}^{3} \int_G (\partial_k \overline{e_j} v_j^1 \overline{e_k} - i \partial_k \overline{e_j} v_j^2 \overline{e_k}) \varphi dG_y + \int_G \overline{v}^{\mathbb{CH}} \alpha \varphi dG_y \\
&= -\sum_{k=1}^{3} \sum_{j=0}^{3} \int_G (\overline{e_j} e_k \partial_k v_j^1 - i \overline{e_j} e_k \partial_k v_j^2) \varphi dG_y + \int_G \overline{v}^{\mathbb{CH}} \alpha \varphi dG_y
\end{aligned}$$

$$
\begin{aligned}
&= \sum_{k=1}^{3}\sum_{j=0}^{3}\left[\int_G (\overline{e_j}v_j^1\partial_k e_k\varphi - i\overline{e_j}v_j^2\partial_k e_k\varphi)dG_y - \int_\Gamma (\overline{e_j}e_k v_j^1 n_k\varphi - i\overline{e_j}e_k v_j^2 n_k\varphi)d\Gamma_y\right] \\
&\qquad + \int_G \overline{v}^{\mathbb{CH}}\alpha\varphi dG_y \\
&= \int_G \overline{v}^{\mathbb{CH}} D\varphi dG_y + \int_G \overline{v}^{\mathbb{CH}}\alpha\varphi dG_y - \int_\Gamma \overline{v}^{\mathbb{CH}} n(y)\varphi(y)d\Gamma_y \\
&= \int_G \overline{v}^{\mathbb{CH}} D_\alpha\varphi dG_y + \int_\Gamma \overline{v}^{\mathbb{CH}}\overline{n(y)}^{\mathbb{CH}}\varphi(y)d\Gamma_y = \overline{\int_\Gamma \overline{\varphi}^{\mathbb{CH}} n(y)v(y)d\Gamma_y}^{\mathbb{CH}}.
\end{aligned}
$$

If we substitute $\varphi := K_\alpha(y - x^l)$, and use the relation $\overline{K_\alpha(y-x^l)}^{\mathbb{CH}} = \widetilde{K}_{\overline{\alpha}}(x^l - y)$ then $(F_{\overline{\alpha}}v)(x^l) = 0$, $x^l \in \Gamma'$. That means $tr_\Gamma v \in imP_{\overline{\alpha}} \cap W_2^{\frac{1}{2}}(\Gamma, \mathbb{CH})$. Hence, there exists a function $h \in \ker D_{\overline{\alpha}} \cap W_2^1(G, \mathbb{CH})$ so that $tr_\Gamma h = tr_\Gamma v$. So far, let $w := v - h \in \overset{\circ}{W}{}_2^1(G, \mathbb{CH})$ then $u = D_{\overline{\alpha}}v = D_{\overline{\alpha}}w \in D_{\overline{\alpha}}\overset{\circ}{W}{}_2^1(G, \mathbb{CH})$. □

Many results that follow, and in particular the following theorem for the existence of two orthoprojections onto the occurring subspaces, are related in one way or another to the previous orthogonal decomposition.

Theorem 3.2. *There exist the orthoprojections*

$$
\begin{aligned}
&\mathbf{P}_\alpha : L^2(G, \mathbb{CH}) \longmapsto \ker D_\alpha \cap L^2(G, \mathbb{CH}), \\
&\mathbf{Q}_\alpha : L^2(G, \mathbb{CH}) \longmapsto D_{\overline{\alpha}}\overset{\circ}{W}{}_2^1(G, \mathbb{CH}) \cap L^2(G, \mathbb{CH})
\end{aligned}
$$

with $\mathbf{Q}_\alpha = I - \mathbf{P}_\alpha$. *Furthermore we have*

$$
\mathbf{P}_\alpha = F_\alpha(tr_\Gamma T_{\overline{\alpha}}F_\alpha)^{-1}tr_\Gamma T_{\overline{\alpha}}
$$

with $\ker \mathbf{P}_\alpha = D_{\overline{\alpha}}\overset{\circ}{W}{}_2^1(G, \mathbb{CH})$, *and* $im\mathbf{P}_\alpha = \ker D_\alpha \cap L^2(G, \mathbb{CH})$.

Proof. We refer to [4, 6, 15] for the proof. □

We are now able to consider the related boundary value problem expressed as follows:

$$
\begin{aligned}
D_\alpha D_{\overline{\alpha}}u &= f \quad \text{in } G, \\
u &= g \quad \text{on } \Gamma
\end{aligned}
$$

where $D_\alpha D_{\overline{\alpha}} = -\Delta + 2Re(\alpha)D + |\alpha|^2$ does not contain any complex term. The following theorem can be proved.

Theorem 3.3. *Let* $f \in W_2^k(G, \mathbb{CH})$ *and* $g \in W_2^{k+\frac{3}{2}}(\Gamma, \mathbb{CH})$, *then the Dirichlet problem*

$$
\begin{aligned}
(-\Delta + 2Re(\alpha)D + |\alpha|^2)u &= f \quad \text{in } G, \\
u &= g \quad \text{on } \Gamma
\end{aligned}
$$

has the unique solution

$$u = F_{\overline{\alpha}} g + T_{\overline{\alpha}} \mathbf{P}_\alpha D_{\overline{\alpha}} h + T_{\overline{\alpha}} \mathbf{Q}_\alpha T_\alpha f,$$

where h denotes a $W_2^{k+2}(G, \mathbb{CH})$-extension of g.

Proof. We seek to show that this function satisfies the Dirichlet problem. The first equation can be rewritten as $D_\alpha D_{\overline{\alpha}} u = f$. In addition, notice that

$$D_\alpha T_\alpha = I, \quad D_\alpha \mathbf{Q}_\alpha = D_\alpha, \quad D_\alpha \mathbf{P}_\alpha = 0, \quad D_\alpha F_\alpha = 0.$$

A direct computation shows that

$$\begin{aligned} D_\alpha D_{\overline{\alpha}} u &= D_\alpha D_{\overline{\alpha}} F_{\overline{\alpha}} g + D_\alpha D_{\overline{\alpha}} T_{\overline{\alpha}} \mathbf{P}_\alpha D_{\overline{\alpha}} h + D_\alpha D_{\overline{\alpha}} T_{\overline{\alpha}} \mathbf{Q}_\alpha T_\alpha f \\ &= D_\alpha T_\alpha f = f. \end{aligned}$$

This function satisfies also the boundary condition. The proof of the uniqueness may be found in [6].

□

In particular, if α is a pure complex number that means $\alpha := i\lambda$ $(\lambda \in \mathbb{R})$ a similar result as in [15] can be obtained:

$$L^2(G, \mathbb{CH}) = \ker D_{i\lambda} \cap L^2(G, \mathbb{CH}) \oplus_{\mathbb{CH}} D_{-i\lambda} \overset{\circ}{W}{}_2^1 (G, \mathbb{CH}).$$

Following the ideas given in [6, 26] we can now consider more general boundary value problems (of order $2n$) in $\mathbb{R}^3$ involving complex potentials. For the convenience, we denote the *left-* and *right-products of the sequences* respectively by

$$\prod_{i=k}^{m\ (l)} A_i := A_m A_{m-1} \dots A_k \,, \qquad \prod_{i=k}^{m\ (r)} A_i := A_k A_{k+1} \dots A_m \,.$$

In the sequel, let α_i $(i = 1, \dots, n)$ be arbitrary complex numbers, then we have:

Theorem 3.4. *Let $f \in L^2(G, \mathbb{CH})$ and $g_i \in W_2^{2n-\frac{4i+1}{2}}(\Gamma, \mathbb{CH})$ $(i = 0, \dots, n-1)$ then the Dirichlet problem*

$$\begin{aligned} &\prod_{i=1}^{n\ (l)} D_{\alpha_i} D_{\overline{\alpha}_i} u = f \quad \text{in } G; \\ &u = g_0,\ D_{\alpha_1} D_{\overline{\alpha}_1} u = g_1,\ \dots, D_{\alpha_{n-1}} D_{\overline{\alpha}_{n-1}} \dots D_{\alpha_1} D_{\overline{\alpha}_1} u = g_{n-1} \quad \text{on } \Gamma \end{aligned}$$

has the unique solution $u \in W_2^{2n}(G, \mathbb{CH})$ given explicitly by the formula

$$u = r_1(g_0) + T_{\overline{\alpha}_1} \mathbf{Q}_{\alpha_1} T_{\alpha_1} r_2(g_1) + \dots + \prod_{i=1}^{n-1\ (r)} T_{\overline{\alpha}_i} \mathbf{Q}_{\alpha_i} T_{\alpha_i} r_n(g_{n-1}) + \prod_{i=1}^{n\ (r)} T_{\overline{\alpha}_i} \mathbf{Q}_{\alpha_i} T_{\alpha_i} f,$$

where with $k = 1, \dots, n$

$$r_k(g_{k-1}) := F_{\overline{\alpha}_k} g_{k-1} + T_{\overline{\alpha}_k} F_{\alpha_k} \left(tr_\Gamma T_{\overline{\alpha}_k} F_{\alpha_k}\right)^{-1} Q_{\overline{\alpha}_k} g_{k-1}.$$

In general, if we assume that $(\alpha_k,\ \beta_k)$ $(k = 1, \ldots, n)$ are pairs of complex numbers, which are chosen such that the boundary value problems

$$\begin{aligned} D_{\alpha_k} D_{\beta_k} u &= f_k \quad \text{in } G, \\ u &= g_{k-1} \quad \text{on } \Gamma \quad (k = 1, \ldots, n), \end{aligned}$$

are uniquely solvable, and $\mathbf{P}_{\alpha_k\beta_k}, \mathbf{Q}_{\alpha_k\beta_k}$ are projections defined by

$$\begin{aligned} \mathbf{P}_{\alpha_k\beta_k} &= F_{\alpha_k} \left(tr_\Gamma T_{\beta_k} F_{\alpha_k}\right)^{-1} tr_\Gamma T_{\beta_k}, \\ \mathbf{Q}_{\alpha_k\beta_k} &= I - \mathbf{P}_{\alpha_k\beta_k}. \end{aligned}$$

In this sense the previous theorem can be generalized and stated as follows:

Theorem 3.5. *Let $f \in L^2(G, \mathbb{CH})$ and $g_i \in W_2^{2n-\frac{4i+1}{2}}(\Gamma, \mathbb{CH})$ $(i = 0, \ldots, n-1)$, then the unique solution of the Dirichlet problem*

$$\begin{aligned} &\prod_{i=1}^{n\ (l)} D_{\alpha_i} D_{\beta_i} u = f \quad \text{in } G; \\ &u = g_0,\ D_{\alpha_1} D_{\beta_1} u = g_1,\ \ldots, D_{\alpha_{n-1}} D_{\beta_{n-1}} \ldots D_{\alpha_1} D_{\beta_1} u = g_{n-1} \quad \text{on } \Gamma \end{aligned}$$

has the explicit representation

$$u = r_1(g_0) + T_{\beta_1} \mathbf{Q}_{\alpha_1\beta_1} T_{\alpha_1} r_2(g_1) + \ldots + \prod_{i=1}^{n-1\ (r)} T_{\beta_i} \mathbf{Q}_{\alpha_i\beta_i} T_{\alpha_i} r_n(g_{n-1}) + \prod_{i=1}^{n\ (r)} T_{\beta_i} \mathbf{Q}_{\alpha_i\beta_i} T_{\alpha_i} f,$$

where

$$r_k(g_{k-1}) := F_{\beta_k} g_{k-1} + T_{\beta_k} F_{\alpha_k} \left(tr_\Gamma T_{\beta_k} F_{\alpha_k}\right)^{-1} Q_{\beta_k} g_{k-1}.$$

REFERENCES

[1] S. Bernstein, *Fundamental solutions of Dirac type operators*, Banach Center Publications, Banach Center Symposium: Generalizations of Complex Analysis, May 30 - July 1 1994, Warsaw, 1996, 37: pp. 159–172 (1996).

[2] S. Bernstein, *On the left linear Riemann problem in Clifford analysis*, Bull. Belg. Math. , 1996, Soc. 3: pp. 557–576.

[3] B. Goldschmidt, *Existence and representation of solutions of a class of elliptic systems of partial differential equations of first order in the space*, Math. Nachr., 1982, 108: pp. 159–166.

[4] K. Gürlebeck and W. Sprößig, *Quaternionic Analysis and Elliptic Boundary Value Problems*, Akademie-Verlag, Berlin, 1989.

[5] K. Gürlebeck and W. Sprößig, *Clifford-Analysis and Elliptic Boundary Value Problems*, In R. Ablamowicz and P. Lounsto (eds.) Clifford algebras and Spinor Structures, Kluwer Academic Publ., 1995, pp. 325–334.

[6] K. Gürlebeck and W. Sprößig, *Quaternionic and Clifford Calculus for Physicists and Engineers*, John Wiley and Sons, Chichester, 1997.

[7] K. V. Khmelnytskaya, V. Kravchenko and V. S. Rabinovich, *Quaternionic fundamental solutions for the numerical analysis of electromagnetic scattering problems*, 2002.

[8] V. Kravchenko and M. Shapiro, *Helmholtz Operator with a Quaternionic Wave Number and Associated Function Theory. II. Integral Representations*, Acta Applicandae Mathematicae 32, 1993, pp. 243–265.

[9] V. Kravchenko and M. Shapiro, *On a generalized system of equations of Cauchy-Riemann type with quaternionic parameters*, Matematika, Doklady Akademii Nauk, 1993, v. 329, Nr. 5, pp. 547–549 (Russian).

[10] V. Kravchenko and M. Shapiro, *Integral representations for spatial models of mathematical physics*, Addison Wesley Longman Inc., 1996.

[11] V. Kravchenko and M. Shapiro, *Helmholtz operator with a quaternionic wave number and associated function theory II*, Integral representations. Acta Applicandae Mathematicae 32, 1993, No. 3: pp. 243–265.

[12] V. Kravchenko and M. Shapiro, *On a generalized system of equations of Cauchy-Riemann type with quaternionic parameters*, Doklady Akademii Nauk 329, 1993, Nr. 5:547-549 (Russian).

[13] V. Kravchenko and M. Shapiro. *Integral Representations for Spatial Models of Mathematical Physics*, Research Notes in Mathematics, Pitman Advanced Publishing Program, London, 1996.

[14] V. Kravchenko. *Applied quaternionic analysis. Research and Exposition in Mathematics*, Lemgo: Heldermann Verlag, 2003.

[15] H. T. Le, J. Morais and W. Sprößig, *An orthogonal decomposition of the complex quaternionic valued Hilbert space and its applications*, Proceedings of the 9th International Conference on Clifford Algebras and their Applications in Mathematical Physics, 2011, 10 pp.

[16] E. I. Obolaschvili, *Multidimensional generalized holomorphic vectors*, Diff. Uravnenija. tom 11, 1975, No. 1: pp. 108–115.

[17] E. I. Obolaschvili, *Effective solutions of some boundary value problems in two and three dimensional cases*, Funct. Anal. Methods in Compl. Anal. and Applications to PO, Trieste, 1988, pp. 149–172.

[18] E. I. Obolaschvili, *Boundary and initial value problems in Clifford analysis*, In Sproessig W. and Gürlebeck K. (eds) Proceedings of the Symposium "Analytical and Numerical Methods in Quaternionic and Clifford Analysis" held at Seiffen, Germany i996, University of Mining and Technology Freiberg, 1997, pp. 145–152.

[19] J. Ryan, *Clifford analysis with generalized elliptic and quasifunctions*, Applicable Analysis 13, 1982, pp. 151–171.

[20] J. Ryan, *Cauchy-Green Type Formula in Clifford Analysis*, University of Arkansas, Transactions of the AMS 347, 1995, pp. 1331–1341 (1995).

[21] I. A. Schischmarov, *Introduction in the theory of elliptic equations*, Moscow University Publ., 1979 (russian).

[22] M. Shapiro and N. L. Vasilevski, *Quaternionic ψ-hyperholomorphic functions, singular operators and boundary value problems I*, Complex Variables, Theory Appl., 1995.

[23] M. Shapiro and N. L. Vasilevski, *Quaternionic ψ-hyperholomorphic functions, singular operators and boundary value problems II*, Complex Variables, Theory Appl., 1995.

[24] M. Shapiro and L. M. Tovar, *On a Class of Integral Representations Related to the Two-Dimensional Helmholtz Operator*, Contemporary Mathematics, 1998, Vol. 213: pp. 229–244.

[25] F. Sommen and Z. Xu, *Fundamental solutions for operators which are polynomials in the Dirac operator*, In: Micali A., Boudet R. and Helmstetter J. (eds), Clifford algebras and their applications in mathematical physics. Kluwer, Dordrecht, 1992, pp. 313–326.

[26] W. Sprößig, *On decompositions of the Clifford Valued Hilbert Space and their Applications to Boundary Value Problems*, Advances in Applied Clifford Algebras, 1995, Vol. 5, No. 2, pp. 167–186.

[27] W. Sprößig, *Boundary Value Problems treated with methods of Clifford analysis*, Contemporary Mathematics, 1998, Vol. 212, pp. 255–268.

[28] W. Sprößig, *Forecasting equations in complex-quaternionic setting*, In: T. E. Simos; Recent Advances in Computational and Applied Mathematics, European Academy of sciences, 2011, pp. 273–287.

[29] I. Stern, *Direct Methods for Generalized Cauchy-Riemann Systems in the Space*, Complex Variables, 1993, Vol. 23. 73-100.

[30] A. Sudbery. *Quaternionic analysis*, Math. Proc. Cambridge Phil. Soc. 85, 1979, pp. 199–225.

[31] V. S. Vladimirov, *Equations of mathematical physics*, N.Y.: Marcel Dekker, 1971, Engl. transl. of the first edition.

[32] U. Wimmer, *Orthogonal Decomposition of the space $L_2(D, \mathbb{CH})$*, Proceedings of the 19-th Summer School "Applications of Mathematics in Engineering", Varna, August 24 - September 02, 1993, pp. 203–210.

[33] Z. Xu, *A function theory for the operator $D - \lambda$*, Complex Variables Theory and Appl. 16, 1991, pp. 27–42.

19th International Conference on the Application of Computer
Science and Mathematics in Architecture and Civil Engineering
K. Gürlebeck, T. Lahmer and F. Werner (eds.)
Weimar, Germany, 04–06 July 2012

THE PROBLEM OF COUPLING BETWEEN ANALYTICAL SOLUTION AND FINITE ELEMENT METHOD

D. Legatiuk*, S. Bock and K. Gürlebeck

**Research Training Group 1462, Bauhaus-University Weimar, Germany*
E-mail: dmitrii.legatiuk@uni-weimar.de

Keywords: FEM, analytical solution, coupling, interpolation, holomorphic functions.

Abstract. *This paper is focused on the first numerical tests for coupling between analytical solution and finite element method on the example of one problem of fracture mechanics. The calculations were done according to ideas proposed in [1]. The analytical solutions are constructed by using an orthogonal basis of holomorphic and anti-holomorphic functions. For coupling with finite element method the special elements are constructed by using the trigonometric interpolation theorem.*

1 INTRODUCTION

The finite element methods is the most popular numerical method for solving partial differential equations in computational mechanics. For many problems it shows high accuracy of results, but for problems which contain different types of singularities (like for instance cracks, gaps, corners) one should make some adaptation and improvement to get an acceptable result. Another approach is to use analytical method for the near-field of the singularity (crack-tip region) and classical finite element method in the far-field.

One of possible modifications of finite element method for singular problems is the eXtended Finite Element Method (XFEM) [2]. In the XFEM the classical finite element approximation is enriched in certain region of interest (the crack-tip region) by using special set of the enrichment functions. But for many problems we have to refine a lot to get desired accuracy, this increased time costs and reduced the rate of convergence.

In the linear elastic fracture mechanics the analytical solution of the crack-tip has been developed by using methods of complex function theory. Based on the *Formulas of Kolosov* the near-field solution of the crack can be represented by only two holomorphic functions $\Phi(z)$ and $\Psi(z)$, $z \in \mathbb{C}$ [5]. Analytical solution based on the complex function theory gives us a high accuracy of solution in the neighborhood of singularity.

A combination of finite element method with analytical solution was proposed by Piltner in [6] and [7]. He has constructed a special elements containing the crack or the hole by using Formulas of Kolosov and coupled it with finite element mesh by nodes on the boundary of this element. The boundary displacements between two adjacent nodes are chosen as piecewise linear or quadratic functions. This approach gives us advantages of analytical solution near singularity, but coupling with finite elements is realized in such a way, that we have a break on the boundary, because, in general, the analytical solution is not necessary the piecewise linear or quadratic functions on the boundary between two methods.

Our idea is to continue work in direction proposed in [1] for method of coupling between analytical solution and finite element method. The main goal of this approach is to get the continuous coupling between analytical solution and finite element method through the whole interaction interface. For that reason we construct a special element which contain analytical solution and transmission or coupling elements. Advantages of such combination can be high accuracy of solution without special refinement, following investigation of model, like for instance error estimations, rate of convergence evaluations. The purpose of this article is to present first numerical results.

In the following section we introduce the global geometrical settings and explain the structure of the special element. The numerical examples are shown and discussed in the Section 3.

2 GEOMETRICAL SETTINGS AND SPECIAL ELEMENT

2.1 Global settings and notations

We work in the field $\mathbb{C}$ of one complex variable, where we identify each point of the complex plane $\mathbb{C}$ with the ordered pair $z = (x, y) \in \mathbb{R}^2$, $x, y \in \mathbb{R}$ or equaivalently with the complex number $z = x + iy \in \mathbb{C}$, where i denotes the imaginary unit.

For constructing the exact solution to the differential equation we will work with the complex linear Hilbert space of square-integrable $\mathbb{C}$-valued functions defined in Ω, that is denoted by

$L_2(\Omega, \mathbb{C})$, with the corresponding inner product [3]

$$\langle f, g\rangle_{L_2(\Omega,\mathbb{C})} = \int_\Omega f\,\bar{g}\,d\sigma, \quad f, g \in L_2(\Omega, \mathbb{C}), \tag{1}$$

where $d\sigma$ denotes the Lebesgue measure in $\mathbb{R}^2$, the functions f and g are $\mathbb{C}$-valued function such that

$$f(z) = f_0(x, y) + if_1(x, y), \quad z \in \Omega$$

and the coordinates $f_j : \Omega \to \mathbb{R} \quad (j = 0, 1)$ are real-valued functions defined in Ω.

For continuously real-differentiable functions $f_j : \Omega \to \mathbb{C}$, the operator

$$D = \frac{\partial}{\partial x} + i\frac{\partial}{\partial y} \tag{2}$$

is called *Cauchy-Riemann* operator. The *conjugate Cauchy-Riemann* operator we denote by

$$\overline{D} = \frac{\partial}{\partial x} - i\frac{\partial}{\partial y}. \tag{3}$$

Also we introduce the polar coordinates by $x = r\cos\varphi$, $y = r\sin\varphi$ and arrive to the representation of the complex number

$$z = re^{i\varphi} = r(\cos\varphi + i\sin\varphi), \qquad 0 \le r < \infty, 0 \le \varphi < 2\pi.$$

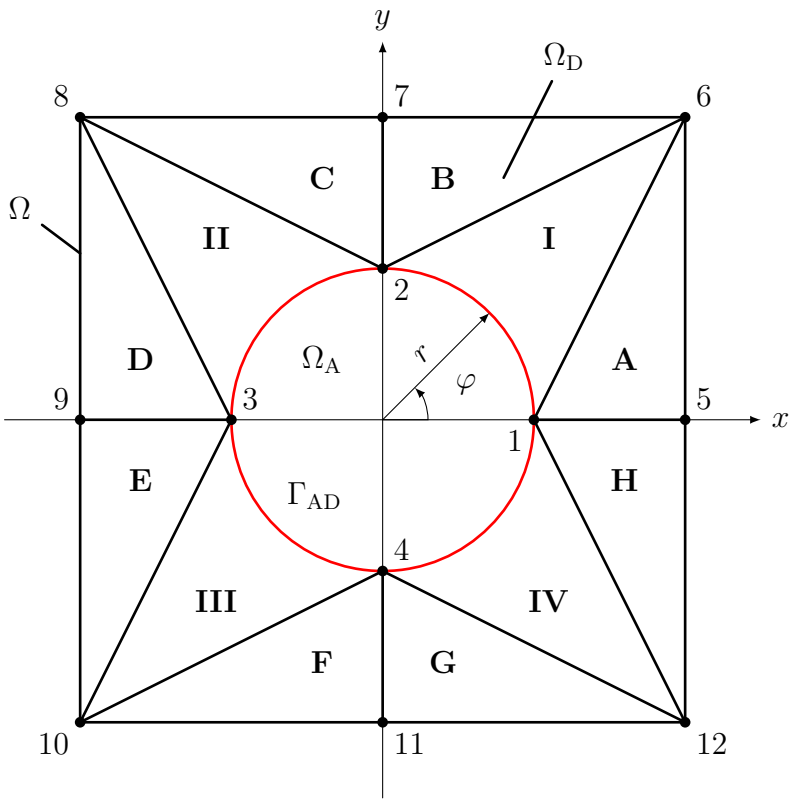

Figure 1: Geometrical setting of special element

Let now $\Omega \subset \mathbb{C}$ be a bounded simply connected domain containing the singularity at the origin (see Figure 1). The domain Ω is decomposed in the two sub-domains $\Omega = \Omega_A \cup \Omega_D$

separated by the fictitious joint interface $\Gamma_{\mathrm{AD}} = \overline{\Omega}_{\mathrm{A}} \cap \overline{\Omega}_{\mathrm{D}}$. The discrete numerical domain, denoted by Ω_{D}, is modeled by two different kinds of elements: the CST-element of class C^0 (in example elements $A-H$) and the Coupling-element of class C^0-C^∞ (in example elements $I-IV$), that couple the discrete domain Ω_{D} with the analytical domain Ω_{A}. We call the sub-domain Ω_{A} analytical in that sense, that the constructed solutions are exact solutions to the differential equation in Ω_{A}. The idea behind this special element is to get the continuous connection through the interface Γ_{AD} by modifying of one side osculating triangles.

2.2 Exact solution to the homogeneous Lamé equation

Inside of Ω_{A} we are going to use the exact polynomial solutions to the homogeneous Lamé by using a basis of holomorphic and anti-holomorphic polynomials. The idea behind is the factorization of the Laplace operator by the Cauchy-Riemann (2) operator and its conjugate (3). First we recall the classical matrix representation of the Lamé equation.

In linear elasticity theory the pysical state of each continuum model is described by three fundamental equations: the equilibrium equations, the constutive equations and the strain-displacement relations. Solving these three equations with respect to unknown displacement vector $\underline{\mathbf{u}} = [u_1(x,y), u_2(x,y)]^T$ we get the Lamé (or Navier) equation in vector form [4]:

$$(\lambda+\mu)\nabla(\nabla\cdot\underline{\mathbf{u}}) + \mu\nabla^2\underline{\mathbf{u}} = -\underline{p}, \tag{4}$$

where λ and μ are material constants (Lamé constants). Also, we can rewrite equation (4) in the classical matrix formulation

$$-\underline{p} = \underline{D}_e\,\underline{\mathbf{E}}\,\underline{D}_k\underline{\mathbf{u}} \tag{5}$$

where $\underline{p} = [p_x, p_y]^T$ denotes the vector of the outer forces and

$$\underline{D}_e \;=\; (\underline{D}_k)^T = \begin{bmatrix} \partial_{,x} & 0 & \partial_{,y} \\ 0 & \partial_{,y} & \partial_{,x} \end{bmatrix}$$

are the adjoint differential operators of equilibrium and kinematics respectively. The matrix

$$\underline{\mathbf{E}} = G\begin{bmatrix} \frac{\kappa+1}{\kappa-1} & -\frac{\kappa-3}{\kappa-1} & 0 \\ -\frac{\kappa-3}{\kappa-1} & \frac{\kappa+1}{\kappa-1} & 0 \\ 0 & 0 & 1 \end{bmatrix}, \quad \text{where} \quad \kappa = \begin{cases} 3-4\nu & \text{plane strain state} \\ \dfrac{3-\nu}{1+\nu} & \text{plane stress state} \end{cases}$$

includes material parameters for a linear elastic, homogeneous and isotropic material in the usual notations.

For complex representation of the Lamé equation we identify the displacement vector $\underline{u}$ with the complex valued function $\mathbf{u} = u_1(x,y) + iu_2(x,y) \in \Omega$ in the bounded simply connected domain $\Omega \subset \mathbb{C}$. A purely complex representation of the homogeneous form of (5) is given by

$$0 = D\tilde{M}^{-1}\overline{D}\mathbf{u}, \tag{6}$$

where D denotes the Cauchy-Riemann operator and $\tilde{M}$ a multiplication operator which is, acting on a function $u = u_0 + iu_1$, defined by

$$\tilde{M}u = \frac{\kappa+1}{\kappa-1}u_0 + iu_1.$$

Proposition 1 *For a fixed $n \in \mathbb{N}_0$ the $4n+2$ polynomials of the system*

$$\begin{array}{rcl} \{f_k(z)\}_{k=0,\ldots,n,} & = & \left\{\varphi_k(z) + \frac{1}{2}(M_0-1)D(\mathbf{M}_p\varphi_k(z))\right\}_{k=0,\ldots,n,} \\ \left\{\hat{f}_l(z)\right\}_{l=0,\ldots,n,} & = & \left\{\psi_l(z) + \frac{1}{2}(M_0-1)D(\mathbf{M}_p\psi_l(z))\right\}_{l=0,\ldots,n,} \end{array} \tag{7}$$

are exact solutions to the homogeneous Lamé equation (6). The operator $\mathbf{M}_p$ is defined by

$$\mathbf{M}_p h(z) = x\mathbf{Sc}\, h(z) + y\mathbf{Vec}\, h(z) = xh_0(x,y) + yh_1(x,y).$$

In the formulas (7) systems $\varphi_k(z)$ and $\psi_k(z)$ are the holomorphic and anti-holomorphic polynomials

$$\begin{array}{rcl} \{\varphi_k(z)\}_{k=0,\ldots,n,} & = & \left\{\sqrt{\frac{k+1}{r_a^{k+1}\pi}}z^k\right\}_{k=0,\ldots,n,} \\ \{\psi_l(z)\}_{l=0,\ldots,n,} & = & \left\{\sqrt{\frac{l+1}{r_a^{l+1}\pi}}\overline{z}^l\right\}_{l=0,\ldots,n,} \end{array} \tag{8}$$

2.3 Construction of the coupling element

The numerical domain Ω_{D} consists of two different kinds of elements. In the far-field of the analytical inclusion we use CST-elements of class C^0, where the primary variables are linearly interpolated and the secondary variables are constantly represented. The second kind of the used elements are the so called *Coupling* elements, that connect the discrete domain Ω_{D} modeled by CST-elements with the analytical domain Ω_{A}. For these special curved triangles we have following restrictions:

- C^0 continuity on two boundaries with CST-elements;
- at least C^0 through the joint interface Γ_{AD} with the analytical domain.

To satisfy these condtions we introduce the special coupling element of polynomial degree $n = c(m+1) - 1$ on Γ_{AD}. The parameters c and m define a discrete point grid for the identity coupling element $\mathbb{T}_n^{c,m}$, where $c \in \mathbb{N}, c \geq 2$ denotes the number of coupling elements used to discretize the joint coupling interface Γ_{AD}. The second parameter $m \in \mathbb{N}_0$ is concerned to the number of nodes used additionally on the boundary Γ_{AD}.

To construct the coupling element we are going to use the *Discrete Fourier Analysis* in $\mathbb{C}$, which based on the following trigonometric interpolation theorem.

Theorem 1 *For given observations $\mathrm{Y}_0, \mathrm{Y}_1, \ldots, \mathrm{Y}_n$ exist a unique function*

$$t_n(\varphi) = \sum_{k=0}^{n} c_k e^{ik\varphi} \tag{9}$$

that satisfies the interpolation conditions $t_n(\varphi_j) = \mathrm{Y}_j$, $j = 0, \ldots, n$. The coefficients c_k are given by

$$c_k = \frac{1}{n+1}\sum_{j=0}^{n} \mathrm{Y}_j e^{-ij\varphi_k}, \tag{10}$$

$\varphi_k = k\frac{2\pi}{n+1}$ denote the $n+1$ equidistant interpolation nodes on the interval $\varphi \in [0, 2\pi)$.

Using (9) and (10) we rearrange the trigonometric interpolation formula and obtain

$$t_n(\varphi) = \sum_{k=0}^{n} S_k(\varphi)\mathrm{Y}_k, \qquad S_k(\varphi) = \frac{1}{n+1}\sum_{j=0}^{n} e^{-i(j\varphi - k\varphi_j)}, \qquad S_k(\varphi), \mathrm{Y}_k \in \mathbb{C}. \tag{11}$$

Proposition 2 *For a fixed discretization* (c, m) *and* $n = c(m+1)-1 \in \mathbb{N}$ *the geometry mapping* $\mathbb{X}_n^{c,m}(\xi, \eta) \in \mathbb{C}$ *for the* $(n+2)$*-node identity coupling element* $\mathbb{T}_n^{c,m}$ *is given by*

$$\mathbb{X}_n^{c,m}(\xi, \eta) = \sum_{q=0}^{n+1} N_q(\xi, \eta) Y_q, \tag{12}$$

where

$$N_q(\xi, \eta) = \begin{cases} \frac{\eta}{n+1} \sum_{j=0}^{n} e^{2\pi i j \frac{(m+1)\xi - q}{c(m+1)}} & : \quad q < n+1 \\ 1 - \eta & : \quad q = n+1 \end{cases}$$

The orientation of the axes ξ and η of local coordinate system of the coupling element is shown in figure 2.

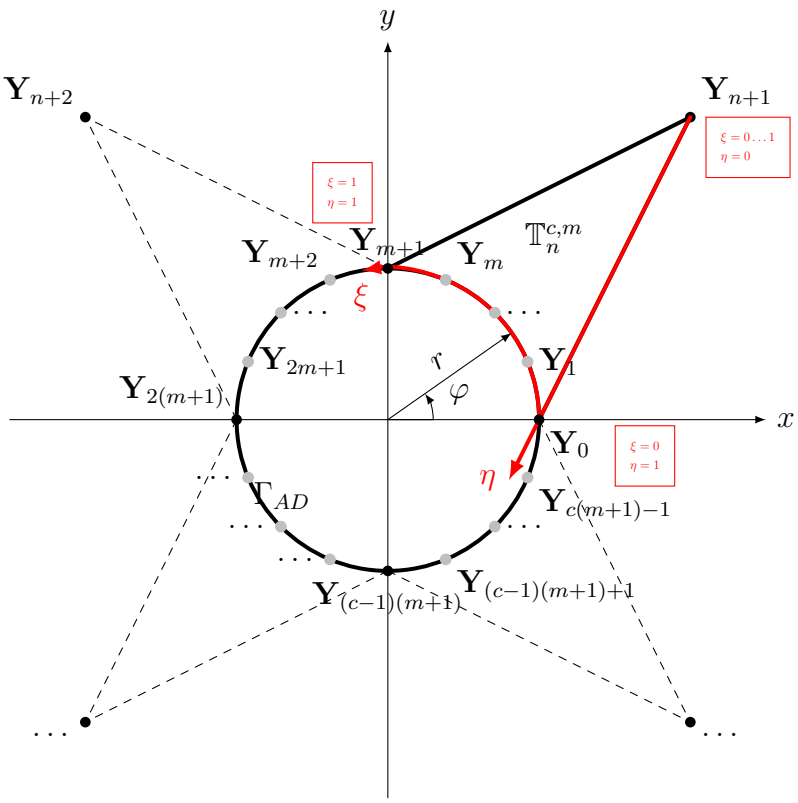

Figure 2: $(n+2)$-node identity coupling element $\mathbb{T}_n^{c,m}$

2.4 Coupling of Ω_{A} and Ω_{D}

The solution of the original boundary value problem in Ω determines the values of unknown displacements $\mathrm{U}_0, \ldots, \mathrm{U}_n$ at the nodes on the fictitious joint interface Γ_{AD}. To interpolate these unknown values at the nodes we use the interpolation formula (9). The point is that then the displacement are continuous also along the arcs between the nodes.

3 FIRST NUMERICAL EXAMPLES

Based on the theory which was presented in the previous section, now we would like to show first numerical tests. A general design model is shown in figure 3.

We have an arbitrary square domain Ω and we discretize it accordantly with scheme proposed in the Section 2. We start our tests with 37 Finite Elements (32 CST-elements, 4 Coupling

elements and 1 analytical domain), and after we make gradually refinment of our finite element mesh up to 973 Elements. The special elements are always located at the origin, but we would like to underline, that is not a restriction. We can use several special elements in one finite element mesh. Also is not restricted to use the special element only of square shape.

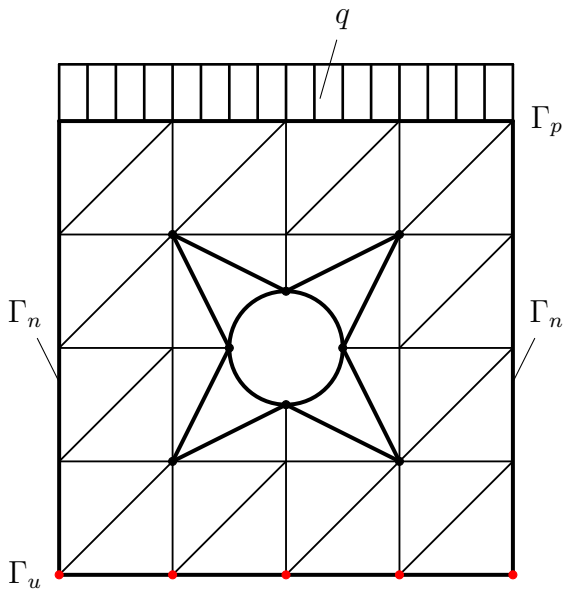

Figure 3: a general design model

All calculation are performed with the boundary condtions:

$$\begin{array}{rcrll} u & = & 0 & \text{on} & \Gamma_u, \\ p_y & = & -q & \text{on} & \Gamma_p, \\ \sigma_{xx} & = & 0 & \text{on} & \Gamma_n. \end{array} \tag{13}$$

The material is supposed to be linear isotropic and the problem is considered under plain strain state. For values of material constant and applying loads we used synthetic data, because at the present moment the goal is to investigate general behaviour of the method and to understand possible ways for improvement.

The displacement field for 973 Elements is presented in figure 4

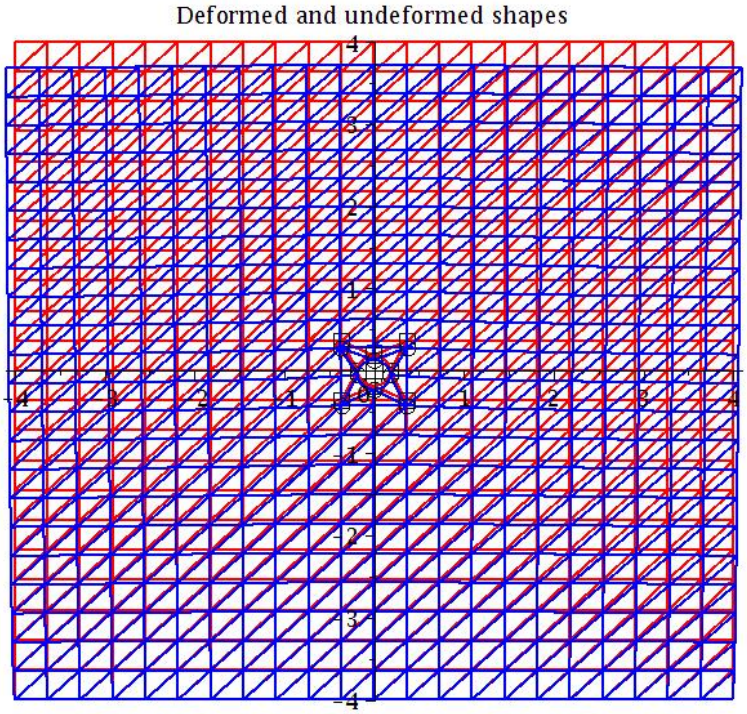

Figure 4: Displacement field for 973 elements

The figure 4 shows the approximation of the displacement field for given boundary conditions. Another important result is that we can easily see how the special element can be integrated to the global finite element mesh. Also, we would like to underline that location and number of special elements are not restricted: we can construct a mesh with several special elements, for instance in case of multiple cracks. The changing of the condition number of the global stiffness matrix with refinement is shown in figure 5

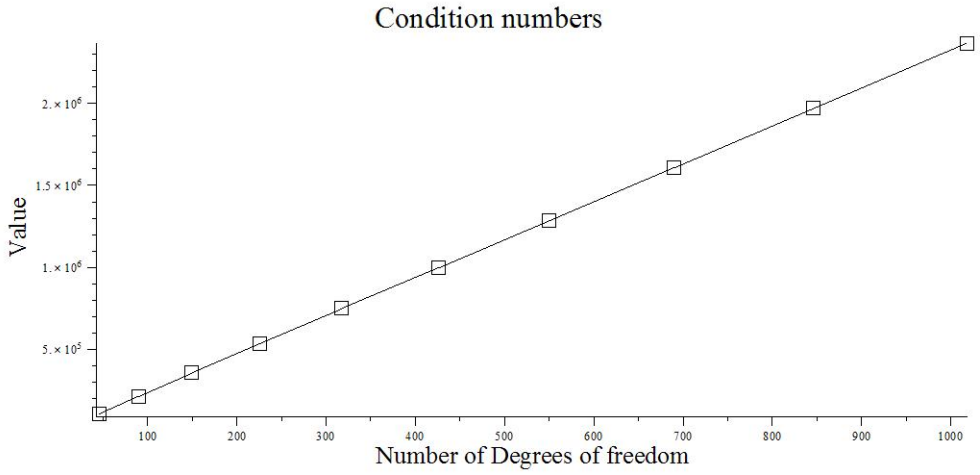

Figure 5: Condition number

We see that the condition number is growing as linear function

To study the flexibility of the method we would like to change a shape of the special element from square to rectangle. The displacement field for 973 Elements is presented in figure 6

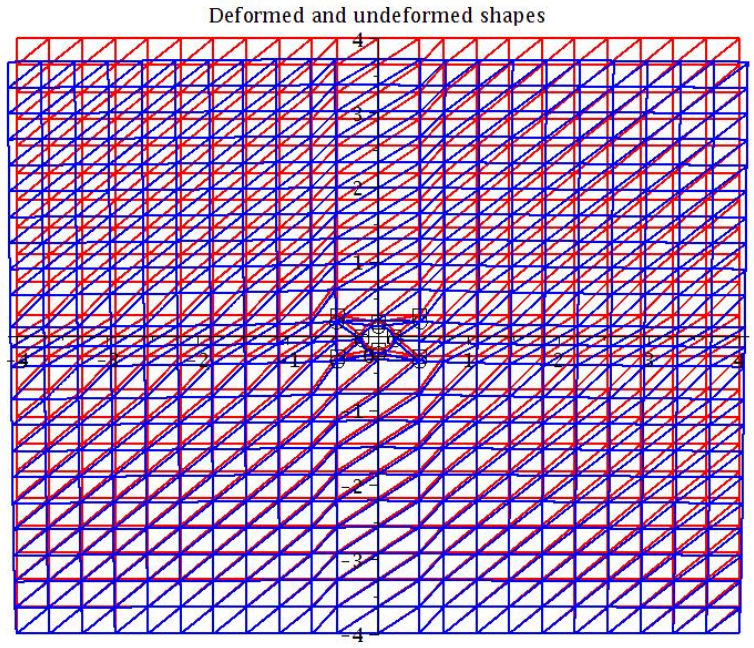

Figure 6: Displacement field for 973 elements for rectangle

The figure 6 shows the approximation of the displacement field for given boundary conditions. The changing of the condition number of the global stiffness matrix with refinement is shown in figure 7

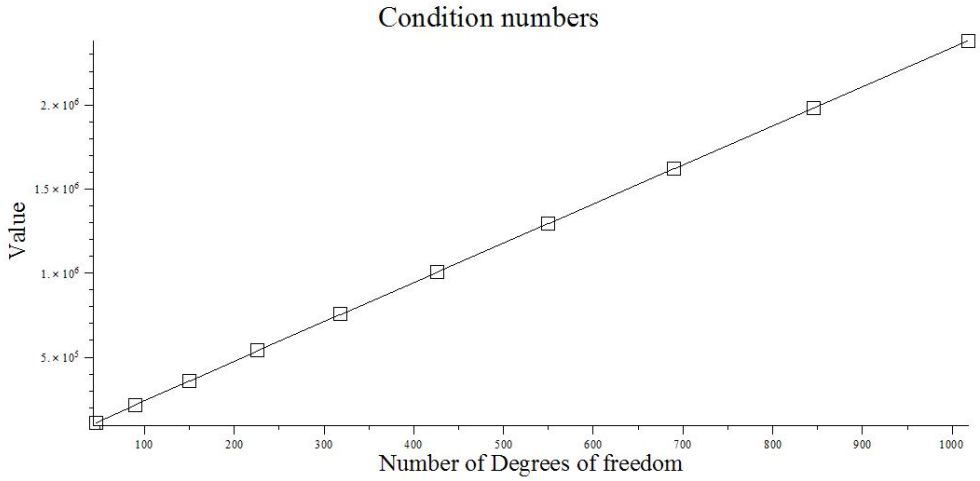

Figure 7: Condition number

Again we see, that the condition number is growing as linear function. Finally, figure 8 shows the comparison of condition numbers between square and rectangle shapes.

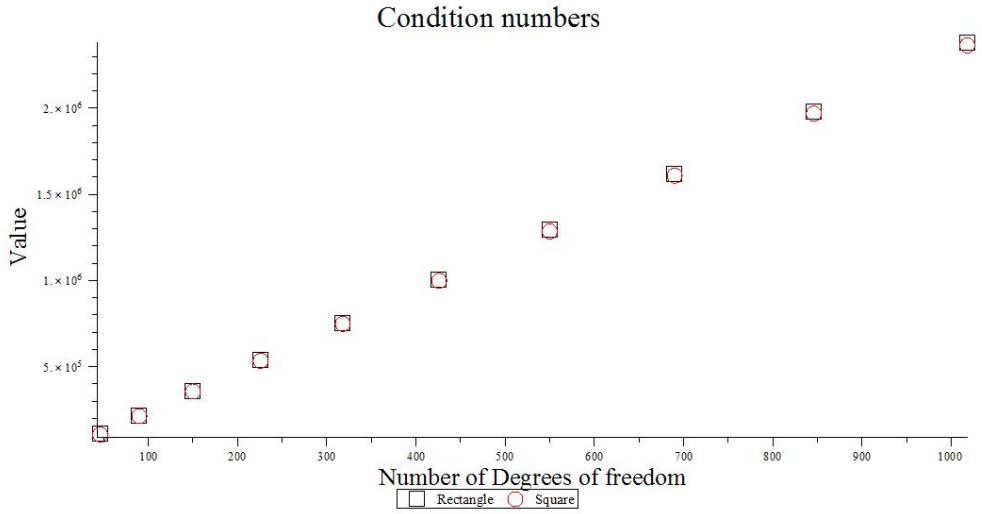

Figure 8: Comparison of condition numbers

As we can see, the condition numbers are growing always as a linear function of total amout degrees of freedom, and, in fact, doesn't depend on the shape of the super element.

4 CONCLUSIONS

The first numerical results for coupling between analytical solution and finite element method were presented. For the shape preserving geometry mapping and continuous coupling of the displacement field the special element was constructed. The behaviour of the condition number during refinement procedure was shown. Flexibility and possible points for improvement were discussed.

LITERATUR

[1] S. Bock, K. Gürlebeck, *A coupled Ritz-Galerkin approach using holomorphic and anti-holomorphic functions*. K. Gürlebeck and C. Könke eds. *17th Conference on the Application of Computer Science and Mathematics in Architecture and Civil Engineering*, Weimar, Germany, 12-14 July 2006

[2] M Fleming, Y.A. Chu, B. Moran and T. Belytschko, *Enriched element-free Galerkin methods for crack tip fields*, International journal for numerical methods in engineering, Volume 40, 1997.

[3] John K. Hunter, Bruno Nachtergaele, *Applied analysis*, World Scientific Publishing, 2005.

[4] Lawrence E. Malvern, *Introduction to the mechanics of a continuous medium*, Prentice-Hall, 1969.

[5] N.I.Mußchelischwili, *Einige Grundaufgaben der mathematischen Elastizitätstheorie*, VEB Fachbuchverlag Leipzig, 1971.

[6] R. Piltner, *Some remarks on finite elements with an elliptic hole*, Finite elements in analysis and design, Volume 44, Issues 12-13, 2008.

[7] R. Piltner, *Special finite elements with holes and internal cracks*, International journal for numerical methods in engineering, Volume 21, 1985.

ACKNOWLEDGEMENTS

This research is supported by the German Research Institute (DFG) via Research Training Group “Evaluation of Coupled Numerical Partial Models in Structural Engineering (GRK 1462)”, which is gratefully acknowledged by the author.

19th International Conference on the Application of Computer
Science and Mathematics in Architecture and Civil Engineering
K. Gürlebeck, T. Lahmer and F. Werner (eds.)
Weimar, Germany, 04–06 July 2012

SYSTEM IDENTIFICATION OF A WIND TURBINE USING ROBUST MODEL UPDATING STRATEGY

X. Liu*, **K. R. Leimbach and D. Hartmann**

**Chair of Computing in Engineering*
Ruhr-University Bochum, Germany
E-mail: xiangqin.liu@rub.de

Keywords: system identification, wind turbine, model updating, global sensitivity analysis.

Abstract. *This paper presents a robust model updating strategy for system identification of wind turbines. To control the updating parameters and to avoid ill-conditioning, the global sensitivity analysis using the elementary effects method is conducted. The formulation of the objective function is based on Müller-Slany's strategy for multi-criteria functions. As a simulation-based optimization, a simulation adapter is developed to interface the simulation software ANSYS and the locally developed optimization software MOPACK. Model updating is firstly tested on the beam model of the rotor blade. The defect between the numerical model and the reference has been markedly reduced by the process of model updating. The effect of model updating becomes more pronounced in the comparison of the measured and the numerical properties of the wind turbine model. The deviations of the frequencies of the updated model are rather small. The complete comparison including the free vibration modes by the modal assurance criteria shows the excellent coincidence of the modal parameters of the updated model with the ones from the measurements. By successful implementation of the model validation via model updating, the applicability and effectiveness of the solution concept has been demonstrated.*

1 INTRODUCTION

The renewable energy sources have gained high attention due to the current energy crisis and the urge to get clean energy. Wind energy as a strong contender, therefore, is becoming more and more popular. As the wind turbine structure, however, suffers from inevitable ageing and degradation resulting from operational actions, continuous system identification based upon long term monitoring is indispensable. By that, the current state of the structure can be determined and possible failures can be revealed in time. To this end, an adequate numerical model is mandatory to predict the structural behavior. This model needs to be validated by a continuous model updating to ensure a reliable and accurate estimation of the structural behavior.

According to [1], the model updating methods can be broadly classified into direct methods, which are essentially non-iterative ones, and iterative methods. A number of methods that were first to emerge belong to the direct category. These methods update directly the elements of stiffness and mass matrices and are one step procedures. Although the resulting updated matrices reproduce measured modal data exactly, they do not generally maintain structural connectivity and the corrections suggested are not always physically meaningful [2]. The methods in the second category are referred to as iterative methods. Iterative methods use changes in physical parameters to update the finite element models and, thereby, generate models that are physically realistic. From earlier work on finite element model updating it is evident that finite element model updating is essentially an optimization method. Here, the design variables are the uncertain parameters in the model. The objective is to minimize the distance between the predicted data by the model and the measured data. Some applications of the iterative optimization methods are reviewed in [3, 4, 5, 6, 7].

However, some key issues in the iterative optimization method of model updating are not fully matured, especially for continuous system identification, e.g. how to control the updating parameters and to avoid ill-conditioning; how to master the sophisticated simulation-based optimization and solve the non-standard optimization problem. To solve these problems, a robust model updating strategy is proposed in this paper, including four main aspects as described in the next section.

2 PROPOSED MODEL UPDATING STRATEGY

2.1 Updating parameter determination

Specifying the updating parameters is one of the most difficult yet most critical steps in the whole updating process. The number of updating parameters should be large enough to cover all the relevant uncertain parameters, but as low as possible to avoid ill-conditioning. An initial selection of the parameters depends on clearly engineering insight of the model. Such parameters typically are associated to unknown material parameters, approximated geometrical parameters, uncertain boundary conditions, parts with a high level of uncertainty (e.g. joints, localized mass), and etc. They can be described by a vector $\mathbf{x}$ in Equation 1.

$$\mathbf{x} = \left(X_1 \dots X_k\right) = \begin{pmatrix} \text{material parameters} \\ \text{geometrical parameters} \\ \text{boundary conditions} \\ \dots \end{pmatrix} \tag{1}$$

To ensure well-conditioned problem, the number of the updating parameters should not exceed the number of the measured responses. It needs to be limited to the variation of a few key model parameters that account for the observable errors. To identify the impact of different parameters on the model errors, the sensitivity analysis can be conducted. The traditional sensitivity analysis, which is also called local sensitivity analysis, is derivative-based approach and only efficient for linear models. As for nonlinear and non-additive models, the global sensitivity analysis should be used, since this method explores the whole space of the input parameters and includes the interaction effect among parameters as well.

There are several different methods that belong to the class of global sensitivity analysis, as described in detail by [8]. The choice of the proper sensitivity analysis technique depends on such considerations as: the computational cost of running the model; the number of input factors; features of the model (e.g. linearity, additivity). Considering a modest model computational expense (e.g. up to 10 minutes per run) and dozens of parameters (e.g. 20 to 100), the elementary effects (EE) method is recommended as a simple but effective way to identify the few important factors among the many contained in the model and cope with nonlinearity and interactions. The fundamental idea behind this method is owed to Morris, who introduced the concept of elementary effects in 1991 [9]. While adhering to the concept of local variation around a base point, the EE method makes an effort to overcome the limitations of the derivative-based approach by introducing wider ranges of variations for the inputs and averaging a number of local measures so as to remove the dependence on a single sample points. An elementary effect is defined as [8]:

$$EE_i = \frac{Y(X_1, X_2, \ldots, X_{i-1}, X_i + \Delta, \ldots, X_k) - Y(X_1, X_2, \ldots, X_k)}{\Delta} \tag{2}$$

The sensitivity measures, μ and σ, proposed by Morris, are respectively the mean and the standard deviation of the elementary effects calculated from finite randomly sampled inputs. The mean μ assesses the overall influence of the factor on the output. The standard deviation σ estimates the ensemble of the factor's effects, whether nonlinear and/or due to interactions with other factors. Campolongo et al. [10] proposed replacing the use of the mean μ with μ^*, which is defined as the mean of the absolute values of the elementary effects. The use of μ^* can prevent cancellation effects when the model is nonmonotonic or has interaction effects. μ^* is a practical and concise measure to use, especially when there are several output variables. Campolongo et al. [10] have also shown that μ^* is a good proxy of the total sensitivity index S_T of the variance-based method [8]. With the aid of the global sensitivity analysis, the few decisive key parameters can be selected as updating parameters for the following process.

2.2 Objective function formulation

The objective function used in model updating evaluates the defect between the model predicted and the measured data. Typical measurements include the modal model (natural frequencies and mode shapes) and the frequency response functions (FRF). Based on Müller-Slany's strategy [11], the error expressions $\varepsilon_i(\mathbf{x})$ between the numerical and measured dynamic properties are components of the vector objective function $\mathbf{f}[\varepsilon(\mathbf{x})]$ in Equation 3. To express errors of natural frequencies and mode shapes, the modal frequency shift [12] and the modal assurance criterion (MAC) [13] can be utilized.

$$\mathbf{f}[\varepsilon(\mathbf{x})] = \begin{bmatrix} \varepsilon_1(\mathbf{x}) \\ \varepsilon_2(\mathbf{x}) \\ \varepsilon_3(\mathbf{x}) \\ \varepsilon_4(\mathbf{x}) \\ \cdots \end{bmatrix} = \begin{bmatrix} \text{error expression of total mass} \\ \text{error expression of natural frequencies} \\ \text{error expression of mode shapes} \\ \text{error expression of FRF} \\ \cdots \end{bmatrix} \tag{3}$$

It is worth noting that the measured and analytical natural frequencies and mode shapes must relate to the same mode, that is, they must be paired correctly. Arranging the natural frequencies in ascending order of magnitude is not sufficient, because the mode orders may not be correct when two modes are close together in frequency, and the finite element model normally provides more degrees of freedom than those can be identified from measurements. The approach to pair the modes is by using the modal assurance criterion (MAC). For a reference mode, the corresponding numerical mode should have the largest MAC value.

After formulating the individual objective functions separately, the linear weighting sum method (LWS) [14], which is based on the concept of aggregation functions, is adopted to combine the multi-objective functions into a scalar objective function of Equation 4, using appropriate weighting factors w_i so that the relative importance of the individual objectives can be reflected:

$$f(\mathbf{x}) = \sum_{i=1}^{k} w_i \varepsilon_i(\mathbf{x}) \tag{4}$$

With the objective function having been formulated, the model updating is established by solving the constrained multi-criteria optimization problem of Equation 5, in which $\mathbf{h}(\mathbf{x})$is the constraint function, while $\mathbf{x}_L$ and $\mathbf{x}_U$ are the lower and upper bounds, respectively.

$$\min_{\mathbf{x}\in\Sigma}\{f(\mathbf{x}) \mid \mathbf{h}(\mathbf{x}) = 0\}, \Sigma := \{\mathbf{x} \in R^n \mid \mathbf{x}_L \leq \mathbf{x} \leq \mathbf{x}_U\} \tag{5}$$

2.3 Optimization algorithm selection

It is crucial to choose a suitable algorithm for the optimization involved in the model updating, because the existence and correctness of the solution as well as the convergence speed largely depend on the nature of the optimization problem. The optimization problem in the model updating has a number of properties, which makes it hard to solve:

- The interdependence between residuals and the updating parameters is highly nonlinear; therefore the common derivative-based approaches are not fully applicable.
- Since a multi-criteria objective function has been formulated, a large number of local minima have to be taken into consideration.
- Due to the complexity of the real-world problem, as a rule, the objective function is not continuously differentiable.
- The presence of numerical noise introduces additional difficulties.

For these reasons, the deterministic techniques, which are efficient for smooth problems, turn out not to be applicable here because of their gradient-based characteristic. Instead, the evolutionary algorithms (EAs), known as derivative free methods, can be considered as a reliable

alternative in such situations. Bäck and Schwefel [15] and Eiben [16] give overviews on EAs. EAs have several advantages compared to gradient-based methods for complex problems. They require only little knowledge about the problem being solved, and they are easy to implement, robust, and most important, inherently parallel. Since most real-world problems involve simultaneous optimization of several concurrent objectives, parallel approaches are advantageous. EAs are well suited to multi-objective optimization problems as they are fundamentally based on multi-membered biological processes which are inherently parallel.

2.4 Optimization process implementation

The model updating process constitutes a simulation-based optimization. In the simulation-based optimization, all or some of the objective and constraint functions depend on the simulation result. In each optimization iteration, the output from simulation is used to compute the objective and constraint functions. If the objective function does not meet the convergence criteria, new values for updating parameters are created according to the logic of the optimization method and used to reform the FE model. Then, the simulation is invoked again to compute new output. Hence, in simulation-based optimization, optimization and simulation work together as a whole.

The respective simulations are commonly accomplished using commercial finite element software because they are powerful numerical analysis tools providing high reliability and numerous capabilities. In the present work, the applied simulation tool is the commercial finite element software ANSYS 11. Regarding the optimization problem, the complex real world structures often lead to optimization problems difficult to solve. In most of the cases, the existing simulation software offers no direct support for nonlinear optimization or has no powerful optimization tools. For instance, the optimization methods provided by ANSYS are entirely derivative-oriented, making it impossible to solve non-standard optimization problems, like nonlinear or discontinues optimization problems. Therefore, in the present work, the java-based optimization framework, MOPACK, is applied to solve the simulation-based optimization problem. MOPACK is the abbreviation for multi-method optimization package and has been implemented by Nguyen et al. [17]. It contains numerous robust optimization strategies, including deterministic methods and stochastic methods. More details about the available methods in MOPACK can be found in [17]. In particular, the graphical user interface (GUI) of MOPACK provides sophisticated tools for visualization and pre and post-processing. Another important issue is that MOPACK is extensible such it can be enriched with new methods and applications.

To solve the simulation-based optimization problem with the aid of MOPACK, intensive interactions are required between the external simulation software ANSYS and the optimization framework MOPACK. Therefore, a simulation adapter is developed for running the optimization using external solvers in the simulation software and the optimization framework simultaneously [18]. The integration of multiple software in the optimization procedure makes the proposed model updating approach robust for complex structural optimization problems.

3 TEST IMPLEMENTATION

The proposed approach is substantiated on a real world wind turbine located in Dortmund, Germany, which has a gearless system and a 40m-diameter rotor. A complete numerical model of the investigated wind turbine is constructed using ANSYS 11.0. This FE model contains

a concrete foundation, a steel tower with flanges, rotor blades and a simplified nacelle. Beam models with coarsely discretized meshes are used for the tower and the blades in order to reduce the development time and to allow parameters to be easily changed and items to be added.

Instead of considering the complete model, it is more reasonable to validate the model components in the first step, in particular the blade model, because several estimations had to be made due to lack of information from the manufacturer.

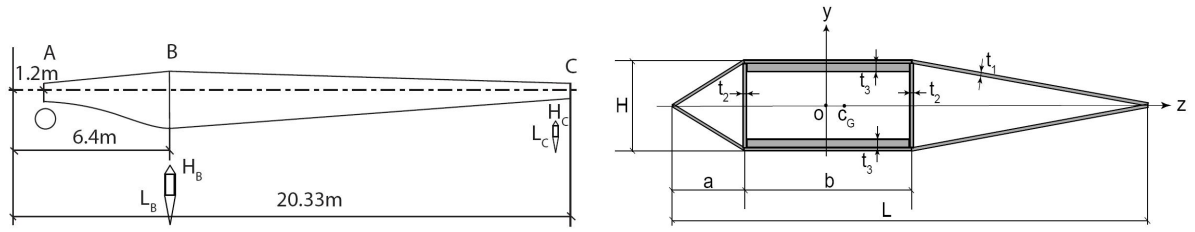

(a) (b)

Figure 1: (a) Illustration of the blade geometry (b) Parameters of the cross section

There is no measurement carried out on the blade in the current research project [19], fortunately, a test article of almost the same physical properties has been built and dynamically tested in [20]. Therefore the first five eigenfrequencies provided by [20] are taken as validation criteria for the current blade model.

Before formulating the optimization problem, sensitivity analysis is conducted on the following six geometrical parameters of the blade cross section:

- X_1: thickness t_1 of the skin;
- X_2: thickness t_2 of the two shear webs;
- X_3: thickness t_3 of the top and bottom spar caps.
- X_4: ratio r_1 between the height H and the chord length L at position B;
- X_5: ratio r_2 between the distance of the two shear webs b and the chord length L;
- X_6: ratio r_3 between the height H and the chord length L at position C;

Some assumptions have been made to reasonably simplify the problem: The parameters t_1, t_2, t_3 and r_2 are considered as constants along the blade. A cosine shape function is used between position A and B to transform the shape smoothly, while a linear shape function is used between position B and C. All parts of the cross section are assumed to consist of GRP (Glass fibre Reinforced Plastic) material having the same modulus of elasticity and shear and the same material density.

By implementing the elementary effects method, three sensitivity measures μ^*, μ and σ are calculated to reveal the influences of the six parameters on the output, which is multiple output including the first five eigenfrequencies. The barplots of μ^*, μ and σ for the multiple output are shown in Figure 2 to Figure 4. As above mentioned, the value of μ^* indicates the total sensitivity, therefore it can be concluded that the flapwise modes are sensitive to parameters X_4

and X_5, while the edgewise modes are sensitive to parameters X_1 and X_6. The influences of the parameters on the output is monotonic because the distributions of μ^* and μ are the same. According to the values of σ, parameters X_1, X_5 and X_6 have large interactions with other parameters.

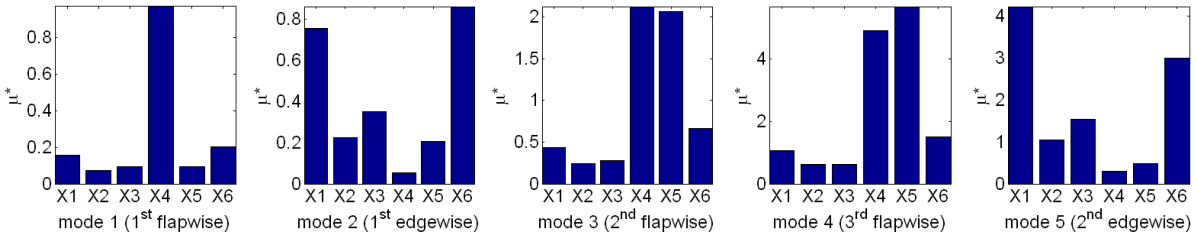

Figure 2: Barplot of μ^* for the first five eigenfrequencies

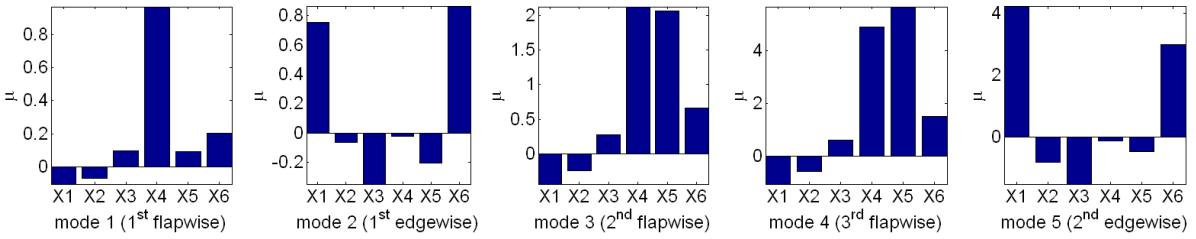

Figure 3: Barplot of μ for the first five eigenfrequencies

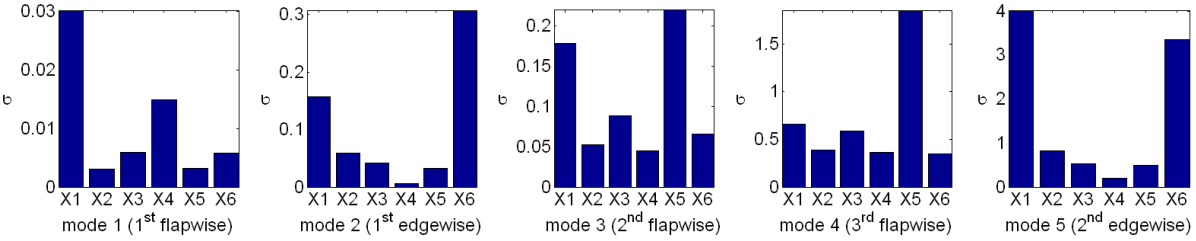

Figure 4: Barplot of σ for the first five eigenfrequencies

Since the number of the initially selected parameters is not large in this case, all of the six parameters are considered in the optimization process. The total weight of the blade serves as a constraint, and the first five eigenfrequencies are computed to compose the objective function. In addition, the modal assurance criterion (MAC) is applied to pair the modes correctly.

Referring to the optimization algorithm, the differential evolution (DE) method, which belongs to the class of EAs, is employed in the present test. The DE is a fairly fast and reasonably robust method with the capability of handling nondifferentiable, nonlinear and multimodal objective functions. It is originally described in [21]. Books [22, 23, 24] have been published on theoretical and practical aspects of using DE in parallel computing, multi-objective optimization and constrained optimizations. The crucial idea behind the DE is using vector differences for perturbing the vector population.

The simulation-based optimization of the blade model has been successfully implemented. Table 1 lists the natural frequencies of the blade model and the deviations (in the parentheses) from the reference before and after model updating. It can be noticed that the defect between the FE model and the reference model has been significantly reduced within the process of model updating.

	blade mode shape	reference frequency	FE model	
		f [Hz]	before updating	after updating
1	1st flapwise mode	1.64 Hz	1.503 Hz (8.35%)	1.617 Hz (1.41%)
2	1st edgewise mode	2.94 Hz	3.313 Hz (12.68%)	2.648 Hz (9.94%)
3	2nd flapwise mode	4.91 Hz	5.158 Hz (5.05%)	4.790 Hz (2.45%)
4	3rd flapwise mode	9.73 Hz	12.054 Hz (23.88%)	10.428 Hz (7.18%)
5	2nd edgewise mode	10.62 Hz	15.708 Hz (47.91%)	12.607 Hz (18.71%)

Table 1: Model updating results of the blade model

To validate the complete wind turbine model, an agent-based monitoring system has been established on the tower of the investigated wind turbine for continuous measurement and automated signal processing [25]. By virtue of operational modal analysis (OMA), the modal properties of the wind turbine have been identified from the measured acceleration time histories using the commercial OMA software ARTeMIS Extractor [26]. As listed in Table 2, the first 6 mode shapes are configured in the global coordinate system, whose origin is at the bottom of the tower, X axis is parallel to the rotation plane, Y axis is perpendicular to the rotation plane and Z axis is up. In association with the updated blade model, the complete FE model of the wind turbine provides modal properties quite close to those identified from on-site measurement. Small deviations of frequencies and high MAC values demonstrate very good consistency between the numerical and measured modes. Considering a certain extent of deviation like 5% (normally not avoidable in OMA result due to measurement errors), the FE model can be taken as a very good approximation for representing the dynamic behavior of the real world wind turbine structure.

	mode shape	measured f [Hz]	FE model f [Hz]	deviation	MAC
1	1st bending in X-Z plane	0.3753	0.3595	4.22%	0.9993
2	1st bending in Y-Z plane	0.3779	0.3611	4.44%	0.9994
3	2nd bending in Y-Z plane	2.217	2.242	1.11%	0.9951
4	2nd bending in X-Z plane	2.171	2.380	9.63%	0.9981
5	3rd bending in Y-Z plane	5.837	5.598	4.09%	0.9724
6	3rd bending in X-Z plane	5.857	6.223	6.25%	0.9944

Table 2: Comparison of the measured and numerical modal properties

4 CONCLUSION

The model updating problem serving as a pivot for system identification has been solved by a novel procedure using simulation-based multi-criteria optimization. The crucial aspects

of the solution concept include: updating parameter determination by global sensitivity analysis; objective function formulation using multi-criteria; optimization process implementation on the basis of an interface between the MOPACK package and the simulation software; and employment of the evolutionary algorithms for complicated optimization problems. The proposed solution concept has been successfully implemented on a real world wind turbine. The numerical models have been validated by measuring the dynamic response of the rotor blade test article, and of the wind turbine in operation.

In continuous system identification, the numerical model could be successively updated if the system has been subjected to structural modification (damage), which opens new opportunities for modern residual lifetime estimation.

5 ACKNOWLEDGEMENT

The financial support of the project [19] through the German Research Foundation (DFG) under project number HA 1463/20-1 and HO 3286/1-2 is gratefully acknowledged.

REFERENCES

[1] M. I. Friswell and J. E. Mottershead, *Finite element model updating in structural dynamics*. Dordrecht, Boston: Kluwer Academic Publishers, 1995.

[2] S. V. Modak, T. K. Kundra, and B. C. Nakra, "Model updating using constrained optimization," *Mechanics Research Communications*, vol. 27, pp. 543–551, 2000.

[3] Y. Liu, Z. Duan, and H. Liu, "Updating finite element model of structures with semi-rigid joints and boundary," in *Proc of SPIE - The Intl Soc for Opt Eng*, vol. 6174, 2006.

[4] B. Schwarz, M. Richardson, and D. L. Formenti, "Fea model updating using sdm," *Journal of Sound and Vibration*, vol. 41, pp. 18–23, 2007.

[5] P. G. Bakir, E. Reynders, and G. d. Roeck, "Sensitivity-based finite element model updating using constrained optimization with a trust region algorithm," *Journal of Sound Vibration*, vol. 305,, no. 1-2, pp. 211–225, 2007.

[6] B. Jaishi and W. Ren, "Finite element model updating based on eigenvalue and strain energy residuals using multiobjective optimisation technique," *Mechanical Systems and Signal Processing*, vol. 21, no. 5, pp. 2295–2317, 2007.

[7] M. Huang and H. Zhu, "Finite element model updating of bridge structures based on sensitivity analysis and optimization algorithm," *Wuhan University Journal of Natural Sciences*, vol. 13, no. 1, pp. 87–92, 2008.

[8] A. Saltelli, *Global sensitivity analysis: The primer*. Chichester, England ;, Hoboken, NJ: John Wiley, 2008.

[9] M. D. Morris, "Factorial sampling plans for preliminary computational experiments," *Technometrics*, vol. 33, no. 2, pp. 161–174, 1991.

[10] F. Campolongo, J. Cariboni, and A. Saltelli, "An effective screening design for sensitivity analysis of large models," *Environ. Model. Softw*, vol. 22, no. 10, pp. 1509–1518, 2007.

[11] H. H. Müller-Slany, "A hierarchical scalarization strategy in multicriteria optimization problems," in *Multicriteria Decision, Proc. Of the 14th Meeting of the German Working Group "Mehrkriterielle Entscheidung"* (Brosowski, Ester, Helbig, and Nehse, eds.), pp. pp69–79, 1993.

[12] R. Pascual, I. Trendafilova, J. C. Golinval, and W. Heylen, "Damage detection using model updating and identification techniques," in *2nd International Conference on Engineering Optimization*, 2010.

[13] R. J. Allemang, "The modal assurance criterion – twenty years of use and abuse," *Sound and vibration*, vol. 37, no. 8, pp. 14–21, August, 2003.

[14] R. Perera, A. Ruiz, and C. Manzano, "Performance assessment of multicriteria damage identification genetic algorithms," *Computers & Structures*, vol. 87, no. 1-2, pp. 120–127, 2009.

[15] T. Bäck and H.-P. Schwefel, "An overview of evolutionary algorithms for parameter optimization," *Evolutionary Computation*, vol. 1,, no. 1, pp. 1–23, 1993.

[16] A. E. Eiben, "Evolutionary computing: the most powerful problem solver in the universe?," *Dutch Mathematical Archive*, pp. 126–131, 2002.

[17] V. V. Nguyen, D. Hartmann, M. Baitsch, and M. König, "A distributed agent-based approach for robust optimization," in *2nd International Conference on Engineering Optimization*, 2010.

[18] K. Musayev, *Simulation based optimization and system identification of structures using FEA software*. PhD thesis, Department of Civil Engineering, November, 2010.

[19] D. Hartmann and R. Höffer, "Lifespan assessment of wind energy converters through system identification (lebensdauerabschätzung von windenergieanlagen mit fortlaufend durch systemidentifikation aktualisierten numerischen modellen) research project funded by the german research foundation (dfg) through the research grant ha 1463/20-1 and ho 3286/1-2.," 2010.

[20] G. C. Larsen, A. M. Hansen, and O. J. D. Kristensen, "Identification of damage to wind turbine blades by modal parameter estimation," 2002.

[21] R. Storn and K. Price, "Differential evolution - a simple and efficient heuristic for global optimization over continuous spaces," *Journal of Global Optimization*, vol. 11, no. 4, pp. 341–359, 1997.

[22] K. V. Price, R. M. Storn, and J. A. Lampinen, *Differential evolution: A practical approach to global optimization : with 292 figures, 48 tables and CD-ROM*. Berlin: Springer, op. 2005.

[23] V. F. Feoktistov, *Differential evolution: In search of solutions*. New York: Springer Science+Business Media, 2006.

[24] J. Kacprzyk and U. K. Chakraborty, *Advances in Differential Evolution*. Berlin, Heidelberg: Springer-Verlag Berlin Heidelberg, online-ausg. ed., 2008.

[25] K. Smarsly and D. Hartmann, "Agent-oriented development of hybrid wind turbine monitoring systems," in *Proceedings of the XVII EG-ICE Workshop on Intelligent Computing in Engineering*, European Group for Intelligent Computing in Engineering, 2010.

[26] Structural Vibration Solutions (SVS), "Artemis software - version 5.3." 2010.

19th International Conference on the Application of Computer
Science and Mathematics in Architecture and Civil Engineering
K. Gürlebeck, T. Lahmer and F. Werner (eds.)
Weimar, Germany, 04–06 July 2012

TOTALLY REGULAR VARIABLES AND APPELL SEQUENCES IN HYPERCOMPLEX FUNCTION THEORY

H. R. Malonek*, **M. I. Falcão, C. Cruz**

**Department of Mathematics*
University of Aveiro
3810-193 Aveiro, PORTUGAL
E-mail: hrmalon@ua.pt

Keywords: Hypercomplex Function Theory, totally regular variables, generalized Appell sequence

Abstract. *The aim of our contribution is to call attention to the relation between totally regular variables and Appell sequences of hypercomplex holomorphic polynomials in Hypercomplex Function Theory. Under some very natural normalization condition the set of all para-vector valued totally regular variables which are also Appell sequences will completely be characterized.*

1 INTRODUCTION

The aim of our contribution is to call attention to the relation between totally regular variables and Appell sequences of hypercomplex holomorphic polynomials (sometimes simply called monogenic power-like functions) in Hypercomplex Function Theory. After their introduction in 2006 by two of the authors of this note (see [1] and the discussion in [2]) on the occasion of the 17th IKM, the latter have been subject of investigations by different authors with different methods and in various contexts. The former concept, introduced by R. Delanghe in [3] and later also studied by Gürlebeck ([4], [5]) for the case of quaternions, has some obvious relationship with the latter, since it describes a set of linear hypercomplex holomorphic functions whose integer powers are also hypercomplex holomorphic. Due to the non-commutative nature of the underlying Clifford algebra, being totally regular variables or Appell sequences are not trivial properties as it is for the integer powers of the complex variable $z = x + iy$. Simple examples show also, that not every totally regular variable and its powers form an Appell sequence and vice versa. Under some very natural normalization condition the set of all para-vector valued totally regular variables which are also Appell sequences will completely be characterized. In some sense the result can also be considered as an answer to a remark of Habetha in [6] on the use of exact copies of several complex variables for the power series representation of any hypercomplex holomorphic function.

2 BASIC NOTATIONS

As usual, let $\{e_1, e_2, \ldots, e_n\}$ be an orthonormal basis of the Euclidean vector space $\mathbb{R}^n$ with a non-commutative product according to the multiplication rules

$$e_k e_l + e_l e_k = -2\delta_{kl}, \quad k, l = 1, \ldots, n,$$

where δ_{kl} is the Kronecker symbol. The set $\{e_A : A \subseteq \{1, \ldots, n\}\}$ with

$$e_A = e_{h_1} e_{h_2} \cdots e_{h_r}, \quad 1 \leq h_1 < \cdots < h_r \leq n, \quad e_\emptyset = e_0 = 1,$$

forms a basis of the 2^n-dimensional Clifford algebra $C\ell_{0,n}$ over $\mathbb{R}$. Let $\mathbb{R}^{n+1}$ be embedded in $C\ell_{0,n}$ by identifying $(x_0, x_1, \ldots, x_n) \in \mathbb{R}^{n+1}$ with

$$x = x_0 + \underline{x} \in \mathcal{A} := \text{span}_{\mathbb{R}}\{1, e_1, \ldots, e_n\} \subset C\ell_{0,n}.$$

Here, $x_0 = \text{Sc}(x)$ and $\underline{x} = \text{Vec}(x) = e_1 x_1 + \cdots + e_n x_n$ are, the so-called, scalar and vector parts of the paravector $x \in \mathcal{A}$. The conjugate of x is given by $\bar{x} = x_0 - \underline{x}$ and its norm by $|x| = (x\bar{x})^{\frac{1}{2}} = (x_0^2 + x_1^2 + \cdots + x_n^2)^{\frac{1}{2}}$.

To call attention to its relation to the complex Wirtinger derivatives, we use the following notation for a generalized Cauchy-Riemann operator in $\mathbb{R}^{n+1}$, $n \geq 1$:

$$\overline{\partial} := \frac{1}{2}(\partial_0 + \partial_{\underline{x}}), \quad \partial_0 := \frac{\partial}{\partial x_0}, \quad \partial_{\underline{x}} := e_1 \frac{\partial}{\partial x_1} + \cdots + e_n \frac{\partial}{\partial x_n}.$$

$\mathcal{C}^1$-functions f satisfying the equation $\overline{\partial} f = 0$ (resp. $f\overline{\partial} = 0$) are called *left monogenic* (resp. *right monogenic*). We suppose that f is hypercomplex-differentiable in Ω in the sense of [7, 8], that is, it has a uniquely defined areolar derivative f' in each point of Ω (see also [9]). Then, f is real-differentiable and f' can be expressed by real partial derivatives as $f' = \partial f$ where,

analogously to the generalized Cauchy-Riemann operator, we use $\partial := \frac{1}{2}(\partial_0 - \partial_{\underline{x}})$ for the conjugate Cauchy-Riemann operator. Since a hypercomplex differentiable function belongs to the kernel of $\overline{\partial}$, it follows that, in fact, $f' = \partial_0 f = -\partial_{\underline{x}} f$ which is similar to the complex case.

In general, $C\ell_{0,n}$-valued functions defined in some open subset $\Omega \subset \mathbb{R}^{n+1}$ are of the form $f(z) = \sum_A f_A(z) e_A$ with real valued $f_A(z)$. However, in several applied problems it is very useful to construct $\mathcal{A}$-valued monogenic functions as functions of a paravector with special properties. In this case we have

$$f(x_0, \underline{x}) = \sum_{j=0}^{n} f_j(x_0, \underline{x}) e_j$$

and left monogenic ($\overline{\partial} f = 0$) functions are also right monogenic functions ($f\overline{\partial} = 0$), a fact which follows easily by direct inspection of the corresponding real system of first order partial differential equations (*generalized Riesz system*).

We use also the classical definition of sequences of Appell polynomials [**?**] adapted to the hypercomplex case.

Definition 2.1 *A sequence of monogenic polynomials $(\mathcal{F}_k)_{k\geq 0}$ of exact degree k is called a generalized Appell sequence with respect to ∂ if*

1. $\mathcal{F}_0(x) \equiv 1$,
2. $\partial \mathcal{F}_k = k\, \mathcal{F}_{k-1},\ k = 1, 2, \ldots$.

The second condition is the essential one while the first condition is the usually applied normalization condition which can be changed to any constant different from zero.

2.1 TOTALLY REGULAR VARIABLES AND GENERALIZED HYPERCOMPLEX APPELL SEQUENCE

To overcome the problem that an integer power of a hypercomplex variable

$$z = x_0 + x_1 e_1 + \ldots + x_n e_n \in \mathcal{A} := \text{span}_{\mathbb{R}}\{1, e_1, \ldots, e_n\} \tag{1}$$

is not hypercomplex holomorphic, Delanghe introduced in [3] the concept of a *totally regular variables* as a linear hypercomplex holomorphic functions whose integer power also are hypercomplex holomorphic. The general Clifford algebra valued case of linear hypercomplex holomorphic functions studied by Delanghe, resulted in very complicated conditions for being totally regular. Restricted to the para-vector case they proved to be only sufficient. Later Gürlebeck ([4], [5]) studied the case of quaternion valued ($\mathbb{H}$ - valued) variables in the form of

$$z = \sum_{k=0}^{3} x_k d_k \tag{2}$$

with $d_k \in \mathbb{H}$ and not necessarily linearly independent.

He found a necessary and sufficient condition expressed by the rank of a reduced coefficient matrix and equivalent with the commutativity of the coefficients d_k.

Here we study only the case of linear paravector valued functions of 3 real variables, subject to a normalization condition with respect to the real variable x_0. The normalization condition

is given in terms of the value of the hypercomplex derivative by demanding that $z' = 1$. This is motivated by the fact that at the same time we are looking for the characterization of all totally regular variables whose integer powers form an Appell sequence in the sense of 2.1 as we know it from the complex case for $z = x + iy$.

That not every totally regular variable and its powers form an Appell sequence and vice versa can be shown by some simple examples. For instance, $z = z_1 = x_1 - x_0 e_1$ is a totally regular variable, because

$$z_1 = \frac{1}{2}(\partial_0 + \partial_{\underline{x}}) z_1 = 0$$

,

but since we have also that

$$z_1' = \frac{1}{2}(\partial_0 - \partial_{\underline{x}}) z_1 = -e_1$$

the sequence $z^n = (z_1)^n = (x_1 - x_0 e_1)^n$ is not an Appell sequence in the sense of 2.1.
From the other side, the standard Appell sequence considered in [1] of the form

$$\mathcal{P}_k^n(x) = \sum_{s=0}^{k} \binom{k}{s} c_s \, x_0^{k-s} \, \underline{x}^s \tag{3}$$

with the *generalized central binomial coefficient* given by

$$c_k := \frac{1}{2^k} \binom{k}{\lfloor \frac{k}{2} \rfloor}, \tag{4}$$

where $\lfloor \, . \, \rfloor$ is the usual floor function, is an Appell sequence which does not consist of totally regular variables.

REFERENCES

[1] Falcão, M.I., Cruz, J, and H.R. Malonek: Remarks on the generation of monogenic functions., 17th Inter. Conf. on the Appl. of Computer Science and Mathematics on Architecture and Civil Engineering, K. Gürlebeck and C. Könke eds., Weimar, 2006.

[2] Bock, S. and K. Gürlebeck, K.: On a generalized Appell system and monogenic power series, Math. Methods Appl. Sci., **33**, 394-411, 2010.

[3] Delanghe, R.: On regular-analytic functions with values in a Clifford algebra, Math. Ann. **185**, 91-111, 1970.

[4] Gürlebeck, K.: Über Interpolation und Approximation verallgemeinert analytischer Funktionen, Wiss. Inf. **34**, TH Karl-Marx-Stadt, 1982.

[5] Gürlebeck, K., Sprössig, W.: Quaternionic analysis and elliptic boundary value problems, Birkhuser Verlag, Basel, 1990.

[6] Habetha, K.: Function theory in algebras, in: Complex analysis. Methods, trends, and applications, E. Lanckau and W. Tutschke eds. Akademie-Verlag Berlin, 225-237, 1983.

[7] K. Gürlebeck and H. R. Malonek, A Hypercomplex Derivative of Monogenic Functions in $\mathbb{R}^{n+1}$ and Its Applications, Complex Variables Theory Appl. **39**, 199–228, 1999.

[8] H. R. Malonek, A New Hypercomplex Structure of the Euclidean Space $\mathbb{R}^{m+1}$ and the Concept of Hypercomplex Differentiability, Complex Variables **14**, 25–33, 1990.

[9] H. R. Malonek, Selected Topics in Hypercomplex Function Theory, in Clifford Algebras and Potential Theory, S.-L. Eriksson, Ed., **7**, University of Joensuu, 111–150, 2004.

19th International Conference on the Application of Computer
Science and Mathematics in Architecture and Civil Engineering
K. Gürlebeck, T. Lahmer and F. Werner (eds.)
Weimar, Germany, 04–06 July 2012

MODEL QUALITY EVALUATION OF COUPLED RC FRAME-WALL SYSTEMS FOR GLOBAL DAMAGE ASSESSMENT

S. Marzban[*], **J. Schwarz**[**]

[*] *Bauhaus-Universität Weimar*
Graduiertenkolleg 1462 'Modellqualitäten',
Berkaer Straße 9, 99423 Weimar, Germany
E-mail: samira.marzban@uni-weimar.de
[**] *Zentrum für die Ingenieuranalyse von Erdbebenschäden - Erdbebenzentrum*
Marienstraße 13B, 99421 Weimar, Germany
Email: schwarz@uni-weimar.de

Keywords: Model quality, Coupled frame-wall systems, global/partial models

Abstract. *Civil engineers take advantage of models to design reliable structures. In order to fulfill the design goal with a certain amount of confidence, the utilized models should be able to predict the probable structural behavior under the expected loading schemes. Therefore, a major challenge is to find models which provide less uncertain and more robust responses. The problem gets even twofold when the model to be studied is a global model comprised of different interacting partial models. This study aims at model quality evaluation of global models with a focus on frame-wall systems as the case study. The paper, presents the results of the first step taken toward accomplishing this goal. To start the model quality evaluation of the global frame-wall system, the main element (i.e. the wall) was studied through nonlinear static and dynamic analysis using two different modeling approaches. The two selected models included the fiber section model and the Multiple-Vertical-Line-Element-Model (MVLEM). The influence of the wall aspect ratio (H/L) and the axial load on the response of the models was studied. The results from nonlinear static and dynamic analysis of both models are presented and compared. The models resulted in quite different responses in the range of low aspect ratio walls under large axial loads due to different contribution of the shear deformations to the top displacement. In the studied cases, the results implied that careful attention should be paid to the model quality evaluation of the wall models specifically when they are supposed to be coupled to other partial models such as a moment frame or a soil-footing substructure which their response is sensitive to shear deformations. In this case, even a high quality wall model would not result in a high quality coupled system since it fails to interact properly with the rest of the system.*

1 INTRODUCTION

In the field of civil engineering the goal is to design structures that, with a certain amount of confidence, will be able to fulfill their purpose of construction i.e. withstand loading and deformation schemes the structure is expected to undergo during its lifetime. In other words a civil engineer aims at designing reliable structures by examining the *probable* response of the structure under *expected* loading conditions. Such terms are normally observed in the civil engineering technical literature due to the facts that the human knowledge about the nature of the phenomena underlying the structural behavior is limited and that many phenomena even have randomness as their inherent characteristic. Consequently, any model which is an abstraction of the phenomena to be studied, also faces deficiencies in terms of knowledge i.e. *uncertainties*. Finding models that can be employed as tools to further design reliable structures has therefore turned into a challenge. As a solution, *model quality criteria* are defined which allow for making decisions over a range of plausible models. Since most of the engineering models, when possible, are discretized into smaller distinct but coupled parts (so called partial models) to ease their study, the model quality evaluation originally starts from the partial models and their coupling. The ongoing study, conducted by the first author, aims at evaluating the global model quality of coupled partial models for damage assessment purposes considering the quality of the partial models and their coupling. To find a general solution coupled reinforced concrete (RC) frame-wall systems are studied as an example of widely used coupled structural systems. In the present study, the model quality evaluation process is started by investigating the wall models since the wall element is the crucial partial model in the coupled system. Based on a literature survey, two of the well known modeling approaches, namely the fiber section model and the Multiple-Vertical-Line-Element-Model (MVLEM) were chosen for further studies. To take the first step, the model responses under cyclic deformation-controlled loading are compared to a selected observed response. To further investigate the differences, the models responses are then compared through static and dynamic analysis. Finally, the results are discussed and conclusions are derived.

2 MODEL QUALITY EVALUATION OF COUPLED SYSTEMS

The main challenge in the model quality evaluation process is to prove the model to be an appropriate representative of the real structural system for its intended purpose of use. The difficulty gets even twofold in the absence of adequate observed data from real and experimental systems to validate the global model. For the specific case of a frame-wall system, for instance, almost negligible amount of experimental data is available for the coupled system (particularly in interaction with the soil-footing substructure). Although, an extensive number of experiments can be found in the literature individually focused on wall or frame elements. So, one of the primary challenges in the field of frame-wall systems, is to validate the global model when there is only a chance to validate its partial models against experimental data. In fact RC structural walls have gained considerable attention in the construction/rehabilitation of new/existing buildings in regions with medium to high seismic hazard. This is mainly because: they provide structures with lateral stiffness, strength and ductility if properly designed/constructed and they have shown reasonable performance during the past earthquakes. In the most common building configuration, the RC walls are combined with a gravity resisting system (usually RC moment frames or slabs) to form an integrated lateral/vertical load-carrying system. In such frame-wall structures the most lateral resisting of the system is supplied by the walls. Therefore, their modeling and design becomes a critical issue, since the structural performance under

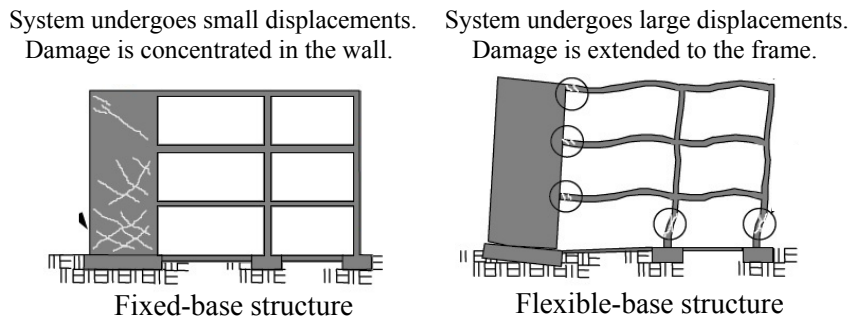

Figure 1: Structural response of a coupled frame-wall system in the presence/absence of the couplings (Originally from [1])

seismic actions relies mainly on their performance. Nevertheless, it has been learned from the past earthquakes that the wall performance can be significantly affected by the interactions with other substructures (see Figure 1).

So far, it is quite well understood that neglecting the coupling effects may lead to a misestimation of the structural response/damage. In spite of being aware of this, however, it has been a common practice to ignore the interaction among the substructures in frame-wall systems. The absence of adequate observed data for the global model to be validated on one hand and the complexity of the available models which does not allow for parametric studies on the global model on the other hand may be the main reasons. For instance, many researchers have focused on the study of RC walls ([28, 11, 13, 19, 5, 12, 6, 18, 15, 24] among the others) whereas quite a few have investigated the coupled frame-wall systems particularly in interaction with the soil-foundation substructure ([23, 3, 16, 27, 21, 26, 4] among the others). Evidently, there is still a crucial need to quantitatively measure the importance of coupling effects by means of tools like the sensitivity analysis. Based on the results from a sensitivity analysis one can decide whether or not the global model under study can be reduced to its partial models by disregarding some uninfluential parameters/aspects/interactions.

3 MODELING APPROACHES

The global model of the system to be studied is constructed by means of coupling different partial models. The choice of a specific modeling approach not only depends on the capabilities of the resulting partial model in representing a part of the whole system, but also on its capacity to interact properly with the rest of the system. In other words, when dealing with global models, the *high quality* of a partial model does not necessarily signify that its application will lead to a *high quality* of the global model. In fact, in cases where the desired degree of coupling to the other partial models can not be reached, the overall quality may even decrease. Finally, one also has to consider the amount of computational time and effort to be supplied when selecting a model out of a number of plausible models.

In the superstructure of a RC frame-wall system at least two partial models can be distinguished, namely: the wall and the frame. According to the technical literature, the numerical modeling of RC frame elements has been well developed ([7, 17, 25, 8] among the others). Distributed and lumped plasticity elements are widely being used to analyze and design RC frames. Distributed plasticity models are mainly based on the fiber section concept which allows for the interaction between flexural and axial behaviors. Models based on this concept provide pow-

erful tools for the analysis of RC frame elements in which the shear deformations are roughly ignorable. The main challenge, however, is to find an appropriate model for the wall element.

Numerous micro/macro models have also been proposed for structural walls ([10] reviews a selected number of the available models). According to the technical literature, the most efficient models, in terms of the capabilities and accuracy on one hand and the required computational time and cost on the other hand, are based on the fiber section concept. This modeling method is considered as a *micro-modeling* approach and thus is able to predict both local and global damages in the wall. The main drawback is that since fibers only undergo axial deformations the model fails to detect shear deformations. This may result in unrealistic predictions of the wall response in the case of squat walls (i.e. aspect ratios less than 2.0, as a practical criteria). Not to mention that the model also fails to consider some observed phenomena like neutral axis shift. To further develop the method macro models have been proposed which not only benefit from the fiber section concept but also from some additional features that cover the shortcomings of the fiber section method. "Multiple Vertical Line Element Model (MVLEM)" is one of the well known solutions. Fibers are individually defined as 'vertical line elements' over the section and a shear spring is added to allow for deformations under shear actions. Although in this case, no interaction between the flexural and shear behaviors is considered which seems to be inconsistent with experimental observations according to [19]. Nevertheless, the MVLEM constructed through the above-mentioned procedure provides a powerful tool to predict RC wall behavior under lateral loadings.

The basic concept for creating the MVLEM is to separate the flexural and shear behaviors of the wall element (see Figure 2). Here the two modes of deformation are assumed to be uncoupled. The flexural and axial behaviors of the wall (and their corresponding interaction) are represented by the contribution of fibers whereas the shear spring constitutes the behavior under shear actions. Relative rotation of the upper bound of the wall to its base is defined by considering a center of rotation. The point is located on the central column of the element at a specific height ch where h is the height of the wall (see Figure 3). c is practically set to be 0.4 for common applications [28]. It is however recommended to include more elements along the height of the wall where significant nonlinear behavior is expected. This is to avoid curvature misestimations in the regions where it is highly variable [8]. Although, the total number of divisions along the height or the length of the wall does not have a significant effect on the overall behavior of the wall. Nevertheless, by adding more elements it is more likely that one can detect the desired local behavior/damage [15, 20].

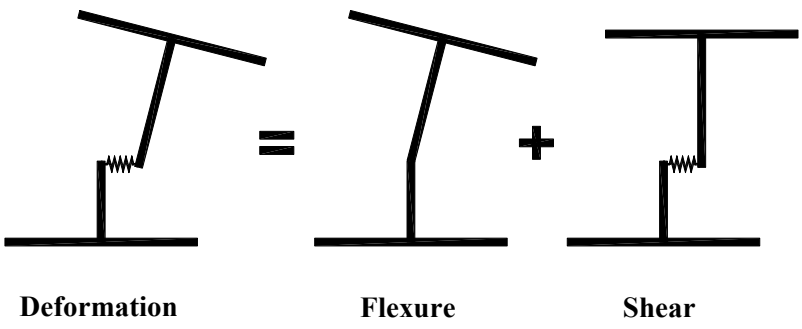

Figure 2: Schematic deformation decoupling of a RC wall element in MVLEM [19]

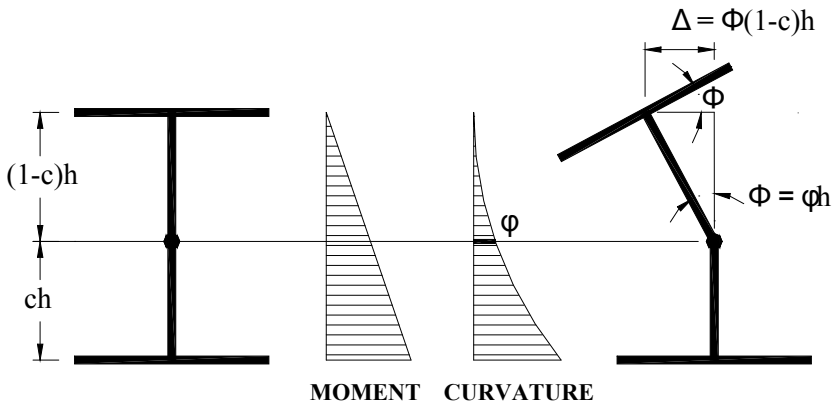

Figure 3: Center of rotation in MVLEM [19]

Quite well known material models are available for concrete (e.g. Kent-Scott-Park model with tensile strength) and steel (e.g. Menegotto-Pinto model) to define the vertical line elements' sectional force-deformation relationships under axial actions. There are also a handful of choices for the hysteretic behavior to be assigned to the shear spring i.e. the sectional force-deformation relationship under shear actions ([16, 9, 19, 29, 15]). Here, the major concern is to represent the low hysteretic energy absorbtion capability in shear. Mostly, this is done by means of origin-oriented or pinching hysteretic materials. In this study a pinching hysteretic material with a trilinear backbone curve was used. Its behavior under cyclic loading is determined by means of some predefined rules. The cracking and yield properties of the backbone curve were calculated according to [16, 22]. The aforementioned hysteretic material allows for pinching of force and deformation, damage due to ductility and energy, and degraded unloading stiffness based on ductility. More details about hysteretic materials can be found in [14].

To study the MVLEM the results from static monotonic and cyclic as well as dynamic analysis of the model were compared to the corresponding results of a fiber section model. Both models were created and analyzed using the OpenSees platform. The fiber section model consisted of a single column defined with *nonlinearBeamColumn* element to which a fiber section was assigned. *Concrete02* (Kent-Scott-Park model with linear tension softening) and *Steel02* (Giuffre-Menegotto-Pinto model) were chosen to represent the constitutive material relationships of the concrete and the reinforcing steel, respectively. In order to consider the deformations due to shear, the force-deformation relationship of the section under shear actions was separately calculated as discussed before and was added to the previously defined fiber section. To create the MVLEM, two MVLEM sets were stacked along the height of the wall each having half the height of the wall. Each of the MVLEM sets consisted of 11 truss elements to which fiber sections with the same material properties as those of the fiber section model were assigned. The truss elements were connected by means of rigid beams at their end nodes. The central columns were divided into two rigid parts at 40% of their heights. Horizontal (shear) and vertical springs were defined to connect the two parts of each central column. The shear spring properties were calculated in the same manner as those of the fiber section model. The two models created through the abovementioned procedures are schematically shown in Figure 4. The numerical results will be presented in the following section.

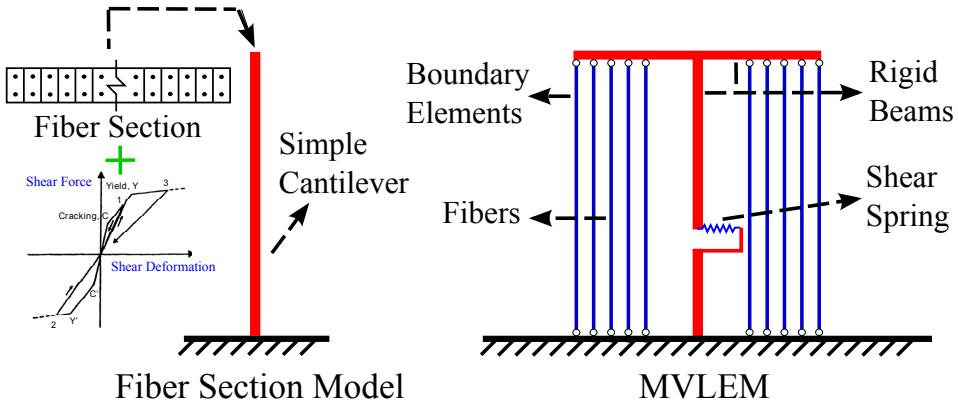

Figure 4: The two studied models: the fiber section model and the MVLEM

4 NUMERICAL RESULTS: MVLEM VS FIBER SECTION MODEL

To take the first step, the MVLEM was verified/validated against observed response of a selected wall specimen to check its potential for further studies. For this purpose, the specimen WSH3, one of the 6 wall specimens tested within an experimental program conducted at the ETH Zurich [6], was chosen as the reference experimental model. During the test the specimens were subjected to a deformation-controlled quasi-static cyclic loading. Details about the loading schemes can be found in [6]. The WSH3 with a height of $4.56m$ had a rectangular section of $2.0m$ length and $0.15m$ thickness. The reinforcement layout is shown in Figure 5. Compressive strength (f'_c) and modulus of elasticity (E_c) for concrete were reported to be 39.2 MPa and 35.2 GPa, respectively. Also, the yield strength of steel (f_y) for boundary and web reinforcements were respectively recorded to be 601.0 MPa and 569.2 MPa. Additional information about the sectional and material properties can be found in [6]. It is worth mentioning that throughout the rest of the study the sectional and material properties are kept unchanged. Comparison of the results from this step are presented in Figure 6. Very good agreement can be seen between the three responses (i.e. MVLEM, fiber section model and the experimental results). The model was therefore qualified to be used for further sensitivity/uncertainty studies.

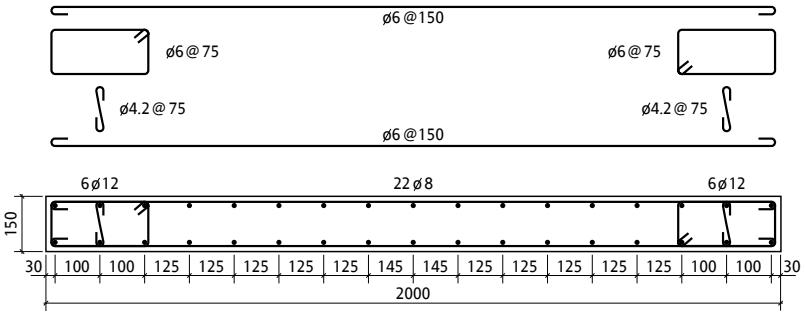

Figure 5: Reinforcement layout for the WSH3 specimen [6]

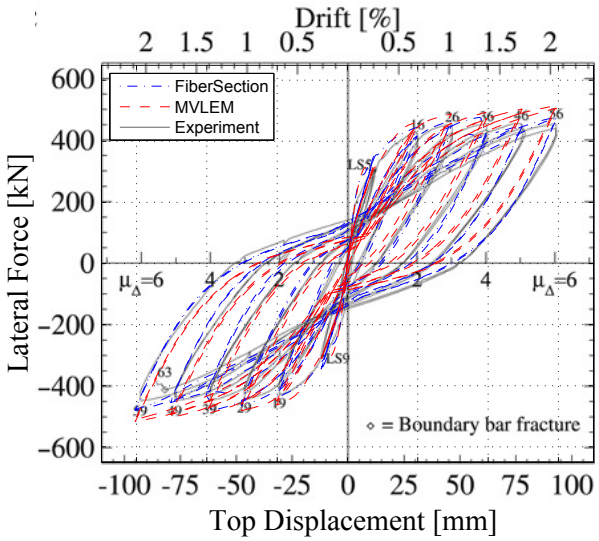

Figure 6: Static cyclic analysis results of the two studied models compared to the experimental results for the WSH3 specimen from [6]

In the next step, sensitivity analysis was used to find out the influence of the wall aspect ratio (H/L) and the amount of the axial load (P) on the response of the wall. The mentioned parameters are known to have noticeable effects on the response of wall elements. The two variables were assumed to have uniformly distributed probability densities over their entire ranges ($[1.0-3.0]$ for the wall aspect ratio and $[100.0-1500.0]$kN for the axial load). Latin Hypercube Sampling method was used to generate 400 samples for the pushover analysis and 100 samples for the dynamic analysis from the marginal probability distributions of the variables. Figure 7 shows the distribution of the studied samples in the case of the dynamic analysis. In the next sections the nonlinear static and dynamic analysis results from the two studied models will be presented, compared and discussed.

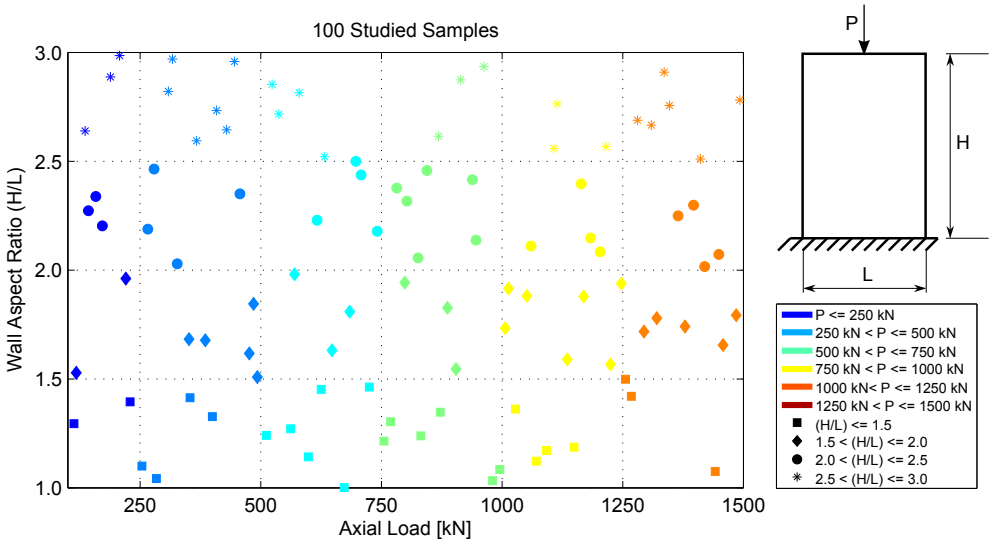

Figure 7: Distribution of the studied samples for the dynamic analysis with regard to the variables

4.1 Static Monotonic Analysis (Pushover)

Primarily, gravity analysis was performed for each model under the sampled axial load. A displacement-controlled pushover analysis was then performed until the top displacement (controlled displacement) reached 2% of the height for each model (2% drift was roughly taken as the failure drift). The resulting pushover curves (i.e. base shear vs top displacement curves) of both the MVLEM and the fiber section model are shown in Figure 8 for 400 samples. As it is obvious from the figure, the models have resulted in similar response curves in the case of less stiff walls (i.e. walls with aspect ratios greater than 2.0). However, failure in fiber section models with aspect ratios less than 2.0 signifies a noticeable difference between the two models.

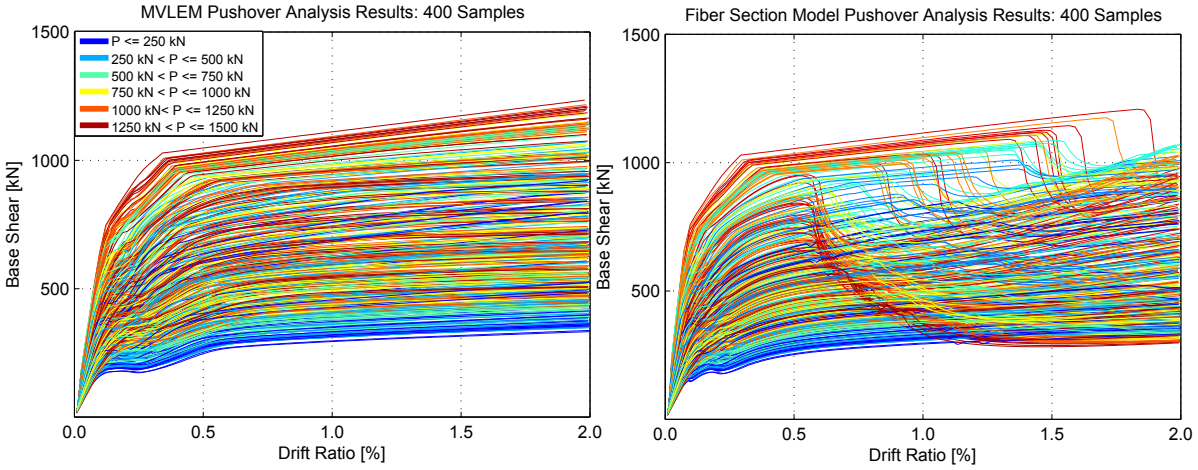

Figure 8: Pushover curves of the studied models

To further investigate the reason for the unlike failure of the fiber section model the contribution of the shear and flexural deformations to the total top displacement was studied. Figures 9 and 10 compare the shear and flexure-induced top displacements of the two models at the last step of the pushover analysis with regard to the wall height and the axial load value. According to Figure 9, shear deformations predicted by the MVLEM are at least two times those predicted by the fiber section model. Under larger axial loads the difference between the estimated shear deformations by the two models becomes even more than a factor of two. In addition, in the case of highly vertically loaded walls with aspect ratios close to 1.5 contribution of the shear deformations to the total top displacement in the MVLEM can be dramatically more than that of the fiber section model. In contrast, the flexural deformations in the MVLEM account for an ignorable portion of the top displacement in the same range (see Figure 10). It can be concluded that for the walls with aspect ratios close to 1.5 which are bearing large axial loads the fiber section model significantly overestimates the contribution of the flexural deformations to the top displacement on one hand and underestimates the contribution of the shear deformations, on the other hand. As a result of noticeable flexural deformations the fiber section model reaches failure at early steps of the pushover analysis. Failure due to shear is not captured in any of the models because no significant strength reduction was considered in the trilinear backbone curve used to define the force-deformation relationship in shear. The above discussion implies that in the studied cases even if both models result in high model qualities in the prediction of the top displacement, they may result in quite different global model qualities when coupled to other

partial models which are sensitive to shear deformations.

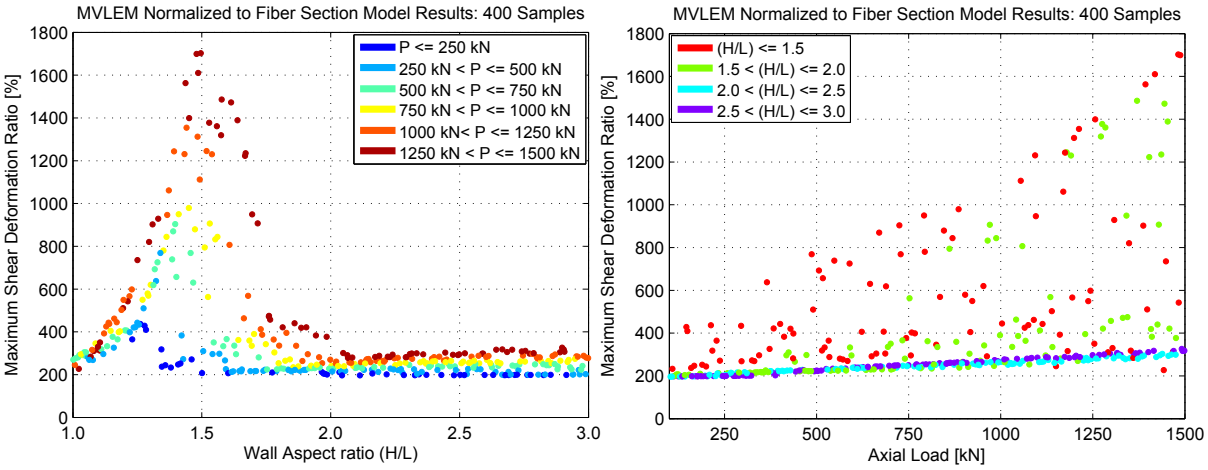

Figure 9: Scatter of the normalized shear-induced top displacement of the studied samples with regard to the variables

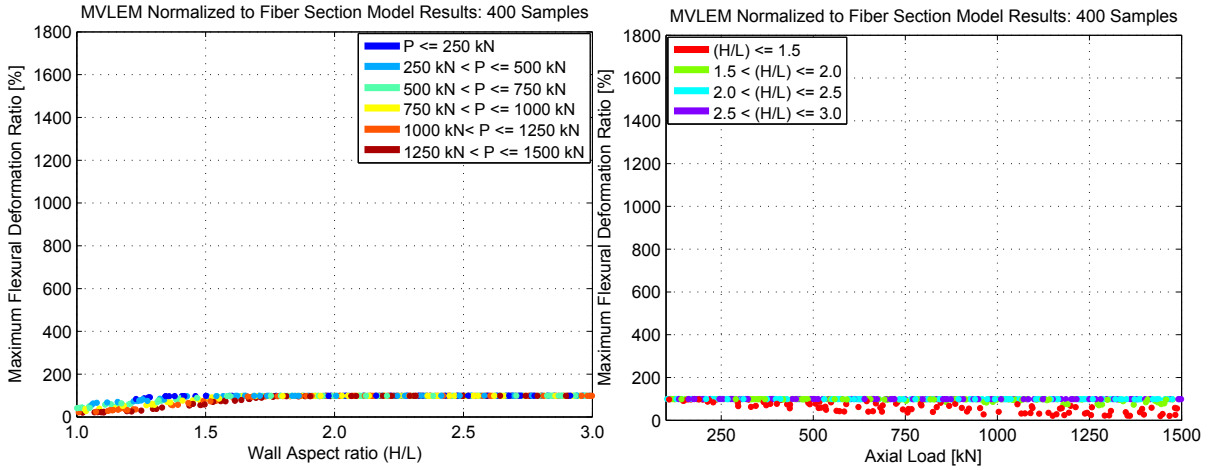

Figure 10: Scatter of the normalized flexure-induced top displacement of the studied samples with regard to the variables

4.2 Dynamic Analysis

44 ground motions were selected according to the far-field record set of FEMAp695 [2] to perform the dynamic analysis. The record set includes twenty-two records (44 individual components) taken from the PEER NGA database. Details about the ground motions can be found in [2]. In sum, 100 samples were chosen which implies a total 440 number of nonlinear dynamic analysis. As in the case of the pushover analysis, each model was imposed to the sampled axial load before the dynamic analysis was performed. The fundamental periods of the models were then computed and used to calculate the spectral accelerations of the models for

each of the 44 selected ground motions. Scatter of the MVLEM fundamental period normalized to that of the fiber section model with regard to the wall height and the axial load value is shown in Figure 11. Clearly, the two models produce almost the same fundamental periods. Only in the range of lower wall aspect ratios the MVLEM estimates the period slightly larger than the fiber section model. The resulting spectral accelerations are also compared for the two models in Figure 12. According to the figure, the most scatter comes from the samples with lower aspect ratios and higher axial loads. As in the case of the pushover analysis, the two models tend to behave differently in this range of the variables due to unlike contribution of the shear deformations to the overall response. The two models were then subjected to the 44 selected ground motions to further compare the dynamic analysis results. Figure 13 depicts the scatter of the resulting maximum top displacement of the MVLEM normalized to that of the fiber section model with respect to the studied variables. Again, the low aspect ratio region accounts for the most differences between the two models' responses. The larger scatter however comes from larger axial load values.

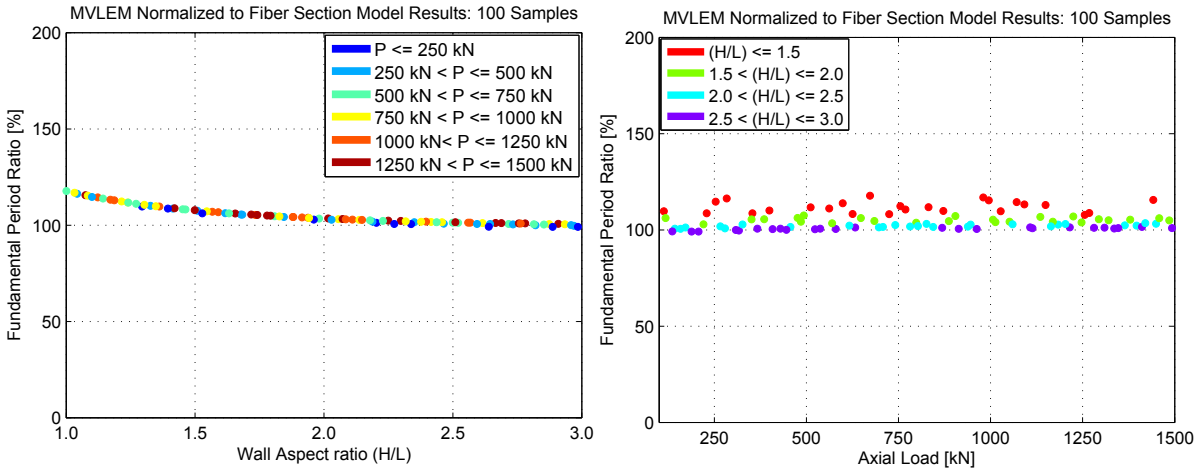

Figure 11: Scatter of the normalized fundamental period of the studied samples with regard to the variables

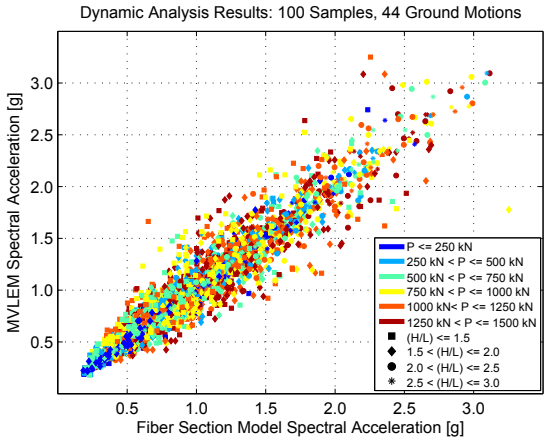

Figure 12: Spectral acceleration at the fundamental period of the studied samples for 44 ground motions

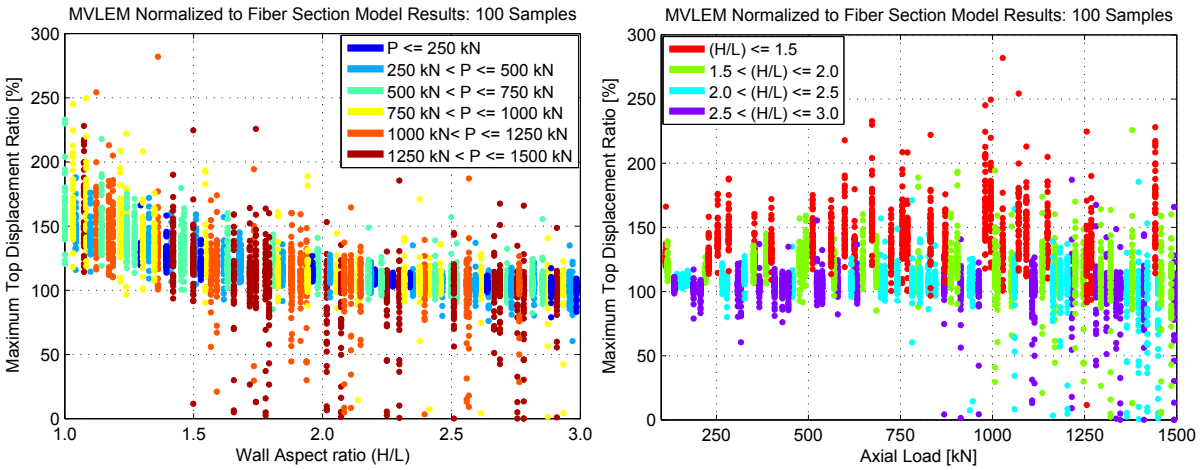

Figure 13: Scatter of the normalized maximum top displacement of the studied samples with regard to the variables

5 CONCLUSIONS

In order to take the first step in the model quality evaluation of coupled frame-wall systems, the main partial model of the system i.e. the wall element was studied through nonlinear static and dynamic analysis. Fiber section model and the Multiple-Vertical-Line-Element-Model (MVLEM) were selected from two major modeling categories (micro- and macro-modeling approaches respectively). To check the potential of the models in the prediction of the wall response, comparison to a selected observed response was made. The models produced responses in close agreement with the observed behavior. Later, the influence of the wall aspect ratio (H/L) and the axial load on the response of the models was investigated through sensitivity analysis. In case of the pushover analysis, the models resulted in quite similar behavior for high aspect ratio walls under low axial loads. However, a dramatic difference was seen between the model responses in the range of low aspect ratio walls under high levels of axial load due to the unlike contribution of the shear deformations to the total top displacement. In the aforementioned range of the variables, the fiber section reached flexural failure at early steps of the pushover analysis since the flexural deformations had to increase significantly in order to fill in for the less contribution of the shear deformations to the top displacement. In the studied cases, this implies that careful attention should be paid to the model quality evaluation of the wall models specifically when they are supposed to be coupled to other partial models. Other partial models may include a moment frame or a soil-footing substructure which their response can be sensitive to shear deformations. If this is the case then even a high quality wall model would not result in a high quality coupled system since it fails to interact properly with the rest of the system. Based on the above discussion, one may be able to define coupling capabilities as one of the properties of a given model. Finally, the dynamic analysis results were presented and compared. According to the results, as in the case of the pushover analysis the most differences between the models' responses is concentrated in the range of low aspect ratios and large axial loads. Further check of the model responses with other models (numerical and physical) is required in order to infer conclusions about the quality of the models. This is the focus of an ongoing research by the first author.

ACKNOWLEDGMENTS

The first author is currently a member of the Research Training Group 1462 (GRK 1462) at the Faculty of Civil Engineering, Bauhaus University of Weimar. The ongoing research is funded by the German Research Foundation (DFG). This support is gratefully acknowledged.

REFERENCES

[1] Applied Technology Council. ATC-40: Seismic Evaluation and Retrofit of Concrete Buildings. Technical report, Seismic Safety Commission, State of California, Redwood, California, US, 1996.

[2] Applied Technology Council. FEMAp695: Quantification of Building Seismic Performance Factors. Technical report, Federal Emergency Management Agency (FEMA), Washington, D.C., US, June 2009.

[3] G. Areiza and C. N. Kostem. Interaction of Reinforced Concrete Frame-Cracked Shear Wall Systems Subjected to Earthquake Loadings. Technical Report 433,4, Fritz Engineering Laboratory, Department of Civil Engineering, Lehigh University, Bethlehem, Pennsylvania, July 1979.

[4] Y. Bao and S. K. Kunnath. Simplified Progressive Collapse Simulation of RC Frame-wall Structures. *Engineering Structures*, 32:3153–3162, 2010.

[5] Y. Belmouden and P. Lestuzzi. Analytical Model for Predicting Nonlinear Reversed Cyclic Behaviour of Reinforced Concrete Structural Walls. *Engineering Structures*, 29:1263–1276, 2007.

[6] A. Dazio, K. Beyer, and H. Bachmann. Quasi-Static Cyclic Tests and Plastic Hinge Analysis of RC Structural Walls. *Engineering Structures*, 31:1556–1571, 2009.

[7] F. C. Filippou and A. Issa. Nonlinear Analysis of Reinforced Concrete Frames Under Cyclic Load Reversals. Technical Report UCB/EERC88/12, Earthquake Engineering Research Center, College of Engineering, University of California, Berkeley, September 1988.

[8] M. Fischinger, T. Vidic, and Fajfar P. *Nonlinear Seismic Analysis and Design of Reinforced Concrete Buildings*, chapter Nonlinear Seismic Analysis Of Structural Walls Using The Multiple-Vertical-Line-Element Model, pages 191–202. Elsevier Applied Science, 1992.

[9] M. Fischinger, T. Vidic, J. Selih, P. Fajfar, H. Y. Zhang, and F.B. Damjanic. Validation of a Macroscopic Model for Cyclic Response Prediction of RC Walls. In *2nd International Coneference on Computer Aided Analysis and Design of Concrete Structures*, volume 2, pages 1131–1142, Zell am See, Austria, 4-6 April 1990.

[10] K. Galal and H. El-Sokkary. Advancement In Modeling of RC Shear Walls. In *14th World Conference on Earthquake Engineering*, Beijing, China, October 12-17 2008.

[11] A. Ghobarah and M. Youssef. Modelling of Reinforced Concrete Structural Walls. *Engineering Structures*, 21:912–923, 1999.

[12] C. K. Gulec and A. S. Whittaker. Performance-Based Assessment and Design of Squat Reinforced Concrete Shear Walls. Technical Report MCEER-09-0010, MCEER, University at Buffalo, State University of New York, September 15 2009.

[13] P. A. Hidalgo, R. M. Jordan, and M. P. Martinez. An Analytical Model to Predict the Inelastic Seismic Behavior of Shear-Wall, Reinforced Concrete Structures. *Engineering Structures*, 24:85–98, 2002.

[14] L. F. Ibarra, R. A. Medina, and H. Krawinkler. Hysteretic Models that Incorporate Strength and Stiffness Deterioration. *Earthquake Engineering and Structural Dynamics*, 34:14891511, 2005.

[15] A. Jalali and F. Dashti. Nonlinear Behavior of Reinforced Concrete Shear Walls Using Macroscopic and Microscopic Models. *Engineering Structures*, 32:2959–2968, 2010.

[16] T. Kabeyasawa, H. Shiohara, S. Otani, and H. Aoyama. Analysis of the Full-Scale Seven-Story Reinforced Concrete Test Structure. *Journal of Faculty of Engineering, University of Tokyo*, 37(2):432 – 478, 1983.

[17] H.-g. Kwak and F. C. Filippou. Finite Element Analysis of Reinforced Concrete Structures under Monotonic Loads. Technical report, Department of Civil Engineering, University of California, Berkeley, Berkeley, California, November 1990.

[18] L. M. Massone. Strength Prediction of Squat Structural Walls via Calibration of a Shear-Flexure Interaction Model. *Engineering Structures*, 32:922–932, 2010.

[19] K. Orakcal, L. M. Massone, and J. W. Wallace. Analytical Modeling of Reinforced Concrete Walls for Predicting Flexural and Coupled-Shear-Flexural Responses. Technical Report PEER 2006/07, Pacific Earthquake Engineering Research Center, October, 2006.

[20] K. Orakcal, J. W. Wallace, and J. P. Conte. Flexural Modeling of Reinforced Concrete Walls-Model Attributes. *ACI Structural Journal*, 101(5):688–398, 2004.

[21] M. Panneton, P. Lger, and R. Tremblay. Inelastic Analysis of a Reinforced Concrete Shear Wall Building According to the National Building Code of Canada 2005. *Canadian Journal of Civil Engineering*, 33(7):854–871, 2006.

[22] Y. J. Park and C. H. Hofmayer. Shear Wall Experiments and Design in Japan. In *5th Symposium on Current Issues Related to Nuclear Power Plant Structures, Equipment and Piping*, Lake Buena Vista, Florida, US, December 1994.

[23] R. Rosman. Stability and Dynamics of Shear-Wall Frame Structures. *Building Science*, 9(1):55–63, 1974.

[24] B. Shafei, F. Zareian, and D. G. Lignos. A Simplified Method for Collapse Capacity Assessment of Moment-Resisting Frame and Shear Wall Structural Systems. *Engineering Structures*, 33:1107–1116, 2011.

[25] E. Spacone, V. Ciampi, and F. C. Filippou. A Beam Element for Seismic Damage Analysis. Technical Report UCB/EERC-92/07, Earthquake Engineering Research Center, College of Engineeruing, University of California, Berkeley, August 1992.

[26] B. Taskin and Z. Hasgr. Monte Carlo Analysis of Earthquake Resistant RC 3D Shear Wall-Frame Structures. *Structural Engineering and Mechanics*, 22(3):371–399, 2006.

[27] A. Vulcano. Use of Wall Macroscopic Models in the Nonlinear Analysis of RC Frame-wall Structures. In *10th World Conference on Earthquake Engineering*, Balkema, Rotterdam, 1992.

[28] A. Vulcano and V. V. Bertero. Analytical Models for Predicting the Lateral Response of RC Shear Wall: Evaluation of Their Reliability. Technical Report UCB/EERC-87/19, Earthquake Engineering Research Center, November 1987.

[29] H. Xiaolei, C. Xuewei, J. Cheang, M. Guiniu, and W. Peifeng. Numerical Analysis of Cyclic Loading Test of Shear Walls based on OpenSees. In *14th World Conference on Earthquake Engineering*, Beijing, China, 12-17 October 2008.

19th International Conference on the Application of Computer
Science and Mathematics in Architecture and Civil Engineering
K. Gürlebeck, T. Lahmer and F. Werner (eds.)
Weimar, Germany, 04–06 July 2012

SYSTEM IDENTIFICATION METHODS FOR GROUND MODELS IN MECHANIZED TUNNELING

S. Miro*, D. Hartmann, T. Schanz, and V. Zarev

**Chair of Computing in Engineering*
Ruhr-University Bochum, Germany
E-mail: shorash.miro@rub.de

Keywords: System Identification, Ground Modeling, Global Sensitivity Analysis, Non-standard Optimization, Handling of Uncertainties, Mechanized Tunneling.

Abstract. *Due to the complex interactions between the ground, the driving machine, the lining tube and the built environment, the accurate assignment of in-situ system parameters for numerical simulation in mechanized tunneling is always subject to tremendous difficulties. However, the more accurate these parameters are, the more applicable the responses gained from computations will be. In particular, if the entire length of the tunnel lining is examined, then, the appropriate selection of various kinds of ground parameters is accountable for the success of a tunnel project and, more importantly, will prevent potential casualties. In this context, methods of system identification for the adaptation of numerical simulation of ground models are presented. Hereby, both deterministic and probabilistic approaches are considered for typical scenarios representing notable variations or changes in the ground model.*

1 INTRODUCTION

In July 2010 a new collaborative research center (**SFB** 837) started at Ruhr-Universitt Bochum Germany, entitled *Interaction Models in Mechanized Tunneling*. The center consists of 14 subprojects and it is funded by the German Research Foundation (**DFG**). This paper is part of the work conducted in the subproject **C2** Methods of System Identification for the Adaptation of Numerical Simulation Models.

The ground model is central to computational tunneling, where a realistic ground model is crucial for predicting the distributions and magnitudes of the strains and, consequently, reducing the surface settlements caused by the TBM propagation. Based upon the information of bore holes sunken in the target area of the tunnel alignment, the ground model describes the detailed spatial distribution of the constitutive soil properties along with the geometry of the stratification. Customary bore holes, however, provide only an approximate insight into the real world geologic realities. As a consequence, only the realization of the system identification approach can result in improved and more sophisticated numerical predictions of the spatiotemporal ground behavior induced by driving the tunnel.

For system identification, a numerical simulation model is required. This model, however, represents a complex, mechanically-hydraulically coupled and a three dimensional initial boundary value problem. Also, it is characterized by various physical nonlinearities as well as various construction stages. For application in a later reference tunnel project, numerical simulation models are needed which enable the appropriate *forward computation* of typical scenarios describing relevant variations or changes in the ground model with respect to prescribed output states.

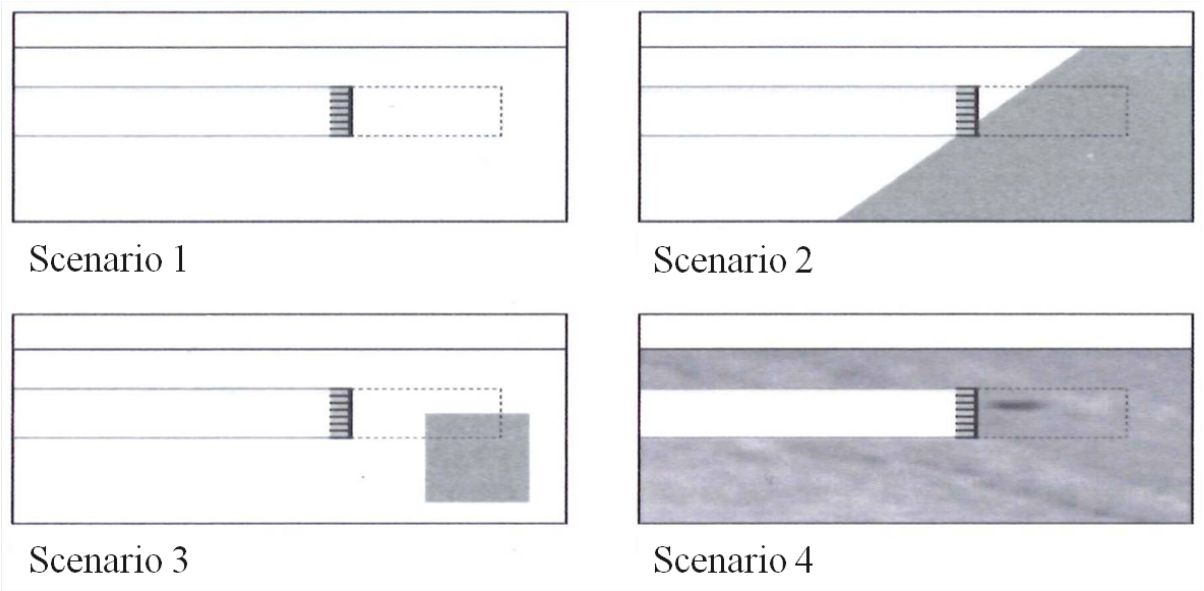

Figure 1: Subsoil scenarios for the forward computation.

According to Figure 1, the following scenarios have been defined:

- Scenario #1: advance in homogeneous soil.
- Scenario #2: advance in two homogeneous sub-soils where the parameters and inclination of the second one are unknown.

- Scenario #3: advance in a homogeneous subsoil with a cubic impediment (unknown in position, dimension and material parameters) in front of the tunnel face.
- Scenario #4: advance in an inhomogeneous subsoil with unknown parameters and spatial distribution.

2 METHODOLOGY

Methodologically, the solution of a system identification problem is based on the concatenation of observations (measurements) and computations (numerical results) using the inverse analysis procedure. By that, the defect between the measurement-based properties and the computed ones is being minimized.

2.1 2.1 Deterministic Approach

In deterministic inverse analysis, the selected numerical model is calibrated by iteratively changing a subset of its parameters until the discrepancies between the calculated/simulated responses and the observed/measured data reach a predefined minimum [1]. This procedure is illustrated in Figure 2.

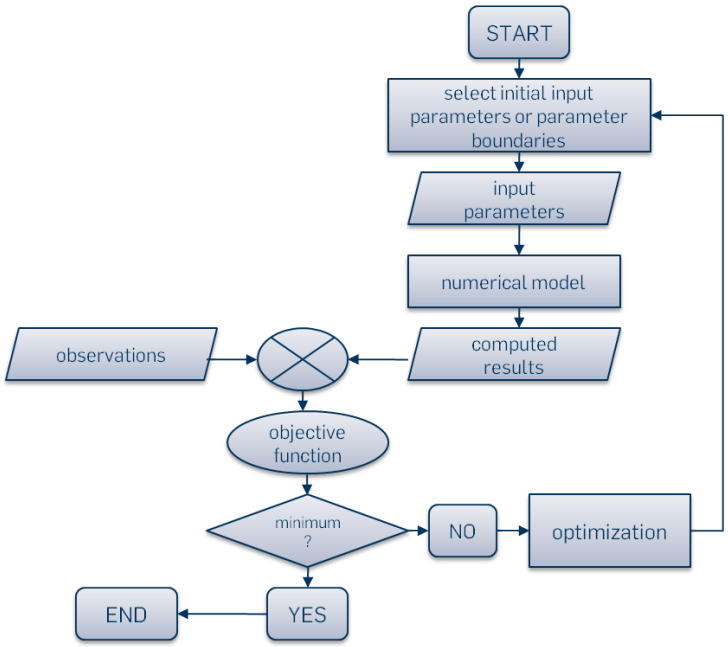

Figure 2: Scheme of inverse analysis procedure.

In the first step of the procedure, a priori estimation or guess of the unknown parameter set is given or a reasonable range of each parameter is defined. After that, the forward model (numerical simulation) is called for the initial guess of the parameters. Subsequently, the obtained numerical results are compared with the observed/measured data in field. The discrepancy between the two sets of data is quantified by an *objective function* which is to be minimized applying an *optimization algorithm*. The set of parameters which minimizes the objective function is the best estimated set of the unknown model parameters. The objective function considered in this approach is the least squares criterion:

$$f(\mathbf{m}) = \sum_{i=1}^{N} (d_{obs}^{i} - g_i(\mathbf{m}))^2 \tag{1}$$

where g_i is the calculated value for the point i, $\mathbf{m}$ is the set of the model parameters, and d_{obs}^{i} is the observed value at the same point.

2.2 Probabilistic Approach

Customarily, the uncertainties associated with the geotechnical applications can be categorized as follows [2]:

- Natural variability (aleatory/objective uncertainty) associated with the inherent randomness of natural processes, like wind flow and geologic layers. In this case samples are taken and inferences are drawn.
- Knowledge uncertainty (epistemic/subjective uncertainty) caused by the lack of data or information about events and processes, and of understanding the physical laws, where the following subcategories may be distinguished:
  - Site characterization uncertainty.
  - Model uncertainty.
  - Parameter uncertainty.

In order to include the aforementioned uncertainties (inherent in the forward model and the measured data) and the prior knowledge about the unknown parameters (indicating the trend of the parameters), a *Probabilistic Approach* based on *Bayes Theorem* (Thomas Bayes, 1702-1761) is incorporated in the inverse problem considered here. This approach yields a solution that provides suitable uncertainty measures [3] as follows:

- The prior information of the model parameters and the uncertainties in the observed data are represented in terms of two *independent* probability density functions (PDFs), $\rho_M(\mathbf{m})$ and $\rho_D(\mathbf{D})$ respectively, with a joint PDF:

  $$\rho(\mathbf{m}, \mathbf{d}) = k\rho_M(\mathbf{m})\rho_D(\mathbf{d}) \tag{2}$$

  where k is the normalization constant.

- The effect of the modeling uncertainties is mapped by a PDF referred to as the forward model probability:

  $$\Theta(\mathbf{m}, \mathbf{d}) = \theta(\mathbf{d}|\mathbf{m})\mu_M(\mathbf{m}) \tag{3}$$

  where $\mu_M(\mathbf{m})$ is the homogeneous probability density over the model space M.

- Combining the prior information and the forward model probability by the *conjunction operation* gives the probabilistic solution (see Figure 3):

$$\begin{aligned}\sigma(\mathbf{m},\mathbf{d}) &= k\frac{\rho(\mathbf{m},\mathbf{d})\Theta(\mathbf{m},\mathbf{d})}{\mu(\mathbf{m},\mathbf{d})} \\ &= k\frac{\rho_M(\mathbf{m})\rho_D(\mathbf{d})\theta(\mathbf{d}|\mathbf{m})\mu_M(\mathbf{m})}{\mu_M(\mathbf{m})\mu_D(\mathbf{d})} \\ &= k\frac{\rho_M(\mathbf{m})\rho_D(\mathbf{d})\theta(\mathbf{d}|\mathbf{m})}{\mu_D(\mathbf{d})} \end{aligned} \quad (4)$$

where $\mu_D(\mathbf{d})$ is the homogeneous probability density over the data space D.

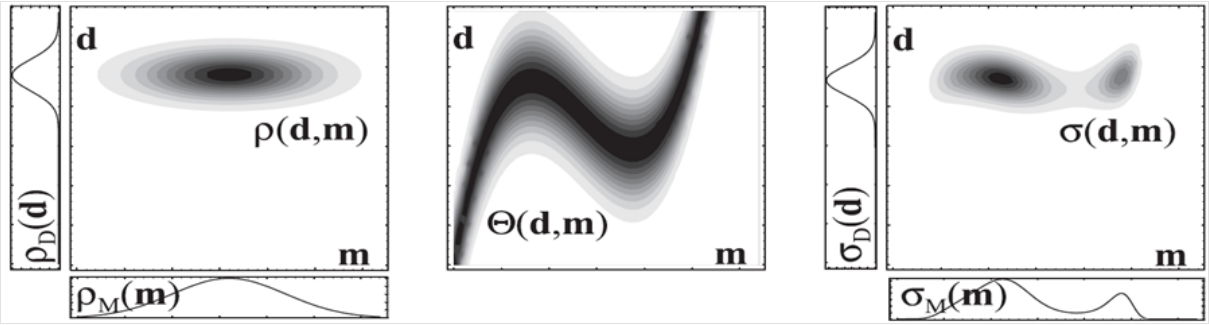

Figure 3: Conceptual depiction of the general probabilistic solution of an inverse problem.

- Once the posteriori probability in the $D\mathrm{x}M$ space has been defined, the posteriori probability in the model space is given by the marginal probability density:

$$\begin{aligned}\sigma(\mathbf{m}) &= k\int_D \sigma(\mathbf{m},\mathbf{d})d\mathbf{d} \\ &= k\int_D \frac{\rho_M(\mathbf{m})\rho_D(\mathbf{d})\theta(\mathbf{d}|\mathbf{m})}{\mu_D(\mathbf{d})}d\mathbf{d} \\ &= k\rho_M(\mathbf{m})\int_D \frac{\rho_D(\mathbf{d})\theta(\mathbf{d}|\mathbf{m})}{\mu_D(\mathbf{d})}d\mathbf{d} \\ &= k\rho_M(\mathbf{m})L(\mathbf{m}) \end{aligned} \quad (5)$$

hereby, $L(\mathbf{m})$ is the *likelihood function* which gives a measure of how good a model $\mathbf{m}$ is in explaining the data.

By assuming Gaussian PDFs for both data and model uncertainties, we have

$$\rho_D(\mathbf{d}) = k\exp(-0.5(\mathbf{d}-\mathbf{d}_{obs})^T\mathbf{C}_D^{-1}(\mathbf{d}-\mathbf{d}_{obs})) \quad (6)$$

$$\theta(\mathbf{d}|\mathbf{m}) = k\exp(-0.5(\mathbf{d}-\mathbf{g}(\mathbf{m}))^T\mathbf{C}_M^{-1}(\mathbf{d}-\mathbf{g}(\mathbf{m}))) \quad (7)$$

and the likelihood function becomes Gaussian having a covariance matrix $\mathbf{C}_L = \mathbf{C}_D + \mathbf{C}_M$:

$$L(\mathbf{m}) = k\exp(-0.5(\mathbf{d}_{obs}-\mathbf{g}(\mathbf{m}))^T\mathbf{C}_L^{-1}(\mathbf{d}_{obs}-\mathbf{g}(\mathbf{m}))) \quad (8)$$

If no prior information about the model parameters is available and the components of the

observed and calculated data $(\mathbf{d}_{obs}, \mathbf{g}(\mathbf{m}))$ are independent as well as identically distributed with standard deviations S_D and S_M , respectively, the probabilistic solution simply becomes:

$$\begin{aligned} \sigma(\mathbf{m}) &= kL(\mathbf{m}) \\ &= k(S_D^2 + S_M^2)^{-N/2} \exp\left[-\frac{1}{2} \underbrace{\frac{\sum_{i=1}^{N}(d_{obs}^i - g_i(\mathbf{m}))^2}{S_D^2 + S_M^2}}_{J(\mathbf{m}, S_D, S_M)} \right] \end{aligned} \tag{9}$$

where $J(\mathbf{m}, S_D, S_M)$ is the *misfit* function or *least squares cost* function.

For fixed values of S_D and S_M over the model and the data spaces, maximizing the likelihood function equals minimizing the least squares cost function. Thus, the probabilistic approach converts to the deterministic approach.

The probabilistic solution is numerically evaluated by direct sampling. Generation of realizations of the probabilistic density solution $\sigma(\mathbf{m})$ is accomplished by using *Monte Carlo Markov Chain* method along with the *Metropolis* acceptance rules [4] and [5]: Given the target probability distribution $\sigma(\mathbf{m}|\mathbf{d})$, we consider a Markov chain with a given sample $\mathbf{m}_n$. The next sample $\mathbf{m}_{n+1}$ is obtained from $\mathbf{m}_n$ as follows:

- Generate a candidate sample $\mathbf{m}$ from a *jumping* probability density function $P(\mathbf{m}^*|\mathbf{m}_n)$.
- Calculate
$$\alpha = \min\left[1, \frac{\sigma(\mathbf{m}^*|\mathbf{d})P(\mathbf{m}_n|\mathbf{m}^*)}{\sigma(\mathbf{m}_n|\mathbf{d})P(\mathbf{m}^*|\mathbf{m}_n)}\right]$$
- Generate a uniformly distributed sample $U \in (0.0; 1.0)$.
- If $U \leq \alpha$ accept $\mathbf{m}_{n+1} = \mathbf{m}^*$ otherwise $\mathbf{m}_{n+1} = \mathbf{m}_n$.

Repeating this sequence shows that the generated Markov Chain converges to the probability distribution function $\sigma(\mathbf{m}|\mathbf{d})$.

2.3 Sensitivity Analysis

Due to the highly nonlinear problem nature of geotechnical applications with respect to both the physical and the geometrical characteristics, the numerical simulation is normally computationally expensive. In order to make the inverse analysis efficient as well as robust, it is favorable to reduce the number of the parameters to be identified by performing a *sensitivity analysis*. This analysis evaluates the importance of each unknown model parameter with respect to the system response resulting in a decrease of the number of the forward calculations.

In this paper, a *variance based global sensitivity analysis*, which explores the space of the input parameters, has been utilized. In this analysis two different sensitivity measures have been introduced, the first index, *first order sensitivity index* [6], measures only the decoupled effect on the system response,

$$S_i = \frac{V_{m_i}(E_{\mathbf{m}_{\sim i}}(g(\mathbf{m})|m_i))}{V(g(\mathbf{m}))} \tag{10}$$

where $V(g(\mathbf{m}))$ is the unconditional variance of the model output and $V_{m_i}(E_{\mathbf{m}_{\sim i}}(g(\mathbf{m})|m_i))$ is the variance of conditional expectation with $\mathbf{m}_{\sim i}$ indicating the matrix of all parameters but m_i.

In order to consider the coupling effects of the input parameters, the second index, *total effect index* [7], has been introduced,

$$S_{Ti} = 1 - \frac{V_{\mathbf{m}_{\sim i}}(E_{m_i}(g(\mathbf{m})|\mathbf{m}_{\sim i}))}{V(g(\mathbf{m}))} \tag{11}$$

where $V_{\mathbf{m}_{\sim i}}(E_{m_i}(g(\mathbf{m})|\mathbf{m}_{\sim i}))$ measures the first order effect of $\mathbf{m}_{\sim i}$ on the system response that does not include any influence corresponding to m_i.

For the estimation of the first and total sensitivity indices a numerical procedure introduced by [8] have been utilized.

2.4 Model Approximation

The forward calculation, which is a three dimensional finite element simulation, needs a significant computation time. Therefore, and due to the large number of the forward calculations that are included in the optimization process of the deterministic approach, or the sampling procedure of the probabilistic approach, or even in the global sensitivity analysis being adopted in this work, using a meta-model that substitutes the finite element simulation runs is unavoidable. For this purpose, an approximation method based on polynomial regression has been implemented.

Customarily, $g(\mathbf{m})$ the system output can be represented by the approximated value and an error ϵ

$$g(\mathbf{m}) = \hat{g}(\mathbf{m}) + \epsilon = \mathbf{p}^T(\mathbf{m})\boldsymbol{\beta} + \epsilon \tag{12}$$

where $\boldsymbol{\beta}$ is the vector of the unknown regression coefficients, and $\mathbf{p}$ is the vector of the polynomial basis functions

$$\mathbf{p}^T(\mathbf{m}) = [1\ m_1\ m_2\ m_3 \dots m_1^2\ m_2^2\ m_3^2 \dots m_1m_2\ m_1m_3 \dots m_2m_3 \dots]. \tag{13}$$

The regression coefficients are estimated according to [9]:

$$\hat{\boldsymbol{\beta}} = (\mathbf{P}^T\mathbf{P})^{-1}\mathbf{P}^T\mathbf{g} \tag{14}$$

where $\mathbf{P}$ is a matrix containing the basis polynomials of the support points and $\mathbf{g}$ is the system responses of the support points.

For the assessment of the approximation quality, the Coefficient of Determination

$$R^2 = 1 - \frac{\sum_{j=1}^{n}(g_j - \hat{g}_j)^2}{\sum_{j=1}^{n}(g_j - \bar{g}_j)^2}$$

according to [10] has been introduced, where, the closer the R^2 value to one is, the better the approximation is.

3 APPLICATION

We use a three dimensional finite element model for scenario #1 of the tunnel excavation (Figure 1), using the FE-code PLAXIS 3D, version 2010. Since the geometry, the material properties, the initial and excavation conditions are in total symmetric with respect to a vertical plane parallel to the tunnel axis (X-axis), only one-half of the model needs to be analyzed (see Figure 4). The chosen slurry shield Tunnel Boring Machine TBM being 9 m long is simulated, along with the tunnel lining, by circular plate elements assuming linear elastic behavior. The ground is modeled by the *Hardening Soil Model* [11]. In Table 1, the parameters of the considered constitutive models are presented. More details about the model can be seen in [12].

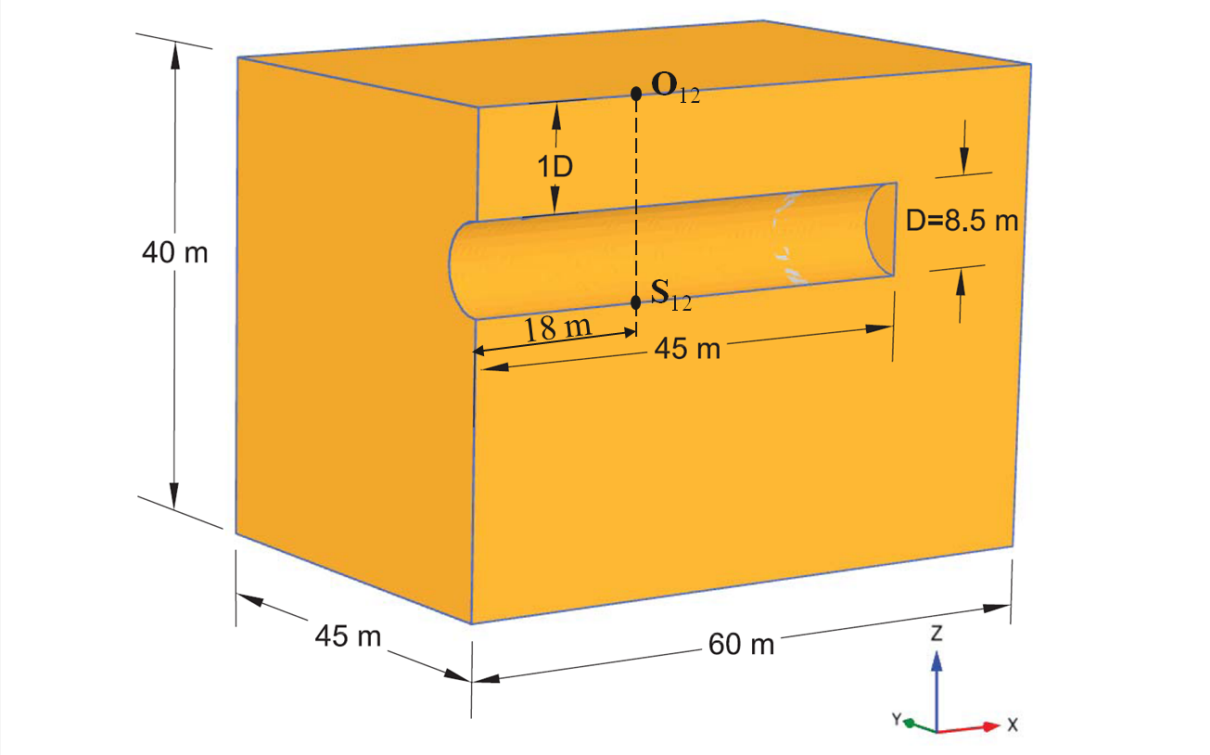

Figure 4: The geometry and properties for a three dimensional model using Plaxis 3D.

In order to identify the ground model (HS-Model) parameters, the following steps have been carried out:

- The model has been run for the parameter values stated in Table 1. Hereby, the vertical displacements at the two points O_{12} and S_{12} (see Figure 4) have been saved as observation measurements $\mathbf{d}_{obs}$ for the whole excavation phases. Subsequently, the HS-Model parameters (i.e. ϕ, c, E_{oed}^{ref}, E_{50}^{ref}, E_{ur}^{ref} with the conditions $E_{oed}^{ref} = E_{50}^{ref}$, $E_{oed}^{ref} \leq E_{ur}^{ref}/2$) are considered as unknowns that need to be estimated from the data set $\mathbf{d}_{obs}$.

- An objective function, representing the discrepancy between the observed and calculated measurements, has been adapted based on the least squares criterion (Equation 1).

- Model approximation for the system response at the observation points O_{12} and S_{12} have been carried out using polynomial regression. The coefficients of determination show a

parameter	Soil Hardening Soil Model	Tunnel lining Linear Elastic	TBM-Shield Linear Elastic
$\phi[^\circ]$	35	-	-
$\psi[^\circ]$	5	-	-
$c[\mathtt{kN/m^2}]$	10	-	-
$E_{50}^{ref}[\mathtt{kN/m^2}]$	35000	-	-
$E_{oed}^{ref}[\mathtt{kN/m^2}]$	35000	-	-
$E_{ur}^{ref}[\mathtt{kN/m^2}]$	10^5	-	-
$P^{ref}[\mathtt{kN/m^2}]$	100	-	-
$m[-]$	0.7	-	-
$R_f[-]$	0.9	-	-
$\nu_{ur}[-]$	0.2	-	-
$\gamma_{unsat}[\mathtt{kN/m^3}]$	17	-	-
$\gamma_{sat}[\mathtt{kN/m^3}]$	20	-	-
$R_{inter}[-]$	0.6	-	-
$E[\mathtt{kN/m^2}]$	-	3.10^7	21.10^7
$\nu[-]$	-	0.1	0.3
$\gamma[\mathtt{kN/m^3}]$	-	24	38
$d[m]$	-	0.2	0.35

Table 1: Material properties for the models used in tunnel simulation for scenario #1.

good approximation for the forward model

$$R^2_{O_{12}} = 0.98759 \quad R^2_{S_{12}} = 0.9997.$$

- A variance based sensitivity analysis has been implemented for deciding which parameters have to be identified. As a result, a parameter with small values for S_i and S_{Ti} has a negligible effect on the considered system response; and can be excluded from the identification. The analysis has shown that the four decisive parameters of the model need to be identified, Figure 5.

- The subsequent identification process has been performed following the inverse analysis procedure presented in Figure 2, where two different optimization algorithms have been applied, (*i*) Particle Swarm Optimization PSO [13], and (*ii*) Differential Evolution Algorithm [14]. In both cases, the objective function is minimized until the parameters match their real world values to a large extend (see Figure 6).

- In the probabilistic approach, we are currently still considering the simple case in which a homogeneous PDF for the a priori information about the model parameters is assumed. Also, Gaussian PDFs are used for both data and model uncertainties, according to Equation 8. The covariance matrix of the measured data (CD) depends usually on sensing devices used in recording the observations. In [15] different devices with their covariance matrices are presented that can be used in our case, as well. For the present example, the forward model is assumed to be exact and the influence of the data (measurements) uncertainty is investigated in two cases with the assumption that the observation errors are independent and identically distributed. In the first case, the standard deviation of

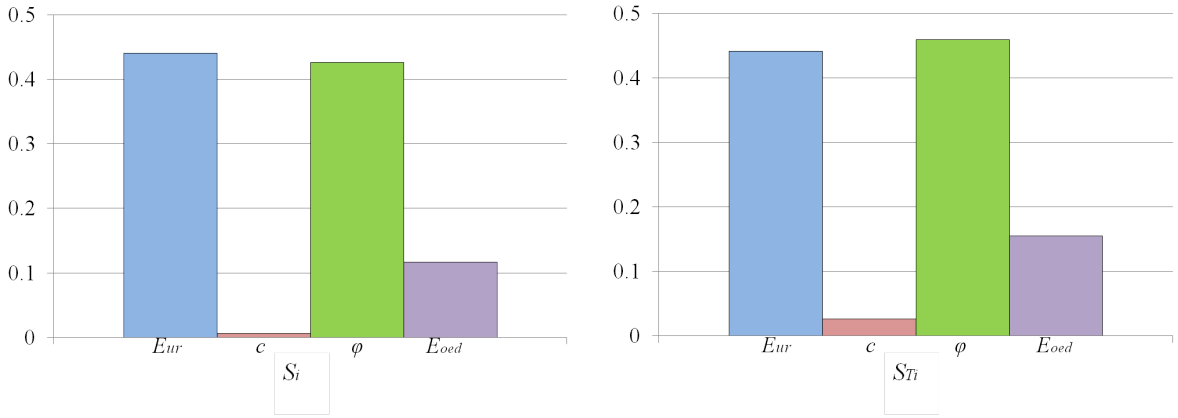

Figure 5: First order and total effect sensitivity indices of the soil parameters.

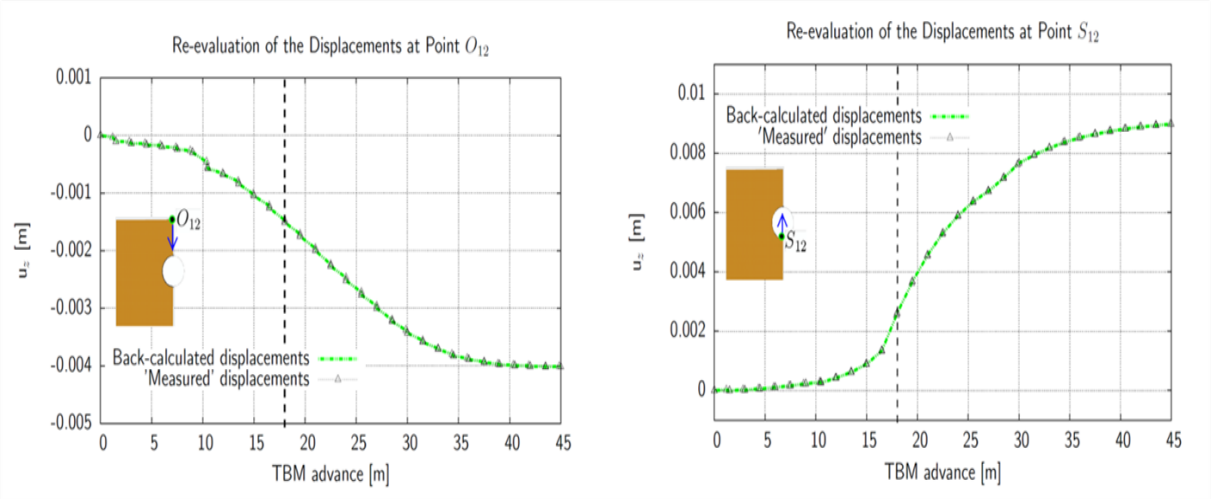

Figure 6: Quality of results; forward solver = back analysis solver.

the observations error S_D is given a relatively small value in comparison to the system response at the observing points, and in the second case, a relatively higher value for S_D is considered. Using Monte Carlo Markov Chain method for sampling the probabilistic solution

$$\begin{aligned} \sigma(\mathbf{m}) &= kL(\mathbf{m}) \\ &= k(S_D^2)^{-N/2} \exp\left[-\frac{1}{2} \frac{\sum_{i=1}^{N} (d_{obs}^i - g_i(\mathbf{m}))^2}{S_D^2} \right] \end{aligned} \tag{15}$$

for both cases. Analysing the generated samples gives the results in Table 2 and Table 3.

Where, the uncertainty of the parameters increases with the data uncertainty. In addition to that, the parameters with higher sensitivity measures can be identified better than those of lower sensitivity measures.

parameter	Exact value	Mean μ	Standard deviation σ	Coefficient of Variation $CoV = \sigma/\mu$
E_{ur}^{ref}	100000	102040	12809	0.1255
c	10	310.989	2.757	0.2508
ϕ	35	333.85	2.1886	0.0655
E_{oed}^{ref}	35000	31941	5101	0.1597

Table 2: Statistical characteristics of the generated samples for the first case (relatively small data uncertainty).

parameter	Exact value	Mean μ	Standard deviation σ	Coefficient of Variation $CoV = \sigma/\mu$
E_{ur}^{ref}	100000	121065	18765	0.155
c	10	310.6	2.82	0.2665
ϕ	35	335.85	3.715	0.1036
E_{oed}^{ref}	35000	35649	7419	0.208

Table 3: Statistical characteristics of the generated samples for the second case (relatively large data uncertainty).

By drawing the relative frequency diagram of two parameters for the tow cases, the distribution of parameters within their bounds is illustrated, Figure 7.

4 CONCLUSIONS ANS OUTLOOKS

The two presented identification approaches, deterministic and probabilistic, are able to estimate the ground model parameters from observations. Where, the second approach is able to capture and quantify parameter uncertainties that result from uncertainties associated with measurement data. Different and more specific investigations are going to be considered in the probabilistic approach for representing more realistic and general cases of uncertainties. Furthermore, the captured and quantifies uncertainties are going to be utilized in the model assessment process that enables choosing the most adequate ground model for the forward model representing the tunnel excavation.

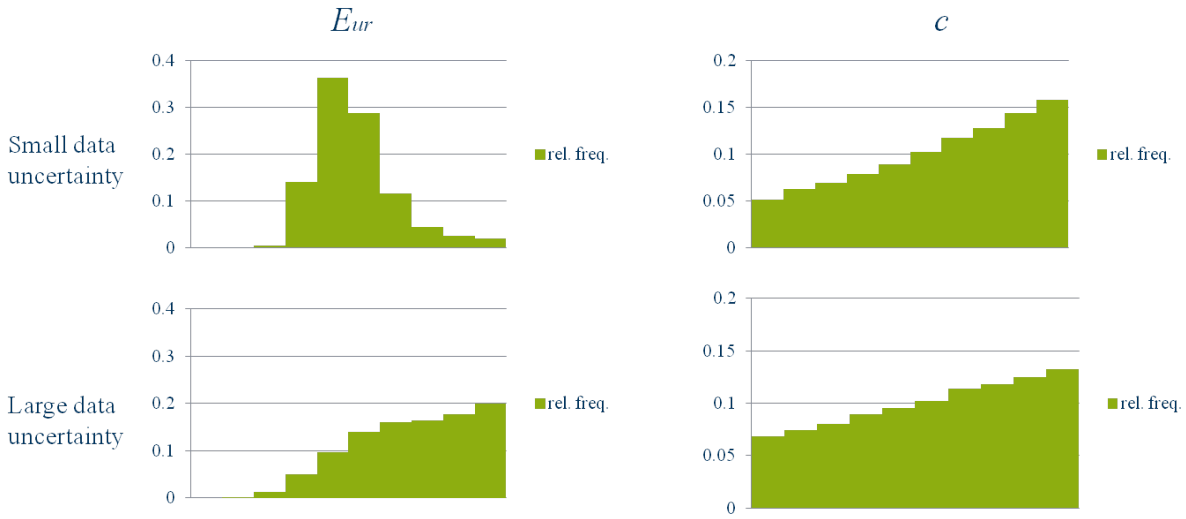

Figure 7: Relative frequencies due to data uncertainties.

5 ACKNOWLEDGEMENTS

This work is part of the subproject **C**2 in the Collaborative Research Center **SFB** 837, funded by the German Research Foundation **DFG**. We greatly appreciate their valuable support.

REFERENCES

[1] T. Schanz, M. M. Zimmerer, M. Datcheva, and J. Meier, "Identification of constitutive parameters for numerical models via inverse approach," *Journal of Felsbau*, vol. 2, pp. 11–21, 2006.

[2] G. Baecher and J. T. Christian, *Reliability and Statistics in Geotechnical Engineering*. England: Wiley, 2003.

[3] A. Tarantola, *Inverse Problem Theory and Methods for Parameter Estimation*. Philadelphia: siam, 2005.

[4] N. Metropolis, A. Rosenbluth, M. Rosenbluth, A. Teller, and E. Teller, "Equation of state calculations by last computing machines," *J. Chem. Phys.*, vol. 21(6), pp. 1087–1092, 1953.

[5] W. K. Hastings, "Monte carlo sampling methods using markov chains and their applications," *Biometrika*, vol. 57(1), pp. 97–109, 1970.

[6] I. M. Sobol, "Sensitivity estimates for nonlinear mathematical models," *Mathematical Modelling and Computational Experiment*, vol. 1, pp. 407–414, 1993.

[7] T. Homma and A. Saltelli, "Importance measures in global sensitivity analysis of nonlinear models," *Reliability Engineering and System Safety*, vol. 52, pp. 1–17, 1996.

[8] A. Saltelli, M. Ratto, T. Andres, F. Campolongo, J. Cariboni, D. Gatelli, M. Saisana, and S. Tarantola, *Global Sensitivity Analysis. The Primer*. John Wiley & Sons, Ltd, 2008.

[9] R. Myers and D. C. Montgomery, *Response Surface Methodology*. John Wiley& Sons, Ltd, 2002.

[10] D. C. Montgomery and G. C. Runger, *Applied Statistics and Probability for Engineers*. John Wiley & Sons, Ltd, 2003.

[11] T. Schanz, P. Vermeer, and P. Bonnier, "The hardening soil model: Formulation and verification," *Beyond 2000 in Computational Geotechnics-10 years of PLAXIS*, Rotterdam, 1999.

[12] V. Zarev, T. Schanz, and M. Datcheva, "Three-dimensional fe-analysis of mechanized tunneling in urban areas," in *13th Inter. Conf. on Civil, Structural and Environmental Engineering Computing*, (Greece), 2011.

[13] J. Kennedy and R. Eberhard, "Particle swarm optimization," in *IEEE International Conference on Neural Networks*, NJ, USA, 1995.

[14] R. Storn and K. Price, "Differential evolution- a simple and efficient adaptive scheme for global optimization over continuous spaces," tech. rep., ICSI, 1995.

[15] A. Ledesma, A. Gens, and A. E.E., "Estimation of parameters in geotechnical backanalysis-1. maximum likelihood approach," *Journal of Computers and Geotechnics*, vol. 18(1), pp. 1–27, 1996.

19th International Conference on the Application of Computer
Science and Mathematics in Architecture and Civil Engineering
K. Gürlebeck, T. Lahmer and F. Werner (eds.)
Weimar, Germany, 04–06 July 2012

COMPLETE ORTHOGONAL SYSTEMS OF 3D SPHEROIDAL MONOGENICS

J. Morais* **and S. Georgiev**

**Departamento de Matemática*
Universidade de Aveiro
Campus Universitário Santiago
3810-193 Aveiro, Portugal
E-mail: joao.pedro.morais@ua.pt

Keywords: Quaternion analysis, Riesz system, Moisil-Théodoresco system, Ferrer's associated Legendre functions, Chebyshev polynomials, hyperbolic functions, monogenic functions, Szegö kernel function.

Abstract. *In this paper we review two distinct complete orthogonal systems of monogenic polynomials over 3D prolate spheroids. The underlying functions take on either values in the reduced and full quaternions (identified, respectively, with $\mathbb{R}^3$ and $\mathbb{R}^4$), and are generally assumed to be nullsolutions of the well known Riesz and Moisil Théodoresco systems in $\mathbb{R}^3$. This will be done in the spaces of square integrable functions over $\mathbb{R}$ and $\mathbb{H}$. The representations of these polynomials are explicitly given. Additionally, we show that these polynomial functions play an important role in defining the Szegö kernel function over the surface of 3D spheroids. As a concrete application, we prove the explicit expression of the monogenic Szegö kernel function over 3D prolate spheroids.*

1 INTRODUCTION

Quaternion analysis is thought to generalize onto the multidimensional situation the classical theory of holomorphic functions of one complex variable, and to provide the foundations for a refinement of classical harmonic analysis. The rich structure of this function theory involves the analysis of monogenic functions defined in open subsets of $\mathbb{R}^3$, which are nullsolutions of higher-dimensional Cauchy-Riemann systems. In this paper we review two distinct complete orthogonal systems of monogenic polynomials over 3D prolate spheroids. We show that these polynomial functions play an important role in defining the monogenic Szegö kernel function over 3D spheroids. The underlying spheroidal prolate functions (C. Flammer [12], E.W. Hobson [21], N.N. Lebedev [24]) were introduced by C. Niven in 1880 while studying the conduction of heat in an ellipsoid of revolution, which lead to a Helmholtz equation in spheroidal coordinates. The prolate spheroidal harmonics are special functions in mathematical physics which have found many important practical applications in science and engineering where the spheroidal coordinate system is used. They usually appear in the solutions of Dirichlet problems in spheroidal domains arising in hydrodynamics, elasticity and electromagnetism. For the solvability of boundary value problems of radiation, scattering, and propagation of acoustic signals and electromagnetism waves in spheroidal structures, spheroidal wave functions are commonly encountered. Recently, there has been a growing interest in developing numerical methods using prolate spheroidal functions as basis functions [2, 3, 41, 42, 43]. These applications have stimulated a surge of new techniques and have reawakened interest in approximation theory, potential theory, and the theory of partial differential equations of elliptic type for spheroidal domains. Higher dimensional extensions of the prolate spheroidal functions were first studied by Slepian in [35], which provided many of their analytical properties, as well as properties that support the construction of numerical schemes (see also A.I. Zayed [44]). Very recently, K.I. Kou et al. [23] introduced the continuous Clifford prolate spheroidal functions in the finite Clifford Fourier transform setting. These generalized spheroidal functions (for offset Clifford linear canonical transform) were successfully applied for the analysis of the energy concentration problem introduced in the early-sixties by D. Slepian and H.O. Pollak [34].
Since the foundations of the theory of approximation of monogenic functions by Fueter [13, 14], the study of orthogonal polynomials in application to certain boundary value problems for elliptic partial differential equations has been of great importance in connection with certain problems of mathematical physics. In our view much of the older theory has progressed considerably upon the study of monogenic polynomial approximations in the context of quaternion analysis. For a detailed historic survey and extended list of references on monogenic approximations we refer to [17]. Most relevant to our study are the intimate connections between monogenic functions and spheroidal structures, and the potential flexibility afforded by a spheroid's non-spherical canonical geometry. Developments are described in the sequence of papers by H. Malonek et al. in [1, 26, 27] (cf. [9]) and J. Morais et al. in [18, 19, 20, 30]. In light of this, in [29, 31] (cf. [16]) a very recent approach has been developed to discuss approximation properties for monogenic functions over 3D prolate spheroids by Fourier expansions in monogenic polynomials of which could be explicitly expressed in terms of products of Ferrer's associated Legendre functions multiplied by Chebyshev polynomial factors (see Theorem 3.1 below). Within the scope of this paper we shall be fully concerned with the polynomials introduced in these notes. Studies have shown that the underlying spheroidal monogenics play an important role in defining the monogenic Szegö kernel function for 3D spheroids [32].

2 PRELIMINARIES

2.1 The Riesz and Moisil-Théodoresco systems

As is well known, a holomorphic function $f(z) = u(x, y) + iv(x, y)$ defined in an open domain of the complex plane, satisfies the Cauchy-Riemann system

$$\begin{cases} \dfrac{\partial u}{\partial x} &= \dfrac{\partial v}{\partial y} \\ \dfrac{\partial u}{\partial y} &= -\dfrac{\partial v}{\partial x} \end{cases}.$$

As in the case of two variables, we may now characterize two possible analogues of the Cauchy-Riemann system in an open domain of the Euclidean space $\mathbb{R}^3$. More precisely, consider the pair $f = (f_0, f^*)$ where f_0 is a real-valued continuously differentiable function defined on an open domain $\Omega \subset \mathbb{R}^3$ and $f^* = (f_1, f_2, f_3)$ is a continuously differentiable vector-field in Ω for which

$$(\mathrm{R}) \quad \begin{cases} \operatorname{div} f^* &= 0 \\ \operatorname{rot} f^* &= 0 \end{cases}. \tag{2.1}$$

Recall that the 3-tuple f^* is said to be an *M. Riesz system of conjugate harmonic functions* in the sense of E.M. Stein and G. Weiß [36, 37], and system (R) is called the *Riesz system* [33]. The Riesz system has a physical relevance as it describes the velocity field of a stationary flow of a non-compressible fluid without sources nor sinks.
The *Moisil-Théodoresco system* is represented by [28] (cf. [22])

$$(\mathrm{MT}) \quad \begin{cases} \operatorname{div} f^* &= 0 \\ \operatorname{grad} f_0 + \operatorname{rot} f^* &= 0 \end{cases}, \tag{2.2}$$

and it is closely related to many mathematical models of relevance in spatial physical problems such as the Lamé and Stokes systems. Both systems are historical precursors that generalize the classical Cauchy-Riemann system in the plane. Obviously (2.1) may be derived from (2.2) by taking $f_0 = 0$.

2.2 Quaternion analysis

To start with, the (R)- and (MT)-systems may be obtained consistently by working with the quaternion algebra. Let $\mathbb{H} := \{\mathbf{z} = z_0 + z_1\mathbf{i} + z_2\mathbf{j} + z_3\mathbf{k} : \ z_l \in \mathbb{R},\ l = 0, 1, 2, 3\}$ be the Hamiltonian skew field, where the imaginary units **i**, **j**, and **k** are subject to the multiplication rules

$$\mathbf{i}^2 = \mathbf{j}^2 = \mathbf{k}^2 = -1;$$
$$\mathbf{ij} = \mathbf{k} = -\mathbf{ji}, \qquad \mathbf{jk} = \mathbf{i} = -\mathbf{kj}, \qquad \mathbf{ki} = \mathbf{j} = -\mathbf{ik}.$$

The scalar and vector parts of $\mathbf{z}$, $\mathbf{Sc}(\mathbf{z})$ and $\mathbf{Vec}(\mathbf{z})$, are defined as the z_0 and $z_1\mathbf{i} + z_2\mathbf{j} + z_3\mathbf{k}$ terms, respectively. Like in the complex case, the conjugate of $\mathbf{z}$ is the reduced quaternion $\overline{\mathbf{z}} = z_0 - z_1\mathbf{i} - z_2\mathbf{j} - z_3\mathbf{k}$, and the norm $|\mathbf{z}|$ of $\mathbf{z}$ is defined by $|\mathbf{z}| = \sqrt{\mathbf{z}\overline{\mathbf{z}}} = \sqrt{\overline{\mathbf{z}}\mathbf{z}} = \sqrt{z_0^2 + z_1^2 + z_2^2 + z_3^2}$.

The *paravector space* is the linear subspace defined by $\mathcal{A} := \mathrm{span}_{\mathbb{R}}\{1, \mathbf{i}, \mathbf{j}\} \subset \mathbb{H}$, with elements of the form $\mathbf{x} := x_0 + x_1\mathbf{i} + x_2\mathbf{j}$. Of course, it is assumed here that $\mathcal{A}$ is a real vectorial subspace, but not a subalgebra of $\mathbb{H}$. Now, let Ω be an open subset of $\mathbb{R}^3$ with a piecewise smooth boundary. We say that

$$\mathbf{f} : \Omega \longrightarrow \mathbb{H}, \qquad \mathbf{f}(x) = [\mathbf{f}(x)]_0 + [\mathbf{f}(x)]_1\mathbf{i} + [\mathbf{f}(x)]_2\mathbf{j} + [\mathbf{f}(x)]_3\mathbf{k} \tag{2.3}$$

is a quaternion-valued function or, briefly, an $\mathbb{H}$-valued function, where the components $[\mathbf{f}]_l$ $(l = 0, 1, 2, 3)$ are real-valued functions defined in Ω. By now, it is clear that the form of a paravector-valued function may be derived from (2.3) by taking $[\mathbf{f}(x)]_3 = 0$. Continuity, differentiability, integrability, and so on, which are ascribed to $\mathbf{f}$ are defined componentwise. We will work with both the real- (resp. quaternionic-) linear Hilbert space of square integrable $\mathcal{A}$- (resp. $\mathbb{H}$-) valued functions defined in Ω, that we denote by $L^2(\Omega; \mathcal{A}; \mathbb{R})$ (resp. $L^2(\Omega; \mathbb{H}; \mathbb{H})$). In this assignment, the scalar and quaternionic inner products are defined by

$$< \mathbf{f}, \mathbf{g} >_{L^2(\Omega;\mathcal{A};\mathbb{R})} = \int_\Omega \mathbf{Sc}(\overline{\mathbf{f}}\,\mathbf{g})\, dV \tag{2.4}$$

and

$$< \mathbf{f}, \mathbf{g} >_{L^2(\Omega;\mathbb{H};\mathbb{H})} = \int_\Omega \overline{\mathbf{f}}\,\mathbf{g}\, dV\,,$$

where dV denotes the Lebesgue measure on Ω. For continuously real-differentiable $\mathcal{A}$-valued functions $\mathbf{f}$, the reader may be familiar with the (reduced) quaternionic operator

$$D = \frac{\partial}{\partial x_0} + \mathbf{i}\frac{\partial}{\partial x_1} + \mathbf{j}\frac{\partial}{\partial x_2},$$

which is called generalized Cauchy-Riemann operator on $\mathbb{R}^3$. From this operator we obtain the usual Dirac operator

$$\partial = \mathbf{i}\frac{\partial}{\partial y_1} + \mathbf{j}\frac{\partial}{\partial y_2} + \mathbf{k}\frac{\partial}{\partial y_3}$$

via the equality $\partial = -\mathbf{j}D\mathbf{i}$, and the identification

$$\mathbf{x} = x_0 + x_1\mathbf{i} + x_2\mathbf{j} \in \mathcal{A} \quad \rightarrow \quad \mathbf{y} = x_2\mathbf{i} + x_1\mathbf{j} + x_0\mathbf{k} \in \mathbb{H}.$$

Namely, a continuously real-differentiable $\mathcal{A}$-valued function $\mathbf{f}$ is said to be *monogenic* in Ω if $D\mathbf{f} = 0 = \mathbf{f}D$ in Ω, which is equivalent to the Riesz system

$$\text{(R)} \quad \begin{cases} \dfrac{\partial[\mathbf{f}]_0}{\partial x_0} - \dfrac{\partial[\mathbf{f}]_1}{\partial x_1} - \dfrac{\partial[\mathbf{f}]_2}{\partial x_2} = 0\,, \\ \dfrac{\partial[\mathbf{f}]_0}{\partial x_1} + \dfrac{\partial[\mathbf{f}]_1}{\partial x_0} = 0, \quad \dfrac{\partial[\mathbf{f}]_0}{\partial x_2} + \dfrac{\partial[\mathbf{f}]_2}{\partial x_0} = 0, \quad \dfrac{\partial[\mathbf{f}]_1}{\partial x_2} - \dfrac{\partial[\mathbf{f}]_2}{\partial x_1} = 0\,. \end{cases}$$

This system can also be written in abbreviated form:

$$\begin{cases} \mathrm{div}\,\overline{\mathbf{f}} &= 0 \\ \mathrm{curl}\,\overline{\mathbf{f}} &= 0 \end{cases}.$$

For the interpretation of the (R)-system in viewpoint of $\mathbb{H} \cong \mathcal{C}\ell^{+}_{0,3}$ we refer to [10]. Following [25], the solutions of the system (R) are customary called (R)-solutions. The subspace of polynomial (R)-solutions of degree n will be denoted by $\mathcal{R}^{+}(\Omega;\mathcal{A};n)$. We also denote by $\mathcal{R}^{+}(\Omega;\mathcal{A}) := L^2(\Omega;\mathcal{A};\mathbb{R}) \cap \ker D$ the space of square integrable $\mathcal{A}$-valued monogenic functions defined in Ω.
The analysis of functions with values in $\mathbb{H}$ requires a different treatment. Namely, an $\mathbb{H}$-valued function $\mathbf{f}$ is called *left* (resp. *right*) monogenic in Ω if $\mathbf{f}$ is in $C^1(\Omega;\mathbb{H})$ and satisfies $\partial\mathbf{f} = 0$ (resp. $\mathbf{f}\partial = 0$) in Ω. Throughout the text we only use left $\mathbb{H}$-valued monogenic functions that, for simplicity, we call monogenic. Nevertheless, all results accomplished to left $\mathbb{H}$-valued monogenic functions can be easily adapted to right $\mathbb{H}$-valued monogenic functions. For any $\mathbb{H}$-valued function $\mathbf{f}$ it is worthy of note that the equation $\partial\mathbf{f} = 0$ is equivalent to the system

$$(\mathrm{MT}) \quad \begin{cases} \dfrac{\partial[\mathbf{f}]_1}{\partial x_0} + \dfrac{\partial[\mathbf{f}]_2}{\partial x_1} + \dfrac{\partial[\mathbf{f}]_3}{\partial x_2} &= 0 \\ \dfrac{\partial[\mathbf{f}]_0}{\partial x_0} - \dfrac{\partial[\mathbf{f}]_2}{\partial x_2} + \dfrac{\partial[\mathbf{f}]_3}{\partial x_1} &= 0 \\ \dfrac{\partial[\mathbf{f}]_0}{\partial x_1} + \dfrac{\partial[\mathbf{f}]_1}{\partial x_2} - \dfrac{\partial[\mathbf{f}]_3}{\partial x_0} &= 0 \\ \dfrac{\partial[\mathbf{f}]_0}{\partial x_2} - \dfrac{\partial[\mathbf{f}]_1}{\partial x_1} + \dfrac{\partial[\mathbf{f}]_2}{\partial x_0} &= 0 \end{cases}$$

or, in a more compact form:

$$\begin{cases} \operatorname{div}(\mathbf{Vec}(\mathbf{f})) &= 0 \\ \operatorname{grad}[\mathbf{f}]_0 + \operatorname{rot}(\mathbf{Vec}(\mathbf{f})) &= 0. \end{cases}$$

For the interpretation of the (MT) system in viewpoint of $\mathbb{H} \cong \mathcal{C}\ell^{+}_{0,3}$ we also refer to [11]. To state our general results we shall need some further notation. The solutions of the (MT)-system are called (MT)-solutions, and the subspace of polynomial (MT)-solutions of degree n is denoted by $\mathcal{M}^{+}(\Omega;\mathbb{H};n)$. In [38], A. Sudbery proved that $\dim \mathcal{M}^{+}(\Omega;\mathbb{H};n) = n+1$. We also denote by $\mathcal{M}^{+}(\Omega;\mathbb{H}) := L^2(\Omega;\mathbb{H};\mathbb{H}) \cap \ker \partial$ the space of square integrable $\mathbb{H}$-valued monogenic functions defined in Ω.

3 COMPLETE ORTHOGONAL SYSTEMS OF MONOGENIC POLYNOMIALS OVER 3D PROLATE SPHEROIDS

3.1 Prolate spheroidal monogenics

A prolate spheroid is generated by rotating an ellipse about its major axis. For the prolate spheroidal coordinate system (μ,θ,ϕ) the coordinate surfaces are two families of orthogonal surfaces of revolution. The surfaces of constant μ are a family of confocal prolate spheroids, and the surfaces of constant θ are a family of confocal hyperboloids of revolution.
In prolate spheroidal coordinates (see e.g. E.W. Hobson [21], N.N. Lebedev [24]), the Cartesian coordinates may be parameterized by $x = x(\mu,\theta,\phi)$, $\mu \in [0,\infty)$, $\theta \in [0,\pi)$, and $\phi \in [0,2\pi)$, such that

$$x_0 = ca\cos\theta, \quad x_1 = cb\sin\theta\cos\phi, \quad x_2 = cb\sin\theta\sin\phi,$$

where c is the prolatness parameter, and $a = \cosh\mu$, $b = \sinh\mu$, are respectively, the semimajor and semiminor axis of the generating ellipse. Using these transformation relations the surfaces of revolution for which μ is the parameter consist of the confocal prolate spheroids:

$$\mathcal{S} : \frac{x_0^2}{c^2\cosh^2\mu} + \frac{x_1^2+x_2^2}{c^2\sinh^2\mu} = 1. \tag{3.1}$$

Accordingly, the surface of $\mathcal{S}$ is matched with the surface of the supporting spheroid $\mu = \alpha$ if we put $c^2\cosh^2\alpha = a^2$, and $c^2\sinh^2\alpha = b^2$. Then we obtain the prolatness parameter $c = \sqrt{a^2-b^2} \in (0,1)$, which means that c is the eccentricity of the ellipse with foci on the x_0-axis: $(-c,0,0)$, $(+c,0,0)$.

In [29] J. Morais found it necessary to focus the discussion on spaces of square integrable functions over $\mathbb{R}$. With this outcome in mind, a complete orthogonal set

$$\{\boldsymbol{\mathcal{E}}_{n,l}, \boldsymbol{\mathcal{F}}_{n,m} : l = 0,\ldots,n+1,\ m = 1,\ldots,n+1\}$$

of polynomial nullsolutions of the well known Riesz system has been developed over 3D prolate spheroids. The mentioned spheroidal monogenics are explicitly given by[1]

Theorem 3.1. *Monogenic polynomials of the form*

$$\begin{aligned}
\boldsymbol{\mathcal{E}}_{n,l}(\mu,\theta,\phi) \;:=\; & \frac{(n+l+1)}{2} A_{n,l}(\mu,\theta)\, T_l(\cos\phi) \\
& + \frac{1}{4(n-l+1)} A_{n,l+1}(\mu,\theta)\,[T_{l+1}(\cos\phi)\mathbf{i} + \sin\phi\, U_l(\cos\phi)\mathbf{j}] \\
& + \frac{1}{4}(n+1+l)(n+l)(n-l+2) A_{n,l-1}(\mu,\theta)\,[-T_{l-1}(\cos\phi)\mathbf{i} + \sin\phi\, U_{l-2}(\cos\phi)\mathbf{j}]\,,
\end{aligned}$$

and

$$\begin{aligned}
\boldsymbol{\mathcal{F}}_{n,m}(\mu,\theta,\phi) \;:=\; & \frac{(n+m+1)}{2} A_{n,m}(\mu,\theta)\sin\phi\, U_{m-1}(\cos\phi) \\
& + \frac{1}{4(n-m+1)} A_{n,m+1}(\mu,\theta)\,[\sin\phi\, U_m(\cos\phi)\mathbf{i} - T_{m+1}(\cos\phi)\mathbf{j}] \\
& - \frac{1}{4}(n+1+m)(n+m)(n-m+2) A_{n,m-1}(\mu,\theta)\,[\sin\phi\, U_{m-2}(\cos\phi)\mathbf{i} + T_{m-1}(\cos\phi)\mathbf{j}]\,,
\end{aligned}$$

for $l = 0,\ldots,n+1$ and $m = 1,\ldots,n+1$, with the notation

$$A_{n,l}(\mu,\theta) := \sum_{k=0}^{\left\lceil \frac{n-l}{2} \right\rceil} \frac{(2n+1-2k)\,(n+l)_{2k}}{(n+1-l)_{2k+1}}\, P_{n-2k}^l(\cosh\mu)\, P_{n-2k}^l(\cos\theta) \tag{3.2}$$

such that $A_{n,-1} = -\frac{1}{n(n+1)^2(n+2)} A_{n,1}$ form a complete orthogonal system for the interior of the prolate spheroid (3.1) in the sense of the scalar product (2.4). Here P_n^l denotes the Ferrer's associated Legendre functions of degree n and order l of the first kind, T_l and U_l are the Chebyshev polynomials of the first and second kinds, respectively. Also, we set $P_n(\cosh\mu) = P_n^0(\cosh\mu)$ and $P_n^l(\cosh\mu) = (-1)^l(\sinh\mu)^l \,\frac{d^l}{dt^l}[P_n(t)]\Big|_{t=\cosh\mu}$.

[1]The first author wishes to thank Mr. N.M. Hung, who has found a misprint in the expressions of the polynomials introduced in [29], and who has shown great interest in questions related to them.

We shall now be able to extend these results to a quaternionic Hilbert subspace; in particular, we exploit a complete orthogonal system of polynomial nullsolutions of the Moisil-Théodoresco system over 3D prolate spheroids. In continuation of [29] (cf. [16]) we designate the new $n+1$ (prolate) spheroidal monogenics by

$$\boldsymbol{\mathcal{S}}_{n,l} := \boldsymbol{\mathcal{E}}_{n,l+1}\,\mathbf{i} + \boldsymbol{\mathcal{F}}_{n,l+1}\,\mathbf{j}, \quad l = 0, \ldots, n, \tag{3.3}$$

namely functions with respect to the variables μ, θ, and the azimuthal angle ϕ of the quaternion form:

$$\begin{aligned}
\boldsymbol{\mathcal{S}}_{n,l}\,(\mu,\theta,\phi) &:= \frac{1}{2}\,(n+2+l)\,(n+1+l)\,(n-l+1)\,A_{n,l}(\mu,\theta)\,T_l(\cos\phi) \\
&+ \frac{1}{2}\,(n+2+l)\,A_{n,l+1}(\mu,\theta)\,T_{l+1}(\cos\phi)\,\mathbf{i} \\
&+ \frac{1}{2}\,(n+2+l)\,A_{n,l+1}(\mu,\theta)\,\sin\phi\,U_l(\cos\phi)\,\mathbf{j} \\
&- \frac{1}{2}\,(n+2+l)\,(n+1+l)\,(n-l+1)\,A_{n,l}(\mu,\theta)\,\sin\phi\,U_{l-1}(\cos\phi)\,\mathbf{k}
\end{aligned}$$

with the subscript coefficient function $A_{n,l}(\mu,\theta)$ given by (3.2). It is easily verified that the polynomials $\boldsymbol{\mathcal{S}}_{n,l}$ are the zero functions for $l \geq n+1$.

Remark 3.2. For the usual applications we define these $n+1$ polynomials in a spheroid which has an infinite boundary, because $P_n^l(\cosh\mu)$ becomes infinite with μ. Of course, the results can be extended to the case of the region outside a spheroid as well. One has merely to replace the Ferrer's associated Legendre functions by the Legendre functions of second kind [21].

These $n+1$ polynomials satisfy the first order partial differential equation

$$\begin{aligned}
0 &= c\,\partial\boldsymbol{\mathcal{S}}_{n,l} \\
&= \mathbf{i}\left(\frac{\cos\theta\sinh\mu}{\sin^2\theta+\sinh^2\mu}\frac{\partial\boldsymbol{\mathcal{S}}_{n,l}}{\partial\mu} - \frac{\sin\theta\cosh\mu}{\sin^2\theta+\sinh^2\mu}\frac{\partial\boldsymbol{\mathcal{S}}_{n,l}}{\partial\theta}\right) \\
&+ \mathbf{j}\left(\frac{\sin\theta\cosh\mu\cos\phi}{\sin^2\theta+\sinh^2\mu}\frac{\partial\boldsymbol{\mathcal{S}}_{n,l}}{\partial\mu} + \frac{\cos\theta\sinh\mu\cos\phi}{\sin^2\theta+\sinh^2\mu}\frac{\partial\boldsymbol{\mathcal{S}}_{n,l}}{\partial\theta} - \frac{\sin\phi}{\sin\theta\sinh\mu}\frac{\partial\boldsymbol{\mathcal{S}}_{n,l}}{\partial\phi}\right) \\
&+ \mathbf{k}\left(\frac{\sin\theta\cosh\mu\sin\phi}{\sin^2\theta+\sinh^2\mu}\frac{\partial\boldsymbol{\mathcal{S}}_{n,l}}{\partial\mu} + \frac{\cos\theta\sinh\mu\sin\phi}{\sin^2\theta+\sinh^2\mu}\frac{\partial\boldsymbol{\mathcal{S}}_{n,l}}{\partial\theta} + \frac{\cos\phi}{\sin\theta\sinh\mu}\frac{\partial\boldsymbol{\mathcal{S}}_{n,l}}{\partial\phi}\right).
\end{aligned}$$

We further assume the reader to be familiar with the fact that ∂ is a square root of the Laplace operator in $\mathbb{R}^3$ in the sense that

$$\begin{aligned}
\Delta_3\boldsymbol{\mathcal{S}}_{n,l} &= -\partial^2\boldsymbol{\mathcal{S}}_{n,l} \\
&= \frac{1}{c^2(\sin^2\theta+\sinh^2\mu)}\left(\frac{\partial^2\boldsymbol{\mathcal{S}}_{n,l}}{\partial\mu^2} + \frac{\partial^2\boldsymbol{\mathcal{S}}_{n,l}}{\partial\theta^2} + \coth\mu\frac{\partial\boldsymbol{\mathcal{S}}_{n,l}}{\partial\mu} + \cot\theta\frac{\partial\boldsymbol{\mathcal{S}}_{n,l}}{\partial\theta}\right) \\
&+ \frac{1}{c^2\sin^2\theta\sinh^2\mu}\frac{\partial^2\boldsymbol{\mathcal{S}}_{n,l}}{\partial\phi^2}.
\end{aligned}$$

Remark 3.3. It is of interest to remark at this point that the Laplacian in (prolate) spheroidal coordinates reduces to the classical Laplacian in spherical coordinates if $a = b$, which occurs as μ appoaches infinity, and in which case the two foci coincide at the origin.

In [31] it is shown that the above-mentioned polynomails are (MT)-solutions and form a complete orthogonal system over the interior of 3D prolate spheroids. The principal point of interest is that the orthogonality of the polynomials in question does not depend on the shape of the spheroids, but only on the location of the foci of the ellipse generating the spheroid. It is shown a corresponding orthogonality over the surface of these spheroids with respect to a suitable weight function.

Theorem 3.4 (see [31]). *The monogenic polynomials $\boldsymbol{\mathcal{S}}_{n,l}(\mu,\theta,\phi)$ $(l=0,\ldots,n)$ form a complete orthogonal system over the surface of a prolate spheroid in the sense of the product*

$$\int_{\partial\mathcal{S}} \overline{\mathbf{f}}\,\mathbf{g}\,\boldsymbol{\omega}\,d\sigma\,, \tag{3.4}$$

where $\partial\mathcal{S}$ is the surface of $\mathcal{S}$ and $d\sigma$ denotes the area element on $\partial\mathcal{S}$, and with weight function

$$\boldsymbol{\omega} := |c^2-(ca\cos\theta+\mathbf{i}\,cb\sin\theta)^2|^{1/2}(\sin^2\theta+\sinh^2\mu)\quad (a>b)$$

equal to the square root of the product of the distances from any point inside of the spheroid to the points $(c,0,0)$ and $(-c,0,0)$, and their norms are given by

$$\begin{aligned}
\|\boldsymbol{\mathcal{S}}_{n,l}\|^2_{L^2(\partial\mathcal{S};\mathbb{H};\mathbb{H})} &= \pi\,(n+2+l)\,\frac{(n+2+l)!}{(n-l)!}\\
&\times\ \Big[(n+1+l)(n-l+1)\,P_n^l(\cosh\alpha)\,\sinh\alpha\,\cosh\alpha\,P_{n+1}^l(\cosh\alpha)\\
&\quad-\frac{(n+1+l)^2(n-l+1)}{2n+3}\,[P_n^l(\cosh\alpha)]^2\,\sinh\alpha\\
&\quad+P_n^{l+1}(\cosh\alpha)\,\sinh\alpha\,\cosh\alpha\,P_{n+1}^{l+1}(\cosh\alpha)\\
&\quad-\frac{(n+2+l)}{2n+3}\,[P_n^{l+1}(\cosh\alpha)]^2\,\sinh\alpha\Big]\,.
\end{aligned}$$

3.2 Properties

This subsection summarizes some basic properties of the prolate spheroidal monogenics.

Proposition 3.5 (see [32]). *The monogenic polynomials $\boldsymbol{\mathcal{S}}_{n,l}$ $(l=0,\ldots,n)$ satisfy the following properties:*

1. $\boldsymbol{\mathcal{S}}_{n,l}(0,0,0)=\begin{cases}\frac{(n+2)(n+1)^2}{2}\sum_{k=0}^{\lceil\frac{n}{2}\rceil}\frac{(2n+1-2k)\,(n)_{2k}}{(n+1)_{2k+1}} & ,\ l=0\\ 0 & ,\ l>0\end{cases}$;

2. $\boldsymbol{\mathcal{S}}_{n,l}(\mu,\theta,\pi)=\frac{(n+2+l)}{2}(-1)^l\Big[(n+1+l)(n-l+1)A_{n,l}(\mu,\theta)-A_{n,l+1}(\mu,\theta)\mathbf{i}\Big]$;

3. $\lim_{\phi\longrightarrow 2\pi}\boldsymbol{\mathcal{S}}_{n,l}(\mu,\theta,\phi)=\frac{(n+2+l)}{2}\Big[(n+1+l)(n-l+1)A_{n,l}(\mu,\theta)+A_{n,l+1}(\mu,\theta)\mathbf{i}\Big]$;

4. $\boldsymbol{\mathcal{S}}_{n,1}(\mu,\theta,\phi)=\frac{(n+3)}{2}\Big[n(n+2)A_{n,1}(\mu,\theta)+A_{n,2}(\mu,\theta)\mathbf{i}e^{-\mathbf{k}\phi}\Big]e^{-\mathbf{k}\phi}$;

5. *The polynomials $\boldsymbol{\mathcal{S}}_{n,l}$ are 2π-periodic with respect to the variable ϕ.*

3.3 Numerical examples

This subsection presents some numerical examples showing approximations up to degree 10 for the image of a prolate spheroid under a special spheroidal monogenic mapping. To begin with, a direct observation shows that for each degree $n \in \mathbb{N}_0$ the polynomial $\boldsymbol{\mathcal{S}}_{n,0}$ is monogenic from both sides ($\partial \boldsymbol{\mathcal{S}}_{n,0} = \boldsymbol{\mathcal{S}}_{n,0}\partial = 0$) and is such that $[\boldsymbol{\mathcal{S}}_{n,0}]_3 = 0$, i.e. $\boldsymbol{\mathcal{S}}_{n,0} : \mathcal{S} \longrightarrow \mathcal{A}$. We use this insight to motivate our numerical procedures for computing the image of a 3D prolate spheroid under $\boldsymbol{\mathcal{S}}_{n,0}$. We did not go further than $n = 10$, as our program becomes very time-consuming. Figures $1-3$ visualize approximations of degrees 3, 7 and 10 for the image of a prolate spheroid with semi-axes $a = 4$ and $b = \sqrt{15}$, and centered at the origin.

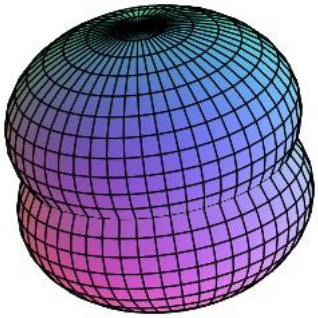

Fig. 1:

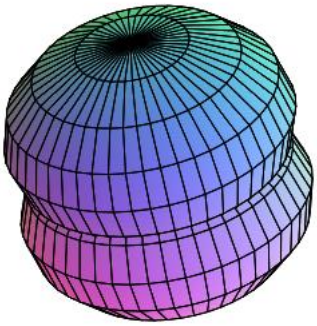

Fig. 2:

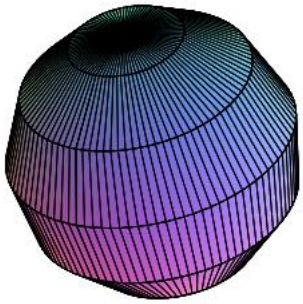

Fig. 3:

3.4 A special Fourier expansion by means of spheroidal monogenics

This subsection discusses a suitable Fourier expansion for monogenic functions over 3D prolate spheroids in terms of orthogonal monogenic polynomials. To begin with, note that for each degree $n \in \mathbb{N}_0$ the set

$$\{\boldsymbol{\mathcal{S}}_{n,l} : l = 0, \ldots, n\} \tag{3.5}$$

is formed by $n + 1 = \dim \mathcal{M}^+(\mathcal{S}; \mathbb{H}; n)$ monogenic polynomials, and therefore, it is complete in $\mathcal{M}^+(\mathcal{S}; \mathbb{H}; n)$. Furthermore, based on the orthogonal decomposition

$$\mathcal{M}^+(\mathcal{S}; \mathbb{H}) = \oplus_{n=0}^{\infty} \mathcal{M}^+(\mathcal{S}; \mathbb{H}; n),$$

and the completeness of the system in each subspace $\mathcal{M}^+(\mathcal{S}; \mathbb{H}; n)$, it follows the result.

Theorem 3.6. *For each n, the set (3.5) forms an orthogonal basis in the subspace $\mathcal{M}^+(\mathcal{S}; \mathbb{H}; n)$ in the sense of the product (3.4) with weight function*

$$\boldsymbol{\omega} := |c^2 - (ca\cos\theta + \mathbf{i}\, cb\sin\theta)^2|^{1/2}(\sin^2\theta + \sinh^2\mu)$$

such that $a > b$. Consequently,

$$\{\boldsymbol{\mathcal{S}}_{n,l} : l = 0, \ldots, n;\ n = 0, 1, \ldots\} \tag{3.6}$$

is an orthogonal basis in $\mathcal{M}^+(\mathcal{S}; \mathbb{H})$.

From now on we shall denote by $\boldsymbol{\mathcal{S}}^*_{n,l}$ $(l = 0, \ldots, n)$ the new normalized basis functions $\boldsymbol{\mathcal{S}}_{n,l}$ in $L^2(\mathcal{S}; \mathbb{H}; \mathbb{H})$ endowed with the inner product (3.4). Yet clearly we can easily write down the Fourier expansion of a square integrable $\mathbb{H}$-valued monogenic function over prolate spheroids in $\mathbb{R}^3$. Next we formulate the result.

Lemma 3.7. *Let* $\mathbf{f} \in \mathcal{M}^+(\mathcal{S}; \mathbb{H})$. *The function* $\mathbf{f}$ *can be uniquely represented with the orthogonal system (3.6):*

$$\mathbf{f}(x) = \sum_{n=0}^{\infty} \sum_{l=0}^{n} \boldsymbol{\mathcal{S}}^*_{n,l}\, a^*_{n,l}\,, \tag{3.7}$$

where for each $n \in \mathbb{N}_0$*, the associated (quaternion-valued) Fourier coefficients are given by*

$$a^*_{n,l} = \int_{\partial\mathcal{S}} \overline{\boldsymbol{\mathcal{S}}^*_{n,l}}\, \mathbf{f}\, \boldsymbol{\omega}\, d\sigma \quad (l = 0, \ldots, n)$$

with weight function

$$\boldsymbol{\omega} := |c^2 - (ca\cos\theta + \mathbf{i}\, cb \sin\theta)^2|^{1/2} (\sin^2\theta + \sinh^2\mu)$$

such that $a > b$.

4 MONOGENIC SZEGÖ KERNEL FUNCTION OVER 3D SPHEROIDS

Due to the absence of a direct analogue of the famous Riemann mapping theorem for higher dimensions, at first glance it seems extremely difficult to get closed formulae for the Szegö kernel on monogenic functions. However, in 2002 D. Constales and R. Kraußhar [4] provided an important breakthrough in this research direction. As far as we know, before their work explicit formulae for the Bergman kernels were only known for very special domains, such as for instance the unit ball and the half-space. In several papers [5, 6, 7, 8], the authors were able to give explicit representation formulae for the monogenic Bergman kernel for block domains, wedge shaped domains, cylinders, triangular channels and hyperbolic polyhedron domains which are bounded by parts of spheres and hyperplanes. Recently R. Kraußhar et al. also managed to set up explicit formulae for the Bergman kernel of polynomial Dirac equations, including the Maxwell-, Helmholtz- and Klein-Gordon equations as special subcases, for spheres and annular shaped domains.

With the help of the above-mentioned polynomials we may now obtain an explicit representation for the monogenic Szegö kernel function over 3D prolate spheroids. Now, since the right linear set $\mathcal{M}^+(\mathcal{S}; \mathbb{H})$ is a subspace of $L^2(\mathcal{S}; \mathbb{H}; \mathbb{H})$, to each $\xi \in \mathcal{S}$, if $\mathbf{K}(x, \xi)$ is a positive definite Hermitian quaternion element in $\mathcal{M}^+(\mathcal{S}; \mathbb{H})$, then it can be easily shown that there exists a uniquely determined Hilbert space of functions admitting the reproducing kernel $\mathbf{K}(x, \xi)$, and such that

$$\mathbf{f}(\xi) = \int_{\partial\mathcal{S}} \overline{\mathbf{f}}\, \mathbf{K}(x, \xi)\, \boldsymbol{\omega}\, d\sigma(x),$$

for any $\mathbf{f} \in \mathcal{M}^+(\mathcal{S}; \mathbb{H})$. The function $\mathbf{K}(x, \xi)$, with $(x, \xi) \in \mathcal{S} \times \mathcal{S}$, is called the monogenic Szegö kernel function of $\mathcal{S}$ with respect to ξ, and is given by

$$\mathbf{K}(x, \xi) = \sum_{n=0}^{\infty} \sum_{l=0}^{n} \boldsymbol{\mathcal{S}}^*_{n,l} \int_{\partial\mathcal{S}} \overline{\boldsymbol{\mathcal{S}}^*_{n,l}}\, \mathbf{K}(x, \xi)\, \boldsymbol{\omega}\, d\sigma(x).$$

Next we formulate our main result.

Theorem 4.1 (see [32]). *The monogenic Szegö kernel of* $\mathcal{S}$

$$\mathbf{K} : \mathcal{S} \times \mathcal{S} \longrightarrow \mathbb{H}$$

is given explicitly by the formula

$$\mathbf{K}\Big((\mu,\theta,\phi),(\eta,\beta,\varphi)\Big) = \frac{1}{4}\sum_{n=0}^{\infty}\sum_{l=0}^{n}\frac{(n+2+l)^2(n+1+l)(n-l+1)}{\|\boldsymbol{\mathcal{S}}_{n,l}\|^2_{L^2(\partial\mathcal{S};\mathbb{H};\mathbb{H})}}\,(A+B+C+D),$$

with the subscript coefficient functions

$$\begin{aligned}
A &= (n+1+l)(n-l+1)A_{n,l}(\mu,\theta)\,A_{n,l}(\eta,\beta)\Big\{\cos[l(\phi-\varphi)]-\sin[l(\phi+\varphi)\mathbf{k}]\Big\},\\
B &= -\frac{A_{n,l+1}(\mu,\theta)\,A_{n,l+1}(\eta,\beta)}{(n+1+l)(n-l+1)}\Big\{\cos[(l+1)(\phi-\varphi)]+\sin[(l+1)(\phi-\varphi)]\mathbf{k}\Big\},\\
C &= A_{n,l}(\mu,\theta)\,A_{n,l+1}(\eta,\beta)\Big\{\cos[l\phi-(l+1)\varphi]\mathbf{i}-\sin[l\phi-(l+1)\varphi]\mathbf{j}\Big\},\\
D &= A_{n,l+1}(\mu,\theta)\,A_{n,l}(\eta,\beta)\Big\{\cos[(l+1)\phi+l\varphi]\mathbf{i}+\sin[(l+1)\phi+l\varphi]\mathbf{j}\Big\}.
\end{aligned}$$

for $l=0,\ldots,n$.

Ultimately, we recall some of the basic properties of $\mathbf{K}$.

Proposition 4.2 (see [32]). *The monogenic Szegö kernel function* $\mathbf{K}$ *satisfies the following properties:*

1. $\mathbf{K}\Big((0,0,0),(0,0,0)\Big) = \begin{cases} \frac{1}{2}\frac{(n+2)^2(n+1)^4}{\|\boldsymbol{\mathcal{S}}_{n,0}\|^2_{L^2(\partial\mathcal{S};\mathbb{H};\mathbb{H})}}\left|\sum_{k=0}^{\lceil\frac{n}{2}\rceil}\frac{(2n+1-2k)\,(n)_{2k}}{(n+1)_{2k+1}}\right|^2 & l=0\\ 0 & l>0 \end{cases};$

2. *The function* $\mathbf{K}$ *is* 2π*-periodic with respect to the variables* ϕ *and* φ.

5 ACKNOWLEDGEMENT

This work was supported by *FEDER* funds through *COMPETE*–Operational Programme Factors of Competitiveness ("Programa Operacional Factores de Competitividade") and by Portuguese funds through the *Center for Research and Development in Mathematics and Applications* (University of Aveiro) and the Portuguese Foundation for Science and Technology ("FCT–Fundação para a Ciência e a Tecnologia"), within project PEst-C/MAT/UI4106/2011 with COMPETE number FCOMP-01-0124-FEDER-022690. Partial support from the Foundation for Science and Technology (FCT) via the post-doctoral grant SFRH/BPD/66342/2009 is also acknowledged by the first author. The second author acknowledges financial support via the grant DD-VU-02/90, Bulgaria. We would also like to thank Mr. N.M. Hung, who has found a misprint in the expressions of the polynomials introduced in [29], and who has shown great interest in recent questions related to them.

REFERENCES

[1] R. Almeida and H. Malonek. *On a Higher Dimensional Analogue of the Joukowski Transformation*. AIP Conf. Proc. 1048, 630-633 (2008).

[2] J.P. Boyd. *Prolate spheroidal wavefunctions as an alternative to Chebyshev and Legendre polynomials for spectral element and pseudospectral algorithms*. J. Comput. Phys., 199(2): 688-716, 2004.

[3] Q.Y. Chen, D. Gottlieb and J.S. Hesthaven. *Spectral methods based on prolate spheroidal wave functions for hyperbolic PDEs*. SIAM J. Numer. Anal., 43(5): 1912-1933, (2005).

[4] D. Constales, R. Kraußhar. *Bergman Kernels for rectangular domains and Multiperiodic Functions in Clifford Analysis*. Mathematical Methods in the Applied Sciences 25 No. 16-18, 1509-1526 (2002).

[5] D. Constales and R. Kraußhar. *The Bergman Kernels for the half-ball and for fractional wedge-shaped domains in Clifford Analysis*. Forum Mathematicum 17 (5), 809-821 (2005).

[6] D. Constales and R. Kraußhar. *Hilbert Spaces of Solutions to Polynomial Dirac equations, Fourier Transforms and Reproducing Kernel Functions for Cylindrical Domains*. Zeitschrift fur Analysis und Ihre Anwendungen 24 (3), 611-636 (2005).

[7] D. Constales and R. Kraußhar. *Bergman Spaces of higher dimensional hyperbolic polyhedron type domains I*. Mathematical Methods in the Applied Sciences 29 (1), 85-98 (2006).

[8] D. Constales and R. Kraußhar. *On the Navier-Stokes equation with Free Convection in three dimensional unbounded triangular channels*. Mathematical Methods in the Applied Sciences 31 (6), 735-751 (2008).

[9] C. Cruz, M. I. Falcão, H. Malonek. *3D Mappings by Generalized Joukowski Transformations*. Computational Science and Its Applications - ICCSA 2011, Lecture Notes in Computer Science, Volume 6784/2011, 358-373, Santander (2011).

[10] R. Delanghe. *On homogeneous polynomial solutions of the Riesz system and their harmonic potentials*. Complex Variables and Elliptic Equations, Vol. 52, No. 10-11, 1047–1062 (2007).

[11] R. Delanghe. *On homogeneous polynomial solutions of the Moisil-Théodoresco system in* $\mathbb{R}^3$, Computational Methods and Function Theory, Vol. 9, No. 1, 199–212 (2009).

[12] C. Flammer. *Spheroidal Wave Functions*. Stanford University Press, Stanford, CA, 1957.

[13] R. Fueter. *Analytische Funktionen einer Quaternionenvariablen*. Comment. Math. Helv., 4, 9-20 (1932).

[14] R. Fueter. *Functions of a Hyper Complex Variable*. Lecture notes written and supplemented by E. Bareiss, Math. Inst. Univ. Zürich, Fall Semester, 1949.

[15] P. Garabedian. *Orthogonal harmonic polynomials*. Pacific J. Math. Vol. 3, No. 3, 585-603 (1953).

[16] S. Georgiev and J. Morais. *On convergence aspects of Spheroidal monogenics*. AIP Conference Proceedings, Vol. 1389, 276-279 (2011).

[17] K. Gürlebeck, K. Habetha and W. Sprößig, *Holomorphic Functions in the Plane and n-dimensional Space*, Birkhäuser Verlag, Basel - Boston - Berlin, 2008.

[18] K. Gürlebeck and J. Morais. *On Local Mapping Properties of Monogenic Functions*, K. Gürlebeck and C. Könke (Editors): Proceedings 18th International Conference on the Applications of Computer Science and Mathematics in Architecture and Civil Engineering, Weimar (2009).

[19] K. Gürlebeck and J. Morais. *Local properties of monogenic mappings*, AIP Conference Proceedings, "Numerical analysis and applied mathematics", 797-800 (2009).

[20] K. Gürlebeck and J. Morais. *Geometric characterization of M-conformal mappings*, Geometric Algebra Computing: in Engineering and Computer Science, Bayro-Corrochano, Eduardo; Scheuermann, Gerik (Eds.), Springer, 1st Edition, 327-342 (2010).

[21] E. W. Hobson. *The theory of spherical and ellipsoidal harmonics*, Cambridge, 1931.

[22] V. Kravchenko and M. Shapiro. *Integral Representations for Spatial Models of Mathematical Physics*. Research Notes in Mathematics, Pitman Advanced Publishing Program, London, 1996.

[23] K.I. Kou, J. Morais and Y. Zhang. *Generalized prolate spheroidal wave functions for offset linear canonical transform in Clifford analysis*. To appear in Mathematical Methods in the Applied Sciences.

[24] N.N. Lebedev. *Special Functions and their Applications*. Dover, New York, Chs. 7, 8, 1972.

[25] H. Leutwiler. *Quaternionic analysis in $\mathbb{R}^3$ versus its hyperbolic modification*. Brackx, F., Chisholm, J.S.R. and Soucek, V. (ed.). NATO Science Series II. Mathematics, Physics and Chemistry, Vol. 25, Kluwer Academic Publishers, Dordrecht, Boston, London (2001).

[26] H. Malonek and M.I Falcão. *3D-mappings by means of monogenic functions and their approximation*. Mathematical Methods in the Applied Sciences, Vol. 33, No. 4, 423-430 (2010).

[27] H. Malonek and R. Almeida. *A note on a generalized Joukowski transformation*. Applied Mathematics Letters, 23, 1174-1178 (2010).

[28] G. Moisil and N. Théodoresco. *Fonctions holomorphes dans l'espace*. Matematica (Cluj) 5, 142-159 (1931).

[29] J. Morais. *A Complete Orthogonal System of Spheroidal Monogenics*. To appear in the Journal of Numerical Analysis, Industrial and Applied Mathematics.

[30] J. Morais and M. Ferreira. *Quasiconformal mappings in 3D by means of monogenic functions*. To appear in Mathematical Methods in the Applied Sciences, 13 pp.

[31] J. Morais. *An orthogonal system of monogenic polynomials over prolate spheroids in* $\mathbb{R}^3$. Submitted for publication.

[32] J. Morais, S. Georgiev, K.I. Kou, T. Qian and W. Sprößig. *Generalized holomorphic Szegö kernel in 3D spheroids*. Submitted for publication.

[33] M. Riesz. *Clifford numbers and spinors*. Institute for Physical Science, Vol. 54, Kluwer Academic Publishers, Dorrecht, 1993.

[34] D. Slepian and H. O. Pollak. *Prolate Spheroidal Wave Functions, Fourier Analysis and Uncertainty, I*, Bell System Tech. J., Vol. 40, 1961, pp. 43-64.

[35] D. Slepian. *Prolate spheroidal wave functions, Fourier analysis and uncertainity. IV. Extensions to many dimensions; generalized prolate spheroidal functions.* Bell System Tech. J., 43:3009-3057, 1964. MR0181766 (31:5993).

[36] E. M. Stein and G. Weiß. *On the theory of harmonic functions of several variables*. Part I: *The theory of* H^p *spaces*. Acta Math. 103, 25-62 (1960).

[37] E.M Stein and G. Weiss. *Generalization of the Cauchy-Riemann equations and representations of the rotation group*, Amer. J. Math. 90, 163-196 (1968).

[38] A. Sudbery. *Quaternionic analysis*. Math. Proc. Cambridge Phil. Soc. 85: 199-225 (1979).

[39] G. Szegö. *A problem concerning orthogonal polynomials*, Trans. Amer. Math. Soc. 37, 196-206 (1935).

[40] G. Szegö. *Orthogonal Polynomials*, Amer. Math. Soc. Colloq. Publ., Vol. 23, New York (1939).

[41] G. Walter and T. Soleski. *A new friendly method of computing prolate spheroidal wave functions and wavelets.* Appl. Comput. Harmon. Anal., 19(3): 432-443, (2005).

[42] G. Walter. *Prolate spheroidal wavelets: Translation, convolution, and differentiation made easy.* J. Fourier Anal. Appl., 11(1): 73-84, (2005).

[43] G. Walter *Wavelets based on prolate spheroidal wave functions.* J. Fourier Anal. Appl., 10(1): 1-26 (2004).

[44] A.I. Zayed. *A generalization of the prolate spheroidal wave functions*. Proc. Amer. Math. Soc., 135(7): 2193-2203 (electronic), 2007.

19th International Conference on the Application of Computer
Science and Mathematics in Architecture and Civil Engineering
K. Gürlebeck, T. Lahmer and F. Werner (eds.)
Weimar, Germany, 04–06 July 2012

A NOTE ON THE CLIFFORD FOURIER-STIELTJES TRANSFORM AND ITS PROPERTIES

J. Morais*, S. Georgiev and W. Sprößig

**Departamento de Matemática*
Universidade de Aveiro
Campus Universitário Santiago
3810-193 Aveiro, Portugal
E-mail: joao.pedro.morais@ua.pt

Keywords: Clifford analysis, Fourier transform, functions of bounded variation, Fourier-Stieltjes integral, convolution.

Abstract. *The purpose of this article is to provide an overview of the real Clifford Fourier-Stieltjes transform (CFST) and of its important properties. Additionally, we introduce the definition of convolution of Clifford functions of bounded variation.*

1 INTRODUCTION

1.1 Function of bounded variation and its Fourier-Stieltjes transform

The concept of functions of bounded variation plays an important role in probability theory. Among the known attempts made in this direction, the most notable ones are due to Beurling [1], Bochner [2, 6], and Cramér [10].

Let $\sigma(x)$ be a nondecreasing real or complex-valued function of the real variable x, having bounded variation on the whole real axis: $\int_{\mathbb{R}} |d\sigma(x)| < \infty$. It is well known that $\sigma(x)$ has at most an enumerable set of discontinuity points. In such a point we define

$$\sigma(x) = \frac{1}{2}[\sigma(x+0) + \sigma(x-0)].$$

For any function $\sigma(x)$ as above, the expression

$$f(t) = \int_{\mathbb{R}} e^{itx} d\sigma(x), \quad -\infty < t < \infty \tag{1}$$

defines the *Fourier-Stieltjes transform* of $\sigma(x)$. The Fourier-Stieltjes transform (FST) is a well-known generalization of the classical Fourier transform, and is frequently applied in certain areas of theoretical and applied probability and stochastic processes contexts.

There has recently been much interest in the construction of higher dimensional counterparts of the Fourier-Stieltjes transform in the framework of quaternion and Clifford analyses [13, 14]. It is the object of the present paper to give an overview on the (real) Clifford Fourier-Stieltjes transform (CFST), and on some of its important properties [13]. The underlying functions are continuous functions of bounded variation defined in $\mathbb{R}^m$ and taking values in a Clifford algebra. We also introduce the definition of convolution of Clifford functions of bounded variation. The convolution is related to pairs of functions belonging to a certain class in the same way as in the classical case.

The used methods also allow a generalization to the case of Clifford functions that satisfy higher dimensional generalizations of Cauchy-Riemann or Dirac systems. We leave the details of this slight generalization to the interested reader.

1.2 Some basic concepts of Clifford analysis

In the present subsection, we review some definitions and basic algebraic facts of a special Clifford algebra of signature $(0, m)$. For more details, we refer the reader to [7, 16].

Let $\{e_1, e_2, \ldots, e_m\}$ be an orthonormal basis of the Euclidean vector space $\mathbb{R}^m$ with a product according to the multiplication rules:

$$e_i e_j + e_j e_i = -2\delta_{i,j}, \quad i, j = 1, \ldots, m,$$

where $\delta_{i,j}$ is the Kronecker symbol. Whence, the set $\{e_A : A \subseteq \{1, \ldots, m\}\}$ with $e_A = e_{h_1} e_{h_2} \ldots e_{h_r}$, $1 \leq h_1 < \ldots < h_r \leq m$, and $e_\phi = 1$ forms a basis of the 2^m-dimensional Clifford algebra $Cl_{0,m}$ over $\mathbb{R}$. Any Clifford number a in $Cl_{0,m}$ may thus be written as $a = \sum_A e_A a_A$, $a_A \in \mathbb{R}$, or still as $a = \sum_{k=0}^{m} [a]_k$, where $[a]_k = \sum_{|A|=k} e_A a_A$ is the so-called *k-vector part* of a $(k = 0, 1, \ldots, m)$. The real vector space $\mathbb{R}^m$ will be embedded in $Cl_{0,m}$ by identifying the element $(x_1, \ldots, x_m) \in \mathbb{R}^m$ with the Clifford vector $\mathbf{x}$ given by

$$\mathbf{x} := e_1 x_1 + \cdots + e_m x_m.$$

It is worth noting that the square of a vector $\mathbf{x}$ is scalar-valued and equals the norm squared up to a minus sign: $\mathbf{x}^2 = -|\mathbf{x}|^2$. Throughout the paper, we consider $Cl_{0,m}$-valued functions defined in $\mathbb{R}^m$, i.e. functions of the form

$$f : \mathbb{R}^m \longrightarrow Cl_{0,m}, \quad f(\mathbf{x}) = \sum_A f_A(\mathbf{x}) e_A, \tag{2}$$

where f_A are real-valued functions defined in $\mathbb{R}^m$. Properties (like integrability, continuity or differentiability) that are ascribed to f have to be fulfilled by all components f_A.

Let

$$L^1(\mathbb{R}^m; Cl_{0,m}) := \{f \in \mathbb{R}^m \longrightarrow Cl_{0,m} : \int_{\mathbb{R}^m} |f(\mathbf{x})| d\sigma(\mathbf{x}) < \infty\}$$

denote the linear Hilbert space of integrable $Cl_{0,m}$-valued functions defined in $\mathbb{R}^m$. The *left-sided Clifford Fourier transform* (CFT) of $f \in L^1(\mathbb{R}^m; Cl_{0,m})$ is given by [9]

$$\mathcal{F}(f) : \mathbb{R}^m \longrightarrow Cl_{0,m}, \quad \mathcal{F}(f)(\boldsymbol{\omega}) := \int_{\mathbb{R}^m} \mathbf{e}(\boldsymbol{\omega}, \mathbf{x})\, f(\mathbf{x})\, d\sigma(\mathbf{x}), \tag{3}$$

where the kernel function

$$\mathbf{e} : \mathbb{R}^m \times \mathbb{R}^m \longrightarrow Cl_{0,m}, \quad \mathbf{e}(\boldsymbol{\omega}, \mathbf{x}) := \prod_{i=1}^{m} e^{-e_{m+1-i}\, \omega_{m+1-i}\, x_{m+1-i}}.$$

For $i = 1, \ldots, m$, x_i will denote the *space* and ω_i the *angular frequency* variables. It is of interest to remark at this point that the product in (3) has to be performed in a fixed order since, in general, $\mathbf{e}(\boldsymbol{\omega}, \mathbf{x})$ does not commute with every element of $Cl_{0,m}$.

Under suitable conditions, the original signal f can be reconstructed from $\mathcal{F}(f)$ by the inverse transform. The *inverse (left-sided) Clifford Fourier transform* of $g \in L^1(\mathbb{R}^m; Cl_{0,m})$ is defined as follows:

$$\mathcal{F}^{-1}(g) : \mathbb{R}^m \longrightarrow Cl_{0,m}, \quad \mathcal{F}^{-1}(g)(\mathbf{x}) = \frac{1}{(2\pi)^m} \int_{\mathbb{R}^m} \overline{\mathbf{e}(\boldsymbol{\omega}, \mathbf{x})}\, g(\boldsymbol{\omega})\, d\sigma(\boldsymbol{\omega}) \tag{4}$$

where $\overline{\mathbf{e}(\boldsymbol{\omega}, \mathbf{x})} := \prod_{i=1}^{m} e^{e_i\, \omega_i\, x_i}$ is called the inverse (left-sided) Clifford Fourier kernel.

2 THE CLIFFORD FOURIER-STIELTJES TRANSFORM AND ITS PROPERTIES

In this section we review the (real) Clifford Fourier-Stieltjes transform (CFST).

2.1 The (real) Clifford Fourier-Stieltjes transform

In the sequel, consider the function

$$\alpha : \mathbb{R}^m \longrightarrow Cl_{0,m}, \quad \mathbf{x} \longmapsto \alpha(\mathbf{x}) := \prod_{i=1}^{m} \alpha^i(x_i)$$

where $\alpha^i : \mathbb{R} \longrightarrow Cl_{0,m}$ are of *bounded variation* on $\mathbb{R}$:

$$\int_{\mathbb{R}} |d\alpha^i(x_i)| := M_i < \infty,$$

and such that $|\alpha^i| \leq \delta_i$ for real numbers $\delta_i < \infty$. From here it follows that α is of bounded variation also, since it holds

$$\int_{\mathbb{R}^m} |d\alpha(\mathbf{x})| = \int_{\mathbb{R}^m} \prod_{i=1}^{m} |d\alpha^i(x_i)| = \prod_{i=1}^{m} M_i := M < \infty$$

and, such that

$$|\alpha(\mathbf{x})| \leq \prod_{i=1}^{m} \delta_i := \delta < \infty.$$

The class of all such functions is denoted by (V). Unless otherwise stated, throughout this paper the product is meant to be performed in a fixed order:

$$\prod_{i=1}^{m} \alpha^i(x_i) := \alpha^1(x_1)\alpha^2(x_2)\ldots\alpha^m(x_m).$$

For the sets of discontinuity points of each $\alpha^i(x_i)$, we further assume that there exist the limits

$$\lim_{x_i \longrightarrow y_i+} \alpha^i(x_i) = \alpha^i(y_i + 0), \quad \text{and} \quad \lim_{x_i \longrightarrow y_i-} \alpha^i(x_i) = \alpha^i(y_i - 0) \quad (i = 1, \ldots, m)$$

(taken over all directions) for which

$$\alpha^i(y_i) = \frac{1}{2}\Big[\alpha^i(y_i + 0) + \alpha^i(y_i - 0)\Big]$$

holds almost everywhere on $\mathbb{R}$. Each function α^i is said to be a *Clifford distribution*.

The idea behind the construction of a Clifford counterpart of the Stieltjes integral is to replace the exponential function in (1) by a suitable (noncommutative) exponential product. Due to the noncommutativity of the algebra, we recall two different types of CFST [13]:

Definition 2.1. The *CFST* $\mathcal{FS}(\alpha) : \mathbb{R}^m \longrightarrow Cl_{0,m}$ of $\alpha(\mathbf{x})$ is defined as the Stieltjes integrals:

1. Right-sided CFST:

$$\mathcal{FS}_r(\alpha)(\boldsymbol{\omega}) := \int_{\mathbb{R}^m} d\alpha(\mathbf{x})\, \overline{\mathbf{e}(\boldsymbol{\omega}, \mathbf{x})}, \tag{5}$$

2. Left-sided CFST:

$$\mathcal{FS}_l(\alpha)(\boldsymbol{\omega}) := \int_{\mathbb{R}^m} \mathbf{e}(\boldsymbol{\omega}, -\mathbf{x})\, d\alpha(\mathbf{x}). \tag{6}$$

The function $\alpha(\mathbf{x})$ which generates (5) and (6) is essentially unique.

Remark 2.2. We recall the reader that, the order of the exponentials in (5)-(6) are fixed because of the noncommutativity of the underlying product. It is of interest to remark at this point that in the case $m = 2$ the formulae above reduce to the definitions for the right- and left-sided QFST introduced by the authors in [14]. Detailed information about the QFST and its properties can be found in [14]. For $m = 1$ the CFST is identical to the classical FST.

Remark 2.3. Throughout this text we may investigate the integral (5) only that, for simplicity, we denote by $\mathcal{FS}(\alpha)$. Nevertheless, all computations can be easily converted for (6). In view of (5) and (6), a straightforward calculation shows that:

$$\mathcal{FS}(\alpha)(\boldsymbol{\omega}) = \overline{\int_{\mathbb{R}^m} \mathbf{e}(\boldsymbol{\omega}, \mathbf{x})\, \overline{d\alpha(\mathbf{x})}} = \overline{\mathcal{FS}_l(\overline{\alpha})(-\boldsymbol{\omega})}.$$

From now on, we denote the class of functions which can be represented as (5) by $\mathcal{B}$. Functions in $\mathcal{B}$ are called *(right) Clifford Bochner functions* and $\mathcal{B}$ will be referred to as the *(right) Clifford Bochner set*. It follows that members of $\mathcal{B}$ are entire functions of the real variables ω_i.

It is immediately clear that $\mathcal{B}$ is a linear space, and every element f of $\mathcal{B}$ is a bounded uniformly continuous function:

$$|f(\boldsymbol{\omega})| \leq \int_{\mathbb{R}^m} |d\alpha(\mathbf{x})| = M < \infty. \tag{7}$$

We recall from [13] the following result.

Theorem 2.4. *If a function belongs to $\mathcal{B}$ and is identically equal to zero for all $\omega_i \leq 0$ ($i = 1, \ldots, m$), then it is the Fourier-Stieltjes transform of an absolutely continuous function.*

Proof. Let f be any function in $\mathcal{B}$. By hypothesis,

$$f(\boldsymbol{\omega}) = \int_{\mathbb{R}^m} d\alpha(\mathbf{x})\, \overline{\mathbf{e}(\boldsymbol{\omega}, \mathbf{x})}, \tag{8}$$

where $\int_{\mathbb{R}^m} |d\sigma(\mathbf{x})| = M < \infty$. For $\mathbf{x} = x_1 e_1 + \cdots + x_m e_m \in Cl_{0,m}$ we set

$$Cl_{0,m} \ni \tilde{\mathbf{x}} := \frac{1}{2} \sum_{i=1}^{m} (x_i^2 + 1) e_i.$$

Let $\mathbb{R}_0^{m,+} := \underbrace{\mathbb{R}_0^+ \times \cdots \times \mathbb{R}_0^+}_{m \text{ times}}$. We define the function $G(\mathbf{x})$ as follows

$$G(\mathbf{x}) := \frac{1}{(2\pi)^m} \int_{\mathbb{R}_0^{m,+}} f(\boldsymbol{\omega})\, \overline{\mathbf{e}(\boldsymbol{\omega}, \tilde{\mathbf{x}})} d\boldsymbol{\omega}.$$

Evidently $G(\mathbf{x})$ is analytic for all x_i $(i = 1, \ldots, m)$ since it is the product of analytic functions for any fixed x_i. We suppose from now on that this condition is satisfied. From the definition of the function f follows that there exists a constant $M > 0$ so that $|f(\boldsymbol{\omega})| \leq M < \infty$. From (8) and since $f(\boldsymbol{\omega}) = 0$ for all $\omega_i \leq 0$ $(i = 1, \ldots, m)$, we may write

$$|G(\mathbf{x})| \leq \frac{1}{(2\pi)^m} \int_{\mathbb{R}_0^{m,+}} |f(\boldsymbol{\omega})| \prod_{i=1}^{m} e^{-\frac{x_i^2+1}{2}\omega_i} d\omega_i \leq \frac{M}{(2\pi)^m} \prod_{i=1}^{m} \frac{2}{x_i^2 + 1}.$$

By straightforward calculation we may show that

$$\int_{\mathbb{R}^m} |G(\mathbf{x})| d\mathbf{x} \leq \frac{M}{(2\pi)^m} \prod_{i=1}^{m} \int_{\mathbb{R}} \frac{2}{x_i^2 + 1} dx_i = M < \infty.$$

This proves the theorem. □

For practical purposes, if $f \in \mathcal{B}$ is given then for any real variables ω_i, and real constants a_i $(i = 1, \ldots, m)$ a direct computation shows that

$$\begin{aligned} |f(\boldsymbol{\omega})| &= \left| \left(\int_{-\infty}^{a_1} + \int_{a_1}^{\infty} \right) \left(\int_{-\infty}^{a_2} + \int_{a_2}^{\infty} \right) \ldots \left(\int_{-\infty}^{a_m} + \int_{a_m}^{\infty} \right) d\alpha(\mathbf{x})\, \overline{\mathbf{e}(\boldsymbol{\omega}, \mathbf{x})} \right| \\ &\leq \prod_{i=1}^{m} \Big(\big| \alpha^i(\infty) - \alpha^i(a_{m+1-i}) \big| + \big| \alpha^i(a_{m+1-i}) - \alpha^i(-\infty) \big| \Big) \end{aligned}$$

since $\left| \overline{\mathbf{e}(\boldsymbol{\omega}, \mathbf{x})} \right| = 1$. If $f \in \mathcal{B}$ is given, then

$$f(\mathbf{0}) = \prod_{i=1}^{m} \Big(\alpha^i(\infty) - \alpha^i(-\infty) \Big).$$

In particular, a simple argument gives

$$f(-\boldsymbol{\omega}) = \int_{\mathbb{R}^m} d\alpha(\mathbf{x})\, \overline{\mathbf{e}(-\boldsymbol{\omega}, \mathbf{x})} = \overline{\int_{\mathbb{R}^m} \mathbf{e}(-\boldsymbol{\omega}, \mathbf{x})\, \overline{d\alpha(\mathbf{x})}} = \overline{g(\boldsymbol{\omega})}, \tag{9}$$

where g is any function which can be represented as $\overline{\mathcal{FS}_l(\overline{\alpha})}(\boldsymbol{\omega})$.

2.2 Lévy's inversion formula

This subsection provides an explicit formula for computing a Clifford function once its Fourier-Stieltjes integral is known.

Theorem 2.5. *For every $\alpha^i : \mathbb{R} \longrightarrow Cl_{0,m}$ $(i = 1, \ldots, m)$, we consider the functions*

$$g_i(\omega_i) = \int_{\mathbb{R}} d\alpha^i(x_i)\, e^{e_i \omega_i x_i}.$$

For any real numbers a and b the following equality holds:

$$\alpha^i(a) - \alpha^i(b) = \lim_{T \longrightarrow \infty} \frac{1}{2\pi} \int_{-T}^{T} g_i(\omega_i) \frac{e^{e_i b \omega_i} - e^{e_i a \omega_i}}{e_i \omega_i} d\omega_i. \tag{10}$$

In particular, it holds

$$\alpha^i(x_i + 0) - \alpha^i(x_i - 0) = \lim_{T \longrightarrow \infty} \frac{1}{2T} \int_{-T}^{T} g_i(\omega_i) e^{-e_i x_i \omega_i} d\omega_i.$$

Proof. We begin with the following observation:

$$\begin{aligned} g_i(\omega_i) \Big(e^{-e_i a \omega_i} - e^{-e_i b \omega_i} \Big) &= \int_{\mathbb{R}} d\alpha^i(x_i)\, e^{e_i \omega_i (x_i - a)} - \int_{\mathbb{R}} d\alpha^i(x_i)\, e^{e_i \omega_i (x_i - b)} \\ &= \int_{\mathbb{R}} d\alpha^i(x_i + a)\, e^{e_i \omega_i x_i} - \int_{\mathbb{R}} d\alpha^i(x_i + b)\, e^{e_i \omega_i x_i} \end{aligned}$$

$$
\begin{aligned}
&= \lim_{T\longrightarrow\infty}\Big[\alpha^i(T+a)e^{e_iT\omega_i} - \alpha^i(-T+a)e^{-e_iT\omega_i} \\
&\qquad -\alpha^i(T+b)e^{e_iT\omega_i} + \sigma^i(-T+b)e^{-e_iT\omega_i} \\
&\qquad -\int_{-T}^{T}\Big(\alpha^i(x_i+a)-\alpha^i(x_i+b)\Big)dx_i\, e^{e_i\omega_i x_i}e_i\omega_i\Big] \\
&= -\int_{\mathbb{R}}\Big(\alpha^i(x_i+a)-\alpha^i(x_i+b)\Big)dx_i\, e^{e_i\omega_i x_i}e_i\omega_i.
\end{aligned}
$$

Therefore, it is easy to see that

$$
g_i(\omega_i)\Big(e^{-e_ia\omega_i}-e^{-e_ib\omega_i}\Big)\frac{1}{-e_i\omega_i} = \int_{\mathbb{R}}\Big(\alpha^i(x_i+a)-\alpha^i(x_i+b)\Big)dx_i\, e^{e_i\omega_i x_i}.
$$

From the last equality and from the inverse Fourier transform formula we find

$$
\alpha^i(x_i+a)-\alpha^i(x_i+b) = \frac{1}{2\pi}\int_{\mathbb{R}} g_i(\omega_i)\frac{e^{-e_ia\omega_i}-e^{-e_ib\omega_i}}{-e_i\omega_i}\, e^{-e_ix_i\omega_i}d\omega_i,
$$

and, in particular taking $x_i = 0$ we find

$$
\alpha^i(a)-\alpha^i(b) = \frac{1}{2\pi}\int_{\mathbb{R}} g(\omega_i)\frac{e^{-e_ia\omega_i}-e^{-e_ib\omega_i}}{-e_i\omega_i}d\omega_i,
$$

and this completes the proof. □

Formula (10) is known as the *Lévy's inversion formula*. It is immediately clear if two Clifford functions have the same Fourier-Stieltjes integral, then they are identical up to an additive (Clifford) constant.

3 UNIFORM CONTINUITY

In this section we discuss uniform continuity and its relationship to CFST. We begin by defining uniform continuity.

Definition 3.1. A Clifford function $f : \mathbb{R}^m \longrightarrow Cl_{0,m}$ is *uniformly continuous* on $\mathbb{R}^m$ if and only if for all $\epsilon > 0$ there exists a $\delta > 0$ such that $|f(\boldsymbol{\omega}) - f(\mathbf{t})| < \epsilon$ for all $\boldsymbol{\omega}, \mathbf{t} \in \mathbb{R}^m$ whenever $|\boldsymbol{\omega} - \mathbf{t}| < \delta$.

We now prove some results related to the asymptotic behaviour of the CFST which run:

Proposition 3.2. *Let f be an element of $\mathcal{B}$. For any natural number n, let $f^n : \mathbb{R}^{m-1} \times [-n, n] \longrightarrow Cl_{0,m}$ be the function given by*

$$
f^n(\boldsymbol{\omega}) = \int_{-n}^{n}\int_{\mathbb{R}^{m-1}} d\alpha(\mathbf{x})\,\overline{\boldsymbol{e}(\boldsymbol{\omega},\mathbf{x})}.
$$

Then $f^n(\boldsymbol{\omega}) \longrightarrow_{n\longrightarrow\infty} f(\boldsymbol{\omega})$ uniformly. Also, if f^n are uniformly continuous functions then f is a uniformly continuous function.

Proof. A first straightforward computation shows that

$$\begin{aligned}\left|f(\boldsymbol{\omega})-f^n(\boldsymbol{\omega})\right| &= \left|\int_{\mathbb{R}^m} d\alpha(\mathbf{x})\,\overline{\mathbf{e}(\boldsymbol{\omega},\mathbf{x})}-\int_{-n}^{n}\int_{\mathbb{R}^{m-1}} d\alpha(\mathbf{x})\,\overline{\mathbf{e}(\boldsymbol{\omega},\mathbf{x})}\right| \\ &= \left|\int_{-\infty}^{-n}\int_{\mathbb{R}^{m-1}} d\alpha(\mathbf{x})\,\overline{\mathbf{e}(\boldsymbol{\omega},\mathbf{x})}+\int_{n}^{\infty}\int_{\mathbb{R}^{m-1}} d\alpha(\mathbf{x})\,\overline{\mathbf{e}(\boldsymbol{\omega},\mathbf{x})}\right| \\ &\leq \prod_{i=1}^{m-1}\left|\alpha^i(\infty)-\alpha^i(-\infty)\right|\left|\alpha^m(-n)-\alpha^m(-\infty)\right| \\ &+ \prod_{i=1}^{m-1}\left|\alpha^i(\infty)-\alpha^i(-\infty)\right|\left|\alpha^m(\infty)-\alpha^m(n)\right|.\end{aligned}$$

Moreover, having in mind that

$$\alpha^m(-n)-\alpha^m(-\infty)\longrightarrow_{n\longrightarrow\infty}0,\quad \text{and}\quad \alpha^m(\infty)-\alpha^m(n)\longrightarrow_{n\longrightarrow\infty}0,$$

and hence, $f^n(\boldsymbol{\omega})\longrightarrow_{n\longrightarrow\infty} f(\boldsymbol{\omega})$ uniformly. In addition, we claim that if $f^n(\boldsymbol{\omega})$ are uniformly continuous functions it follows that $f(\boldsymbol{\omega})$ is an uniformly continuous function. □

In like manner, we have an analogous result.

Proposition 3.3. *Let f be an element of $\mathcal{B}$. For any natural number n, let $f^n:[-n,n]\times\mathbb{R}^{m-1}\longrightarrow Cl_{0,m}$ be the function given by*

$$f^n(\boldsymbol{\omega})=\int_{\mathbb{R}^{m-1}}\int_{-n}^{n} d\alpha(\mathbf{x})\,\overline{\boldsymbol{e}(\boldsymbol{\omega},\mathbf{x})}.$$

Then $f^n(\boldsymbol{\omega})\longrightarrow_{n\longrightarrow\infty} f(\boldsymbol{\omega})$ uniformly. Also, if f^n are uniformly continuous functions then f is a uniformly continuous function.

Proposition 3.4. *Let f be an element of $\mathcal{B}$. For any natural number n, let $f^n:[-n,n]^m\longrightarrow Cl_{0,m}$ be the function given by*

$$f^n(\boldsymbol{\omega})=\int_{[-n,n]^m} d\alpha(\mathbf{x})\,\overline{\boldsymbol{e}(\boldsymbol{\omega},\mathbf{x})}.$$

Then $f^n(\boldsymbol{\omega})\longrightarrow_{n\longrightarrow\infty} f(\boldsymbol{\omega})$ uniformly. Also, if f^n are uniformly continuous functions then f is a uniformly continuous function.

Proof. For simplicity and without loss of generality we will prove the case $m=2$ only. We set

$$A:=d\alpha^1(x_1)d\alpha^2(x_2)\,e^{e_1\omega_1x_1}\,e^{e_2\omega_2x_2}.$$

The key to the proof is the simple observation that:

$$\begin{aligned}\int_{-\infty}^{\infty}\int_{-\infty}^{\infty}A-\int_{-n}^{n}\int_{-n}^{n}A &= \int_{-\infty}^{-n}\int_{-\infty}^{-n}A+\int_{-\infty}^{-n}\int_{-n}^{n}A+\int_{-\infty}^{-n}\int_{n}^{\infty}A \\ &+ \int_{-n}^{n}\int_{-\infty}^{-n}A+\int_{-n}^{n}\int_{n}^{\infty}A \\ &+ \int_{n}^{\infty}\int_{-\infty}^{-n}A+\int_{n}^{\infty}\int_{-n}^{n}A+\int_{n}^{\infty}\int_{n}^{\infty}A.\end{aligned}$$

For the remaining part of the proof, we use similar arguments as in Proposition 3.2. □

We come now to the main result of this section.

Theorem 3.5. *Let $f \in \mathcal{B}$ be given, and $g : \mathbb{R}^m \longrightarrow Cl_{0,m}$ be a continuous and absolutely integrable function. For any $\alpha : \mathbb{R}^m \longrightarrow Cl_{0,m}$ the following relations hold:*

1. $\displaystyle\int_{\mathbb{R}^m} f(\mathbf{t})g(\boldsymbol{\omega}-\mathbf{t})d\mathbf{t} = \int_{\mathbb{R}^m} d\alpha(\mathbf{x}) \int_{\mathbb{R}^m} \overline{\boldsymbol{e}(\boldsymbol{\omega},\mathbf{x})}\, g(\boldsymbol{\omega}-\mathbf{t})d\mathbf{t}$;

2. $\displaystyle\int_{\mathbb{R}^m} f(\mathbf{t})g(\mathbf{t})d\mathbf{t} = (2\pi)^m \int_{\mathbb{R}^m} d\alpha(\mathbf{x})\, \mathcal{F}^{-1}(g)(\mathbf{x})$.

Proof. Assume $g : \mathbb{R}^m \longrightarrow Cl_{0,m}$ to be a continuous and absolutely integrable function. For any real variables ρ_i $(i = 1, \ldots, m)$ let $\Omega_{\rho_i} := [-\rho_1, \rho_1] \times \cdots \times [-\rho_m, \rho_m] \subset \mathbb{R}^m$. We now define the function

$$R : \mathbb{R}^m \times \mathbb{R}^m \longrightarrow Cl_{0,m}, \quad (\mathbf{x}, \boldsymbol{\rho}) \longmapsto R(\mathbf{x}, \boldsymbol{\rho}) := \int_{\Omega_{\rho_i}} \prod_{i=1}^{m} e^{e_i t_i x_i} g(\mathbf{t})d\mathbf{t}.$$

Take

$$f^n(\mathbf{t}) = \int_{[-n,n]^m} d\alpha(\mathbf{x}) \prod_{i=1}^{m} e^{e_i t_i x_i}.$$

Using the fact that g is an absolutely integrable function it follows

$$\begin{aligned}
\int_{\Omega_{\rho_i}} f^n(\mathbf{t})g(\mathbf{t})d\mathbf{t} &= \int_{\Omega_{\rho_i}} \left(\int_{[-n,n]^m} d\alpha(\mathbf{x}) \prod_{i=1}^{m} e^{e_i t_i x_i} \right) g(\mathbf{t})d\mathbf{t} \\
&= \int_{[-n,n]^m} d\alpha(\mathbf{x}) \int_{\Omega_{\rho_i}} \prod_{i=1}^{m} e^{e_i t_i x_i} g(\mathbf{t})d\mathbf{t} \\
&= \int_{[-n,n]^m} d\alpha(\mathbf{x}) R(\mathbf{x}, \rho). \qquad (11)
\end{aligned}$$

From the last proposition we know that $\lim_{n\longrightarrow\infty} f^n(\boldsymbol{\omega}) = f(\boldsymbol{\omega})$ uniformly. Moreover, since $g(\mathbf{t})$ is an absolutely integrable function it follows that $R(\mathbf{x}, \boldsymbol{\rho})$ is a uniformly continuous function. Hence

$$\lim_{n\longrightarrow\infty} \int_{\Omega_{\rho_i}} f^n(\mathbf{t})g(\mathbf{t})d\mathbf{t} = \int_{\Omega_{\rho_i}} f(\mathbf{t})g(\mathbf{t})d\mathbf{t}. \qquad (12)$$

With this argument at hand, and from (11) we conclude that

$$\lim_{n\longrightarrow\infty} \int_{\Omega_{\rho_i}} f^n(\mathbf{t})g(\mathbf{t})d\mathbf{t} = \int_{\mathbb{R}^m} d\alpha(\mathbf{x})R(\mathbf{x}, \boldsymbol{\rho}). \qquad (13)$$

From the last equality and from (12) we obtain

$$\int_{\mathbb{R}^m} d\alpha(\mathbf{x})R(\mathbf{x}, \boldsymbol{\rho}) = \int_{\Omega_{\rho_i}} f(\mathbf{t})g(\mathbf{t})d\mathbf{t}.$$

In addition, we have

$$R(\mathbf{x},\boldsymbol{\rho}) \longrightarrow \begin{array}{l}\rho_i \longrightarrow \infty \\ (i=1,\ldots,m)\end{array} \quad \int_{\mathbb{R}^m} \prod_{i=1}^{m} e^{e_i t_i x_i} g(\mathbf{t}) d\mathbf{t}$$

and hence, for any fixed a_i it follows

$$\int_{\Omega_{a_i}} d\alpha(\mathbf{x}) R(\mathbf{x},\boldsymbol{\rho}) \longrightarrow \begin{array}{l}\rho_i \longrightarrow \infty \\ (i=1,\ldots,m)\end{array} \quad \int_{\Omega_{a_i}} d\alpha(\mathbf{x}) \int_{\mathbb{R}^m} \prod_{i=1}^{m} e^{e_i t_i x_i} g(\mathbf{t}) d\mathbf{t}. \tag{14}$$

For the sake of simplicity, in the considerations to follow we will often omit the argument and write simply R instead of $R(\mathbf{x},\boldsymbol{\rho})$. Since R is uniformly bounded then there exists a positive constant M so that $|R| \leq M$ for all real numbers x_i and ρ_i. Without loss of generality, we will prove the case $m = 2$ only. A direct computation shows that

$$\begin{aligned} I \;:=\; & \left| \int_{-\infty}^{-a_1}\int_{-\infty}^{-a_2} d\alpha^1(x_1) d\alpha^2(x_2) R + \int_{-a_1}^{a_1}\int_{-\infty}^{-a_2} d\alpha^1(x_1) d\alpha^2(x_2) R \right. \\ & + \int_{a_1}^{\infty}\int_{-\infty}^{-a_2} d\alpha^1(x_1) d\alpha^2(x_2) R + \int_{-\infty}^{-a_1}\int_{-a_2}^{a_2} d\alpha^1(x_1) d\alpha^2(x_2) R \\ & + \int_{a_1}^{\infty}\int_{-a_2}^{a_2} d\alpha^1(x_1) d\alpha^2(x_2) R + \int_{-\infty}^{-a_1}\int_{a_2}^{\infty} d\alpha^1(x_1) d\alpha^2(x_2) R \\ & \left. + \int_{-a_1}^{a_1}\int_{a_2}^{\infty} d\alpha^1(x_1) d\alpha^2(x_2) R + \int_{a_1}^{\infty}\int_{a_2}^{\infty} d\alpha^1(x_1) d\alpha^2(x_2) R \right|. \end{aligned}$$

Therefore, we obtain

$$\begin{aligned} I \;\leq\; & M\Big[\left|\alpha^1(-a_2)-\alpha^1(-\infty)\right| \left|\alpha^2(-a_1)-\alpha^2(-\infty)\right| \\ & + \left|\alpha^1(-a_2)-\alpha^1(-\infty)\right| \left|\alpha^2(a_1)-\alpha^2(-a_1)\right| + \left|\alpha^1(-a_2)-\alpha^1(-\infty)\right| \left|\alpha^2(\infty)-\alpha^2(a_1)\right| \\ & + \left|\alpha^1(a_2)-\alpha^1(-a_2)\right| \left|\alpha^2(-a_1)-\alpha^2(-\infty)\right| + \left|\alpha^1(a_2)-\alpha^1(-a_2)\right| \left|\alpha^2(\infty)-\alpha^2(a_1)\right| \\ & + \left|\alpha^1(\infty)-\alpha^1(a_2)\right| \left|\alpha^2(-a_1)-\alpha^2(-\infty)\right| + \left|\alpha^1(\infty)-\alpha^1(a_2)\right| \left|\alpha^2(a_1)-\alpha^2(-a_1)\right| \\ & + \left|\alpha^1(\infty)-\alpha^1(a_2)\right| \left|\alpha^2(\infty)-\alpha^2(a_1)\right| \Big] \longrightarrow_{a_1,a_2\longrightarrow\infty} 0. \end{aligned}$$

Extending the last inequality to a total of 2^m terms $(m > 2)$, and using (14) we get

$$\lim_{a_i\longrightarrow\infty} \int_{\Omega_{a_i}} d\alpha(\mathbf{x}) R(\mathbf{x},\boldsymbol{\rho}) = \int_{\mathbb{R}^m} d\alpha(\mathbf{x}) \int_{\mathbb{R}^m} \prod_{i=1}^{m} e^{e_i t_i x_i} g(\mathbf{t}) d\mathbf{t}.$$

From here and (13) we find

$$\int_{\mathbb{R}^m} f(\mathbf{t}) g(\mathbf{t}) d\mathbf{t} = \int_{\mathbb{R}^m} d\alpha(\mathbf{x}) \int_{\mathbb{R}^m} \prod_{i=1}^{m} e^{e_i t_i x_i} g(\mathbf{t}) d\mathbf{t} = (2\pi)^m \int_{\mathbb{R}^m} d\alpha(\mathbf{x})\, \mathcal{F}^{-1}(g)(\mathbf{x}).$$

Making the change of variables $t_i \longrightarrow \omega_i - t_i$ $(i = 1,\ldots,m)$ in the definition of g we finally find

$$\int_{\mathbb{R}^m} f(\mathbf{t}) g(\boldsymbol{\omega}-\mathbf{t}) d\mathbf{t} = \int_{\mathbb{R}^m} d\alpha(\mathbf{x}) \int_{\mathbb{R}^m} \prod_{i=1}^{m} e^{e_i t_i x_i}\, g(\boldsymbol{\omega}-\mathbf{t}) d\mathbf{t}.$$

□

4 CONVOLUTION

In this section we introduce the definition of convolution of Clifford functions. The convolution is related to pairs of Clifford functions belonging to (V).

Definition 4.1. Let $\alpha, \beta : \mathbb{R}^m \longrightarrow Cl_{0,m}$ belong to (V). The convolution $\alpha \odot \beta$ of α and β is the uniquely determined function $\gamma : \mathbb{R}^m \longrightarrow Cl_{0,m}$ given by

$$\gamma \;=\; \alpha \odot \beta \;:=\; \int_{\mathbb{R}^m} \alpha(\mathbf{x}-\mathbf{y})\, d\beta(\mathbf{y}) \tag{15}$$

for every $\mathbf{x}, \mathbf{y} \in \mathbb{R}^m$.

We underline that due to the noncommutativity of the quaternionic product, $\alpha \odot \beta$ does not coincide with $\beta \odot \alpha$ in general. We notice that the function γ given by (15) is well defined since it obviously holds

$$|\gamma(\mathbf{x})| \leq \int_{\mathbb{R}^m} |\alpha(\mathbf{x}-\mathbf{y})||d\beta(\mathbf{y})| \leq \delta \int_{\mathbb{R}^m} |d\beta(\mathbf{y})| < \infty.$$

Let α, β, ζ be elements of (V), and λ a Clifford constant. In particular, the convolution retains the following properties:

1. $(\alpha \odot \beta) \odot \zeta = \alpha \odot (\beta \odot \zeta)$;
2. $\alpha \odot (\beta \pm \zeta) = \alpha \odot \beta \pm \alpha \odot \zeta$;
3. $\lambda(\alpha \odot \beta) = (\lambda\alpha) \odot \beta, \quad (\alpha \odot \beta)\lambda = \alpha \odot (\beta\lambda)$;
4. $\lambda(\alpha \odot \beta) \neq \alpha \odot (\lambda\beta)$ in general.

Next we formulate the results of this section.

Proposition 4.2. *If α and β are elements of (V) then the function γ defined by (15) belongs to (V).*

Proof. Let $\mathbf{x}, \mathbf{z} \in \mathbb{R}^m$. Since α is a continuous function then for every $\epsilon > 0$ there exists a real $\delta = \delta(\epsilon) > 0$ such that

$$|\alpha(\mathbf{x}) - \alpha(\mathbf{z})| < \frac{\epsilon}{M}$$

whenever $|\mathbf{x} - \mathbf{z}| < \delta$. The constant $M > 0$ is chosen so that $\int_{\mathbb{R}^m} |d\beta(\mathbf{y})| = M$ for every $\mathbf{y} \in \mathbb{R}^m$. Hence, it holds

$$|\gamma(\mathbf{x}) - \gamma(\mathbf{z})| = \left| \int_{\mathbb{R}^m} (\alpha(\mathbf{x}-\mathbf{y}) - \alpha(\mathbf{z}-\mathbf{y}))\, d\beta(\mathbf{y}) \right| < \epsilon.$$

Consequently γ is a continuous function in $\mathbf{x}$. Since $\mathbf{x} \in \mathbb{R}^m$ is arbitrarily chosen it follows that γ is also continuous. □

Proposition 4.3. *Let α and β be elements of (V). If $\alpha \in L^1(\mathbb{R}^m; Cl_{0,m})$ then it holds*

$$\|\gamma\|_{L^1(\mathbb{R}^m;Cl_{0,m})} \leq M\|\alpha\|_{L^1(\mathbb{R}^m;Cl_{0,m})}.$$

Proof. Let α and β be any functions in (V). A first straightforward computation shows that

$$\begin{aligned}
\|\gamma\|_{L^1(\mathbb{R}^m;Cl_{0,m})} &= \int_{\mathbb{R}^m} |\gamma(\mathbf{x})| d\sigma(\mathbf{x}) \\
&= \int_{\mathbb{R}^m} \Big| \int_{\mathbb{R}^m} \alpha(\mathbf{x}-\mathbf{y}) d\beta(\mathbf{y}) \Big| d\sigma(\mathbf{x}) \\
&\leq \int_{\mathbb{R}^m} \Big(\int_{\mathbb{R}^m} |\alpha(\mathbf{x}-\mathbf{y})| d\sigma(\mathbf{x}) \Big) |d\beta(\mathbf{y})| \\
&= M\|\alpha\|_{L^1(\mathbb{R}^m;Cl_{0,m})}.
\end{aligned}$$

□

In consequence, the following result holds:

Corollary 4.4. *Let α, β and α^n be elements of (V). If $\alpha, \alpha^n \in L^1(\mathbb{R}^m; Cl_{0,m})$ then it holds*

$$\|\gamma^n - \gamma\|_{L^1(\mathbb{R}^m;Cl_{0,m})} \longrightarrow 0$$

when $n \longrightarrow \infty$, where $\gamma^n = \alpha^n \odot \beta$ and $\gamma = \alpha \odot \beta$.

Proof. From the previous proposition a direct computation shows that

$$\|\gamma^n - \gamma\|_{L^1(\mathbb{R}^m;Cl_{0,m})} \leq M\|\alpha^n - \alpha\|_{L^1(\mathbb{R}^m;Cl_{0,m})},$$

and from this follows our assertion. □

5 ACKNOWLEDGEMENT

This work was supported by *FEDER* funds through *COMPETE*–Operational Programme Factors of Competitiveness ("Programa Operacional Factores de Competitividade") and by Portuguese funds through the *Center for Research and Development in Mathematics and Applications* (University of Aveiro) and the Portuguese Foundation for Science and Technology ("FCT–Fundação para a Ciência e a Tecnologia"), within project PEst-C/MAT/UI4106/2011 with COMPETE number FCOMP-01-0124-FEDER-022690. Partial support from the Foundation for Science and Technology (FCT) via the post-doctoral grant SFRH/BPD/66342/2009 is also acknowledged by the first author. The second author acknowledges financial support via the grant DD-VU-02/90, Bulgaria.

REFERENCES

[1] A. Beurling. *Sur les intégrales de Fourier absolument convergentes et leur application à une transformation fonctionnelle*. Neuvième congrès des mathédmaticiens scandinaves. Helsingfors, 1938.

[2] S. Bochner. *Monotone funktionen, Stieltjessche integrate, und harmonische analyse*. Math. Ann., Vol. 108 (1933), pp. 378-410.

[3] S. Bochner. *A theorem on Fourier-Stieltjes integrals*. Bull. Amer. Math. Soc. 40 (1934).

[4] S. Bochner. *Completely monotone functions of the Laplace operator for torus and sphere*. Duke Math. Journ., Vol. 3 (1937), pp. 488-502.

[5] S. Bochner. *A theorem on analytic continuation of functions of several complex variables*. Annals of Math., Vol. 39 (1938), pp. 14-19.

[6] S. Bochner. *Lectures on Fourier integrals*. Priceton, New Jersey, Priceton University Press, 1959.

[7] F. Brackx, R. Delanghe, and F. Sommen. *Clifford Analysis*. Pitman, Boston - London - Melbourne, 1982.

[8] T. Bülow. *Hypercomplex spectral signal representations for the processing and analysis of images*. Ph.D.Thesis, Institut für Informatik und Praktische Mathematik, University of Kiel, Germany, 1999.

[9] T. Bülow, M. Felsberg and G. Sommer. *Non-commutative hypercomplex Fourier transforms of multidimensional signals*. In G. Sommer (ed.), Geom. Comp. with Cliff. Alg., Theor. Found. and Appl. in Comp. Vision and Robotics, Springer (2001), pp. 187-207.

[10] H. Cramér. *Random variables and probability distributions*. Cambridge Tracts No. 36, 1937.

[11] J. Ebling and G. Scheuermann. *Clifford Fourier transform on vector fields*. IEEE Transactions on Visualization and Computer Graphics, Vol. 11, No. 4 (2005), pp. 469-479.

[12] S. Georgiev, J. Morais and W. Sprößig, *Trigonometric integrals in the framework of Quaternionic analysis*. Proceedings of the 9th International Conference on Clifford Algebras and their Applications in Mathematical Physics (2011), 15 pp.

[13] S. Georgiev, J. Morais, and W. Sprößig. *A note on the Clifford Fourier-Stieltjes transform*. Clifford analysis, Clifford algebras and their applications. Vol. 1, No. 1 (2012), pp. 86-96.

[14] S. Georgiev and J. Morais, *Bochner's Theorems in the framework of Quaternion Analysis*. Accepted for publication in Eckhard Hitzer and Steve Sangwine, Quaternion and Clifford Fourier Transforms and Wavelets, Springer, Birkhauser Trends in Mathematics Series, 20 pp. (2012).

[15] S. Georgiev, J. Morais, K.I. Kou and W. Sprößig, *Bochner-Minlos Theorem and Quaternion Fourier Transform*. Accepted for publication in Eckhard Hitzer and Steve Sangwine, Quaternion and Clifford Fourier Transforms and Wavelets, Springer, Birkhauser Trends in Mathematics Series, 17 pp. (2012).

[16] K. Gürlebeck, K. Habetha, and W. Sprößig. *Holomorphic Functions in the Plane and n-dimensional Space*, Birkhäuser Verlag, Basel - Boston - Berlin, 2008.

19th International Conference on the Application of Computer
Science and Mathematics in Architecture and Civil Engineering
K. Gürlebeck, T. Lahmer and F. Werner (eds.)
Weimar, Germany, 04–06 July 2012

UNCERTAINTY QUANTIFICATION AND SENSITIVITY ANALYSIS ON CYCLIC CREEP PREDICTION OF CONCRETE

HB. Motra*, A. Dimmig-Osburg and J. Hildebrand

* *Research Training Group 1462*
Bauhaus-Universität Weimar
Berkaerstr. 9
99423, Weimar
Germany
E-mail: hem.bahadur.motra@uni-weimar.de

Keywords: Cyclic Creep, Input Variables, Stochastic, Sensitivity Analysis, Uncertainty Analysis, Monte Carlo Simulation.

Abstract. *This paper presents a methodology for uncertainty quantification in cyclic creep analysis. Several models- , namely BP model, Whaley and Neville model, modified MC90 for cyclic loading and modified Hyperbolic function for cyclic loading are used for uncertainty quantification. Three types of uncertainty are included in Uncertainty Quantification (UQ): (i) natural variability in loading and materials properties; (ii) data uncertainty due to measurement errors; and (iii) modelling uncertainty and errors during cyclic creep analysis. Due to the consideration of all type of uncertainties, a measure for the total variation of the model response is achieved. The study finds that the BP, modified Hyperbolic and modified MC90 are best performing models for cyclic creep prediction in that order. Further, global Sensitivity Analysis (SA) considering the uncorrelated and correlated parameters is used to quantify the contribution of each source of uncertainty to the overall prediction uncertainty and to identifying the important parameters. The error in determining the input quantities and model itself can produce significant changes in creep prediction values. The variability influence of input random quantities on the cyclic creep was studied by means of the stochastic uncertainty and sensitivity analysis namely the Gartner et al. method and Saltelli et al. method. All input imperfections were considered to be random quantities. The Latin Hypercube Sampling (LHS) numerical simulation method (Monte Carlo type method) was used. It has been found by the stochastic sensitivity analysis that the cyclic creep deformation variability is most sensitive to the Elastic modulus of concrete, compressive strength, mean stress, cyclic stress amplitude, number of cycle, in that order.*

1 INTRODUCTION

Creep of concrete under a sustained static load is a well-known phenomenon. Much research has been carried out in this context [1-2]. Under actual operating condition many structures are subjected to dynamic loading in addition to static loading. The effect of traffic loads on bridge and pavement, vibrating machinery on floor system, wave load on offshore structures and wind load on slender buildings are familiar examples. Such structures under repeated loads must be designed to control deformation due to static and dynamic creep. Numerous researches on the cyclic creep in concrete found the increase in creep under cyclic loading as cyclic creep and it is important to realize that cyclic creep is measured relative to creep under sustained load equal to the mean cyclic stress and not the creep under a sustained load equal to the upper cyclic stress [2]. Actually, time-dependent nonlinearity also grows during cyclic loading especially under higher strains. Cyclic creep is a nonlinear phenomenon.

Many studies have examined the stress-strain behaviour of drying and confined concrete under cyclic compression and tension and numerous concrete models have been proposed in the last years but very few studies addressed the long term time-dependent behaviour of concrete under cyclic load. Since probably the first works attempting to characterize the behaviour of concrete under a rapidly fluctuating (1 Hz) stress of given duration were published [3-4] a significant research effort has been devoted to that field and found the irreversible deformation to increase with the number of cycles. The decrease of the non-elastic deformation with an increase in the age at application of cyclic load, this behaviour is similar to that under static loading. Many others mathematical and experimental models have been documents in the literatures like [5-12].

The investigation of uncertainties for time-dependent behaviour of plain concrete under sustained loading much research has been carried out but under cyclic loading very less work has been done. The study on the uncertainties in creep and shrinkage effects has been continuously an area of significant efforts. The external or parameters uncertainty and internal (model uncertainty, measurement uncertainty and uncertainty of the creep phenomenon) uncertainty has given to the references [13-20].Uncertainty Quntification (UQ) of creep models under sustained loading by using the Latin Hypercube Sampling were proposed [21]. However, most of the existing UQ and Sensitivity Analysis (SA) techniques assume input variables independence, and a few studies have focused on the UQ and SA of the correlated input variables and degradation materials behaviour under cyclic loading, which is usually the common case in concrete structures.

Different UQ and SA techniques will perform better for specific type of models. One method of UQ and SA of models by considering the uncorrelated and correlated parameters is proposed by [22 and 28]. The distinction between uncorrelated and correlated contribution of uncertainty for an individual variable is very important and output response and input variables is approximately linear in this method. One of the most important and basic concepts is that results of any scientific experiment always has a degree of uncertainty which is known as experimental uncertainty. The problem of quantifying the contribution of systematic error and measurement uncertainty considered for the calculation of the uncertainty. In fact, since its first edition [24] of the Guide to the Expression of the Uncertainty in Measurement (GUM), and still in the last one [25], the GUM attempts to completely set aside the concepts of the true value and measurement error, whose connection with that of measurement uncertainty is considered (Clause E.5.1). GUM uncertainties are standard deviation of probability distribution and as a degree of

belief, quantified by means of a subjective probability distribution (Clause 3.3.5). The GUM Supplement 1 [26] is based on one general concept of propagating probability density function (PDF) where in order to obtain PDF for the measured of the Monte Carlo method (MCM) use was suggested. Consequently, the law of propagation of uncertainties is based on a construction of a linear approximation of the model function [27]. The GUM uncertainty framework- GUF [26] and MCM are approximate methods where the first methods are exact and second one is never exact. Apart from that MCM is more valid than the GUF for large class of problems [26].

In this work, a statistical framework is discussed for cyclic creep function. As a first step, four cyclic creep models in plain concrete are discussed briefly: BP model [6-7], modified MC90/EC2 [8-9], Whaley and Neville model [5] and modified Hyperbolic function [10-12]. Subsequently, the influences of input parameters are discussed in 2 steps. The Monte Carlo simulation with Latin Hypercube Sampling (LHS) technique is used for determining the UQ and SA, measurement, phenomenon , model uncettainties, which explained in step 3. In step 4 explain the overview of UQ and SA [22-26] and measurement UQ according to GUM methods. Further, using the stochastic UQ and SA, it is determined the uncertainty level of different models and analysed the quality of model and to what degree does the randomness of an input quantity influence the variability of the output. The present paper has considered the amount of degradation with respect of both strength and stiffness of the concrete.

2 CYCLIC CREEP MODELS

Several experimental and mathematical models have been developed for estimating cyclic creep strain. The most widely used mathematical models are the BP models, Whaley and Neville model. Modified MC90/EC2 and modified Hyperbolic function, experimental cyclic creep models: Gaede 1962, Kern et al. 1962, Neville et al. 1973, Sutter et al. 1975, Hirst et al. 1977. This study also includes these four mathematical models.

Based on the test data Whaley and Neville model [5] has shown that the cyclic creep strain can be expressed as the sum of the two strain component, a mean strain component and a cyclic strain component. We consider uniaxial stress decribe as:

$$\sigma = \sigma_0 + \frac{1}{2}\Delta sin(2\Pi\omega t) \tag{1}$$

where, σ_0 = mean stress, $\frac{1}{2}\Delta$ = cyclic stress amplitude, and ω = circular frequency.
The mean strain component is the creep strain produced by the static mean stress $(\sigma_m) = \left[\frac{\sigma_{max}-\sigma_{min}}{2}\right]$. The additional cyclic creep component was found to dependent on both mean stress (σ_m) and the stress range $(\Delta) = [\sigma_{max} - \sigma_{min}]$. They proposed the following predictive equation for the total cyclic creep strain:

$$\epsilon(t - t_0) = 129\sigma_m(1 + 3.87\Delta)t^{\frac{1}{3}} * 10^{-6} \tag{2}$$

$$\Phi(t - t_0) = \frac{1}{\sigma}\left[\epsilon_{el}(t_0) + \epsilon(t - t_0)\right] = \frac{1}{E_c(t_0)} + \frac{\epsilon(t - t_0)}{\sigma} \tag{3}$$

where, $\epsilon(t - t_0)$ is the cyclic creep strain, σ_m is the mean stress expressed as a fraction of the compressive strength, Δ is the stress-range expressed as a fracton of the compressive strength, and $\Phi(t - t_0)$ is the creep functuion.

The above the static and dynamic components of dynamic creep as a function of time. It can be expressed as a function of number of cycles also:

$$\epsilon(t-t_0) = 129\sigma_m t^{\frac{1}{3}} + 17.8\sigma_m \Delta N^{\frac{1}{3}} \tag{4}$$

The above equation is fit for $\sigma_m < 0.45$ and $\Delta < 0.3$. The cyclic creep specimens 76 mm x 76 mm x 203 mm cast vertically, fog-cured for 14 days at 20±1°C. During enclosed in polyethylene bags containing some water nut water was not in direct contact with the specimens. The cyclic load varied sinusoidally at 9.75 (Hz) cycles per second.

BP model [6] takes into consideration both shrinkage strain and mechanical strain. According to the BP model, cyclic creep function $\Phi(t-t_0) = \frac{\epsilon}{\sigma_{mean}}$, where ϵ is the strain mean level of cycle, is as follows:

$$\phi(t-t_0) = \left[\frac{1}{E} + C_{oc}(t-t_0) + C_d(t-t_0-t_d)g\sigma - C_p(t-t_0-t_d)\right] f\sigma \tag{5}$$

where,

$$C_{oc}(t-t_0) = \frac{\varphi_1}{E_0}(t_0^{-m} + \alpha)(1 + k_w\varphi_\sigma\sigma_{pp}^2\omega^n(t-t_0)^n \tag{6}$$

and this equation modified:

$$\Phi(t,t_0,\sigma) = q_1 + F(\sigma)\left[C_{oc}(t,t') + C_d(t_{dc},t't_0) + C_p(t_{dc},t',t_0)\right] \tag{7}$$

In which t_{dc} can be calculated as:

$$t_{dc} = t' + (t-t')\left[1 + 10\omega^{\frac{1}{4}}\Delta^2F^3\sigma_{max}\right] \tag{8}$$

Here ω is the frequency (Hz), k_ω is the empirical constant and the the function $F(\sigma_{max})$ is the nonlinearity over proportionality factors.

The long-time material model presented in the 1990 CEB Model Code (MC90) [8] was chosen as the model. Static creep tests within the previously mentioned and the modified by [9] cyclic creep function is defined as:

$$\Phi(t-t_0) = \frac{1}{E_c(t_0)} + \frac{\varphi_c(t-t_0)}{E_c(28d)} + \frac{\varphi_{cc}(t-t_0)}{E_c(28d)} \tag{9}$$

In these expression $\varphi_c(t-t_0)$ is the static creep ratio and φ_{cc} is the cyclic creep ratio, t' the concrete age at loading and t the actual time. The cyclic creep ratio is defined as:

$$\varphi_{cc}(t-t_0) = \beta(t_0)\beta(f_{cm})\beta(S_m)\beta(\Delta)\varphi_{cc}\beta(N,\omega) \tag{10}$$

In this expression f_{cm} is the average compressive cylinder strength at 28 days, S_m the ratio between the mean stress and the concrete strength at the start of testing, Δ the relative stress amplitude, N is the number of load cycles and ω is the frequency $N = (t-t_0)\omega$:

$$\beta(N,\omega) = N^n - 1 = ((t-t_0)86400\omega)^n - 1, with, n = 0.022 \tag{11}$$

The general expression for cyclic creep term is then written as:

$$\varphi_{cc}(t-t_0) = 1.39\beta(t_0)\beta(f_{cm}(1 + 10.5(S_m - 0.4)^2))\Delta(N^n - 1) \tag{12}$$

This expression is basically derived for high strength concrete and it is applicable also plain concrete with different constants parameters.

The hyperbolic function form German code 1045-1 or DAfStb booklet 525 [DIN5] modified by [10] and give the final equation as:

$$\varphi(t-t_0) = \left(\frac{t-t_0}{a+(t-t_0)}\right)^b \varphi_\infty(t_0) = \left(\frac{t-t_0}{a+(t-t_0)}\right)^b * c * \frac{1}{d+t_0^e} \tag{13}$$

$$c = \varphi_{RH} * \beta(f_{cm}) = \left(1 + \frac{1-\frac{RH}{100}}{0.10 * h_0^{\frac{1}{3}}} * \left(\frac{35}{f_{cm}}\right)^{0.7}\right) * \left(\frac{35}{f_{cm}}\right)^{0.2} * \left(\frac{16.8}{(f_{cm})^{\frac{1}{2}}}\right) \tag{14}$$

The constant a, b, d, and e are determined from cyclic creep experimental data. For concrete compressive strength 52.00 MPa, the value of a, b, d and 318.22, 0.30, 0.10 and 0.20 found, respectively.

3 SOURCES OF UNCERTAINTY

This section describe to include the different sources of uncertainty in the cyclic creep prediction. These sources of uncertainty can be classified into three different types-physical or natural uncertainty, data uncertainty and model uncertainty as shown in Fig.1.

Fig.1 shows the different sources of error and uncertainty considered in this paper for the sake of illustration of the proposed methodology. There are several otheres sources of uncertaint that are not considered here. Each of these different sources of uncertainty is briefly discussed below.

3.1 Physical or Natural Uncertainty

Physical or natural uncertainty refers to the uncertainty or fluctuations in the environment, test procedures, instruments, observer, etc. Hence, repeated obervations of the same physical quantity do not yield identical results. This paper considers the physical uncertainty in loading, environment and materials properties. The uncertainty in the systematic errors to the measuement, human error, the variability in others materials properties such as Poisson ratio, supplementary cementaing materials, the curing time period, temperatures, etc. is not considered.

3.2 Data Uncertainty

Experimental data are available in literature to characterize the distribution of materials properties such as young modulus of elascity, compressive strength of concrete, etc. These data may be sparse and cause uncertainty regarding the probability distribution type and parameters, these errors are not considered in this paper and the quantification of these errors is trivial; these errors will be considered in future work. The measurement uncertainty calculated from the GUM [23-25] and Monte Carlo method. Bayesian model screening is implemented using Monte Carlo methode, which is described in literature [25]. The study found that the experimental error between 0.08 - 0.13 is reasonables for diffeent test.

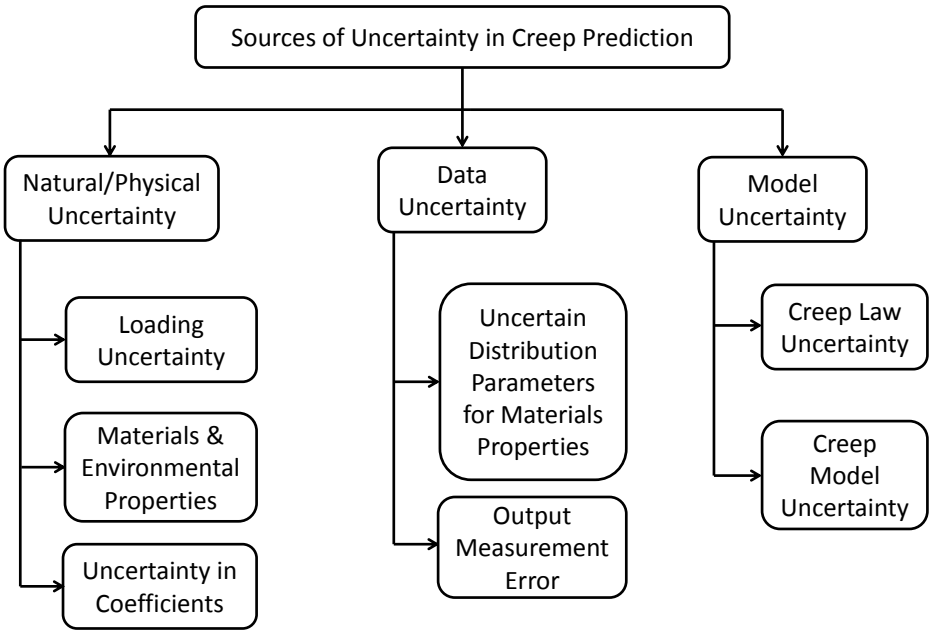

Figure 1: Sources of Uncertainty in Creep Prediction

3.3 Model Uncertainty

More than 10 different creep prediction laws have been proposed in the literatures. Each of these models has its own limitation and uncertainty. The uncertainty in cyclic creep prediction can be subdivided into two different type: creep model error and uncertainty in model coffi-cients. This error is assumed to represent the difference between the model prediction and the experimental obervations. The variation from the experiments are determined by [28-29] for the comparison with measurements data. The statistical analysis of cyclic creep data no body done and there is no data existing data bank for cyclic loading. The all pervious comparison based on RILEM data bank for sustained loading. The effect of cyclic loading to calculate variation in experiments are neglected so far might be non-negligible for big structures, such as bridge with many lanes or with dense traffic of heavy trucks. Assuming the $CV_{\psi,\alpha} \approx 0.08$ and $CV_{\psi,\beta} \approx 0.05$. The coefficient of variation of the creep phenomenon α and the measurements β determined the coefficient of variation of the model uncertainties. The model uncertainty factor is normally distributed with an expected value of $E(\psi_{cr,cyc}) = 1$. Discretization error is not considered in this paper; this error will be considered in future work. There appears to be an influence of frequency of loading on cyclic creep, creep generally decreasing with an increase in frequency so that under very rapid cycles the behaviour of concrete becomes more elastic. Furthermore, uniform cycling causes less creep than an irregular pattern within the same range of stresses. Table 1 list the comparision of the total coefficient of variation of four models based on using statistic input variables. In all these comparision, model BP is found to be the best model. The MCM calculation method of measurement uncertainty is discussed in Section 4.1.

Table 1: Model uncertainty

Model	BP	mod.MC90	mod. Hyperbolic	Neville
$CV_{\psi,cr,cyc}$	0.283	0.306	0.300	0.380

4 UNCERTAINTY QUANTIFICATION IN MODEL PARAMETERS

4.1 Bayes Method

This section explain the Bayesian technique used to uncertainty anylsis for measurement: MCM using the experimental data. A fundamental parameter in order to obtain reliable results through MCM is the number M of trails or evaluation be performed by the model. M value 10^6 is often considered approprite in order to provide a coverage interval of 95 percentage ; however, the random nature of the process and the nature of the probability distribution of the output quantity Y have an influence on the value needed for M, which will very in each case. Each value of standard uncertainty y_r $(r = 1, ..., M)$ is obtained by performing a random sampling of each of the probability density functions of the input quantities X_i and evaluating the model with the values found. The M values of Y thus obtained must be arranged in a non-decreasing order. The output quantity and the associated standard uncertainty can be calculated as follows:

The average:

$$\bar{y} = \frac{1}{M}\sum_{r=1}^{M} y_r \tag{15}$$

and the standarddeviation is taken as the standard uncertainty $u(y)$ associated with y:

$$u^2(\bar{y}) = \frac{1}{M-1}\sum_{r=1}^{M}(y_r - \bar{y})^2 \tag{16}$$

4.2 Global sensitivity analysis

The objective of SA is to identify critical inputs variables of a model and quantifying how input uncertainty impacts model outcomes. The sensitivities are solved at nominal values, cannot take account of the variation effect of the input variables, and thus those sensitivities are local. Compared with the local sensitivity, the uncertainty importance measure is defined as the uncertainty in the output cab be apportioned to different sources of uncertainty in the model input, and the importance measures is also called global sensitivity. [22-23] Methods are used in this paper and method is approximately linear output response and input variables. For a model $y = (x_1, x_2, x_3, ...x_i...x_k)$ and the main effect of each variables, the model can be simplified as follows:

$$y = \beta_0 + \sum_{i}^{K} \beta_i x_i + e, \tag{17}$$

Where $\beta_0...\beta_k$ are regression coefficients and e is the error. The partial variance (V_i) and total variance (V) can be estimate for uncorrelated variables as follows. The sensitivity indices can be calculated as follows:

$$S_i = \frac{V_i}{\hat{V}} \tag{18}$$

$$S_i^U = \frac{V_i^U}{\hat{V}} \tag{19}$$

$$S_i^C = \frac{V_i^C}{\hat{V}} \tag{20}$$

where, V_i, V_i^U, V_i^c are the partial variancs, uncorrelated variance and correlated variance, respectively.

5 UQ AND SA OF CYCLIC CREEP FUNCTION

5.1 Input Parameter and Parameters Correlation

The cyclic creep models uncertainty factors compressive strength of concrete (f_c), young modulus of elasticity (E_c), relative humidity (RH), water-cement ratio (w/a), sand-aggregate ratio (a/c), geometry factor (ks), cement content (c), frequency of loading (ω), mean stress (σ_m), stress amplitude (Δ), number of cycle (N) are assumed to be random quantities. All statistic properties of concrete given in Table 2. For the determination of dynamic modulus of concrete, E_d, dynamic compressive shear strength of concrete, f_d, are contradictory part for the analysis of the cyclic creep function because these quantities are depend on the strain rate, and number of cycle. Numerous empirical relationships are available in the literatures. However, "Lifetime-Oriented Structural Design Concepts" and "Deterioration of Materials and Structures" [31] published the overview of degradation of concrete under cyclic loading and are used in this paper. The deformation of concrete at any instant are defined as follow:

$$Totalstrain = elasticstrain + creep + shrinkage \tag{21}$$

If the elastic strain under a constant stress is assumed to diminish with time, then merely assume that creep is increased by a corresponding amount to insure that the total strain is correct. Under cyclic loading, is the precise interpretation of elastic strain very important, because change in elastic strain due to change in elastic modulus are generally small compared with the sum of others quantities. The correlation of $\rho = 0.4$ and $\rho = 0.8$ further additional small range of correlation $\rho = 0.1$ are determined, but neglected in the stochastic analysis due to insignificance. These models are not intended (e.g. temperature effect on creep).

Table 2: Statistic properties of the input variables for mathematical cyclic creep model

Variables	Mean	Std.	CoV	Distribution	Models	Sources
$f_{c,28}$	52.00 MPa	3.12	0.06	Log-normal	1,2,3,4	34
f_d	50.70 MPa	3.00	0.06	Log-normal	1,2,3,4	30
$E_{ci,28}$	34144 MPa	3414.4	0.10	Log-normal	1,2,3,4	30
$E_{cm,28}$	29394 MPa	2994.0	0.10	Log-normal	1,2,3,4	34
E_d	33290 MPa	3329.0	0.10	Log-normal	1,2,3,4	30
Humidity (RH)	0.65 [-]	0.026	0.04	Normal	1,2,3	32
Cement content	362 kg/m^3	36.20	0.10	Normal	1,3	33
Water-cement ratio	0.50 [-]	0.10		Normal	1	33
Sand-cement ratio	5.16 [-]	0.516	0.10	Normal	1	33
Fine-aggregate ratio	0.50 [-]	0.05	0.10	Normal	1	33
Geometry factor, ks	1.15 [-]	0.057	0.05	Normal	1,2,3	33
Frequency	9.0 Hz	0.72	0.08	Normal	1,2,3,4	Assumed
Mean stress	$0.40 f_c$	0.016	0.04	Normal	1,2,3,4	Assumed
Stress amplitude	$0.20 f_c$	0.008	0.04 6	Normal	1,2,3,4	Assumed
Number of cycles	10^6	40000	0.04	Normal	1,2,3,4	Assumed
a	318.22	31.82	0.10	Normal	3	Assumed
b	0.30	0.03	0.10	Normal	3	Assumed
d	0.10	0.010	0.10	Normal	3	Assumed
e	0.20	0.02	0.10	Normal	3	Assumed

1 = BP, 2 = modified MC90/CE 2 , 3 = modified Hyperbolic , 4 = Neville

The input variables correlation of the model Neville, modified MC90/CE2, modified Hyperbolic function and BP are shown in Tables 3-6.

Table 3: Correlation matrix Neville

Variables	f_c	E_c	σ_m	Δ
f_c	1	0.8	0	0
E_c		1	0	0
σ_m			1	0
Δ		Symm.		1

Table 4: Correlation matrix mod. MC90/EC

Variables	RH	ks	f_c	E_c	σ_m	Δ	N
RH	1	0	0	0	0	0	0
ks		1	0	0	0	0	0
f_c			1	0.8	0	0	0
E_c				1	0	0	0
σ_m					1	0	0
Δ						1	0
N			Symm.				1

Table 5: Correlation matrix mod. Hyperbolic model

Variables	RH	ks	f_c	E_c	a	b	d	e
RH	1	0	0	0	0	0	0	0
ks		1	0	0	0	0	0	0
f_c			1	0.8	0	0	0	0
E_c				1	0	0	0	0
a					1	0	0	0
b						1	0	0
d							1	0
b			Symm.					1

Table 6: Correlation matrix BP

Variables	RH	c	w/c	a/c	ks	f_c	ω	Δ
RH	1	0	0	0	0	0	0	0
c		1	-0.4	-0.4	0	0.4	0	0
w/c			1	0	0	-0.4	0	0
a/c				1	0	-0.4	0	0
ks					1	0	0	0
f_c						1	0	0
ω							1	0
Δ			Symm.					1

5.2 Uncertainty of cyclic creep strain

The mean value of the predicted cyclic function of the four models for short time is presented in Fig 2. Because the initial elastic strains were not reported, because, due to pronounced short-time creep duration, they had to be assumed, and so the compressions are relevant only to the part of strain representing the creep increase due to the part of strain cycling. Significant errors have often been caused by combining the creep coefficient with an incompatible value of the conventional elastic modulus. Thus analysis must properly be based on the cyclic creep function. In Fig. 2 the data of all four models shows quit different values in the first hour of testing and at 100 hours the difference showed small despite the use of a similar concrete and testing condition. This may be fluctuation in time to the physical mechanism of creep. The modified MC90/EC2, Neville and modified hyperbolic model are based only on the set of data and may not be applicable for conditions substantially different than these during the experiments.

Fig. 3 and 4 shows that the result of the uncertainty analysis of four different models. The both Fig. showed that the correlated and uncorrelated contribution of input variables have important contribution to the uncertainty in model output. The uncorrelated input variables uncertainty of Neville model is very small, only the contribution of four variable. On the other hand the input variables are notable effect on the output because there in more variables and complex model and model uncertainty is small. The correlated and uncorrelated input variables for model Neville shows largest uncertainty $CV_{par,crcyc}(t - t_0) = 0.08$ at t = 1 h and uncertainty $CV_{par,crcyc}(t - t_0) = 0.06$ at t = 100 h, the uncertainty goes to decreasing with the increasing the time under load. The uncorrelated input quantities uncertainty of

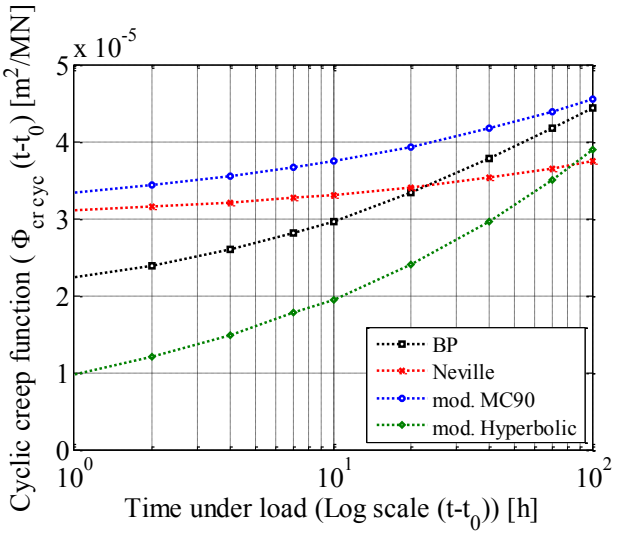

Figure 2: Mean value of creep function

model mod. MC90 and mod. Hyperbolic $CVpar, crcyc(t - t_0) = 0.10$ and almost independent with time. Model BP has strongly time-dependent uncertainty varying in the range of $CV_{par,crcyc}(t - t_0) = 0.11 \cdots 0.08$. Taking into the input variables real correlation of model Neville the input variables increase significantly $CV_{par,crcyc}(t-t_0) = 0.08$ may cause this effect strong correlation of strength and young modulus of elasticity. Comparing the total uncertainty of the models from Fig. 4, we conclude that the model and measurement paly the important role on the uncertainty behaviour of models. In comparison of all models, BP has the lowest total uncertainty $CV_{par,crcyc}(t - t_0) = 0.30$ and model Neville has highest total uncertainty $CV_{tot,crcyc}(t - t_0) = 0.40$. The models mod. MC90, mod. Hyperbolic and Neville are based on the experimental data and also, assumed strain-time equation do to always satisfactory fit the experimental data, so that long-term values cannot be estimate with confidence. Generally, the time over which creep have actually been measured the better the prediction. The CV in the initial time of loading shows higher and decreasing with increasing the time. Because the initial time more uncertainty in measurement. The most important variable at short-time creep is model uncertainty factor for all models.

Total model quality (MQ) can be used to balance the better response of the model to its uncertainty in order to select the model that is most for a certain response. Fig. 5 show the time-dependent model quality. MQ dependent total uncertainty considering the correlated input quantities. The MQ is slight time dependent. For this reason the time interrogation according to the [32] and results given in Fig 5. In all these comparisons, model BP is found to be the best. CEB-MC90/EC2 model [8], which modifies his original model MC90/EC 2 [9] by co-opting key aspects of cyclic loading (the mean stress and stress amplitude function and dependence on the number of cycles would simply mean a loading frequency), comes out as the second best. Considerably worse but the third best overall is seen to be the modified Hyperbolic model. Since the current Neville model, labelled Neville, is the simplest, introduced in 1973 on the basis of Neville's research [2], it is not surprising that it comes out as the worst because based on only four variables and there is no consideration of concrete composition and environmental variables.

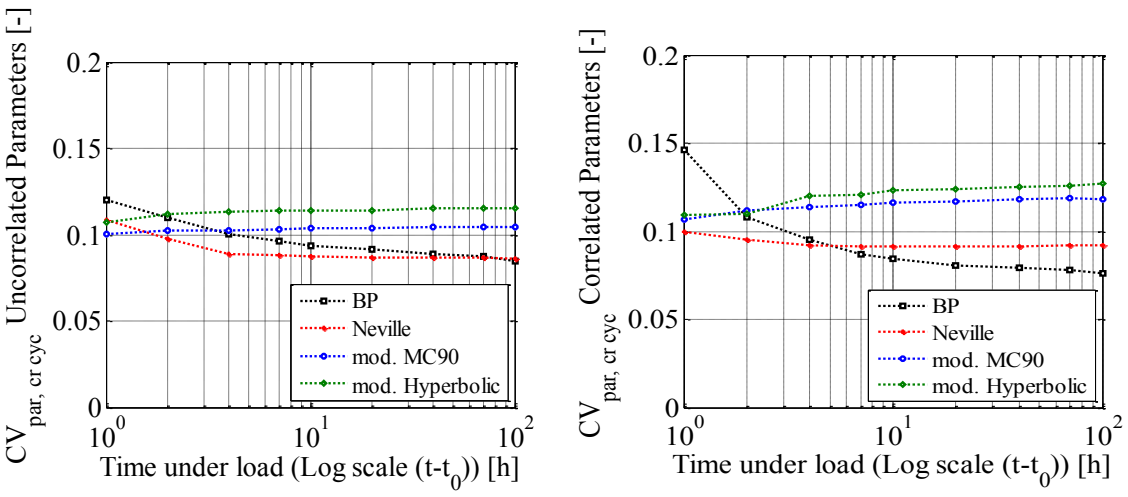

Figure 3: Input variables uncertainty of cyclic creep prediction

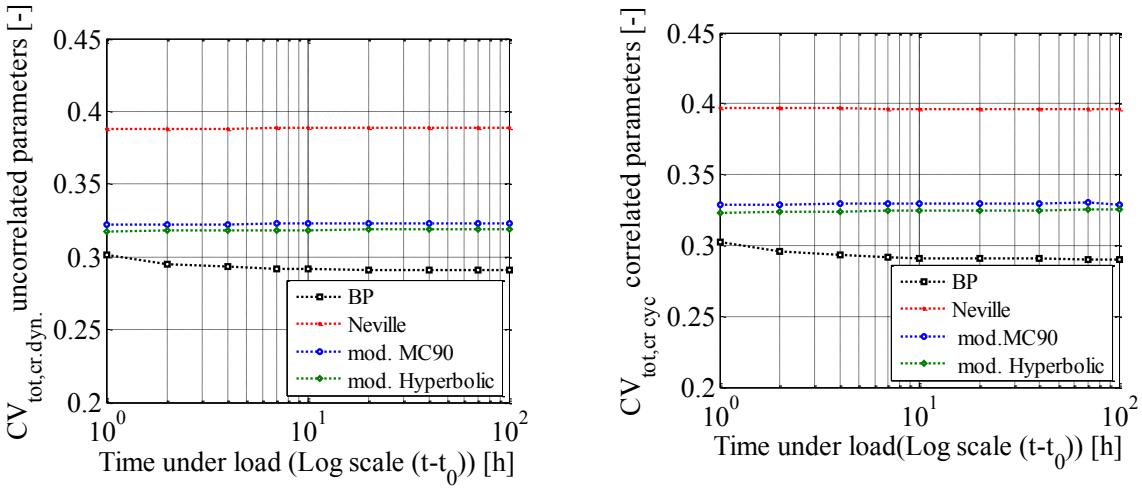

Figure 4: Input variables and model uncertainty of cyclic creep prediction

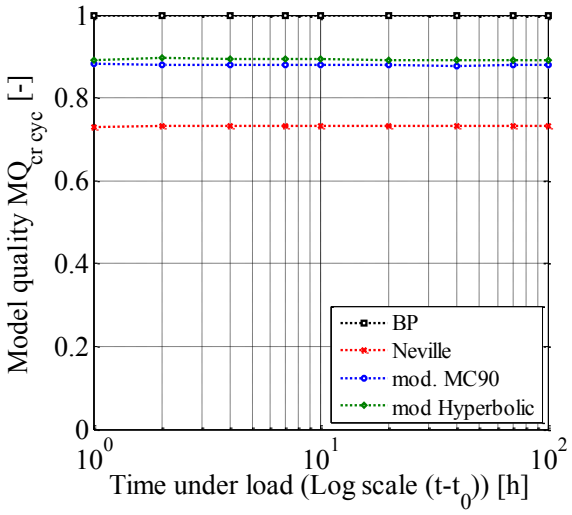

Figure 5: Model quality (MQ) of cyclic creep prediction

5.3 Sensitivity analysis of the cyclic creep strain

SA require to find out the dominant effect of the variability of input random variables on the cyclic creep strain. Figs 6-9 show the results of the sensitivity analysis of uncorrelated and correlated variables. For the calculation of the sensitivity the model uncertainty is not considered. It is assumed that the sensitivity indices are up to $\sum_{p'=1}^{pK} S_p = 1$. The normalization is necessary due to consideration of correlation, which may the results of sensitivity indices $Sp \geq 1$. This arise the difficulties in the comparison between the uncorrelated and correlated indices. High value of sensitivity S_p means highly influential on the uncertainty. For example $Sp = 1$ means only this quantities affect the output. The input quantities sensitivity of model Neville is presented in Fig.6. All input quantities are approximately time-independent. The reason behind this is the expression is depend on the value of the mean stress, stress amplitude, compressive strength an modulus of concrete and there is other input quantities considered in this model and this quantities is assumed constant with respect to time. The strength and modulus is not exactly constant over the time but it is much complicated to consider. It is seen that the most sensitive quantities turn out to be elastic modulus and followed by compressive strength. The mean stress and stress amplitude is not much influence as compared above two quantities. The variables correlation is strongly influence the sensitivity indices. However, E_c and f_c are most influence quantities.

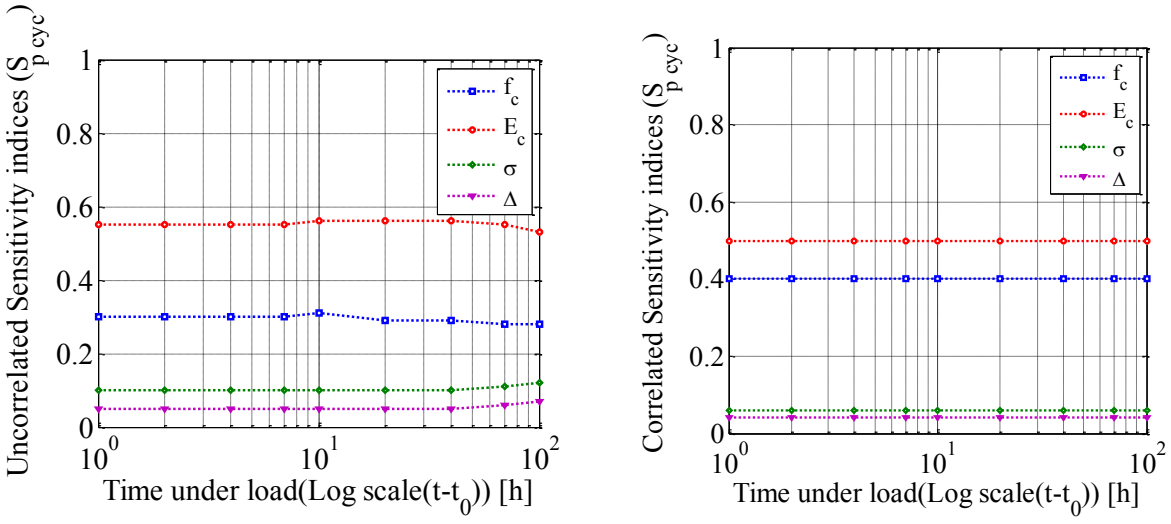

Figure 6: Uncorrelated and correlated sensitivity indices of model Neville

Model modified hyperbolic shows also constant sensitivity indices of all input quantities over the time. In this model the time is account only this $\left(\frac{t-t_0}{a+(t-t_0)}\right)^b$ quantities and the influence of both a and b is much smaller as compared the other quantities. The elastic modulus most influenced variable and followed strength of concrete. The correlation showed the valuable influences the sensitivity indices. The Fig. 7 shows the sensitivity indices of all input variables of modified hyperbolic.

The sensitivities of model modified MC90 remain approximately constant over the time. The humidity influence the time function by factor β_H, but the influence is relatively small. The sensitivity indices of E_c, f_c and σ_m fluctuate over the time. The main reason for this is these variables affect by the time under loading but the influence is small. As compared the sensitivity

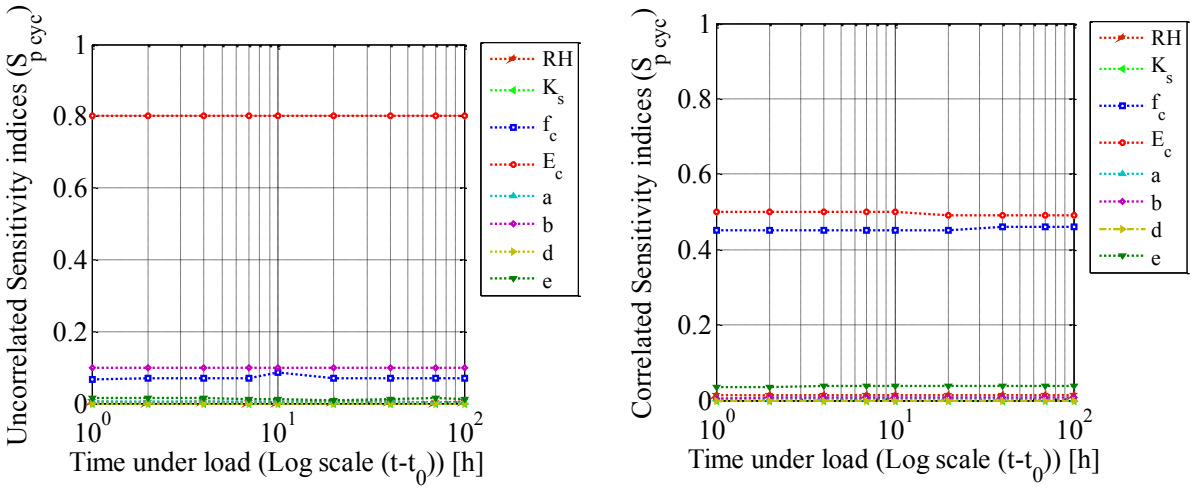

Figure 7: Uncorrelated and correlated sensitivity indices of model modified Hyperbolic

indices between the uncorrelated and uncorrelated, it seem clearly large difference for most influent quantities. In the case of input quantities uncorrelated, E_c is the most dominating input quantities. Oh the other hand, the E_c and f_c are sensitive quantities turns out due to the strong correlation. The numbers of cycle, mean stress and stress amplitude have small influence.

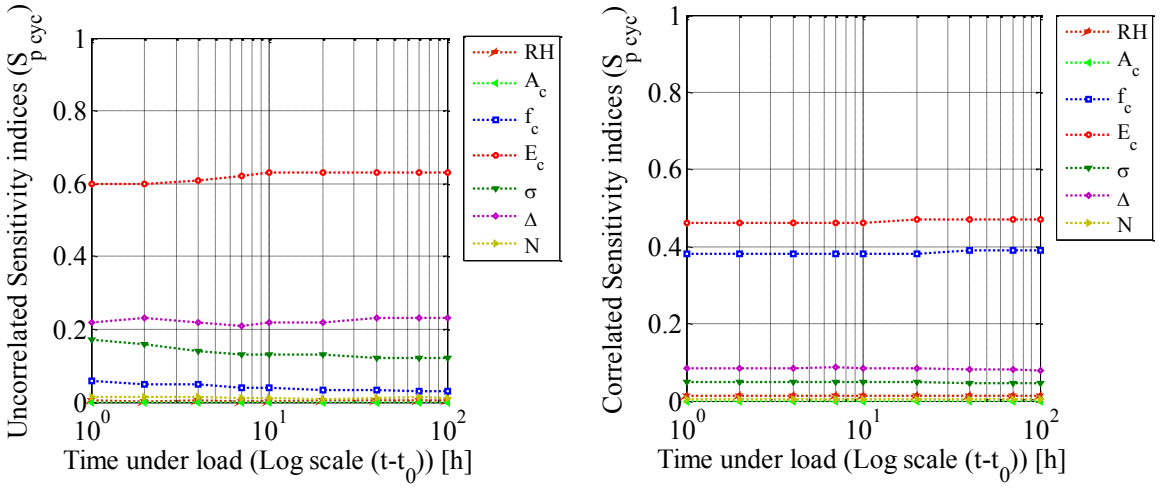

Figure 8: Uncorrelated and correlated sensitivity indices of model modified MC90/CE2

The model BP seen a more time dependent sensitivity indices over the time. The main reason behind this is the more combination of time function with the input quantities. It is seen that the most sensitive quantities turn out to be concrete strength. In the second place the content of the cement when quantities are assuming the uncorrelated. Further, the stress amplitude and frequency is the third and fourth influence quantities. The influence of water-cement ratio, aggregate-sand ratio and humidity also considerable. The concrete strength is most dominating quantities when considering the quantities correlation. The second dominant quantity is the cement content and stress amplitude. The sensitivity indices of cement content

and stress amplitude small decrease with increasing time. The cyclic parameter is seen that the considerable influence.

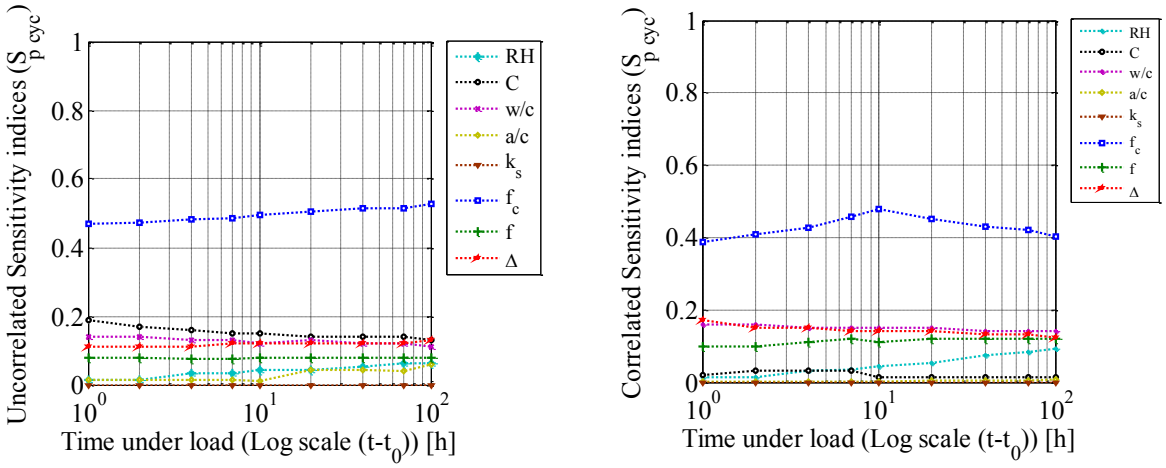

Figure 9: Uncorrelated and correlated sensitivity indices of model BP

6 CONCLUSION

In the present study, a probabilistic framework is suggested for the predicting the cyclic creep of plain concrete considering four different cyclic creep models. Different sources of uncertainty- physical variability, data uncertainty, and model error/uncertainty- were included in the cyclic creep analysis. Different types of model error cyclic creep model error. The input quantities which drive the cyclic creep such as, elastic modulus, concrete strength, mean stress, cyclic stress amplitude, number of cycle, humidity, cement content, water-cement ratio, sand-cement ratio, geometric factor have been considered as random variables. The uncertainty and sensitivity analysis is computed using the LHS sampling technique. It is seen from the uncertainty analysis the complex cyclic creep model BP has the good MQ and less uncertainty but the simple model Neville has higher uncertainty and lower model quality. In contrast, the complex model needs computational effort and more input variables. Stochastic sensitivity analysis is performed to determine the predominant factor amongst the input variables, which influences the cyclic creep prediction. It is observed that cyclic creep is more sensitive to the elastic modulus and strength of concrete, followed by mean stress, stress amplitude, frequency, cement content, humidity, water- cement ratio, in that order. Further, the present study of cyclic creep models brings some interesting point. The most of the creep analysis is only sustained load; the cyclic loading effect is neglected. Cyclic effect, neglected so far, might non-negligible for long span bridge with many lanes or with a dense traffic of heavy trucks. This may cause the excessive time-dependent deflection of concrete structures. The concrete structure can lose their stiffness by (i) the degradation of concrete, (ii) the creep of concrete etc. The relation between the frequency of the structure and its age is important fo the study of the long-term bahaviour of materials, possibly for the detection of its damage. Significant is the change of the modulus of elasticity of concrete dur to cyclic creep. Also, the proposed approach for UQ and SA is applicable to several engineering disciplines and the domain of cyclic creep analysis was

used only as an illustration to develop the methodology. In general, the proposed methodology provides a fundamental framwork in which multiple models can be connected through a Bayes network and the confidence in the overall model prediction can be assessed quantitatively.

ACKNOWLEDGMENT

This research is supported by the German Research Institute (DFG) via Research Training Group "Evaluation of Coupled Numerical Partial Models in Structural Engineering (GRK 1462)", which is gratefully acknowledged by the author.

REFERENCES

[1] Z.P. Bažant, *Matehmatical modelling of creep and shrinkage of concrete*, John Wiley. New York, 1988.

[2] A.M. Neville, W.H. Dilger, J.J. Dilger, *Creep of plain and structural concrete*, Construction Press, London and New York, 1983.

[3] E. Probst, *The influence of rapidly alternating loading on concrete and reinforced concrete* The Structural Engineer, **9**, 1931, pp.410-29.

[4] E. Probst, *Pastic flow in plain and reinforced concrete arches*, ACI Journal, 30, 1933, pp. 137-41.

[5] C.P. Whaley, A.M. Neville, *Non-elastic deformation of concrete under cyclic compression* Mag. Concrete Res. 1973, **25** (84) 145-154.

[6] Z.P. Bažant , L. Panula, *Practical prediction of time-dependent deformation of concrete (Part IV: Cyclic creep, nonlinearity and statistical scatter)* J. Mat. Struct. 1979, **12** (69), pp. 175-183

[7] Z.P. Bažant, J. Kim, *Improved prediction model for time-dependent deformation of concrete: (Part 5- Cyclic load and cyclic humidity)*, J. Mat. Struct. 1992, **25**. pp 163-169.

[8] *CEB - Comite Euro-International du Beton: CEB-FIP Model Code 1990 / Comite Euro-International du Beton. 1993. - Technical report 43*.

[9] K. Terje , P. Gordana, *Material model for high strength concrete exposed to cyclic loading , Fracture mechanics and concrete structures Edited by Z.P Bažant*, 1992.

[10] E. Schwabach, *Verformungs- und Degradationsverhalten von niederzyklisch uniaxial druckbeanspruchtem Beton*. Dissertation an der Fakultt Bauingenieurwesen der Bauhaus-Universitt Weimar, 2005.

[11] A.D. Ross, *Concrete creep data*, The structural engineer, **15**, No.8. 1937, pp 314-26.

[12] W.R. Lorman, *The theory of concrete creep*, proc. ASTM, 40. 1940. Pp. 1082-1102.

[13] CQ. Li, RE. Melchers, *Reliability analysis of creep and shrinkage effects*. J Struct Eng ASCE 1992, **118**(9):2323-37.

[14] T. Tsubaki *Uncertainty of prediction*. In: Proceedings offifth international RILEM symposium, Barcelona, Spain,1993. pp. 831-47.

[15] Z.P. Bažant , S. Baweja, *Justification and refinement of model B3 for concrete creep and shrinkage-1. Statistics and sensitivity*. Mater Struct 1995, **28**(181):415-30.

[16] B. Teply, Keršner, Z. Keršner, D. Novăk, *Sensitivity study of BP-KX and B3 creep and shrinkage models*. Mater Struct 1996, **29**(192):500-5.

[17] *ACI 209R-92. Prediction of creep, shrinkage and temperature effects in concrete structures*. ACI Manual of Concrete Practice, Part 1, American Concrete Institute, Detroit, 1992.

[18] *Comite Euro-International du Beton (CEB). CEB-FIP model code for concrete structures*. Lausanne, Switzerland, 1990.

[19] M.J. Smith, DG. Goodyear, *A practical look at creep and shrinkage in bridge design*. PCI J 1988,**93**(3):108-21.

[20] P. Bjerager, S. Krenk, *Parametric sensitivity in first order reliability theory*. J Eng Mech ASCE 1989**115**(7):1577-82.

[21] Z.P. Bažant, K-L Liu, *Random creep and shrinkage in structures:sampling*. J .Struc. Eng. 1985**111**(5):1113-34.

[22] C.Xu, G.Z. Gertner, *Uncertainty and Sensitivity Analysis for Models with Correlated Parameters*. In: Reliability Engineering and System Safety, **93** (2008), S. 1563-1573 7, 61.

[23] T. Most, Variance-based sensitivity analysis in the presence of correlatrd input variables.

[24] *International Organization for Standardization, Guide to the Expression of Uncertainty in Measurement (GUM)*, first ed., ISO, 1993, (withdrawn).

[25] *International Organization for Standardization, ISO/IEC Guide 98-3:2008 - Uncertainty of Measurement - Part 3: Guide to the Expression of Uncertainty in Measurement (GUM)*, ISO, 2008.

[26] *JCGM, Evaluation of measurement data-Supplement 1 to the 'Guideto the Expression of Uncertainty in Measurement'-Propagation of distributions using a Monte Carlo method*, 2008.

[27] G. Wubbeler, M. Krystek, C. Elster*Evaluation of measurement uncertainty and its numerical calculation by a Monte Carlo method, Meas. Sci. Technol.***19** (2008).

[28] Li, Z. Lu, C. Zhou *Importance analysis for models with correlated input variables by the state dependent parameters method Computers and Mathematics with Applications*, **62** (2011) 4547-4556.

[29] H. Madsen, Z. P. Bažant, *Uncertainty analysis of creep and shrinkage effects in concrete structures*. ACI J B 1983, **80**:116-27.

[30] Z.P. Bažant, G.-H. Li, *Unbiased Statistical Comparison of Creep and Shrinkage Prediction Models*. In: ACI Materials Journal, **105**(6) (2008).

[31] S. Friedhelm, B. Rof, O. T. Bruhns, D. Artmann, H. Ruediger, K. Detlef and G. Meschke, *Lifetime-Oriented Structural Design Concepts* 2009 Springer-Verleg-Berlin Heidelberg Chapter 3 "Deterioration of Materials and Structures"

[32] H. Keitel, *Evaluation Methods for the Prediction Quality of Creep Models of Concrete*,Bauhaus-Universitt Weimar, Dissertation, 2011

[33] D. Diamantidis, H. Madsen, R. Rackwitz, *On the variability of the creep coefficient of structural concrete*. Mater Constr 1984, **17**(100):321-8.

[34] H. Madsen, Z.P. Bažant, *Uncertainty analysis of creep and shrinkage effects in concrete structures*. ACI J B 1983, **80**:116-27

[35] T. Vrouwenvelder *Probabilistic model code*. 12th draft. Tech. rep. Joint Committee on Structural Safety. 2002.

19th International Conference on the Application of Computer
Science and Mathematics in Architecture and Civil Engineering
K. Gürlebeck, T. Lahmer and F. Werner (eds.)
Weimar, Germany, 04–06 July 2012

ROTATIONAL DUCTILITY OF CRACK IN STATIC AND DYNAMIC CALCULATIONS OF REINFORCED CONCRETE BAR STRUCTURES

M. Musiał *, **A. Ubysz**

* *Wroclaw University of Technology, Institute of Building Engineering*
Pl. Grunwaldzki 1, 50-377 Wroclaw, Poland
E-mail: michal.musial@pwr.wroc.pl

Keywords: crack, ductility, dynamics, reinforced concrete, statics.

Abstract. *In this paper experimental studies and numerical analysis carried out on reinforced concrete beam are partially reported. They aimed to apply the rigid finite element method to calculations for reinforced concrete beams using discrete crack model. Hence rotational ductility resulting from crack occurrence had to be determined. A relationship for calculating it in static equilibrium was proposed. Laboratory experiments proved that dynamic ductility is considerably smaller. Therefore scaling of the empirical parameter was carried out. Consequently a formula for its value depending on reinforcement ratio was obtained.*

1 INTRODUCTION

Some research concerning reinforced concrete beams [1, 2] including own research [3] exhibit differences in terms of static and dynamics issues. Those differences are reflected by deflections (statics) and natural frequencies. Those quantities, however, could not be directly compared. Nonetheless, based on their values and known scheme stiffness of elements can be computed [4] (static based on deflections and dynamic based on natural frequencies). Research carried out thus far proved, those are not the same quantities.

The approach presented by authors draws on discrete crack model in rigid finite elements method [5, 6]. Hence, formulae for equivalent stiffness (both static and dynamic) could not be used. The rigid finite element method requires on the other hand implementing ductility dictated by crack occurrence. This paper discusses method of scaling relationship expressing dynamic rotational ductility based on the static one. Scaling was carried out based on own experimental studies.

2. EXPERIMENTAL STUDIES CHARACTERIZATION

Experimental studies were performed on reinforced concrete beams in half-natural scale. Each of the elements had the dimensions of 3300 mm x 250 mm x 150 mm. The cross-sections with a reinforcement are shown in figure 1.

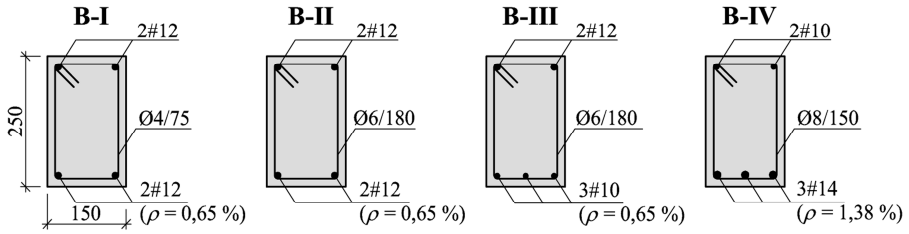

Figure 1: Investigative elements (dimensions in mm)

Series B-I, B-II, B-III had the same tensile reinforcement ratio of 0,65 %. The B-IV beams series were reinforced stronger (1,38 %). The elements were made of the C25/30 class concrete. The basic material properties are listed in table 1.

Table 1: Basic material properties

Material	Property	Series			
		B-I	B-II	B-III	B-IV
Concrete	Mean compressive strength f_{cm} [MPa]	51,7	51,2	45,0	41,1
	Mean splitting tensile strength $f_{ctm,spl}$ [MPa]	3,58	3,21	3,03	2,79
	Mean Young modulus E_{cm} [GPa]	30,3	29,6	28,5	30,0
Steel (longitudinal rebars)	Mean yield strength f_{ym} [MPa]	563	563	548	555
	Mean Young modulus E_{sm} [GPa]	202	202	200	202

The beams' deflections were registered with the inductive gauges with accuracy of 0,001 mm. The beams were loaded with concentrated force applied at the mid-span (three points bending test).

A Brüel & Kjær data acquisition and processing system was used in the dynamic measurements. The system uses the operational version of the modal analysis [7] – presently, a popular tool for nondestructive testing of engineering structures and machines. The system registers the beam's response (acceleration of certain points) on external random forces. The vibrations in the beams are caused randomly by the setup environment, and include: acoustic noise, air flow, gentle strokes in investigative element. The measurements yield basic dynamic parameters of the object investigated (eigenfrequencies, eigenforms, damping parameters). It was decided to carry out the dynamic experiments with using the suspended beam scheme. This approach is commonly used in investigating mechanisms and their characteristics [8].

Each test was preceded by the dynamic analysis of a suspended beam. Followingly, the element under tests was placed on the supports and loaded at the mid-span with a concentrated force of a given value. The beam deflection was acquired once it stabilized. Subsequently, beam was unloaded and taken from the supports for the dynamic analysis. In the next step, the beam was once again placed on the bearings and loaded with a higher force than in the previous step. The aforementioned procedure was repeated till the beam failure. When the load-bearing capacity was exhausted the modal analysis was performed in the suspended position. The detailed description of the experimental studies is included in [3].

3. STIFF FINIE ELEMENTS METHOD

3.1. General description of the method

In this method beam model consists of stiff mass discs which represent force of inertia of a structure. Discs are connected by elastic constraints (one rotation and two translation) responsible for elastic features of a structure. Movement of each mass discs is described by three general coordinates. In case of transverse vibrations which are considered in this paper, elastic constraints and general coordinates are reduced to two. Example scheme and calculation model of a beam divided into four elements are shown in figure 2. The wider description of the method is included in [9].

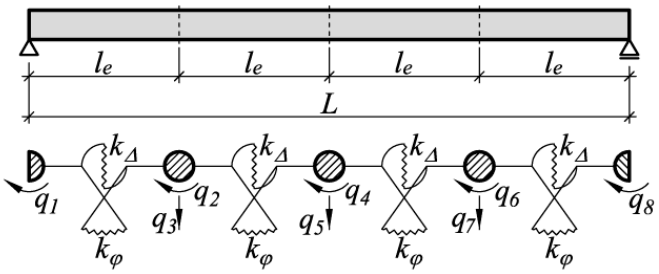

Figure 2: Scheme and numerical model of homogenous beam

The presented approach enables to include local discontinuities (among others cracks) in a discrete way [5, 6]. Adequate division into finite elements allows the introduction of cracks by means of reduction of stiff rotation constraints while calculations are performed as for the homogenous beam.

Stiffnesses of constraints k_φ, k_Δ are commuted using the element stiffness in phase I (EI_I). The stiffness of rotation constraints is reduced and has value k_φ^{cr} in the place where the cracks appear. The scheme and calculation model of the segment of beam with cracks is shown in figure 3.

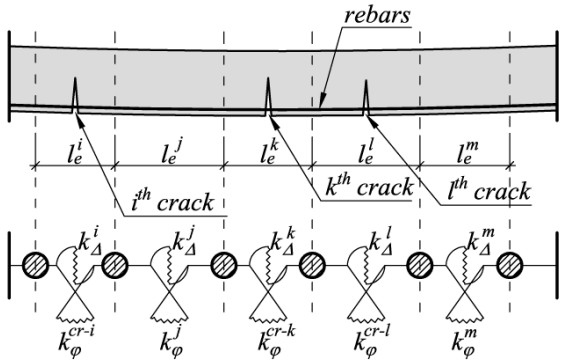

Figure 3: Scheme and numerical model of the reinforced concrete beam with cracks

3.2. Rotational ductility in static calculation

The rotational ductility resulted from crack was estimated on the basis of elementary relations of geometry and strength of materials. The scheme as in figure 4 was considered.

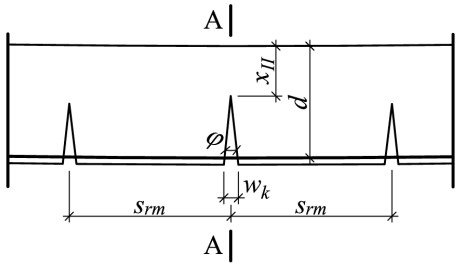

Figure 4: Considered model of beam with cracks

Forces acting in the cross-section (A-A) in the place of crack occurrence are shown in figure 5. Triangular stress distribution in compressed concrete was assumed.

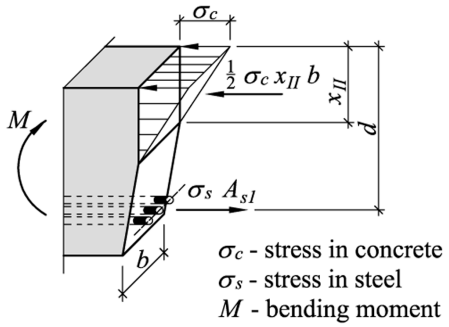

Figure 5: Forces acting in cross-section

Figures 4 and 5 enable to formulate following expression allowing to calculate the rotational susceptibility which is consequence of crack occurrence in static solution:

$$d_{\varphi,static}^{cr-i} = \frac{\psi_z\ s_{rm}}{E_s\ A_{s1}\,(d - \frac{x_{II}}{3})(d - x_{II})}, \tag{1}$$

where: ψ_z – coefficient describing violation of interaction between steel and concrete calculated according to (2), s_{rm} – average crack spacing, E_s – Young's modulus of steel, A_{s1} –

reinforcement cross-sectional area, d – useful beam height, x_{II} – height of the compressed zone in phase II.

$$\psi_z = 1.3 - s\frac{M_{cr}}{M}, \tag{2}$$

where: s – 1.1 in case of immediate loading, 0.8 in case of long-term loading, M_{cr} – cracking moment, M – maximum moment up to which the cross-section was overloaded.

3.3. Comparison with experimental results

In line with above-mentioned assumptions, proprietary program was used to compute deflections of reinforced concrete beams. Results of calculations along experimental results are shown on charts (fig. 6 – 9). Solid line traces equilibrium paths recorded during experiment, points represent analytical results for each load increment. Individual elements from different series had different colours.

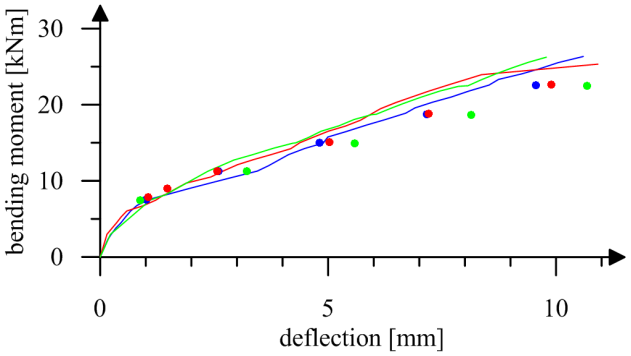

Figure 6: Deflection vs. bending moment for B-I series

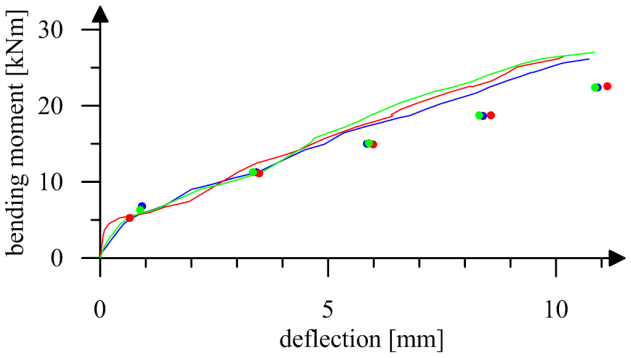

Figure 7: Deflection vs. bending moment for B-II series

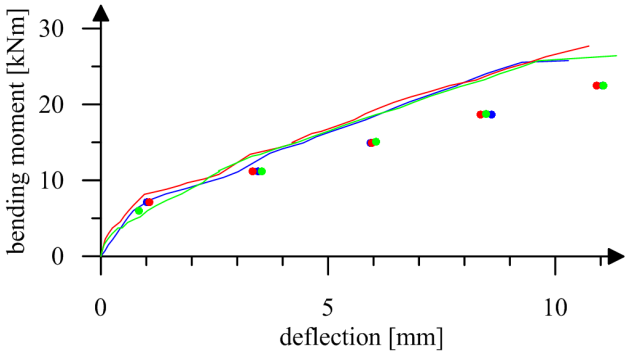

Figure 8: Deflection vs. bending moment for B-III series

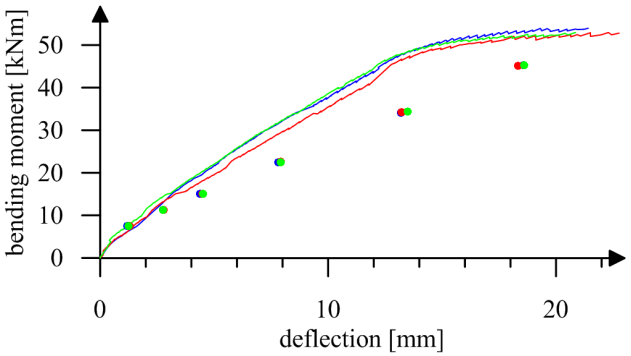

Figure 9: Deflection vs. bending moment for B-IV series

Obtained results proved highly consistent, especially up to 50% load applied to lightly reinforced beams (series B-I, B-II, B-III) and up to 30% load applied to highly reinforced beams (series B-IV). Results outside that range show greater inconsistencies (approx. 30%). Deflection could have been overestimated, because computations included every macroscopically observable during the experiment crack. Cracks occurring under heavier loads (closer to supports) were not as deep as cracks occurring under lighter loads. The proposed numerical model envisages every crack penetrating to natural axis of beam. Results of calculations have therefore confirmed correctness of the model and usability of presented method in computing static deflection of cracked reinforced concrete beams.

4. SCALING OF PARAMETER

As aforementioned in preliminary section of the paper, static and dynamic ductility of cracked reinforced concrete beams might vary. Hence it is fair to say that rotational ductility resulted from crack will differ from dynamic one. Hence:

$$d_{\varphi,dynamic}^{cr-i} = \alpha_d \cdot d_{\varphi,static}^{cr-i}, \tag{3}$$

where: α_d – empirical coefficient.

The parameter was scaled iteratively. During laboratory experiments at each load increment, crack perpendicular to element's axis were macroscopically catalogued. After cataloguing, cracks were sketched. Example sketch for B-I-1 beam is shown in figure 10. Next to each crack is given the load that caused it.

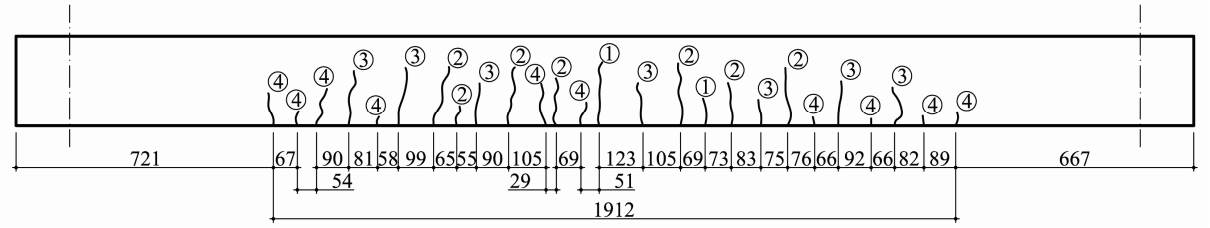

Figure 10: Sketch of crack - element B-I-1 (mm)

For each load increment, computations were then carried out using proprietary program. Each model was recalculated several times for different α_d parameters. Selected were values where inconsistencies between analytical and experimental natural frequency were the smallest. Example chart illustrating the process of scaling the B-I-1 beam is shown in figure 11.

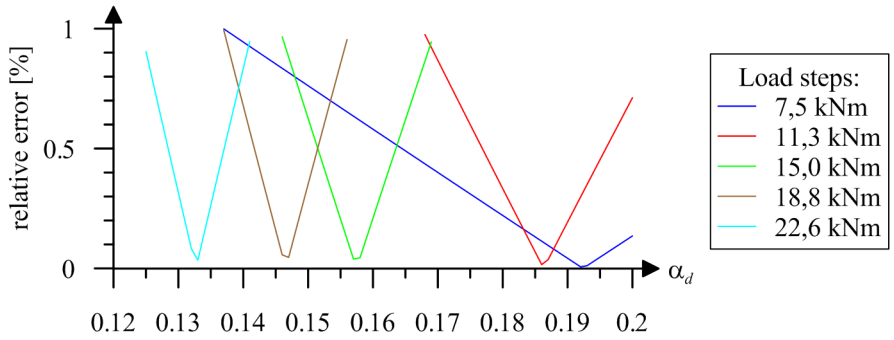

Figure 11: Relative difference depending on α_d parameter for individual load increments

Results of calculations for individual beams were analysed and function describing scaled parameter selected. Tested initial functions are shown in table 2.

Table 2: Functions describing parameter α_d

No.	Function	Relative function error [%]				
		B-I	B-II	B-III	B-I, B-II, B-III $\rho = 0{,}65$ %	B-IV $\rho = 1{,}38$ %
1	$e^{-\beta x}$	0,46	1,03	0,48	0,67	0,42
2	$\alpha \cdot e^{-\beta x}$	0,09	0,53	0,36	0,33	0,16
3	$\alpha \cdot \gamma^{-\beta x}$	0,10	0,57	0,39	-	0,17
4	$\alpha + x^{-\beta}$	**0,09**	**0,51**	**0,35**	**0,32**	**0,13**
5	$Cot(\alpha \cdot x^{\beta}) + \gamma$	0,09	0,56	0,38	0,33	0,14
6	$\alpha + e^{-\beta x}$	0,10	0,55	0,46	0,36	0,20

e – Eulerian number
α, β, γ – parameters
$x = M/M_R$ (effort level)

Model exhibiting the smallest error (function no. 4) was selected and used for further analyses. Values of parameters α and β are given in table 3.

Table 3. Parameters of used model

Parameter	B-I	B-II	B-III	B-I, B-II, B-III $\rho = 0{,}65$ %	B-IV $\rho = 1{,}38$ %
α	-0,916	-0,926	-0,947	-0,929	-0,958
β	0,0941	0,0955	0,157	0,116	0,0732

Due to negligible difference in the α parameter for both lightly and highly reinforced concrete, it was averaged for further calculations. Moreover, the β was assumed linearly variable as the function of reinforcement ratio given by the relationship:

$$\beta = -0{,}154 + 5{,}823 \cdot \rho \,. \tag{4}$$

The final formula for calculating the α_d coefficient given by:

$$\alpha_d = -0{,}944 + \left(M / M_R \right)^{-0{,}154+5{,}823\,\rho} \,. \tag{5}$$

Figure 11 shows nomograph of the parameter for selected reinforcement ratios.

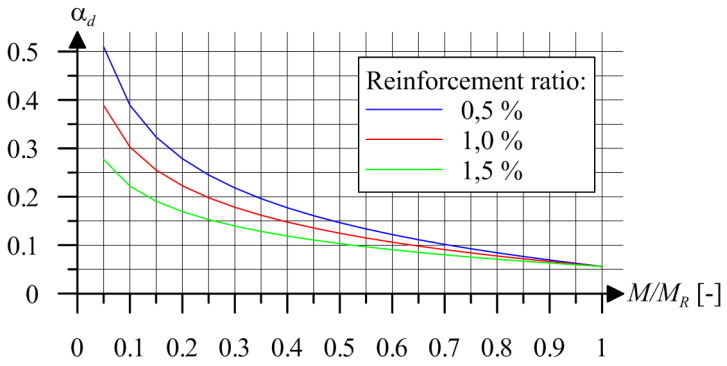

Figure 11: Nomograph of the α_d parameter for selected reinforcement ratios

5. FINAL REMARKS AND CONCLUSIONS

Carried out analyses proved differences in static and dynamic behaviour between reinforced concrete beams pertain not only to the global parameter of flexural rigidity. It was observed they also concern aspects of local description. In this paper used were the rigid finite element method and discrete crack modelling. Hence rotational ductility resulting from crack appearance had to be determined. For static issues an own relationship was used (1), derived based on elementary relationships from strength of materials. Proposed model showed promising results in terms of static calculations.

For dynamic calculations the relationship (1) was modified by introducing the empirical coefficient of α_d. Scaling was carried out based on own experimental studies. It was proved that dynamic ductility decreases relative to static ductility. It is the lower the higher the overload of element. The research has thus far proved that this difference depends also on the reinforcement ratio (fig. 11).

REFERENCES

[1] S. Jerath, M. M. Shibani: Dynamic Stiffness and Vibration of Reinforced Concrete Beams. ACI Journal, **82-18**, 196-202, 1985.

[2] K. C. Johns, M. D. Belanger: Dynamic Stiffness of Concrete Beams. ACI Journal, **78-18**, 201-205, 1981.

[3] M. Musiał: Vibrations of reinforced concrete beams with consideration of discrete crack model (in Polish) – PhD dissertation. Wroclaw University of Technology, Wroclaw, 2010.

[4] M. Musiał: Static and dynamic stiffness of reinforced concrete beams. Archives of Civil and Mechanical Engineering, **12**, 186-191, 2012.

[5] M. Kamiński, M. Musiał, A. Ubysz: Eigenfrequencies of the reinforced concrete beams – methods of calculations. Journal of Civil Engineering and Management, **17**, 278–283, 2010.

[6] M. Musiał, M. Kamiński, A. Ubysz: Free vibration frequencies the cracked reinforced concrete beams-methods of calculations. K. Gürlebeck and C. Könke eds. 18th

International Conference on the Applications of Computer Science and Mathematics in Architecture and Civil Engineering, IKM 2009, Weimar, Germany, 2009.

[7] M. Batel: Operational Modal Analysis – Another Way of Doing Modal Testing. Sound and Vibration, 22-27, August 2002.

[8] A. S. Ghods, B. Moghaddasie: Evaluating the dynamic characteristics of reinforced concrete beams. M. Motavalli ed. Fourth International Conference on FRP Composites in Civil Engineering, CICE 2008, Zurich, Switzerland, 2008.

[9] J. Langer: Dynamics of structures (in Polish). Wroclaw University of Technology Publishing House, Wroclaw, 1980.

Formel-Kapitel 1 Abschnitt 1 19th International Conference on the Application of Computer Science and Mathematics in Architecture and Civil Engineering
K. Gürlebeck, T. Lahmer and F. Werner (eds.)
Weimar, Germany, 04–06 July 2012

MODEL DESCRIBING STATIC AND DYNAMIC DISPLACEMENT OF SILO WALLS DURING DISCHARGE OF GRANULAR SOLID

M. Musial*, A. Ubysz and P. Ulatowski

* *Institute of Building Engineering, Wroclaw University of Technology, Poland address*
E-mail: michal.musial @ pwr.wroc.pl

Keywords: wall vibration, displacement model, silo design

Abstract.*Correct evaluation of wall displacements is a key matter when designing silos. This issue is important from both the standpoint of design engineer (load-bearing capacity of structures) and end-consumer (durability of structures). Commonplace methods of silo design mainly focus on satisfying limit states of load-bearing capacity. Current standards fail to specify methods of dynamic displacements analysis.*
Measurements of stressacting on silo walls prove that the actual stress is sum of static and dynamic stresses. Janssen came up with differential equation describing state of static equilibrium in cross-section of a silo. By solving the equation static stress of granular solid on silo walls can be determined. Equations of motion were determined from equilibrium equations of feature objects. General solution, describing dynamic stresses was presented as parametric model.
This paper presents particular integrals of differential equation, which enable analysing displacements and vibrations for different rigidities of silo walls, types of granular solid and its flow rate.

1 INTRODUCTION - TECHNICAL PROBLEM STATEMENT

Silos for storing grain or other granular solids, under normal operating conditions exhibit wall vibration caused by flow of material generating friction against silo wall. That vibration normally has quasi-harmonic waveform alternately increasing and decreasing. Its strength depends on various factors, however, observations made thus far prove that crucial parameters are wall flexibility and its decrement rate.

Stresspeaks upon silo emptying are widely known phenomena. Since those greater stresses used to cause silo failures, it is currently a common practice to factor them in and compensate their impact through experimentally determined by increasing coefficients. Those coefficients usually enable satisfying limit states of structural capacity, however, they could not be used to: compute maximum amplitudes in walls, determine material fatigue hazards or potential resonance threats.

The Authors set out to develop a computational model for describing fluctuation of vibration in silo walls during granular solid and grain flows. The model was devised based on analysis of continuous stress on silo walls.

2. ASSUMPTIONS TAKEN FOR MODELLING

The following assumptions were taken to formulate the model:

- Actual stress is superposition of static and dynamic stress (fig. 1):
- Vibration has harmonic waveform alternately increasing and decreasing.
- Conditions for static equilibrium defined by Janssen

$$\frac{\mathrm{dp_v}}{dx} + \mathrm{p_v\ k\ tg}\delta\frac{\mathrm{U}}{\mathrm{F}} = \gamma \tag{1.1}$$

p_v – vertical stress; F – silo cross-sectional area; U – silo circumference; δ - angle of wall friction; γ – bulk solid weight by volume;

Solution to differential equation (1) in accordance with Janssen:

$$p_h^{stat} = \frac{\gamma F}{k\,tg\delta\ U}\left(1 - e^{-\frac{k\ tg\delta\ U\,z}{F}}\right)$$

- The displacement equation should be a variable dependent on silo height *z* and time *t*, and other derivatives will enable solving for longitude of the nodal line φ(z,t), bending moment *M*(z,t) and transverse force *V*(z,t);
- The model factors in wall give and decrement rate of the structure;

Special assumption taken to describe self-excited vibration is proportionality of exciting force - stressp_h(x,t), with derivatives of perpendicular translations relative to silo wall – w(x,t), $\frac{dw(x,t)}{dt}$, $\frac{d^2w(x,t)}{dt^2}$.

Pomiar naporu na ściany silosu z ciągłą rejestracją naporu na taśmie magnetycznej (badania dr Jerzego Kmity) [7]

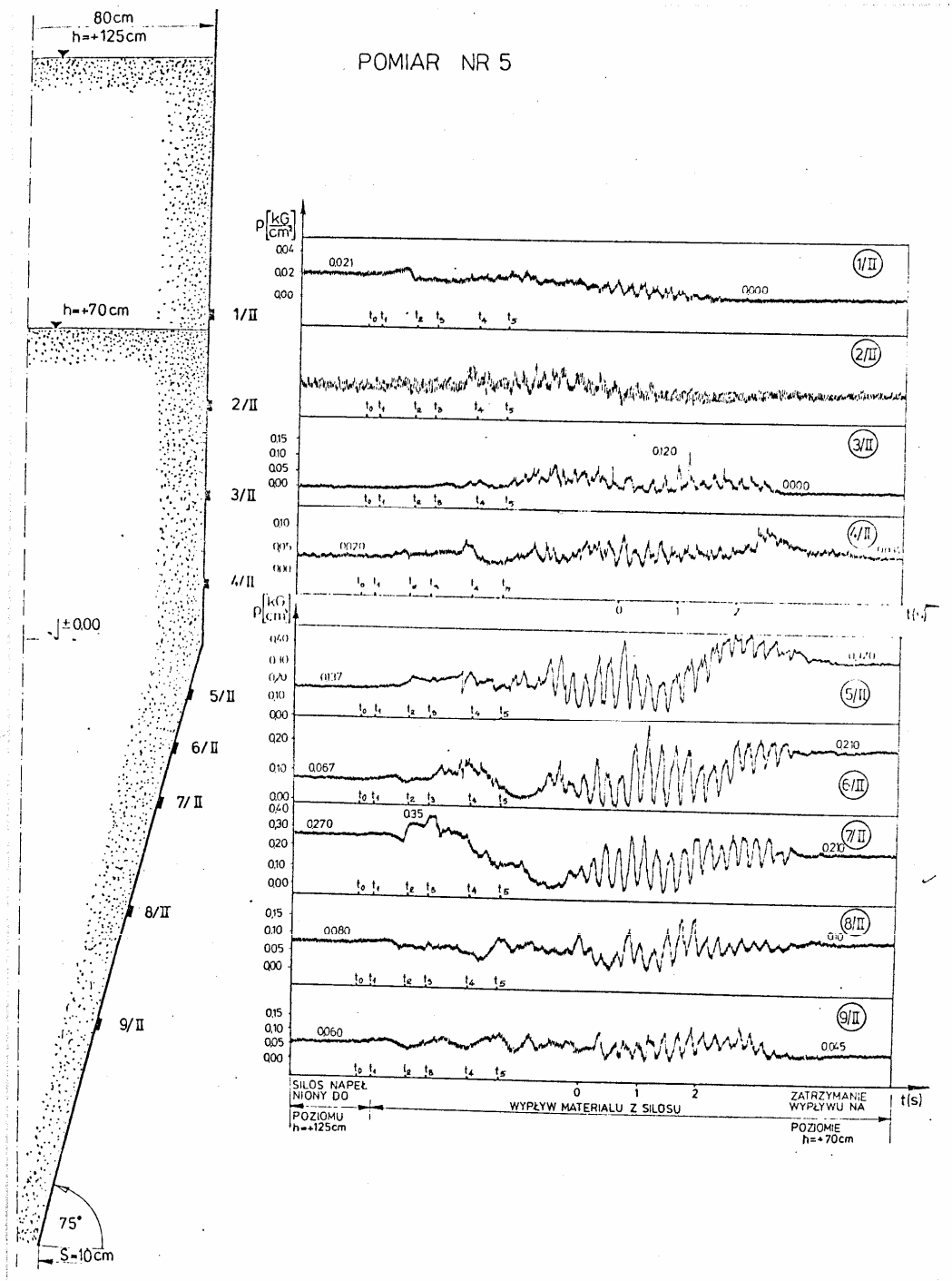

Fig. 2.1. Stress σ_n acting on cylindrical silo wall [Kmita, Ubysz].
Continuous recording silo wall stress measurement

3. FORMULATION OF THE MODEL

According to Boroch [2] and Langer [7] physical objects are continuous systems with indefinite degrees of freedom. Mathematics normally tends to discretise tasks. An assumption can be made that desired effect is obtained through force acting as point mass (granular solid, physical discretisation). The mass, however, can be divided into regular partitions, and the state of displacements can be given by limited number of parameters (mathematical discretisation). The latter method was employed to develop model describing silo wall displacement under load of granular solid.

The square one is equations of motion for uni-dimensional continuous arrangements and underlying dynamics assumptions. This model is justified by silo geometry. In many case this task could be approximately reduced to one dimension.

An important part of every analysis is defining the right-hand side of the equation. In order to correctly describe effect of self-excited vibration, the exciting force has to be proportional to derivatives of perpendicular translations relative to silo wall. In order to more comprehensively analyse experimentally a given phenomenon and more accurately describe vibrations, adequate parameters have to be introduced into RHS of equation. In many cases, numerous parameters would prevent from obtaining a closed solution and that is the objective authors did set for themselves.

Another issue important from viewpoint of modelling is rigidity of the silo wall. As far as dynamic parameters are concerned - frequency and amplitude - the wall is approximated by a beam of adequate flexural rigidity, or by membrane (string) whose flexural rigidity is ignored.

3.1. Linear membrane model of self-excited system

Base model was assumed as unit width membrane, fixed at both ends. The task was reduced down to unit width. In authors' view this is the most fundamental model taken from classic mechanics, which gives a good representation of self-excited vibration generated by dry friction. Figure 3.1 illustrates cut-out of wall under horizontal stress $p_{h1}(x)$ and quasi-harmonic stress $p_{h2}(x,t)$. N(x,t), N(x+Δx,t) expresses local longitudinal force, α(x,t), α(x+Δx,t) – vertical tilt. The load applied to membrane $p_{h2}(x,t)$ is a transverse force per unit of length. From condition for equilibrium Σx (vertical axis) factoring in forces generated by motion and forces of inertia (D'Alembert's principle) we get:

$$N(x+\Delta x,t)\sin\alpha(x+\Delta x,t) - N(x,t)\sin\alpha(x,t) = \Delta x\left[m\frac{d^2w(x,t)}{dt^2} - p_h(x,t)\right] \tag{3.1}$$

m - mass per unit of length, $\frac{d^2w(x,t)}{dt^2}$ - acceleration

Formulation m is an inertial force inferred from II Newton's laws of motion.

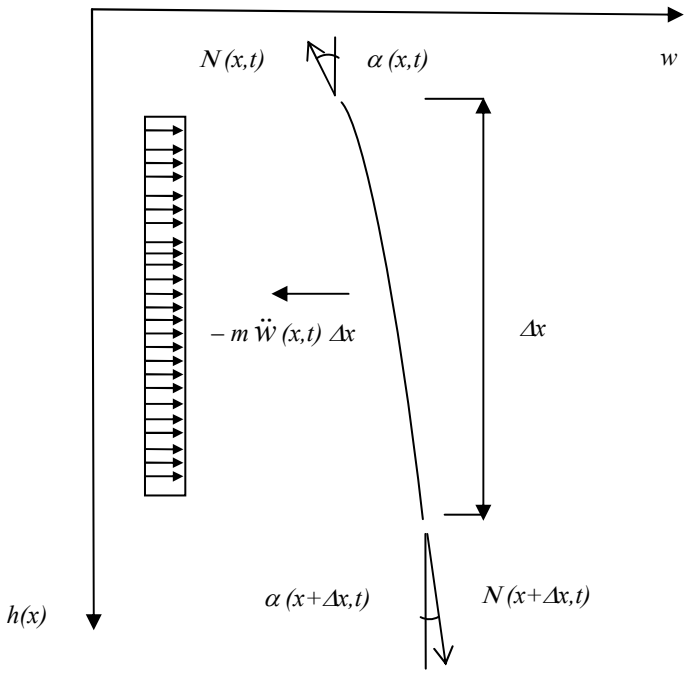

Fig. 3.1. Cut-out of membrane and distribution of forces.

By dividing both sides of equation 3.1 by Δx we get difference quotient on LHS and given $\Delta x \rightarrow 0$ we get derivative at dx (from definition of derivative). For constant x over segment Δx at small angles $\sin \alpha \rightarrow dw/dx$ we get longitudinal force N:

$$N - m\frac{d^2w(x,t)}{dt^2} = -p_h(w,t) \qquad (3.2)$$

This equation, however, has more a general nature. For the exciting force to generate self-excited vibration it has to depend on displacement and its derivatives. Here, on wall displacement, its speed and acceleration. Some authors take static friction f_s as an auxiliary parameter. Forces occurring in the self-excited system, however, have to be explicitly separated from static and quasi-static stress generated through storage, filling and discharging the silo. Hence the general form of non-homogeneous equation can be written as:

$$N\frac{d^2w(x,t)}{dx^2} - m\frac{d^2w(x,t)}{dt^2} = -p_{h1}(w,t) - p_{h2}\left(w, \frac{dw(x,t)}{dt}, \frac{d^2w(x,t)}{dt^2}, f_s, t\right) \qquad (3.3)$$

– $p_{h1}(w,t)$ – static component of stress; $p_{h2}\left(w, \frac{dw(x,t)}{dt}, \frac{d^2w(x,t)}{dt^2}, f_s, t\right)$ – dynamic component of stress.

In similar fashion both the linear flexural model of self-excited system and the model of vibration along generatrix of silo's plating can be described. This will be discussed in dissertation currently in progress. Their final shape is presented in the following subsection.

3.2. Linear flexural membrane model of self-excited system

In case of silo wall with little give, its rigidity has to be factored in as well. Hence - similarly to flexible wall - the entire side surface is assumed to have the same rigidity. From general relationships from strength of materials, geometric relationships and by factoring in physical conditions, we get for small displacements:

$$M(x,t) = - EI\,(x)\,\frac{d^2 w(x,t)}{dx^2} \tag{3.4}$$

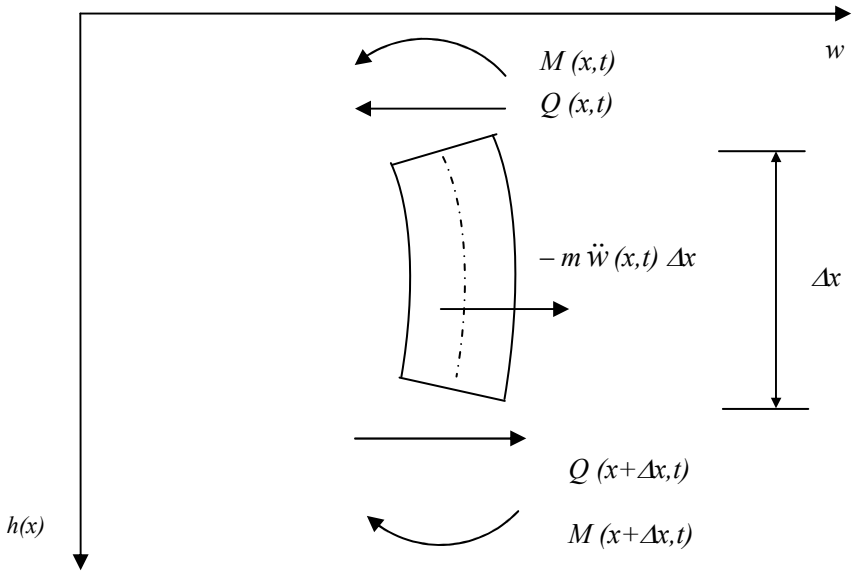

Fig. 3.2. Cut-out of silo wall and distribution of forces.

From conditions for equilibrium (fig. 3.2) we get:

$$- m\,\ddot{w}\,(x,t)\,\Delta x + Q\,(x+\Delta x,t) - Q\,(x,t) + p_h(x,t)\,\Delta x = 0 \tag{3.5}$$

Similarly to equation 3.1, the equation 3.5 can be divided by Δx, and given Δx→0 we get:

$$Q'(x,t) = m\,\frac{d^2 w(x,t)}{dx^2} - p_h(x,t) \tag{3.6}$$

From equation 3.4 we get:

$$Q(x,t) = \frac{d}{dx} M(x,t) = \frac{d}{dx}\left[- EI\,(x)\,\frac{d^2 w(x,t)}{dx^2}\right] \tag{3.7}$$

After substituting (3.7) to (3.6) we get:

$$\frac{d^2}{dx^2} M(x,t) = \frac{d^2}{dx^2}\left[- EI\,(x)\,\frac{d^2 w(x,t)}{dx^2}\right] = m\,\frac{d^2 w(x,t)}{dx^2} - p_h(x,t) \tag{3.8}$$

In majority of cases, silos have high longitudinal rigidity constant across segments, hence EI(x) = const. and 3.8 is reduced to:

$$EI\,(x)\left[\frac{d^4 w(x,t)}{dx^4}\right] + m\,\ddot{w}\,(x,t) = p_h(x,t) \tag{3.9}$$

Similarly to previous case, the component of excitation generated by vibration in self-excited system can by isolated:

$$EI(x)\left[\frac{d^4 w(x,t)}{dx^4}\right] + m\ddot{w}(x,t) = p_{h1}(x,t) + p_{h2}(x, \frac{dx}{dt}, \frac{d^2x}{dt^2}, f_s, t) \tag{8.9}$$

3.3. Model of vibration along generatrix of silo's plating

In high silos elastic strain occurs along generatrix of the silo. Here, vibrations are excited longitudinally. System of forces along the wall is illustrated in figure 3.3 and equation 3.10 shows equilibrium:

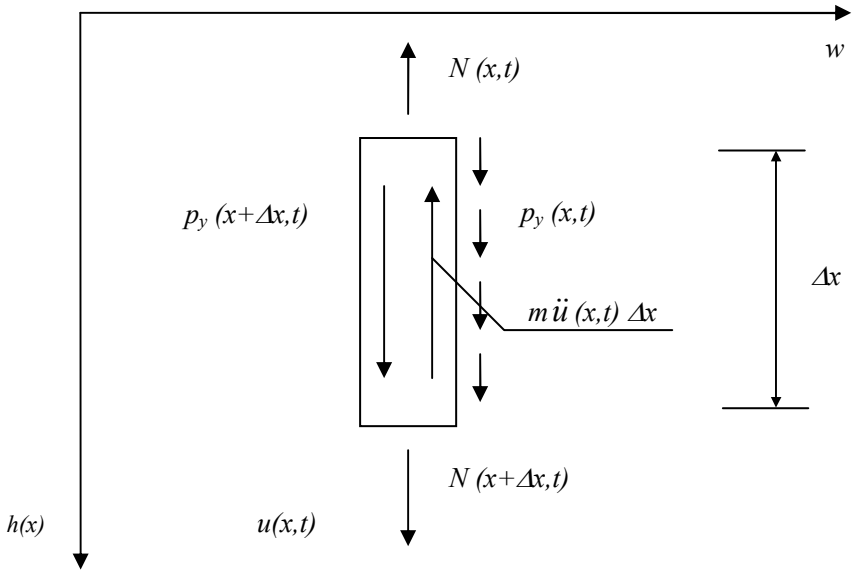

Fig. 3.3. Cut-out of silo wall and distribution of forces.

$$N(x+\Delta x,t) - N(x,t) = m\ddot{u}(x,t)\,\Delta x - p_v(x,t)\,\Delta x \tag{3.10}$$

Similarly dividing by Δx in line with definition of differential quotient, given Δx→0, the differential equation is:

$$\frac{dN}{dx} = m\ddot{u}(x,t) - p_v(x,t) \tag{3.11}$$

Then in accordance with physical relationship (Hooke's law) we get:

$$\sigma = E\,\varepsilon \tag{3.12}$$

$$\frac{N}{A} = E\frac{du}{dx} \tag{3.13}$$

By substituting (3.13) to (3.11):

$$\frac{d}{dx}\left(E\,A\frac{du}{dx}\right) = m\ddot{u}(x,t) - p_v(x,t) \tag{3.14}$$

and for quantities constant over segments EA = const.:

$$E\,A\frac{d^2u}{dx^2} = m\ddot{u}(x,t) - p_v(x,t) \tag{3.15}$$

After rearranging equation 3.15 and singling out factor generating self-excited vibration it becomes:

$$m\ddot{u}(x,t) - E A \frac{d^2u}{dx^2} = p_{v1}(x,t) + p_{v2}(x, \frac{dx}{dt}, \frac{d^2x}{dt^2}, f_s, t) \quad (3.16)$$

However, terms p_v are significantly lower than p_h, are recorded longitudinal vibrations have amplitudes significantly lower than vibrations perpendicular to silo walls. Thus they are considerably less important for silo wall vibrations.

4. SOLUTIONS TO SELECTED MODELS DESCRIBING SILO WALL VIBRATION

Models of self-excited systems were based on equations of motion. Solutions were sought after for complete structure of mass and using approximated description of state of displacements with limited number of parameters expressing characteristics of silo wall stresses.

4.1. Laminar flow stress

Stress generated by granular solid acting on silo walls - provided there is no pulsation (laminar) - can be described by differential equation, which - since stress is assumed proportional to horizontal translation of silo wall - will take form of general equation of motion. If there is no pulsation upon bulk solid being discharged from the silo (laminar flow), the phenomenon can be expressed by the following differential equation:

$$\frac{\partial^2 u(x,t)}{\partial t^2} = -t^n \frac{\partial u(x,t)}{\partial t} - u(x,t); \qquad n \in \langle ½; 2\rangle \quad (4.1)$$

For initial conditions:

$$u(x,t) = 0;\ u'(x,t) = 1 \quad (4.2)$$

we get relationship describing silo wall displacements over time. This is the case where there are no extra loads applied of oscillatory nature. By following up on the assumption wall displacements are proportional to wall stress, we get relationship expressing that stress over discharge time. Depending on assumed *n*, usually between <½; 2>, the stress will fade over various time. This corresponds to different readings of measurements taken at different heights. Due to sheer complexity of factors influencing actual stresses, the following models use theoretical normal stress $p_h^* = 1$, which for given silo has to be multiplied by static stress at given height determined through e.g. Janssen equations. The following figures show example stress over time charts. To better illustrate the function, waveforms of stress fluctuations were shown for three levels: upper, middle and lower part of the silo. According to the function, the highest stress occurs once the discharge process starts and is most intensive towards the hopper.

Due to numerous factors influencing stress acting on different levels of silo, a parametric function is envisaged to describe the phenomenon.

$$p_h(x,t) = m t^L e^{\frac{-ht}{n\pi}} + c_1 t + c_2 \quad (4.3)$$

This function is general integral of equation (4.2) expressed in real numbers. Initial and boundary conditions for determining parameters and constants of integration are determined based on results of experimental study. Parameters of "low vulnerability" to function fluctuation were taken for further deliberations as constants:

m = coefficient describing initial discharge <0,7÷1,00> – assumed 0.8;

L = coefficient describing variability of the function fluctuation - assumed 0.1

h = coefficient describing variability of the function fluctuation (convexity, concavity, inflection point) - assumed 0.005

The solids discharge starts at t_0. Hereunder the function is:

$$p_h(x,t) = \begin{cases} 1 & t \le t_0 \\ m t^{0,1} e^{\frac{-0,005\, t}{n\pi}} & t > t_0 \end{cases} \qquad (4.4)$$

Both the function fluctuation and parameters were taken based on experimental data. Arriving at the solution enables adjusting (correcting) those parameters for flow of different substances

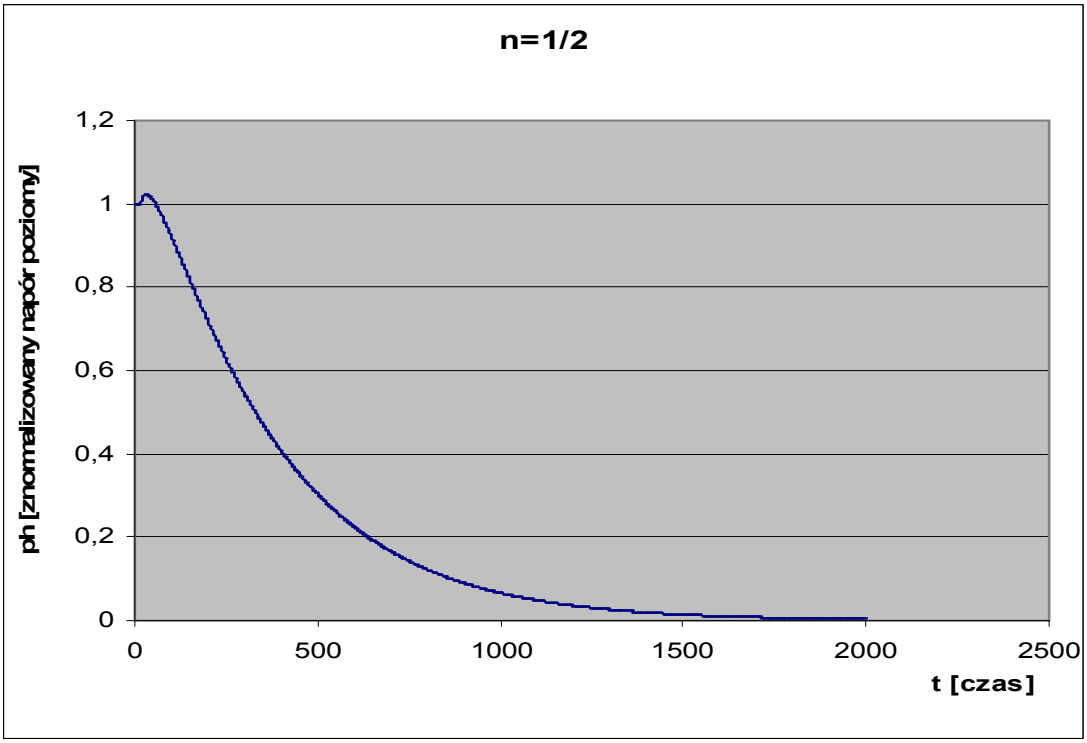

$$p_h(x,t) = 0,8\, t^{0,1} e^{\frac{-0,005\, t}{0,5\pi}} \qquad (4.5)$$

Fig. 4.1. Relationship between horizontal stress and time - upper silo section (n = ½).

4.2. Stress at flow with self-excited vibration

Solids discharge from silo is often distorted by dynamic factors occurring over the course of that process. The most important from the viewpoint of day-to-day operation are seemingly:

- tumble of overburden material due to arching or doming;
- vibration generated by turbulent flow;
- vibration excited by "dry friction" as called in literature self-excited vibration.

The nature on impact stress exerts depends on multiple factors and can be vary both qualitatively and quantitatively. Some of the factors are:

- caking (humidity, granulation, re-solidification),
- angle of internal friction of bulk solid,
- wall friction coefficient,
- silo wall give,
- flow rate of bulk solid,
- boundary conditions (wall joints, silo supports, foundation),
- mass flow problems (relief equipment, segregation);
- other.

Presented next is model built based on available to authors results of experimental study, where parameters of bulk solid (sand) can be assumed homogeneous, the silo is regular shape and discharge flow is consistent. Silo walls show some give, and the wall where wall stress measurements were taken had natural frequency ν = 33 Hz.

For purposes of formulating the model, only tape sections where vibrations were the strongest were used. Based on continuous readings it was concluded that an important oscillatory factor is self-excited vibration.

The equation describing silo wall strain over time was formulated using forecasting method. Presented was superposition function of carrier wave and function describing oscillation. The function describing carrier wave was described in detail in subsection 4.5.1. The function describing the oscillatory wave was introduced with - apart from conditions enabling modulation of frequency and amplitude - conditions enabling to describe excitation and extinction of vibration.

The function describing horizontal displacement of silo wall in any given section is also given by:

$$u(x,t) = u_1(x,t) + u_2(x,t), \tag{4.6}$$

where: $u_1(x,t) = Ate^{-Bt}(\sin Ct - \sin Dt)$, (4.7)

$$u_2(x,t) = M\,t^L\,e^{-Ht}. \tag{4.8}$$

Thus the full equation is:

$$u(x,t) = Ate^{-Bt}(\sin Ct - \sin Dt) + M\,t^L\,e^{-Ht} \tag{4.9}$$

or

$$u(x,t) = Ate^{-Bt}\sin Ct - Ate^{-Bt}\sin Dt + M\,t^L\,e^{-Ht} \tag{4.10}$$

Next in this subsection presented is rearrangement of the function, leading to final differential equation describing silo wall vibration. To keep working outs concise, derivative symbol used for single-variable function $(\,)^{\prime}$ was substituted into the RHS of equation.

$$\frac{\partial u(x,t)}{\partial t} = \left(Ate^{-Bt}\right)^{\prime}(\sin Ct - \sin Dt) + Ate^{-Bt}\left((\sin Ct - \sin Dt)\right)^{\prime} + \left(M\,t^L\right)^{\prime}e^{-Ht} + M\,t^L\left(e^{-Ht}\right)^{\prime}$$

(4.11)

$$\left(Ate^{-Bt}\right)' = Ae^{-Bt} + A(-B)te^{-Bt}$$

$$\left((\sin Ct - \sin Dt)\right)' = \left(C\cos Ct - D\cos Dt\right)$$

$$\left(M\,t^{L}\right)' e^{-Ht} + M\,t^{L}\left(e^{-Ht}\right)' = MLt^{(L-1)}e^{-Ht} + M(-H)t^{L}\,e^{-Ht}$$

$$\frac{\partial u(x,t)}{\partial t} = \left(Ae^{-Bt} - AB\,te^{-Bt}\right)(\sin Ct - \sin Dt) + Ate^{-Bt}\left(C\cos Ct - D\cos Dt\right) + ML\,t^{(L-1)}\,e^{-Ht} - MH\,t^{L}\,e^{-Ht}$$

$$\frac{\partial u(x,t)}{\partial t} = \left(Ae^{-Bt}\sin Ct - AB\,te^{-Bt}\sin Ct - Ae^{-Bt}\sin Dt + AB\,te^{-Bt}\sin Dt\right) +$$

$$+\left(Ate^{-Bt}C\cos Ct - Ate^{-Bt}D\cos Dt\right) + ML\,t^{(L-1)}\,e^{-Ht} - MH\,t^{L}\,e^{-Ht}$$

$$\frac{\partial^2 u(x,t)}{\partial t^2} = \left(\left(Ae^{-Bt} - AB\,te^{-Bt}\right)(\sin Ct - \sin Dt) + Ate^{-Bt}\left(C\cos Ct - D\cos Dt\right) + ML\,t^{(L-1)}\,e^{-Ht} - MH\,t^{L}\,e^{-Ht}\right)'$$

$$\frac{\partial^2 u(x,t)}{\partial t^2} = \left(\begin{array}{l}\left(Ae^{-Bt}\sin Ct - AB\,te^{-Bt}\sin Ct - Ae^{-Bt}\sin Dt + AB\,te^{-Bt}\sin Dt\right) + \\ \\ +\left(Ate^{-Bt}C\cos Ct - Ate^{-Bt}D\cos Dt\right) + ML\,t^{(L-1)}\,e^{-Ht} - MH\,t^{L}\,e^{-Ht}\end{array}\right)'$$

$$\left(Ae^{-Bt}\sin Ct\right)' = -ABe^{-Bt}\sin Ct + ACe^{-Bt}\cos Ct$$

$$\left(ABte^{-Bt}\sin Ct\right)' = \left(ABe^{-Bt} + AB(-B)te^{-Bt}\right)\sin Ct + ABCte^{-Bt}\cos Ct$$

$$\left(ABte^{-Bt}\sin Ct\right)' = ABe^{-Bt}\sin Ct - AB^{2}te^{-Bt}\sin Ct + ABCte^{-Bt}\cos Ct$$

$$\left(Ae^{-Bt}\sin Dt\right)' = -ABe^{-Bt}\sin Dt + ACe^{-Bt}\cos Dt$$

$$\left(ABte^{-Bt}\sin Dt\right)' = \left(ABe^{-Bt} + AB(-B)te^{-Bt}\right)\sin Dt + ABDte^{-Bt}\cos Dt$$

$$\left(ABte^{-Bt}\sin Dt\right)' = ABe^{-Bt}\sin Dt - AB^{2}te^{-Bt}\sin Dt + ABDte^{-Bt}\cos Dt$$

$$\left(ACte^{-Bt}\cos Ct\right)' = \left(ACe^{-Bt} + AC(-B)te^{-Bt}\right)\cos Ct - AC^{2}te^{-Bt}\sin Ct$$

$$\left(ACte^{-Bt}\cos Ct\right)' = ACe^{-Bt}\cos Ct - ABCte^{-Bt}\cos Ct - AC^{2}te^{-Bt}\sin Ct$$

$$\left(ADte^{-Bt}\cos Dt\right)' = \left(ADe^{-Bt} + AD(-B)te^{-Bt}\right)\cos Dt - AD^2te^{-Bt}\sin Dt$$

$$\left(ADte^{-Bt}\cos Dt\right)' = ADe^{-Bt}\cos Dt - ABDte^{-Bt}\cos Dt - AD^2te^{-Bt}\sin Dt$$

$$\left(ML\,t^{(L-1)}e^{-Ht}\right)' = ML(L-1)t^{(L-2)}e^{-Ht} + ML(-H)t^{(L-1)}e^{-Ht}$$

$$\left(ML\,t^{(L-1)}e^{-Ht}\right)' = ML(L-1)t^{(L-2)}e^{-Ht} - MLH\,t^{(L-1)}e^{-Ht}$$

$$\left(MH\,t^{L}e^{-Ht}\right)' = MHLt^{(L-1)}e^{-Ht} + MH(-H)t^{L}e^{-Ht}$$

$$\left(MH\,t^{L}e^{-Ht}\right)' = MHLt^{(L-1)}e^{-Ht} - MH^2\,t^{L}e^{-Ht}$$

$$u(x,t) = u_1(x,t) + u_2(x,t) = Ate^{-Bt}\sin Ct - Ate^{-Bt}\sin Dt + M\,t^{L}e^{-Ht}$$

$$\frac{\partial u(x,t)}{\partial t} = \left(Ae^{-Bt}\sin Ct - AB\,te^{-Bt}\sin Ct - Ae^{-Bt}\sin Dt + AB\,te^{-Bt}\sin Dt\right) +$$

$$+\left(Ate^{-Bt}C\cos Ct - Ate^{-Bt}D\cos Dt\right) + ML\,t^{(L-1)}e^{-Ht} - MH\,t^{L}e^{-Ht}$$

$$\left(Ae^{-Bt}\sin Ct\right)' = -ABe^{-Bt}\sin Ct + ACe^{-Bt}\cos Ct$$

$$-\left(ABte^{-Bt}\sin Ct\right)' = -ABe^{-Bt}\sin Ct + AB^2te^{-Bt}\sin Ct - ABCte^{-Bt}\cos Ct$$

$$-\left(Ae^{-Bt}\sin Dt\right)' = ABe^{-Bt}\sin Dt - ADe^{-Bt}\cos Dt$$

$$\left(ABte^{-Bt}\sin Dt\right)' = ABe^{-Bt}\sin Dt - AB^2te^{-Bt}\sin Dt + ABDte^{-Bt}\cos Dt$$

$$\left(ACte^{-Bt}\cos Ct\right)' = ACe^{-Bt}\cos Ct - ABCte^{-Bt}\cos Ct - AC^2te^{-Bt}\sin Ct$$

$$-\left(ADte^{-Bt}\cos Dt\right)' = -ADe^{-Bt}\cos Dt + ABDte^{-Bt}\cos Dt + AD^2te^{-Bt}\sin Dt$$

$$\left(ML\,t^{(L-1)}e^{-Ht}\right)' = ML\,(L-1)t^{(L-2)}e^{-Ht} - MLH\;t^{(L-1)}e^{-Ht}$$

$$-\left(MH\,t^{L}e^{-Ht}\right)' = -MHLt^{(L-1)}e^{-Ht} + MH^2\,t^{L}e^{-Ht}$$

After substitution:

$$\frac{\partial^2 u_1(x,t)}{\partial t^2} = \left(B^2 - C^2\right)u_1(x,t) - 2B\frac{\partial u_1(x,t)}{\partial t} + AB\,te^{-Bt}(\sin Ct - \sin Dt) + 2Ae^{-Bt}(C\cos Ct - D\cos Dt)$$

and

$$\frac{\partial^2 u_2(x,t)}{\partial t^2} = ML(L-1)t^{(L-2)}e^{-Ht} - 2MLH\,t^{(L-1)}e^{-Ht} + MH^2\,t^L\,e^{-Ht} + (2MH^2\,t^L\,e^{-Ht} - 2MH^2\,t^L\,e^{-Ht})$$

and after rearranging

$$\frac{\partial^2 u_1(x,t)}{\partial t^2} = \left(B^2 - 2B - C^2\right)u_1(x,t) - 2B\frac{\partial u_1(x,t)}{\partial t} + \frac{2}{t}\frac{\partial u_1(x,t)}{\partial t} - \left(\frac{2}{t^2} + \frac{B}{t}\right)u_1$$

$$\frac{\partial^2 u_2(x,t)}{\partial t^2} = -2M\frac{\partial u_2(x,t)}{\partial t} - u_2(x,t) + ML(L-1)t^{(L-2)}e^{-Ht}$$

When considering complete solids discharge, the parameter of time might reach high values and last two equation components will tend to naught. Then the final equations of motion become:

$$\frac{\partial^2 u_1(x,t)}{\partial t^2} - \left(B^2 - 2B - C^2\right)u_1(x,t) + 2B\frac{\partial u_1(x,t)}{\partial t} = \frac{2}{t}\frac{\partial u_1(x,t)}{\partial t} - \left(\frac{2}{t^2} + \frac{B}{t}\right)u_1 \qquad (4.12)$$

$$\frac{\partial^2 u_2(x,t)}{\partial t^2} + 2M\frac{\partial u_2(x,t)}{\partial t} + u_2(x,t) - ML(L-1)t^{(L-2)}e^{-Ht} = 0 \qquad (4.13)$$

In equation (4.12) the RHS is the function of displacement and first derivative of displacement - this is consistent with initial assumptions made for self-excited vibrations. The equation (4.13) can be interpreted as "main wave" –describing characteristics of stress on silo wall during solids discharge.

Similarly to laminar flow, stress was assumed proportional to horizontal translations of silo walls, however, as opposed to that case, apart from regular stress upon solids discharge, also other loads occur with oscillatory waveform. Based on that assumption, we get the relationship between stress and solids discharge time. To make possible comparing graphs of functions, the parameter was assumed to fluctuate within n = <½; 2>. Hence, those stresses will be described for different levels of silo wall. These models also use the theoretical normal stress $p_h^* = 1$, which for given silo has to be multiplied by actual stress at given height. The following figures show example stress over time charts. To better illustrate the function, waveforms of stress fluctuations were shown for three levels: upper, middle and lower part of the silo.

The function describing stress acting on silo wall is given by superposition of main wave and oscillatory stresses. Introduced parameters enable experimentally describing the function both in terms of its graph and expected values.

$$p_h(x,t) = Ate^{-Bt}(\sin Ct - \sin Dt) + M\,t^L\,e^{\frac{-ht}{n\pi}} + c_1 t + c_2 \qquad (4.14)$$

Similarly to solution for laminar flow, the function is general integral of equation () expressed in real numbers. Initial and boundary conditions for determining parameters and constants of integration are determined based on results of experimental study.

Parameters found in equations have the following physical representation:

- A - vibration amplitude; when describing stress acting on silo wall where amplitude of oscillatory component to fixed component is 5 ÷ 20 %, the parameter fluctuates within <0,0005 ÷ 0,002>;
- $B = \frac{b}{n\pi}$, b – range of damping; n ∈<½; 2>; when self-excited vibrations extinct at 0.7 p_h acting on silo wall, b = 0.03, provided self-excited vibrations extinct at 0.2 p_h, b = 0.07;
- C, D - parameters describing frequency of resonant excitation; quantities closest to observed excitations are obtained for C/D=<0,85 ÷ 0,95>;

and previously assumed for laminar flow

- m = coefficient describing initial discharge <0,7÷1,00> – assumed 0.8;
- L = coefficient describing variability of the function fluctuation - assumed 0.1;
- $H = \frac{h}{n\pi}$ h = coefficient describing variability of the function fluctuation (convexity, concavity, inflection point) - assumed 0.005

The solids discharge starts at t_0. Finally the formula became:

$$p_h(x,t) = \begin{cases} 1 & t \le t_0 \\ Ate^{-Bt}\left(\sin 0{,}9t - \sin t\right) + M\, t^{0,1}\, e^{\frac{-0{,}005t}{n\pi}} & t > t_0 \end{cases} \qquad (4.15)$$

In case of rigid silos with high decrement rate vibration has nature of short-term excitation, which causes temporary overload of the silo wall. For that eventuality silo overload was modelled for stresses beyond 1.2 p_h. Because overload has short-term nature, silo overload has characteristics similar to random structural overload during solids discharge, where expected stresses are a band of expected loads as opposed to non-ambiguous values.

In case of dynamically flexible walls with high decrement rate, higher amplitude vibrations might occur, but they who quickly extinct (fig. 4.2).

Another example is dynamically susceptible wall with low decrement rate, where periodically excited are cyclical high-amplitude vibrations. Description of these vibrations is rather characteristic with explicit self-excited vibration (fig.4.3).

Selected examples are seemingly the most representative based on available experimental studies as far as analysis of vibrations and stresses acting on silo walls are concerned.

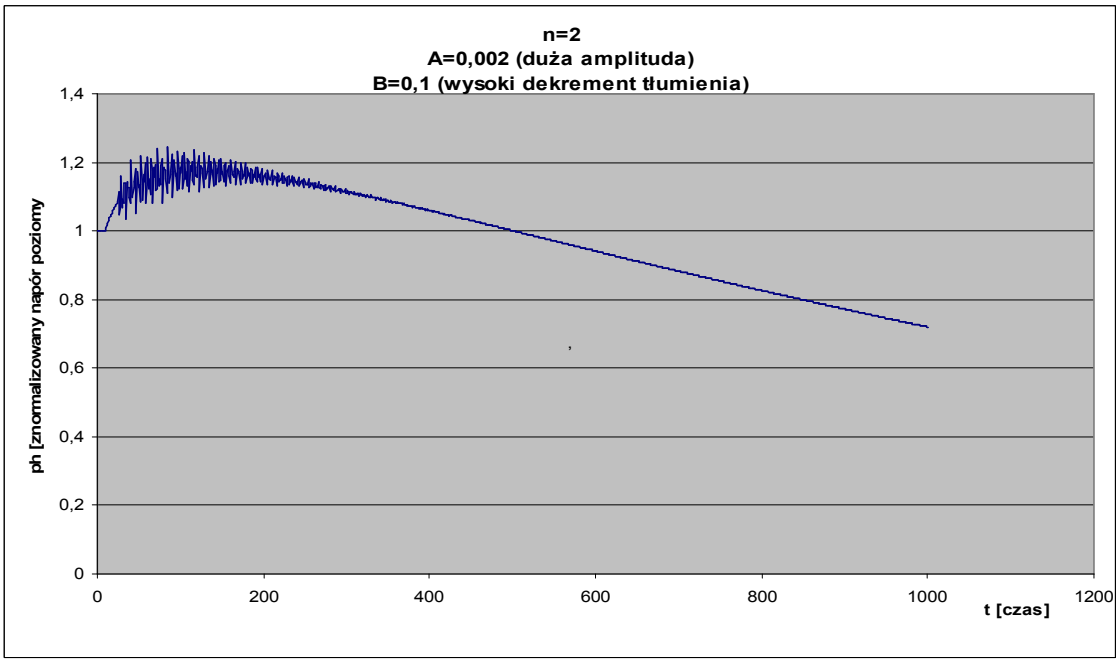

Fig. 4.2.Horizontal stress acting on silo flexible wall to vibration with high decrement rate.

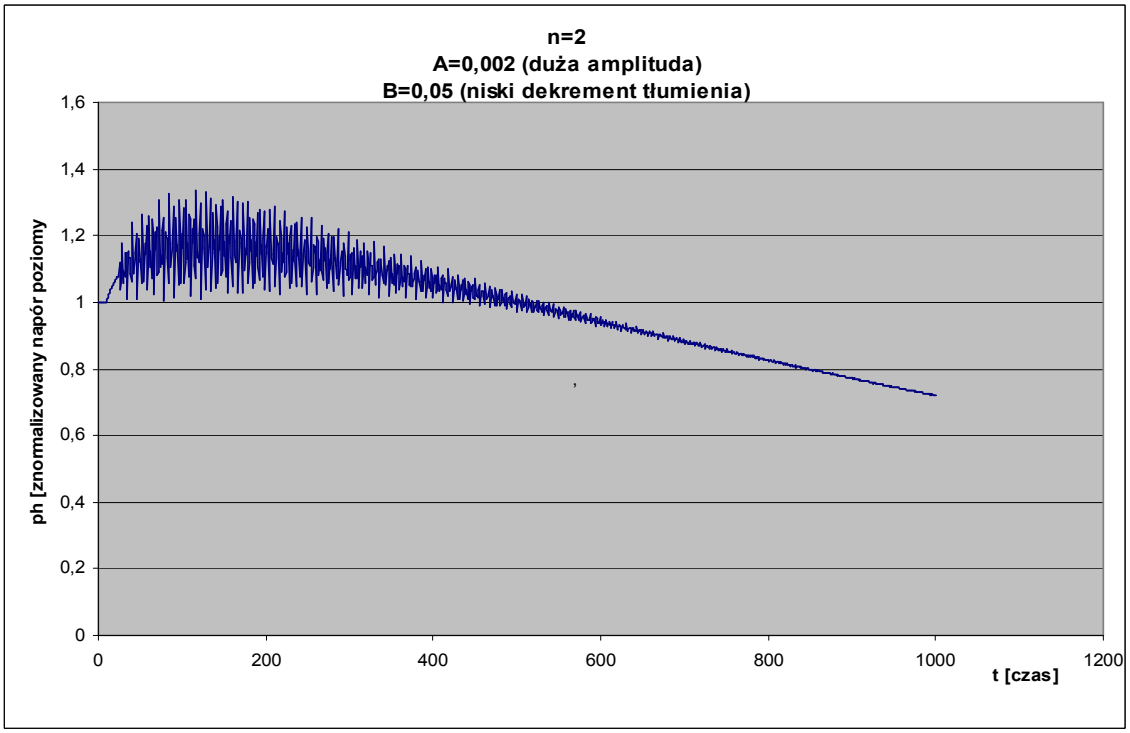

Fig. 4.3. Deformable wall with low decrement rate.

5. SUMMARY, RESEARCH PROBLEMS AND SUPPLEMENTARY RESEARCH PLAN

From designer's point of view, issues of stress acting on silo wall are synonymously related to wall displacements, strength of materials problems and fatigue problems. The proposed model is a tool intended for forecasting loads and some processes related to day-to-day silo operation.

This proposition of stress&strain model was devised to give original contribution to current state of arts in behaviour of silo wall during storage, filling and discharging. This particularly applies to subject area most extensively covered in specialist publications which seems crucial from standpoint of structural safety i.e. real stresses generated by granular solid acting on silo wall. The proposed model aims to make computational models more true to real structural behaviour.

In this paper, authors attempted to compromise between universality of model and its practical applicability, hence it was limited to analyse variability of only selected elements. Taken assumptions are the square one in developing more complex models which would describe with greater accuracy existing cases or enable analysing new practical cases, which were not included in this paper.

Practical applications for the model are:

- Approximated description of vibration cycles (amplitude and frequency of vibrations), key for determining fatigue strength of material,
- Estimation of expected stress acting on silo wall during granular solid flow.

This model - based on research data - requires further verification against greater number of experimental data from natural-scale structures. Beyond doubt, however, it can serve well for purposes of experimental studies.

REFERENCES

[1]. Borcz A., Kmita J., Ubysz A., Drgania samowzbudne podczas wypływu materiału z silosu o ścianach odkształcalnych. Pr. Nauk. Inst, Bud. Polit. Wrocł. Nr 33

[2]. Boroch H. Monographic lecture, TU Wrocław, Wrocław 1976

[3]. Eibl J., Landachl H., Haussler U., Gladen W. Zur Frage des Silodrückes. Beton und Stahlbetonbau 4, 1982 s. 104-110

[4]. Jenike A., Johanson J.R.: On the theory of bin loads, Trans. ASME. J. Eng. Ind. Vol. 91. ser. B2/1969

[5]. Kamiński M. Untersuchungen des Getreidedrücks in Silozellen Die Bautechnik 58, 1981, H. 1, s. 19-23

[6]. Kmita J., Silo as a system of self-induced vibration. Journal of Structural Engineering, vol. 111, nr 1985, s. 190–204

[7]. Langer J.: Dynamika budowli. Wyd. Polit. Wrocł. Wrocław 1980.

[8]. Pieper K., Wenzel F.: Druckverhältnisse in Silozellen, Berlin-München, Verlag von Wilhelm Ernst und Sohn. Berlin 1964

[9]. Schwedes J. , Wilms H. Spannungs Verteilung in divergenten Bunkern. Aufbereitungs-technik H.11, 1979 s. 603-608

[10]. Tejchman J., Niedostatkiewicz M., Experimental and theoretical studies on resonance dynamic effects during silo flow. Powder Handling & Processing, 15, 1 (2003), pp. 36–42.

[11]. Wenzel K, Probleme des Silodruckes. Dissertation TU Braunschweig 1971.

18th International Conference on the Application of Computer
Science and Mathematics in Architecture and Civil Engineering
K. Gurlebeck and C. Konke (eds.)
Weimar, Germany, 07–09 July 2009

ANALYSIS OF THE MODE OF DEFORMATION OF THE SUB-PULLEY STRUCTURES ON SHAFT SLOPING HEADGEAR STRUCTURES

A.Ye. Nechytailo* and Ye.V. Horokhov, V.N. Kushchenko

**Donbas National Academy of Civil Engineering and Architecture*
Derzhavin str., 2,
86123 Makeyevka, Ukraine

**Research Training Group 1462, Bauhaus-University Weimar,*
Research Training Group "Model Validation in Structural Engineering"
Berkaer Str. 9,
99425 Weimar, Germany
E-mail: ae.nechitaylo@mail.ru

Key words: shaft frame-type sloping headgear, sub-pulley structures, joint of a guide pulley resting, design diagram, mode of deformation, local stresses.

Abstract. *A numerical analysis of the mode of deformation of the main load-bearing components of a typical frame sloping shaft headgear was performed. The analysis was done by a design model consisting of plane and solid finite elements, which were modeled in the program «LIRA». Due to the numerical results, the regularities of local stress distribution under a guide pulley bearing were revealed and parameters of a plane stress under both emergency and normal working loads were determined.*
In the numerical simulation, the guidelines to improve the construction of the joints of guide pulleys resting on sub-pulley frame-type structures were established. Overall, the results obtained are the basis for improving the engineering procedures of designing steel structures of shaft sloping headgear.

1 INTRODUCTION

Sloping shaft headgear structures are crucial to the surface facilities of mines. Failure of the shaft headgears have disastrous consequences on the system and can lead to prolonged stoppages. The causes of failure are due to: a) heavy loads; b) intense dynamic loads; c) technical modifications of cables without a proper engineering study.

In the design of the frame supporting the sloping headgears, simplified computational models consisting of rod finite elements are used. The headgear calculations are carried out using equivalent static loading to simulate the hoisting cable tension. However, not all elements of the frame sloping headgears can be represented in the form of rods. For example, sub-pulley components, because these elements have a depth to length ratio ranging between: 1:2 and 1:5 (see Figs. 1-3).

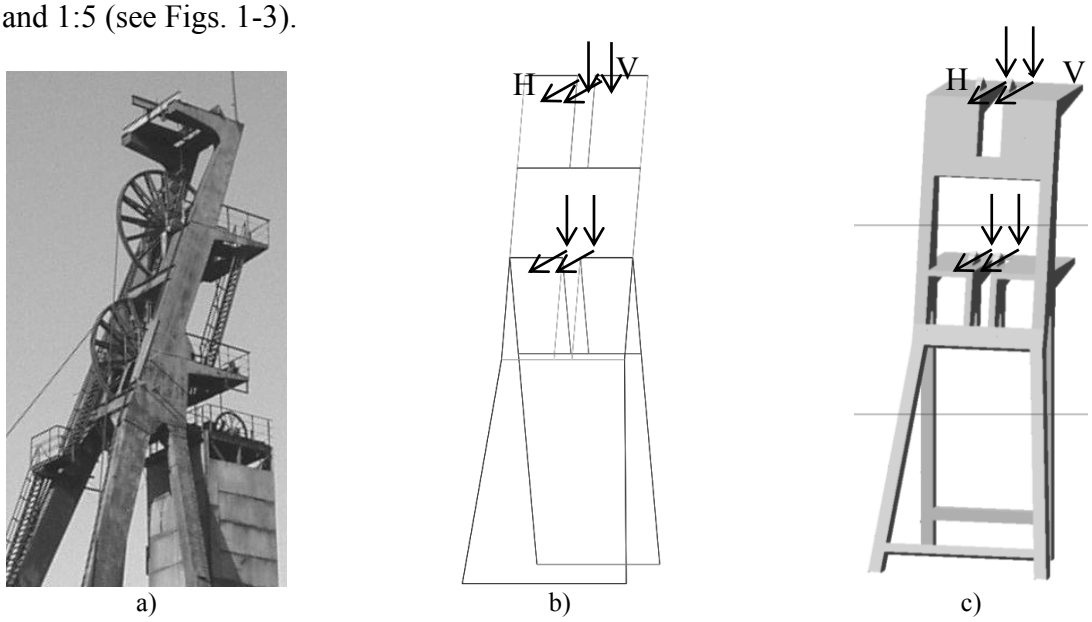

Figure 1: The general view and basic design models of the sub-pulley components:
a) a fragment of the general view of the typical sub-pulley components; b) a fragment of the design model of the sub-pulley rod components; c) a fragment of the design model of the sub-pulley of the lamellar elements (H, V are horizontal and vertical components of the resultant of the hoisting cable tension)

The parameters of the plane mode of deformation of bearing structures of shaft headgears are not calculated accurately enough, for example, in the joints of guide pulley resting on the sub-pulley construction, as well as in the areas of sudden changes in the sections of the structural elements. Thus, the analysis of the plane mode of deformation of the sub-pulley structure elements and their joints is a significant scientific task.

1.1 Object of the study

The object of the study is a sub-pulley structure of a typical sloping frame-type shaft headgear system. Sloping frame-type shaft headgears are a part of the shaft hoisting plant and consist of the following structural parts (see Fig. 2): 1 – sub-pulley structures; 2 – stay legs; 3 – vertical supports (pillars); 4 – a bench; 5 – a sub-headgear frame; 6 – a stay leg and pillar foundation.

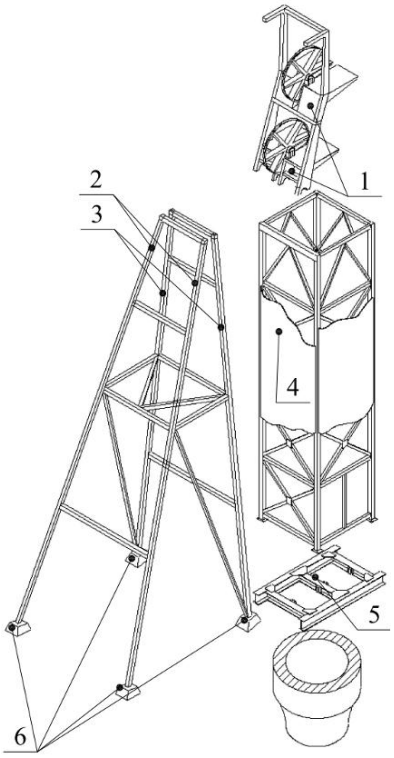

Figure 2: The arrangement of frame-type sloping headgears

Due to the nature of the connection between the above structural parts, there exist several frame-type sloping shaft headgears systems as follows (see Fig. 3):

• Semi-hipped (sub-pulley structures rest on a space frame consisting of a vertical support (pillar) and a stay leg, see Fig. 3a);

• Hipped (sub-pulley structures rest on a hipped roof consisting of two stay legs which form a space frame, see Fig. 3b);

• Combined (sub-pulley structures rest on a bench or on a heap-stead building, see Fig. 3c).

a) b) c)

Figure 3: The structural systems of the frame-type sloping shaft headgears:
a) semi-hipped system; b) hipped system; c) combined system

The most vital joints and elements of the frame-type sloping shaft headgears are depicted schematically in Fig. 4.

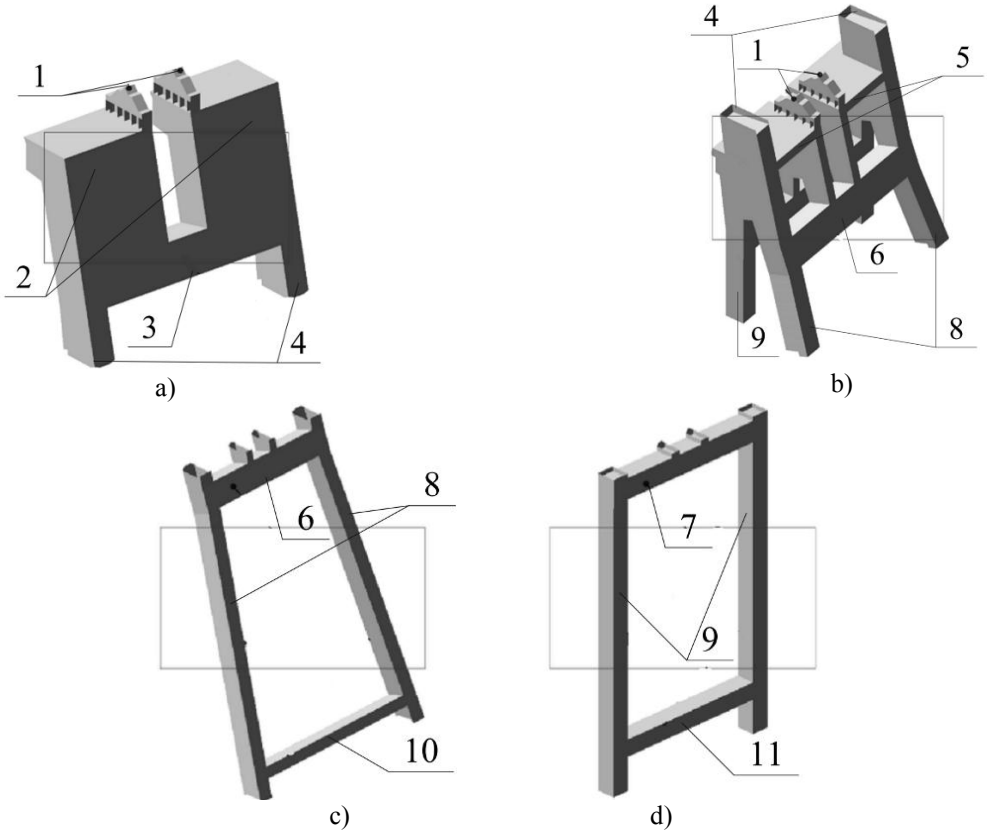

Figure 4**:** The major joints and elements of a frame-type box-like headgear: a) a segment of the upper sub-pulley structure; b) a segment of the lower sub-pulley structure; c) a segment of the upper part of a stay leg; d) a segment of the upper part of a vertical support (pillar). Component numbering: 1-support bearings of a pulley; 2 – a sub-pulley pillar of the upper sub-pulley platform; 3 – the main girder of the stay leg of the upper sub-pulley platform; 4 – the branches of the stay leg between the sub-pulley platforms; 5 – a pillar of the lower sub-pulley platform; 6 – the main girder of the stay leg of the lower sub-pulley platform; 7 – the main girder of the vertical supports of the lower sub-pulley platform; 8 – the stay leg branches; 9 – the vertical support body; 10 – the stay leg girder; 11 – the girder of vertical supports)

The sub-pulley structures of the frame-type sloping shaft headgears are for guide pulleys to rest on. In this paper, the sub-pulley structures of the upper pulley are considered. According to the arrangement of the sub-pulley structure, a frame with the vertical posts inclined to the horizontal is considered. In the place where a guide pulley bearing rests, a change of the frame girder section is provided by adding from above a T-section of 320 mm in height with a flange of 300 mm in width to the main section of the girder (see Fig. 5).

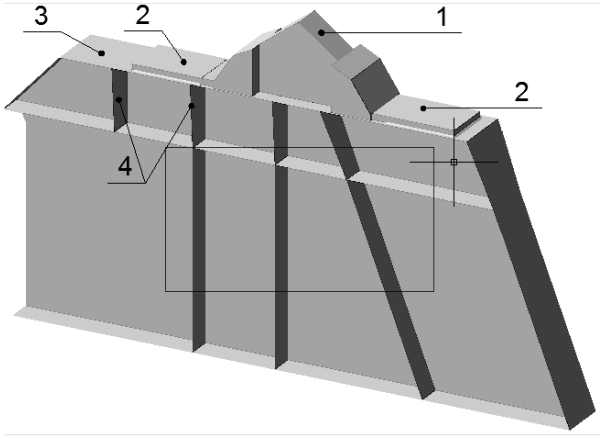

Figure 5: A supporting joint of the guide pulley (1 – a supporting bearing of the guide pulley; 2 – the front and back stops; 3 – the bearing surface area; 4 – the webbing of the supporting joint of the guide pulley)

The supporting joint of the guide pulley (see Fig. 4, 5) consists of a supporting bearing (position 1), the front and back stops (position 2), the bearing surface area (position 3), and the webbing (position 4). The supporting bearing of the guide pulley is secured vertically by bolts, and horizontally, it is secured by dressed wedges between the stops, which are fastened by fillet welds to the upper girder chord of the sub-pulley frame.
The photos of the sub-pulley structures and the resting nodes of the pulleys of the upper sub-pulley platform are shown in Fig. 6.

a) b)

Figure 6: The sub-pulley structures of the upper sub-pulley platform: a) View from below; b) Resting nodes of the guide pulley

1.2 Purpose of the work

The purpose of the work is to analyze the mode of deformation of the sub-pulley structures of a typical, frame-type, sloping, semi-hipped, shaft headgear and to improve the engineering design methods of the node structures of the guide pulley resting on the sub-pulley structures.

1.3 Research tasks

The research tasks are a) to reveal the areas of distributing local tensions in the resting node of a guide pulley at different parameters of the resultant of a hoisting cable tension; b) to determine of the parameters of a plane mode of deformation of the sub-pulley structures; c) establishment of the principles of the rational designing of sub-pulley structures.

2 EXPLORATORY PROCEDURES

A typical skip semi-hipped frame-type sloping shaft headgear was chosen for the study. The headgear has the following technical characteristics: the headgear height – 39.3 m; the spread of the stay leg branches – 11.0 m; the section of the stay leg branches – box-like; the structure material – steel C255 (see Fig. 7).

a) b)

Figure 7: The object of the study – a semi-hipped skip frame-type sloping shaft headgear: a) the general view of the headgear studied; b) the geometry of the headgear

To fulfill the assigned task, computer simulation techniques were implemented with the help of the software package LIRA. The investigation of the mode of deformation of the structure was investigated in two stages:

The 1st stage - The simulation of the mode of deformation of the structure on the spatial design model approximated by laminated finite elements.

The 2nd stage - The simulation of the mode of deformation of a separate sub-pulley structure on the spatial design model approximated by laminated and three-dimensional finite elements.

The design was completed for the following load scenarios: a) normal operating conditions (normal hoisting cable tension, pulley weight, and permanent load); b) emergency loading and breaking of the upper pulley cable, calculated in accordance with the regulations [2]. Loads on a cable are transferred to the nodes of the guide pulley in the form of vertical and horizontal components of the resultant of the hoisting cable branch tension (see Fig. 8).

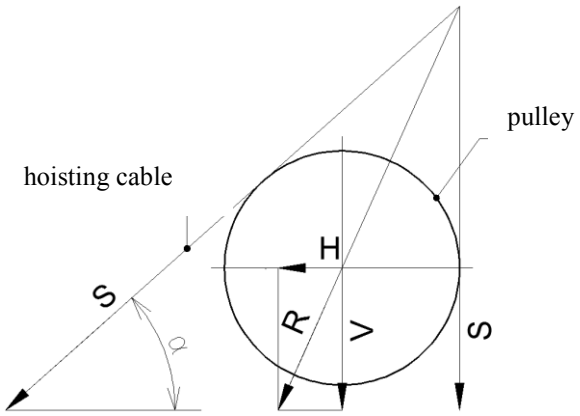

Figure 8: Diagram of load transfer of hoisting cable tension where S is the tension in a cable branch; R is the resultant of a hoisting cable tension; V is the vertical component of the resultant; H is the horizontal component of the resultant; α is the inclination of a hoisting cable to the horizon

The 1st stage. On the spatial design model approximated by laminated finite elements (see Fig. 9) it was obtained: the principal (σ_1, σ_2) and reduced ($\sigma_{red.}$) tensions; characteristics of the self-excited vibrations and elastic displacement of the elements.

Figure 9: The finite-element model generated in the software package LIRA

The 2nd stage. The sub-pulley frame of the upper pulley was thoroughly modeled as a spatial lamellar system in LIRA in the form of an add-on system with regards to the interaction boundary conditions (see Fig. 10).

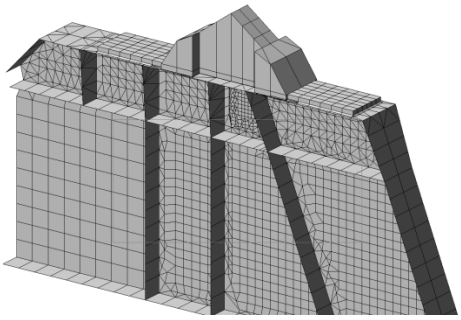

Figure 10: A segment of the design model approximated by plates

The elastic interaction of the sub-pulley frame and the rest of the stay leg structure was simulated by adding resilient flexing ties (FE 266), which simulated the axial and flexural rigidity of an abutment node.

The guide pulley bearing was simulated by the three-dimensional finite elements (FE 34, 36) in such a way that the model dimensions correspond to the structure of the guide pulley supporting bearing. The bearing base resting on the frame, and operating at tension, was simulated with the help of the unilateral elastic tie elements (FE 262) that are horizontally compliant. The stops were three-dimensional elements (FE 36). The stop fastening was modeled by fillet welds with legs of 10 mm which, in turn, were simulated by the three-dimensional finite elements (FE 34).

Breaking cable load, operation tension, and weight of the guide pulleys were applied to a three-dimensional element of the design model, to the simulation bearing of the guide pulley in the form of the vertical and horizontal components of the resultant (see Fig. 11).

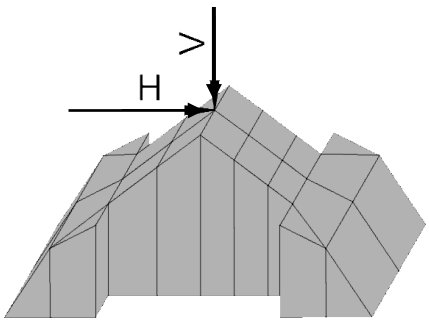

Figure 11: Load transfer diagram of the hoisting cable tension in the lamellar approximation where V – the vertical component of the resultant; H – the horizontal component of the resultant

Because of the varying processes of different shaft hoisting plants, the inclination of the cable can change. In the process of the numerical experiment, we evaluated the influence of the cable inclination on the plane mode of deformation. The inclination of the resultant of the hoisting cable tension varied within 30º and 65º in 5º increments.

3 ANALYSIS

In the first stage, the main stresses (σ_1, σ_2), reduced stresses ($\sigma_{red.}$), normal stresses (σ_x, σ_y), and tangential stresses (τ_{xy}) were obtained. In the analysis of the mode of deformation,

the headgear structures were zoned according to the nature and intensity of the mode of deformation (see Fig. 12 and Table 1).

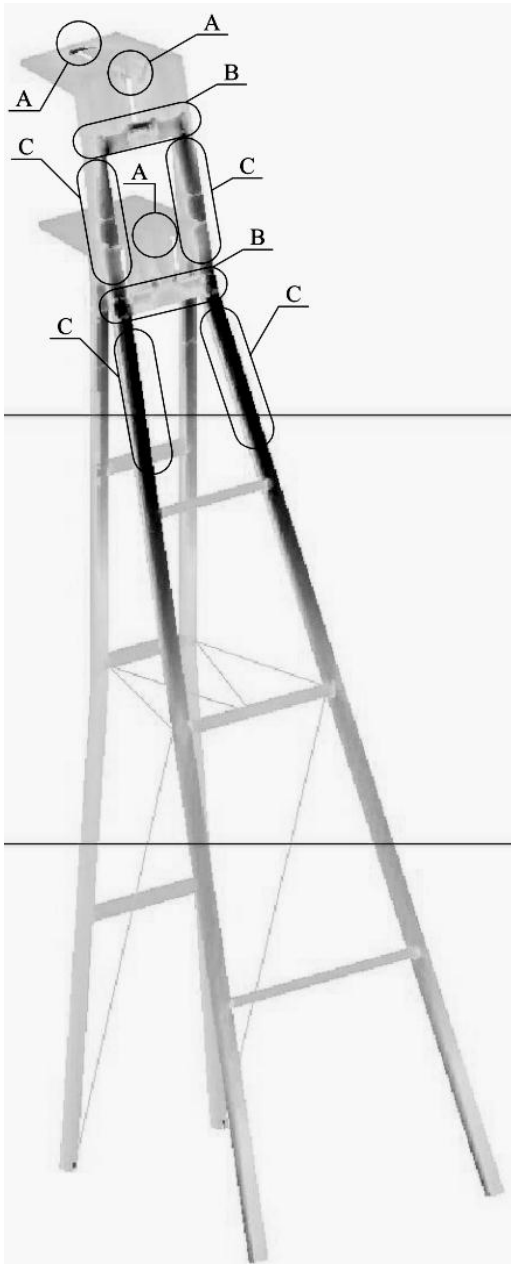

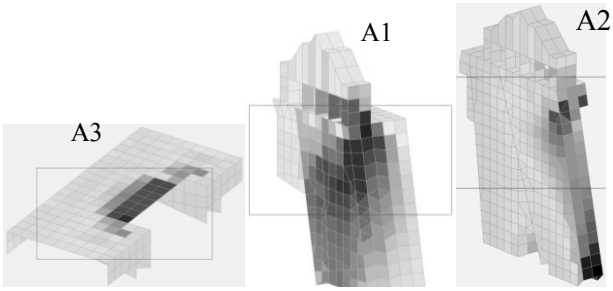

Zone – A

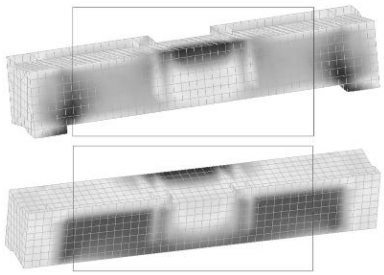

Zone – B (the girder of the upper sub-pulley structure on both sides B1)

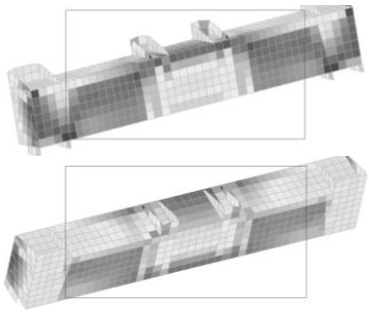

Zone – B (the girder of the lower sub-pulley structure on both sides B2)

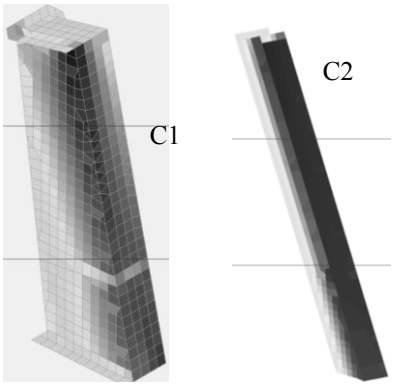

Zone – C

Figure 12: Zoning of the headgear structures by nature and intensity of the mode of deformation:
A – zones of local tension;
B – zones of tension concentration;
C – zones that showed highest stresses.

Table 1: Zoning according to type of plane mode deformation in the headgear elements and the maximum stress values obtained

Zone of stresses		Zone linear dimensions, m	Of the accident design load combinations				Of the operation design load combinations			
			σ_1, MPa	σ_2, MPa	Σ_{red}, MPa	τ_{max}, MPa	σ_1, MPa	σ_2, MPa	Σ_{red}, MPa	τ_{max}, MPa
A	A1 – the area of the upper pulley resting (connection of elements 1 and 2 Fig. 12a)	0.5x0.3	2.33	-33.6	34.8	18.0	0.48	-6.08	6.3	3.3
	A2 – the area of the lower pulley resting (connection of elements 1 and 5 Fig. 12b)	1.8x0.4	-2.6	-71.2	69.9	34.3	-0.43	-7.21	7.00	3.4
	A3 – the area where the sub-pulley platform section changes	2.2x0.4	-0.3	-67.0	66.9	33.4	-0.06	-16.5	16.42	8.2
B	B1 – the girder of the upper sub-pulley structure (element 3 Fig. 12a)	-	49.2	0.28	49.0	24.4	13.4	0.075	13.34	6.7
	B2 – the girder of the lower sub-pulley structure (element 6 Fig. 12b, c)	-	47.9	0.15	47.8	23.9	11.3	0.048	11.23	5.6
C	C1 – the stay legs between the sub-pulleys platforms (element 8 Fig. 12c)	3.1x2.2	-1.2	-70.3	69.7	34.5	-0.05	-6.8	6.86	3.4
	C2 – the stay leg branch (element 4 Fig. 12a,b)	8.4x0.8	0.34	-85.7	84.7	43.0	0.07	-6.46	6.64	3.4

From the above table, it is evident that the maximum values of σ_1 occur in the nodes of resting of the guide pulley and the maximum values of σ_2 were calculated in the stay leg branches in connection with the sub-pulley structures.

In the second stage, the mode of deformation was analyzed for the sub-pulley structures and the nodes of resting of the guide pulleys of the sloping shaft headgear. It was found that the typical parameters affected by cable inclination change were local stresses in the resting node of a guide pulley, the basic stresses (σ_1, σ_2), reduced stresses (σ_{red}), normal stresses (σ_x, σ_y), tangential stresses (τ_{xy}), and stress concentration coefficients (C_u). See Fig. 13.

Analysis of the mode of deformation of the given design model showed the following ranges in the local stress distribution in the resting node of a guide pulley: «*A*» – the range of the local stress distribution under the support bearing foot (see Fig. 13, Table 2, 3); «*B*» – the range of the plane mode of deformation in the wall of the pulley attachment point (see Fig. 13, Table 2, 3); «*C*» – the range of the plane mode of deformation in the girder wall (see Fig. 13, Table 2, 3); «*D*» – the range of the steady mode of deformation in the girder wall (see Fig. 13, Table 2, 3).

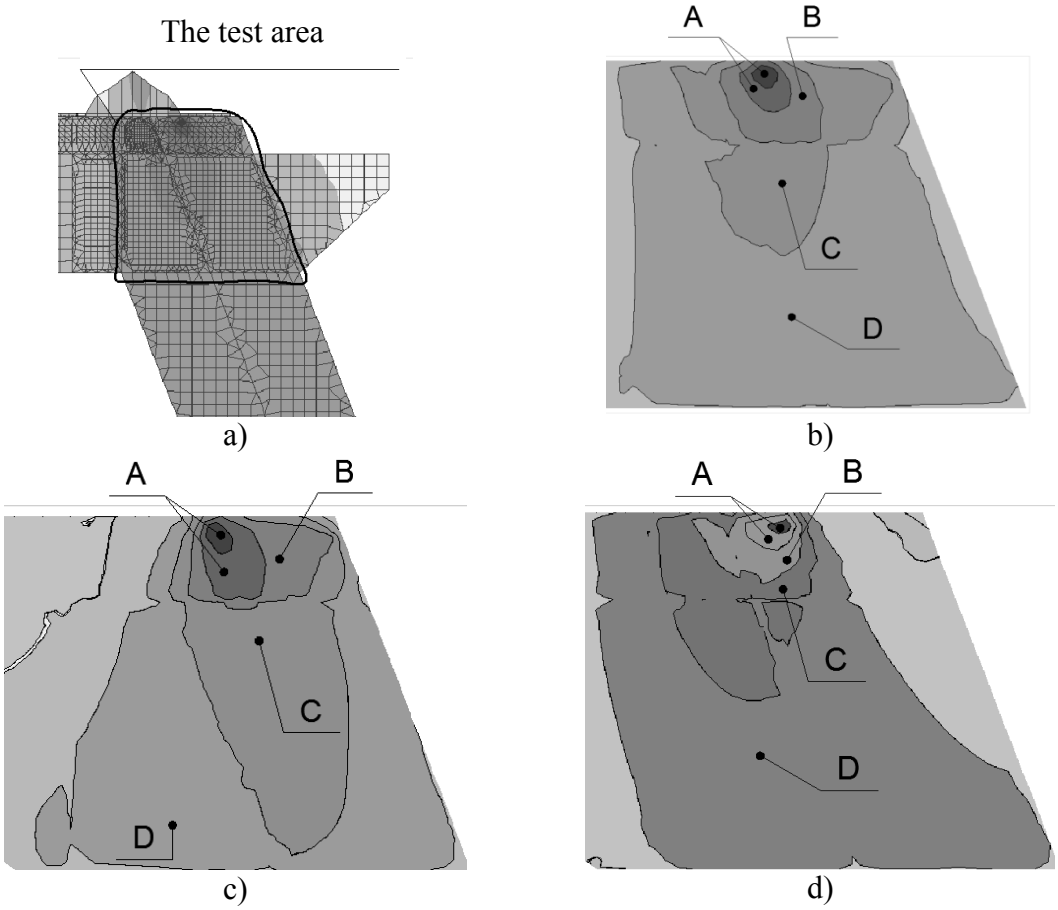

Figure 13: Areas of the local stress distribution in the resting node of the guide pulley (stress iso-fields): a) segment of the sub-pulley frame; b) σ_{red}; c) σ_x; d) τ_{xy}

From the above figure it is evident that the area of the local stress distribution (area «*A*») is under the front end of the guide pulley bearing. The area of the plane mode of deformation (area «*B*») is in the wall of the pulley attachment and is limited by a compartment under the front stop of the pulley bearing. The area of the plane mode of deformation (area «*C*») covers both the wall of the pulley attachment point and the girder wall. The area of the steady mode of deformation (area «*D*») covers the girder wall and connects to a slant leg of the sub-pulley frame.

The linear dimensions of the typical areas, connections to the pulley axis of rotation and the ratio of the height (*h*) and width (*d*) of the typical area to the length of the support bearing foot (*b*) are given in Table 2.

Table 2: Dimensions of local stress areas in the resting node of the guide pulley

Type of stresses	Area of stresses	Linear dimensions of the area (d x h), cm	Connection to the axis of rotation of the pulley, cm		d/b	h/b
			horizontally	vertically		
Σ_{red}	A	16 x 16	41	42	0.20	0.20
	B	39 x 30			0.49	0.38
	C	86 x 91			1.08	1.14
	D	150 x 135			1.88	1.69
σ_x	A	20 x 13	38	42	0.25	0.16
	B	40 x 25			0.50	0.31
	C	60 x 69			0.75	0.86
	D	150 x 135			1.88	1.69
τ_{xy}	A	25 x 31	46	46	0.31	0.39
	B	54 x 35			0.68	0.44
	C	66 x 127			0.83	1.59
	D	150 x 135			1.88	1.69

Note: b – the length of the guide pulley bearing foot; d – the area width; h – the area height. The intensities of the mode of deformation in the areas under study and the ratios of $\sigma_{max1}/\sigma_{max2}$, $\sigma_{xmax}/R_y\gamma_c$, $\sigma_{red}/1.15R_y\gamma_c$, and $\tau_{max}/0.58R_y\gamma_c$ are given in Table 3.

Table 3. The extremes of the local stresses in the resting node of the guide pulley

Stress area	σ_{max1}, MPa	σ_{max2} MPa	σ_{red} MPa	σ_{xmax}, MPa	τ_{max}, MPa	$\sigma_{max1}/\sigma_{max2}$	$\sigma_{max}/\sigma_{aver}$	$\sigma_{xmax}/R_y\gamma_c$	$\Sigma_{red}/1.15R_y\gamma_c$	$\tau_{max}/0.58R_y\gamma_c$
A	6.5	-361.0	364.3	-277.6	172.2	-0.018	3.8	0.99	1.1	1.1
B	49.5	-147.9	177.9	-163.7	105.6	-0.335	1.9	0.58	0.6	0.6
C	25.6	-121.2	135.8	-128.0	63.9	-0.212	1.4	0.46	0.4	0.4
D	9.0	-103.2	108.0	-81.7	47.7	-0.087	1.1	0.29	0.3	0.3

From the above table it is evident that areas «A» and «D» have a stress condition close to the mode of deformation with the ratios $\sigma_{max1}/\sigma_{max2}$ equal to 0.018 and -0.087, respectively. The areas «B» and «C» are the areas of the plane and stress state with the ratios $\sigma_{max1}/\sigma_{max2}$ equal to 0.335 and 0.212, respectively. The area «A» does not meet the strength requirements

because of the tangential and reduced stresses in the case of a combination of loads that will result in failure.

The maximum values of σ_{max1}, σ_{max2}, σ_{red}, $\sigma_{x\ max}$, $\sigma_{y\ max}$, τ_{max} in the resting node of the guide pulley at different parameters of the resultant of the cable tension and the ratios of the maximum to the average stresses in the area of study ($\sigma_{max}/\sigma_{aver}$) are given in Table 4 and Fig. 14.

Table 4. The extreme values of local stresses in the resting node of the guide pulley as the resultant inclination changes

α, degrees	σ_1, MPa	σ_2, MPa	Σ_{red}, MPa	$\sigma_{x\ max}$, MPa	$\sigma_{y\ max}$, MPa	$\tau_{max.}$ MPa	σ_1/σ_2	$\sigma_{max}/\sigma_{aver}$
30	10.2	-369.7	374.9	-334.0	-56.5	171.2	-0.028	4.57
35	9.3	-369.2	373.9	-332.4	-58.3	172.3	-0.025	4.33
40	8.3	-367.1	371.3	-329.2	-59.8	172.7	-0.023	4.09
45	7.2	-363.1	366.8	-324.3	-61.1	172.3	-0.020	3.86
50	6.1	-357.4	360.5	-317.7	-62.2	171.1	-0.017	3.65
55	5.0	-350.1	352.6	-309.6	-63.1	169.2	-0.014	3.44
60	3.9	-341.1	343.0	-299.9	-63.7	166.5	-0.011	3.24
65	2.7	-330.6	332.0	-288.8	-64.1	163.0	-0.008	3.04

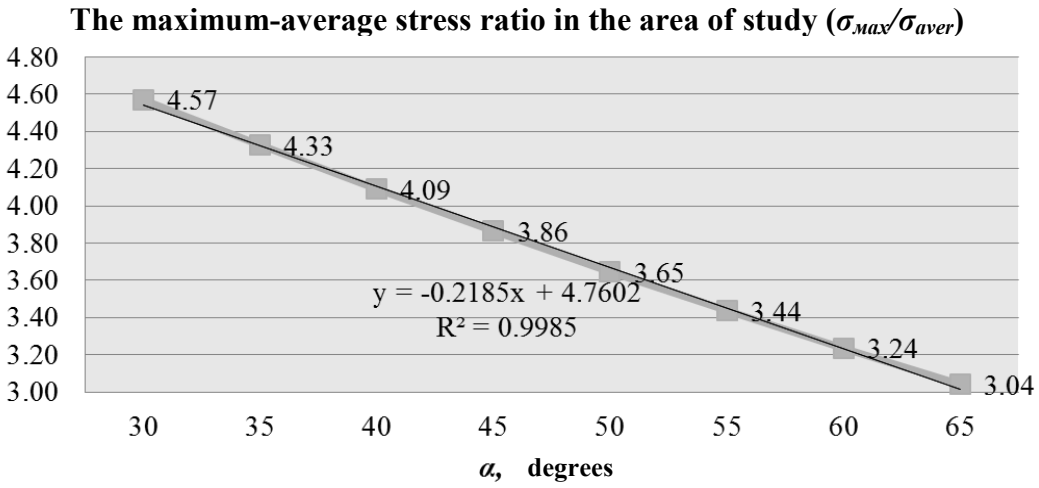

Figure 14: The maximum-average stress ratio in the area of study at different parameters of the resultant of the hoisting cable tension.

With regards to local stresses in the sub-pulley structures, it was discovered that strength capacity limits were reached due to tangential and reduced stresses. Two methods of enhancing the node were theorized. Additional cross ribs could be placed under the exposed

face of the support bearing: a) vertical rib; b) inclined rib (the rib inclination corresponds to the inclination of the resultant of the cable tension), see Fig. 15 and Table 5.

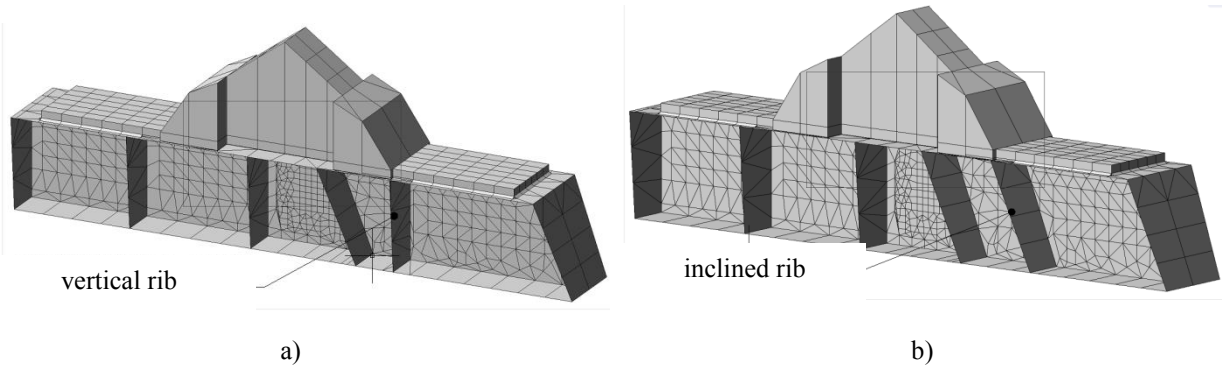

Figure 15: Cross ribs under the exposed face of the support bearing: a) vertical rib; b) inclined rib

Table 5. The extreme values of local stresses in the resting node of the guide pulley for two different additional cross ribs placements

Rib arrange-ment	σ_{max1}, MPa	σ_{max2} MPa	$\sigma_{прив.}$ MPa	σ_{xmax}, MPa	$\tau_{max.}$ MPa	$\sigma_{max1}/\sigma_{max2}$	$\sigma_{max}/\sigma_{aver}$	$\sigma_{xmax}/R_y\gamma_c$	$\sigma_{red}/1.15R_y\gamma_c$	$\tau_{max.}/0.58R_y\gamma_c$
Vertical	72.5	-185.2	230.2	-153.8	117.8	-0.4	2.0	0.5	0.7	0.7
Inclined	145.6	-178.4	281.1	-169.7	121.0	-0.8	2.2	0.6	0.9	0.7

From the above table it is evident that a vertical rib arrangement under the exposed face of the support bearing is more effective than an inclined rib arrangement, because the maximum-average stress ratios ($\sigma_{max}/\sigma_{aver}$) are lower in the area of study.

4 CONCLUSIONS

1. In the study, an excess of the reduced stresses in the sub-pulley structures was revealed. The reason for this lies in a zone of local stresses in the nodes of resting of the guide pulley bearings.

2. As a result of the numerical experiment, the following typical areas of distribution of local stresses in the resting node of the guide pulley were revealed: : «*A*» – the area of the local stress distribution under the support bearing foot close to the linear stressed state ($\sigma_{max1}/\sigma_{max2}$ = -0.018); «*B*» – the area of the plane mode of deformation in the wall of the pulley attachment point ($\sigma_{max1}/\sigma_{max2}$ = -0.335); «*C*» – the area of the plane mode of deformation in the girder wall ($\sigma_{max1}/\sigma_{max2}$ = -0.212); «*D*» – the area of the steady mode of deformation in the girder wall close to the linear stressed state ($\sigma_{max1}/\sigma_{max2}$ = -0.087).

In the area of local stresses «A» in the girder wall of the sub-pulley structure an area for which no strength by tangential and reduced stresses (σ_{red} /$1.15R_y\gamma_c$=1.1; $\tau_{max.}/0.58R_y\gamma_c$=1.1) was provided in case of the accidental combination of loads.

3. To provide the strength of the girder walls in the resting nodes of the guide pulley, it is recommended to place additional double vertical ribs under the exposed face of the support bearing in accordance with the diagram given in Fig. 15.

4. The maximum-average stress ratio ($\sigma_{max}/\sigma_{aver}$) in the girder wall of the sub-pulley structure in the zone of local stresses «A» changes from 4.57 to 3.04 as the inclination of the resultant of the hoisting cable tension changes in the range of 30^0 … 65^0.

5. The connection between the center of the area of local stresses (area «A») to the pulley axis of rotation is constant as the inclination of the resultant of the hoisting cable tension changes. Both the width and height of this area increases 1.7 times as the inclination of the resultant changes. This relationship has linear characteristics.

REFERENCES

[1] Standard II-23-81*. Codes of design. Steel structures /— M.: CITP Gosstroy of the USSR, 1991. — 96 p.

[2] Standard 1.2-2:2006. Loads and effects. – Kyiv: Minstroy of Ukraine, 2006 – 78 p.

[3] Standard 12.005-94. Metal structures of the shaft headgears. Operation demands. K.: Gosugleprom of Ukraine, 1994. — 68 p.

[4] Standard 12.003-92. The order and organization of observation of bearing metal structures of shaft headgears. K.: Gosugleprom of Ukraine, 1993. — 102 p.

[5] Standard 12.011-96. Buildings and structures of the technological complexes of the mining site. Operation demands. K.: Gosugleprom of Ukraine, 1996. — 75 p.

[6] Standard 46-75. Instructions to determine loads on buildings and structures of the coal mining industry. Donetsk, 1977. – 89 p.

[7] Instructions to determine the normative loads and coefficients of overloads for mine yard and structures of the coal mining industry. K.: Budivel'nyk, 1964. – 81 p.

[8] Gorokhov E.V., Kushchenko V.N. Reserves of the bearing ability of steel structures under short-time dynamic effects // Proc. Prospects of the development and ways of increasing the efficiency of using light and specially light metal structures. – K., 1984. – P. 103-104.

[9] Kushchenko V.N., Nechitailo A.E. Analysis of the mode of deformation of the main bearing elements of the frame-type sloping shaft headgears // Metal Structures. – Vol. 17. – No.3. – Makiyivka, 2011. – P. 151-165.

[10] Zherbin M.M. Development of the civil engineering science and technique in the UkSSR: in 3 volumes // AS UkSSR. – K.: Naukove Dumka, 1989. – 308 p.

[11] Zherbin M.M., Vladimirsky V.A. Investigation of the static effects of the wind flow on the tower headframes / Abstract information about the completed researches at the universities. – Civil Engineering, Architecture, Building materials and items. Vol. 6. –

K.: Higher School, 1972. – P. 22-25.

[12] Kushchenko V.N., Kostritsky A. S. An experimental study of the dynamics of the shaft headgear structures. – Visnyk DonDABA 2003-2 (39). Vol. 2. Building structures: materials, structures, technologies. – P. 46-52.

[13] Kushchenko V.N., Kostritsky A. S., Nekrasov Yu.P. Methods and results of the dynamic tests of the sloping shaft headgear // Visnyk DonDABA. Building structures. 2003-2 (39). – P. 116-125.

[14] Balkarey I.M. Determination of the extreme dynamic loads on the structures of shaft headgears // Proc. III Conference of Young Civil Engineering Scientists. Issues of the Up-to-date construction and architecture // K.: Budivel'nyk, 1965. – P. 274-283.

[15] Balkarey I.M. Special loads on the structures of mine and shaft headgears // In: Dynamics and strength of structures. K.: Budivel'nyk, 1965. – P. 60-63.

[16] Balkarey I.M., Koltakova G.V. Vibrations of sloping headgears at a special fracture of the mine hoisting rope // In: Dynamics and strength of building structures. K.: Budivel'nyk, 1965. – P. 50-64.

[17] Perel'muter A.V., Slivker V.I. Design models of structures and a possibility of their realization. – K.: Kompas, 2001. – 446 p.

[18] Metal Structures. In 3 vol./ Ed.: V.V. Kuznetsov (N.L. Mel'nikov DNIIproektstal'konstruktsiya). – M.: ACB Publishing House, 1998. – (Designer's Handbook).

[19] Murgewski J. Reliability: State-of-Art, EX International Conference on Metal Structures,. Final Report. – Krakov, Poland, 1996. – P. 99-112.

[20] Recommendation for Loading and Safety Regulations for Structural Design Nordic Committee on Duilding Regulations, 1978.

19th International Conference on the Application of Computer
Science and Mathematics in Architecture and Civil Engineering
K. Gürlebeck, T. Lahmer and F. Werner (eds.)
Weimar, Germany, 04–06 July 2012

ON M-CONFORMAL MAPPINGS AND GEOMETRIC PROPERTIES

Nguyen Manh Hung* **and Klaus Gürlebeck**

**Institute of Mathematics and Physics - Bauhaus Universität Weimar*
Coudray Str. 13B, 99423 Weimar, Germany
E-mail: hung.manh.nguyen@uni-weimar.de

Keywords: M-conformal mappings, monogenic functions, solid angles, geometric mapping properties.

Abstract. *Monogenic functions play a role in quaternion analysis similarly to that of holomorphic functions in complex analysis. A holomorphic function with non-vanishing complex derivative is a conformal mapping. It is well-known that in $\mathbb{R}^{n+1}, n \geq 2$ the set of conformal mappings is restricted to the set of Möbius transformations only and that the Möbius transformations are not monogenic. The paper deals with a locally geometric mapping property of a subset of monogenic functions with non-vanishing hypercomplex derivatives (named M-conformal mappings). It is proved that M-conformal mappings orthogonal to all monogenic constants admit a certain change of solid angles and vice versa, that change can characterize such mappings. In addition, we determine planes in which those mappings behave like conformal mappings in the complex plane.*

1 INTRODUCTION

The complex function theory is considered as the theory of holomorphic functions, which are null solutions of the Cauchy-Riemann operator. In quaternionic analysis, monogenic functions are a generalization of holomorphic functions in the sense that they are null solutions of the so-called generalized Cauchy-Riemann operator and they share with holomorphic functions so many common properties such as integral representations, mean value theorems, maximum principles, series expansions and etc.

One of the most interesting points of a holomorphic function is that it realises in a domain $\Omega \subset \mathbb{C}$ a conformal mapping providing that its $\mathbb{C}$-derivative is different from zero in Ω. It is well known that in $\mathbb{R}^n,\ n > 2$, only Möbius transformations have the property of conformality and they are not monogenic. Similarly to the complex analysis, we say that a monogenic function with non-vanishing hypercomplex derivative realises in a domain a M-conformal mapping (M stands for monogenic). It arises naturally a question: which geometric mapping properties characterize M-conformal mappings, or how can we generalize the result of conformality from complex case to higher dimensional spaces?

There are several attempts to describe geometric mapping properties of M-conformal mappings. Among others, H. Malonek proved that M-conformal mappings preserve angles where angles in his sense must be understood in terms of "Clifford measures" (see also [7]), while in [8, 9] J. Morais showed that locally M-conformal mappings map a ball to a specific type of ellipsoids with the property that the length of one semi-axis is equal to sum of lengths of two other semi-axes. In fact, in [7] apart from introducing the "Clifford measures" of a surface, the author measures not angles between curves, but angles between hypersurfaces. That means a generalization of angles from the complex plane (between curves) to higher dimensional spaces (between hypersurfaces). These results motivate us to study actions of M-conformal mappings on solid angles in $\mathbb{R}^3$.

In section 3, we have proved that actually M-conformal mappings change also solid angles. However, there exists a subclass of monogenic functions which admits a certain change of a specific type of solid angles. These are monogenic functions with non-vanishing hypercomplex derivatives and orthogonal to all monogenic constants. The inversion theorem is also true, i.e a mapping admits such a change of such solid angles must be in that subclass. Therefore that geometric mapping property can characterize some M-conformal mappings. These results are stated for linear mappings only but it holds for general mappings. The fact is that the actions of general mappings on solid angles are completely determined by their linear parts and based on the relation between the linear part and the whole function at the origin (see also [8]), one can state the results for both of them. The section 4 is about the role of M-conformal mappings on some planes analogously to that of holomorphic functions on the complex plane. They are not conformal with respect to every angles between curves but we determine some planes where they preserve such angles.

2 PRELIMINARIES

2.1 Some Definitions and Notations

Let $\mathbb{H}$ be the skew field of real quaternions with basic elements $\{1, e_1, e_2, e_3\}$ satisfying:

$$e_i e_j + e_j e_i = -2\delta_{ij}, \quad (i, j = 1, 2, 3)$$

Denote by $\mathcal{A} := span_{\mathbb{R}}\{1, e_1, e_2\}$ a subset of $\mathbb{H}$. Each $x := (x_0, x_1, x_2) \in \mathbb{R}^3$ can be identified with $x := x_0 + x_1e_1 + x_2e_2 \in \mathcal{A}$. As usual, we define $Sc(x) := x_0$, $\overline{x} := x_0 - x_1e_1 - x_2e_2$ and $|x| := \sqrt{x_0^2 + x_1^2 + x_2^2}$, respectively.

Let $f : \mathbb{R}^3 \supset \Omega \to \mathcal{A}$, $f(x) = [f(x)]_0 + [f(x)]_1e_1 + [f(x)]_2e_2$, be a reduced quaternion-valued function where $[f(x)]_i$ $(i = 0, 1, 2)$ are real-valued functions. Denote by $L_2(\Omega; \mathcal{A}; \mathbb{R})$ the real-linear Hilbert space of square integrable A-valued functions defined in Ω endowed with the scalar-valued inner product:

$$\langle f, g\rangle_{L_2(\Omega,\mathcal{A},\mathbb{R})} := \int_\Omega Sc(\overline{f}g)dV \tag{1}$$

We introduce a so-called generalized Cauchy-Riemann operator by

$$D := \frac{\partial}{\partial x_0} + \frac{\partial}{\partial x_1}e_1 + \frac{\partial}{\partial x_2}e_2$$

Definition 2.1. *A C^1-function f is called monogenic in a domain Ω if it satisfies $Df = 0$ in Ω.*

With the adjoint Cauchy-Riemann operator $\overline{D} := \frac{\partial}{\partial x_0} - \frac{\partial}{\partial x_1}e_1 - \frac{\partial}{\partial x_2}e_2$, it is well-known that the Laplacian operator in $\mathbb{R}^3$ can be decomposed into $\Delta = D\overline{D} = \overline{D}D$. It means that the class of monogenic functions is a subset of harmonic functions.

Definition 2.2. *Let f be a monogenic function in Ω. The expression $\frac{1}{2}\overline{D}f$ is called the hypercomplex derivative of f in Ω.*

Definition 2.3. *A C^1-function is called a monogenic constant if it is monogenic and its hypercomplex derivative is equal to zero.*

Example: $f = x_1e_1 - x_2e_2$ is a monogenic constant.

Remark 2.1. *In [7], H. Malonek introduced the definition of M-conformal mappings and proved that these are equivalent to monogenic functions with non-vanishing hypercomplex derivatives.*

2.2 Complete Elliptic Integrals

We introduce *Complete Elliptic Integrals* of the *first, second and third kind* which will be used in the next sections

$$\mathcal{K}(k) := \int_0^1 \frac{dt}{\sqrt{(1-t^2)(1-k^2t^2)}},$$

$$\mathcal{E}(k) = \int_0^1 \sqrt{\frac{1-k^2t^2}{1-t^2}}dt,$$

$$\Pi(n,k) := \int_0^1 \frac{dt}{(1-nt^2)\sqrt{(1-t^2)(1-k^2t^2)}}.$$

They have the following properties:

- $\mathcal{K}(0) = \Pi(0,0) = \frac{\pi}{2}$.
- $\frac{d}{dk}\mathcal{K}(k) = -\frac{1}{k}\mathcal{K}(k) + \frac{1}{k(1-k^2)}\mathcal{E}(k)$.
- $\frac{\partial}{\partial n}\Pi(n,k) = \frac{1}{2(k^2-n)(n-1)}[\mathcal{E}(k) + \frac{k^2-n}{n}\mathcal{K}(k) + \frac{n^2-k^2}{n}\Pi(n,k)]$.
- $\frac{\partial}{\partial k}\Pi(n,k) = \frac{k}{n-k^2}\left(\frac{1}{k^2-1}\mathcal{E}(k) + \Pi(n,k)\right)$.

For more information, see also [5, 6].

3 M-CONFORMAL MAPPINGS WITH SOLID ANGLES

We investigate now the change of solid angles under linear M-conformal mappings $F(x) = ax_0 + bx_1e_1 + cx_2e_2$, where a, b, c are real, non-zero and have same signs. We refer readers to J. Morais' dissertation [8] to see how general linear monogenic mappings can be transformed to our case.

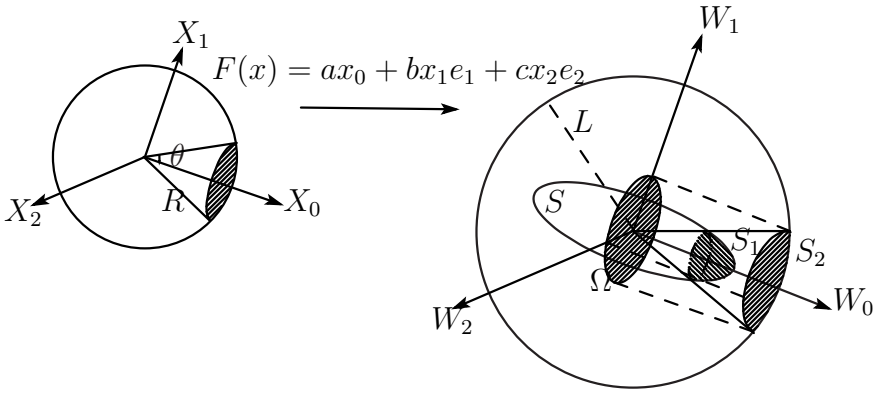

Figure 1: The mapping $F(x)$ changes the solid angle

Let's consider a cone around the x_0-axis characterized by an angle θ as shown in the Figure 1. In order to calculate the solid angle of such a cone, we draw a sphere with the radius R. The area of the surface on the sphere which lies inside the θ-cone can be computed as follow:

$$S_x = \iint_D \sqrt{1 + \left(\frac{\partial x_0}{\partial x_1}\right)^2 + \left(\frac{\partial x_0}{\partial x_2}\right)^2}\, dx_1 dx_2,$$

where $D = \{(x_1, x_2) : x_1^2 + x_2^2 \leq R^2 \sin^2(\theta)\}$ is the projection of the considered surface on the plane $\mathbb{R}^2(x_1, x_2)$ and $x_0 = \sqrt{R^2 - x_1^2 - x_2^2}$. With simple calculations, it leads to:

$$S_x = 2\pi R^2(1 - \cos(\theta)).$$

Then the solid angle of the cone is:

$$\frac{S_x}{R^2} = 2\pi(1 - \cos(\theta)). \tag{2}$$

By applying the linear mapping $F(x) = ax_0 + bx_1e_1 + cx_2e_2$, where a, b, c are all real positive (or negative) numbers, the sphere of radius R transforms into an ellipsoid S, the cone changes to ellipse-based cone and the surface on the ellipsoid restricted by the ellipse-based cone becomes S_1. In order to calculate the solid angle in this case, we draw another sphere with radius L, then project S_1 onto the L-sphere according to the ellipse-based cone and get S_2.

It can be proved that the projection of S_2 on the plane $\mathbb{R}^2(w_1, w_2)$, namely Ω, is an ellipse with the two semi-axes:

$$\begin{cases} A_1 &= L\frac{\delta \tan(\theta)}{\sqrt{1+\delta^2 \tan^2(\theta)}} \\ A_2 &= L\frac{\varepsilon \tan(\theta)}{\sqrt{1+\varepsilon^2 \tan^2(\theta)}} \end{cases}$$

where $\delta = b/a$, $\varepsilon = c/a$.

Similarly, the changed solid angle restricted by S_2 can be calculated:

$$\frac{S_w}{L^2} = 2\pi + \frac{4A_1A_2}{L\sqrt{L^2-A_2^2}}\mathcal{K}\left(\sqrt{\frac{A_1^2-A_2^2}{L^2-A_2^2}}\right) - \frac{4LA_1}{A_2\sqrt{L^2-A_2^2}}\Pi\left(\frac{A_2^2-A_1^2}{A_2^2}, \sqrt{\frac{A_1^2-A_2^2}{L^2-A_2^2}}\right). \tag{3}$$

Remark 3.1. *In fact, S_w/L^2 does not depend on L. However for a short expression, we prefer the formula (3).*

We define the change of such a solid angle under the mappings $F(x)$ by:

$$K_F(\theta) := \frac{S_w/L^2}{S_x/R^2} = \frac{1}{2\pi(1-\cos(\theta))}\frac{S_w}{L^2}. \tag{4}$$

Theorem 3.1. *Let $F(x) = ax_0 + bx_1e_1 + cx_2e_2$ be a bijective linear mapping on $\mathbb{R}^3$. Moreover suppose that F is monogenic and orthogonal to all monogenic constants. Then F changes the solid angle characterized by the angle θ around the x_0-axis by*

$$K_0(\theta) = \frac{1}{1-\cos(\theta)}\left(1 - \frac{2}{\sqrt{4+\tan^2(\theta)}}\right). \tag{5}$$

Proof. If $F(x)$ is monogenic and orthogonal to all monogenic constants, then $a = 2b = 2c$. The result follows directly. □

One is asking whether the quantity $K_0(\theta)$ characterizes uniquely mappings which are monogenic and orthogonal to all monogenic constants?

Theorem 3.2. *Let $F(x) = ax_0 + bx_1e_1 + cx_2e_2$ be a bijective linear mapping in $\mathbb{R}^3$, where a, b, c are real and have the same signs. The necessary and sufficient condition for $F(x)$ to be monogenic and orthogonal to all monogenic constants is that it changes the solid angle characterized by θ around the x_0-axis by $K_0(\theta)$ as in* (5)*.*

Consider the function

$$f(\varepsilon) = \frac{\pi}{2} + \frac{\varepsilon}{\sqrt{16\varepsilon^2+1}}\mathcal{K}\left(\sqrt{\frac{1-16\varepsilon^4}{16\varepsilon^2+1}}\right) - \frac{1+\varepsilon^2}{\varepsilon\sqrt{16\varepsilon^2+1}}\Pi\left(\frac{16\varepsilon^4-1}{\varepsilon^2(16\varepsilon^2+1)}, \sqrt{\frac{1-16\varepsilon^4}{16\varepsilon^2+1}}\right). \tag{6}$$

We have

Lemma 3.1. *Let $f(\varepsilon)$ have the form as in* (6)*, then the derivative of $f(\varepsilon)$ is given as follows:*

$$f'(\varepsilon) = \frac{1}{(\varepsilon^2+1)\sqrt{16\varepsilon^2+1}(1-16\varepsilon^4)} \times \left((16\varepsilon^4+32\varepsilon^2+1)\mathcal{E}\left(\sqrt{\frac{1-16\varepsilon^4}{16\varepsilon^2+1}}\right) - (32\varepsilon^4+32\varepsilon^2)\mathcal{K}\left(\sqrt{\frac{1-16\varepsilon^4}{16\varepsilon^2+1}}\right)\right). \tag{7}$$

Proof. It comes directly from the properties of the complete elliptic integrals. □

Proof. (theorem 3.2)

- Consider the equation $K_F(\theta) \equiv K_0(\theta)$.
- At $\theta = 0 \implies \delta = \frac{1}{4\varepsilon}$
- At $\theta = \pi/4$, we obtain

$$K_F(\frac{\pi}{4}) = \frac{2}{\pi(1 - \frac{\sqrt{2}}{2})} f(\varepsilon). \tag{8}$$

The Figure 2 shows that $f(\varepsilon)$ and therefore $K_F(\frac{\pi}{4})$ takes the maximum value at $\varepsilon = 1/2$.

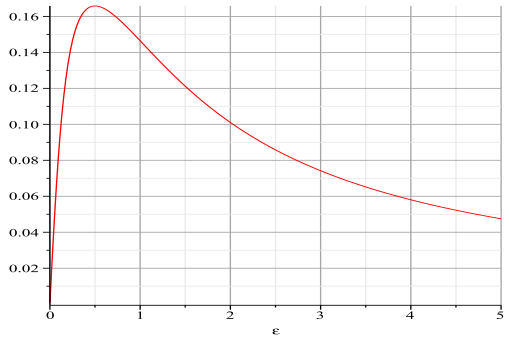

Figure 2: The graph of function $f(\varepsilon)$

This can be proved according to the lemma 3.1. It means that $K_0(\frac{\pi}{4}) = K_F(\frac{\pi}{4})$ has the unique solution $\varepsilon = 1/2$. This completes the proof.

□

4 M-CONFORMAL MAPPINGS ON PLANES

We have proved that on the x_0-direction, a mapping $F(x) = ax_0 + bx_1e_1 + cx_2e_2$ admits a certain change of solid angles providing that it is monogenic and orthogonal to all monogenic constants. In addition, $F(x)$ maps a ball to a prolate spheroid which is symmetric with respect to x_0-axis. A question follows: How does the mapping $F(x)$ behave on planes which are perpendicular to the x_0-axis?

Theorem 4.1. *Let $F(x) = ax_0 + bx_1e_1 + cx_2e_2$ be a function defined in a domain $\Omega \subset \mathbb{R}^3$ with non-vanishing Jacobian determinant. Suppose further that $F(x)$ is monogenic and orthogonal to all monogenic constants, then $F(x)$ preserves angles on planes which are perpendicular to the x_0-axis.*

Proof. Without loss of generality, let's consider the plane $\mathbb{R}^2(x_1, x_2)$. Then

$$F(x)\Big|_{\mathbb{R}^2(x_1,x_2)} = bx_1e_1 + cx_2e_2 \tag{9}$$

is identified with a (linear) complex function, $f(z) = bx + icy$. The assumptions in the theorem lead to $\partial_{\overline{z}} f(z) = 0$, and consequently $f(z)$ is a holomorphic function. This means that the restriction of $F(x)$ to the plane $\mathbb{R}^2(x_1, x_2)$ is a conformal mapping. □

Remark 4.1. *This is a special property because usually the restriction of a monogenic function to a plane is not a holomorphic function there.*

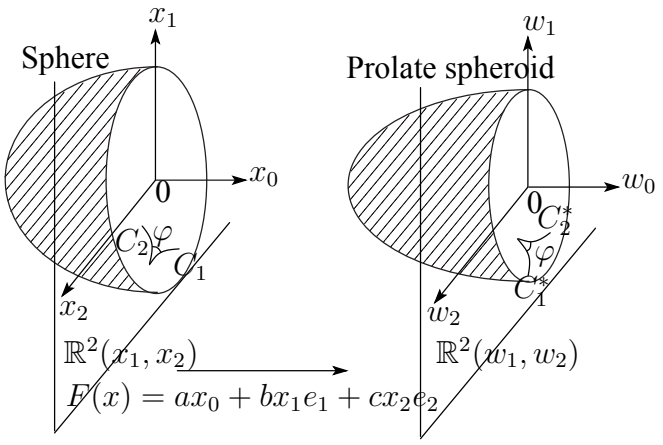

Figure 3: Monogenic mappings preserves angles on the plane $\mathbb{R}^2(x_1, x_2)$.

REFERENCES

[1] F. Brackx, R. Delanghe and F. Sommen: Clifford Analysis, Pitman Publishing, Boston-London-Melbourne, 1982.

[2] K. Gürlebeck and W. Sprößig: Quaternionic Analysis and Elliptic Boundary Value Problems, Akademie Verlag, Berlin, 1989.

[3] K. Gürlebeck and H. Malonek: A hypercomplex derivative of monogenic functions in Rn+1 and its applications, Complex Variables 39, 199-228, 1999.

[4] K. Gürlebeck and J. Morais: On mapping properties of monogenic functions, CUBO A Mathematical Journal, Vol. 11, No. 1, 73-100, 2009.

[5] Harris Hancock: Lectures on Theory of Elliptic Functions, John Wiley & Sons Inc, 1910.

[6] Harris Hancock: Elliptic Integrals, John Wiley & Sons Inc, 1917.

[7] Helmuth R. Malonek: Contributions to a Geometric Function Theory in Higher Dimensions by Clifford Analysis Methods: Monogenic Functions and M-conformal mappings, Kluwer Academic Publishers, 2001.

[8] J. Morais: Approximation by homogeneous polynomial solutions of the Riesz system in $\mathbb{R}^3$, PhD. diss., Bauhaus-Universität Weimar, 2009.

[9] J. Morais - K. Gürlebeck: On local mapping properties of monogenic functions, 18th International Conference on the Application of Computer Science and Mathematics in Architecture and Civil Engineering, Weimar, 2009.

19th International Conference on the Application of Computer
Science and Mathematics in Architecture and Civil Engineering
K. Gürlebeck, T. Lahmer and F. Werner (eds.)
Weimar, Germany, 04–06 July 2012

ROBUSTNESS IN CIVIL ENGINEERING - INFLUENCES OF THE STRUCTURAL MODEL ON THE EVALUATION OF STRUCTURAL ROBUSTNESS

F. Scheiber* **and F. Werner**

**Bauhaus-Universität Weimar, Faculty of Civil Engineering*
DFG Research Training Group 1462
Berkaer Str. 9, 99423 Weimar
E-mail: frank.scheiber@uni-weimar.de

Keywords: IKM 2012, Civil Engineering, Structural Robustness, Model Quality

Abstract. *The topic of structural robustness is covered extensively in current literature in structural engineering. A few evaluation methods already exist. Since these methods are based on different evaluation approaches, the comparison is difficult. But all the approaches have one in common, they need a structural model which represents the structure to be evaluated. As the structural model is the basis of the robustness evaluation, there is the question if the quality of the chosen structural model is influencing the estimation of the structural robustness index.*

This paper shows what robustness in structural engineering means and gives an overview of existing assessment methods. One is the reliability based robustness index, which uses the reliability indices of a intact and a damaged structure. The second one is the risk based robustness index, which estimates the structural robustness by the usage of direct and indirect risk. The paper describes how these approaches for the evaluation of structural robustness works and which parameters will be used. Since both approaches needs a structural model for the estimation of the structural behavior and the probability of failure, it is necessary to think about the quality of the chosen structural model. Nevertheless, the chosen model has to represent the structure, the input factors and reflect the damages which occur. On the example of two different model qualities, it will be shown, that the model choice is really influencing the quality of the robustness index.

1 INTRODUCTION

A large amount of design parameters exist in structural engineering, which have to be taken into account during the design process. A very crucial, but sometimes neglected design parameter is the structural robustness. However, a number of structural collapses in the past [1] have led to a growing importance of this topic. Therefore the topic of structural robustness has been increasingly addressed in literature in recent years. Such that the discussions regarding the development of a practical measurement for the determination of structural robustness have already started. Several approaches for the evaluation of the structural robustness were developed and already exist [2].

The evaluation approaches are based on the probability of failure according to a given input scenario. So it is necessary to evaluate the structural behavior. The basis for this is a structural model, which has to represent all significant input factors. That means it must be able to represent the structural system as well as the influencing loads. For the evaluation of robustness it is necessary that damage in the structural system occurs. That being the case, the structural model must also be able to reflect damage. This shows that the right choice of the structural model highly influences the evaluation process for the structural robustness.

Also, the Eurocodes addresses the topic of structural robustness in DIN-EN 1990 [3] and DIN-EN 1991-1-7 [4]. An overview and also some additional background information are given in [5]. This shows that the topic of structural robustness is gaining more and more attention. Therefore, it is essential to consider the quality of the existing approaches and the influences of the used structural models.

2 THE TERM ROBUSTNESS

2.1 Robustness in other disciplines

The word robust originated from the Latin word *rōbustus*, which means *hard, resistant, strength*. The word robustness is often used in the field of science and describes the property of an object or activity. But as shown in table 1, the meaning of the word robustness sometimes differs.

In technical disciplines, robustness is a sign of high quality. Thus, for example, robust machines can work without any problems under a substantial number of difficult conditions. A partial overload or short-term incorrect use does not lead to damages [6]. That means, an increase of robustness are always equated with an increase in product quality. Therefore, the goal of a more robust product is clearly comprehensible and can be implemented effectively.

2.2 Robustness in structural engineering

In structural engineering, the definition of robustness is not so transparent like in technical disciplines. Because of that, there are some cases where wrong definitions of the term structural robustness exist. The common definition of robustness in structural engineering is related to the behavior of a structure, to resist an occurred input scenario, which temporarily exceeds the limit state of the structure. Thereby, a part of the structural system directly fails by reaching the load bearing capacity. But the rest of the structure has to be stable and rearrange the loads in such a way that no further structural elements fails. This means that the average of damage has to be proportional to the resulting input scenario [7]. Another scenario which has to be considered

Table 1: Different disciplines - Different definitions of robustness [8]

Discipline	Definition
Structural Standards	The consequences of structural failure are not disproportional to the effect causing the failure...
Software Engineering	The ability...to react appropriately to abnormal circumstances (i.e., circumstances "'outside of specifications"'). A system may be correct without being robust...
Product Development	The measure of the capacity of a production process to remain unaffected by small but deliberate variations of internal parameters so as to provide an indication of the reliability during normal use...
Statistics	A robust statistical technique is insensitive against small deviations in the assumptions...
Design Optimization	A robust solution in an optimization problem is one that has the best performance under its worst case...

for a robust structure, is the ability of the structure to compensate for deviations between the designed model and the created structure. Since human errors during the building process are sometimes not negligible, the structure needs to be stable against variations in the execution. Also, human errors can occur during the design process. However, since the topic of human errors in structural engineering is expansive, it will not be further addressed in this paper. For further information, there is an ample amount of available literature (e.g. [9] to [12]).

The requirements for structural robustness are sometimes implicitly integrated in the existing codes and design methods, without using the word robustness. Thus, the structural engineer is sometimes more connected with the subject of robustness than he/she is aware of. One example is the design of redundant structures. By the design of more support conditions than necessary, the system includes unused bearing capacities, which can be exhausted in the case of local damage (formation of plastic hinges). Another example is the structural design of a Gerber girder. The arrangement of the hinges has to be in such a way, that the failure of one part of the girder does not lead to a collapse of the overall system.

There are also structural properties which really have to be separated from the topic of structural robustness. The requirement that a structural system has to announce a failure or collapse with high deformations or by the formation of cracks is not related to the term robustness. This is only the request on ductility. Ductility also includes the usage of non-brittle materials. An example, where non-existing ductility leads to a structural collapse is the progressive collapse of power line towers in Westphalia in the year 2005. Due to the structures being more than 50 years old, the codes in existence at this time did not consider the topic of ductility - the structures were constructed with converter steel [7]. Today this type of steel is not allowed in structural engineering, since the problems of ductility and sensitivity to aging is common knowledge nowadays.

2.3 Non-robust structures

History has shown that there were several structural collapses in the past, which could be related to non-robust structures. This means that the consequences of damage were extensively higher than the original causes. One of the most famous structural failures according to a less robust structure is the "'Ronan Point Disaster"' in 1968 in East London [13]. Due to a small explosion in one of the upper floors, a section of the building completely collapses, shown in figure 1. The insufficient design of a connection point, which was not resistant against horizontal loads led to this disaster. Another example for a collapse of a structure related to a non-robust system is the collapse of the exhibition hall in Katowice (Poland) in the year 2006 [14]. The structural system consisted of a very light weight construction and an overload of only 20 % of snow led to the total collapse.

Figure 1: Progressive collapse of the Ronan Point Tower [7]

By considering the topic of structural robustness, it is important to have in mind that robust structures also cannot resist each input action. The design according to the actual standards leads to a bearing capacity dimensioning of each structural member and connection point regarding the given design loads, such that the structure is also robust against this loads. Thus, it is essential to note that an increasing of the assumed loads, an extraordinary load or a pre-damage in the structure leads to a decreasing of the structural robustness and thus to an increase in the probability of failure. The existing approaches for structural robustness uses these differences in the probability of failure to quantify the structural robustness of a system. An overview for different evaluation approaches is given in section 3.

As it is not feasible to check and establish the structural robustness for all potential loads and load histories in the lifetime of a structure, as well as all variations in the execution during the building process, it is necessary to think about the right choice of lifetime scenarios. In any case, the fact that with increasing robustness against several factors or scenarios the structure is also more and more expensive has to be considered.

3 QUANTIFICATION OF STRUCTURAL ROBUSTNESS

The quantification of structural robustness is one of the aspiring topics in structural engineering in the last years. The new Eurocodes addresses the topic and require, that structures have to be robust. This means that the structure has to react in such a way that the overall damage does not extend disproportionately to the original cause [3]. Thus, if an input scenario occurs and a part of the structural system exceeds the limit state and fails, the rest of the system must be able to be stable on its own. Since this declaration is not very comprehensible, different approaches for the evaluation of the structural robustness were developed. Two of them are the reliability based robustness index, which is described in section 3.1 and the risk based robustness index, which is shown in section 3.2. Other approaches are also available in the literature.

3.1 Reliability based robustness index

According to the fact that the probability of failure of a structural system changes with every modification of the loads or any damage scenario, it is possible to evaluate the structural robustness with the help of the system reliability index β, according to the approach of Frangopol and Curly [15]. The reliability index β is defined in equation 1, where Φ is the normal distribution function with $\overline{X} = 0$ and $\sigma = 1$ and P_f is the probability of failure of the considered system. In the safety concepts of structural engineering the reliability index β is strongly embedded, since the determination of the reliability level of a structure is already done by the reliability index β.

$$\beta = -\Phi^{-1}(P_f) \tag{1}$$

The reliability based robustness index by Frangopol and Curly [15], which is defined in equation 2, is based on two different reliability indices. The reliability of the intact structure, with normal design loads and without any damage is described by β_{intact}. Wherein $\beta_{damaged}$ is describing the reliability of the damaged system, which reaches the load bearing capacity by an extraordinary input scenario.

$$I_{Rob} = \frac{\beta_{damaged}}{\beta_{intact}} \tag{2}$$

The defined robustness index I_{Rob} could take values between zero and one, if both reliability indices are positive values. If the probability of failure from one of the systems is higher than 50 %, the robustness index becomes negative. In that case, the robustness is very low, since a robustness of one indicates the best robustness. That means if the robustness index of a structural system is one, there would be no change in the probability of failure after some damage has occurred.

The estimation of the probability of failure could be done by stochastic modeling and the usage of structural reliability methods according to the probabilistic model code [16].

3.2 Risk based robustness index

Another approach for the evaluation of the robustness of a structural system, is the risk based

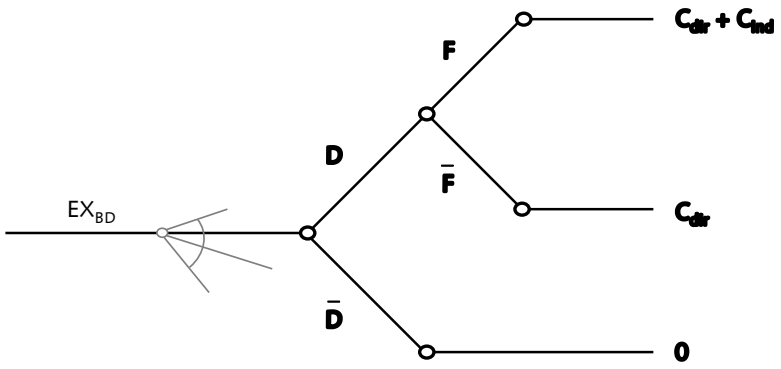

Figure 2: An event tree for robustness quantification [17]

The initial situation for the evaluation of the structural robustness is given by a structural model. This model describes the structural system and must be able to represents all the failure mechanisms and load or damage scenarios. By adding the first exposure EX_{BD}, the system has the potential to react in two different ways. The best way is, that the system is picking up the load without any damage, which leads to path $\overline{D}$ and no consequences appears. If the load is too high and some damage occurs, the system is following path D. The consequences arising from this damage, may be direct (C_{dir}) or indirect (C_{ind}). Direct consequences are those that result explicitly from the first exposure. In this case, damage occurs and one or more structural members fails. Afterwards the load rearranges to other structural members and the new system works independently. If damage occurs and the new system is not able to pick up all the rearranged loads and new damage occurs, it will be described by C_{ind} as indirect consequences. It is also possible, that in this way the whole structure fails. As a result, the consequences increase to a maximum.

Since the robustness index in the approach of Baker *et al.* [17] is defined by the ratio of direct and overall risk, as shown in equation 5, it is necessary to determine the risk of the structure. The term risk is defined as the effect of uncertainty on objectives [18], which means that in the context of structural engineering, risk is the probability of failure of a predefined input scenario multiplied with the consequences of this event [19]. In the case of the event tree shown, the direct risk could therefore be described by equation 3 and the indirect risk can be estimated by equation 4.

$$R_{Dir} = \int_x \int_y C_{Dir}\, f_{D|EX_{BD}}(y|x)\, f_{EX_{BD}}(x)\, dy\, dx \tag{3}$$

$$R_{Ind} = \int_x \int_y C_{Ind}\, P(F|D=y)\, f_{D|EX_{BD}}(y|x)\, f_{EX_{BD}}(x)\, dy\, dx \tag{4}$$

The robustness index I_{Rob} as shown here can assume values between zero and one, where one indicates a structure without any indirect risk. This means one indicates the highest robustness, where no additional failure occurs. To make this a little bit clearer, there is an application of this risk based robustness evaluation in section 5.

$$I_{Rob} = \frac{R_{Dir}}{R_{Dir} + R_{Ind}} \tag{5}$$

4 STRUCTURAL MODELS

A high number of partial models are already in existence in structural engineering. These could be used to model and evaluate the structural behavior or the load bearing capacity of a structural system. Therefore it is necessary, to really think about the right choice of models which will be used during the design process. Each design goal and every influencing parameter has to be implemented in the used model. This could be done by the usage of an overall, global model, or by coupling of several partial models. This means that in each case there is an increase of model complexity.

One way to choose the models for the design process is by selection based on the experience of the engineer. However, this is not very credible. Another way is the evaluation of the prognosis quality of different coupled partial models. An approach for this was developed by Reuter [20] within Research Training Group 1462 at Bauhaus-Universität Weimar. By coupling of different partial models, it is possible to evaluate the quality of the overall model answer. In this

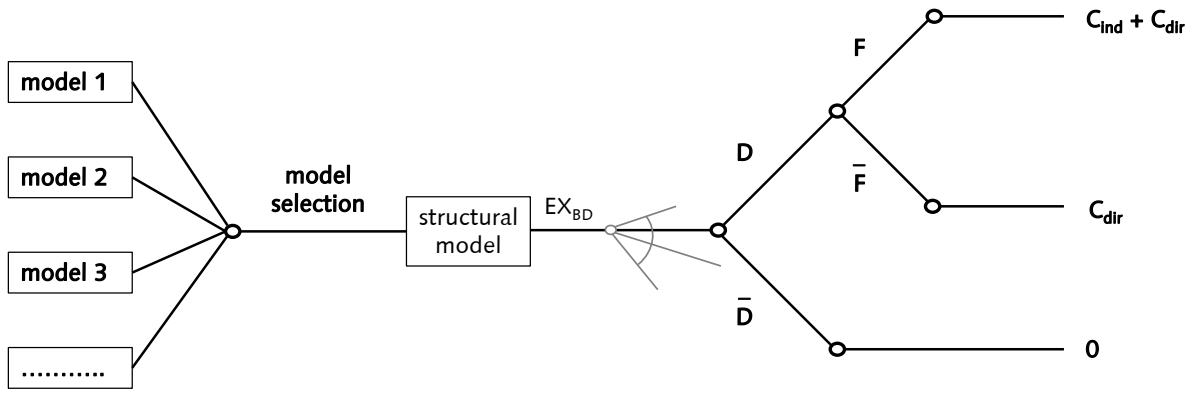

Figure 3: Expanded event tree for model choice and robustness quantification

As mentioned before, there are several approaches to evaluate the robustness of structural systems. One of these is the risk based robustness index, which is described in section 3.2. As recommended in section 3.2, the evaluation will be done by the estimation of direct and indirect risk. To that effect, there was shown an event tree, which is necessary in order to identify the different model outcomes. As also mentioned before, there are no limitations or quality checks for the structural models which will be used to reflect the structure. Shown in figure 3 is a scenario how this event tree expands if the model choice or model evaluation is added.

The different input models could be different partial models, which have to be combined to a global model. But also global models, which describes the whole structural behavior with different approaches. Thus, it is for example possible to describe the supporting conditions of a structural model by fixed nodal supports, by implementation of springs or by modeling of a soil half-space. Another example for different structural models is the choice between linear and nonlinear material behavior. Thus, all models are more or less able to represent the structural system, but the quality of this approximation is sometimes very different. In order to make this clearer, find an example given in the next section.

5 APPLICATION ON A STRUCTURAL MODEL

To show that the model choice is influencing the assessment of the structural robustness, there is an example given in this section. The model describes a system of several steel columns under pressure load such that the structural system leads to buckling failures, which is a sub-area of stability failures.

The worst structural failures in steel constructions are caused by stability problems. Since failures according to stability problems are usually very abrupt and without any prior notice, the chance to prevent the collapse or evacuate people before the collapse takes place is very low. To

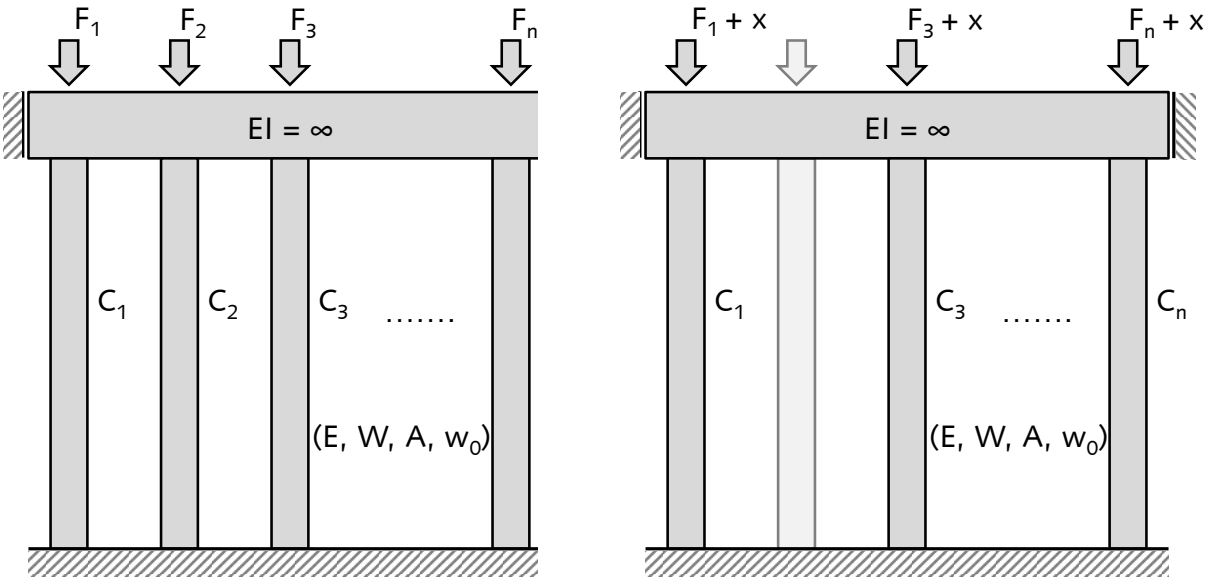

Figure 4: Structural system before and after damage occurs

avoid this type of failures, a variety of computational models still exists. These models belong to the review of load bearing capacity and the need for compliance is governed by the codes. However, the codes did not prescribe an approach for the evaluation of the structural robustness. Therefore, it is necessary to think about the usage of the risk based robustness index.

The chosen system, which is shown in figure 4, describes a structure of n columns under pressure load. These columns are arranged in a row and coupled by a beam with stiffness $EI = \infty$. The connection points of the columns are hinged, which means Euler case II. The input parameters of the structural model are stochastic, to reflect the scattering in real structures. This means that the cross-sections, material parameters, input loads and also imperfections will be described as scattering values. To show the influences of two different structural models, the evaluation was done by two different model approaches. The first model uses nonlinear kinematics to estimate the load bearing capacity, which means the deformation of the structure will be taken into account. The second model uses only linear kinematics. Thus, this means that the second model has a much poorer model quality, since it overestimates the structural behavior by a large margin.

The evaluation of the risk based structural robustness of the example shown will be done according to the event tree in figure 3. After the first exposure (EX_{BD}) occurs, the algorithm calculates the load bearing capacity of each structural member. With this, it is possible to separate into two different model responses. If there is no damage in the structure, the model response is path $\overline{D}$ - no damage occurs, and if damage occurs, the structure goes to path D. So it is possible, to estimate the probability of failure for the first step, which describes the direct failures. After damage occurs, the model rearranges the loads from the failed members to the rest of the structure. This is shown in figure 4, where x indicates the rearranged load from the failed component. By the use of the new loads, the system calculates the load bearing capacity

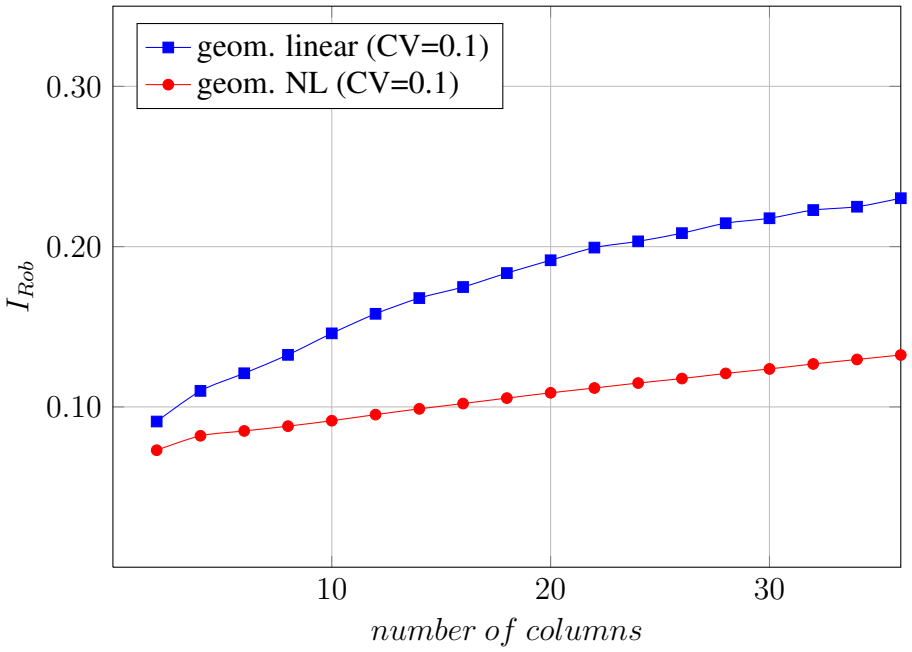

Figure 5: Risk Based Robustness Index for two different models

again. If new damage occurs the structure follows path F, and if there is no additional damage the system follows path $\overline{F}$.

According to the approach of the risk based robustness index, it is necessary to distinguish between direct and indirect risk. As mentioned before, direct risk is the probability of failure of the intact system (D), multiplied with the consequences from this direct failure. The estimation is done according to equation 3. The indirect risk is estimated according to equation 4, where the probability of failure is described by D and F. For the definition of the consequences, some assumptions were made: the consequences for the failure of one component are counted by 10, the consequences for the failure of the whole structure are counted by 1000. Thus, a failure of the whole structure will be penalized strongly.

The evaluation of the risk based robustness index is carried out for the two structural models, with geometrical linearity and nonlinearity. As shown in figure 5, the difference in the model response is really high. With an increasing number of columns in the structural models, the robustness index of both models is also increasing. But with an increasing number of columns, the difference in the model output is increasing as well. As shown, the model with the better model quality (geometrical nonlinear model), estimates a lower robustness index. This means that the model with the poor model quality overestimates the robustness of the given structure.

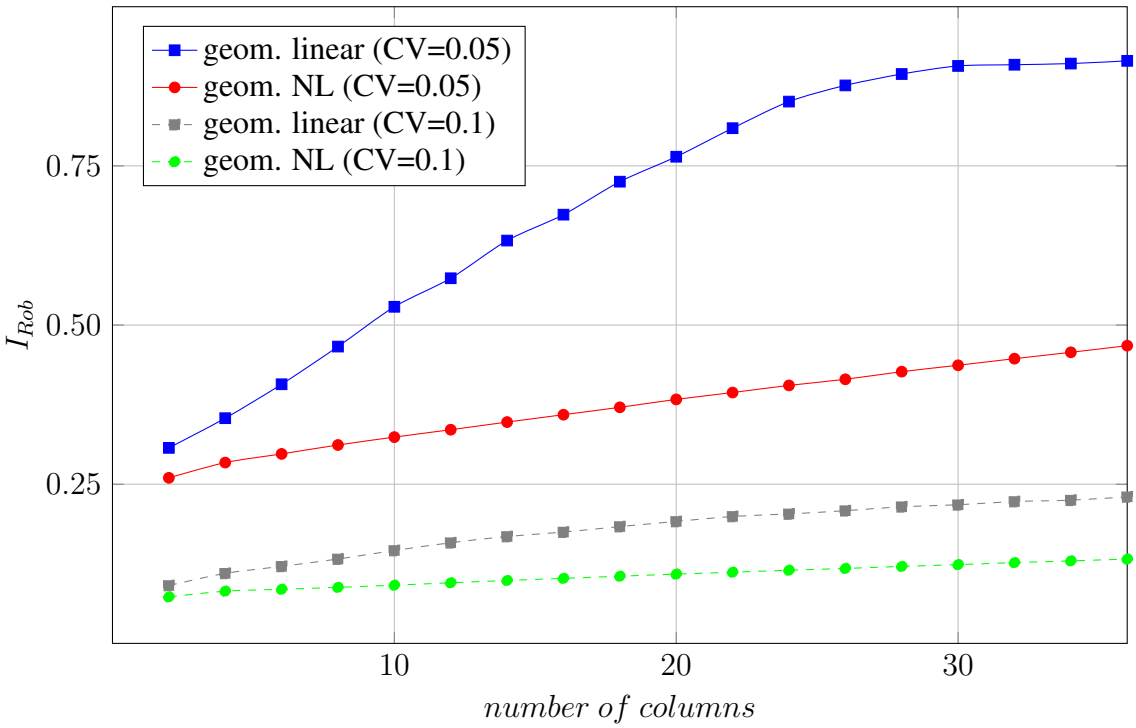

Figure 6: Robustness index for two different models and different coefficient of variation

Figure 6 shows the model outputs for both models, with a different coefficient of variation for the model input parameters. As can be seen, a smaller coefficient of variation in the input parameters leads to a higher robustness of the structural models. But the problem is that the overestimating of the poor model also increases. The linear model estimates a model robustness of up to 0.91, wherein the nonlinear model estimates a model robustness of 0.47. This means

that the linear model identifies a very robust structure, wherein the nonlinear model identifies a less robust structure. So it is shown, that the influence from the structural model on the evaluation of the robustness index is very high. A correct model choice in front of the evaluation of the structural robustness is recommendable.

During the research an attempt was also made to evaluate the structural robustness for both models according to the reliability based robustness index. However, there was the problem that the usage of the reliability indices leads to a very high scattering in the model answers. Since the probabilities of failure in the used models are sometimes very small, a high scattering in the reliability indices occurs and as such, the evaluation was not meaningful. Perhaps, a model with a lesser number of stochastic input parameters will lead to usable model outputs.

6 CONCLUSIONS

In structural engineering a lot of design parameters which have to be taken into account during the design process are already in existence. One of them is the structural robustness index. However, since there is no common definition for the term *robustness* and no universal evaluation algorithm already in existence, most of the engineers did not consider this design parameter.

The topic of structural robustness has been addressed in engineering literature several times during the last years. Thereby, several evaluation approaches were developed. Two of them are the reliability based and the risk based robustness index, which have been described in this paper. For the evaluation of the risk based robustness index, an event tree that shows the different model answers according to robustness problems currently exists. The starting point of this event tree and also the basis for each robustness evaluation is the structural model. Since all the approaches for the evaluation of the structural robustness have no requirements to the quality of the used structural models, this paper shows that the chosen structural model highly influences the robustness index. In the given example of n columns under pressure load, the model with the less quality was strongly overestimating the structural robustness. This means that a poor model leads to an overestimation of the structural robustness. Thus, the question regarding the right model choice for the structural model is of utmost importance.

In the next steps, the structural model of a multi-storage frame will be used to evaluate the influences of different partial models more in detail. There, it will also be possible to show the influences of different static systems. By adding a model quality evaluation process in front of the robustness estimation, it may be possible to improve the quality of the structural robustness indices.

ACKNOWLEDGMENT

This research is supported by the German Research Foundation (DFG) via Research Training Group "'Evaluation of Coupled Numerical Partial Models in Structural Engineering (GRK 1462)"', which is gratefully acknowledged by the author.

REFERENCES

[1] J. Agarwal, M. Haberland, M. Holický, M. Sykora, S. Thelandersson, Robustness of Structures: Lessons from Failures. *Structural Engineering International*, **22**(1), 105–111, 2012.

[2] J.D. Sørensen, Framework of robustness assessment of timber structures. *Engineering Structures*, **33**, 3087–3092, 2011.

[3] DIN-EN 1990, *Eurocode: Basis of Structural Design*, CEN 2002.

[4] DIN-EN 1991-1-7, *Eurocode: Actions on Structures: Part 1-7: Accidental Actions*, CEN 2006.

[5] H. Gulvanessian, T. Vrouwenvelder, Robustness and the Eurocodes. *Structural Engineering International*, **16**(2), 2006.

[6] M. Pötzl, Robuste Tragwerke - Vorschlge zu Entwurf und Konstruktion. *Bauingenieur*, **71**, 481–488, 1996.

[7] R. Harte, W.B. Krätzig, Y.S. Petryna, Robustheit von Tragwerken - ein vergessenes Entwurfsziel?. *Bautechnik*, **84**(4), 2007.

[8] M.H. Faber, M.A. Maes, D. Straub, J. Baker, On the quantification of robustness of structures. *Proceedings of the 25th International Conference on Offshore Mechanics and Arctic Engineering*, 2006.

[9] D.P. Brosnan, Human Error and Structural Engineering. *Structure magazine*, 46–49, September 2008. http://www.structuremag.org

[10] D.C. Epaarachchi, M. G. Stewart, Human Error and Reliability of Multistory Reinforced-Concrete Building Construction. *Journal of Performance of Constructed Facilities*, **18**(1), 12–20, 2004.

[11] R.E. Melchers, Human Error in Structural Design Tasks. *Journal of Structural Engineering*, **115**(7), 1989.

[12] D.M. Frangopol, Human errors and structural failure probability. *International Journal of Materials and Product Technology*, **3**(1), 1–10, 1988.

[13] H. Griffiths, A.G. Pugsley, O. Saunders, *Report of the inquiry into the collapse of flats at Ronan Point, Canning Town*, Her Majesty's Office, London, 1968.

[14] A. Biegus, K. Rykaluk, Zum Einsturz der Messehalle in Kattowitz. *Bauingenieur*, 517–522, 12-2006.

[15] D.M. Frangopol, J.P. Curley, Effects of damage and redundancy on structural reliability. *Journal of structural engineering*, **113**, 1533–1549, 1987.

[16] Joint Committee on Structural Safety, *Probabilistic model code*. JCSS Publication, 2001.

[17] J. W. Baker, M. Schubert, M. H. Faber, On the assessment of robustness. *Structural Safety*, **30**(2), 253–267, 2008.

[18] ISO 31000, *Risk management - principles and guidelines*, 2009.

[19] A. Mann, Risk in structural engineering. *The Structural Engineer*, **81**(10), 12–17, 2003.

[20] M.C. Reuter, Multicriterial Evaluation Method for the Prognosis Quality of Complex Engineering Models. *Schriftenreihe des DFG Graduiertenkollegs 1462 Modellqualitäten*, **3**, Verlag der Bauhaus-Universität, Weimar, 2012.

[21] H. Keitel, G. Karaki, T. Lahmer, S. Nikulla, V. Zabel, Evaluation of coupled partial models in structural engineering using graph theory and sensitivity analysis. *Engineering Structures*, **33**, 3726–3736, 2011.

ON INTERPOLATION FUNCTION OF THE BERNSTEIN POLYNOMIALS

Yilmaz Simsek
Department of Mathematics, Faculty of Science University of Akdeniz TR-07058 Antalya, Turkey, ysimsek@akdeniz.edu.tr

Abstract

The Bernstein polynomials are used for important applications in many branches of Mathematics and the other sciences, for instance, approximation theory, probability theory, statistic theory, number theory, the solution of the differential equations, numerical analysis, constructing Bezier curves, q-calculus, operator theory and applications in computer graphics. The Bernstein polynomials are used to construct Bezier curves. Bezier was an engineer with the Renault car company and set out in the early 1960's to develop a curve formulation which would lend itself to shape design. Engineers may find it most understandable to think of Bezier curves in terms of the center of mass of a set of point masses. Therefore, in this paper, we study on generating functions and functional equations for these polynomials. By applying these functions, we investigate interpolation function and many properties of these polynomials.

Key Words and Phrases. Bernstein polynomials, Bezier curve, Generating function, Interpolation function, Mellin transformation, Gamma function, , Bernoulli polynomials of higher-order, Stirling numbers of the second kind.

2000 Mathematics Subject Classification. 14F10, 12D10, 26C05, 26C10, 30B40, 30C15, 11B68, 11M06, 33B15, 33B15, 65D17.

1. Introduction

In this section we can use the following notation:

$$[x : q] = \frac{1 - q^x}{1 - q}.$$

Observe that

$$\lim_{q \to 1} [x : q] = x.$$

If $q \in \mathbb{C}$, we assume that $\mid q \mid < 1$. If $q \in \mathbb{R}$, we assume that $0 < q < 1$.

In this paper, we modify generating functions for the q-Bernstein polynomials, which are many applications: in approximations of functions, in statistics, in numerical analysis, in p-adic analysis and in the solution of differential equations. Using the functional equations for the generating functions and Laplace transform, we derive fundamental properties and some identities of the q-Bernstein polynomials.

The remainder of this paper is summarized as follows:

Section 2: We construct generating function of the q-Bernstein basis functions. Using these generating, some identities and properties of the q-Bernstein basis functions can be given.

Section 3: We give some properties for the q-Bernstein basis functions (Partition of unity, Alternating sum, Subdivision property).

Section 4: We give recurrence retaliations and derivative of the q-Bernstein basis functions.

Section 5: We give application related to the Laplace transform and generating function.
Section 6: We construct interpolation function for the q-Bernstein polynomials.
Section 7: We give further remarks on the q-Bezier curves and integral representation for the q-Bernstein basis functions.

2. Modified the generating function for the q-Bernstein basis type functions

Definition 1. *Let $x \in [0,1]$. Let k and n be nonnegative integers with $n \geq k$. Then we define*

$$\mathfrak{b}_k^n(x;q) = \begin{pmatrix} n \\ k \end{pmatrix} [x:q]^k q^{(n-k)x} \left[(1-x):q\right]^{n-k}, \tag{2.1}$$

where

$$\begin{pmatrix} n \\ k \end{pmatrix} = \frac{n!}{k!(n-k)!}$$

and $k = 0, 1, 2, ..., n$.

Generating functions for the q-Bernstein basis functions $\mathfrak{b}_k^n(x;q)$ can be defined as follows:

Definition 2. *Let $x \in [0,1]$ and $t \in \mathbb{C}$. Let k be nonnegative integers. Then we define*

$$\mathcal{F}_{k,q}(t,x) = \sum_{n=0}^{\infty} \mathfrak{b}_k^n(x;q) \frac{t^n}{n!}. \tag{2.2}$$

Observe that there is one generating function for each value of k.
We modify generating function for the q-Bernstein type basis functions as follows:

Theorem 1. *Let $x \in [0,1]$ and $t \in \mathbb{C}$. Then we have*

$$\mathcal{F}_{k,q}(t,x) = \frac{1}{k!} t^k [x:q]^k \exp\left(q^x \left[(1-x):q\right] t\right). \tag{2.3}$$

Proof. By substituting (2.1) into the right hand side of (2.2), we obtain

$$\begin{aligned} \mathcal{F}_{k,q}(t,x) &= \sum_{n=0}^{\infty} \left(\begin{pmatrix} n \\ k \end{pmatrix} [x:q]^k q^{(n-k)x} \left[(1-x):q\right]^{n-k} \right) \frac{t^n}{n!} \\ &= \frac{t^k [x:q]^k}{k!} \sum_{n=k}^{\infty} \frac{\left(q^x \left[(1-x):q\right] t\right)^{n-k}}{(n-k)!}. \end{aligned}$$

The right hand side of the above equation is a Taylor series for

$$\exp\left(q^x \left[(1-x):q\right] t\right),$$

thus we arrive at the desired result.

3. Some properties for the q-Bernstein basis functions are given as follows

In [13] and [14], Simsek present much background material on computations functional equation of the generating function for the Bernstein basis functions. We give some functional equations which are used to find some new identities related to the q-Bernstein basis functions. Our method is similar to that of Simsek's [13].

3.1. **Partition of unity.** The polynomials $\mathfrak{b}_k^n(x;q)$ have **partition of unity**, which is given by the following theorem.

Theorem 2. *(Sum of the polynomials $\mathfrak{b}_k^n(x;q)$)*

$$\sum_{k=0}^{n} \mathfrak{b}_k^n(x;q) = 1.$$

Proof. By using (2.3), we have

$$\sum_{k=0}^{\infty} \mathcal{F}_{k,q}(t,x) = \exp\left(q^x \left[1-x:q\right] t\right) \sum_{k=0}^{\infty} \frac{1}{k!} t^k [x:q]^k.$$

The right hand side of the above equation is a Taylor series for

$$\exp\left(\left[x:q\right] t\right),$$

thus we obtain

$$\sum_{k=0}^{\infty} \mathcal{F}_{k,q}(t,x) = \exp\left(\left(q^x \left[1-x:q\right] + \left[x:q\right]\right) t\right). \tag{3.1}$$

If we substitute the following identity

$$\left[a+b:q\right] = \left[a:q\right] + q^a \left[b:q\right],$$

into the right-hand side of (3.1), we find that

$$\sum_{k=0}^{\infty} \mathcal{F}_{k,q}(t,x) = \exp(t).$$

By using (2.2) and Taylor expansion of $\exp(t)$ in the above equation, we get

$$\sum_{n=0}^{\infty} \left(\sum_{k=0}^{n} \mathfrak{b}_k^n(x;q) \right) \frac{t^n}{n!} = \sum_{n=0}^{\infty} \frac{t^n}{n!}.$$

By comparing the coefficients of $\frac{t^n}{n!}$ on both sides, we arrive at the desired result.

Remark 1. *Simsek and Acikgoz* [15] *defined the q-Bernstein type basis functions as follows:*

$$Y_n(k,x;q) = \left(\begin{array}{c} n \\ k \end{array} \right) \left[x:q\right]^k \left[1-x:q\right]^{n-k}. \tag{3.2}$$

*The polynomials $Y_n(k,x;q)$ have not **partition of unity**. That is*

$$\sum_{k=0}^{n} Y_n(k,x;q) = \left(\left[x:q\right] + \left[1-x:q\right]\right)^n \neq 1. \tag{3.3}$$

By using (2.1) and (3.2), one can easily see that

$$\mathfrak{b}_k^n(x;q) = q^{x(n-k)} Y_n(k,x;q).$$

Thus generating functions of the polynomials $\mathfrak{b}_k^n(x;q)$ give us modification that of the polynomials $Y_n(k,x;q)$.

Remark 2. *In the special case when $q \to 1$, Definition 1 immediately yields the corresponding well known results concerning the classical Bernstein basis functions $B_k^n(x)$:*

$$B_k^n(x) = \left(\begin{array}{c} n \\ k \end{array} \right) x^k (1-x)^{n-k}, \tag{3.4}$$

where $k = 0, 1, \cdots, n$ and $x \in [0,1]$ cf. ([1]-[15]).

Since

$$q^x \left[(1-x) : q \right] = 1 - \left[x : q \right],$$

we modify Definition 1 as follows:

$$\mathfrak{b}_k^n(x;q) = \left(\begin{array}{c} n \\ k \end{array} \right) \left[x : q \right]^k \left(1 - \left[x : q \right] \right)^{n-k}$$

or

$$\mathfrak{b}_k^n(x;q) = B_k^n \left(\left[x : q \right] \right).$$

3.2. **Alternating sum.** By using (2.3), we obtain the following functional equation:

$$\sum_{k=0}^{\infty} (-1)^k \mathcal{F}_{k,q}(t,x) = \exp\left(\left(q^x \left[1 - x : q \right] - \left[x : q \right] \right) t \right). \tag{3.5}$$

By using same method with the author [14] and (3.5), we derive a formula for the alternating sum which is given the following Theorem:

Theorem 3. *(Alternating sum)*

$$\sum_{k=0}^{n} (-1)^k \mathfrak{b}_k^n(x;q) = \left(1 - 2 \left[x : q \right] \right)^n. \tag{3.6}$$

Remark 3. *If we let $q \to 1$ in (3.6), then we arrive at the well-known Goldman's results* [4]-[3, Chapter 5, pages 299-306] *and see also* [14]*:*

$$\sum_{k=0}^{n} (-1)^k B_k^n(x) = (1-2x)^n.$$

3.3. **Subdivision property.** By using similar method of Simsek's [13], we define the following functional equation:

$$\mathcal{F}_{k,q}(t, xy) = \mathcal{F}_{k,q}(t \left[y : q^x \right], x) \exp\left(q^{xy} \left[1 - y : q^x \right] t \right). \tag{3.7}$$

By using the above functional equation, we derive subdivision property for the q-Bernstein basis functions by the following theorem:

Theorem 4. *Then the following identity holds:*

$$\mathfrak{b}_j^n(xy;q) = \sum_{k=j}^{n} \mathfrak{b}_j^k(x;q) \mathfrak{b}_k^n(y;q^x).$$

Remark 4. *If we let $q \to 1$ in Theorem 4, we have*

$$B_j^n(xy) = \sum_{k=j}^{n} B_j^k(x) B_k^n(y). \tag{3.8}$$

The above identity is fundamental in subdivision property for the Bernstein basis functions cf. ([4]-[3, Chapter 5, pages 299-306], [14], [13]).

4. Recurrence retaliations and derivative of the q-Bernstein basis functions:

In this section, we give higher order derivatives of the Bernstein basis functions. We define

$$\mathcal{F}_{k,q}(t,x) = g_{k,q}(t,x)h_q(t,x), \tag{4.1}$$

where

$$g_{k,q}(t,x) = \frac{t^k\,[x:q]^k}{k!}$$

and

$$h_q(t,x) = \exp\left(q^x\,[1-x]\,t\right).$$

In this section we are going to differentiate (4.1) with respect to t to derive a recurrence relation for the Bernstein basis functions.

Using Leibnitz's formula for the vth derivative, with respect to t, we obtain the following *higher order partial differential equation*:

$$\frac{\partial^v \mathcal{F}_{k,q}(t,x)}{\partial t^v} = \sum_{j=0}^{v} \begin{pmatrix} v \\ j \end{pmatrix} \left(\frac{\partial^j g_{k,q}(t,x)}{\partial t^j}\right)\left(\frac{\partial^{v-j} h_q(t,x)}{\partial t^{v-j}}\right). \tag{4.2}$$

From the above equation, we have the following theorem:

Theorem 5.

$$\frac{\partial^v \mathcal{F}_{k,q}(t,x)}{\partial t^v} = \sum_{j=0}^{v} \mathfrak{b}_j^v(x;q)\mathcal{F}_{k-j,q}(t,x). \tag{4.3}$$

By same method in [14] and [13], Theorem 5 is proved by induction on v using (4.2).

Using (2.2) and (3.4) in Theorem 5, we obtain a recurrence relation for the Bernstein basis functions:

Theorem 6.

$$\mathfrak{b}_k^n(x;q) = \sum_{j=0}^{v} \mathfrak{b}_j^v(x;q)\mathfrak{b}_{k-j}^{n-v}(x;q). \tag{4.4}$$

Proof. By substituting right hand side of (2.2) into (4.3), we get

$$\frac{\partial^v}{\partial t^v}\left(\sum_{n=0}^{\infty} \mathfrak{b}_k^n(x;q)\frac{t^n}{n!}\right) = \sum_{n=0}^{\infty}\left(\sum_{j=0}^{v} \mathfrak{b}_j^v(x;q)\mathfrak{b}_{k-j}^{n-v}(x;q)\right)\frac{t^n}{n!}.$$

Therefore

$$\sum_{n=v}^{\infty} \mathfrak{b}_k^n(x;q)\frac{t^{n-v}}{(n-v)!} = \sum_{n=0}^{\infty}\left(\sum_{j=0}^{v} \mathfrak{b}_j^v(x;q)\mathfrak{b}_{k-j}^{n-v}(x;q)\right)\frac{t^n}{n!}.$$

From the above equation, we get

$$\sum_{n=v}^{\infty} \mathfrak{b}_k^n(x;q)\frac{t^{n-v}}{(n-v)!} = \sum_{n=v}^{\infty}\left(\sum_{j=0}^{v} \mathfrak{b}_j^v(x;q)\mathfrak{b}_{k-j}^{n-v}(x;q)\right)\frac{t^{n-v}}{(n-v)!}.$$

Comparing the coefficients of $\frac{t^n}{n!}$ on the both sides of the above equation, we arrive at the desired result. □

Remark 5. *If we let $q \to 1$ in (4.5), then we arrive at Theorem 9 in* [14].

By using (2.3), we derive derivative of the q-Bernstein basis functions for in the next theorem:

Theorem 7. *Let $x \in [0,1]$. Let k and n be nonnegative integers with $n \geq k$. Then we have*

$$\frac{d}{dx}\mathfrak{b}_k^n(x;q) = \frac{q^x \log(q^n)}{q-1}\left(\mathfrak{b}_{k-1}^{n-1}(x;q) - \mathfrak{b}_k^{n-1}(x;q)\right). \tag{4.5}$$

Remark 6. *If we let $q \to 1$ in (4.5), then we arrive at Corollary 1 in* [14].

5. Applications

In this section we apply Laplace transform to the generating function for the q-Bernstein basis function. We derive new identity.

From (2.3), we get the following generating functions:

$$e^{[x]t}\sum_{n=0}^{\infty}\mathfrak{b}_k^n(x;q)\frac{t^n}{n!} = \frac{[x:q]^k}{k!}t^k e^t. \tag{5.1}$$

$$e^{-t}\sum_{n=0}^{\infty}\mathfrak{b}_k^n(x;q)\frac{t^n}{n!} = \frac{[x:q]^k}{k!}t^k e^{-[x]t}. \tag{5.2}$$

$$e^{-q^x[1-x]t}\sum_{n=0}^{\infty}\mathfrak{b}_k^n(x;q)\frac{t^n}{n!} = \frac{[x:q]^k}{k!}t^k. \tag{5.3}$$

Theorem 8.

$$\sum_{n=0}^{\infty}[x]\,\mathfrak{b}_k^n(x;q) = 1. \tag{5.4}$$

Proof. Integrate equation (5.2) (by parts) with respect to t from zero to infinity, we have

$$\sum_{n=0}^{\infty}\frac{\mathfrak{b}_k^n(x;q)}{n!}\int_0^{\infty}e^{-t}t^n dt = \frac{[x:q]^k}{k!}\int_0^{\infty}t^k e^{-[x:q]t}dt. \tag{5.5}$$

We here assume that

$$x > 0.$$

of the following Laplace transform of the function $f(t) = t^k$:

$$\mathcal{L}(t^k) = \frac{k!}{[x:q]^{k+1}},$$

on the both sides of (5.5), we find that

$$\sum_{n=0}^{\infty}\mathfrak{b}_k^n(x;q) = \frac{1}{[x:q]}.$$

Thus we arrive at the desired result.

Remark 7. *If we let $q \to 1$ in (5.4), then we arrive at Theorem 15 in* [14].

6. Interpolation Function

In this section, we construct interpolation function for the q-Bernstein polynomials. This function interpolates the q-Bernstein polynomials at negative integers.

Let $s \in \mathbb{C}$, and $x \in R$ with $x \neq 1$. By applying the Mellin transformation to (2.3), we give integral representation of the interpolation function $I_q(s,k;x)$ as follows:

$$I_q(s,k;x) = \frac{1}{\Gamma(s)} \int_0^\infty t^{s-1} \mathcal{F}_{k,q}(-t,x)dt,$$

where $\Gamma(s)$ denotes the Euler gamma function. By using the above integral representation, we are now ready to define interpolation function of the q-Bernstein polynomials.

Definition 3. *Let k be a nonnegative integer. Let $s \in \mathbb{C}$, and $x \in R$ with $x \neq 1$. The interpolation function $I_q(s,k;x)$ is defined by*

$$I_q(s,k;x) = (-1)^k \frac{\Gamma(s+k)}{\Gamma(s)\Gamma(k+1)} \frac{[x:q]^k}{q^{x(k+s)}\,[1-x:q]^{k+s}}.$$

Theorem 9. *Let n be a positive integer. Then we have*

$$I_q(-n,k;x) = \mathfrak{b}_k^n(x).$$

Proof of this theorem is same as that of Theorem 12 in [12]. So we omit it.

7. Further remarks

7.1. **Bezier curve.** The Bezier curves are constructed by the Bernstein polynomials and control points. The Bezier curves are widely used in computer graphics to model smooth curves. The history of the Bezier curves can be traced back to Pierre Bezier, who was an engineer with the Renault car company and set out in the early 1960's to develop a curve formulation which would lend itself to shape design. Engineers may find it most understandable to think of the Bezier curves in terms of the center of mass of a set of point masses.

q-Bezier curves $B(x:q)$ with control points $P_0,\cdots, P_n$ is defined by

$$B(x:q) = \sum_{k=0}^{n} P_k \mathfrak{b}_k^n(x).$$

Observe that if $q \to 1$, we have the standard Bezier curves

$$B(x:1) = B(x) = \sum_{k=0}^{n} P_k B_k^n(x) \text{ cf. [2].}$$

If we substitute $\mathfrak{b}_k^n(x;q) = B_k^n([x:q])$ into the above equation, then q-Bezier curves have same properties as standard Bezier curves. Because the q-Bernstein basis functions are parametrization of the standard Bernstein basis functions. The the q-Bernstein basis functions might be the **affect** of q on the **shape of the curves**.

7.2. **Integral representation for the q-Bernstein basis functions.** In this section we derive very powerful result related to integral representation for the q-Bernstein basis functions, which can be obtained from generating function.

Integral representation for the q-Bernstein basis functions is given as follows:

$$\mathfrak{b}_k^n(x;q) = \frac{n!}{2\pi i} \int_{\mathcal{C}} \mathcal{F}_{k,q}(z,x) \frac{dz}{z^{n+1}}, \tag{7.1}$$

where $\mathcal{C}$ is a circle around the origin and the integration is in positive direction, $z \in \mathbb{C}$, $n \in \mathbb{Z}^+ = \{1, 2, 3, \cdots\}$ and $x \in [0, 1]$.

In [12], we give integral representation for the q-Bernstein basis functions. Here we give in detail about this representation as follows:

By substituting (2.3) into (7.1) and using Cauchy Residue Theorem, we obtain

$$\frac{n!}{2\pi i}\int_{\mathcal{C}} \mathcal{F}_{k,q}(z,x)\frac{dz}{z^{n+1}} = \frac{n!}{2\pi i}\left(2\pi i Res\left(\frac{\mathcal{F}_{k,q}(t,x)}{z^{n+1}}, 0\right)\right).$$

We now compute residue of $\frac{\mathcal{F}_{k,q}(t,x)}{z^{n+1}}$ at $z = 0$ by Laurent series as follows:

$$\mathfrak{b}_0^n(x;q)\frac{1}{z^{n+1}} + \mathfrak{b}_k^n(x;q)\frac{1}{z^n} + \cdots + \frac{\mathfrak{b}_k^n(x;q)}{n!}\frac{1}{z} + \mathfrak{b}_k^{n+1}(x;q) + \cdots .$$

By using the above Laurent series, we have

$$Res\left(\frac{\mathcal{F}_{k,q}(t,x)}{z^{n+1}}, 0\right) = \frac{\mathfrak{b}_k^n(x;q)}{n!}.$$

Consequently, one can obtain easily arrive at (7.1).

We note that our method same as of that of Lopez and Temme' [9] and Kim et al [7].

Acknowledgement 1. *The second author is supported by the research fund of Akdeniz University.*

References

[1] S. N. Bernstein, Démonstration du théorème de Weierstrass fondée sur la calcul des probabilités, Comm. Soc. Math. Charkow Sér. 2 t. 13, 1-2 (1912-1913).

[2] Goldman R.: An Integrated Introduction to Computer Graphics and Geometric Modeling, *CRC Press, Taylor and Francis*, New York, 2009.

[3] R. Goldman Pyramid Algorithms: A Dynamic Programming Approach to Curves and Surfaces for Geometric Modeling, Morgan Kaufmann Publishers, Academic Press, San Diego, 2002.

[4] R. Goldman, Identities for the Univariate and Bivariate Bernstein Basis Functions, Graphics Gems V, edited by Alan Paeth, Academic Press, (1995), 149-162.

[5] G. Morin and R. Goldman, On the smooth convergence of subdivision and degree elevation for Bézier curves, Computer Aided Geometric Design. 18(7), 657-666 (2001).

[6] L.-C. Jang, W.-J. Kim, and Y. Simsek, A study on the p-adic integral representation on $\mathbb{Z}p$ associated with Bernstein and Bernoulli polynomials, Adv. Difference Equ. 2010, Art. ID 163217, 6 pp.

[7] T. Kim, L.-C. Jang, and H. Yi, A note on the modified q-Bernstein polynomials, Discrete Dyn. Nat. Soc. 2010, Article ID 706483, 12 pages, 2010.

[8] M.-S. Kim, D. Kim, T. Kim, On q-Euler numbers related to the modified q-Bernstein polynomials, Abst. Appl. Anal. 2010, Article ID 952384, 15 pages.

[9] Lopez, L., Temme, N. M.: Hermite polynomials in asymptotic representations of generalized Bernoulli, Euler, Bessel and Buchholz polynomials, Modelling. Analysis and Simulation (MAS), MAS-R9927 September 30, (1999).

[10] G. M.Phillips, Bernstein polynomials based on the q-integers, The heritage of P. L. Chebyshev: a Festschrift in honor of the 70th birthday of T. J. Rivlin, Annals of Numerical Math. 1-4, 511-518 (1997).

[11] G. M. Phillips, A survey of results on the q-Bernstein polynomials, IMA Journal of Numerical Analysis Advance Access published online on June 23, 1-12 (2009).

[12] Y. Simsek, Interpolation function of generalized q-Bernstein type polynomials and their application, Curve and Surface, Springer Verlag Berlin Heidelberg 2011, LNCS 6920, (2011), 647-662.

[13] Y. Simsek, Generating functions for the Bernstein polynomials: A unified approach to deriving identities for the Bernstein basis functions. arXiv:1012.5538v1 [math.CA].

[14] Y. Simsek, Functional equations from generating functions: a novel approach to deriving identities for the Bernstein basis functions, arXiv:1111.4880v1 [math.CA].

[15] Y. Simsek, M. Acikgoz, A new generating function of (q-) Bernstein-type polynomials and their interpolation function, Abst. Appl. Anal. 2010, Article ID 769095, 12 pp.

19th International Conference on the Application of Computer
Science and Mathematics in Architecture and Civil Engineering
K. Gürlebeck, T. Lahmer and F. Werner (eds.)
Weimar, Germany, 04–06 July 2012

EVALUATION OF SOIL-STRUCTURE INTERACTION MODELS USING DIFFERENT MODEL-ROBUSTNESS APPROACHES

H. Stutz* **and F. Wuttke**

**Training Research Group 1462 "Evaluation of Coupled Numerical Partial Models in Structural Engineering"*
Berkaer Str. 9, 99423 Weimar
E-mail: Henning.Stutz@uni-weimar.de

Keywords: Soil-structure interaction, macro-element, finite element method, variance based model–robustness measure, mathematical model–robustness approach, shallow foundation

Abstract. *The aim of this study is to show an application of model robustness measures for soil-structure interaction (henceforth written as SSI) models. Model robustness defines a measure for the ability of a model to provide useful model answers for input parameters which typically have a wide range in geotechnical engineering. The calculation of SSI is a major problem in geotechnical engineering. Several different models exist for the estimation of SSI. These can be separated into analytical, semi-analytical and numerical methods. This paper focuses on the numerical models of SSI specific macro-element type models and more advanced finite element method models using contact description as continuum or interface elements. A brief description of the models used is given in the paper. Following this description, the applied SSI problem is introduced. The observed event is a static loaded shallow foundation with an inclined load. The different partial models to consider the SSI effects are assessed using different robustness measures during numerical application. The paper shows the investigation of the capability to use these measures for the assessment of the model quality of SSI partial models. A variance based robustness and a mathematical robustness approaches are applied. These different robustness measures are used in a framework which allows also the investigation of computational time consuming models. Finally the result shows that the concept of using robustness approaches combined with other model–quality indicators (e.g. model sensitivity or model reliability) can lead to unique model–quality assessment for SSI models.*

1 INTRODUCTION

Soil-Structure Interaction can be defined as a certain kind of structure which is embedded within the soil. Hereby, the interaction between both materials reaction to each other is important. Typical topics for SSI analysis are deep foundations, shallow foundations and excavations, geosynthecial reinforcements to name a few [1]. SSI effects are important topics which have to be considered in a wide range of geotechnical and structural engineering applications. SSI can be modeled using one or more of a high amount of approaches which have been published in the past. The different available models can be split into analytical, semi-analytical and numerical models considering SSI effects in diverse ways.
The major problem in dealing with SSI effects is the great amount of model and the rising question of what the best suitable model is, in regards to model–robustness, model–uncertainty and/or model–complexity. These different model attributes are important to quantify to select the most suitable model [2]. [1] states that it is important to consider the best suitable model to allow predictions and back calculations. [3] points out that less attention is paid to validate the models and investigate their capability for reliable simulation results. [4] shows a benchmark test where it is obvious that the model choice and modeling techniques have a major influence on the results which consider SSI effects.
Recent approaches are presented to assess the modelquality in geotechnical engineering [5] to validate the use of the constitutive soil models. In general, it can be pointed out that there is great need to continue this work, in particular for different SSI models. These different SSI models are so-called ill-posed problems, because for the identification of the most suitable model it is important to consider changes in the structure as well as in the soil. This paper focuses on the use of numerical finite element models and so called macro–element approaches. These models are introduced briefly.
The purpose of this paper is to clarify the use of such different SSI models, taking into account the model–robustness. Therefore a variance–based model robustness and a mathematical robustness approaches are used. These two slightly different ways for the model robustness are applied to a shallow foundation with a transient inclined static loading. Thus a scheme is proposed to evalute the model robustness especially for boundary value problems which have a large computational time. For this statistical analysis, different methods presented which can be used to evaluate the most influencing parameter to the model response are presented. Following this preliminary study, a meta–model is generated for the further evaluation of the model–robustness. During the consideration of this meta–model the mathematical model robustness is evaluated.

2 SOIL-STRUCTURE INTERACTION MODELING

In this section the different SSI modelling techniques are briefly introduced. The main focus is on the Finite–Element Method, but the SSI modeling using a macro–element approach is also captured.

2.1 Modelling SSI with macro-element approach

A macro element approach is a simplified approach which combines the soil half–space, interface between the soil and the structure, and the foundation into on single model which can be solved using a parabolic function. A general description of different kinds of macro–elements to calculate SSI effects are given in [6].
A number of parallel studies have been conducted on the subject of macro–element modeling for a static loaded strip footing by e.g. [7, 8, 9]. Using an incremental plasticity model consisting of constitutive description to account for the interaction between the forces of structure and the plastic displacement, it is possible to use an elasto-plastic strain hardening macroelement which can predict the behaviour of SSI [7]. Some examples are shown by [10, 11]. These macro–element use a yield function Eq. (1) given by [7]

$$f\left(\mathbf{Q}, \rho_c\right) = h^2 + m^2 - \xi^2 \left[1 - frac\xi\rho_c\right]^{2\beta} = 0 \tag{1}$$

Where $h = H/\left(\mu V_m\right)$, $m = M/\left(_m\right)$, $\xi = V/V_m$, ρ_c is a loading history parameter, H the horizontal load, M the generated moment, V the vertical force, V_m the maximum vertical load capacity of the macroelement, μ the slope of failure envelope in the H-V plane, ψ Slope of the failure envelope in the M-V plane, B width of the foundation and β is a constitutive parameter which controls the shape of the failure envelope. The plastic potential can be written as developed by [7]:

$$g\left(\mathbf{Q}\right) = \lambda^2 h^2 + \chi^2 m^2 - \xi^2 \left[1 - frac\xi\rho_g\right]^{2\beta} = 0 \tag{2}$$

Where $= \mu/\mu_g$ and $\chi = \psi/\psi_g$. Both of these parameters must be determined experimentally. If $f\left(\mathbf{Q}, \rho_c\right) = g\left(\mathbf{Q}\right)$ the flow rule is associated. Both functions can be used with an incremental plasticity scheme to calculate the displacement in respect to the load. For the interested reader, refer to [10, 7] for a detailed description.

2.2 Modelling with Finite Elemente Methode SSI

Generally, if a structure is loaded, relative movements with regards to the soil can occur. Therefore, the use of conventional finite elements can create compatibility problems prohibiting relative movements into soil structure interaction modeling. Due to discretization as shown in Figure 1a the nodal compatibility in the finite elements method is constrained, such that the soil and the structure move together. To prevent this occurrence, so-called interface or joints elements could be used. Particular advancement also is that it is possible to use a different material formulation for this interaction zone (e.g. maximum wall friction angle). Another important point is that with such elements it is possible to allow separation or sliding.
Undergoing research to use finite element analysis to investigate SSI has been considered since the early 70s. There are different proposed methods and models used. The different groups are tackled here in the following:

1. node to node contact
2. using conventional continuum finite elements (e.g. [12, 13])
3. zero thickness / thin layered interface elements (e.g. [14, 18, 16])

Figure 1 shows the different types of SSI modelling. These three methods are used in a finite element analysis. In the following a brief description follows the methodology and the constitutive models.

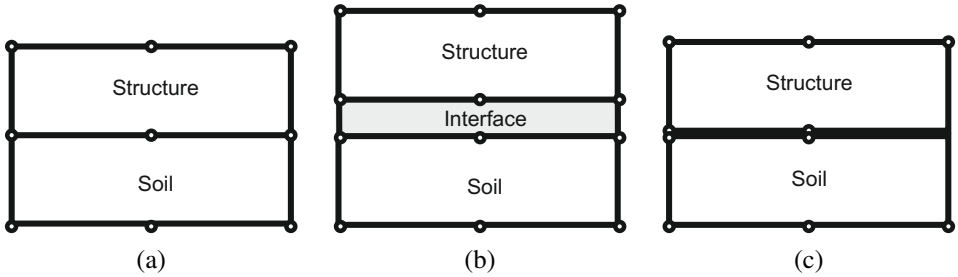

Figure 1: (a) node to node contact (b) use of continuum element as interface (c) use of interface element according to [17]

All of these different techniques can be used under conditions where their utilization is justified.

Node to node contact

Modeling the SSI using only node to node contact is a rough method with which to model the phenomenas which appear these transition zones. Clearly there is a big disadvantage in using such kinds of SSI models due to the fact that the nodes for the soil and structure must fulfill the nodal compability. This is due to the fact that if the structure is loaded, relative movements can occur [17]. Due the discretization shown in Fig. 1(a) the nodal compatibility in the finite elements method is constrained such that the soil and structure tend to move together.
Also, it is important to point out that the use of such a modeling technique for SSI can lead to unrealistic high failure loads. This is due to the fact that at corner points singularity points, will occur which reduces the accuracy of the global finite element mesh [18].
The use of these modeling methods can not recommended but it is quite often that in practical engineering applications using interface elements are forgotten or the effect is underestimated by the engineer.

Using conventional finite elements

[12] proposes the use of conventional finite elements (Fig. 1(b)) in cases where the slip of a foundation structure must not be considered. [12, 13] shows that the conventional finite element formulation is able to predict SSI effects in efficient quality. If the finite element model should be used to model slipping of the structure in a great range over the soil it is not suitable for this propose [12].
Another advantage is also that it is possible to use a different material formulation for this interaction zone (e.g. maximum wall friction angle). As with interface elements it is possible to use the same constitutive material formulation than in the surrounding soil.

Zero-thickness interface elements

[15] shows the first use of special interface elements in finite element analysis which can model discontinuity like joints in rock mechanics. This pioneer work from [15] are followed by a huge amount of different proposed interface element formulation from 6-10 node isoparametric interface element to different material descriptions from linear elastic material behavior to bi–linear models of the *Mohr-Coulomb* friction material model to more advanced material models like Damage models [20], Critical State Soil Mechanics [21] framework and advanced elasto–plastic formulations [19].
The use of thin continuum interface elements (e.g. [16, 22]) for soil–structure interaction can lead to problems due to the fact that the thickness of the interface is unknown and the determination of the input parameters used is difficult without conducting special laboratory tests [19]. Special interface formulation are developed which ensure of singular points at the corner of SSI modelling [18].
The interface models used are in respect to the finite element formulation in the commercial software used. 6 or 15 noded triangular elements are used in this publication. The associated interface elements are 6 or 10 noded joint elements. Both types of elements for the continuum and interface are shown in Fig. 2. The rate of interface traction t and the displacement discontinuity Δu is a combination of linear elasticity and perfect plasticity therefore the elasto–plastic relationship can express the following equation:

$$t = \mathbf{D}_c^e \Delta u^e = \mathbf{D}_c^e \left(\Delta u - \Delta u^p \right) \tag{3}$$

Eq. (3) relates the objective rate of traction t to the relative displacement over the full length of the interface surface Δu^e. The following D–Matrix can be generated for isotropic linear elastic behavior (4):

$$\mathbf{D}_c^e = \begin{bmatrix} k_s & 0 \\ 0 & k_n \end{bmatrix} \tag{4}$$

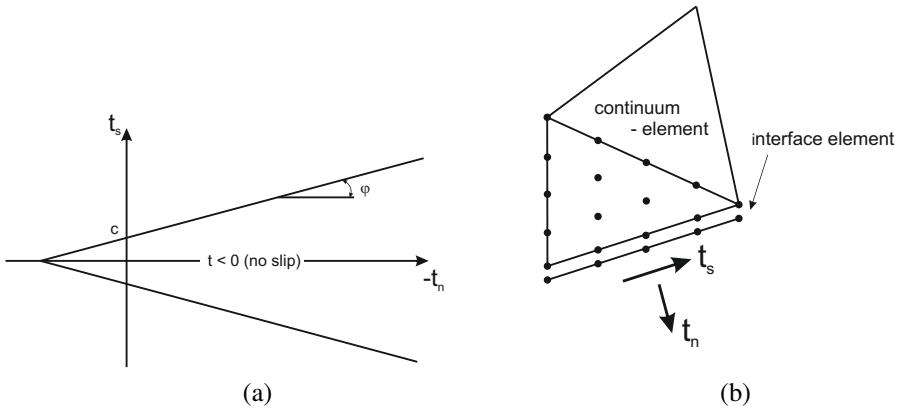

Figure 2: (a) Yield function and (b) interface element assmbly according to [18]

where the interface stiffness is related to the mean element length l, G the shear modulus of the soil and v Possions ratio.

$$k_s = \mu\,(G/l) \qquad\qquad k_n = \mu G/\,(1-2\nu) \tag{5}$$

In the present study only a simple *Mohr-Coulomb* yield function is considered. This yield function is combined with a non-associated plastic potential. Fig. 2a shows a repesentation of the yield function in a t_s–t_n space. The yield function and plastic potential can be described with:

$$f(t) = t_s + t_n \tan\varphi_c - c_c \qquad\qquad g(t) = t_s + t_n \tan\psi_c \tag{6}$$

Where φ_c is the friction angle and c_c the adhesion in the interface zone. For the plastic potential ψ_c is the dilation angle which controls the plastic dilation. As described in [23] the use of a non-associated flow rule $\varphi_c > \psi_c$ prevents a unrelastic high plastic dilation. For some special cases this can result in an overestimation of the contact pressure and consequently of the shear strength. Using the plastic potential the plastic slip can be derived using the following equation:

$$\Delta u^p = \alpha\lambda\,(\partial g/\partial t) \tag{7}$$

where α is a coefficent defined as:

$$\alpha = 0 \quad \text{if} \quad f < 0 \text{or}\,[\partial f/\partial t]^T\,\mathbf{D}\Delta(u) < 0 \tag{8}$$

$$\alpha = 1 \quad \text{if} \quad f = 0 \text{with}\,[\partial f/\partial t]^T\,\mathbf{D}\Delta(u) \geq 0 \tag{9}$$

using this switch on and off coefficient α the multiplier λ can be solved with the help of the consistency equation $f = 0$. To solve these constitiutive equations a *Newton-Cotes* algorithm is applied. Considering this integration scheme, a lumped interface stiffness matrix can be archieved.
The advantages of using this interface elements is that it is not necessary to care about the interface thickness and the special needed material parameters which are uncertain and difficult to obtain by using conventional laboratory tests.

3 MODEL – ROBUSTNESS

Model–robustness is defined as the capability of a model to given consistent output over the full range for which it is generated of possible input parameters. Two different types of robustness measures are used. Both of these robustness approaches are based on global model–robustness.

3.1 Variance-based robustness measure

The variance based robustness measure is also called *Taguchis* robustness and is defined as an adapted "'signal-to-noise"' ratio discussed in [24] and can be expressed in Eq. (10):

$$T = -10 \log \left(\frac{1}{\sigma_Y^2} \right) \tag{10}$$

Where the standard derivation σ_Y^2 is used to estimate the model–robustness. The robustness measure by *Taguchi* has some drawbacks described in [24].

3.2 Mathematical robustness approach

The principal idea of the mathematical robustness approach is directly derived from the definition of model–robustness, that the model will generate an input which is completely conneted to the output. As an example the change in input will be related to the change of output. Therefore the input–output relationship of the SSI models will be investigated.
There can be three different model robustness classes defined. Robust, partial robust and non-robust models as shown in Fig. 3.

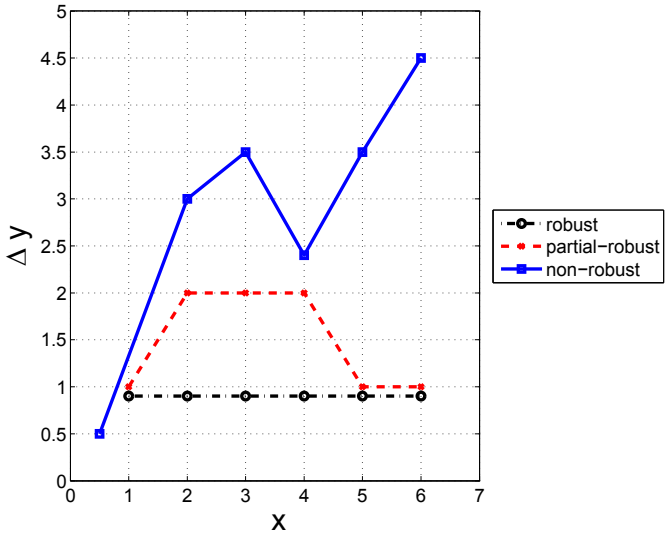

Figure 3: Input–Output relation for **robust**, **partial-robust** and **non-robust** model

Plotting $\Delta y - x$ diagram shows different possible cases. If the plot shows a straight horizontal line the input-output relation is linear and it is a quite robust model. Shows the input–output relation some fluctuations, it is partial robust. The third case is that if the model shows a complete irregular behavior for the output it can be called non-robust. If $\Delta y = 0$ the parameter does not influence on the output. This means the parameter has no influence on the model response.
To calculate this, the model input will be split in n numbers of intervals. Using n intervals for all important input variables used. These are used to compute all possible combinations as model response. The number of combinations will be quite high, as the following Eq. 11 shows:

$$nC_i = n^{np} \tag{11}$$

where nC_i is the amount of different possible combinations and np are the number of parameters. For all these combinations the global response of the model is computed. Therefore

one parameter is frozen and all other combinations are computed.

$$E(Y|X_i) \tag{12}$$

From these ouptut the mean (μ_Y) is calculated for all combinations. Using these mean values the Δy for every single parameter interval is calculated by:

$$\Delta y = E\left(\hat{Y}_n|\mathbf{X}_i\right) - E\left(\hat{Y}_{n+1}|\mathbf{X}_i\right)$$

These Δy are plotted against the parameter input x to estimate the robustness of a model graphically.

4 METHODOLOGY FOR THE ASSESSMENT OF MODEL – ROBUSTNESS

The first step in the determination of the robustness measures are the concept as show in Fig. 4. The different step as shown in Fig. 4 are explained in the next paragraphs.

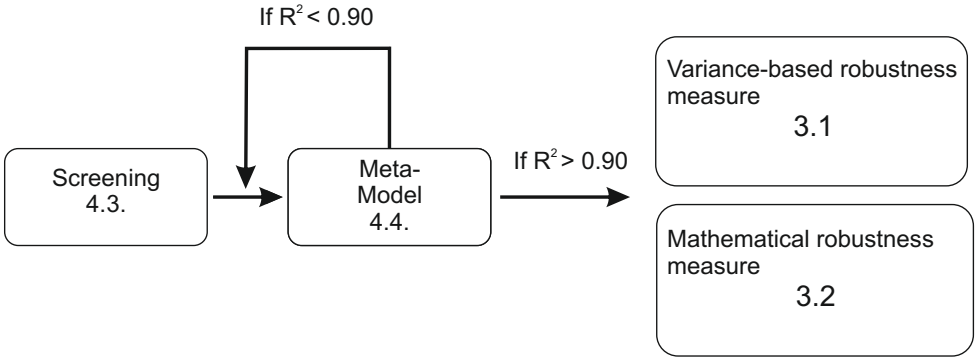

Figure 4: Methodology for the assement of the model–robustness

4.1 Application to an inclined loaded shallow foundation

The application for the comparison of these different robustness approaches described above is a shallow foundation which is loaded with an inclined load. Figure 5 shows the boundary conditions.
This boundary value problem is assumed for all the 4 different partial models. For the three different finite element models, the contact description is different according to section 2.2. Model 1 (M1) uses a simple node–node contact, Model 2 (M2) uses an interface element and Model 3 (M3) uses the continuum approach. The macro–element model is the fourth type of model which is used. To exclude mesh dependencies and errors due to other modeling issues, some comparison with different meshes are conducted in order to ensure that such effects could not happen. Please note that these investigations are not shown here.

The gray scaled areas in Fig. 5 are the meshed parts of the model. For the discretization, 15-noded triangular elements with a fourth order interpolation for displacements are used. These elements have 12 Gauss points (stress points) for each element (also shown in Fig. **??**).
The model has a plane strain boundary condition with the width of 9.00 m and height of 4.00 m. Fig. 5 uses the same element formulation for the beam embedded in the soil. For the material

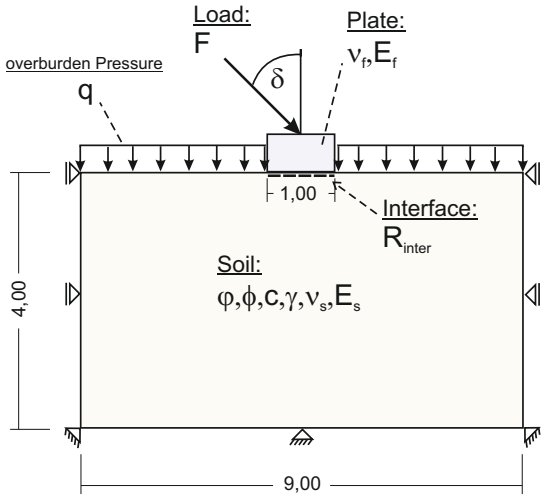

Figure 5: Applied boundary value problem

model of the foundation a simple linear-elastic "*Hookes law*" model is chosen. This requires 2 material parameter. The Young's Modulus E_f and the Possion's ratio ν_f
The constitutive material model for the soil is the *Mohr–Coulomb* model which is a classical model used in geotechnical engineering. It is a linear–elastic perfectly plastic model with a fixed yield surface in principal stress space. For a more detailed description see for example [6]. The model uses five different parameters to describe the constitutive behavior of soils and rocks in a wide range. The different parameters are φ the friction angle, ψ dilatancy angle, c cohesion, E_s Youngs modulus and ν_s Possions ratio. For a more detailed description, [6] is referenced.
Considering this boundary value problem, the SSI models are applied. Consequently, this means that three finite element analysis and one macro-element calculation is conducted. The macroelement approach is also applied for the shown boundary in Fig. 5. Due to its modelreduction it is not explicitly drawn here, for a pictorial representation is refered to [8] .
For comparsion of the different models a fixed load level of 75 kN is applied and all results are shown in respect to the displacement by this load level.

4.2 Parameters used in the different SSI models

The parameters which are used are listed in the following Tab. 1. The sampling of the parameter is performed as uniformed distributed sampling as described by [25]. The meta model sampling is also uniformly distributed. These uniform distribution is chosen to hold each variable for the model input independent of each other.

4.3 Preliminary Study for Elementary Effects

The different models were first screened with the help of a screening technique proposed by [25]. The idea of this is to search the elementary effects of the entire design space. Therefore, a randomized sampling plan is generated where so-called Elementary Effects (EE) can be calculated using Equation (13). With the help of these EE the input parameters can be ranked in order of their importance. These EEs can not give a statement of the importance quantifiably. The basic assumption from [25] is that the objective function from the underlying computational model is deterministic.

Table 1: Parameter input for the analysis

Parameter [unit]	Baseline	Minimum	Maximum
Friction angle φ []	35	28	45
Dilation angle ψ []	5	0	10
Cohesion c [kN/m^3]	1	0.0001	5
Possions ratio (soil) ν_s [-]	0.25	0.2	0.38
Youngs modulus (soil) E_s [kN/m^2]	30000	20000	45000
Unit weight (soil) [kN/m^3]	18	15	19.5
Youngs modulus (foundation) E_f [MN/m^2]	30000	20000	100000
Possions ratio (foundation) ν_f [-]	0.45	0.3	0.495
Friction cofficient R_{inter} [-]	0.8	0.3	1
Load inclination angle δ []	22.5	0.1	45

Soil	Foundation	Interaction	Load

To estimate EEs the mean and standard deviation is calculated. These indicators shows the importance to the global response and the non–linearity / interaction. In computational regard this scheme is quite efficient because with the help of one simulation run two sensitivity values can be examined.

$$d_i(\mathbf{x}) = \frac{y(x_1,x_2,\cdots,x_{i-1},x_i+\Delta,\cdots,x_k) - (y(\mathbf{x}))}{\Delta} \tag{13}$$

Where $\Delta = \xi/(p-1)$, $\xi \in \mathbb{N}$ and $\mathbf{x} \in D$ such that the components $x_i \leq 1-\Delta$ and $\mathbf{x} \in D = [0,1]^2$ for scaling issues, k amount of input variables, p number of discrete values along each dimension. The basic idea of a parameter in regarding to [25] is that a parameter with a large measure of central tendency indicates a major influence to the objective function. Further, [25] considers that a significant measure of spread indicates that the variable is involved in non–linear effects and/or interacts with other parameters.
With estimation of the sample mean and the sample standard deviation, for a set of $d_i(x)$ values overspanned to the design space. Of major importance for this purpose is to generate a sampling plan that each evaluation of the objective function f participates in the estimation of two elementary effects. Therefore the sampling has to give us a defined number r elementary effects for each variable. A more detailed discussion is given by [25].

The sampling can generate with the help of Eq. (14).

$$\mathbf{B}^* = (1_{k+1,1}\mathbf{x}^* + (\Delta/2)\left[(2\mathbf{B} - 1_{k+1,k})\,\mathbf{D}^* + 1_{k+1,k}\right])\,\mathbf{P}^* \tag{14}$$

Here, B is the basic sampling matrix, $P^\star$ is the random permutation matrix and $D^\star$ randomly generated matrix with $+1$ or -1 on the diagonal. For the calculation of r EEs for each variable, the screening plan is built from r random orientations using Eq. (15):

$$\mathbf{X} = \begin{bmatrix} \mathbf{B}_1^* \\ \mathbf{B}_2^* \\ \cdots \\ \mathbf{B}_r^* \end{bmatrix} \tag{15}$$

The advantage of the method presented is to generate a more efficient and accurate response surface with a less of computational time. The result of these screening is shown as a bar plot in Fig. 6. Therefore, the parameters scaled to show the influence of the different parameters correlated under each other. These scaling is done with the following Eq. 16:

$$EE_i^{scale} = \frac{\mu_Y}{\max(\mu_Y^2)} + \frac{\sigma^2}{\max(\sigma_Y^2)} \tag{16}$$

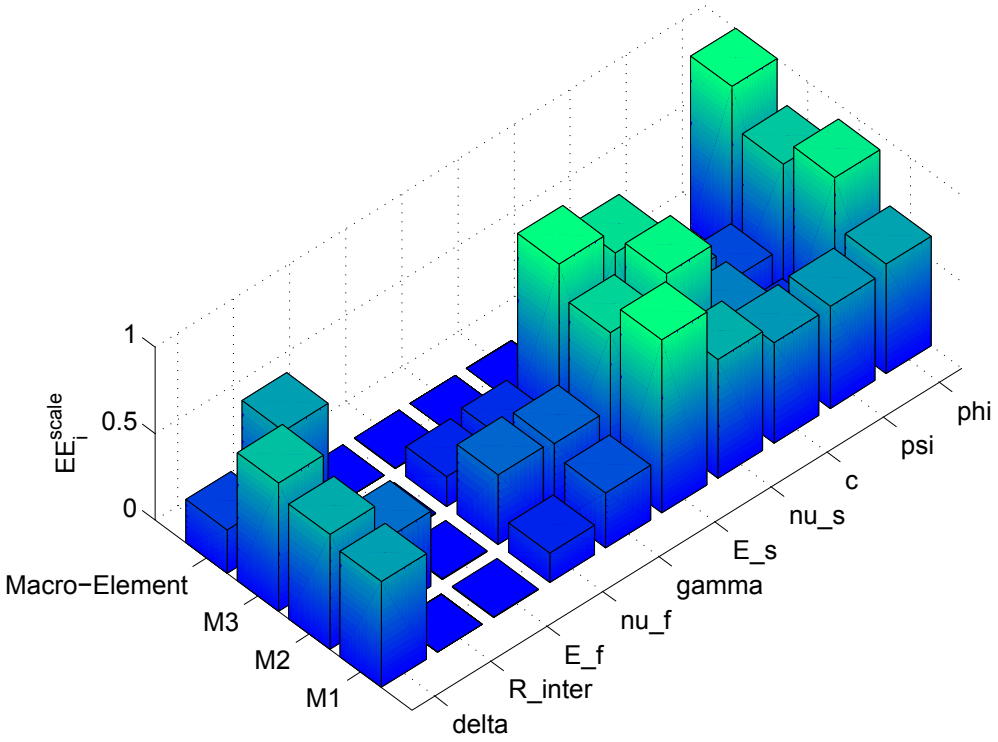

Figure 6: Scaled Elementary Effects

4.4 Meta-Modeling

Due to the computational time consuming finite element models, this models are replaced by different meta–models. For these, only those from the screening important model input parameters are considered. For the investigation of the robustness criterion it was important that the model input are considered as uncorrelated input, to generate also uncorrelated meta–models. To control and build the response surfaces a multi–linear regression was used. The object function of the observed model will be idealized by the following equation. For the regression linear, quadratic and mixed terms Eq. 17 are used:

$$\begin{aligned}\hat{Y} = \beta_0 + \beta_1 X_1 + \beta_2 X_2 + \cdots + \beta_{Pk} X_{Pk} + \beta_{11} X_{11}^2 + \beta_{22} X_{22}^2 + \cdots \\ + \beta_{PkPk} X_{PkPk}^2 + \beta_{12} X_1 X_2 + \cdots + \beta_{Pk-1Pk} X_{Pk-1} X_{Pk} + \mathbf{e}\end{aligned} \tag{17}$$

Here, $\hat{Y}$ is the regression equation for the approximation of the model response, β the regression coefficient, X_i the i-th parameter set. The regression coefficents β are calculated using Eq. (18):

$$\beta = \left(\mathbf{X}^T\mathbf{X}\right)^{-}1\mathbf{X}^T\mathbf{Y} \tag{18}$$

For the control of correctness of the used response surface the coefficient of determination R^2 is calculated using Eq. 19.

$$R^2 = 1 - \left(\frac{SS_E}{SS_T}\right) \tag{19}$$

If the coefficient of determination is smaller than 0.90 the number of samplings must be higher to reach a higher accuracy of the meta–models.
The different coefficient of determination are shown in Fig. 7a. For the generation of the meta–model, 500 samples are used. The macro–element is not replaced by a meta–model. The plane in the bar plot shows the value of the coefficient of determination. All meta-models can be used with a number of 500 samples.

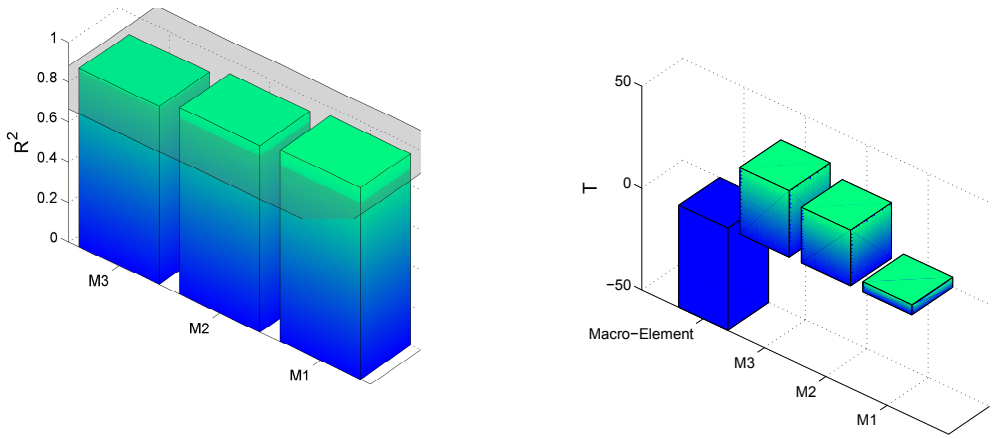

(a) (b)

Figure 7: (a) R^2 for meta–models (b) Results for the *Taguchi* robustness

4.5 Robustness approaches

At the end of the concept show in Fig. 4 both robustness approaches are investigated, to investigate the model–robustness.

Results: Variance–based robustness measure

Fig. 7b visualizes the results for the variance based robustness measure. Based on the *Taguchi* robustness measure it can stated that the most robust model is the model M3 followed by M2.

Results: Mathematical based robustness approach

Currently for the mathematical robustness, there are no clear mathematical formulation to express the robustness of a model in scalar in existence. However, generally the concept for the

evaluation of the model–robustness presented above can identify the model–robustness for each model parameter independently (see Fig. 8).
In Fig. 8a the results for all four different models are shown for the load inclination angle. In general can be stated that all models have parts where they are robust. In Fig. 8b shows the results for the friction angle φ.

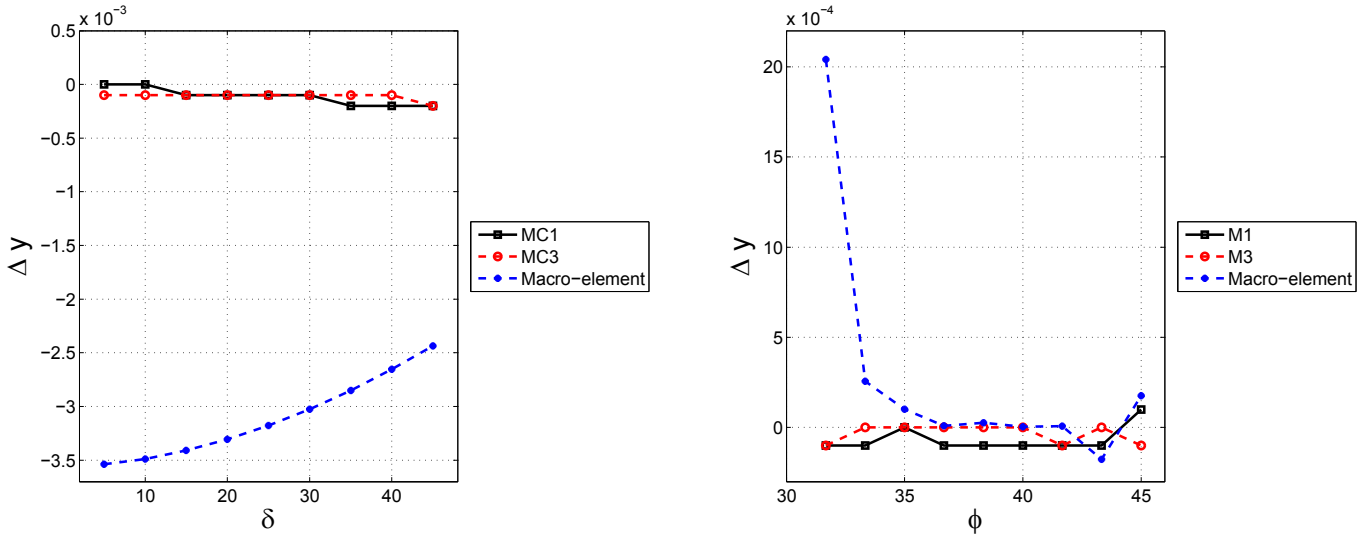

(a) (b)

Figure 8: (a) mathematical robustness inclination angle δ (b) mathematical robustness for the friction angle φ

5 CONCLUSION

Both of these robustness approaches can be applied to soil–structure coupling models. In the case of the *Taguchi* robustness measure, the different models shows really different results. The mathematical robustness approach have to be completed. This approach has to be refined as a mathematical formulation. This will helps to compare models in the sense of model–robustness and model–quality. Furthermore, some effort has to be done on the question of which model delivers a reference model robustness and what happens if the models tends to be show a non-linear behavior.
This paper shows the applicability of using two different model robustness assement approachs for the model robustness. This paper concludes with an outlook on the development of a straight-forward mathematical formulation of model–robustness.

6 ACKNOWLEDGEMENT

The author gratefully acknowledges the support of the German Research Foundation (DFG) through the Research Training Group 1462 ”Evaluation of Coupled Numerical Partial Models in Structural Engineering” in Weimar.

REFERENCES

[1] R. J. Jardine, D. M. Potts, A. B. Fourie and J. B. Burland,Studies of the influence of non–linear stress–strain charateristics in soil–structure interaction,*Gotechnique*, **36** 3, 377-396, 1986.

[2] T. Lahmer, T. Knabe, S. Nikulla and M. Reuter, Bewertungsmethoden fr Modelle des konstruktiven Ingenieurbaus. *Bautechnik Sonderdruck*, **88**(6), 60–64,2011

[3] J.P.Carter, C.S.Desai, D.M.Potts, H.F.Schweiger and S.W.Sloan, Computing and Computer Modelling in Geotechnical Engineering, *Proc.GeoEng2000*, Melbourne, Technomic Publishing, Lancaster, Vol.1, 1157-1252, 2000.

[4] H. F. Schweiger, Results from the ERTC7 benchmark exercise, H. Schweiger eds., *Numerical Methods in Geotechnical Engineering*, Graz, 2006.

[5] T. Knabe, Assessment of constitutive approaches for soil in civil engineering applications,*Schriftenreihe des DFG Graduiertenkollegs 1462 Modellqualitäten* **6** Bauhaus-Universität Weimar, 2011.

[6] D. M. Wood, *Geotechnical Modelling*, Spoon Press Taylor and Francis Group, 360–381, 2004.

[7] R. Nova and L. Monterasio, Settlements of shallow foundations on Sand, *Geotechnique*, **41**(2), 243-256, 1991.

[8] C. Cremer, A. Pecker and L. Davenne, Cyclic macroelement for soil-structure interaction: materials and geometrical nonlinearities, *Int. Jour. Num. Anal. Meth. Geomech.* **25**(13), 1257–1284, 2001.

[9] C. M. Martin and G. T. Houlsby, Combined loading of spudcan foundations on clay: numerical modelling, *Geotechnique*, **51**(8), 687-699, 2001.

[10] A. Kisse, Entwicklung eines Systemgesetzes zur Beschreibung der Boden-Bauwerk-Interaktion flachgegründeter Fundamente auf Sand, *Universität Duisburg-Essen, Mitteilungen aus dem Fachgebiet Grundbau und Bodenmechanik*, Heft **34**, VGE Verlag, 2008.

[11] F. Wuttke, H.–G. Schmidt, V. Zabel, B. Kafle and I. Stade, Vibration induced building settlement assessment and calculation, G De Roeck, G. Degrande, G. Lombart and G. Müller eds. *Proceedings of the 8th International Conference on Structural Dynamics*, EURODYN2011, Leuven, Belgium, 901-908, 2011.

[12] D.V. Griffiths, Modelling of interfaces using conventional finite elements, T. Kawamoto, Y. Ichikawa eds. *Fifth International Conference on Numerical Methods in Geomechanics*, Nagoya, Japan, 837–844 , 1985.

[13] A. Francavilla and O.C. Zienkievicz, A note on numerical computations of elastic contact problems, *Int. J. Numer. Methods Eng.* **9**, 913-924, 1975

[14] R. A. Day and D. M. Potts, Zero thickness interface elements – Numerical stability and application *Int. Journ. Num. Anal. Meth. Geomech.*, **18**, 689-708, 1994.

[15] R. E. Goodman, R. L. Taylor and T. L. Brekke, A model for the mechanics of jointed rock. *J. Soil Mech. Found. Div., ASCE*, **94**, 637-659, 1968

[16] C. S. Desai, M. M. Zaman, J. G. Lightner and H. J. Siriwardane, Thin-layer element for interfaces and joints, *Int. J. Numer. Anal. Methods Geomech.*, **8**, 19-43 ,1984.

[17] D. M. Potts, L. Zdravkovic, *Finite Element Analysis in Geotechnical Engineering: Theory*, London Thomas Telford, 1999.

[18] H. Van Langen and P. A. Vermeer, Interface elements for singular plasticity points *Int. J. Numer. Anal. Methods Geomech.*, **15**, 301–315 ,1991.

[19] M. Boulon, P. Garnica and P. A. Vermeer, Soil-structure interaction: FEM Computations, A. P. S. Selvaduari and M. J. Boulon eds. *Mechanics of Geomaterial Interfaces*, 1995.

[20] L. Hu and J. Pu, Testing and modeling of soil–structure interface, *Jour. Geot. Geoenviro. Eng.*, **130**, 8, 851–860,2004

[21] H. Liu and H. I. Ling, Constitutive description of interface behavior including cyclic loading and particle breakage withn the framework of critical state soil mechanics, *Int. Jour. Num. Anal. Meth. Geomech.*, **32**, 1495–1514, 2008

[22] J. Ghaboussi, E. L. Wilson and J. Isenberg, Finite elements for rock joints and interfaces, *Journal of Soil Mechanics and Found. Div. ASCE*, **99**, SM10, 833-848,1973

[23] P. A. Vermeer and R. de Borst, Non-associated plasticity for soils, concrete and rocks, *Heron*, 1984.

[24] G. Box, S. Bisgaard and C. Fung, An explanation and critique of Taguchis contributions to qualtiy engineering, *Quality and Reliability Enginerring International*, **4** 2, 123-131, 1988.

[25] M. D. Morris, Factorial Sampling for prelimary computional experiments. *Technometrics*, **33**(2), 161–174, 1991.

19th International Conference on the Application of Computer
Science and Mathematics in Architecture and Civil Engineering
K. Gürlebeck, T. Lahmer and F. Werner (eds.)
Weimar, Germany, 04–06 July 2012

CONSTITUTIVE MODELING OF STEEL WITH TEXTURE CHARACTERISTICS

I. Wudtke*

**Bauhaus-Universität Weimar*
Research Training Group 1462
Berkaer Str. 9, 99423 Weimar
E-mail: idna.wudtke@uni-weimar.de

Keywords: texture, heat affected zone, multiscale, RVE, grain size function

Abstract. *The optimal utilization of modern steels for building industry requires the description of microscopic constitution of these materials. The disparity in the quantity of their macroscopic properties (e.g. Youngs modulus, yield strength, ultimate strength, ductility) is purposely changed by means of microscopic constitutive differences. The hierarchical multiscale approaches give an opportunity to extend the phenomenological material description of macroscopic scale by means of microscopic information. This paper introduces an enrichment multiscale approach applicable for textured steel materials, typically occurring in hot rolled members or welded joints. Hence, texture is manifested in crystalline materials as a regular crystallographic structure and crystallite orientation, influencing macroscopic material properties. The grain texture has been described on a mesoscopic scale (μm) according to a RVE-approach and coupled with macroscopic constitutive relations by means of homogenization. On both spatial scales material has been taken into account as a continuum. The influence of manufacturing and fabrication has been incorporated into the macroscopic material description by a local grain size function. The approach has been developed for structures under static loading underlaying macroscopically elastic material responses.*

1 INTRODUCTION

Modern manufacturing technologies allow an optimal and purpose-oriented utilization of steel materials in the building industry. Thereby, the desired metallurgical constitution is created by obtaining a particular microscopic state, since all material phenomena, affecting the behavior of the structure, rely on physical effects which interact in different spatial scales from subatomic to microscopic and macroscopic range. One of early beginnings of research of this particular issue can be dated to the end of 19th century [10]. In the first half of 20th century, different approaches of homogenization methods were developed by [4][9][5][1]. These coupling approaches are oriented on transferring the results and informations obtained on lower spatial scales to the macroscopic scale. Since then, the micromechanical modelling techniques have been developing rapidly, since they are applicable in a wide range of research fields, such as mechanical engineering, biomechanics, electronics, etc. This regards mostly the application to new materials with limited number of alloys and a certain degree of similarity in microstructural constitution. Since steel materials vary in their microscopic constitution, this prospective approach can be find rarely in the field of structural steel engineering. In the context of civil engineering, all steel materials are generalized and described qualitatively by the same phenomenological material laws, differing in quantities of their properties (e.g. Youngs modulus, yield strength, ultimate strength, ductility). If the material is microscopically heterogenic and macroscopically homogeneous, it might be appropriate to use phenomenological models for civil engineering applications. This might be timesaving, but it also has limited potential to increase the reliability of the prognosis of behavior, since the material response is always closely related to microscopic state. Aside from this, these models are insufficient for steel materials with microscopic characteristics such as texture, that typically occur in hot rolled steel members or heat affected zones of welded joints. Hence, texture is manifested in crystalline materials as a regular morphological structure and crystallite orientation, that influences macroscopic material properties.

2 CONCEPTION AND METHODOLOGY

2.1 General Context

The method has been developed for materials under static loading, characterized by texture. In order to distinguish the metallurgical diversity, microscopic material law has been enriched purposely by microscopic constituents. The concerned approach will be shown on an example of a welded joint of a hot rolled ferritic/pearlitic steel, S460TM (1, a), where different microscopic states of particular zones in a narrowed area of heat affected zone and parent material are distinctive. During the manufacture of parent material (e.g. hot rolling) the grains obtained preffered cristallographic orientation. The non-randomnes of cristallographic texture reveals a macroscopic anisotropy of crystaline materials. In addition, the parent material is characterized by banded microscopical structure (1, b), which also contributes to the macroscopic anisotropy of material. The degree of anisotropy is influenced by grain size ratio in rolling direction and thickness direction (morpholgic anisotropy). The constitution of S460TM is characterized by courser bands of ferrite grains, elongated in rolling direction, and fine pearlite bands, consisting of ferrite and cementite constituents. Due to the fact that grain size and cristallographic orientation influence the macroscopic material properties, these issues will be the focus of this. The heat affected zone (HAZ) of a welded joint is a thermally and metallurgically affected area,

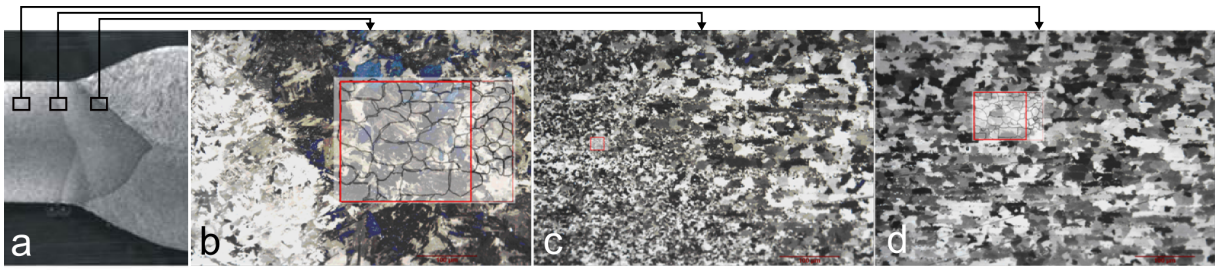

Figure 1: a) Welded joint and heat affected zone, S460TM, b) coarse grain zone, c) pearlite decomposition zone (fine grain zone), d) microstructure banding

where the initial constitution of the parent material is changed. This zone is mainly characterized by brittle and high strength constituents, martensite and bainite. The grain size varies from the course grain zone in a fusion line of a joint and a HAZ and fine grain zone in a pearlite decomposition area which is the outside margin of a HAZ (1, c and d). Every welded joint and its HAZ is unique in its structure, due to the non reproducibility of the welding process as well as inclusions, voids and microcracks. To incorporate the metallographic structure into the procedure of the response calculation of engineering structures, it is necessary to describe microscopic constitution explicitly. For this purpose, the methods of micromechanics are appropriate.

2.2 Meso-Macro Approach to Constitutive Modelling

The methodology has been derived following the principals of the micromechanical approach of the Reference Volume Element (RVE). This hierarchical multiscale method is based on the consecutive modeling of material on different spatial scales by RVE and connecting them to upper scales. Besides the scale of interest (e.g. macroscopic scale), the mesoscopic scale (μm)

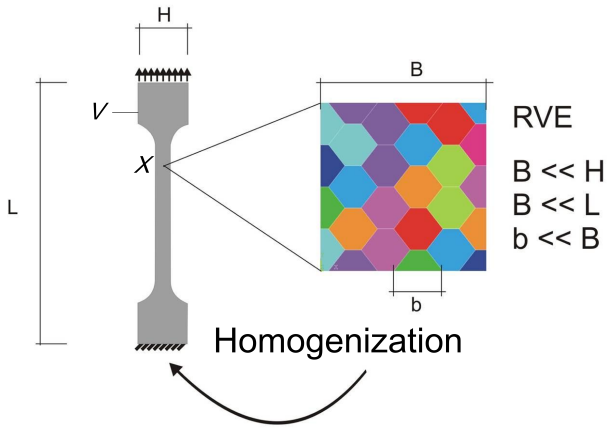

Figure 2: Principle of hierarchical multiscale approach

has been taken into account in the present example. The necessity of the description on the mesoscopic scale is given by the fact, that the constitutive parameters, which mainly influence macroscopic anisotropy of textured steels can be described on this scale. Within the context of this approach, on the macroscopic scale, body V consists of a set of infinitesimal material points X. The material point $X \in V$ has to be constitutively and geometrically described on

the lower scale (meso scale), thus demanding representativity. The models on the considered spatial scales are coupled by means of homogenization techniques to derive the mechanical relation between the microscopic components and macroscopic material response. The basic principle has been shown in figure 2. The original micromechanical approach is based on the demand of homogeneity of the material on the macroscopic scale. This demand retains the representativity of the RVE for every material point on the macroscopic body. The application to materials that obey particular local effects, such as in heat affected zones, has to be modified. Hence the homogeneity demand can not be met. The amendment consists of an adoptation of a grain size function (GSF), that describes the grain size as a function of position in a HAZ. Thus enables a consistent application of an RVE-concept for the presented purpose. An approximated grain size function of a HAZ of a butt welded S460TM connection is shown in 3. A multiple linear regression according to [6] has been used to identify the GSF. The measured grain sizes of an existing joint have been used as a response vector Y. The coordinates in thickness- and width-direction are represented by the input parameter matrix X. The approximation of the responce surface $\hat{Y}$ obey the following equation:

$$\hat{Y} = X\beta + e \tag{1}$$

By minimizing the vector of error term e, the regression coefficient vector β can be obtained according to [6]:

$$\frac{\delta SS_E}{\delta \beta} = 0, \;\; \hat{\beta} = (X^T X)^{-1} X^T Y \tag{2}$$

The quality of the approximation has been obtained by the coefficient of determination R^2:

$$R^2 = 1 - \frac{SS_E}{SS_T}, \; 0 \leq R^2 \leq 1 \tag{3}$$

which relates the sum of error squares SS_E and model response variance SS_T:

$$SS_E = e^T e, \;\; e = Y - \hat{Y}, \tag{4}$$

$$SS_T = (\hat{Y} - \bar{Y})^T (\hat{Y} - Y) \tag{5}$$

Within the measured area of HAZ, the calculated coefficient of determination $R^2 = 0.92$ shows a good approximation quality. The quality decreases for the prediction of the grain size outside of the approximation area ($R^2 = 0.67$). This result shows a potential to expand the input parameter set and incorporate the parameters, such as cooling time and temperature gradient, with the intention of effectively integrating the welding process into the expression of a GSF. As mentioned, material constitution on a mesoscopic scale is described by means of RVE. The material properties have been derived from material properties of a body-centered Fe-crystal (4). The orientation of grains within the RVE is assumed to be normally distributed. To relate the different cristallographic orientations to the global orientation of an RVE, a decomposed transformation of material tensor C_{pqrs} for every grain according to their Eulerian angles has been preformed. The transformed material tensor C_{ijkl} is calculated according to following equation:

$$C_{ijkl} = R_{ip} R_{jq} R_{kr} R_{ls} C_{pqrs} \tag{6}$$

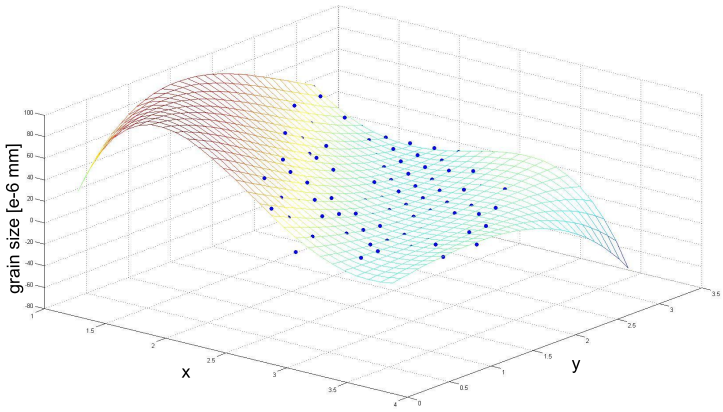

Figure 3: Approximated response curface of a GSF in a HAZ of S460TM

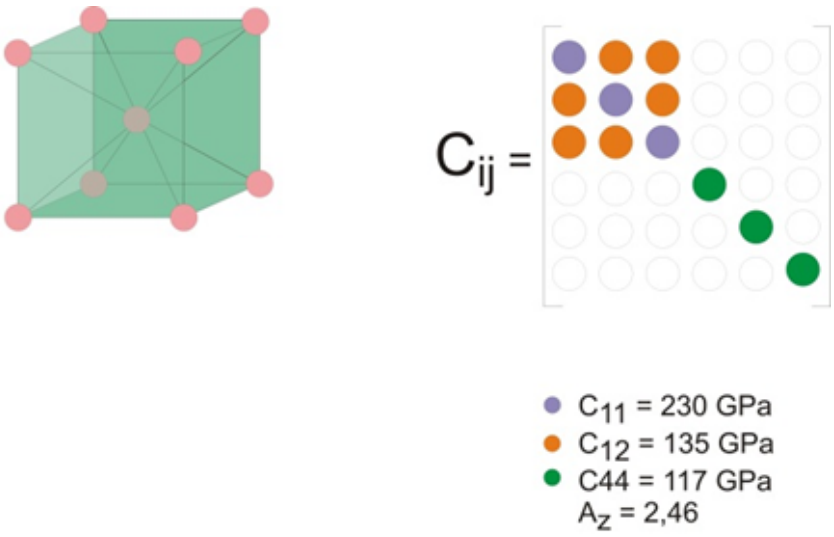

Figure 4: Material matrix of a body-centered Fe-crystal

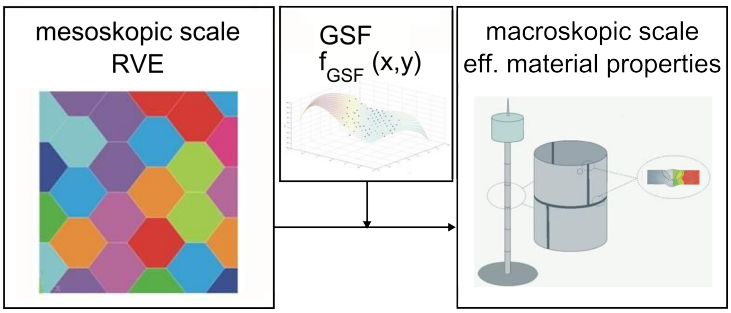

Figure 5: Principle of a meso-macro-approach

where R describes decomposed rotation matrices of three Eulerian angles [3]. To obtain effective material properties on the macroscopic scale, considering the textured structure of a mesoscale, homogenization techniques are preformed. The local strain- or stress-fields within the RVE have to be derived and homogenized over the volume [2]:

$$\langle \sigma_{makro} \rangle = \frac{1}{|V|} \int_V \sigma(x) dV, \quad \langle \epsilon_{makro} \rangle = \frac{1}{|V|} \int_V \epsilon(x) dV \tag{7}$$

The physical consistency of these approaches has been requested by equality of strain energy density on both scales:

$$\langle \sigma_{meso}(x) : \epsilon_{meso}(x) \rangle = \langle \sigma_{makro} \rangle : \langle \epsilon_{makro} \rangle \tag{8}$$

The homogenised macroscopic material tensor C^*_{ijkl} is relating the mean values of stress and strain-fields over the volume:

$$\langle \sigma_{ij} \rangle = C^*_{ijkl} : \langle \epsilon_{kl} \rangle \tag{9}$$

Within the application of the RVE-concept, periodic boundary conditions have been implemented, fulfilling the following relation [7]:

$$u_i^B i - u_i^A = \epsilon_{ij}(x_j^B - x_j^A) \tag{10}$$

where the displacement u_i of opposite boundaries A and B has been determined by means of strain ϵ_{ij} and the distance of the respective locations x_j. The application of periodic boundary condition is an RVE-concept based constraint, where all macroscopic material points, represented by RVE, obey identical behavior on their opposite boundaries. For the calculation of all components of the macroscopic material tensor, six uniform loading conditions of the RVE are necessary: three axial strains and three sher strains. With the presented approches and assumptions, an exemplary method has been derived, which incorporates the metallurgical material state into the constitutive material model used for calculation of response of steel structures. In figure 5, a main principle of the method is shown. The first calculations of RVE are focused on identification of relevant influencing factors, to assure the representativity of the model. For this purpose, the effect of grain size, grain shape and RVE-size have been investigated. The influence of grain geometry has been performed on two-dimensional models, considering rectangular and truncated octahedral grains. The representativity of the RVE is apparent when the influence of the number of grains on the macroscopic material properties is investigated. Additional analysis has been performed on a three-dimensional model with cubic formed grains.

The deviation of RVE-models with respect to their size, has been investigated by means of an error estimate according to [8]. This error estimator is formulated as a ratio of a standard deviation of an equivalent von Mises stress and a representative equivalent von Mises stress of an RVE-model with 2744 grains:

$$err = \frac{S(\sigma_{vM})}{\sigma_{vM}^{2744}} \tag{11}$$

3 RESULTS

The size of the RVE has been investigated with respect to the derived effective Young's modulus of the macroscopic material. In addition, the grain shapes have been analysed. The results of the effective Young's modulus in the rolling direction with respect to RVE-size for rectangular and truncated octahedral grains are shown in figure 6. The derived results show

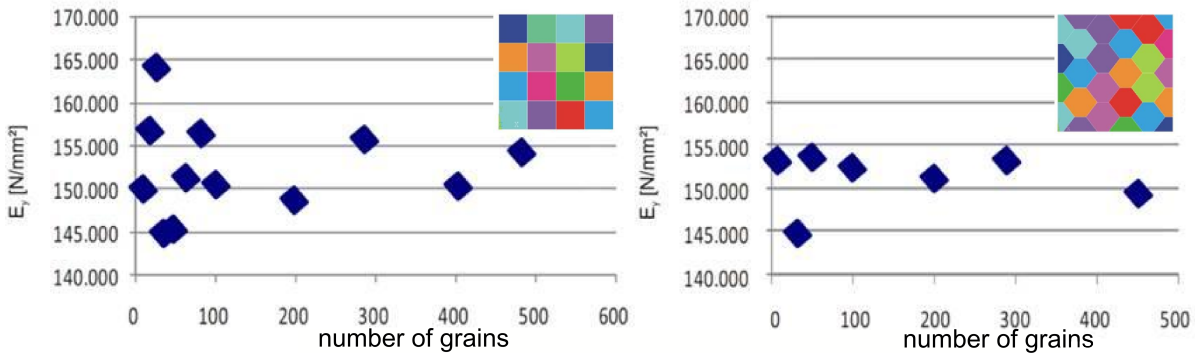

Figure 6: Influence of grain shape and RVE size on effective Young's modulus

negligible influence of grain shape on the Young's modulus on macroscopic scale. As the RVE size increases, the effect on Young's modulus decreases. The RVE-models with appr. 400 grains vary 3%. Hence, for further three dimensional investigations, a cubic grain shape has been assumed. The analysis of the error estimate according to 11, reveals asymptotic behavior, as shown in figure 7. The variation of error is insignificant for RVE with more than 1000 grains. The presented investigations create a basis for analysis of the influence of the grade of banded

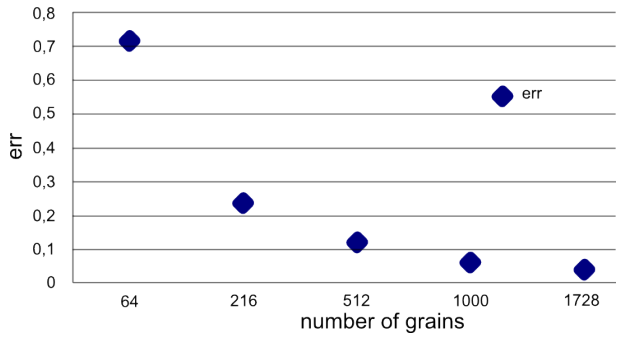

Figure 7: Error estimate based on equivalent von Mises stress for different RVE size according to equation 11

microscopic structure on the anisotropy on the macroscopic scale. The purpose of this analysis is to adaptively integrate the method into calculations on a macroscopic scale.

4 CONCLUSIONS

The proposed method enables the description of the metallurgical state of steel materials for the purpose of the analysis of structural responses in civil engineering applications. There are advantages to the possibility of including a grain size function for the specification of local effects such as heat affected zones of welded joints. The first numerical investigations show negligible influence of grain shape. The error estimation analysis, based on equivalent von Mises stress, has been used and a representative RVE-size have been derived. An outlook for the next investigations has been given. With the presented methodology, a first step has been taken towards a new basis of calculation, as well as an effective design procedure for steel structures.

ACKNOWLEDGMENT This research is supported by the German Research Foundation (DFG) within the Research Training Group "Evaluation of Coupled Numerical Partial Models in Structural Engineering (GRK 1462)", which is gratefully acknowledged by the author.

REFERENCES

[1] J.D. Eshelby, *The determination of the elastic field of an ellipsoidal inclusion and related problems*. Proceedings of the Royal Society, A241, London, 376–396, 1957.

[2] A. Fröhlich, *Mikromechanisches Modell zur Ermittlung effektiver Materialeigenschaften von piezoelektrischen Polykristallen*. Dissertation, Universität Karlsruhe, 2001.

[3] K. Helming, *Texturapproximation durch Modellkomponenten*. Habilitation, TU Clausthal, 1995.

[4] R. Hill, *The Elastic Behaviour of a Crystalline Aggregate*. Proceedings of the Physical Society, A65, London, 1952.

[5] E. Kröner, *Berechnung der elastischen Konstanten des Vielkristalls aus den Konstanten des Einkristalls*. Zeitschrift für Physik, 151, 504–518, 1958.

[6] D.C. Montgomery, G. C. Runger *Applied Statistics and Probability for Engineers*. Wiley, 2003.

[7] M. Nygards, P. Gudmundson *Micromechanical modeling of ferritic/pearlitic steels*. Materials Science and Engineering, A325, 435–443, 2002.

[8] M. Nygards, P. Gudmundson *Three-dimensional periodic Voronoi grain models and micromechanical FE-simulations of a two-phase steel*. Computational Materials Science, 24, 513–519 2002.

[9] A. Reuss, *Berechnung der Fließgrenze von Mischkristallen auf Grund der Plastizitätsbedingung fr Einkristalle*. Zeitschrift fr angewandte Mathematik und Mechanik, Bd. 9, 49, pp. 49–58, 1929.

[10] W. Voigt, *Theoretische Studien ber die Elasticitätsverhältnisse der Kristalle*. Abhandlungen der königlichen Gesellschaft der Wissenschaften zu Göttingen, Göttingen, 53–100, 1887.